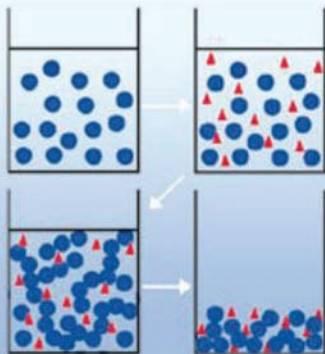
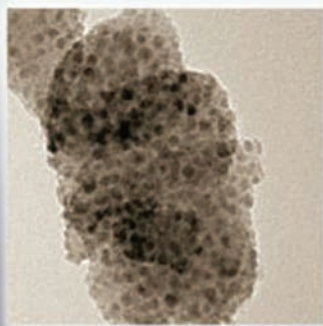


Edited by Krijn P. de Jong

WILEY-VCH

Synthesis of Solid Catalysts



Synthesis of Solid Catalysts

Edited by
Krijn P. de Jong

Related Titles

Jackson, S. D., Hargreaves,
J. S. J. (ed.)

Metal Oxide Catalysis

2009

ISBN: 978-3-527-31815-5

Mizuno, N. (ed.)

Modern Heterogeneous Oxidation Catalysis

Designs, Reactions and Characterization

2009

ISBN: 978-3-527-31859-9

van Santen, R. A., Sautet, P. (eds.)

Computational Methods in Catalysis and Materials Science

**An Introduction for Scientists and
Engineers**

2009

ISBN: 978-3-527-32032-5

Ozkan, U. (ed.)

Design of Heterogeneous Catalysts

**New Approaches based on Synthesis,
Characterization and Modeling**

2009

ISBN: 978-3-527-32079-0

Ding, K., Uozumi, Y. (eds.)

Handbook of Asymmetric Heterogeneous Catalysis

2008

ISBN: 978-3-527-31913-8

Ertl, G., Knözinger, H., Schüth, F.,
Weitkamp, J. (eds.)

Handbook of Heterogeneous Catalysis

8 Volumes

2008

ISBN: 978-3-527-31241-2

Astruc, D. (ed.)

Nanoparticles and Catalysis

2008

ISBN: 978-3-527-31572-7

Chorkendorff, I., Niemantsverdriet, J. W.

Concepts of Modern Catalysis and Kinetics

2007

ISBN: 978-3-527-31672-4

Centi, G., van Santen, R. A. (eds.)

Catalysis for Renewables

**From Feedstock to Energy
Production**

2007

ISBN: 978-3-527-31788-2

Sheldon, R. A., Arends, I., Hanefeld, U.

Green Chemistry and Catalysis

2007

ISBN: 978-3-527-30715-9

Synthesis of Solid Catalysts

Edited by
Krijn P. de Jong



WILEY-
VCH

WILEY-VCH Verlag GmbH & Co. KGaA

The Editor

Prof. Dr. Krijn P. de Jong

Inorganic Chemistry and Catalysis
Utrecht University
Sorbonnelaan 16
3548 CA Utrecht
The Netherlands

All books published by Wiley-VCH are carefully produced. Nevertheless, authors, editors, and publisher do not warrant the information contained in these books, including this book, to be free of errors. Readers are advised to keep in mind that statements, data, illustrations, procedural details or other items may inadvertently be inaccurate.

Library of Congress Card No.: applied for

British Library Cataloguing-in-Publication Data

A catalogue record for this book is available from the British Library.

Bibliographic information published by the Deutsche Nationalbibliothek

The Deutsche Nationalbibliothek lists this publication in the Deutsche Nationalbibliografie; detailed bibliographic data are available on the Internet at <http://dnb.d-nb.de>.

© 2009 WILEY-VCH Verlag GmbH & Co.
KGaA, Weinheim

All rights reserved (including those of translation into other languages). No part of this book may be reproduced in any form – by photoprinting, microfilm, or any other means – nor transmitted or translated into a machine language without written permission from the publishers. Registered names, trademarks, etc. used in this book, even when not specifically marked as such, are not to be considered unprotected by law.

Cover Design Adam Design, Weinheim
Typesetting Laserwords, Chennai, India
Printing betz-druck GmbH, Darmstadt
Binding Litges & Dopf GmbH, Heppenheim

Printed in the Federal Republic of Germany
Printed on acid-free paper

ISBN: 978-3-527-32040-0

Contents

Preface XIII

List of Contributors XV

Abbreviations XIX

Part I Basic Principles and Tools

1 General Aspects 3

Krijn P. de Jong

- 1.1 Importance of Solid Catalysts 3
- 1.2 Development of Solid Catalysts 4
- 1.3 Development of Solid Catalyst Synthesis 5
- 1.4 About This Book 10
- References 10

2 Interfacial Chemistry 13

Alexis Lycourghiotis

- 2.1 Introduction 13
- 2.2 Interfacial and Bulk Deposition 14
- 2.3 The Surface of the Oxidic Supports: Surface Ionization Models 15
 - 2.3.1 The Charged Surface of the Oxidic Supports 15
 - 2.3.2 Homogeneous Surface Ionization Models 16
 - 2.3.3 The Music Model 17
- 2.4 The Size and the Structure of the Interface 18
- 2.5 The Arrangement of the Ions Inside the Interface and the Deposition Modes 20
 - 2.5.1 Indifferent Ions 20
 - 2.5.2 Transition-Metal Ionic Species 22
- 2.6 Determining the Mode of Interfacial Deposition and the Surface Speciation/Structure of the Deposited Precursor Species 23
 - 2.6.1 Introductory Remarks 23

2.6.2	Methodologies Based on Macroscopic Adsorption Data and Potentiometric Titrations as well as on Microelectrophoretic Mobility or Streaming Potential Measurements	23
2.6.3	Spectroscopic Investigations	25
2.6.4	Quantum-Mechanical Calculations	26
2.6.5	Electrochemical (Equilibrium) Modeling	26
2.7	A Case Study: The Deposition of $\text{Co}(\text{H}_2\text{O})_6^{2+}$ Aqua Complex on the Titania Surface	27
2.7.1	Experimental Investigation	27
2.7.2	Quantum-Mechanical Calculations	28
2.7.3	Electrochemical (Equilibrium) Modeling	29
	References	30
3	Electrostatic Adsorption	33
	<i>John R. Regalbuto</i>	
3.1	Introduction	33
3.2	Purely Electrostatic Adsorption	37
3.3	Electrostatic Adsorption with Metal Respeciation	38
3.4	Electrostatic Adsorption and Ion Exchange	41
3.5	Electrostatic Adsorption and Deposition-Precipitation	45
3.6	Electrostatic Adsorption and Surface Reaction	46
3.7	Electrostatics and Dissolution, Reaction, and Redeposition	47
3.8	Electrostatics-Based Design	48
3.8.1	Well-Dispersed Single Metals	49
3.8.2	Selective Adsorption onto Promoters	51
3.8.3	Bimetallic Catalysts	54
3.9	Summary	57
	References	57
4	Impregnation and Drying	59
	<i>Eric Marceau, Xavier Carrier, and Michel Che</i>	
4.1	Introduction	59
4.2	Impregnation	61
4.2.1	Methods of Impregnation	61
4.2.2	Physical Models for Impregnation	62
4.3	Drying	64
4.4	The Chemistry	67
4.4.1	Concentrations and pH	67
4.4.2	Precursor-Support Interactions	69
4.4.2.1	Adsorption: From Electrostatic Interactions to Grafting	69
4.4.2.2	The Formation of Mixed Phases	70
4.4.3	Ligands	71
4.4.4	Counterions	73
4.5	Impregnation and Drying of an $\text{MoO}_x/\text{Al}_2\text{O}_3$ Catalyst	74
4.5.1	Molybdenum Speciation and Its Consequences	74

4.5.2	Degrees of Freedom: Drying Parameters and Ligands in Solution	76
4.6	Conclusions	77
	References	78
5	Sol-Gel Processing	83
	<i>Miron V. Landau</i>	
5.1	Introduction	83
5.2	Physicochemical Basis and Principles of Sol-Gel Processing	85
5.2.1	Activation	86
5.2.2	Polycondensation	87
5.2.3	Gelation/Aging/Washing	89
5.2.4	Gel Drying/Desolvation	90
5.2.5	Stabilization of Xero- and Aerogels	90
5.3	Application of Sol-Gel Processing for the Preparation of Solid Catalysts	91
5.3.1	Bulk Catalytic Phase Materials: Xero- and Aerogels	91
5.3.1.1	Monometallic Catalytic Materials	91
5.3.1.2	Multimetallc Composite Catalytic Phases	94
5.3.2	Catalytic Materials and Modifiers Entrapped in Porous Matrices	97
5.3.2.1	Atoms or Molecular Substances Entrapped by Cocondensation at the Colloidization Step	98
5.3.2.2	Molecular Substances Adsorbed or Entrapped at the Gelation Step	103
5.4	Summary	106
	References	106
6	Deposition Precipitation	111
	<i>Krijn P. de Jong</i>	
6.1	Introduction	111
6.2	Theory and Practice	112
6.3	Mechanistic Studies	115
6.3.1	Kinetics	115
6.3.2	Molecular Details	118
6.4	Case Studies	120
6.4.1	pH Increase	120
6.4.2	Reduction Deposition Precipitation	124
6.4.3	Ligand Removal	128
6.4.4	Miscellaneous Methods	129
6.5	Summary, Conclusions, and Outlook	131
	Acknowledgments	131
	References	132
7	Coprecipitation	135
	<i>Martin Lok</i>	
7.1	Introduction	135

7.2	Basic Principles of Precipitation and Nucleation	136
7.3	Raw Materials	139
7.4	Precipitation Conditions	141
7.5	Process Operation	141
7.6	Examples	145
7.6.1	High Metal Nickel/Alumina Catalysts	145
7.6.2	Single-Step Sulfur-Promoted Nickel/Alumina Catalyst	146
7.6.3	Copper/Zinc Methanol Catalysts	147
7.6.4	Iron-Based Fischer–Tropsch Catalysts	148
7.6.5	Unsupported Metal Sulfide Catalysts for Hydrotreating	148
7.7	New Developments in Process Monitoring	148
	Acknowledgments	149
	References	149
8	Clusters and Immobilization	153
	<i>Sophie Hermans</i>	
8.1	Introduction	153
8.2	The Surface of Common Supports	154
8.3	Clusters in Catalysis	157
8.4	Reaction with Unmodified Surface	160
8.5	“Ship-in-a-Bottle” Synthesis	163
8.6	Tethering	167
8.7	Concluding Remarks	168
	References	169
9	Shaping of Solid Catalysts	173
	<i>Bettina Kraushaar-Czarnetzki and Steffen Peter Müller</i>	
9.1	Objectives of Catalyst Shaping	173
9.2	Fixed-Bed Reactors – Particle Beds	177
9.2.1	Pelleting	177
9.2.2	Granulation	179
9.2.3	Extrusion	181
9.2.4	Tailoring of the Pore-Size Distribution	184
9.2.5	Fixed-Bed Egg-Shell Catalysts	186
9.3	Fixed-Bed Reactors – Monoliths	187
9.3.1	Honeycombs	187
9.3.1.1	Ceramic Honeycombs	188
9.3.1.2	Metallic Honeycombs	190
9.3.2	Open-Cell Foams	192
9.3.3	Coating of Monoliths	194
9.4	Catalysts for Moving-Bed Reactors	195
9.5	Catalysts for Fluidized Beds	196
	References	198

10	Space and Time-Resolved Spectroscopy of Catalyst Bodies	201
	<i>Bert M. Weckhuysen</i>	
10.1	Introduction	201
10.2	Space- and Time-Resolved Methods Applied to Catalyst Bodies	201
10.2.1	Invasive Methods	202
10.2.2	Noninvasive Methods	205
10.3	Case Studies	209
10.3.1	Keggin-Type Co-Mo Complexes in Catalyst Bodies	209
10.3.2	Speciation of Co Complexes in Catalyst Bodies	212
10.4	Future Prospects	215
	Acknowledgments	215
	References	216
11	High-Throughput Experimentation	217
	<i>Uwe Rodemerck and David Linke</i>	
11.1	Introduction	217
11.2	Synthesis Strategies	219
11.2.1	Combinatorial Strategies	220
11.2.2	Methods to Reduce Experiments	220
11.3	Catalyst Libraries for Primary Screening	223
11.3.1	Wafer-Based Preparation	223
11.3.2	Single Pellets	224
11.3.3	Single Beads	225
11.4	Catalyst Libraries for Secondary Screening	225
11.4.1	Impregnation Techniques	226
11.4.2	Precipitation	226
11.4.3	Hydrothermal Synthesis	230
11.4.4	Sol-Gel Chemistry	231
11.4.5	Drying, Calcination, and Shaping	231
11.5	Catalyst Libraries for Special Reactor Types	234
11.6	An Industrial Point of View	234
11.7	Conclusions	235
	References	236
Part II	Case Studies	
12	Concepts for Preparation of Zeolite-Based Catalysts	243
	<i>Metin Bulut and Pierre A. Jacobs</i>	
12.1	Introduction and Scope	243
12.2	Zeolite Effects in Catalysis	245
12.2.1	Brønsted Acidity in Metallosilicate Zeolites	245
12.2.2	Zeolite Protonic Superacidity	246
12.2.3	Brønsted Acidity in Substituted Four-Coordinated Aluminophosphates	247
12.2.4	Zeolite Shape Selectivity	250

12.2.5	Concentration Effects by Specific Adsorption	253
12.2.6	Site Isolation or the Role of Zeolites as Solid Solvents	254
12.3	Zeolitization	254
12.3.1	Overall Steps in Zeolite Crystallization	255
12.3.2	Classic Model for Zeolite Growth	257
12.3.3	The Aggregation Model	259
12.3.4	Zeolitization Parameters	260
12.3.5	Nanocrystalline Zeolites	264
12.3.6	Zeolite Synthesis via the Dry Gel Route	265
12.3.7	AlPO ₄ -n-Based Molecular Sieve Zeolites	266
12.3.8	Ionothermal Synthesis Method	267
12.3.9	Zeolites with Pores Beyond the 12-MR	267
12.3.10	Upscaling of Zeolite Synthesis	268
	References	268
	Further Reading	276
13	Ordered Mesoporous Materials	277
	<i>Ying Wan and Dongyuan Zhao</i>	
13.1	Introduction	277
13.2	Mesoporous Silica	277
13.2.1	MCM-41	279
13.2.2	SBA-15	280
13.2.3	MCM-48	281
13.2.4	Pore-Size Control	282
13.3	Organic Group Functionalized Mesoporous Silicates	284
13.3.1	Organic Groups Anchored to Mesoporous Silicates	284
13.3.2	Periodic Mesoporous Organosilicas	285
13.3.3	Adsorption and Catalysis	285
13.4	Metal-Substituted Mesoporous Silica Molecular Sieves	287
13.5	Carbon	289
13.5.1	The Hard-Templating Approach	289
13.5.2	The Supramolecular-Templating Approach	290
13.6	Nonsiliceous Oxides	293
13.6.1	The Supramolecular-Templating Approach	293
13.6.2	The Hard-Templating Approach	294
13.7	Nonoxides	294
13.7.1	SiC-Based Materials	294
13.7.2	Metal Sulfides	296
13.8	Summary and Remarks	296
	Acknowledgments	297
	References	297
14	Hydrotreating Catalysts	301
	<i>Sonja Eijssbouts</i>	
14.1	Introduction	301

14.2	Typical Hydrotreating Catalyst	302
14.2.1	Typical Catalyst Composition	302
14.2.2	Literature Describing the Preparation of Hydrotreating Catalysts	302
14.3	Support Preparation	303
14.3.1	Precipitation of γ -Alumina	303
14.3.2	Addition of SiO_2	305
14.3.3	Addition of Other Components (e.g. Zeolites) and Extrusion	305
14.3.4	Drying and Calcination of Al_2O_3 and $\text{SiO}_2\text{-Al}_2\text{O}_3$ Supports	307
14.4	Metal Comixing/Coextrusion and Coprecipitation Routes	307
14.4.1	Addition of Metals to the Al_2O_3 Dough	307
14.4.2	Bulk Catalysts	308
14.4.3	Drying and Calcination of Catalysts Prepared by Comixing/Coextrusion and Coprecipitation Routes	308
14.5	Impregnation of Metals	309
14.5.1	Typical Additives and Solution Stabilizers	309
14.5.2	Pore-Volume Impregnation versus Dipping/Equilibrium Impregnation of Compacted Support Particles	310
14.5.3	Sequential versus Coimpregnation	314
14.5.4	Drying and Calcination	315
14.6	Presulfiding as the Last Stage in Hydrotreating Catalyst Preparation	318
14.6.1	Presulfiding Goals	318
14.6.2	Gas-Phase versus Liquid-Phase Presulfiding	319
14.6.3	<i>Ex-situ</i> versus <i>In-situ</i> Presulfiding	320
14.7	Industrial Process for the Production of the Oxidic Catalyst	323
14.7.1	Industrial Equipment	323
14.7.2	Health, Safety, and Environmental Issues	323
14.8	Summary	324
	References	324
15	Methanol Catalysts	329
	<i>S. Schimpf and M. Muhler</i>	
15.1	Binary Cu/ZnO Catalysts	329
15.2	Coprecipitation	331
15.2.1	Precipitation	333
15.2.2	Aging	334
15.2.3	Washing	337
15.2.4	Drying and Calcination	337
15.2.5	Reduction	339
15.3	The Role of Alumina in Ternary Catalysts	341
15.4	Alternative Preparation Routes	344
15.4.1	Alternative Anions	344
15.4.2	Chemical Vapor Deposition	347
15.4.3	Promising Strategies	347
15.5	Conclusions	348

Acknowledgment	348
References	349

16 Case Studies of Nobel-Metal Catalysts 353

Stuart Soled

16.1	Introduction	353
16.2	Optimization of Catalyst Preparation	354
16.2.1	Electrostatic Interactions and the Use of Zeta Potential Measurements	355
16.2.2	Noble-Metal Impregnation Example onto a Modified Silica-Alumina Support	356
16.2.3	A Novel Approach for the Preparation of Dispersed Ru on Silica	358
16.2.4	Other Metals that Form Similar Supported Complexes as Ru	363
16.2.5	Conclusions	365
	Acknowledgments	366
	References	366

17 Gold Catalysts 369

Catherine Louis

17.1	Introduction	369
17.2	Preparations Involving Aqueous Solutions	370
17.2.1	Impregnation to Incipient Wetness	370
17.2.2	Anion Adsorption	371
17.2.3	Small Particles from $\text{HAuCl}_4 \cdot 3\text{H}_2\text{O}$	371
17.2.4	Deposition-Precipitation with NaOH	373
17.2.5	Gold Complex Interaction with Oxide Supports	375
17.2.6	Deposition-Precipitation with Urea	376
17.2.7	Cation Adsorption	378
17.3	Preparations Involving Organometallic Precursors	379
17.3.1	Impregnation of Phosphine-Based Gold Complexes	379
17.3.2	Impregnation of Other Organogold Complexes	380
17.4	Deposition of Gold Nanoparticles	380
17.4.1	Deposition of Gold Colloids	380
17.4.2	Deposition of Dendrimer-Encapsulated Gold Nanoparticles	384
17.5	One-Step Preparations	384
17.5.1	Coprecipitation	385
17.5.2	Sol-Gel Method	386
17.6	Special Methods	386
17.6.1	Photochemical Deposition	386
17.6.2	Sonochemical Techniques	387
17.7	Conclusion	387
	References	388

Index	393
-------	-----

Preface

Solid catalysts are used in modern energy, chemical and environmental processes. Catalyst performance – activity, selectivity and stability – is largely determined by their preparation. In this respect, catalyst synthesis may be considered as one of the most influential ‘unit operations’ in industry. This book provides an introduction to basic concepts and research tools relevant to catalyst synthesis followed by a number of case studies. In this way it is an introduction to the field of catalyst synthesis for students and newcomers as well as a reference book for experienced scientists and practitioners. I hope that this book will stimulate the research field of catalyst synthesis and that it will support research and applications of solid catalysts by facilitating reliable and reproducible synthesis of materials.

For me it has been a privilege to work with so many colleagues in developing this book. I thank all of the lead authors as well as their co-authors for working with me on this project. It has been rewarding and I hope that we can continue to work together to foster and develop the field of catalyst synthesis.

I would like to thank Jos van Dillen and John Geus. They taught me as a graduate student at Utrecht University that catalyst synthesis is a research topic in its own right. For many years colleagues at the Shell Research Laboratories in Amsterdam provided a stimulating environment to synthesize and use solid catalysts. More recently at Utrecht University, staff, students and postdoctoral fellows have worked with me in the field of catalyst synthesis. Working with them has been a pleasure and is acknowledged.

Utrecht, December 2008

Krijn P. de Jong

List of Contributors

Metin Bulut

KU Leuven
COK, Dept. M2S
23 Kasteelpark Arenberg
3001 Leuven (Heverlee)
Belgium

Xavier Carrier

Laboratoire de Réactivité
de Surface
(UMR 7197 CNRS)
UPMC (Université Pierre et
Marie Curie)
Tour 54-55
4 Place Jussieu
75252 Paris Cedex 05
France

Michel Che

Laboratoire de Réactivité
de Surface
(UMR 7197 CNRS)
UPMC (Université Pierre et
Marie Curie)
Tour 54-55
4 Place Jussieu
75252 Paris Cedex 05
France

Krijn P. de Jong

Utrecht University
Inorganic Chemistry
and Catalysis
Sorbonnelaan 16
3584 CA Utrecht
The Netherlands

Sonja Eijsbouts

Albemarle Catalysts Company BV
Research Centre Catalysts
1022 AB Amsterdam
The Netherlands

Sophie Hermans

Catholic University of Louvain
Departement de Chimie
Place Louis Pasteur, 1 bte. 3
1348 Louvain-la-Neuve
Belgium

Pierre A. Jacobs

KU Leuven
COK, Dept. M2S
23 Kasteelpark Arenberg
3001 Leuven (Heverlee)
Belgium

Bettina Kraushaar-Czarnetzki

University of Karlsruhe
Institute of Chemical Process
Engineering CVT
Kaiserstr. 12
76128 Karlsruhe
Germany

Miron V. Landau

Ben-Gurion Univ. of the Negev
Dept. of Chem. Engineering
Ben-Gurion av. 1
Beer-Sheva 84105
Israel

Dr. David Linke

Leibniz-Institut für Katalyse
Albert-Einstein-Str. 29a
18059 Rostock
Germany

Martin Lok

Johnson Matthey Catalysts
Belasis Avenue, Billingham
Cleveland, TS23 1LB
UK

Catherine Louis

Laboratoire de Réactivité
de Surface
(UMR 7197 CNRS)
UPMC (Université Pierre et
Marie Curie)
Tour 54-55
Lab. de Reactions de Surfactants
4 Place Jussieu
75252 Paris Cedex 05
France

Alexis Lycourghiotis

University of Patras
Department of chemistry
26500 Patras
Greece

Eric Marceau

Laboratoire de Réactivité
de Surface
(UMR 7197 CNRS)
UPMC (Université Pierre et
Marie Curie)
Tour 54-55
4 Place Jussieu
75252 Paris Cedex 05
France

Martin Muhler

Ruhr-Universität Bochum
LS für Technische Chemie
Universitätsstr. 150
44780 Bochum
Germany

Steffen Peter Müller

University of Karlsruhe (TH)
Institute of Chemical Process
Engineering CVT
Kaiserstr. 12
76128 Karlsruhe
Germany

John R. Regalbuto

University of Illinois
Chemical Engineering
810 South Clinton Street
Chicago, IL 60607
USA

Uwe Rodemerck

Leibniz-Institut für Katalyse
Albert-Einstein-Str. 29a
18059 Rostock
Germany

Sabine Schimpf

Ruhr-Universität Bochum
LS für Technische Chemie
Universitätsstr. 150
44780 Bochum
Germany

Stuart Soled

ExxonMobil Research and
Engineering Company
Corporate Strategic Research
1545 Rt. 22 East
Annandale, NJ 08801
USA

Ying Wan

Shanghai Normal University
Department of Chemistry
Guilin Road 100
Shanghai 200234
P. R. China

Bert M. Weckhuysen

Utrecht University
Inorganic Chemistry and Catalysis
Sorbonnelaan 16
3584 CA Utrecht
The Netherlands

Dongyuan Zhao

Fudan University
Laboratory of Advanced Materials
Department of Chemistry
Handan Road 220
Shanghai 200233
P.R. China

Abbreviations

<i>AHM</i>	ammonium-hexa-molybdate
<i>BM</i>	base metal
<i>ccp</i>	cubic close packing
<i>CNF</i>	carbon nanofiber
<i>CNT</i>	carbon nanotube
<i>CT</i>	charge transfer
<i>CVD</i>	chemical vapor deposition
<i>D4R</i>	double four-ring
<i>D6R</i>	double six-ring
<i>DFG</i>	Deutsche Forschungsgemeinschaft
<i>DI</i>	dry impregnation
<i>DoE</i>	design of experiment
<i>DP</i>	deposition precipitation
<i>DTG</i>	differential thermal gravimetry
<i>EDF</i>	equilibrium deposition filtration
<i>EDTA</i>	ethylene diamine tetraacetic acid
<i>EDX</i>	energy-dispersive X-ray spectroscopy
<i>EPR</i>	electron paramagnetic resonance
<i>EXAFS</i>	extended X-ray absorption fine structure spectroscopy
<i>FCC</i>	fluid catalytic cracking
<i>FTIR</i>	Fourier transform infrared
<i>hcp</i>	hexagonal close packing
<i>HDMe</i>	hydrodemetallation
<i>HDN</i>	hydrodenitrogenation
<i>HDO</i>	hydrodeoxygenation
<i>HDS</i>	hydrodesulfurization
<i>HPA</i>	heteropolyacid
<i>IA</i>	ion adsorption
<i>ICI</i>	Imperial Chemical Industries
<i>iep</i>	isoelectric point
<i>IE</i>	ion exchange
<i>IL</i>	ionic liquid
<i>IR</i>	infrared

<i>IWI</i>	incipient wetness impregnation
<i>IZA</i>	International Zeolite Association
<i>MAS-NMR</i>	magic-angle sample spinning nuclear magnetic resonance
<i>MMA</i>	methyl methacrylate
<i>MOF</i>	metal organic framework
<i>MRI</i>	magnetic resonance imaging
<i>MTBE</i>	methyl tert-butylether
<i>(M)HC</i>	(mild) hydrocracking
<i>NMR</i>	nuclear magnetic resonance
<i>NM</i>	noble metal
<i>NTA</i>	nitrilo triacetic acid
<i>OHP</i>	outer Helmholtz plane
<i>Pc</i>	phthalocyanine
<i>PMO</i>	periodic mesoporous organosilica
<i>PTA</i>	platinum tetraammine
<i>PZC</i>	point of zero charge
<i>QMS</i>	quadrupole mass spectroscopy
<i>RDP</i>	reduction deposition precipitation
<i>RFC</i>	reactive frontal chromatography
<i>RPA</i>	revised physical adsorption
<i>RT</i>	room temperature
<i>SAPO</i>	SiAlPO ₄
<i>SCR</i>	selective catalytic reduction
<i>SDA</i>	structure-directing agent
<i>SEA</i>	strong electrostatic adsorption
<i>SRGO</i>	straight run gas oil
<i>STY</i>	space time yield
<i>3D</i>	three-dimensional
<i>TEA</i>	triethanolamine
<i>TEDDI</i>	tomographic energy-dispersive diffraction imaging
<i>TEM</i>	transmission electron microscope
<i>TEOS</i>	tetraethylorthosilicate
<i>TMA</i>	tetramethylammonium
<i>TMB</i>	trimethyl benzene
<i>TPA</i>	tetrapropylammonium
<i>TPD</i>	temperature-programmed desorption
<i>TPR</i>	temperature-programmed reduction
<i>2D</i>	two-dimensional
<i>USY</i>	ultrastable Y
<i>UV-VIS</i>	ultraviolet-visible spectroscopy
<i>VOC</i>	volatile organic compound
<i>XPS</i>	X-ray photoelectron spectroscopy
<i>XRD</i>	X-ray diffraction

PART I

Basic Principles and Tools

1

General Aspects

Krijn P. de Jong

1.1

Importance of Solid Catalysts

Catalysis is essential to modern energy conversion, chemicals manufacture, and environmental technology. From the start, oil refining and bulk chemicals manufacture have relied largely on the application of solid catalysts. In the meantime, in specialty and fine-chemicals production catalysis is used frequently too. According to current estimates about 85% of all chemical processes make use of catalysis, while all molecules in modern transportation fuels have been confronted with one or more solid catalysts.

Heterogeneous catalysts, or more specifically solid catalysts, dominate industrial catalysis. Of all industrial catalytic processes, 80% involves the use of solid catalysts with the remaining 20% for homogeneous catalysts (17%) and biocatalysts (3%). The world catalyst sales in 2004 amounted to 15 billion US\$/a, with 12 billion US\$/a for solid catalysts. The growth rate foreseen for catalyst sales amounts to about 5% per year (see Table 1.1) [1]. Although the catalyst sales comprise a significant market, the economic impact of catalysts is amplified by their use. The products (mainly fuels and chemicals) obtained by catalysts usage generate a margin that is a multiple of the catalysts costs. Data are scarce but indicative figures have been reported. For zeolite catalysis a paper by Naber and coworkers quotes figures on the costs of zeolites and their upgrading in heavy-oil cracking [2]. From their figures one can estimate the ratio of product margin divided by zeolite costs to be around 100 for fluid catalytic cracking as well as hydrocracking. If all energy and chemical industries are involved a ratio of 100–300 has been published [3] and it seems sufficient for the sake of argument that the total gross margin of the “catalysis industry” amounts to more than 100 times the catalyst sales, that is, more than 1500 billion US\$/a. The importance of research and manufacture of catalysts relates to this gross margin of their application.

Next to the economic importance we mention the environmental impact of catalysis. The amount of energy and raw materials needed for fuels and

Table 1.1 World catalyst demand and forecast (billion US\$/a) by application [1].

	2007	2010	2013	AAGR ^a
Refining	4.35	4.98	5.85	5.7
Petrochemicals	3.03	3.64	4.34	7.2
Polymers	3.24	3.75	4.30	5.4
Fine chemicals/other	1.47	1.59	1.70	2.5
Environmental	5.51	6.28	6.93	4.3
Total	17.6	20.2	23.1	~5

^a Average annual growth rate (%).

chemicals manufacture is much reduced by using catalysts. In fact today, many products could not be obtained without catalysis. Although sulfur removal from oil products started as extraction processes, today's low-sulfur diesel and gasoline could not be produced in an acceptable manner without hydrodesulfurization (HDS) catalysis. Exhaust catalysis has enabled the widespread use of cars, while selective catalytic reduction of nitrogen oxides has removed the brown plumes from power and chemical plants. In the future, the importance of catalysis will grow as raw materials for chemicals diversify and alternative energy sources and end use come into play. Building blocks in new energy chains, such as water electrolysis and fuel cells, also rely on solid catalysts.

1.2

Development of Solid Catalysts

In Table 1.2 selected solid catalysts are shown together with their main use. Bulk and supported catalysts as well as zeolite-based catalysts are listed. Many of the examples shown have been known for decades. However, a continuous and spectacular progress over the years is noted for many catalytic processes. We discuss two examples hereafter.

Based on the development of both catalysts and reactors [4, 5], the Fischer–Tropsch synthesis activity and selectivity of cobalt catalyst have increased as illustrated in Figure 1.1. The volume-based activity has increased by a factor of 10 going from 1940 at space time yield (STY) = 10 to 1990 at STY = 100, and another factor of 3 is expected to lead to STY = 300 by 2010. Most importantly, with increasing activity the catalysts displayed improved selectivities to higher hydrocarbons.

The second example, shown in Figure 1.2, involves the increase of the weight-based activity for HDS of NiMo catalysts over the years [6]. For quite a long period, say 1975–1995 the increase of activity has been modest, whereas a steep increase is apparent over the last decade. Low costs for HDS catalysts have been the predominating market factor for previous decades, whereas legislation for low-sulfur diesel has been a major driver lately. Market pull had

Table 1.2 Survey of selected catalysts with their main applications.

Catalyst	Applications
Ni/SiO ₂	Hydrogenation
K ₂ O/Al ₂ O ₃ /Fe	Ammonia synthesis
Ag/ α -Al ₂ O ₃	Epoxidation
CrO _x /SiO ₂	Polymerization
CoMoS ₂ / γ -Al ₂ O ₃	Hydrotreating
Co/SiO ₂	Fischer–Tropsch synthesis
Cu/ZnO/Al ₂ O ₃	Methanol synthesis
Zeolite Y composite	Catalytic cracking
Pt/Mordenite	Hydroisomerization of light alkanes
V ₂ O ₅ /TiO ₂	NO _x abatement
Pt/C	Hydrogenation; fuel cell

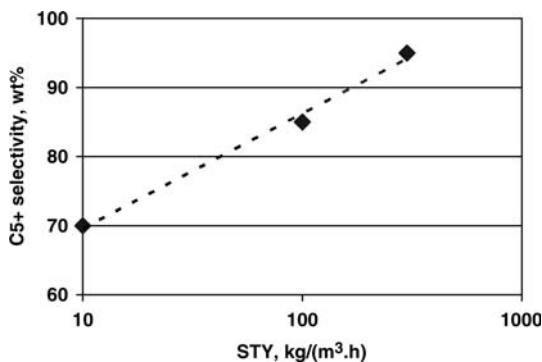


Figure 1.1 Development of cobalt-based Fischer–Tropsch synthesis in terms of both activity (STY = space time yield) and selectivity to hydrocarbons of five or more C-atoms. Data from 1940 to 2010 with data points from left to right at years 1940, 1990, and 2010, respectively.

quite an impact at all stages and it shows the great flexibility and potential of catalyst preparation to respond quickly.

One could easily put forward many other examples where catalyst preparation has been the basis for new and improved processes, such as methanol synthesis, ethene epoxidation, and acrylic acid production. However, for the topic of this book it is more important to discuss in which ways catalyst preparation has allowed these new developments.

1.3 Development of Solid Catalyst Synthesis

Depending on the application, macroscopic catalyst bodies differ in size and shape. For slurry and fluid-bed applications the size is in the range of

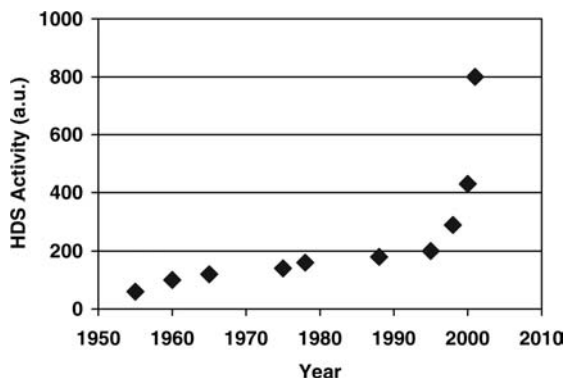


Figure 1.2 Development of hydrodesulfurization (HDS) catalyst activity over the years [6].

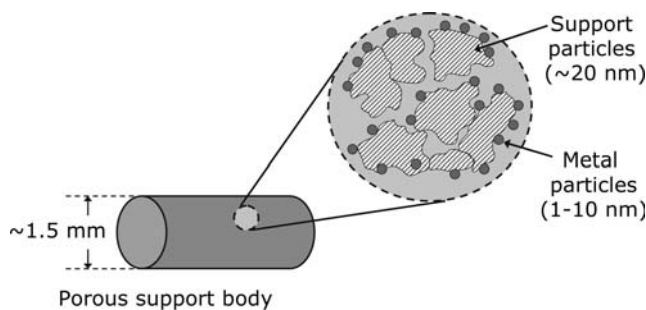


Figure 1.3 Structure at different length scales of catalyst extrudate.

tens of micrometers, whereas fixed-bed applications require millimeter-sized particles. Next to particles, monoliths are used with macroscopic sizes well beyond that of particles (Chapter 9). A typical structure for a cylindrically shaped catalyst body for fixed-bed application is shown in Figure 1.3. This figure also reveals the multiple length scales involved in solid catalysts. The microscopic scale involves the structure of the active sites, the mesoscopic scale the pore system and the sizes of support particles as well as the particles of the active phase. The macroscopic length scale involves the size and shape of the catalyst bodies. The importance of the microscopic scale goes without saying as it determines the intrinsic activity and selectivity of the catalyst. The mesoscopic length scale affects, amongst others, the intraparticle mass transfer of the catalysts. The macroscopic size and shape is relevant for properties such as pressure drop (fixed-bed reactor), mechanical strength, and attrition resistance.

In catalyst manufacturing a final catalyst is usually obtained in multiple steps. Building blocks of the final catalyst may be obtained from sol-gel type processes with support materials such as alumina and silica as prime examples. Also, zeolites and carbon are relevant catalyst building

Table 1.3 Generations of solid catalysts according to manufacturing techniques.

Period	Material type	Key production step	Example – material and process
~1890	Natural	Shaping	Bauxite; Claus process
~1930	Natural	Shaping	Clays; catalytic cracking
~1940	Synthetic	Impregnation	Pt/Al ₂ O ₃ ; reforming
~1970	Synthetic	Precipitation	Cu/ZnO/Al ₂ O ₃ ; methanol synthesis
~1980	Synthetic	Hydrothermal	ZSM-5; methanol-to-gasoline
>2000	Nanostructured	Templating, CVD	MCM-41, SBA-15, CNF, CNT

See main text for an explanation of abbreviations.

blocks. The synthesis of these “building blocks” mostly leads to primary particles in the nanometer or micrometer range that have to be shaped to macroscopic sizes (Chapter 9). Subsequently, shaped particles can be loaded with active components via methods such as impregnation and drying or ion adsorption.

The development of the manufacture of solid catalyst synthesis is summarized in Table 1.3. The first solid catalysts comprised of supports and active phase available from nature. Bauxite and clays are examples of active phases, while “diatomaceous earth” or “kieselguhr” is a natural source of silica support material. Using sol-gel chemistry synthetic support materials have been developed. Application techniques for the active phase based on impregnation and drying emerged during the twentieth century. Hydrothermal synthesis has been important for synthetic zeolites such as ZSM-5. Using micelle templating nanostructured silica (MCM-41, SBA-15) and other oxides have been produced during the last two decades. Using chemical vapor deposition (CVD) techniques nanostructured carbon materials such as carbon nanofibers (CNFs) and carbon nanotubes (CNTs) have been produced and explored as catalyst supports [7].

Figure 1.4 displays three generations of support materials, that is, natural silica (kieselguhr), silica gel and ordered mesoporous silica. Moving from natural (Figure 1.4a) to synthetic (Figure 1.4b) materials has greatly improved the control over composition and texture of the support in question. Although diatomaceous earth has been named “nature’s nanotechnology”, one should realize that, next to a low specific surface area and broad pore-size distribution, the variation in properties is a major issue. The latest advancement of synthetic nanostructured supports (Figure 1.4c) has not yet resulted in many new industrial catalysts. For fundamental studies on catalyst preparation, however, these materials are of great value with results that can be translated to more conventional support materials [8].

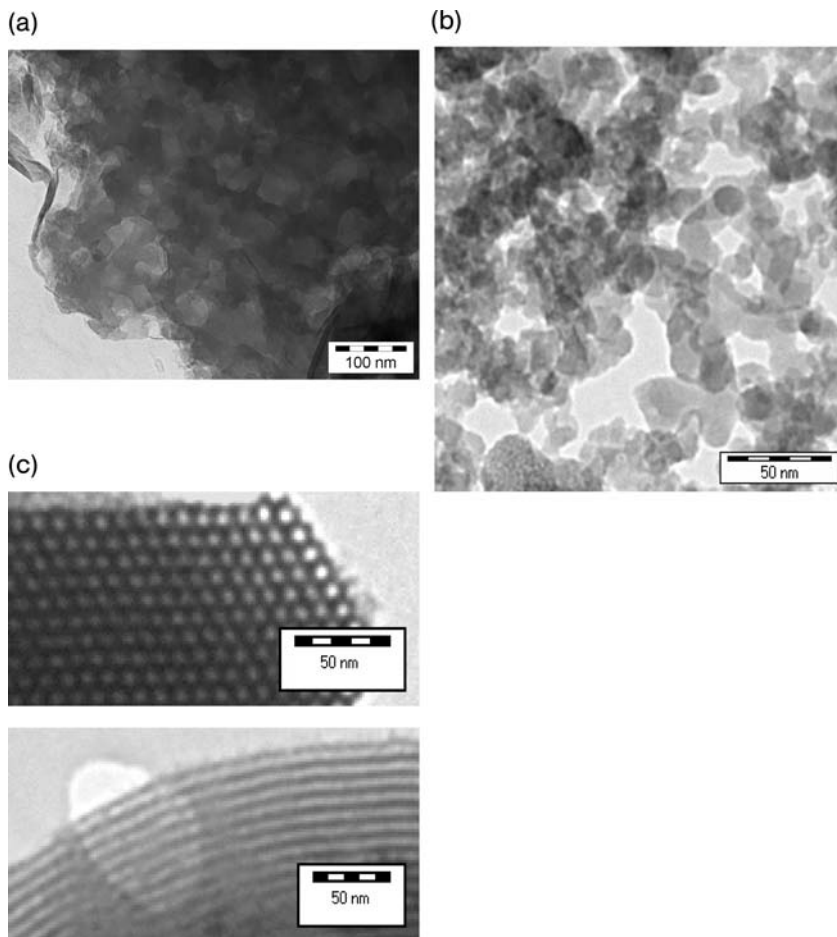


Figure 1.4 Silica materials that have been used catalyst support. (a) Natural silica, kieselguhr ($\sim 20 \text{ m}^2 \text{ g}^{-1}$); (b) silica gel ($\sim 500 \text{ m}^2 \text{ g}^{-1}$); and (c) ordered mesoporous silica, SBA-15 ($\sim 500 \text{ m}^2 \text{ g}^{-1}$).

Here, we illustrate the impact of new supports, on the one hand, and new catalyst synthesis methods, on the other hand, by considering the showcase of the preparation of silica-supported cobalt catalysts for Fischer–Tropsch synthesis. In Figure 1.5 different generations of cobalt catalysts are shown. In Figure 1.5a a kieselguhr-supported cobalt catalyst is shown that has been prepared according to a recipe from the 1940s reported by Anderson [9] that involves precipitation in the presence of the support. The large amount of cobalt separate from the support is apparent as well as clustering of the cobalt particles. Using a synthetic silica gel and impregnation with aqueous cobalt

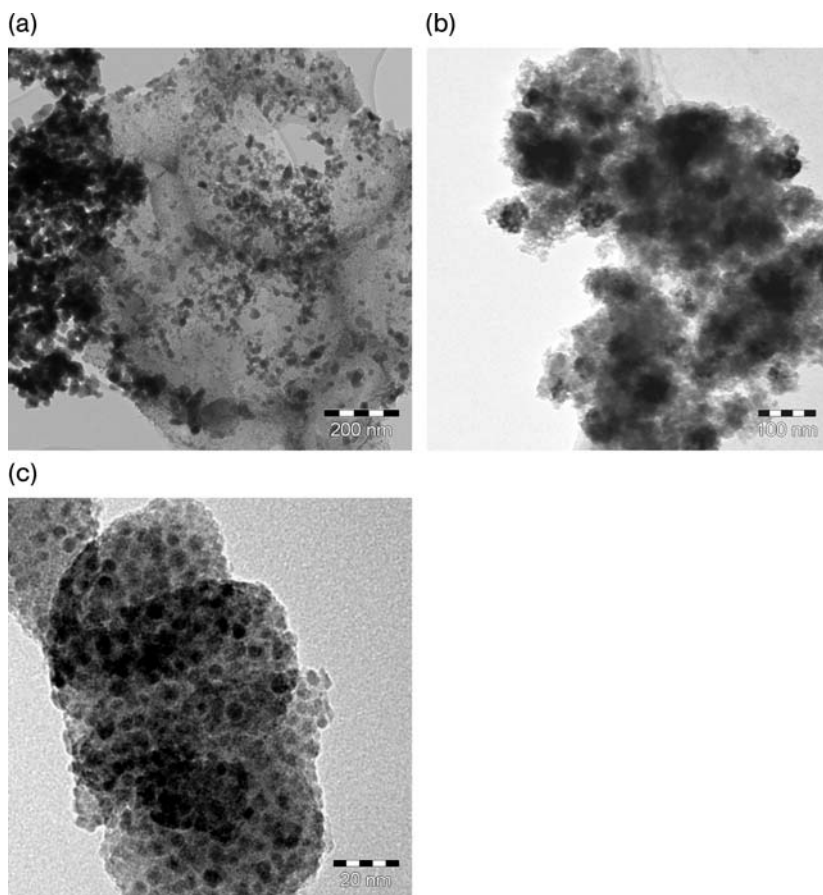


Figure 1.5 Three generations of silica-supported cobalt catalyst. (a) 50 wt% Co/kieselguhr prepared by precipitation; (b) 18 wt% Co on silica gel obtained by calcination in NO/He flow; and (c) 18 wt% Co on silica gel obtained by calcination in air flow.

nitrate solution followed by drying and calcination in air the catalyst shown in Figure 1.5b has been prepared. A fairly high dispersion (~ 10 nm Co particles) but still extensive clustering of the cobalt particles is apparent. Using the same support and the same steps of impregnation and drying but applying a new calcination treatment in diluted nitrogen oxide [8], the catalyst displayed in Figure 1.5c has been obtained. The small Co particle size (~ 5 nm) together with the uniform dispersion of the Co particles over the support, illustrate the progress made in the synthesis of solid catalysts.

Next to new support materials continuous advancement in sol-gel chemistry, zeolite synthesis, and new classes of materials such as metal organic frameworks provide an impetus to catalyst preparation. Molecular details about the

interaction of catalyst precursor species with support materials have provided great insights. New tools to study catalyst synthesis are emerging that either speed up research (high-throughput experimentation) or provide molecular details resolved in time and space (microspectroscopy). These new tools provide us with unprecedented numbers and details of catalysts preparation and facilitate new avenues to nanostructured catalysts. Further advancements making use of developments from colloidal chemistry and nanotechnology are foreseen too [10].

1.4

About This Book

Catalyst synthesis literature has been summarized in the proceedings of the conference series “Scientific basis for the preparation of heterogeneous catalyst”. A number of books have appeared, such as those edited by Ertl *et al.* [11] and by Regalbuto [12]. The current book has been organized by, first, dealing with basic principles and tools and, second, dealing with case studies. The basic principles comprise fundamentals of interfacial chemistry (Chapter 2) that play a role in a number of deposition techniques. Preparation of supported catalysts using a previously produced support material involves electrostatic adsorption (Chapter 3), impregnation and drying (Chapter 4), deposition precipitation (Chapter 6), and immobilization of organometallic precursors (Chapter 8). Sol-gel chemistry (Chapter 5) and coprecipitation (Chapter 7) deal with support and catalyst preparation in a single step. Two chapters of this book deal with new tools to study catalyst preparation. Chapter 10 on microspectroscopy treats spatially and time-resolved studies of impregnation, drying, and calcination processes over support bodies. Chapter 11 on high-throughput experimentation is based on extensive experience over the last decade. The case studies of materials and catalyst synthesis involve zeolite synthesis (Chapter 12), ordered mesoporous materials (Chapter 13), hydrotreating catalysts (Chapter 14), methanol catalysts prepared by coprecipitation (Chapter 15), noble-metal catalysts prepared by impregnation (Chapter 16) and drying, and gold catalyst produced via, amongst others, deposition precipitation (Chapter 17).

References

1. The Catalyst Group Resources (2008) Chemical Week April 28. Spring House.
2. Naber, J.E., de Jong, K.P., Stork, W.H.J., Kuipers, H.P.C.E. and Post, M.F.M. (1994) *Stud. Surf. Sci. Catal.*, **84**, 2197.
3. de Jong, K.P. (1998) *CatTech*, **2**, 87.
4. Pichler, H. (1952) *Adv. Catal.*, **4**, 271.
5. Geerlings, J.J.C., Wilson, J.H., Kramer, G.J., Kuipers, H.P.C.E., Hoek, A. and Huisman, H.M. (1999) *Appl. Catal. A*, **186**, 27.

6. http://www.dct.tudelft.nl/race/education/ce3081/akzo_2003.pdf data on HDS.
7. de Jong, K.P. (2006) *Oil Gas Sci. Technol. Rev. Inst. Fr. Petrol*, **61**, 527.
8. (a) Sietsma, J.R.A., Meeldijk, J.D., den Breejen, J.P., Versluijs-Helder, M., van Dillen, A.J., de Jongh, P.E. and de Jong, K.P. (2007) *Angew. Chem. Int. Ed.*, **46**, 4547; (b) Sietsma, J.R.A., Meeldijk, J.D., Versluijs-Helder, M., Broersma, A., van Dillen, A.J., de Jongh, P.E. and de Jong, K.P. (2008) *Chem. Mater.*, **20**, 2921; (c) Sietsma, J.R.A., Friedrich, H., Broersma, A., Versluijs-Helder, M., van Dillen, A.J., de Jongh, P.E. and de Jong, K.P. (2008) *J. Catal.*, **260**, 227.
9. Anderson, J.R. (1975) *Structure of Metallic Catalysts*, Academic Press, p. 455.
10. (a) Bell, A.T. (2003) *Science*, **299**, 1688; (b) Somorjai, G.A., Tao, F. and Park, J.Y. (2008) *Top. Catal.*, **47**, 1.
11. Ertl, G., Knözinger, H. and Weitkamp, J. (eds) (1999) *Preparation of Solid Catalysts*, Wiley-VCH Verlag GmbH, Weinheim.
12. Regalbuto, J. (ed.) (2007) *Catalyst Preparation, Science and Engineering*, CRC Press, Boca Raton.

2

Interfacial Chemistry

Alexis Lycourghiotis

2.1

Introduction

In the preparation of supported catalysts we disperse bidimensional species, nanocrystallites or amorphous nanoparticles of the catalytically active phase on the surface of a rather limited number of supports. These are oxides (e.g. γ - Al_2O_3 , α - Al_2O_3 , SiO_2 , TiO_2) or carbons with convenient surface characteristics. The supported nanoparticles of the final catalysts are in the oxidic, metallic, or sulfidic state. The nature of the forementioned species, the size of the supported nanoparticles and their interactions with the support determine to a great extent the catalytic behavior of the supported catalysts. In most cases the main preparative goal is the formation of very small nanoparticles (e.g. <10 nm) along with a high loading of the active element, for obtaining a relatively highly active surface. In this respect the choice of a suitable preparation method and preparation conditions is indeed critical.

The general (impregnation) procedure usually followed for the preparation of a supported catalyst involves several steps. These are illustrated in Figure 2.1. We may classify these steps into two groups. The first involves the steps 1–4 while the second the steps 5 and 6. In the steps of the first group the support grains or pellets are in contact with the impregnating solution containing one or more than one species of the active element to be deposited. The deposition of the precursor species on the support surface takes place in one of these steps. Therefore, chemical processes taking place in the solution or at the solid/liquid interface are important. In the latter case the concepts of the *liquid/solid interfacial chemistry* are proved to be very useful for understanding fundamental aspects of deposition related with the preparation of supported catalysts [1]. On the other hand, as we shall see, the methodologies of liquid/solid interfacial chemistry help us to control the preparation procedure [1].

Gas–solid surface reactions take place in the last two steps: oxidation during the air-calcination step resulting to oxidic catalysts and reduction/sulfidation in the activation step resulting in metallic/sulfided catalysts. Sintering

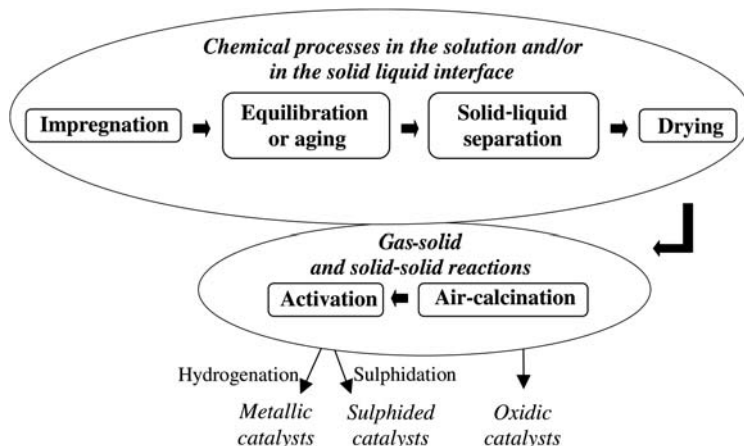


Figure 2.1 General procedure based on impregnation, drying and thermal treatment followed for the preparation of a supported catalyst.

phenomena and *solid–solid* reactions also take place in the last two steps, at relatively high temperatures. There is no doubt that the high-temperature reactions taking place in the last two steps may modify drastically the precursor species deposited in the first four steps.

However, it has been realized that the characteristics of the precursor species frequently affect the surface features of the final catalyst and thus its catalytic behavior [1–3]. This is why the control of the deposition taking place in one of the first four steps is actually significant.

2.2

Interfacial and Bulk Deposition

Suitable characteristics of the aforementioned precursor species may be achieved to some extent by imposing the appropriate *deposition mode* [1, 4, 5]. This may be realized by selecting the proper impregnation technique and suitable impregnation parameters. The appropriate deposition mode leads to convenient surface characteristics of the final catalysts and thus to desirable catalytic behavior.

The first critical choice is between *bulk* and *interfacial* deposition. Bulk deposition may be realized following *incipient wetness impregnation*, while interfacial deposition employing *equilibrium deposition filtration* (otherwise called *equilibrium adsorption*) [1] or *homogeneous deposition precipitation* [6–9]. In fact, applying the first technique (and small aging times) the impregnation solution is rapidly transferred inside the pores of the support through capillary forces. During *drying*, and due to the solvent evaporation, the transition-metal ionic species (TMIS) are precipitated/crystallized in the *bulk solution* being

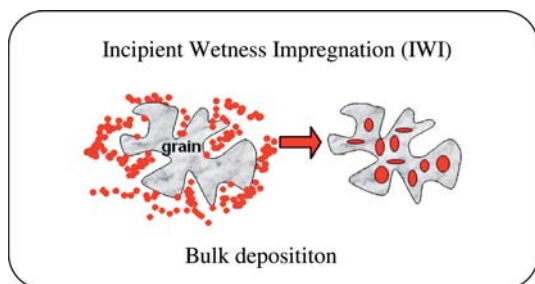


Figure 2.2 Schematic representation of bulk deposition.

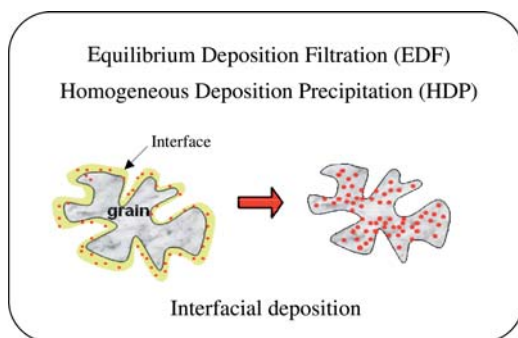


Figure 2.3 Schematic representation of interfacial deposition.

inside the pores. The supported particles formed by bulk deposition are weakly bound to the surface of the support and transformed into relatively large oxidic supported nanoparticles during the air-calcination step (Figure 2.2).

In contrast, employing equilibrium deposition–filtration or homogeneous deposition–precipitation the deposition takes place during the *equilibration step* (Figure 2.1) *inside the interface developed between the surface of the support particles and the impregnating solution*. This results in relatively small supported nanoparticles. The small size of the supported nanoparticles is largely imposed by the relatively small size of the interface (Figure 2.3).

2.3

The Surface of the Oxidic Supports: Surface Ionization Models

2.3.1

The Charged Surface of the Oxidic Supports

A finer tuning of the nature of the bidimensional supported species and of the size and the physicochemical characteristics of the supported nanoparticles could be in principle obtained by “selecting” *the particular mode of interfacial*

deposition and regulating the *interface speciation/structure* of the deposited precursor species. This is not an easy task. In order to explain how to do this it is necessary to look at the interface developed between the support grains and the impregnating solution. In this and in the following subsections we shall discuss very briefly the reason for the development of the interface and the surface structure of the oxidic supports. The structure of the interface will be discussed in the next section.

It is known that on the surface of an oxidic support one or more than one kind of single or double coordinated (with the cation) hydroxyls may be developed, as a result of the interaction of the surface oxygen ions and cations of the oxidic support with water molecules [10]. These are charged and may be protonated/deprotonated in aqueous suspensions [1, 11–13]. Thus, depending on the pH of the impregnation solution, the surface charge may be negative, neutral or positive. The surface charge causes the development of surface potential. Under the influence of this potential, ions with opposite charges (counterions) are accumulated from the solution near to the surface, thus forming the interfacial region. At the interfacial region, the TMIS, containing the active ion to be deposited, are also located.

2.3.2

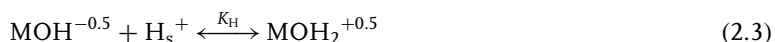
Homogeneous Surface Ionization Models

Let us now concentrate our attention on the surface of the support grains, more precisely on the surface of the support nanoparticles that constitute the grains. In spite of the progress with respect to the surface structure of the oxidic supports thanks to crystallography or IR spectroscopy, rather *hypothetical* homogeneous *surface ionization* (or *surface binding* or *surface complexation*) models have been used to describe their protonation/deprotonation behavior in aqueous solutions.

According to the most familiar “one-site/two-pK model” [14] only one generic kind of oxo-/hydroxo-groups is developed on the surface of an oxide in contact with water. Depending on the pH of the impregnating solution these groups may be protonated/deprotonated.



Only one generic kind of surface of oxo-/hydroxo-groups is also assumed in the context of the “one-site/one-pK model” [15–17].



In the above equilibria by H_s^+ we denote the hydrogen ions located near to the surface. According to the first model, the surface oxygens, with an arbitrary

charge equal to $-1e$, may undergo two successive protonation steps, while according to the second model, the surface oxygens, with an arbitrary charge equal to $-0.5e$, undergo a single protonation.

2.3.3

The Music Model

The much more *realistic multisite surface complexation (music)* model recognizes that different kinds of oxo-/hydroxo-groups are developed on the surface of the oxidic supports [18]. Thus, single $MO(H)$, double $M_2O(H)$ and/or triple M_3O coordinated oxo-/hydroxo-groups may be developed on the surface. Moreover, this model provides a very simple formula for estimating the surface charge of the surface oxo-/hydroxo-groups.

$$\begin{aligned} \text{Surface charge of the group} = & -2 + (+1) \times (\text{number of protons}) \\ & + \sum_{\text{cat}} \{(\text{formal charge of the cation})/(\text{coordination number of} \\ & \text{the cation in the bulk})\} \end{aligned} \quad (2.4)$$

The ratio in the sum of the right-hand side of this equation is defined as the *Pauling valence bond* of the given cation [19–22]. Let us take an example. It concerns the surface group, $Al_{td}-OH-Al_{oh}$, developed on the γ -alumina surface, namely an oxygen coordinated with one proton, one tetrahedral and one octahedral Al^{3+} . Application of the above relationship provides: surface charge of the group $= -2 + (+1) \times (1) + (+3)/(4) + (+3)/(6) = +0.25$. Following the same formula we may calculate the surface charge for the corresponding oxo-group, $Al_{td}-O-Al_{oh}$: surface charge of the group $= -2 + (+1) \times (0) + (+3)/(4) + (+3)/(6) = -0.75$.

It is obvious that the surface charge of an oxo-group differs by one unit charge from the surface charge of the corresponding hydroxo-group.

In order to obtain a more reliable value for the charge of a surface group, it is necessary to take into account that a surface oxo-/hydroxo-group may form hydrogen bonds with water molecules being near to the surface. It has been proposed that $+0.2$ units of charge are transferred from the group (water molecule) to the water molecule (surface group) per hydrogen bond formed in which the hydrogen atom is donated by the surface hydroxo-group (water molecule) to the water molecule (surface oxo-/hydroxo-group). It has been, moreover, proposed that an MO group forms two hydrogen accepting bonds, whereas an $MO(H)$ group forms two hydrogen bonds, one donating and one accepting. The M_3O group may form only one accepting hydrogen bond. As to the $M_2O(H)$ it is involved in one or two hydrogen bonds. In some cases it is necessary to use the actual instead of the Pauling valence, when these parameters have different values. In fact, the former may be slightly different

from the latter because for the determination of the actual valence we also take into account the length of the cation–oxygen bonds for a certain kind of oxo– or hydroxo-groups.

Finally, the music model provided the following empirical equation for calculating the protonation constants of the oxo– and hydroxo-groups.

$$\log K = -19.8 (\text{charge of the oxo/hydroxo-group}) \quad (2.5)$$

In principle, a more reliable value for the charge of an oxo/hydroxo-group could be obtained by performing *ab-initio* calculations in the frame of the *density functional theory*. The first example of catalytic interest, recently reported, concerns the oxo/hydroxo-groups developed on anatase [23].

2.4

The Size and the Structure of the Interface

Let us now go from the surface to the interface. Various models describe the structure of the interfacial region developed between the surface of the support aggregates and the impregnating solution as well as the arrangement of the ions inside the interface [24–34]. According to a modern picture the interface is divided by three charged *planes* into three subregions (*layers*). The detailed structure of the titania/aqueous solution interface is illustrated, as an example, in Figure 2.4 [23]. This structure as well as the mean concentration of the counterions inside the interface were recently determined by applying a novel surface ionization model developed for the titania surface (which is based on *ab-initio* calculated charges of the oxo/hydroxo-groups) in conjunction with potentiometric titrations, microelectrophoresis and streaming potential measurements [23].

The first and the second subregion are uncharged. Plane 1 is usually located at the oxygen atoms of the first or second layer of water molecules surrounding the support surface. These are retained by forming hydrogen bonds with the surface (hydr)oxo-groups and lateral hydrogen bonds between adjacent water molecules as well. Plane 2 is usually located at the center of the second or third layer of water molecules. Taking into account the above, it is understandable that the size of each subregion is of the order of very few angstroms. The first two regions constitute the so-called *compact layer* of the interface.

The third subregion, called *diffuse part of the interface*, is charged because in this region the counterions are accumulated. The size of the diffuse part depends strongly on the ionic strength of the impregnating solution. Assuming a planar solid/water interface, its thickness (L) may be approximately estimated by the formula

$$L = \frac{1}{(3.29I^{1/2})} \quad (2.6)$$

where L is given in nm and I in mol/L.

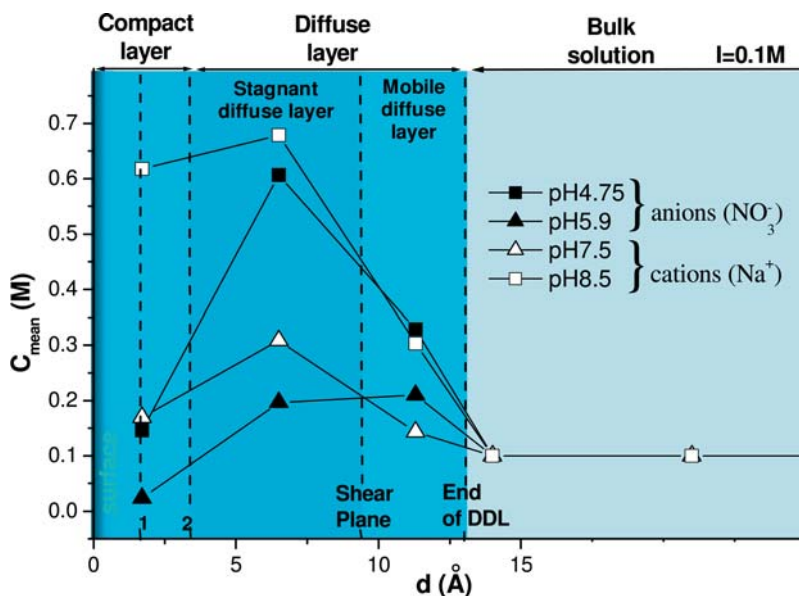


Figure 2.4 The structure of the “titania/aqueous solution” interface and the mean concentration of the counterions inside the various layers of the interface.

Application of this approximate formula shows that the thickness of the diffuse part of the interface is equal to 3, 10, 30, and 96 Å for an ionic strength equal to 1, 0.1, 0.01, and 0.001 M, respectively. It is obvious that for a relatively high value of the ionic strength the diffuse part of the interface is considerably compressed and the interface is practically reduced into its compact part.

In order to accomplish the picture for the structure of the interface it is necessary to mention the so-called *shear plane*. It is the plane that divides the interface into two parts: the *stagnant* one, which “accompanies” the support aggregates when they are moved under the influence of an electric field by applying an electrokinetic technique (e.g. microelectrophoresis), and the external part that is separated from the moving aggregates. Thus, the diffuse layer is divided into the *stagnant-diffuse layer* and the *mobile-diffuse layer*. Traditionally, the *shear plane* was considered to coincide with the plane 2. However, quite recently it was deduced that the distance, d , of the shear plane from the plane 2 is related with the ionic strength by the following empirical relationship [23, 35].

$$\log d = -0.5115 \log I - 0.7229 \quad (2.7)$$

Application of this relationship provides a distance equal to 2, 6, 20, and 65 Å for an ionic strength equal to 1, 0.1, 0.01, and 0.001 M, respectively. Comparison of these values with the corresponding ones calculated for the

size of the diffuse part of the interface indicates that in the most of cases the stagnant part of the interface comprises the compact layer and about $1/3 - 2/3$ of the diffuse part [23].

2.5

The Arrangement of the Ions Inside the Interface and the Deposition Modes

2.5.1

Indifferent Ions

The impregnating solutions used for the preparation of supported catalysts usually contain two kinds of ions: (i) one or more TMIS of the active element to be deposited (e.g. $\text{Co}(\text{H}_2\text{O})_6^{2+}$, $\text{Mo}_7\text{O}_{24}^{6-}$) and (ii) several ions involved in the precursor salts or used for regulating the pH and/or the ionic strength of the impregnating solution (e.g. Na^+ , K^+ , NH_4^+ , NO_3^- ions). It should be noted that the cations are hydrated in solutions. The various modes of interfacial deposition of the TMIS and the aforementioned ions are illustrated in Figure 2.5.

Let us first look at the second kind of ions. It is obvious that cations (anions) are in any case accumulated at the interface when the surface is negatively (positively) charged. The simple accumulation in the diffuse

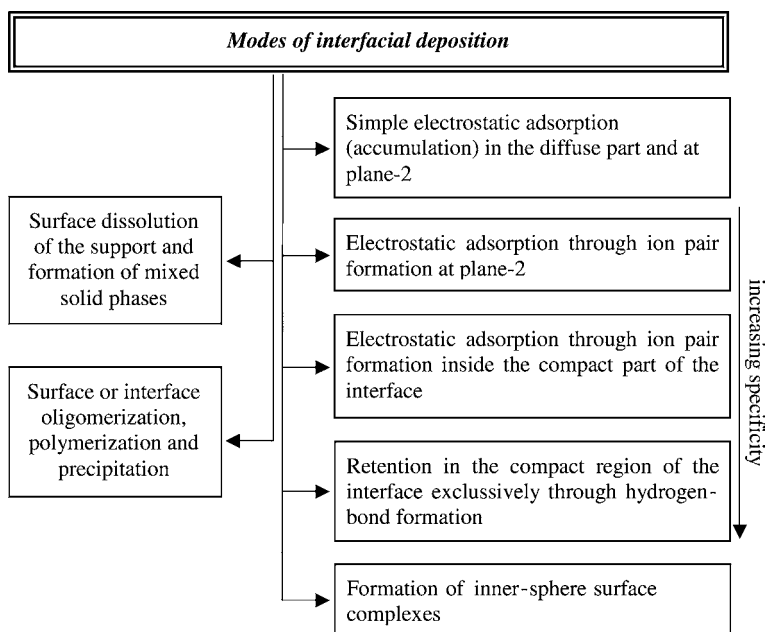


Figure 2.5 Modes of interfacial deposition.

part of the interface and at the plane 2, considered as the front end of the diffuse part, without any specific interaction with the surface oxo/hydroxo-groups, is the simplest mode of deposition (*simple electrostatic adsorption*). The model corresponding to this type of deposition is called *Stern–Gouy–Chapmann* [24, 25]. It is obvious that following this model only two planes, the surface and the plane 2 (now called the outer Helmholtz plane (OHP)) are necessary to be considered. This simple model describes adequately the deposition of the second kind of ions for most of the oxidic supports. An even simpler model, called *diffuse layer model* [26], does not take into account that the ions are hydrated and thus considers that the front end of the diffuse layer coincides with the surface plane. In this case the diffuse part covers the whole interface. This model describes well the *simple electrostatic adsorption* of the second kind of ions only on silica. This actually does not mean that the ions are not hydrated. It has been attributed to the fact that due the surface structure of silica the water molecules may penetrate the first surface layer allowing a closer approach of the ions to the surface [18]. For the other supports the *diffuse layer model* does not work well.

An even more realistic deposition mode for the ions of the second kind and most of the catalytic supports is the *electrostatic adsorption through ion-pair formation at plane 2*. The only difference between this deposition mode and the *simple electrostatic adsorption* is that the ions located at the front end of the diffuse part of the interface form ion pairs with the surface oxo/hydroxo-groups of opposite charge. The cations involved in the ion pairs retain their hydration sphere. The model related with this deposition mode is called *basic Stern* [32] and, as the *Stern–Gouy–Chapmann* model, it involves only two planes (the surface plane and the plane 2).

A recent application of theoretical (*ab-initio* calculations in the frame of the density functional theory and molecular dynamic simulations) and experimental methodologies (*in-situ* synchrotron X-ray studies including crystal truncation rod and Bragg X-ray standing wave) has indicated that at very high pH values, where the support surface has a relatively high negative charge, a *small portion* of the cations of the second kind penetrate the compact part of the interface undergoing a partial dehydration from the surface side [36, 37]. These cations are located at the plane 1 (*triple-layer model/extended Stern model*) [30, 31] and interact directly with the surface (hydr)oxo-groups. Alternatively, these cations may be located between the planes 1 and 2 or between the surface and the plane 1, by sharing properly their charge in two of the three charged planes (*three plane model*) [23, 34, 38]. In all these cases the larger portion of the ions of the second kind are located in the diffuse part of the interface and at the plane 2 as well. The distribution of the common ions of the second kind inside the interfacial region has been very recently determined for the “anatase/impregnation solution” interface [23]. A typical example is illustrated in Figure 2.4.

2.5.2

Transition-Metal Ionic Species

Thanks to the extensive work reported in the last three decades by a rather small number of research teams, we may now better understand the factors that determine the deposition mode of TMIS containing catalytically active ions. The relevant papers reported are mentioned in a recent review [1]. The nature of the *ligand* of the TMIS, the nature of the support and the impregnation parameters (pH, concentration of TMIS, ionic strength and temperature of the impregnating solution) are indeed the principal factors.

Let us start with the influence of *ligands* on the deposition mode. Water is a common ligand of the TMIS used in catalyst preparation. In fact, the transition metals of the groups 8–10 (Fe, Co, Ni) as well as group 11 (Cu) are usually deposited as aqua complexes. It has been well established that one or more of the water ligands are rather easily exchanged with the surface hydr(oxo) groups of the supports leading to the formation of surface inner-sphere complexes. In these complexes the metal is located inside the compact layer, usually at plane 1. The formation of these complexes is corroborated by the observation that replacement of one or more than one of water molecules by organic ligands changes the deposition behavior [39].

Going from the aqua complexes to the oxo-species, frequently used for mounting the transition-metal ions of the group 6 (e.g. Cr^{6+} , Mo^{6+} , W^{6+}) or group 5 (V^{5+}) ions, the deposition mechanism is, more or less, different. The deposition mode depends on the size of the TMIS. Thus, the monomeric species (e.g. CrO_4^{2-} , MoO_4^{2-} , WO_4^{2-}) are retained by the surface hydr(oxo) groups through hydrogen/coordinative bonds. The interface speciation and the detailed structure of the surface inner-sphere complexes formed (e.g. monosubstituted or disubstituted, mononuclear or binuclear) depends on the pH and the kind of the transition metal as well. In these cases the TMIS are located in the compact layer, usually between the plane 1 and the support surface. In contrast, the polymeric species (e.g. $\text{Mo}_7\text{O}_{24}^{6-}$, $\text{W}_7\text{O}_{24}^{6-}$) are usually retained through hydrogen bonds/electrostatic attraction covering the range between the plane 1 and the first layers of the diffuse part of the interface adjacent to the plane 2. Depending on their size they cover a considerable number of the receptor hydr(oxo)-groups, for instance each $\text{Mo}_7\text{O}_{24}^{6-}$ species adsorbed on titania covers about 14 surface sites [40].

The simple electrostatic adsorption (accumulation) in the diffuse part of the interface and at the plane 2 is rather the predominant mode in most cases when ammonia or halogen complexes are used for depositing noble metals (e.g. $\text{Pt}(\text{NH}_3)_4^{2+}$, PtCl_6^{2-}) under conditions where these complexes remain intact in the impregnating solutions.

The role of the support is also important. Thus, γ -alumina and silica favor the surface polymerization and then the surface precipitation of the inner-sphere complexes formed upon deposition of the cobalt or nickel aqua complexes. This allows the successful application of the *homogeneous deposition-precipitation*

technique. In contrast, only oligomerization takes place on the titania surface at room temperature. Moreover, the surface reactivity of silica and γ -alumina is higher than that of titania. In fact, under rather severe impregnating conditions silica and γ -alumina may react with the deposited precursor species, whereas the titania surface is rather inactive. Specifically, the formation of Ni(II) and Co(II) hydrotalcite-like mixed phases with γ -alumina, the formation of an Anderson-type alumino heteropolymolybdate and heteropolytungstate as well as the formation of Ni(II) phyllosilicates have been reported [41].

The variation of the impregnation parameters mentioned before may change the speciation in the solution, in cases where more than one of TMIS are present, and the surface speciation of the receptor hydro(oxo)-groups. Thus, this variation may cause dramatic changes in the mode of interfacial deposition and the surface speciation/structure of the deposited precursor species as well.

2.6

Determining the Mode of Interfacial Deposition and the Surface Speciation/Structure of the Deposited Precursor Species

2.6.1

Introductory Remarks

Having presented the main characteristics of the interfacial region and the modes of the interfacial deposition, we now present an outline of a general approach *for determining*, under various impregnating conditions, the particular mode of interfacial deposition and the surface speciation/structure of the deposited precursor species. This allows the selection of the suitable type of interfacial deposition and the optimization of the aforementioned speciation/structure by adjusting the impregnation parameters. Thus, a fine tuning of the size and the physicochemical characteristics of the supported nanoparticles in the final catalysts could be, in principle, feasible.

The aforementioned general approach is schematized in Figure 2.6. It involves the application of several methodologies based on macroscopic adsorption data and potentiometric titrations as well as microelectrophoretic mobility or streaming potential measurements, the application of spectroscopic techniques as well as the application of electrochemical (equilibrium) modeling, quantum-mechanical calculations and dynamic simulations.

2.6.2

Methodologies Based on Macroscopic Adsorption Data and Potentiometric Titrations as well as on Microelectrophoretic Mobility or Streaming Potential Measurements

The determination of the extent of deposition of the TMIS at various pH values and constant ionic strength (adsorption edge) is a very useful methodology [1, 4].

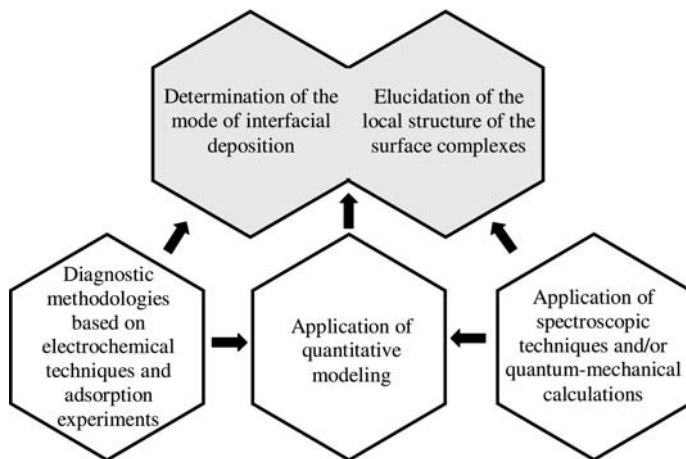


Figure 2.6 A general approach for determining the particular mode of interfacial deposition and the speciation/structure of the deposited precursor species on the support surface.

Considerable adsorption at point of zero charge (pzc) or at pH values where the surface charge has the same sign with the charge of the TMIS suggests formation of inner-sphere complexes. On the contrary, slight (negligible) adsorption under the above conditions suggests retention through hydrogen bonds (electrostatic forces).

The determination of the change of pH upon deposition is a rapid and very simple methodology to investigate the deposition mode [1, 4]. When electrostatic adsorption or adsorption through hydrogen bonding takes place, the receptor groups remain practically intact and the pH does not change markedly. In contrast, upon adsorption of a TMIS with a positive (negative) charge through coordinative bonds, the receptor or neighboring surface oxygens are deprotonated (protonated) in order to compensate the positive (negative) charge transferred to the surface. Therefore, a considerable decrease (increase) of pH due to the adsorption of positive (negative) species is a strong indication for the formation of inner-sphere complexes.

The deposition mode may be also investigated by determining the *microelectrophoretic mobility* or *streaming potential curves*, both in the absence and presence of TMIS [1, 4]. These curves depict the variation, with pH, of the *electrokinetic charge* or *ζ potential* at the shear plane of the interfacial region (Figure 2.4). The *isoelectric point* (*iep*) is the pH value where these parameters take a zero value. When a kind of electrostatic adsorption takes place (Figure 2.5), the aforementioned curves, recorded in the presence of the TMIS, as well as the *iep* value should be rather identical with those observed in the absence of these species at the same ionic strength. In contrast, when the adsorption of cationic TMIS occurs through coordinative or hydrogen bonds, the values of the electrokinetic charge or that of the *ζ potential* should increase

over the whole pH range studied. This is due to the accumulation of positive TMIS inside the stagnant part of the interfacial region (Figure 2.4). On the other hand, the iep should be shifted to a higher value. This is because a surface deprotonation is required to restore the electrokinetic charge at zero value. The magnitude of these effects increases with the amount of the adsorbed cationic TMIS. When a critical amount is exceeded a *charge reversal* could be observed. In this case the electrokinetic charge or ζ -potential takes positive values even at pH values where the surface charge is negative. The opposite effects are expected when negative species are adsorbed through coordinative or hydrogen bonds.

Another method is based on the *determination of pzc both in the absence and presence of the TMIS to be mounted* [1, 4]. As already explained, the surface adsorbs protons upon adsorption of anionic TMIS through coordinative bonds. Thus, its proton charge increases. This takes place at all pH values and obviously at pzc, where the surface was neutral before adsorption. Therefore, in the presence of the so-adsorbed anionic TMIS we need more hydroxyls in the solution in order to deprotonate additional surface groups and restore a zero charge at the surface. Therefore, a shift of the pzc to a higher value is rather expected. The opposite shift should be expected upon adsorption of cationic TMIS.

A recent methodology [1, 4] is based on the determination of the ratio “*amount of H^+ ions released (adsorbed)/amount of cationic (anionic) TMIS adsorbed.*” This ratio is determined by the slope of the corresponding linear plots determined at a fixed pH and under conditions favoring *complete adsorption of TMIS*. A very low value for the above ratio (<0.5) indicates some kind of electrostatic adsorption. On the other hand, values in the range ~ 0.8 – 2.5 suggest formation of inner-sphere surface complexes. Intermediate values could suggest adsorption through hydrogen bonds. This ratio may be also used to determine *the number of surface oxygens participating in the local structure of the inner-sphere surface complexes formed on the support surface*. Thus, the aforementioned structure may be investigated using this ratio.

2.6.3

Spectroscopic Investigations

Several spectroscopic techniques are used for investigating the surface speciation/structure of the deposited precursor species [39–46]. The X-ray absorption fine structure (EXAFS) related techniques are very useful. These allows identification of the kind of atoms surrounding a transition element deposited on the support surface as well as the number of each kind of these atoms and the distances of the transition element from the surrounding atoms. The first and the second coordination sphere can be rather safely probed. Deposition studies on polycrystalline oxidic supports or on monocrystals exposing a certain crystal face have been reported (e.g. the deposition of the

Co(II) aqua complexes on the (1 1 0) rutile termination). In the first case we mainly examine whether a surface inner-sphere complex is actually formed and investigate the general characteristics of its structure. In the second case we try to approach the exact structure of this complex.

ATR (FTIR), DR (UV-Vis-near-IR), NMR, EPR, and RAMAN spectroscopies have been also used to examine whether inner-sphere complexes are formed upon the deposition of TMIS on the surface of an oxidic support and, in some cases, to find the interface speciation. The structure of a deposited TMIS could be changed upon drying. Thus, the application of a spectroscopic technique before drying is in some cases critical. In this respect ATR is very useful because it allows the strong IR absorption of the water molecules to be overcome and interfacial species to be identified.

2.6.4

Quantum-Mechanical Calculations

Ab-initio calculations in the frame of the density functional theory or semiempirical calculations have been recently used to help the investigation of the local structure of the deposited precursor species [23]. Generally speaking, these methodologies may provide the most stable local structure among several tentative ones. However, the simplifications necessarily adopted in these calculations do not frequently meet the usual impregnating conditions. For example, these calculations concern adsorption of a TMIS on only one crystal face among others exposed by the nanocrystals comprised the support grains. Therefore, at present, these calculations may be considered as a part of the whole approach illustrated in Figure 2.6.

2.6.5

Electrochemical (Equilibrium) Modeling

The joint use of the aforementioned adsorption–electrochemical and spectroscopic techniques, *over a wide range of impregnation parameters*, allows the predominant *mode of interfacial deposition and the interface speciation/structure* of the deposited precursor species to be approached, for each value of these parameters. The next step is to use this information, and eventually information drawn from quantum-mechanical calculations, in order to depict several *tentative pictures* for the interface, for a given set of impregnation parameters. These pictures should be tested quantitatively by applying the proper combination of a *surface ionization/interfacial model*.

In view of the considerations involved in the section entitled “*the surface of the oxidic supports: surface ionization models*”, it is understandable that the accuracy of the modeling increases using the more realistic multisite site approach, instead of the hypothetical one-site/two-pK or one-site/one-pK models. In this

context the calculation of the charge of the receptor hydr(oxo) groups following a quantum-mechanical method instead of the Pauling valence bond empirical method increases further the accuracy of the modeling. On the other hand, the interfacial model chosen should be compatible with the tentative pictures under testing. In this respect the modern *three plane model* is very useful [1, 40].

The modeling takes into account the mass and the charge balance equations as well as the equilibrium equations for each species being at the various planes (or layers) of the interface and in the solution as well. It is performed at three steps. First, in the impregnating *solution*, that is in the absence of the support grains, to obtain the speciation of the TMIS in the solution. Second, in the impregnating *suspension* in the presence of the indifferent ions *but in the absence* of the TMIS to be deposited. In the second step the capacity values for the first two layers, the protonation constants for the surface (hydr)oxo-groups and the constants of the ion-pair formation of indifferent ions are determined by fitting the experimental potentiometric titration data, taken at various ionic strengths, with the corresponding potentiometric titration curves calculated on the basis of the surface ionization/interfacial model adopted. Finally, the modeling is performed in the impregnating *suspension* in the presence of both the indifferent ions and the TMIS to be deposited. The parameters determined in the second step are used in the final one.

A successful modeling *must* describe the macroscopic adsorption data (adsorption isotherms, adsorption edges, the aforementioned plots “amount of the H^+ ions released (adsorbed) vs. amount of cationic (anionic) TMIS adsorbed”, potentiometric titrations, microelectrophoretic mobility or steaming potential data over a wide range of pH, ionic strength and concentrations of the TMIS in the solution, using the minimum number of adjustable parameters.

The subtitle modeling is performed using various calculating programs developed for the computation of chemical equilibrium composition both in the bulk solution and inside the interface [47–50].

2.7

A Case Study: The Deposition of $\text{Co}(\text{H}_2\text{O})_6^{2+}$ Aqua Complex on the Titania Surface

2.7.1

Experimental Investigation

Following the general approach illustrated in Figure 2.6 we attempted to elucidate the mode of interfacial deposition and the local structure of the deposited title species on the titania surface [51]. The system was studied at 25°C , pH range 6.0–7.5, metal concentration range $10^{-3} - 2 \times 10^{-2}$ M and ionic strength $I = 0.1$ N. Polycrystalline titania rich in anatase (Degussa P25) has been used.

First, there was no experimental evidence for interface polymerization and precipitation or titania surface dissolution. Moreover, considerable deposition was found even at pzc and a considerable decrease of pH upon adsorption. Moreover, it was observed that the presence of the aqua complexes in the impregnating solution brings about an important shift of the pzc (iep) to lower (higher) values and an increase of the electrokinetic charge or ζ -potential values determined at various pHs. Finally, a value equal to about 2 was determined for the ratio “amount of H^+ ions released/amount of cationic species adsorbed”. The above indicated the formation of rather mononuclear and perhaps a small quantity of oligonuclear inner-sphere complexes under our experimental conditions. Moreover, the value for the aforementioned ratio suggested a rather disubstituted local structure for the deposited Co(II) mononuclear precursor species. The DR spectra recorded after the equilibration of the suspensions and filtration also indicated the formation of surface inner-sphere complexes.

2.7.2

Quantum-Mechanical Calculations

Semiempirical quantum-mechanical calculations performed for the anatase (1 0 1) and (1 0 0) crystal faces showed that at relatively low and medium Co(II) surface concentration the mononuclear disubstituted configuration (BO–TO) in which two water ligands of the $Co(H_2O)_6^{2+}$ aqua complex are exchanged with two surface oxygens is very stable. The one surface oxygen is terminal bonded with *one* surface titanium atom (TO) and the other is bridging bonded with *two* surface titanium atoms (BO). A disubstituted configuration where both surface oxygens are terminal ones was proved to be also very stable (TO–TO).

The above are in line with geometrical findings. In fact, by determining the distances BO–TO for the low-index terminations of the anatase [(1 0 1), (1 0 0), (0 0 1)] we found that in all cases this distance is very close to the O–O distance for two adjacent equatorial oxygens of the $Co[(H_2O)_6]^{2+}$ aqua complex. Thus, the formation of the above disubstituted structure does not require considerable displacement of the titania surface oxygens. In contrast, the BO–BO distance in the anatase low-index terminations is greater than the aforementioned distance in the aqua complex, whereas the displacements of the surface oxygen atoms in this quite rigid structure are very difficult. In contrast, this displacement is easier in the more flexible TO–TO structure and this renders this structure energetically more favorable than the BO–BO one, though the initial O–O distance in the TO–TO structure is equal to that in the BO–BO structure. The quite unstable monosubstituted TO configuration was stabilized provided that the mononuclear Co(II) complex forms two additional hydrogen bonds with two adjacent terminal oxygens (TO..TO..TO configuration). The pure monosubstituted TO and BO configurations are rather unstable. *The above indicate that there is perhaps an inherent tendency*

for increasing the number of the coordinative bonds between $\text{Co}(\text{II})$ and surface oxygens provided that this is geometrically feasible. This is corroborated by the transformation of the $\text{TO}-\text{TO}$ into the $\text{TO}-\text{TO}-\text{TO}$ structure on the anatase (1 0 0) crystal face and the high stability of the latter as well. In fact, in this crystal phase there is a suitable arrangement of three terminal oxygens that allow the aforementioned transformation.

2.7.3

Electrochemical (Equilibrium) Modeling

Taking into account the above experimental and theoretical results, we have tested several more or less possible tentative structures (BO , TO , $\text{BO}-\text{BO}$, $\text{BO}-\text{TO}$, $\text{TO}-\text{TO}$, $\text{TO}\dots\text{TO}\dots\text{TO}$, $\text{TO}-\text{TO}-\text{TO}$). It was found that none of these structures may describe our adsorption and electrochemical results. In contrast, assuming hydrolysis of one (two) water ligand(s) of the tested inner-sphere complexes it was found that the aforementioned very stable $[\text{BO}-\text{TO}][(\text{TO}-\text{TO})]$ structure may describe very well the experimental results at low and medium $\text{Co}(\text{II})$ surface concentrations and over the whole range of *pHs and ionic strengths*. As an example, these structures are illustrated for the anatase (1 0 0) crystal face (Figure 2.7).

In order to describe the experimental results even at relatively high $\text{Co}(\text{II})$ surface concentrations, it was assumed that an oligonuclear $\text{Co}(\text{II})$ complex is formed in addition to the mononuclear one. The interface speciation achieved has shown that the surface concentration of this oligonuclear $\text{Co}(\text{II})$ complex, being negligible at low and medium $\text{Co}(\text{II})$ surface concentrations, becomes considerable at relatively high $\text{Co}(\text{II})$ surface concentrations. The formation of the above inner-sphere complexes is in line with previous EXAFS results taken on polycrystalline anatase [52–54].

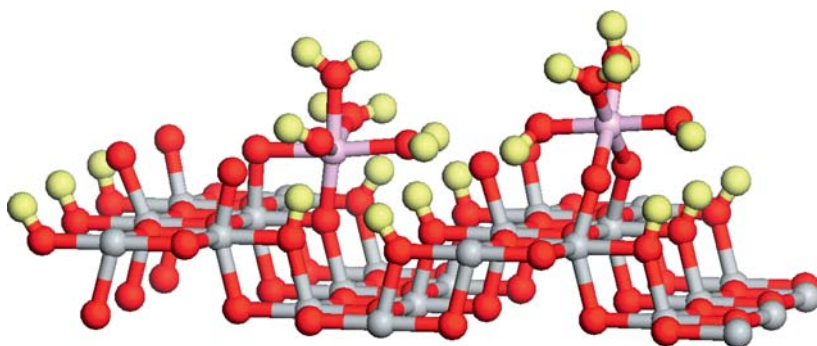


Figure 2.7 The $\text{TO}-\text{TO}$ (right) and $\text{BO}-\text{TO}$ (left) configurations of the $\text{Co}(\text{II})$ inner-sphere complexes formed on the anatase (1 0 0) crystal face: the O, Ti, H, and Co atoms are represented respectively by red, gray, yellow, and pink balls.

References

1. Bourikas, K., Kordulis, Ch. and Lycourghiotis, A. (2006) *Catal. Rev.*, **48**, 363.
2. Lycourghiotis, A., Kordulis, Ch. and Bourikas, K. (2002) *Encyclopedia of Surface and Colloid Science*, Marcel Dekker, New York, p. 1366.
3. Ataloglou, T., Vakros, J., Bourikas, K., Fountzoula, Ch., Kordulis, Ch. and Lycourghiotis, A. (2004) *Appl. Catal. B*, **57**, 299.
4. Bourikas, K., Panagiotou, G.D., Petsi, Th., Kordulis, Ch. and Lycourghiotis, A. (2006) *Stud. Surf. Sci. Catal.*, **162**, 809.
5. Panagiotou, G.D., Petsi, Th., Stavropoulos, J., Bourikas, K., Garoufalis, Ch.S., Kordulis, Ch. and Lycourghiotis, A. (2006) *Stud. Surf. Sci. Catal.*, **162**, 251.
6. Bitter, J.H., van der Lee, M.K., Slotboom, A.G.T., van Dillen, A.J. and de Jong, K.P. (2003) *Catal. Lett.*, **89**, 139.
7. Toebes, M.L., van der Lee, M.K., Tang, L.M., Huis in't Veld, M.H., Bitter, J.H., van Dillen, A.J. and de Jong, K.P. (2004) *J. Phys. Chem. B*, **108**, 11611.
8. Patil, N.S., Uphade, B.S., McCulloh, D.G., Bhargava, S.K. and Choudhary, V.R. (2004) *Catal. Commun.*, **5**, 681.
9. Bezemer, G.L., Radstake, P.B., Koot, V., van Dillen, A.J., Geus, J.W. and de Jong, K.P. (2006) *J. Catal.*, **237**, 291.
10. Thiel, P.A. and Madey, T.E. (1987) *Surf. Sci. Rep.*, **7**, 211.
11. Bourikas, K., Kordulis, Ch., Vakros, J. and Lycourghiotis, A. (2004) *Adv. Colloid Interface Sci.*, **110**, 97.
12. Bourikas, K., Kordulis, Ch. and Lycourghiotis, A. (2006) *Adv. Colloid Interface Sci.*, **121**, 111.
13. Bourikas, K., Kordulis, Ch. and Lycourghiotis, A. (2006) *J. Colloid Interface Sci.*, **296**, 389.
14. Parks, G.A. (1965) *Chem. Rev.*, **65**, 177.
15. Bolt, G.H. and Van Riemsdijk, W.H. (1982) *Soil Chemistry B: Physico-Chemical Models*, 2nd edn (ed. G.H. Bolt), Elsevier, Amsterdam.
16. Van Riemsdijk, W.H., Bolt, G.H., Koopal, L.K. and Blaakmeer, J. (1986) *J. Colloid Interface Sci.*, **109**, 219.
17. Van Riemsdijk, W.H., De Wit, J.C.M., Koopal, L.K. and Bolt, G.H. (1987) *J. Colloid Interface Sci.*, **116**, 511.
18. Hiemstra, T., Venema, P. and Van Riemsdijk, W.H. (1996) *J. Colloid Interface Sci.*, **184**, 680.
19. Pauling, L. (1929) *J. Am. Chem. Soc.*, **51**, 1010.
20. Brown, I.D. (1977) *Acta Cryst. B*, **33**, 1305.
21. Brown, I.D. (1978) *Chem. Soc. Rev.*, **7**, 359.
22. Brown, I.D. and Altermatt, D. (1985) *Acta Cryst. B*, **41**, 244.
23. Panagiotou, G.D., Petsi, Th., Bourikas, K., Garoufalis, Ch.S., Kamarianakis, G., Spanos, N., Kordulis, Ch. and Lycourghiotis, A. (2008) *Adv. Colloid Interface Sci.*, **142**, 20.
24. Stern, O. (1924) *Z. Electrochem.*, **30**, 508.
25. Bowden, J.W., Posner, A.M. and Quirk, J.P. (1977) *Aust. J. Soil. Res.*, **15**, 121.
26. Stumm, W., Huang, C.P. and Jenkins, S.R. (1970) *Croat. Chem. Acta*, **42**, 223.
27. Hohl, H. and Stumm, W. (1976) *J. Colloid Interface Sci.*, **55**, 281.
28. Kummert, R. and Stumm, W. (1980) *J. Colloid Interface Sci.*, **75**, 373.
29. Yates, D.E., Levine, S. and Healy, T.W. (1974) *J. Chem. Soc. Faraday Trans. I.*, **70**, 1807.
30. Davis, J.A., James, R.O. and Leckie, J.O. (1978) *J. Colloid Interface Sci.*, **63**, 480.
31. Westall, J. and Hohl, H. (1980) *Adv. Colloid Interface Sci.*, **12**, 265.
32. Hiemstra, T. and Van Riemsdijk, W.H. (1991) *Colloids Surf.*, **59**, 7.
33. Hiemstra, T. and Van Riemsdijk, W.H. (1996) *J. Colloid Interface Sci.*, **179**, 488.

34. Rahnemaie, R., Hiemstra, T. and Van Riemsdijk, W.H. (2006) *J. Colloid Interface Sci.*, **293**, 312.
35. Bourikas, K., Hiemstra, T. and Van Riemsdijk, W.H. (2001) *Langmuir*, **17**, 749.
36. Predota, M., Zhang, Z., Fenter, P., Wesolowski, D.J. and Cummings, P.T. (2004) *J. Phys. Chem. B*, **108**, 12061.
37. Zhang, Z., Fenter, P., Cheng, L., Sturchio, N.C., Bedzyk, M.J., Predota, M., Bandura, A., Kubicki, J.D., Lvov, S.N., Cummings, P.T., Chialvo, A.A., Ridley, M.K., Benezeth, P., Anovitz, L., Palmer, D.A., Machesky, M.L. and Wesolowski, D.J. (2004) *Langmuir*, **20**, 4954.
38. Hiemstra, T. and Van Riemsdijk, W.H. (2006) *J. Colloid Interface Sci.*, **301**, 1.
39. Boujday, S., Lambert, J.F. and Che, M. (2004) *Chem. Phys. Chem.*, **5**, 1003.
40. Bourikas, K., Hiemstra, T. and Van Riemsdijk, W.H. (2001) *J. Phys. Chem. B*, **105**, 2393.
41. Carrier, X., Lambert, J.F. and Che, M. (1997) *J. Am. Chem. Soc.*, **119**, 110137.
42. Shelimov, B., Lambert, J.F., Che, M. and Didillon, B. (1999) *J. Catal.*, **185**, 462.
43. Vakros, J., Bourikas, K., Perlepes, S., Kordulis, Ch. and Lycourghiotis, A. (2004) *Langmuir*, **20**, 10542.
44. Louis, C. and Che, M. (1992) *J. Catal.*, **135**, 156.
45. Spieker, W.A., Liu, J., Hao, X., Miller, J.T., Kropf, A.J. and Regalbuto, J.R. (2003) *Appl. Catal. A*, **243**, 53.
46. Lefevre, G. (2004) *Adv. Colloid Interface Sci.*, **107**, 109.
47. Schecher, W.D. and McAvoy, D.C. (1998) MINEQL+ A Chemical Equilibrium Modeling System: Version 4.0 for Windows User's Manual. Environmental Research Software, Hallowell, Maine.
48. Gustafsson, J.P. (2005) Visual MINTEQ Version 2.40. Department of Land and Water Resources Engineering, Royal Institute of Technology, Stockholm.
49. Keizer, M.G. and Van Riemsdijk, W.H. (1998) ECOSAT: Technical Report of the Department of Soil Science and Plant Nutrition. Wageningen University, Wageningen.
50. Papelis, G., Hayes, K.F. and Leckie, J.O. (1988) Hydraql: A Program for the Computation of Chemical Equilibrium Composition of Aqueous Batch System Including Surface Complexation Modeling of Ion Association at the Oxide/Solution Interface. Technical Report No. 306. Stanford University, Stanford.
51. Petsi, Th., Garoufalidis, Ch.S., Bourikas, K., Panagiotou, G.D., Kordulis, Ch., Stathi, P., Deligiannakis, Y. and Lycourghiotis, A. to be submitted.
52. Chisholm-Browse, C.J., O'Day, P.A., Brown, G.E. Jr. and Parks, G.A. (1990) *Nature*, **348**, 528.
53. O'Day, P.A., Chisholm-Browse, C.J., Towle, S.N., Parks, G.A. and Brown, G.E. Jr. (1996) *Geochim. Cosmochim. Acta*, **60**, 2515.
54. Towle, S.N., Brown, G.E. Jr. and Parks, G.A. (1999) *J. Colloid Interface Sci.*, **217**, 299.

3

Electrostatic Adsorption

John R. Regalbuto

3.1

Introduction

Among the many methods to prepare supported metal catalysts, impregnation is the simplest and most prevalent. In this type of preparation, metal complexes are typically dissolved in water, and these metal-bearing solutions are contacted with the porous catalyst supports that ultimately serve to anchor the reduced metal particles against sintering during high-temperature operation in a catalytic reactor. Small particle size is normally preferred since it maximizes the metal area available for the reaction. The practical challenge of supported metal catalyst preparation is how to prepare the smallest, most stable metal particles by the simplest and cheapest method. The fundamental challenge of preparation is to understand the mechanism of the adsorption process. With sufficient insight, the “art” of catalyst preparation may be turned into a “science.”

In this chapter, it will be suggested that an electrostatic view of metal adsorption onto support surfaces may in many cases provide a simple and effective basis not only of the practical aspects of catalyst preparation but also as a starting point for rational catalyst design. Components of an electrostatic adsorption mechanism are illustrated in Figure 3.1a. An oxide surface contains terminal hydroxyl groups that are protonated or deprotonated depending of the acidity of the impregnating solution. The pH at which the hydroxyl groups overall are neutral is termed the point of zero charge (PZC). Below this pH, the hydroxyl groups are protonated and become positively charged, and the surface can adsorb anionic metal complexes such as hexachloroplatinate, $[\text{PtCl}_6]^{-2}$ (commonly denoted as CPA, since it arises from chloroplatinic acid). Above the PZC, the hydroxyl groups are deprotonated and become negatively charged, and cations such as platinum tetraammine (PTA), $[(\text{NH}_3)_4\text{Pt}]^{+2}$, can be strongly adsorbed.

This electrostatic mechanism was advanced for catalyst preparation in the seminal paper of Brunelle [1] and the pioneering work of Schwarz [2–5] and Contescu and Vass [6]. Our own work has involved the qualitative

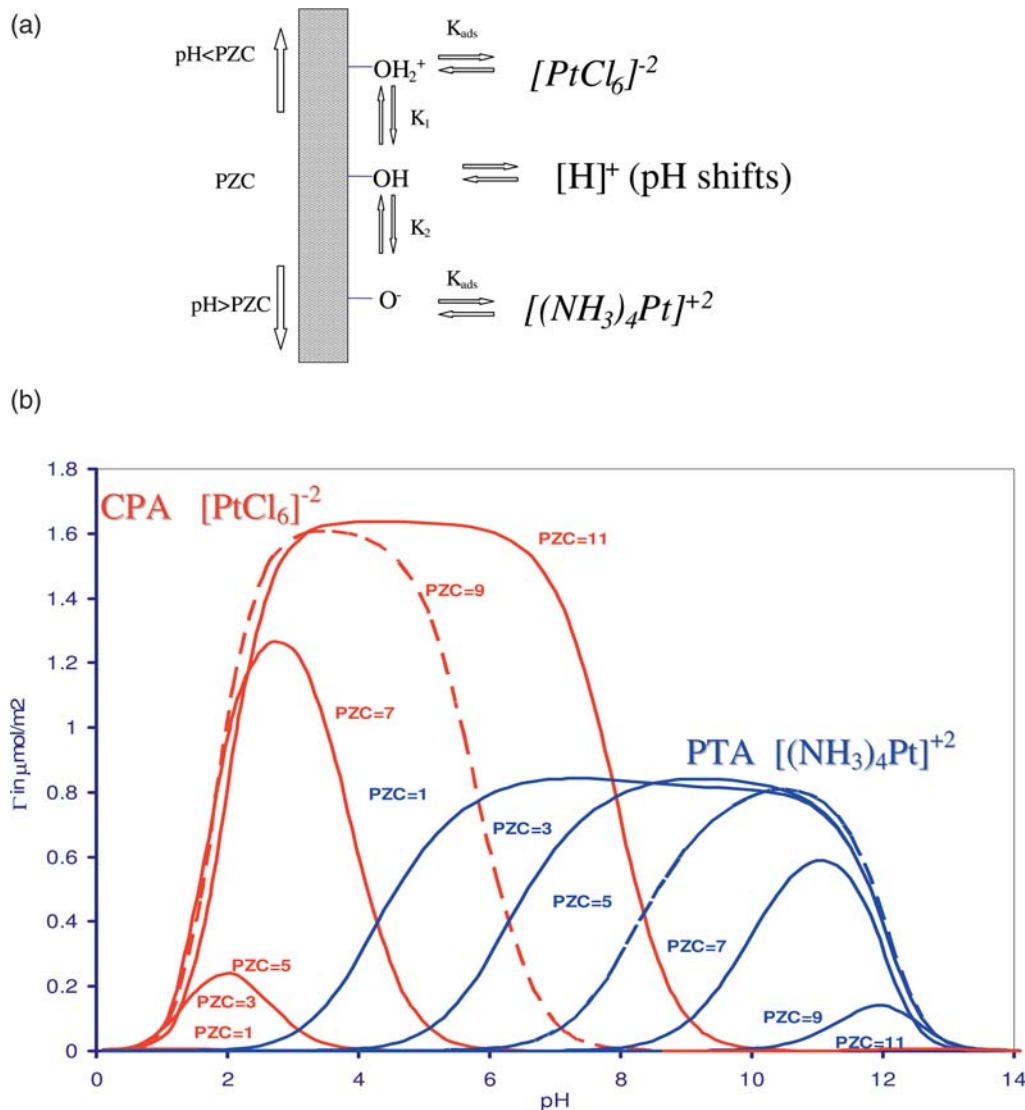


Figure 3.1 Electrostatic adsorption, (a) components of an electrostatic adsorption mechanism: surface charging, metal adsorption, and proton transfer, (b) simulation of uptake versus pH, for

surfaces of various PZCs of the revised physical adsorption model. The left-side curves correspond to the uptake of anionic CPA, the right side to cationic PTA.

establishment of the electrostatic mechanism [7, 8] as well as the quantification of proton transfer [9] and the adsorption mechanism [10, 11] that was adapted from the electric double-layer model of James and Healy [12] from the colloid

science literature. The historical development of this approach has been detailed in a separate review [13].

The “revised physical adsorption” (RPA) model [11] is illustrated in Figure 3.1b, in which the uptake of charged complexes is simulated over surfaces of various PZCs. In the left-hand set of curves, anionic platinum hexachloride, $[\text{PtCl}_6]^{-2}$, is taken as the adsorbate, while on the right the cationic PTA complex, $[(\text{NH}_3)_4\text{Pt}]^{+2}$ is assumed. Curves representative of silica (PZC near 4) and alumina (PZC near 8.5) are indicated by the dashed lines in Figure 3.1b. For CPA, Pt uptake increases as the pH falls from the PZC of each material, as the surface charges increase. At the low-pH extreme, adsorption is inhibited over all surfaces by high ionic strength [8, 11]. The materials with the highest PZC can attain the highest surface charge before the onset of high ionic strength inhibition, and so adsorb the highest density of Pt. A set of CPA adsorption data taken over a series of aluminas [8] reflects the dashed curve (PZC 9) on the left side of the figure. Analogously, it is the lowest PZC materials that adsorb the greatest amounts of the cationic Pt complex at high pH. High ionic strength inhibition also occurs at the high-pH extreme [14]. A set of PTA adsorption data taken over a series of silicas [14] reflects the dashed curve (PZC 5) in the right-hand side of the figure.

The maximum Pt uptake of both complexes appears to be dictated by a steric maximum, which can be calculated as a close-packed monolayer of complexes that retain either one hydration sheath in the case of the anionic chloride complexes, or two sheaths in the case of the cationic ammine complexes [7, 8, 11, 14]. On an areal basis, the maximum loading of CPA is about $1.6 \mu\text{mol}/\text{m}^2$ or about 1 complex/ nm^2 , and that of PTA is about $0.84 \mu\text{mol}/\text{m}^2$ or 1 complex/ 2 nm^2 . These densities are well below hydroxyl group densities, which are typically cited as $8 \text{ OH}/\text{nm}^2$ for alumina, and $5 \text{ OH}/\text{nm}^2$ for silica [13].

Impregnation can be termed wet or dry depending on whether the volume of impregnating solution is in excess or equal to the pore volume of the support. Dry impregnation (DI), in which the amount of metal-loaded solution is added to a porous oxide in just the amount needed to fill the pore volume is alternatively termed “incipient wetness impregnation” as well as “pore filling.” Wet impregnation in general refers to the use of an amount of liquid in excess of the substrate pore volume. In both of these methods, pH is usually not controlled, and the final pH of the impregnating solution can vary quite dramatically and often ends up near the support PZC, at which point no metal precursor–support interaction occurs [9]. This has been referred to as the oxide’s pH buffering effect; it stems from the fact that the hydroxyl-group density of common catalysts supports, combined with the high specific surface area of such supports, means that the total number of OH groups on a support surface is very large relative to the protons or hydroxyl groups initially present in an impregnating solution. Solutions that are only mildly acidic or basic (say pH 3 or 11) do not contain sufficient proton cations or hydroxyl anions to protonate or to deprotonate a significant fraction of the surface. The relatively

small amount of proton transfer that does occur, however, brings the solution pH to the support PZC.

A key parameter when considering impregnation fundamentals such as the pH buffering effect is “surface loading,” or the area of support surface per volume of surface, with units m^2/l . DIs correspond to the highest achievable surface loadings, which are often several hundred thousand m^2/l , while typical laboratory wet impregnations can be orders of magnitude below that. Proton transfer to and from the support surface, shown in Figure 3.1a, was quantified in the context of catalyst preparation over a decade ago [9] and can be quite drastic, even for moderate surface loadings. This is evidenced by Figure 3.2, in which representative pH shifts are given for an alumina of PZC 8 and with a specific surface area of $180 \text{ m}^2/\text{g}$. For a slurry of only 5 wt% alumina, or about $1000 \text{ m}^2/\text{l}$, an initial pH of 3 will equilibrate at a final pH of over 7. This is well away from the optimal pH for the adsorption of CPA, for example, which occurs at a pH of about 3–4 (Figure 3.1).

The whole idea of strong electrostatic adsorption (SEA), then, is to control the pH of the excess liquid so as to arrive at the optimal pH where metal complex–surface interaction is strongest. Calculations and experimental validation such as seen in Figures 3.1b and 3.2 can be used to anticipate the initial pH that gives the optimal final pH. The pH buffering effect has been reviewed in more detail [15] and will be discussed further in the last section of this chapter.

Electrostatic adsorption is not, of course, the only mechanism through which metals interact with high surface area supports. Ion exchange (IE) most appropriately applies to a microscopic electrostatic driving course at framework aluminum sites in zeolites, which is very strong and largely independent of solution pH. A direct exchange of a metal cation and an H^+ or Na^+ counterion occurs. Other impregnation methods often involving the manipulation of

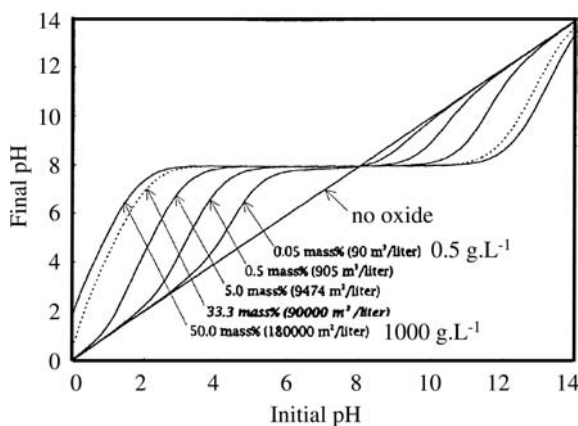


Figure 3.2 pH shifts (pH final versus pH initial) as a function of surface loading for alumina with PZC = 8.

solution pH are deposition-precipitation (DP) or coprecipitation, which are comprehensively reviewed in Chapters 6 and 7 of this book. The general idea is that by slowly and homogeneously altering solution conditions, metal complexes can be induced to precipitate in a controlled fashion on the support surface as small particles, even at high loadings over oxide [16, 17] as well as carbon [18, 19] supports. Impregnation sometimes involves reaction, as in the formation of Ni phyllosilicates when Ni is contacted with amorphous silica [20]. In fact, chemical interactions between precursors and supports can be understood in terms of a coordination chemistry or geochemical mechanism, the driving force for which is the chemical potential for the formation of a new solid phase such as phyllosilicates [20], hydrotalcites [21], or mixed-metal oxides [22]. These impregnations can be collectively termed “reactive adsorption.”

In many of these cases it appears that electrostatic adsorption plays a role in these more complicated mechanisms. From (i) the simplest, most purely electrostatic case, the adsorption mechanism can get more complicated if (ii) the metal coordination complex undergoes respeciation in response to the local conditions at the adsorption plane, (iii) if IE accompanies electrostatic adsorption, or if electrostatic adsorption precedes or accompanies (iv) DP, (v) surface reaction, or (vi) support dissolution, reaction, and redeposition. Each of these cases will be treated in a subsequent section.

It will be suggested that the role of electrostatics in each is central enough to allow at least a qualitative design of many more sophisticated catalyst materials, with a procedure that is simple and scalable. Beyond single metals, examples will be given of the design of promoted catalysts in which the active metal can be steered onto the promoter phase and not the support phase, and bimetallic catalysts in which one metal can be directed onto another and not the support, in all cases with metal particles that are very well dispersed.

3.2

Purely Electrostatic Adsorption

The most straightforward case of electrostatic adsorption occurs with the most stable metal complexes such as platinum or palladium tetraammines, $[(\text{NH}_3)_4\text{Pt}]^{+2}$ and $[(\text{NH}_3)_4\text{Pd}]^{+2}$ or PTA and PdTAs, respectively. Over the wide pH and concentration ranges that can be employed during syntheses from the lab to the industrial scale, the relatively strongly bound ammine ligands of these coordination complexes remain intact. This has been most directly confirmed in the case of Pt by extended X-ray absorption fine structure (EXAFS) analysis of PTA solutions and adsorbed species [23], and for PdTAs less directly by XPS [24].

Since these are cationic species, low PZC supports that deprotonate and charge negatively at high pH are good candidates for strong electrostatic interactions at high pH. The uptake of PTA and PdTAs versus pH are shown

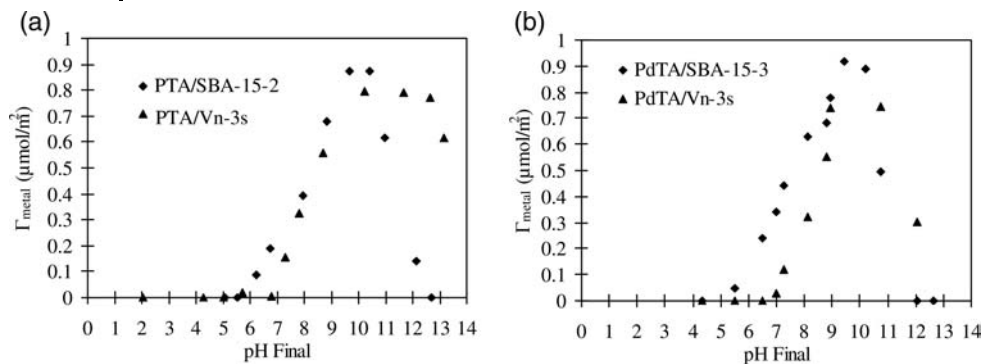


Figure 3.3 Pure electrostatic uptake versus pH of (a) PTA and (b) PdTAs over nonordered silica and ordered mesoporous silica.

in Figure 3.3 over both a nonordered silica [14, 24] and ordered mesoporous SBA-15 [24], both of which have PZCs near 4. These uptake–pH surveys, similar to those seen in Figure 3.1b, have been conducted with a constant metal concentration, usually in excess of a monolayer, and are a central component of the SEA method. The great difference in the surface areas of these silicas ($175 \text{ m}^2/\text{g}$ for the Vn-3 s and 575 and $998 \text{ m}^2/\text{g}$ for the SBA-15-2 and -3, respectively) was accounted for by using different masses of each that gave the same surface loading, $1000 \text{ m}^2/\text{l}$ in this case. In this way, the metal species “sees” the same amount of surface for each material. In all cases the uptake curves are similar over the two materials. The adsorption maximum occurs at about a pH of 11 for the amorphous silica, and 10 for the SBA-15 s.

Electron micrographs of the SEA-prepared Pt and Pd materials after reduction [24] are given in Figure 3.4 for both the nonordered supports (Figures 3.4a and b) and ordered mesoporous silica (Figures 3.4c and d). For both metals over both supports, particles only slightly larger than 1 nm, with relatively narrow particle sizes, have been produced. It is notable that these small sizes have been obtained at relatively high weight loadings; 2.8 and 9.2 wt% for the microporous and mesoporous Pt materials, and 2.2 and 8.7 wt% for the analogous Pd materials. In contrast, DI preparations give much larger average particle sizes with much broader size distributions [24]. Representative micrographs from a DI mesoporous Pt sample and a DI microporous Pd sample are given in Figures 3.4e and f.

3.3

Electrostatic Adsorption with Metal Respeciation

While the volcano-shaped uptake curve of the CPA complex on alumina such as seen in Figure 3.2b can be well simulated by the RPA model [8], there is a subtle variation in this case stemming from the instability of the hexachloroplatinate

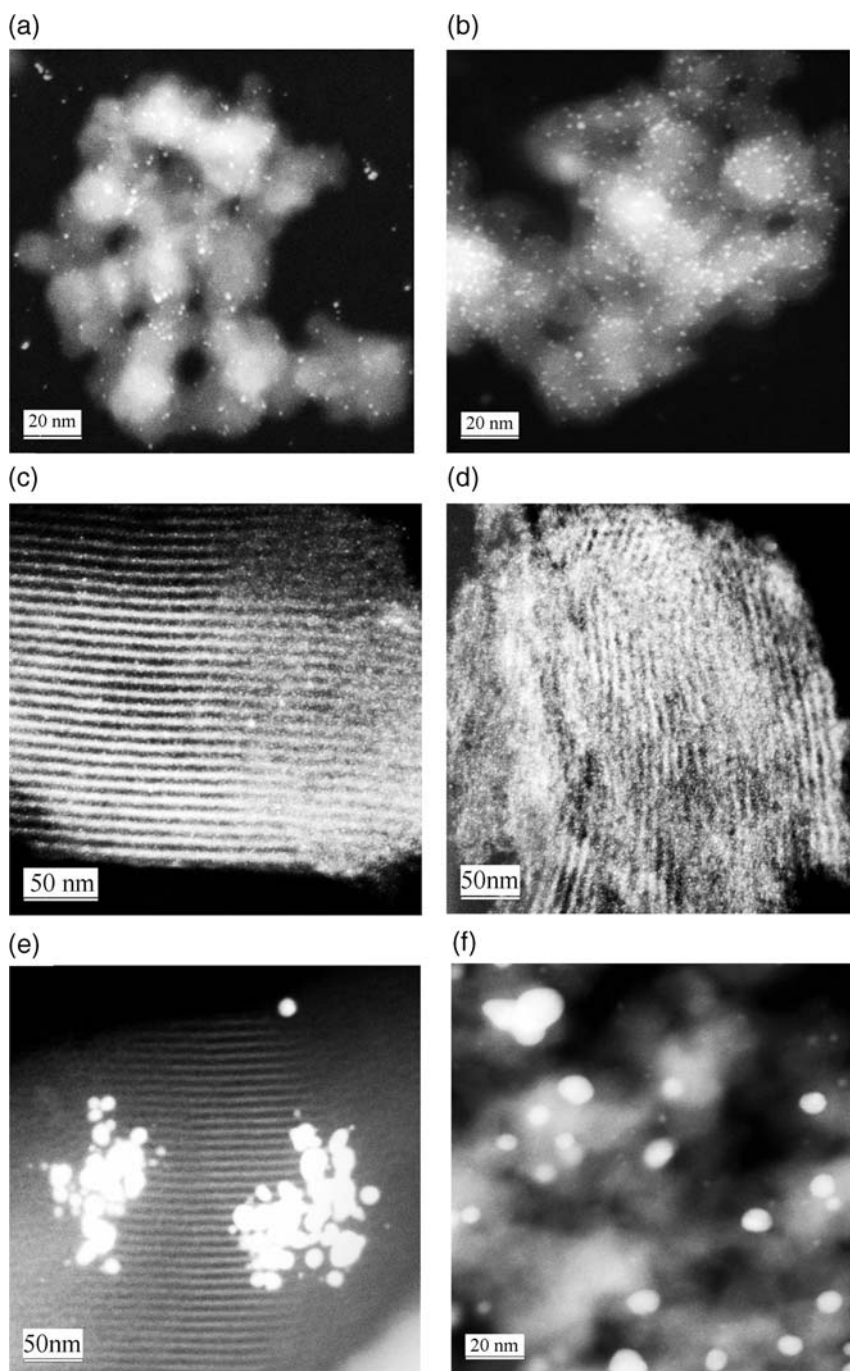


Figure 3.4 Electron micrographs of SEA on ordered mesoporous silica, and prepared (a) 2.8 wt% Pt and (b) 2.2 wt% Pd on nonordered silica and (c) 9.2 wt% Pt and (d) 8.7 wt% Pd on ordered mesoporous silica, and DI preparations of (e) 9.2 wt% Pt and (f) 8.7 wt% Pd on nonordered silica. (From [24] with permission from Elsevier.)

species $[\text{PtCl}_6]^{-2}$. The most recent speciation study of dilute CPA solutions was performed using EXAFS [25] and revealed a much more extensive speciation pathway than had previously been proposed.

In this matrix the hexachloro species is present only at high concentrations and low pH; aquo and hydroxo ligands exchange for chloride as solutions become more dilute or “background” chloride concentration is lowered. For example, when 200 ppm CPA is dissolved in water with no background Cl^- , it was surmised that three chloride ligands immediately exchange for water ligands, after which a slower hydroxyl–water exchange occurs that is evidenced by a slow decrease in solution pH. These ligand exchange reactions occur over several days, but may be catalyzed by a solid surface [25]. The long-term species may be something like $[\text{PtCl}_2(\text{OH})_4]^{-2}$. Since this species has the same valence and about the same size (remembering that the radius of the Pt complex is washed out by an additional diameter of the water sheath), the RPA model can be applied without incorporating different adsorbing species.

An interesting EXAFS analysis of solution versus adsorbed species is given in Table 3.1 from [26]. By adding background chloride to dilute CPA solutions, hexachloro species could be prepared at the same pH values that chloroaquo-hydroxo species would otherwise predominate. Adsorbed onto alumina, both the high chloride and the low chloride bulk liquid species assumed the same composition at the surface (Table 3.1); the high-chloride species lost a great deal of chloride (about four ligands on average), and the low-chloride species lost a little (perhaps one ligand on average). The speciation of these adsorbed complexes falls in between that of fresh and aged solution species containing no excess chloride.

The explanation for this behavior draws on electric double-layer theory [26]; the local pH is a function of the distance from the adsorption plane and can vary quite considerably (several pH units) from the bulk. Presumably the local chloride concentration reduces in the same way, as the Pt anion-filled surface is approached. It can be argued that the respeciation of Pt evidenced in Table 3.1 is simply in response to the local solution conditions at the adsorption plane.

Table 3.1 EXAFS Pt–Cl coordination number (± 0.3) as a function of added NaCl and surface loading (series A).

Sample	Target wt.% Pt	Surface loading (m^2/l)	NaCl (mol/l)	Initial pH	CN Cl liquid	Final pH	CN Cl solid	Actual wt.% Pt
A 1	1	5000	–	2.63	2.7	4.34	1.6	1.0
A 2	1	5000	0.1	2.60	6	5.59	1.5	0.7
A 3	4.8	1000	–	2.59	2.7	2.84	2.1	3.7
A 4	4.8	1000	0.1	2.54	6	3.43	1.9	1.9
A 5	7.2	650	–	2.50	2.7	2.81	2.1	4.1
A 6	7.2	650	0.01	2.55	(6) ^a	2.87	2.2	3.2

^aEstimated from [1], not measured.

The same argument has been advanced more quantitatively for the respeciation of gold chlorides adsorbed onto alumina [27]. The adsorbed Au complexes contain less chloride than those in solution at the same bulk pH, however, when the data for the adsorbed species was replotted at the estimated surface pH, the speciation agreed reasonably well with the bulk-solution species.

Electrostatic adsorption with respeciation has also been suggested for cationic ammine species of copper [28] that appear to be less stable than the Pt and Pd amines. In the typical uptake–pH and pH shift experiments of the SEA method, shown in Figure 3.5, the speciation of Cu tetraammine is indicated by several factors. First, the uptake of Cu at $2.5 \mu\text{mol}/\text{m}^2$ (Figure 3.5a) is much higher than is normally seen (PTA is shown for the sake of reference). Second, the pH shifts seen with the copper tetraammine (CuTA) solutions are different from the control experiments (Figure 3.5b). When a stable complex like PTA is adsorbed, the pH shifts that occur in the metal adsorption experiment are essentially the same as pH shifts from a metal-free control experiment due to oxide buffering. The similarity of the PTA and the control pH shift data are seen in Figure 3.5b. In fact, the pH shift data of the adsorption experiment is a good diagnostic for the mechanism of adsorption; when pH shifts are essentially the same with and without metal, it can be assumed that proton exchange and adsorption occur independently, which is consistent with electrostatic adsorption.

An electrostatic mechanism with respeciation provides a reasonable explanation for the formation of the hydroxyl-bridged Cu dimer reported in the literature [28] in preparations with Cu amines; the tetraammine complex is electrostatically attracted to the silica surface, and when it approaches the surface it respeciates according to the local pH. The copper dimer species is more compact than monomeric Cu amines, and so attains a higher Cu surface density.

The uptake–pH surveys of a number of other metals (Ru(II), Ru(III), Co, and Ni beyond Cu, Pt and Pd) over amorphous and mesoporous silica have recently been reported [24]. It is believed in all cases that adsorption is all or mostly electrostatic, with minor deviations due to metal-complex respeciation (or in the case of Co, phyllosilicate formation at the highest pH, as will be discussed later). When synthesized at the optimal pH (10–11), very well dispersed particles form (with the exception once again of Co since Co amines reduce on silica only at temperatures in excess of 700°C , where sintering cannot be prevented). DI, on the other hand, yielded much larger particles for all metals over both types of supports.

3.4

Electrostatic Adsorption and Ion Exchange

The deposition of metal amines complexes onto silica at high pH is often referred to as “ion exchange.” In several recent papers we have suggested that electrostatic adsorption is a much better description of this phenomenon [14,

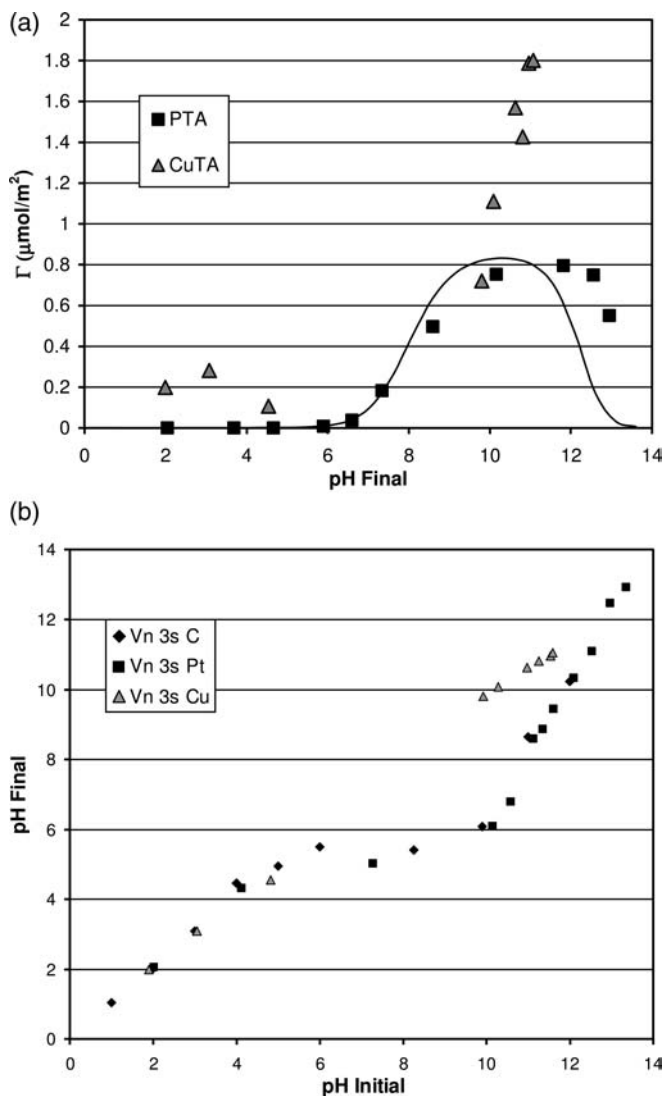


Figure 3.5 Copper tetraammine uptake onto silica Vn-3s: (a) uptake versus pH, with PTA added for comparison and (b) pH shifts, with PTA and a metal-free control experiment added for comparison. (Adapted from [28].)

24, 28] since the uptake (i) is very pH dependent yet produces no pH shifts that differ from metal-free control experiments and (ii) does not occur at the 2 : 1 proton : divalent cation stoichiometry of IE.

Perhaps the best example of IE in the realm of catalyst preparation is the uptake of cations into zeolites, usually in ratios that correspond to the amount

of framework aluminum, and that is largely pH independent [28]. On the other hand, there have been many reports of “overexchanged” zeolites, for zeolites with very low amounts of framework aluminum. Several studies suggest that an electrostatic adsorption mechanism may also apply under certain conditions on some zeolites [29, 30]. The excess exchange capacity of Pt amines into highly silicious zeolites under basic conditions has been associated with the presence of internal silanol groups [29]; this study concluded that there were two distinct adsorbed platinum species: one at the aluminum exchange sites and the other “exchanged” at silanols.

It has been amply demonstrated that Cu amines adsorb over silica in a pH-dependent fashion [24, 31–35] as in Figure 3.5 above, and that the uptake of copper into mordenite increased in ammonia [36–39].

It was hypothesized [28], therefore, that overexchange in zeolites is caused by electrostatic adsorption, and occurs only when the number of internal silanol groups greatly outnumbers the amount of framework aluminum. The interplay between IE and electrostatic adsorption mechanisms is illustrated in Figure 3.6. In Figure 3.6a three separate uptake curves are represented. The first is for pH-independent IE, which for a zeolite with an alumina content of 1 wt% and a surface area of $450 \text{ m}^2/\text{g}$ (typical of H-ZSM5) yields a metal surface density of $0.4 \text{ } \mu\text{mol}/\text{m}^2$. The second curve is for pH-dependent electrostatic adsorption of cations at the silanol groups, which is characteristically volcano-shaped with a maximum around pH 10–11. The maximum attainable surface density via electrostatic adsorption, as mentioned previously, corresponds to a close-packed layer of cationic complexes that retain two hydration sheaths. For Pt, this gives a density of $0.84 \text{ } \mu\text{mol}/\text{m}^2$. If both mechanisms are operative, the two curves would be coadded, producing the upper, third curve.

The relative importance and dependence of SEA and IE on the aluminum content of a zeolite is conveyed in Figure 3.6b in which the maximum surface density of exchanged and electrostatically adsorbed Pt is plotted versus wt% Al in a zeolite of surface area $400 \text{ m}^2/\text{g}$. The surface density of electrostatically adsorbed Pt appears as the horizontal dashed line at $0.84 \text{ } \mu\text{mol}/\text{m}^2$, while the maximum amount of platinum able to exchange into zeolites is determined by the aluminum content. The diagonal dotted line represents 100% exchange of metal, increasing linearly with Al content. Two regimes are delineated; to the left of the intersection of the SEA and IE curves, maximum uptake by SEA can be much greater than by IE. Such would be the case for typical ZSM% materials, which contain relatively little aluminum. The ZSM5 and ZSM11 materials referred to earlier [29] were in this range. On the other hand, to the right of the intersection IE dominates SEA and overexchange becomes negligible at high Al content.

This hypothesis has been confirmed [28] by Pt and Cu ammine adsorption experiments conducted with ZSM5, mordenite, and Y-54 zeolites with the aluminum contents indicated in Figure 3.6b, anticipating the hybrid uptake curve of Figure 3.6a in the case of overexchange. Results for the Pt and Cu ammine complexes were similar, which supports the notion of the last section

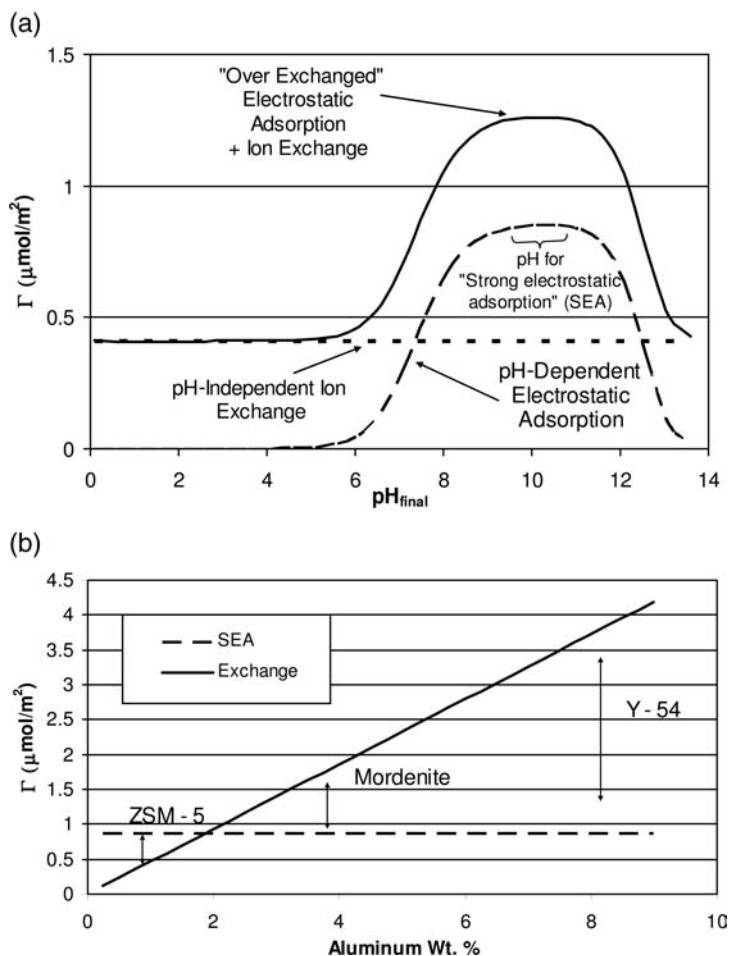


Figure 3.6 Hypothesis to explain metal uptake in zeolites: (a) uptake versus pH for ion exchange and SEA and (b) the prevalence of IE and SEA as a function of aluminum weight per cent. (Adapted from [28].)

that the Cu-adsorption mechanism is predominantly electrostatic. For the low-alumina zeolite (ZSM-5) the SEA maximum is achieved (or superseded in the case of Cu, for the reasons argued in the last section), giving rise to "overexchange." While the exchange capacities of the higher Al content zeolites were not exceeded, the influence of the electrostatic mechanism is evidenced by a volcano-shaped pH dependence in the high-pH range of these experiments. A small electrostatic component appears for both metals even in the highest Al content material, Y-54. The uptake of metal amines by zeolites appears to occur more by coadditive mechanisms than by a single, hybridized one.

3.5

Electrostatic Adsorption and Deposition-Precipitation

DP might be viewed as an extended case of adsorption with respeciation, presented earlier. Electrostatic adsorption and DP can be seen in the same context in Figure 3.7a, which contains one row of Pd solutions at various pH values (top row, from low pH on the left to high pH on the right) and another row of a similar set of Pd solutions that has been contacted with alumina. The conversion of 400 ppm yellow $[\text{PdCl}_4]^{-2}$ complexes into brown Pd aquohydroxides, which precipitate in the liquid phase over the course of hours, is seen when the pH is raised above about 4. This is accompanied by a drop in pH (pH values are written on the sides of the bottles) as there is a net replacement of Cl^- ligands with OH^- ligands, which releases protons. The types of Pd species that can form on an alumina surface are reflected in the colors of the alumina powders seen at the bottom of the lower row of bottles in Figure 3.7a. At the lowest pH, the powder is yellow, indicating that the species adsorbed is the chloride species. As the pH increases, the powder turns a homogeneous brown color, indicating the surface deposition of precipitates. With further increases in pH the brown Pd precipitate forms in solution and settles over the alumina powder, which remains white; this is bulk precipitation. This latter state indicates no interaction of the Pd precursors with the alumina support and the Pd particle size is controlled by aggregation in the liquid phase; very poor dispersion would normally result.

The origin of the surface precipitated phase may in fact be an extension of the adsorption and respeciation mechanism suggested earlier. It can be argued that, since the pH at the alumina surface is higher than the bulk pH, adsorption starts electrostatically and then the adsorbates respond to the local pH of the adsorption plane. This could well be the DP mechanism of Pd chlorides on alumina. Of course, the syntheses illustrated in Figure 3.7 are only very crude renderings of the DP procedure, as care is taken in the real procedure (see Chapter 6) to raise the pH very slowly.

A more detailed analysis of the transition of electrostatic adsorption to DP shown in Figure 3.7b was performed with EXAFS [40]. The solutions in the top row of bottles are the parent solutions of those contacted with alumina, shown in the bottom row. Whereas the pHs of the solutions at pH below 4.0 are stable, the pH of the alumina-contacted samples rose in response to the buffering effect of the alumina. EXAFS revealed that the parent solutions vary in composition from $[\text{PdCl}_4]^{-2}$ at the lowest pH values to $[\text{PdCl}_x(\text{OH})_y(\text{H}_2\text{O})_z]^n$ at the highest pH. EXAFS was also performed on the adsorbed species; Pd-contacted slurries were filtered and analyzed while still wet. Over alumina, there is little uptake at the lowest pH, as the alumina is almost white. This is expected for the lowest pH, highest ionic strength solutions. What does adsorb, though, remains as $[\text{PdCl}_4]^{-2}$. As the pH increases, the uptake of Pd increases as the alumina becomes more yellow and the adsorbing species remains as $[\text{PdCl}_4]^{-2}$. However, from a parent solution of pH 3.0 or 3.5 (top

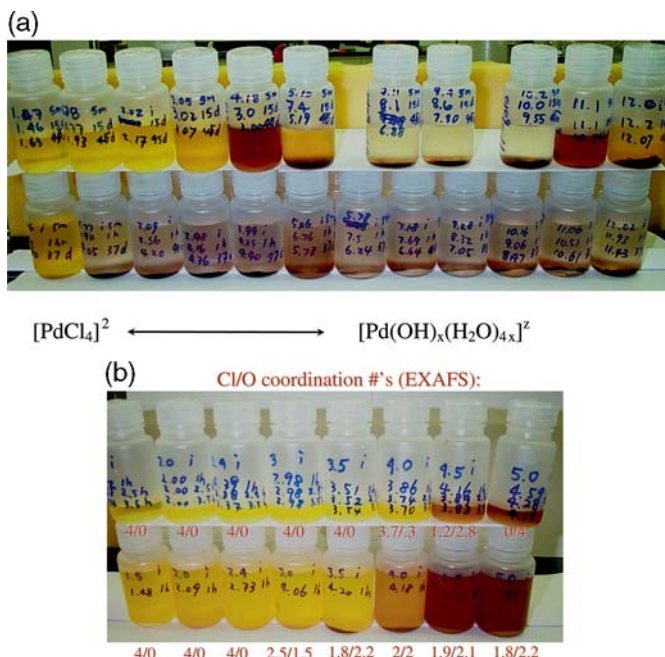


Figure 3.7 (a) Hydrolysis of Pd chloride solutions in solution and contacted with alumina; pH values with time listed on bottles and (b) Another set of parent and alumina contacted solutions with Cl/O coordination numbers from EXAFS.

row, fourth and fifth bottles from the left), in which the $[\text{PdCl}_4]^{-2}$ species and the pH were stable, the adsorbed species have lost considerable chloride and gained OH^- or H_2O ligands, to the extent that the adsorbate from the pH 3.5 solution has turned brown. They behave as if in the liquid phase at higher pH, which is explained not only by the buffering effect of the alumina, but also the increase of the local pH at the adsorption plane.

The reader is referred to Chapter 6 for an in-depth discussion of the DP method. The advantage of this method over SEA is that there is no monolayer adsorption limit with DP; it is possible to achieve acceptably high metal dispersions at metal loadings higher than can be achieved with SEA. In many cases this might compensate for the higher complexity of the DP process.

3.6

Electrostatic Adsorption and Surface Reaction

Metal-complex adsorption can directly lead to surface reaction, as has been observed recently for cobalt ammine complexes adsorbing over carbon substrates [41, 42]. The uptake of cobalt hexaammine (CoHA), $[(\text{NH}_3)_6\text{Co}]^{+3}$

was compared over silica and a graphitic carbon that both had PZCs of about 4. The pH shift and adsorption data for these two substrates are shown in Figure 3.8. A first indication of a different mechanism is the much higher uptake of Co over carbon than over silica, as seen in Figure 3.8a. The close clustering of final pH values is also notable, and is better seen in Figure 3.8b, in which final versus initial pH is plotted for the two adsorption experiments of Figure 3.8a, in addition to three control experiments for Co-free silica, carbon, and Co_3O_4 . The pH shift data for the silica and the CoHA/silica systems are about the same, and show a pH plateau near 5, typical of low surface loading silica with PZC 4 [41]. The pH plateau of the carbon substrate is at the same value, however, the CoHA/carbon plateau occurs at pH 9, which is close to the value of bulk Co_3O_4 . This result implies that the majority of area in the Co/C material is in fact cobalt oxide. Powder X-ray diffraction and X-ray absorption near-edge structure (XANES), and EXAFS of the just-dried CoHA/carbon sample revealed that the CoHA had converted to Co_3O_4 upon contact with the carbon [41]. The formation of Co_3O_4 has also been recently reported over carbon nanofibers as a cobalt carbonate precursor was deposited via DP at high pH [43]. Meanwhile, the cobalt hexammine adsorbed onto silica was tremendously robust; it did convert to Co(II) tetraammine at elevated calcination temperatures but thereafter could be reduced only at temperatures in excess of 650°C [41].

The striking difference in the behavior of CoHA over silica and carbon is illustrated in Figures 3.8c and d. The dried CoHA sample over silica shows no Co features and appears to be completely dispersed over silica (Figure 3.8c). The Co particles produced with a high-temperature reduction average about 6 nm in diameter [41] (not shown). On the other hand, the Co_3O_4 crystallites that result from a dried CoHA/carbon sample are about 16 nm in diameter (Figure 3.8d) and shrink to about 12 nm after reduction [41].

This reductive deammination [43] can be attributed to the more complex functionality of the carbon surface, which besides various types of oxygen-containing groups, contains pi bonds and pyridine-N-oxide groups [44] that give rise to the oxidation–reduction reaction wherein the metal complex is reduced and the carbon surface is oxidized. Carbon has also been shown to reduce Pt^{+4} chloride and oxychloride complexes to Pt^{+2} at acidic conditions, where in the same pH range the Pt^{+4} is completely stable over alumina [45, 46].

3.7

Electrostatics and Dissolution, Reaction, and Redeposition

Chemical interactions between precursors and supports can be understood in terms of a coordination chemistry or geochemical mechanism [22], the driving force for which is the chemical potential for the formation of a new solid

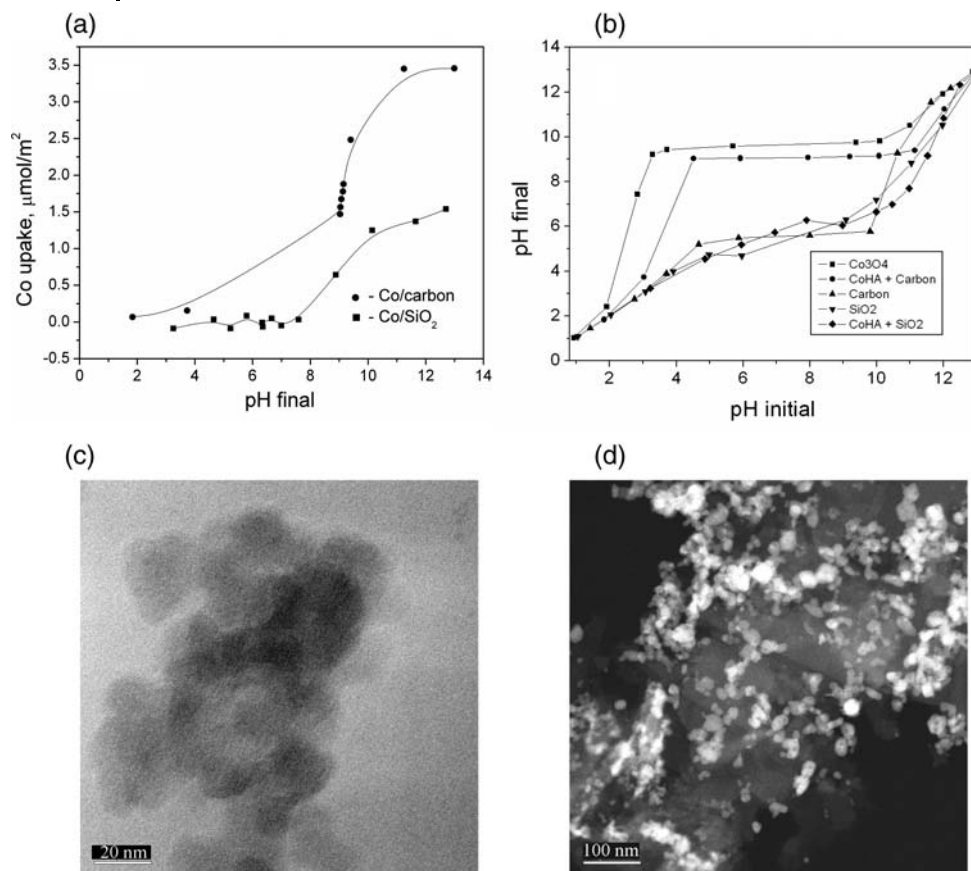


Figure 3.8 Cobalt hexaammine adsorption over silica and carbon with similar PZCs (4): (a) uptake versus pH, and (b) pH shifts, (c) 450°C calcined 1.8 wt% cobalt species on silica, and (d) 200°C calcined 5.15 wt% Co particles on carbon. (From [41] with permission from Elsevier.)

phase such as phyllosilicates [20], hydrotalcites [21], or mixed-metal oxides [22]. Electrostatic adsorption can accompany these chemical mechanisms, as occurs, for example, in the case of copper tetraammine adsorption concurrent with copper phyllosilicate formation [33].

3.8 Electrostatics-Based Design

In the preceding sections it has been demonstrated that metal coordination complexes often interact with common support surfaces via an electrostatic mechanism, as the sole mechanism or in combination with other mechanisms.

Even when other mechanisms are operative, a master impregnation variable would appear to be solution pH, and in particular, final pH. The two main experiments of the SEA method, the $\text{pH}_{\text{initial}}-\text{pH}_{\text{final}}$ plot and the pH–uptake survey might be used for many systems to diagnose the type of adsorption mechanism and to determine the optimal impregnation conditions. These features of the SEA method will be reviewed for a single metal catalyst system, and then applied to composite oxide surfaces for the synthesis of promoted and bimetallic catalysts.

3.8.1

Well-Dispersed Single Metals

The steps to apply the SEA method for the synthesis of a single supported metal are as follows:

1. determination of support PZC
2. metal uptake–pH survey (also recording pH shifts)
3. synthesis at optimal pH and tune pretreatment to optimize dispersion.

To further illustrate the SEA method for a single metal, the synthesis of well-dispersed platinum over a high surface area ($345 \text{ m}^2/\text{g}$), pure anatase TiO_2 support (Hombikat UV 100, Sacthleben) will be considered. The first step in the SEA approach is to determine the PZC of the support. The pH shifts for the Hombikat sample are shown in Figure 3.9a for a surface loading of $10\,000 \text{ m}^2/\text{l}$. The pH plateau, which corresponds to the PZC, is readily visible at a pH of 5.7. The higher the surface loading, the wider the plateau, and if the support is cheap and plentiful, a high surface loading can be used. The highest practical surface loading corresponds to DI; at this condition a pH electrode designed for semisolids can be used to measure the paste pH [9]. However, for reasonably high surface area materials, surface loadings of $100\,000 \text{ m}^2/\text{l}$ can normally be employed and will result in enough excess liquid that pH can be measured using a standard electrode.

Since the PZC is not far from neutral, either anionic or cationic precursors can be employed. The PTA cation was selected for the uptake–pH survey, and results are shown in Figure 3.9b. Two surface loadings were selected, 1000 and $10\,000 \text{ m}^2/\text{l}$, to check for consistency. The pH shift results from the metal-containing and metal-free experiments (not shown) closely overlap and suggest that metal adsorption and proton transfer are independent and the adsorption is largely electrostatic.

The pH shift plot of Figure 3.9a is useful in determining the initial pH ranges for the adsorption experiment of a particular surface loading. The desired final pH values are indicated along the y-axis of the plot (from 5 to 13); the corresponding initial pH values are determined by finding the intersection of the S-shaped $\text{pH}_{\text{initial}}-\text{pH}_{\text{final}}$ curve of the control experiment, and then

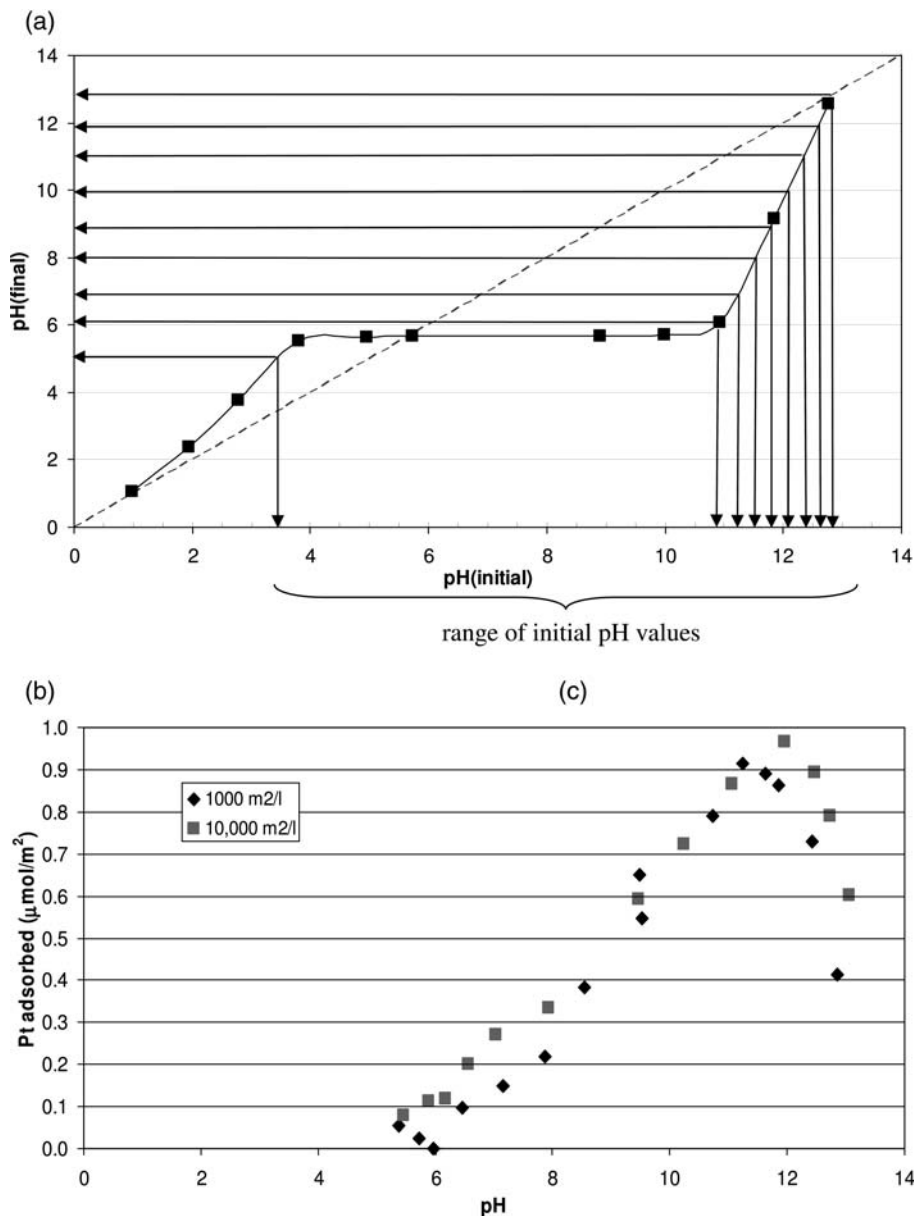


Figure 3.9 The SEA method applied to a high surface area titania: (a) pH shift plots for 10 000 m²/l and (b) PTA uptake versus pH for 1000 and 10 000 m²/l.

dropping down to the initial pH. The initial pH values span the very wide pH plateau; the initial value is at pH 3.4, the rest are from 10.8 to 13. Final pH can also be attained in practice by adjusting the pH after the solution is contacted with the support, however, it is simpler and quicker to anticipate the pH shift

that will occur due to oxide buffering. This works best, of course, when metal adsorption is independent of proton transfer.

The uptake curves for both surface loadings (Figure 3.9b) were very similar, exhibiting a sharp maximum at about 11.5. The uptake curve is noticeably narrower than those for silica (Figure 3.3) since the PZC is about two units higher. Adsorbing at this optimal pH and reducing directly at 200 °C (with no calcination) led to 4-nm Pt particles [47]. A trial and error series of pretreatments revealed that a 500 °C calcination followed by a 500 °C reduction resulted in 1.6-nm particles.

Monolayer adsorption via the SEA method yields well-dispersed metal particles, except as in the case of Co amines [24], when the reduction temperature is very high. The maximum metal loadings of well-dispersed particles attainable by SEA can be easily calculated from the monolayer loading limit of a particular metal complex. This calculation is given in [24] for cationic ammine complexes; from the maximum surface density achievable for a particular complex, which is from 0.5 to 1 complex per nm² for these cations the metal weight per cent achievable is a simple function of support surface area. For example, the surface area of an amorphous silica such as Vn-3 S, 175 m²/g, allows for loadings in the 1.5–3 wt% range, while a high surface area SBA-15 material (about 1000 m²/g) can support up to 14 wt% Pt. The Pd and Pt on SBA-15 materials shown earlier in Figure 3.6 contained almost 10 wt% of each metal, at particle sizes smaller than 2 nm.

Should higher loading be desired, the SEA procedure can be repeated after the metals from a prior impregnation are reduced.

A sampling of support PZCs measured in our own lab, and the suitability of adsorbing cations and/or anions is shown in Table 3.2 and is similar to the 2 offered by Brunelle three decades ago [1]. This information is useful in designing a well-dispersed single-metal catalysts as shown above, or in the extension of electrostatic adsorption to promoted and bimetallic catalysts to be discussed next.

3.8.2

Selective Adsorption onto Promoters

The idea of extending the SEA method to supported oxides is illustrated in Figure 3.10. The surface potential of niobia and alumina are plotted in Figure 3.10a; since niobia has a very acidic PZC and alumina a mildly basic one, there exists a wide pH range over which the respective oxides carry opposite charge. Between the pH values of 2 and 8 the niobia surface will be negatively charged, and the alumina positively charged. If niobia is considered the promoted phase and it is desired to have the promoter in close proximity to the Pt sites, the cationic PTA precursor could be chosen and it should adsorb selectively onto the niobia phase.

Table 3.2 PZCs and suitable metal complexes for common supports.

Support	PZC	Complex
MoO ₃	<1	Cations
Nb ₂ O ₅	2–2.5	Cations
SiO ₂	4	Cations
Oxidized carbon black	2–4	Cations
Oxidized activated carbon	2–4	Cations
Graphitic carbon	4–5	Cations
TiO ₂	4–6	Cations (or anions)
CeO ₂	7	Cations or anions
ZrO ₂	8	Cations or anions
Co ₃ O ₄	7–9	Cations or anions
Al ₂ O ₃	8.5	(Cations or) anions
Activated carbon	8–10	Anions
Carbon black	8–10	Anions

The steps to apply the SEA method for the synthesis of promoted metals are as follows:

1. determination of support and promoter PZC (with bulk powders of each)
2. metal uptake–pH surveys over each pure component (also recording pH shifts)
3. an adsorption experiment at the optimal pH over a physical mixture of the two oxides, which can be identified separately in electron microscopy, to confirm the partitioning of the metal onto the desired oxide
4. synthesis over the supported promoter oxide and characterization via scanning transmission electron microscope (STEM), EXAFS, and ultimately activity and selectivity testing to confirm the adsorption selectivity.

Adsorption studies of PTA over pure niobia and alumina powders, and a physical mixture of the two, are shown in Figure 3.10b [48]. PTA adsorbs over niobia in a wide pH range, given its very low PZC, while the alumina does not accrue a strong negative charge in the basic pH range and adsorbs only small amounts of PTA. The physical mixture results appear to be a simple coaddition of the individual materials.

STEM analysis of a physical mixture synthesized at a final pH of 6 is shown in Figure 3.10c. Adsorption is seen to be essentially 100% selective onto the niobia phase, and the resulting Pt particles formed on niobia after a 250 °C reduction are seen to be on the order of 1.1 nm. More details and extensive characterization of selective Pt adsorption over alumina-supported niobia are found elsewhere [48, 49]. The same principles have been used to steer Pt onto the alumina support of a silica-bound alumina extrudate [50].

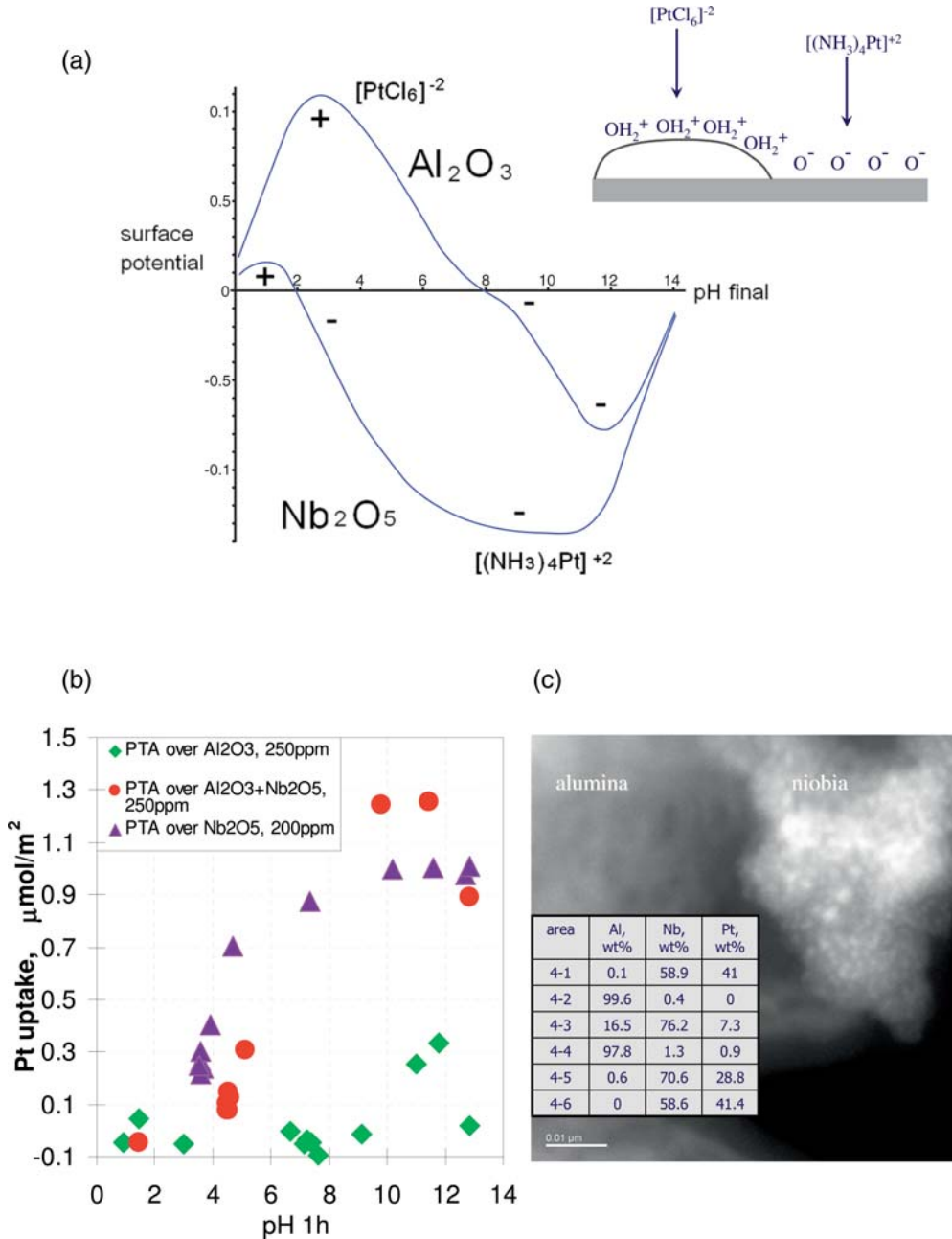


Figure 3.10 SEA extended to mixed-oxide surfaces: (a) surface potential versus pH for niobia and alumina surfaces, (b) uptake versus pH over pure niobia, pure alumina, and a physical mixture of the two, and

(c) STEM analysis demonstrating selective partitioning and the small particle size of PTA onto niobia in niobia/alumina physical mixtures.

Table 3.3 Selective metal partitioning over mixed-metal oxides.

Metals	Catalyst	Charged species at SEA pH	Probe reaction
(Cationic complex)/(acidic promoter)/(basic support)			
BM	Co/Nb ₂ O ₅ /Al ₂ O ₃	$[(\text{NH}_3)_6\text{Co}]^{+3}/(\text{Nb-O}^-)/(\text{Al-OH}_2^+)$	WGS*, FTS*
NM	Pt/Nb ₂ O ₅ /Al ₂ O ₃	$[(\text{NH}_3)_4\text{Pt}]^{+2}/(\text{Nb-O}^-)/(\text{Al-OH}_2^+)$	CO oxidation
(Anionic complex)/(basic promoter)/(acidic support)			
BM	Cu/ZnO/SiO ₂	$[\text{CuCl}_4]^{-2}/(\text{Zn-OH}_2^+)/\text{SiO}_2(\text{Si-O}^-)$	WGS
NM	Pt/ZrO ₂ /SiO ₂	$[\text{PtCl}_6]^{-2}/(\text{Zr-OH}_2^+)/\text{SiO}_2(\text{Si-O}^-)$	CO oxidation
(Cationic complex)/(acidic promoter)/(neutral support)			
BM	Co/MnO ₂ /TiO ₂	$[(\text{NH}_3)_6\text{Co}]^{+3}/(\text{Mn-O}^-)/(\text{Ti-OH}_2^+)$	WGS, FTS
(Anionic complex)/(basic promoter)/(neutral support)			
NM	Pt/ZrO ₂ /TiO ₂	$[\text{PtCl}_6]^{-2}/(\text{Zr-OH}_2^+)/(\text{Ti-O}^-)$	CO oxidation

*WGS, water gas shift; FTS, Fischer–Tropsch synthesis.

A number of examples for which SEA can be applied to promoted catalysts are given in Table 3.3. To achieve adsorptive partitioning over supported promoters, the farther apart the PZCs of promoter and oxide, the better. This precludes the SEA method for placing Cu anions on alumina-supported ZnO, for example, since the PZCs of alumina and ZnO are 8 and 9, respectively. Silica (PZC 4) can be used as support instead of alumina when adsorbing Cu anions onto ZnO, or Pt anions onto zirconia. On the other hand, alumina is a good support for acidic niobia (PZC 2.5). Co ammine can be expected to be selectively adsorbed onto the niobia phase, as is Pt ammine (Figure 3.10). Co and Pt amines behave similarly over pure silica [14, 24]. Titania might be employed as support for acidic or basic promoter oxides. The PZC for zirconia is about 8, while that for MnO₂ should be close to 4.

3.8.3

Bimetallic Catalysts

In the previous example the supported metal oxide onto which the metal precursor was adsorbed did not reduce; which will be the case for many promoted systems. In many systems, however, the supported metal oxide will reduce, especially through hydrogen spillover, and a bimetallic catalyst can be synthesized. The idea is illustrated in Figure 3.11a for the Pd/Co/C electrocatalyst system. The idea will be to adsorb Pd complexes onto a well-dispersed, carbon-supported Co₃O₄ phase, and reduce to get bimetallic Pd/Co particles that are perhaps core-shell in morphology.

As before, much benefit is derived from studying the uptake of Pd over Co₃O₄ and carbon independently. The steps to apply the SEA method for the synthesis of bimetallic materials are as follows:

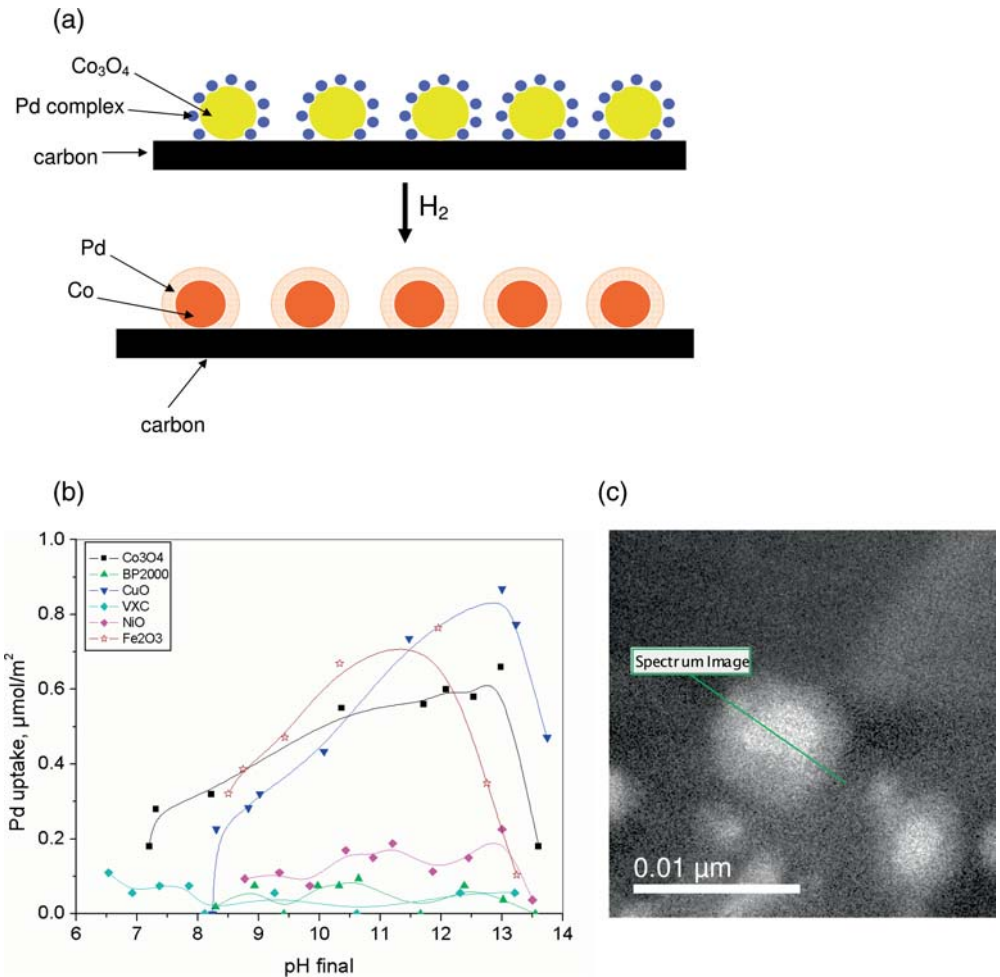


Figure 3.11 The extension of SEA for the production of bimetallic catalysts; (a) Pd complexes are adsorbed selectively onto supported Co₃O₄; both metals subsequently reduce to form bimetallic particles, (b) uptake versus pH of PdTAs over various oxides and carbons, and (c) z-contrast image of Pd/Co core-shell particle.

1. determination of support and second metal oxide PZC (with bulk powders of each)
2. metal uptake–pH surveys over each pure component
3. an adsorption experiment at the optimal pH over a physical mixture of the two oxides, which can be identified separately in electron microscopy, to confirm the partitioning of the metal onto the desired oxide
4. synthesis over the supported oxide, reduction, and characterization via STEM, TPR, EXAFS, and ultimately activity and selectivity testing to

confirm the adsorption selectivity and homogeneity of bimetallic particle composition.

Uptake data for PdTAs onto a number of oxides (Co_3O_4 , CuO , NiO , and Fe_2O_3) and carbons (Vulcan XC72, BP2000) is shown in Figure 3.11b. The carbons, which are unoxidized and have PZCs around 9, do not take up the ammine complex, whereas iron, copper, and cobalt oxides that have somewhat lower PZCs, do. Supporting cobalt on an unoxidized carbon such as Vulcan XC72 should then give high selectivity of Pd adsorption onto the cobalt oxide phase. In EDXS and STEM analysis of physical mixtures it has been confirmed that the selectivity of Pd and Pt ammine adsorption onto the cobalt phase is 80% [51]. Furthermore, detailed analysis of individual particles has revealed a core-shell structure; the majority of X-ray line scans through numerous particles reveal a Co core and Pd shell; an electron energy loss spectroscopy (EELS) analysis of the particle shown in Figure 3.11c also revealed a 5-nm Co core and 2-nm Pd shell [51].

A number of examples for which the SEA method can be applied to make bimetallic catalysts are shown in Table 3.4. Bimetallic preparations can be performed with noble metals (NMs) and base metals (BMs), in combinations of NM/NM, NM/BM, or BM/BM, matched to supports with appropriate PZC. The NMs that form stable oxides are +4 valent (PtO_2 , PdO_2 , ReO_2 , RuO_2) and are expected to be acidic, as oxide PZCs roughly vary with the valence of the metal: MgO (+2) has PZC 12, Al_2O_3 (+3) is 8, TiO_2 and SiO_2 (+4) are 6 and 4, Nb_2O_5 (+5) is 2.5, MoO_3 (+6) is about 1. Thus, a NM/NM bimetallic via SEA may not be possible over low PZC supports.

Table 3.4 Selective metal partitioning for bimetallic catalyst synthesis.

Metals	Catalyst	Intermediate charged species	Probe reaction
(Anionic complex)/(basic oxide precursor)/(acidic support)			
NM/BM	Pt/Co/SiO ₂	$[\text{PtCl}_6]^{-2}/\text{Co}_3\text{O}_4(\text{Co-OH}_2^+)$ /SiO ₂ (Si-O ⁻)	WGS, FTS
	Pt/Co/C _{ox} *	$[\text{PtCl}_6]^{-2}/\text{Co}_3\text{O}_4(\text{Co-OH}_2^+)$ /C(C-O ⁻)	
BM/BM	Cu/Co/SiO ₂	$[\text{CuCl}_4]^{-2}/\text{Co}_3\text{O}_4(\text{Co-OH}_2^+)$ /SiO ₂ (Si-O ⁻)	WGS, FTS
(Cationic complex)/(acidic oxide precursor)/(basic support)			
NM/NM	Pt/Re/Al ₂ O ₃	$[(\text{NH}_3)_4\text{Pt}]^{+2}/\text{ReO}_2(\text{Re-O}^-)$ /Al ₂ O ₃ (Al-OH ₂ ⁺)	Isomerization
NM/BM	Pt/Sn/Al ₂ O ₃	$[(\text{NH}_3)_4\text{Pt}]^{+2}/\text{SnO}_2(\text{Sn-O}^-)$ /Al ₂ O ₃ (Al-OH ₂ ⁺)	DHC*
BM/BM	Co/Mo/Al ₂ O ₃	$[(\text{NH}_3)_6\text{Co}]^{+3}/\text{MoO}_3(\text{Mo-O}^-)$ /Al ₂ O ₃ (Al-OH ₂ ⁺)	SR*

*C_{ox}, oxidized carbon; DHC, dehydrocyclization; SR, steam reforming.

3.9

Summary

NM and BM coordination complexes such as chlorides and ammines often adsorb over oxide and carbon catalyst supports via an electrostatic mechanism, sometimes in conjunction with other chemical mechanisms. SEA can be induced when the support buffering effect is overcome, that is, when the final pH of the impregnating solution is brought far enough away from the PZC of the surface for the surface to be strongly charged (protonated or deprotonated). SEA results in a monolayer of the metal precursor complex that usually retains high dispersion after the metal is reduced. Deposition via SEA is limited to one monolayer of metal complexes, which is typically in the range 0.5–1.5 $\mu\text{mol}/\text{m}^2$. For high surface area supports, relatively high metal weight loadings can be achieved; higher loadings over any one support can be achieved with successive SEA impregnations.

Electrostatic control of adsorption can also be employed to steer a metal onto the promoter oxide of a promoted catalyst, or onto a reducible metal oxide in the preparation of bimetallic catalysts. Thus, SEA is a useful tool for the rational preparation of catalysts.

References

1. Brunelle, J.P. (1978) *Pure Appl. Chem.*, **50**, 1211.
2. Heise, M.S. and Schwarz, J.A. (1985) *J. Colloid Interface Sci.*, **107**, 237.
3. Heise, M.S. and Schwarz, J.A. (1986) *J. Colloid Interface Sci.*, **113**, 55.
4. Heise, M.S. and Schwarz, J.A. (1988) *J. Colloid Interface Sci.*, **123**, 51.
5. Schwarz, J.A. and Heise, M.S. (1990) *J. Colloid Interface Sci.*, **135**, 461.
6. Contescu, C. and Vass, M.I. (1987) *Appl. Catal.*, **33**, 259.
7. Santhanam, N., Conforti, T.A., Spieker, W.A. and Regalbuto, J.R. (1994) *Catal. Today*, **21**, 141.
8. Regalbuto, J.R., Navada, A., Shadid, S., Bricker, M.L. and Chen, Q. (1999) *J. Catal.*, **184**, 335.
9. Park, J. and Regalbuto, J.R. (1995) *J. Colloid Interface Sci.*, **175**, 239.
10. Shah, A. and Regalbuto, J.R. (1994) *Lancet*, **10**, 500.
11. Hao, X., Spieker, W.A. and Regalbuto, J.R. (2003) *J. Colloid Interface Sci.*, **267**, 259.
12. James, R.O. and Healy, T.W. (1972) *J. Colloid Interface Sci.*, **40**, 65.
13. Regalbuto, J.R. (2006) in *Surface and Nanomolecular Catalysis*, (ed. R. Richards), Taylor & Francis, CRC Press, Boca Raton, p. 161.
14. Schreier, M. and Regalbuto, J.R. (2004) *J. Catal.*, **225**, 190.
15. Regalbuto, J.R. (2007) in *Catalyst Preparation: Science and Engineering*, (ed. J.R. Regalbuto), Taylor & Francis, CRC Press, Boca Raton, p. 297.
16. Moreau, F., Bond, G.C. and Taylor, A.O. (2005) *J. Catal.*, **231**, 105.
17. Zanella, R., Delannoy, L. and Louis, C. (2005) *Appl. Catal.*, **291**, 62.
18. Bitter, J.H. et al. (2003) *Catal. Lett.*, **89**, 139.
19. Toebes, M.L. et al. (2004) *J. Phys. Chem. B*, **102**, 11611.
20. Burattin, P., Che, M. and Louis, C.J. (1998) *Phys. Chem. Glasses*, **102**, 6171.
21. Paulhiac, P. and Clause, O. (1995) *J. Am. Chem. Soc.*, **117**, 11471.

22. Carrier, X., Lambert, J.F. and Che, M. (2000) *Stud. Surf. Sci. Catal.*, **130**, 1049.
23. Miller, J.T., Schreier, M., Kropf, A.J. and Regalbuto, J.R. (2004) *J. Catal.*, **225**, 203.
24. Jiao, L., and Regalbuto, J.R. (2008) *J. Catal.*, **260**, 329.
25. Spieker, W.A., Liu, J., Hao, X., Miller, J.T., Kropf, A.J. and Regalbuto, J.R. (2002) *Appl. Catal.*, **232**, 219.
26. Spieker, W.A., Liu, J., Hao, X., Miller, J.T., Kropf, A.J. and Regalbuto, J.R. (2003) *Appl. Catal.*, **243**, 53.
27. Yang, J.H. *et al.* (2005) *Appl. Catal.*, **291**, 73.
28. Schreier, M., Terens, S., Belcher, L. and Regalbuto, J.R. (2005) *Nanotechnology*, **16**, S582.
29. Woolery, G.L., Alemany, L.B., Dessau, R.M. and Chester, A.W. (1986) *Zeolites*, **6**, 14.
30. Smirnov, A.V. *et al.* (2002) *J. Catal.*, **194**, 266.
31. Trouillet, L., Toupance, T., Villain, F. and Louis, C. (2000) *Phys. Chem. Chem. Phys.*, **2**, 2005.
32. Toupance, T., Kermarec, M. and Louis, C. (2000) *J. Phys. Chem. B*, **104**, 965.
33. Toupance, T., Kermarec, M., Lambert, J.F. and Louis, C. (2002) *J. Phys. Chem. B*, **106**, 2277.
34. Arrua, L.A. *et al.* (1997) *Appl. Catal.*, **165**, 259.
35. Arrua, L.A. *et al.* (2000) *Appl. Catal.*, **204**, 33.
36. Torre-Abreu, C., Ribeiro, M.F., Henriques, C. and Delahay, G. (1997) *Appl. Catal.*, **B**, **14**, 261.
37. Shimokawabe, M., Takodoro, K., Sasaki, S. and Takezawa, N. (1998) *Appl. Catal.*, **166**, 215.
38. Shimokawabe, M., Hirano, K. and Takezawa, N. (1998) *Catal. Today*, **45**, 117.
39. Cheung, T., Bhargava, S.K., Habday, M. and Foger, K.J. (1996) *J. Catal.*, **158**, 301.
40. Miller, J.T. and Regalbuto, J.R., unpublished results.
41. D'Souza, L.D., Regalbuto, J.R. and Miller, J.T. (2006) *J. Catal.*, **248**, 165.
42. D'Souza, L.D., Regalbuto, J.R. and Miller, J.T. (2007) *J. Catal.*, **248**, 165.
43. Bezemer, G.L. *et al.* (2006) *J. Catal.*, **237**, 291.
44. Montoya, A., Gil, O.J., Mondragon, N.T. and Truon, N.T. (2002) *Am. Chem. Soc., Div. Fuel Chem.*, **47**, 424.
45. Van Dam, H.E. and van Bekkum, H. (1991) *J. Catal.*, **131**, 335.
46. Hao, X. (2004). Ph. D. Dissertation, University of Illinois, Chicago.
47. Schreier, M., D'Souza, L.D. and Regalbuto, J.R., manuscript in preparation.
48. Zha, Y. (2004). Ph. D. Dissertation, University of Illinois, Chicago.
49. Hao, X., Regalbuto, J.R., Miller, J.T., and Kropf, A.J., manuscript in preparation.
50. Spieker, W.S. (2000). Ph. D. Dissertation, University of Illinois, Chicago.
51. D'Souza, L.D., Klie, R. and Regalbuto, J.R., manuscript in preparation.

4

Impregnation and Drying

Eric Marceau, Xavier Carrier, and Michel Che

4.1

Introduction

As their name indicates, supported catalysts consist of a catalytically active phase dispersed over a support. Requirements for their preparation are threefold as far as the introduction of the active phase is concerned:

- in order to achieve dispersion, the precursor of the active phase should be distributed uniformly.
- the number of operations needed for the precursor introduction should be limited.
- because precursors can be costly, their complete deposition should be ensured.

The first requirement can be reached by dissolving the precursor in a liquid. The solution is then introduced into the voids of the support, after which the solvent is eliminated. The former step of the procedure is called *impregnation* and the latter step, usually thermally activated, is called *drying*. Altogether, they allow fulfilling the second and the third requirements, because the number of unit operations is only two and the whole of the solute remains on the support after solvent elimination.

Impregnation is often described on a container/contents basis and does not need chemistry to be comprehended. However, simplicity from a practical point of view does not necessarily mean simpler physical and chemical phenomena. The present chapter provides guidelines to help the reader understand what lies behind this method of preparation, which is still deemed the favorite by the industry and the most convenient at the laboratory scale for the reasons stated above.

The term “impregnation” belongs to the traditional vocabulary of industrial chemistry. It refers to the contacting of a solid and a liquid phase, and absorption of the latter by the former, be it wood or textile. It is difficult to ascertain who introduced this term in the field of catalysts preparation, but a plausible candidate is the English industrialist Henry Deacon, a former

student of Michael Faraday who invented a process of oxidation of HCl to Cl₂ over copper compounds. Only 33 years after Berzelius had coined the term “catalysis”, procedure and rationale for the use and choice of a support were exposed by Deacon with striking clarity [1]:

“... Of the compounds of copper, I prefer the sulphate of copper, which may be employed in the following manner: Into a strong solution of sulphate of copper, I dip, or immerse, or **impregnate** common clay, or fire-clay bricks, or pipes, which, after saturation, I place in retorts or flues heated externally [...] One advantage arising from the employment of compounds of copper, is the comparatively low temperature at which they act, but for practical purposes they require to be mixed with some other body or compounds to prevent their fusing together. Burnt clay will be found to be efficient for this purpose.”

The examination of two later patents [2, 3] allows us to identify some important parameters that will be detailed below, and to realize that some preoccupations of that time are still topical:

1. During impregnation, the dissolved precursor migrates in the pores of the support, on which it may adsorb.
2. The support can be used as a powder but most often in industry it appears in the form of extrudates or pellets of specific size and shape, implying a transport of matter in the solid at a macroscopic scale and a distribution that might not be homogeneous.
3. The impregnation solution contains several chemical species: the metal precursor of the active phase, its counterions, coimpregnants; precursors are also selected according to their physicochemical properties and cost.
4. Choice of parameters such as concentration and temperature is critical. Depending on these, different physicochemical phenomena may lead to different types of deposited phases and ultimately to more or less active catalysts.

Having defined impregnation, it remains to specify what drying is, or, more precisely, when drying stops and calcination starts, as far as thermal treatments are concerned. In this chapter, drying will be considered as the thermally activated step during which the solvent, submitted to evaporation and still present in its molecular form, is able to influence the transport of its chemical partners or to react with them. Calcination concerns a system in which the solid/solvent interface has been replaced by a solid/gas interface, on which new transformations take place (decomposition of ligands, ion diffusion, etc.).

Over the last 10 years, aspects of impregnation and drying have been treated in a number of chapters of books and reviews devoted to the preparation of supported catalysts or to one class of catalysts in particular; a selection can be found in [4–11].

In the first part of this chapter (Sections 4.2 and 4.3), we describe the procedures of impregnation and drying from an experimental point of view

and shed light on transport phenomena by using simple physical models. The description of the events will be limited to molecular migration, displacement or elimination. The chemical reactions taking place between precursor, support, and solvent will be detailed in Section 4.4. As a case study we discuss in Section 4.5 the preparation of alumina-supported molybdenum oxide catalysts.

4.2 Impregnation

Impregnations can be classified in two categories, according to the volume of solution added. Specific problems that arise from the impregnation of extrudates, as used in industrial reactors (Chapter 9), are also described.

4.2.1 Methods of Impregnation

The simplest way to execute impregnation is by contacting a previously dried support, of pore volume V_{PT} , with a volume $V = V_{PT}$ of solution containing the precursor of the active phase. The solution is drawn into the pores by capillary suction (hence “capillary impregnation”) [12–14]. In the case of proper wetting no excess of solution remains outside the pore space and the procedure is also called “dry” or “incipient wetness” impregnation.

The penetration of the liquid phase requires the elimination of air from the pores. If the pore radius is very small, capillary pressure is much larger than the pressure of the entrapped air; compressed air dissolves or escapes from the solid through larger pores [13, 14]. Sometimes, the mechanical strength of the support is not sufficient to withstand forces imposed by the transitory formation of bubbles and the catalyst grains may burst [13]. This can be remedied by impregnation under vacuum or addition of a surfactant to the solution.

Heat is generally released when a solid/gas interface is replaced by a solid/liquid interface. This might influence the quality of impregnation if the precursor solubility decreases when the temperature increases or if detrimental reactions involving the support take place due to a temperature rise. These drawbacks can be avoided by exposing the support to water vapor before impregnation and thus stabilizing the interface with a hydrous film.

Impregnation can also be carried out in diffusional conditions, that is, by immersing a water-filled support in the precursor solution (“wet” impregnation) [12–14]. Before water filling, air can be replaced by a water-soluble gas like ammonia to avoid gas bubbles in the pores [13]. Wet impregnation should be avoided when the interaction between precursor and support is too weak to guarantee the deposition of the former [15].

For powders, it can be convenient to suspend the support in an excess of solution and evaporate the solvent under regular stirring. Such a method can be used for the introduction of poorly soluble compounds, but leads to a dispersed phase *only* if seeds serving the subsequent growth of the particles have time to form all over the support surface before crystallization starts. It is thus advised to check by microscopic methods if the final distribution of the active phase is homogeneous at the scale of the support grain.

So as to combine conventional stirring and the use of a low volume of precursor solution, a two-solvent method has been proposed, in which a dry hydrophilic support is first suspended into a large volume of an organic solvent with a relatively low surface tension [16]. A volume V_{PT} of precursor solution in water is then poured into the suspension. It moves into the pores where it replaces the organic solvent that has a lower affinity for the support surface.

These procedures apply to supports whatever their granulometry. However, in industry one prefers to use millimeter-sized extrudates or pellets, in which impregnation may lead to uniform or heterogeneous distributions of the active phase precursor depending on the conditions (“egg-shell”, “egg-yolk” profiles; for more detail, see also Chapters 9, 10, and 14 of this book). “Competitor” molecules introduced in the impregnation solution help to obtain a large number of metal distribution profiles between the periphery and the center of the support grain, depending on the strength of their interaction with the support compared with that of the precursor [17–23].

4.2.2

Physical Models for Impregnation

Basically, impregnation has been rationalized following two physical models. For the sake of clarity, their presentation starts with the simplest one (wet/diffusional impregnation) that will be further completed to describe dry impregnation.

In diffusional impregnation, the distribution of the solute inside the wet porosity of the pellet is assumed to be governed by two phenomena [24–27] (Figure 4.1a): the diffusion of the solute into the pores of the pellet, described by Fick’s law, and the adsorption of the solute onto the support, which depends on the adsorption capacity of the surface and on the adsorption equilibrium constant. These two parameters are experimentally determined from adsorption isotherms, but the final distribution is not fundamentally changed if equilibrium is not reached and adsorption is ruled by kinetics [28].

The distribution of the precursor along the pellet depends on the balance between diffusion and adsorption: when the precursor adsorbs on the support surface, its concentration in solution decreases and as a consequence, diffusion decreases too. Diffusion can be enhanced by imposing a high concentration

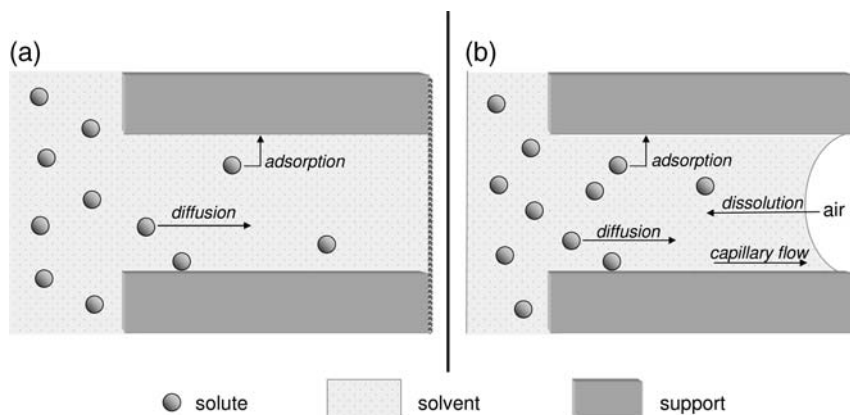


Figure 4.1 Phenomena of transport involved in (a) wet impregnation and (b) dry impregnation. The *solute* migrates into the pore from the left to the right of the figures.

outside the pellet. The characteristic time τ required to attain equilibrium in a pellet of radius R is proportional to R^2 [24] and is thus appreciably reduced by diminishing the size of the beads: with beads having a radius of 1 or 0.5 mm instead of 2 mm, τ is divided by 4 and 16, respectively. In all cases, wet impregnation in diffusional conditions is far from being instantaneous (several hours).

In models used for dry impregnation (Figure 4.1b), another equation based on Poiseuille steady states or on the related Darcy's law is added to represent the pressure-driven capillary flow of the solution inside the empty pores [28, 29]. For low concentrations, strong adsorption of the solute or short times, egg-shell distributions are expected [29, 30]. If the adsorption of the solute is weak and time is long enough, distribution should tend to uniformity. For powders, equilibrium is reached within a few minutes, but it can take a few hours to reach a uniform distribution of the precursor inside a pellet [19, 31]. A blockage of the pores by "bulky species" has been invoked in some cases, when egg-shell distributions persist even after long durations [26, 32]. It must be noted that in physical models, the contact time between support and solvent is treated as a variable influencing only the transport of the precursor through the pellet. Examples presented in Section 4.4.2 will show that dramatic changes concerning the support may take place during this "aging" period.

An important parameter from the introduction of Darcy's law is the solution viscosity μ . In the case of aqueous solutions and in the common range of concentrations used for impregnation, viscosity increases almost proportionally with concentration [18]. It also increases with the presence of organic ligands attached to the metal ions [33]. Viscosity and concentration behave contrariwise as far as the precursor diffusion is concerned: a high concentration tends to favor the diffusion of the solute toward the center

of the pellet, while a high viscosity tends to curb it. Moreover, it may be more difficult to eliminate entrapped air from the pores when a viscous solution is used [18]. Nevertheless, a very high viscosity is sometimes searched for. An original procedure has been developed by Iglesia *et al.* to obtain thin egg-shell profiles [34]. It consists in spilling molten cobalt nitrate hexahydrate over extrudates placed in a vacuum funnel. The high viscosity of the liquid phase prevents it from penetrating into the core of the pellets.

Temperature of impregnation has seldom been investigated as a parameter determining the profile in a pellet. It may act on the adsorption equilibrium of the precursor [30] but has been considered a minor factor as far as the precursor distribution is concerned [29].

4.3

Drying

The step after impregnation is the elimination of the solvent. Typically, the impregnated system, spread in fine layers, is heated in an oven up to the boiling point of the solvent or at a lower temperature for gentle drying, in static conditions or under a flow of gas. The elimination of water from the pores leads to an increase of the precursor concentration up to saturation and crystallization, preferably on seeds resulting from the interactions with the support, if one wants to obtain a highly dispersed phase. However, hydrated salts like nitrates melt at moderate temperature [35, 36], which may cause the coalescence of their initially dispersed particles, or even their exclusion from the pores.

Drying may also cause the thermally activated elimination of molecules other than the solvent. Depending on the temperature, hydrated salt crystallites dehydrate into, for example, hydroxynitrate phases [33, 37, 38]; isolated complexes lose ligands and graft onto the support surface [39, 40]; volatile compounds introduced in the impregnation solution as competitors or pH-adjusters evaporate (HCl, NH₃).

Temperature is not the sole parameter that governs drying, as is shown by two examples (Figure 4.2). Komiyama *et al.* prepared Ni/Al₂O₃ catalysts from nickel chloride and found that a heating rate of 10°C min⁻¹ up to 110°C led to small particles disseminated all over alumina, whereas a six-fold lower rate resulted in a segregation of matter to the mouth of the pores [41]. In contrast, when the precursor is [Ni(NH₃)₆](NO₃)₂, it is a fast heating up to 200°C that results in an egg-shell distribution [31].

In fact, drying confronts centrifugal phenomena that favor a displacement of the precursor toward the outer part of the pellet, where the solvent evaporation occurs, and centripetal phenomena that favor migration of the solute in the opposite direction [13, 14, 17, 21]. In physical models, one should take into account:

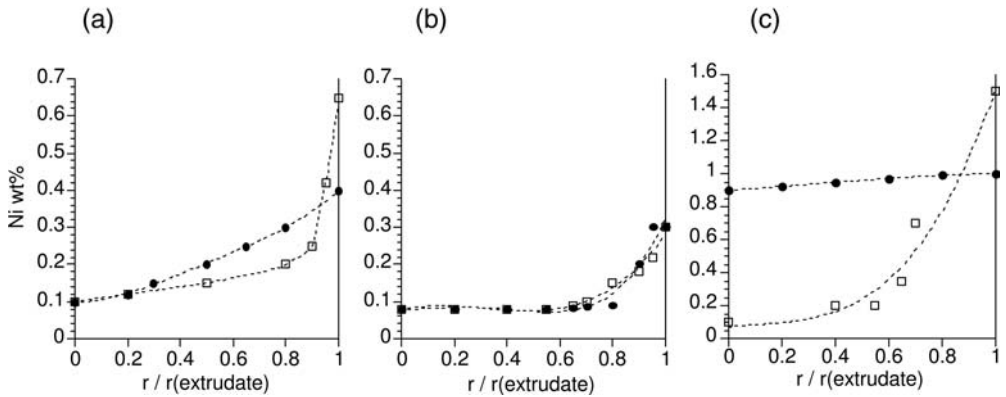


Figure 4.2 Profiles of nickel content in spherical extrudates before drying (black circles) and after drying (white squares). The origin of axis x corresponds to the center of the extrudate. (a) Low drying rate to 110°C; (b) high drying rate to 110°C; and (c) drying at 200°C. (Data have been collected from [41] (a and b) and [31] (c).)

- the interactions between the precursor and the support surface, which have been established during the preceding step of impregnation or will develop at some point during drying
- a centrifugal convective flow of liquid toward the pellet surface, modeled by Darcy's law, and the associated centrifugal flow of the solute; they are favored by a low viscosity of the solution
- a microconvective flow inside the evaporating liquid, which rejects and concentrates matter at its periphery (difficult to model and usually overlooked) [42]
- a centripetal backdiffusion of the solute, modeled by Fick's law, which lives on the consequences of convection, that is, the increase of concentration in precursor near the outer surface of the pellet.

The distribution of the precursor phase in the pellet, or its segregation at the outer surface, results from the balance between adsorption, convection, and backdiffusion, at least as long as the flow of solvent is high enough to counterbalance the vapor removal (constant-rate period) [14] (Figure 4.3a). When this is no longer the case, the solvent front recedes inside the pores and evaporation occurs inside the pellet (falling-rate period) [14, 21] (Figure 4.3b). The drying regime is defined as slow if the constant-rate period predominates, and as fast if it is the falling-rate period [12, 14]. Compared with slow drying, fast drying, usually associated with high heating rate and drying temperature, tends to block all movements of the solute toward the outside and may even lead to centripetal flows due to the receding solvent front [18, 21].

Unfortunately, the criteria on which one can implement slow or fast drying are difficult to identify, because the frontier between the two regimes is also a

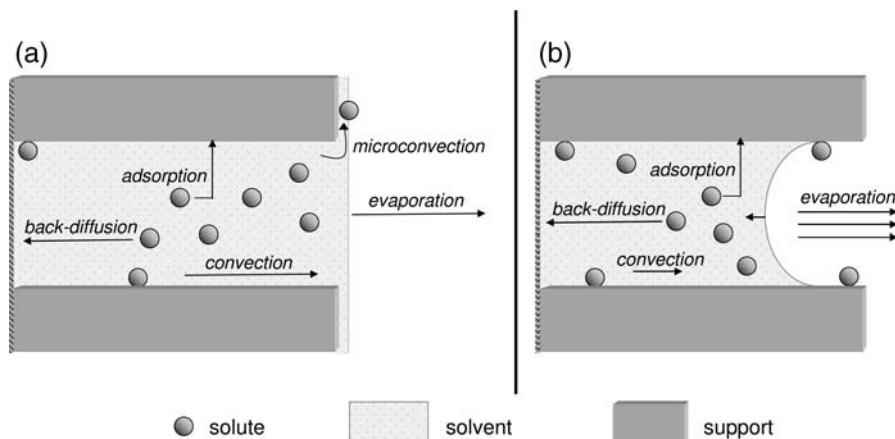


Figure 4.3 Phenomena of transport involved in (a) the constant-rate period of drying and (b) the falling-rate period of drying. The *solvent* migrates from the left to the right of the figures. Microconvection is not mentioned in (b) for the sake of clarity.

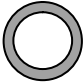
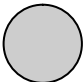
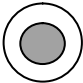
function of parameters that cannot be tuned or quantified easily, such as the permeability of the solid – in other terms, the accessibility of the liquid phase to the outer surface – or the “strength” of the precursor-support interactions before drying starts and during drying [14, 43]. A slow gentle drying at room temperature, which limits the solvent convective flow and provides time for the precursor to diffuse back, does not much modify the distribution obtained after impregnation [17, 30]. The same holds whatever the drying regime, if strong interactions have been created during the impregnation step [14, 44].

Finally, since during drying different parts of the support in contact with different quantities of water are submitted to different temperatures, the reactions between precursor and support may be not uniform. As a consequence, the number of seeds on which particles nucleate may not be the same along the axis of the pellet, resulting in differences in particle size inside the extrudate [17]. This explains why often drying is optimized on the basis of trial and error, rather than by using models.

As a conclusion, Table 4.1 provides a summary of the various conditions of impregnation and drying leading to different types of precursor distributions: egg-shell, uniform, or egg-yolk.

Two other methods of drying are mentioned in the literature, but due to technical constraints, they are not widely applied. Microwave heating provides a homogeneous drying of large systems [45–47]. Freeze drying, in which water is sublimated at temperatures below 0°C and under low pressure, has been applied to powders and small volumes of materials but also to monoliths [47–49]. In this case, the transport of dissolved species is blocked by the transformation of liquid water into ice.

Table 4.1 Influence of the conditions of impregnation and drying on the precursor distribution inside a pellet.

Distribution	Conditions of impregnation and drying
 Egg-shell	<ul style="list-style-type: none"> • Strong adsorption of the precursor during impregnation • Impregnation with a very viscous solution • Slow drying regime, in the case of solutions of low concentration and viscosity, or weakly adsorbing precursors
 Uniform	<ul style="list-style-type: none"> • Precursors and competitors equally interacting with the surface^a • Weakly interacting precursor + drying at room temperature • Drying a concentrated, viscous solution (e.g., addition of hydroxyethyl cellulose [50] or citrate ligands [51]) • If the migration of the solute has started during drying, transition from the constant-rate period to the falling-rate period
 Egg-yolk	<ul style="list-style-type: none"> • Competitor interacting more strongly with the surface than the precursor^a • Fast drying regime with predominant back-diffusion

^aAs long as drying does not modify the precursor distribution obtained during impregnation.

4.4 The Chemistry

Because various forms of the precursor exist in the solution or on the support, depending on the location in the pellet and on the moment the impregnated or dried system is examined, chemistry in the pore system during impregnation and drying is more complex than what a simplistic approach of the support as a “container” suggests. Impregnation and drying, with their specificities, are investigated in this section from a molecular point of view, in order to clarify what lies behind the expressions “adsorption of the precursor,” “strong precursor–support interactions” or “contact with the solvent,” which have been used intuitively in Sections 4.2 and 4.3. It should be noted that in this part of the chapter, we will focus on water as the solvent, since it is the most commonly used for convenience, cost, and safety.

4.4.1 Concentrations and pH

Due to the low volume of solution used in incipient wetness impregnation, the concentration of the precursor in water is often high and sometimes close to the limit of solubility (which depends much on the counterion chosen and on the presence of ligands surrounding the metal ion).

For values higher than 0.5 mol l^{-1} , activities should be used instead of concentrations to predict the evolution of reactions, because the behavior of ions is influenced by that of the surrounding charged species (including coimpregnants) and the ionic strength acts on adsorption equilibria [44, 52, 53]. High concentrations also lead to an increase of the solution viscosity (Section 4.2).

It is also possible to prepare catalysts by contacting the support with a suspension in which the precursor is not totally dissolved (“slurry” or “solvent-assisted spreading”) [54, 55]. The equilibrium of dissolution is shifted by the adsorption of the precursor on the support surface, which depletes progressively the liquid phase from the dissolved ions. Molybdenum-containing catalysts have been prepared from MoO_3 by this method, with high yields in metal deposition [55]. Thanks to their viscosity, slurries are also convenient to impregnate foams [56].

It is finally recalled here that gases may be dissolved in the impregnation solution. Dissolved oxygen can cause the oxidation of air-sensitive complexes, possibly leading to less-soluble species [57]. Carbon dioxide contributes to the deposition of carbonate ions onto the support [58]. Upon NH_3 dissolution (Section 4.2.1), the solution pH may change and pH-related reactions of precipitation or complexation occur.

The pH is an important parameter in the impregnation process and its influence on the liquid and solid parts of the interface has been described in Chapters 2 and 3. The impregnation solution consists of a mixture of acidic and basic species, whose initial concentrations have been fixed to meet several constraints (mainly the active phase content and its distribution in the pores) and that are subjected to various pH-dependent and interrelated reactions of association or dissociation till equilibrium is reached. On the solid side, the pH rules the sign of the global surface charge and the number of charged sites, and it affects the dissolution of the oxide support both thermodynamically and kinetically.

In the simplest cases, a proper choice of pH should allow one to select the most abundant species in solution to be deposited onto the support. HNO_3 , carboxylic acids or NH_3 are usually chosen as pH adjusters, because these molecules decompose or desorb during thermal treatments. However, in the case of incipient wetness impregnation involving solutions that are neither very acidic nor very basic, the pH in the pore space is regulated by the acidobasic surface hydroxyls of the support (“buffer effect”) [59]; it is thus brought close to the point of zero charge (PZC) of the oxide (see also Chapter 3).

pH measurement and control *inside the pore system* is still a challenge, especially for nonequilibrium conditions, for example when the transport of the solute is under diffusional control and the composition of the solution is nonuniform inside the pellet. Devices based on fiber-optic sensors are being developed that might help resolve this problem [60].

4.4.2

Precursor-Support Interactions

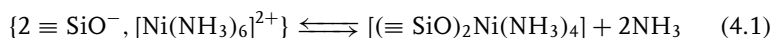
As far as the dispersion of the active phase is concerned, interactions between metal ions and an oxide surface are an important matter of study for two reasons. If the precursor concentration is low (for example when costly noble metals are to be deposited), these interactions are the driving force for the adsorption of individual metal ions on the support surface. If the precursor salt concentration is high, the species interacting with the surface act as seeds for the crystallization of the salt upon drying. In multistep impregnation, these seeds are formed in a first step, using a small quantity of precursor, while the rest of the precursor, which nucleates on the seeds, is introduced through successive sequences of impregnation and drying [61]. The building of the precursor–support interactions often involves the solvent, as an acidobasic species, as a ligand or as a reactant. This section presents a summary of the main interactions established between the chemical partners during impregnation and drying. A more thorough approach can be found in Chapters 2 and 3 of this book or in references devoted to interfacial coordination chemistry [62].

4.4.2.1 Adsorption: From Electrostatic Interactions to Grafting

If the support is considered as an inert receptacle for the ions, two types of interactions are usually considered as “strong” enough to drive the precursor adsorption. Both involve the hydroxyl groups of the surface, but one of them may be preferred depending on the pH of the solution, degree of hydroxylation of the surface, charge of the metal complex, and temperature of impregnation or drying.

The first type of interaction is electrostatic, between surface groups and the precursor complex if their charges are of opposite signs [63]. Typical examples are the use of acidic solutions of H_2PtCl_6 and basic solutions of $[\text{Pt}(\text{NH}_3)_4](\text{OH})_2$ in the preparation of $\text{Pt}/\text{Al}_2\text{O}_3$ catalysts. In the former case, the alumina surface ($\text{PZC} = 8$) is charged positively due to the low pH and $-\text{OH}_2^+$ groups attract anionic $[\text{PtCl}_6]^{2-}$ complexes. In the latter case, the alumina surface is charged negatively due to the high pH and $-\text{O}^-$ groups attract cationic $[\text{Pt}(\text{NH}_3)_4]^{2+}$ complexes. In contrast, on silica ($\text{PZC} = 2$), the electrostatic interactions between the oxide and H_2PtCl_6 are limited by the low quantity of positive surface charges, even in a very acidic solution. Interactions are better favored with $[\text{Pt}(\text{NH}_3)_4]^{2+}$, even in solutions that are not basic, and a precursor like $[\text{Pt}(\text{NH}_3)_4]\text{Cl}_2$ in a neutral solution can be employed [63–66].

The second type of interactions occurs when surface groups enter the coordination sphere of the metal ion by ligand substitution, leading to an entropy-driven chemical grafting of the ion onto the oxide that acts as a supermolecular ligand, such as in [39]:



This process requires bond scissions and creations; it can take place in solution but more often upon thermal activation during drying. The strength of this interaction is a function of the bond between metal ion and surface and some grafting reactions are reversible. ^{195}Pt NMR showed that chloroplatinate complexes grafted on silica dissociate from the surface upon exposure to ambient humidity, in contrast with the case of alumina (Figure 4.4) [40, 67]. Nongrafted chloroplatinates self-reduce into platinum dichloride and platinum metal upon thermal treatment, with an associated decrease of the metal dispersion.

4.4.2.2 The Formation of Mixed Phases

In fact, the support surface is not inert. The oxide/water system is thermodynamically metastable and a realistic description of its interface should take into account the oxide hydration and its possible dissolution. The kinetic factor, which is often overlooked for the two types of interactions described above, is here a parameter of prime importance, because the transformations involving the support are far from being instantaneous and should be favored by a long contact time between support and impregnation solution (“aging”).

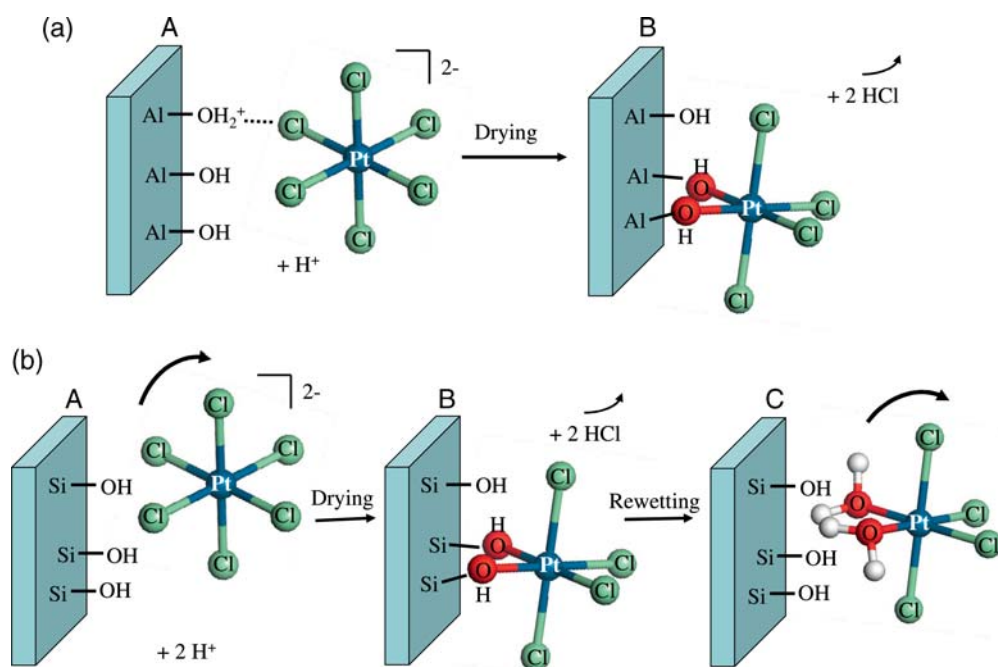


Figure 4.4 (a) Change in the adsorption mode of Pt^{IV} in $\text{H}_2\text{PtCl}_6/\text{Al}_2\text{O}_3$. A: after deposition and b: after drying. (b) Change in the adsorption mode of Pt^{IV} in $\text{H}_2\text{PtCl}_6/\text{SiO}_2$. A: after deposition, B: after drying, and C: after rehydration (rewetting).

Upon contact with water, an anhydrous oxide can transform into superficial oxyhydroxide or hydroxide phases detectable by X-ray diffraction, such as in the case of MgO or Al₂O₃, or gel-like hydrated layers, such as in the case of SiO₂ [68–70]. Temperature accelerates the diffusion and fixation of the ions inside the superficial hydrated layer; for instance, it was observed that the quantity of Ni²⁺ ions eliminated from alumina by washing after drying diminishes as the temperature of drying increases [71].

On the other hand, species released by the support dissolution can react with the precursor and form mixed phases. These are the compounds that are subsequently transformed during thermal treatments, and not the precursor as introduced initially. Typical extended mixed phases and their conditions of formation are presented in Table 4.2. The building of layered compounds resulting from the partial dissolution of alumina or magnesia takes place during impregnation. The case of silicates is not so clear-cut. For instance, zinc silicate is not detected at all after impregnation and drying at 25°C [37] and in certain conditions, the formation of silicates does not originate from a dissolution process during impregnation but from the temperature-activated reaction between hydroxynitrates and silica [38]. The formation of molecular mixed compounds, such as heteropolyanions, takes place when the catalyst is prepared from molybdates and tungstates [72–77]; the case of molybdates is detailed in Section 4.5.

Metal ions that are embedded inside a mixed phase at the support surface can be used as seeds for the subsequent growth of the active phase particles [61]. Unless the mixed phase decomposes during calcination, these ions are not accessible for catalysis. Subsequent thermal treatments trigger their further diffusion into the support bulk, where they can hardly be reduced. The resulting oxidic phases can, nevertheless, be useful; for example, nonreduced NiAl₂O₄ is reported to inhibit the sintering of nickel particles at high temperatures [85].

4.4.3 Ligands

The precursor used for impregnation is usually a commercial salt of low cost, in which, most often, the molecule bonded to the cation is H₂O, coming from the solvent or present in the crystals. However, it can be decided to add a ligand to the impregnation solution for several reasons:

- The charge of the ligand determines the global charge of the metal complex, which can therefore differ from that of the precursor ion. As a result, anionic chloro complexes of noble metals cations can adsorb electrostatically onto alumina at pH lower than 8, for which the alumina surface is charged positively.
- From a kinetic point of view, the substitution of aqua ligands by polydentate amines increases the lability of the remaining aqua ligands, favoring the chemical grafting of the complexes onto the oxide [86].

Table 4.2 Influence of the conditions of impregnation and drying on the formation of extended mixed phases. Italics identify the step considered by the authors as crucial for the formation of the mixed phase.

Support	Composition of the impregnation solution	Conditions of impregnation	Conditions of drying	Mixed phase	Ref.
SiO ₂	Ni(II) nitrate	IW, $t = 2$ h	$T = 90^{\circ}\text{C}$, $t \geq 72$ h	Ni(II) phyllosilicate	[38]
	Ni(II) nitrate + NH ₄ NO ₃ + NH ₃	<i>IW</i> , $pH \geq 6.9$	$T = 80\text{--}120^{\circ}\text{C}$, $t = 15$ h	Ni(II) phyllosilicate	[72]
	Mg(II) nitrate + NH ₄ NO ₃ + NH ₃	<i>ES</i> , $pH > 8$, $t = 15$ h	$T = 120^{\circ}\text{C}$, $t = 15$ h	Mg(II) hydrous silicate	[73]
	Co(II) nitrate	IW	<i>Vacuum</i> , $T = 100^{\circ}\text{C}$, $t = 24$ h+ $T = 200^{\circ}\text{C}$, $t = 5$ min	Co(II) silicate	[74]
	Co(II) nitrate + urea	IW, $pH \geq 5$, $t = 15$ min	Microwave, $t = 30$ min	Co(II) silicate	[75]
	Zn(II) nitrate	IW	$T = 120\text{--}200^{\circ}\text{C}$, $t = 24$ h	Zn(II) silicate	[37]
Al ₂ O ₃	Ni(II) chloride + NaOH	<i>ES</i> , $4 \leq pH \leq 7$, $t = 14$ h	$T = 120^{\circ}\text{C}$, $t = 15$ h	Hydrotalcite-like compounds (also named as Feitknecht phases)	[76]
	Co(II), Ni(II) or Zn(II) nitrates + NH ₄ NO ₃	<i>ES</i> , $7 < pH < 8.2$, $t > 30$ min	$T = 100^{\circ}\text{C}$, $t = 12$ h		[77]
MgO	Ni(II) nitrate	IW	$T = 120^{\circ}\text{C}$, $t = 15$ h	Ni(II)-containing Mg(OH) ₂	[78]

IW: incipient wetness impregnation; ES: impregnation in excess of solution.

- Ligands such as ammonia or ethylenediamine, which are not bridging, hinder the formation of ill-dispersed oligomers or mixed phases [87].
- Solutions containing chelates with multidentate ligands (such as citrate ions $^{-}\text{OOC}-\text{CH}_2-\text{C}(\text{OH})(\text{COO}^{-})-\text{CH}_2-\text{COO}^{-}$) give an amorphous viscous deposit sticking to the support surface upon drying [51]. The phase obtained after thermal treatments is more dispersed than with crystallized precursors.

Coimpregnants also influence the precursor speciation by their coordinating properties. HCl acts not only as a competitor but also as a stabilizing agent for the coordination sphere of platinum when hexachloroplatinic acid is used. It

has been shown that the PtCl_6^{2-} anion can lose two or four chloride ligands after a few hours in the absence of hydrochloric acid, modifying its tendency to graft onto the support surface [88].

4.4.4

Counterions

The precursor salt introduced by impregnation should be (i) soluble and (ii) easily transformed into an oxidic or metallic phase upon heating. The choice of the counterions balancing the charge of the precursor complexes is steered by these two criteria.

If we consider metals from the Mn–Zn series, chlorides and sulfates are readily soluble, but chloride ions may act as poisons for the active phases [89] and sulfate ions do not decompose at moderate temperatures. However, their presence is sometimes searched for due to the acidity they can induce on the support [90]. The most used precursors are metal nitrates sold under the dualistic formula $\text{M}(\text{NO}_3)_x \cdot y\text{H}_2\text{O}$, which associate a high solubility (respectively, 8.5 and 4.6 mol per l of water at room temperature for nickel or cobalt, respectively) to the possibility of decomposing nitrate ions by calcination between 250 and 350°C [91]. Carboxylates such as formates or acetates have been sometimes used, though they are more than three times less soluble than nitrates [92]. These anions also have coordinative properties toward the cations in solution or in the crystals, as is the case for the acetylacetonate anion, which gives precursors soluble in organic solvents.

In the case of anionic precursors like molybdate, vanadate, or tungstate ions, it is the cation that must leave the support during thermal treatment. Alkaline cations should thus be discarded. Salts are thus preferred in their ammonium or protonic form (for instance $(\text{NH}_4)_6\text{Mo}_7\text{O}_{24}$, $(\text{NH}_4)_2\text{Mo}_2\text{O}_7$, H_2MoO_4). Late transition-metal ions (rhodium, palladium, iridium, platinum) are usually supplied in a complexed form, with chloride ions or NH_3 molecules as ligands, and H^+ , OH^- or NH_4^+ as counterions. It is important to note that unlike nitrates or chlorides, these three ions, whose concentration is fixed by the imperatives of the impregnation procedure, determine the pH of the impregnating solution (Section 4.3.1). The same can be said of carboxylate anions.

The presence of these counterions throughout the preparation is a marked difference from other processes of precursor introduction such as ion exchange. It is the overall system including the counterions that is transformed during the thermal treatments: to influence the final nature of the catalytic system, one can take advantage of the reducing properties of NH_4^+ toward the metal ion or of the oxidizing properties of NO_3^- toward ligands and/or metal ion. For example, large precursor crystals containing organic ligands and oxidizing anions may decompose into smaller particles when the process of decomposition involves the release of gaseous products [33, 71].

4.5

Impregnation and Drying of an $\text{MoO}_x/\text{Al}_2\text{O}_3$ Catalyst

A number of reviews has been published on the structure of alumina-supported oxidic Mo systems [93–97]. A hydrode sulfurization (HDS) catalyst prepared by incipient wetness impregnation contains about 10 wt% Mo, which implies an impregnation solution in which the Mo concentration is $1\text{--}2\text{ mol l}^{-1}$. The precursor salt is usually ammonium heptamolybdate, known for its high solubility [98]. According to Raman spectroscopy studies [99–101], monomeric fourfold coordinated Mo species are present after calcination on the alumina surface if the Mo loading lies below 3 Mo wt% (about 1 Mo at nm^{-2} for a typical specific surface area of $200\text{ m}^2\text{ g}^{-1}$), but these species coexist with polymeric sixfold coordinated Mo species at higher loadings, MoO_3 being detected above 7 Mo wt% (2.5 Mo at nm^{-2}). Is there a relationship between the speciation of Mo in the impregnation solution and the speciation of Mo on alumina after calcination? Can impregnation and drying parameters be varied so as to modify this speciation?

4.5.1

Molybdenum Speciation and Its Consequences

In solution, molybdenum (VI) presents a pH-dependent aqueous chemistry based on the existence of monomeric and polymeric oxoanions [102]. At low concentration and $\text{pH} \geq 4$, Mo is mainly present as monomeric species, described as a fourfold coordinated MoO_4^{2-} or sixfold coordinated $[\text{MoO}_2(\text{OH})_2(\text{H}_2\text{O})_2]$ [103]. At higher Mo concentration, hepta- or octamolybdates resulting from the polymerization of octahedral oxoanions are formed [103, 104]. In the presence of Al^{III} ions, a new species appears in the Mo speciation diagram [104]: an Anderson-type heteropolyanion made of six edge-sharing octahedra surrounding one $\text{Al}(\text{OH})_6$ octahedron (Figure 4.5). At the natural pH of an ammonium molybdate solution and in the presence of Al^{III} ions, one of the predominant Mo-containing species may thus be $[\text{Al}(\text{OH})_6\text{Mo}_6\text{O}_{18}]^{3-}$ (denoted $[\text{AlMo}_6]$).

Luthra and Cheng [105] and Sarrazin *et al.* [106] studied Mo speciation *in solution* by liquid-state ^{95}Mo NMR during alumina impregnation. The former authors showed that starting from a heptamolybdate solution at initial $\text{pH} = 5.5$ (5.4 Mo wt%), MoO_4^{2-} was the only species actually detected in the wet porosity. The depolymerization of heptamolybdates to monomolybdates was assigned to a pH increase resulting from the buffer power of the support (see Section 4.4.1 and Chapter 3). Alternatively, Sarrazin *et al.* [106] suggested that MoO_4^{2-} was present because the overall concentration [Mo] in the liquid phase had decreased, driven by the preferential adsorption of more condensed species; 97% of the Mo initially present in the impregnation solution was

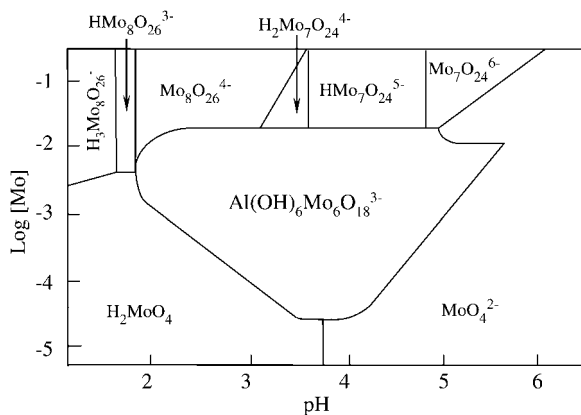
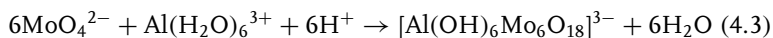
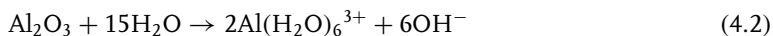


Figure 4.5 Predominance diagram of Mo(VI)-containing species at $[\text{Al}]_{\text{tot}} = 10^{-3}$ M. (Reproduced with permission from *Inorg. Chem.* **1989**, 28, 3629–3632. Copyright 1989 American Chemical Society.)

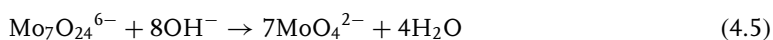
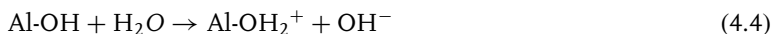
supposed to be adsorbed and only a minor fraction of the Mo species was detected with liquid-state NMR.

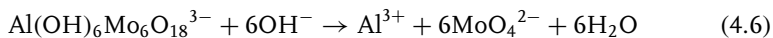
The chemistry of Mo adsorption on alumina was later reconsidered by two groups [75, 76] assuming that Al^{III} ions resulting from the dissolution of alumina had a role to play. Using Raman spectroscopy, ^{27}Al and ^{95}Mo NMR, it was shown that during impregnation, $[\text{AlMo}_6]$ was the predominant Mo-containing species both in solution and on the support. In fact, the total amount of solubilized Al increases because the reaction with Mo oxoanions (2) shifts the alumina dissolution equilibrium (Equation 4.2) to the right (ligand-promoted support dissolution [75]).



It was further demonstrated [48] than in the conditions of dry impregnation (i.e. with a high Mo concentration, about 2.1 M), $(\text{NH}_4)_3[\text{Al}(\text{OH})_6\text{Mo}_6\text{O}_{18}]$ precipitates on the support (solubility: $[\text{Mo}] = 0.13$ M [107]).

Taking into account Equations 4.3–4.5 it can be calculated under which conditions heptamolybdates or $[\text{AlMo}_6]$ deposit on the support or decompose into monomolybdate monomers [48].





The amount of OH^- in the intraporous liquid is assumed to be fixed by the buffer power of alumina and the amount of ionizable basic OH groups on alumina is evaluated to a maximum of $3.5 \mu\text{mol m}^{-2}$ [108, 109]. Calculations show that $[\text{AlMo}_6]$ is the predominant species for Mo loadings above 6.3 Mo wt%, while heptamolybdates would predominate for a lower Mo weight content. However, depolymerization into monomolybdates occurs for a Mo loading lower than 5.6 Mo wt%. These values fit quite well with the figures reported above. A validation of this estimate can be found in the work of Le Bihan *et al.* [76]. These authors demonstrated that the preparation of a catalyst containing 4 wt% Mo from a solution of $[\text{AlMo}_6]$ leads to the deposition of tetrahedrally coordinated molybdates.

As a conclusion, only in a very restricted number of cases is the original precursor, heptamolybdate, deposited as the main species on the alumina surface. Due to pH effects inherent in the impregnation procedure, at low concentrations, it decomposes totally or partly into monomers that are still detected after calcination. Due to chemical equilibria involving the support, at high concentrations, it forms a poorly soluble polymeric species that precipitates as large crystals in the course of the impregnation, as confirmed by X-ray diffraction (XRD) [48], and later transforms into MoO_3 during thermal treatments.

4.5.2

Degrees of Freedom: Drying Parameters and Ligands in Solution

The low dispersion of molybdenum after calcination is not the only problem brought about by the formation of poorly soluble species upon impregnation. Impregnation of extrudates by molybdate solutions is usually followed by an aging step carried out either in air or in a water-saturated atmosphere for a duration ranging from a few minutes to a few hours. This step is justified by the need to let the solute diffuse into the support pores in order to achieve a homogeneous distribution of molybdenum in the pellet. However, the results of Goula *et al.* [30] challenged this intuitive reasoning since these authors showed that long impregnation time (up to 3 hours) and high concentration favor a sharp egg-shell distribution with deposition of Mo at the outer parts of the extrudates.

In fact, as can be deduced from the previous section, more time for aging also means more time for alumina dissolution and thus for $[\text{AlMo}_6]$ formation and precipitation, which may lead to pore blocking. This has been confirmed by Raman microscopy locally applied to cross-sections of impregnated alumina extrudates [110]. After 24 hours of aging, the main species detected after drying are large clusters of $[\text{AlMo}_6]$ on the outer section of the pellets, while the concentration in molybdates is low inside. The aging period would thus favor an egg-shell distribution of ill-dispersed Mo phases.

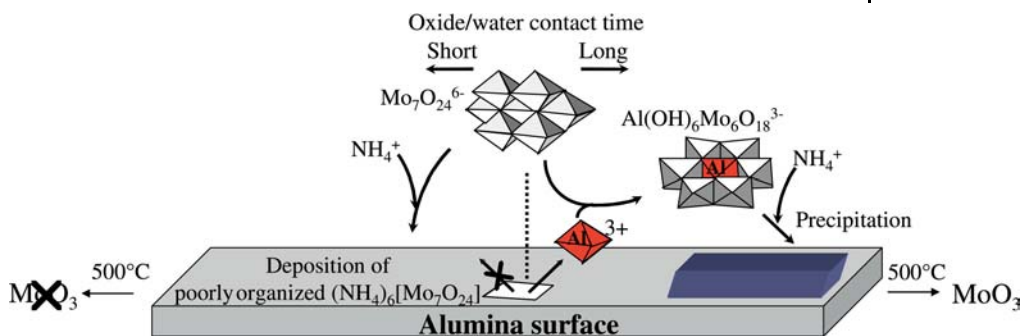


Figure 4.6 Schematic representation of the molecular-scale phenomena occurring at the oxide/water interface (impregnation) and oxide/gas interface (calcination) during alumina-supported Mo catalysts preparation. (Reprinted from *J. Mol. Struct.*, 656, X. Carrier *et al.*, Influence of aging on MoO₃ formation in the preparation of alumina-supported Mo catalysts, 231–238, Copyright 2003, with permission from Elsevier.)

How can this situation be changed? This could be by adjusting kinetic parameters during the drying step [48] or by changing the composition of the impregnating solution via the addition of ligands [110].

Indeed, the oxide/water contact time is drastically reduced if one freezes the impregnated catalyst with liquid nitrogen a few seconds after impregnation, and then freeze-dries the solvent in vacuum [48]. The consequence of this procedure is to limit the extent of MoO₃ formation after calcination (Figure 4.6): alumina dissolution and [AlMo₆] precipitation have been inhibited, whereas conventional drying at about 100–120°C probably speeds up the alumina dissolution rate, especially since liquid water is initially present.

As far as extrudates are concerned, Bergwerff *et al.* [110] have succeeded in limiting [AlMo₆] formation by using Mo complexing agents such as citrate and phosphate. In these cases, stable and soluble Mo complexes (such as P₂Mo₅O₂₃⁶⁻ and Mo₄(Hcitrate)₂O₁₁⁴⁻) diffuse in the pores of the pellets, which leads to a more homogeneous Mo distribution. It has also to be kept in mind that these anionic ligands (phosphate and citrate) act as competitors with Mo for adsorption sites that is another favorable parameter to obtain a uniform Mo profile [30]. These results have important practical implications since the addition of organic additives in the impregnation solution is currently one of the research directions for improving the activity of HDS catalysts [111].

4.6 Conclusions

Contacting a porous solid with a solution and subsequently evaporating the solvent are unit operations that technically speaking are easy to implement,

both at the laboratory and at the industrial scales. However, a closer look at the physics and chemistry inherent in impregnation and drying reveals differences as far as their optimization is concerned.

The impregnated system is heavily determined by the conjunction of inter-related parameters (concentrations, pH, viscosity, choice of counterions and competitors, use of water as a solvent). Improving the quality of impregnation thus requires investigation of the chemistry of the system in its whole complexity and to take advantage of the few degrees of freedom left (adjusting the pH, introducing ligands or organic additives, using time as a variable influencing chemistry) in order to imagine new rationalized procedures. In contrast, a large number of parameters can be varied in the drying step (temperature, heating rate, gas flow and pressure, time) but regrettably they have seldom been studied in a systematic way. Moreover, some variables are not easy to quantify beforehand (“strength” of the precursor – support interactions) or remain semiempirical (permeability, tortuosity of the support). It can be suggested that in order to optimize drying for a given system, dual studies should be undertaken on powders and on extrudates, so as to first decouple the chemical aspects from the physical phenomena of transport.

The examples presented in this chapter concern oxides impregnated with aqueous solutions but the field of nonaqueous solvents, which exhibit different coordinative properties, dielectric constant, viscosity, and boiling temperature, and in which precursors like carboxylates and acetylacetonates can be dissolved, should probably be explored more thoroughly. The use of supercritical fluids can also be considered. The fact that more catalysts are being prepared on supports such as carbon fibers or polymers, whose interfacial chemistry is less known than that of oxides, adds interest to these directions of research.

As has been shown by the example of $\text{MoO}_x/\text{Al}_2\text{O}_3$ catalysts, the speciation of the active phase after thermal treatments often is connected to the speciation of the precursor after impregnation and drying. Improving the properties of a catalyst thus needs the combined efforts of industry, who identify obstacles to overcome and assess the feasibility of any change in the unit operations, of the chemical engineering, to increase the reliability of the models via the input of experimental data, and of molecular chemists for the analysis of the physico-chemical conditions, investigation of the reactions paths, and suggestions for alternative procedures.

References

1. Deacon, H. (1868) US Patent 85,370, Dec. 19th, 1868.
2. Deacon, H. (1872) US Patent 123,875, Feb. 20th, 1872.
3. Deacon, H. (1873) US Patent 141,333, July 29th, 1873.
4. Geus, J.W. (2007) in *Catalyst Preparation* (ed. J. Regalbuto), CRC Press LLC, Boca Raton, p. 341.
5. Bourikas, K., Kordulis, C. and Lycourghiotis, A. (2006) *Catal. Rev. Sci. Eng.*, **48**, 363.

6. Hutchings, G.J. and Vedral, J.C. (2004) *Springer Ser. Chem. Phys.*, **75**, 217.
7. Perego, C. and Villa, P. (1997) *Catal. Today*, **34**, 281.
8. Regalbuto, J.R. and Antos, G.J. (2004) *Chem. Ind.*, **100**, 141.
9. Toebes, M.L., van Dillen, J.A. and de Jong, K.P. (2001) *J. Mol. Catal. A*, **173**, 75.
10. Bond, G.C. and Thompson, D.T. (1999) *Catal. Rev. Sci. Eng.*, **41**, 319.
11. Iglesia, E. (1997) *Appl. Catal. A*, **161**, 59.
12. Neimark, A.V., Kheifets, L.I. and Fenelonov, V.B. (1981) *Ind. Eng. Chem. Prod. Res. Dev.*, **20**, 439.
13. Lee, S.Y. and Aris, R. (1985) *Catal. Rev. Sci. Eng.*, **27**, 207.
14. Lekhal, A., Glasser, B.J. and Khinast, J.G. (2001) *Chem. Eng. Sci.*, **56**, 4473.
15. Gavrilidis, A., Varma, A. and Morbidelli, M. (1993) *Catal. Rev. Sci. Eng.*, **35**, 399.
16. Lopes, I., El Hassan, N., Guerba, H., Wallez, G. and Davidson, A. (2006) *Chem. Mater.*, **18**, 5826.
17. Qin, Q. and Ramkrishna, D. (2005) *Ind. Eng. Chem. Res.*, **44**, 6466.
18. Galarraga, C., Peluso, E. and de Lasa, H. (2001) *Chem. Eng. J.*, **82**, 13.
19. Papageorgiou, P., Price, D.M., Gavrilidis, A. and Varma, A. (1996) *J. Catal.*, **158**, 439.
20. Le Page, J.F. (1987) *Applied Heterogeneous Catalysis*, Technip, Paris, p. 12.
21. Hepburn, J.S., Stenger, H.G. and Lyman, C.E. Jr. (1989) *Appl. Catal.*, **55**, 287.
22. Hegedus, L.L., Chou, T.S., Summers, J.C. and Potter, N.M. (1979) *Stud. Surf. Sci. Catal.*, **3**, 171.
23. Wang, J., Zhang, J. and Pang, L. (1983) *Stud. Surf. Sci. Catal.*, **16**, 37.
24. (a) Weisz, P.B. (1967) *Trans. Faraday Soc.*, **63**, 1801; (b) Weisz, P.B. and Hicks, J.S. (1967) *Trans. Faraday Soc.*, **63**, 1807.
25. Hanika, J., Janousek, V. and Sporka, K. (1987) *Collect. Czech. Chem. Commun.*, **52**, 663 672.
26. Maitra, A.M., Cant, N.W. and Trimm, D.L. (1986) *Appl. Catal.*, **27**, 9.
27. Harriott, P. (1969) *J. Catal.*, **14**, 43.
28. Vincent, R.C. and Merrill, R.P. (1974) *J. Catal.*, **35**, 206.
29. Assaf, E.M., Jesus, L.C. and Assaf, J.M. (2003) *Chem. Eng. J.*, **94**, 93.
30. Goula, M.A., Kordulis, C. and Lycourghiotis, A. (1992) *J. Catal.*, **133**, 486.
31. Li, W.D., Li, Y.W., Qin, Z.F. and Chen, S.Y. (1994) *Chem. Eng. Sci.*, **49**, 4889.
32. Pizzio, L.R., Cáceres, C.V. and Blanco, M.N. (1995) *Catal. Lett.*, **33**, 175.
33. Négrier, F., Marceau, E., Che, M. and de Caro, D. (2003) *C. R. Chim.*, **6**, 231.
34. Iglesia, E., Soled, S.L., Baumgartner, J.E. and Reyes, S.C. (1995) *J. Catal.*, **153**, 108.
35. Cseri, T., Békassy, S., Kennesey, G., Liptay, G. and Figueras, F. (1996) *Thermochim. Acta*, **288**, 137.
36. Mhamdi, M., Marceau, E., Khaddar-Zine, S., Ghorbel, A., Che, M., Ben Taarit, Y. and Villain, F. (2005) *Z. Phys. Chem.*, **219**, 963.
37. Chouillet, C., Villain, F., Kermarec, M., Lauron-Pernot, H. and Louis, C. (2003) *J. Phys. Chem. B*, **107**, 3565.
38. Louis, C., Cheng, Z.X. and Che, M. (1993) *J. Phys. Chem.*, **97**, 5703.
39. Bonneviot, L., Legendre, O., Kermarec, M., Olivier, D. and Che, M. (1990) *J. Colloid Interface Sci.*, **134**, 534.
40. Lambert, J.F., Marceau, E., Shelimov, B., Lehman, J., Le Bel de Penguilly, V., Carrier, X., Boujday, S., Pernot, H. and Che, M. (2000) *Stud. Surf. Sci. Catal.*, **130B**, 1043.
41. Komiyama, M., Merrill, R.P. and Harnsberger, H.F. (1980) *J. Catal.*, **63**, 35.
42. Deegan, R.D., Bakajin, O., Dupont, T.F., Huber, G., Nagel, S.R. and Witten, T.A. (2000) *Phys. Rev. E*, **62**, 756.
43. Uemura, Y., Hatate, Y. and Ikari, A. (1986) *J. Chem. Eng. Jpn.*, **19**, 560.

44. Santhanam, N., Conforti, T.A., Spieker, W. and Regalbuto, J.R. (1994) *Catal. Today*, **21**, 141.
45. Villegas, L., Masset, F. and Guilhaume, N. (2007) *Appl. Catal. A*, **320**, 43.
46. Hwang, Y.K., Kim, D.K., Mamman, A.S., Park, S.E. and Chang, J.S. (2007) *Chem. Lett.*, **26**, 186.
47. Vergunst, T., Kapteijn, F. and Moulijn, J.A. (2001) *Appl. Catal. A*, **213**, 179.
48. Carrier, X., Lambert, J.F., Kuba, S., Knözinger, H. and Che, M. (2003) *J. Mol. Struct.*, **656**, 231.
49. Johnson, D.W., Gallagher, P.K., Schnettler, F.J. and Vogel, E.M. Jr. (1979) *Am. Ceram. Soc. Bull.*, **56**, 785.
50. Kotter, M. and Rieker, L. (1983) *Chem. Eng. Fundament.*, **2**, 21 31.
51. (a) van de Loosdrecht, J., van der Haar, M., van den Kraan, A.M., van Dillen, A.J. and Geus, J.W. (1997) *Appl. Catal. A*, **150**, 365; (b) Soled, S.L., Iglesia, E., Fiato, R.A., Baumgartner, J.E., Vroman, H. and Miseo, S. (2003) *Top. Catal.*, **26**, 101; (c) van Dillen, A.J., Terörde, R.J.A.M., Lensveld, D.J., Geus, J.W. and de Jong, K.P. (2003) *J. Catal.*, **216**, 257.
52. Ruckenstein, E. and Karpe, P. (1989) *Langmuir*, **5**, 1393.
53. Shah, A.M. and Regalbuto, J.R. (1994) *Langmuir*, **10**, 500.
54. Ben Boubaker, H., Mhamdi, M., Marceau, E., Khaddar-Zine, S., Ghorbel, A., Che, M., Ben Taarit, Y. and Villain, F. (2006) *Microporous Mesoporous Mater.*, **93**, 62.
55. (a) Zdrzil, M. (1994) *Appl. Catal. A*, **115**, 285; (b) Gulkova, D., Kaluza, L., Vit, Z. and Zdrzil, M. (2006) *Catal. Lett.*, **112**, 193.
56. Giani, L., Cristiani, C., Groppi, G. and Tronconi, E. (2006) *Appl. Catal. B*, **62**, 121.
57. Dumond, F., Marceau, E. and Che, M. (2007) *J. Phys. Chem. C*, **111**, 4780.
58. Lee, D.H. and Condrate, R.A. Sr. (1995) *Mater. Lett.*, **23**, 241.
59. Spieker, W.A. and Regalbuto, J.R. (2001) *Chem. Eng. Sci.*, **56**, 3491.
60. Lin, J. (2000) *Trends Anal. Chem.*, **19**, 541.
61. Che, M., Cheng, Z.X. and Louis, C. (1995) *J. Am. Chem. Soc.*, **117**, 2008.
62. (a) Lepetit, C. and Che, M. (1995) *J. Mol. Catal.*, **100**, 147; (b) Lambert, J.F. and Che, M. (2000) *J. Mol. Catal. A*, **162**, 5.
63. Brunelle, J.P. (1978) *Pure Appl. Chem.*, **50**, 1211.
64. Sermon, P.A. and Sivalingam, J. (1992) *Colloids Surf.*, **63**, 59.
65. Mang, T., Breitscheidel, B., Polanek, P. and Knözinger, H. (1993) *Appl. Catal. A*, **106**, 239.
66. Miller, J.T., Schreier, M., Kropf, J.A. and Regalbuto, J.R. (2004) *J. Catal.*, **225**, 203.
67. Boujday, S., Lehman, J., Lambert, J.F. and Che, M. (2003) *Catal. Lett.*, **88**, 23.
68. Parks, G.A. (1965) *Chem. Rev.*, **65**, 177.
69. (a) Lefèvre, G., Duc, M., Lepeut, P., Caplain, R. and Fédoroff, M. (2002) *Langmuir*, **18**, 7530; (b) Carrier, X., Marceau, E., Lambert, J.F. and Che, M. (2007) *J. Colloid Interface Sci.*, **308**, 429.
70. Vigil, G., Xu, Z., Steinberg, S. and Israelachvili, J. (1994) *J. Colloid Interface Sci.*, **165**, 367.
71. Négrier, F., Marceau, E., Che, M., Giraudon, J.M., Gengembre, L. and Löfberg, A. (2005) *J. Phys. Chem. B*, **109**, 2836.
72. Bañares, M.A., Hu, H. and Wachs, I.E. (1995) *J. Catal.*, **155**, 249.
73. Kasztelan, S., Payen, E. and Moffat, J.B. (1988) *J. Catal.*, **112**, 320.
74. van Veen, J.A.R. and Hendriks, P.A.J.M. (1986) *Polyhedron*, **5**, 75.
75. Carrier, X., Lambert, J.F. and Che, M. (1997) *J. Am. Chem. Soc.*, **119**, 10137.
76. Le Bihan, L., Blanchard, P., Fournier, M., Grimblot, J. and Payen, E. (1998) *J. Chem. Soc., Faraday Trans.*, **94**, 937.
77. Carrier, X., d'Espinose de la Caillerie, J.B., Lambert, J.F. and

- Che, M. (1999) *J. Am. Chem. Soc.*, **121**, 3377.
78. (a) Clause, O., Kermarec, M., Bonneviot, L., Villain, F. and Che, M. (1992) *J. Am. Chem. Soc.*, **114**, 4709; (b) Kermarec, M., Carriat, J.Y., Burattin, P., Che, M. and Decarreau, A. (1994) *J. Phys. Chem.*, **98**, 12008.
 79. d'Espinose de La Caillerie, J.B., Kermarec, M. and Clause, O. (1995) *J. Phys. Chem.*, **99**, 17273.
 80. Coulter, K.E. and Sault, A.G. (1995) *J. Catal.*, **154**, 56.
 81. Ming, H. and Baker, B.G. (1995) *Appl. Catal.*, **123**, 23.
 82. de Bokx, P.K., Wassenberg, W.B.A. and Geus, J.W. (1987) *J. Catal.*, **104**, 86.
 83. (a) Paulhiac, J.L. and Clause, O. (1993) *J. Am. Chem. Soc.*, **115**, 11602; (b) d'Espinose de la Caillerie, J.B., Kermarec, M. and Clause, O. (1995) *J. Am. Chem. Soc.*, **117**, 11471.
 84. Malet, P., Martin, M., Montes, M. and Odriozola, J.A. (1997) *Solid State Ion.*, **95**, 137.
 85. Bolt, P.H., Habraken, F.H.P.M. and Geus, J.W. (1995) *J. Catal.*, **151**, 300.
 86. (a) Lambert, J.F., Hoogland, M. and Che, M. (1997) *J. Phys. Chem. B*, **101**, 10347; (b) Boujday, S., Lambert, J.F. and Che, M. (2004) *ChemPhysChem*, **5**, 1003.
 87. Kermarec, M., Carriat, J.Y., Burattin, P., Che, M. and Decarreau, A. (1994) *J. Phys. Chem.*, **98**, 12008.
 88. (a) Shelimov, B., Lambert, J.F., Che, M. and Didillon, B. (1999) *J. Am. Chem. Soc.*, **121**, 545; (b) Shelimov, B., Lambert, J.F., Che, M. and Didillon, B. (1999) *J. Catal.*, **185**, 462.
 89. Richardson, J.T., Ortego, J.D., Coute, N. and Twigg, N.V. Jr. (1996) *Catal. Lett.*, **41**, 17.
 90. Sohn, J.R. and Park, W.C. (2003) *Appl. Catal. A*, **239**, 269.
 91. Yuvaraj, S., Lin, F.Y., Chang, T.H. and Chuin-Tih, Y. (2003) *J. Phys. Chem. B*, **107**, 1044.
 92. (a) Rosynek, M.P. and Polansky, C.A. (1991) *Appl. Catal.*, **73**, 97; (b) Boudjahem, A.G., Monteverdi, S., Mercy, M., Ghanbaja, D. and Bettahar, M.H. (2002) *Catal. Lett.*, **84**, 115.
 93. Topsøe, H., Clausen, B.S. and Massoth, F.E. (1996) *Hydrotreating Catalysis*, Springer-Verlag, Berlin.
 94. Knözinger, H. (1989) Proceedings of the 9th International Congress Catalysis, Vol. 5, The Chemical Institute of Canada, Calgary, Ottawa, p. 20.
 95. Grimblot, J. (1998) *Catal. Today*, **41**, 111.
 96. Blanchard, P., Lamonnier, C., Griboval, A. and Payen, E. (2007) *Appl. Catal. A*, **322**, 33.
 97. Breyse, M., Afanasiev, P., Geantet, C. and Vrinat, M. (2003) *Catal. Today*, **86**, 5.
 98. Tsigdinos, G.A., Chen, H.Y. and Streusand, B.J. (1981) *Ind. Eng. Chem. Prod. Res. Dev.*, **20**, 619.
 99. Jeziorowski, H. and Knözinger, H. (1979) *J. Phys. Chem.*, **83**, 1166.
 100. Payen, E., Grimblot, J. and Kasztelan, S. (1987) *J. Phys. Chem.*, **91**, 6642.
 101. Hu, H., Wachs, I.E. and Bare, S.R. (1995) *J. Phys. Chem.*, **99**, 10897.
 102. Baes, C.F. and Mesmer, R.E. (1976) *The Hydrolysis of Cations*, John Wiley & Sons, Inc., New York.
 103. Pope, M.T. (1983) *Heteropoly and Isopoly Oxometalates*, Springer-Verlag, Berlin.
 104. Öhman, L.O. (1989) *Inorg. Chem.*, **28**, 3629.
 105. Luthra, N.P. and Cheng, W.C. (1987) *J. Catal.*, **107**, 154.
 106. Sarrazin, P., Mouchel, B. and Kasztelan, S. (1991) *J. Phys. Chem.*, **95**, 7405.
 107. Filatenko, L.A., Ivanov-Emin, B.N., Ol'GinKin'ones, S., Zaitsev, B.E., Ivlieva, V.I. and Ezhov, A.I. (1973) *Russ. J. Inorg. Chem.*, **18**, 419.
 108. Spanos, N., Vordonis, L., Kordulis, C. and Lycourghiotis, A. (1990) *J. Catal.*, **124**, 301.

109. van Veen, J.A.R., Hendriks, P.A.J.M., Romers, E.J.G.M. and Andrea, R.R. (1990) *J. Phys. Chem.*, **94**, 5275.
110. (a) Bergwerff, J.A., Visser, T., Leliveld, B.R.G., Rossenaar, B.D., de Jong, K.P. and Weckhuysen, B.M. (2004) *J. Am. Chem. Soc.*, **126**, 14548; (b) Bergwerff, J.A., Jansen, M., Leliveld, B.R.G., Visser, T., de Jong, K.P. and Weckhuysen, B.M. (2006) *J. Catal.*, **243**, 292.
111. Costa, V., Marchand, K., Digne, M. and Geantet, C. (2008) *Catal. Today*, **130**, 69.

5

Sol-Gel Processing

Miron V. Landau

5.1

Introduction

Sol-gel processing is one of the routes for the preparation of porous materials by their solidification from a true solution phase [1]. Its physicochemical principles and applications are well described in the literature [2, 3]. The method is characterized by the formation of stable colloidal solutions ("sol") in the first step followed by anisotropic condensation of colloidal particles (micelles) producing polymeric chains with entrapped solution of condensation by-products, resulting in the formation of a "xero- or hydrogel" or "monolith" when external solvent is not used. After washing out the by-products the solvent removal produces "xero-" or "aerogels," depending on the drying mode, with distinct structure of the primary particles, and their packing manner (texture) [4, 5]. For clarity of terminology, the sol-gel method should be distinguished from other routes of materials solidification from solutions: precipitation and deposition-precipitation, crystallization from melts, expansion of supercritical solvent, supercritical antisolvent method, supramolecular assembling, and others. The main peculiarity, making the sol-gel route unique and clearly discernible, is formation of a clear colloidal solution due to primary condensation of dissolved molecular precursors. The second peculiarity is the merging of these colloidal particles during the subsequent gelation stage into polymeric chains by chemical bonding between local reactive groups at their surface. This prevents flocculation being a result of isotropic micelle aggregation (Figure 5.1). The porous solids (xero- or aerogels) are produced in the next, the desolvation step depending on the drying mode (Figure 5.1).

Both stages are controlled by condensation chemistry that can include, as a first step, hydrolysis of hydrated metal ions or metal alkoxide molecules [6, 7] (hydrolytic sol-gel processing). The condensation chemistry in this case is based on ololation/oxolation reactions between hydroxylated species. The hydroxylated species for further condensation can be formed also by a non-hydrolytic route, that is, by reactions between metal chlorides and alcohols with electron-donor substituents [8]. The nonhydrolytic sol-gel processing may

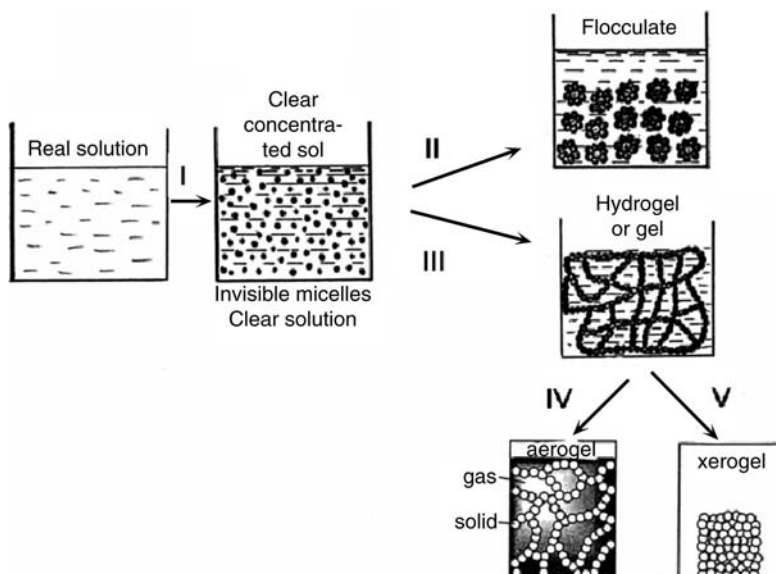


Figure 5.1 General scheme of sol-gel processing in the preparation of solid materials: I – colloidization; II – flocculation; III – gelation; IV – supercritical fluid processing; and V – drying by evaporation.

also proceed without intermediate formation of hydroxylated species when it is based on esterification of metal chelate complexes with free carboxylic groups and polyalcohols [9, 10]. Another nonhydrolytic/nonhydroxylating sol-gel route relies on direct condensation reactions between metal alkoxides and metal chlorides or acetates with elimination of alkylchlorides or esters [9, 11].

The characteristics of sol-gel processing allow the application of different strategies for the preparation of solid catalytic materials. A schematic representation is shown in Figure 5.2. The gelation of colloidal solution followed by desolvation of the obtained gel can be applied for the preparation of three types of materials:

- bulk uniphase materials, that is, mono- or multimetallic xero- or aerogels (I→II)
- bulk multiphase materials where molecular moieties or condensed phases are entrapped between polymeric chains of the gel matrices and/or cogenerated from a mixed colloidal solution ((I + III)→IV)
- porous uni- and multiphase coatings and nanometric films prepared by conducting the gelation inside a thin film of colloidal solution at the surface of a supporting material (substrate) (I→II→V; (I + III)→V).

In the present chapter the physicochemical basis of the sol-gel processing will be discussed, as well as synthesis parameters that control the properties of the obtained materials – structure/texture and catalytic performance. The attention

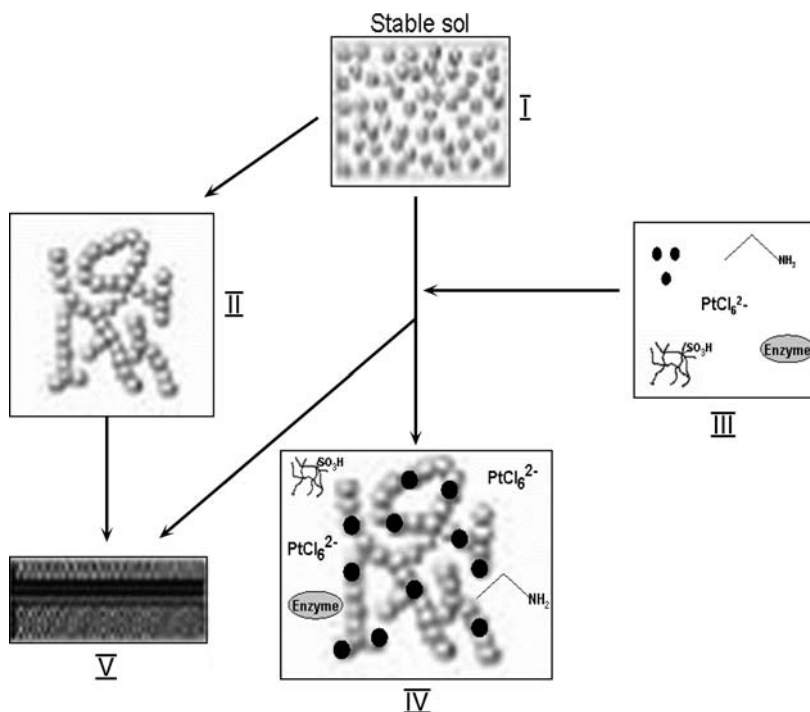


Figure 5.2 Schematic diagram showing different applications of sol-gel processing for the preparation of catalytic materials: I – stable sol; II – gel; III – sources of additional catalytic chemical functionality; IV – gel with included sources of additional catalytic chemical functionality; and V – catalytic coating.

is focused on the sol-gel synthetic strategies for preparation of mono- and multimetallic oxide phases and catalytic materials entrapped in porous matrices. Only those catalytic materials will be considered where the sol-gel principle is an essential part of the preparation strategy. Deposition, grafting or anchoring of catalytic phases or functionalized molecular moieties on sol-gel-derived supports or coatings as well as methods not using the full sequence of sol-gel processing, like spray drying of colloidal solutions, are dealt with in other chapters.

5.2

Physicochemical Basis and Principles of Sol-Gel Processing

Sol-gel processing is a sequence of operations including chemical reactions and physical processes (phase separation, dissolution, evaporation, phase transition, etc.) leading to the formation of porous solids (metal oxides or oxide-free materials) from liquid solutions of molecular precursors. Its general principles and the physicochemical basis of separate steps are well described and analyzed in many comprehensive books and reviews [2, 3,

5–7, 9, 12–18]. The sol-gel processing sequence includes the following seven main stages: (i) conversion (activation) of dissolved molecular precursors to the reactive state; (ii) polycondensation of activated molecular precursors into nanoclusters (micelles) forming a colloidal solution – sol; (iii) gelation; (iv) aging; (v) washing; (vi) drying; and (vii) stabilization as shown in Figure 5.3. The chemical nature of the selected precursors determines the reactions involved in sol-gel processing, the required additives (solvents, reagents, catalysts) and the conditions needed to control the properties of a porous solid (pH, reaction time, concentrations, temperature, drying mode). The choice of the chemical strategy depends on the possibility to control the rates of activation/condensation reactions determining the materials texture, cost/availability of corresponding precursors and ease of their handling.

5.2.1

Activation

Activation of sol-gel precursors is needed when they are chemically inert and cannot participate in condensation reactions directly. It most often involves hydrolysis of solvated metal ions in aqueous solutions or metal alkoxides in

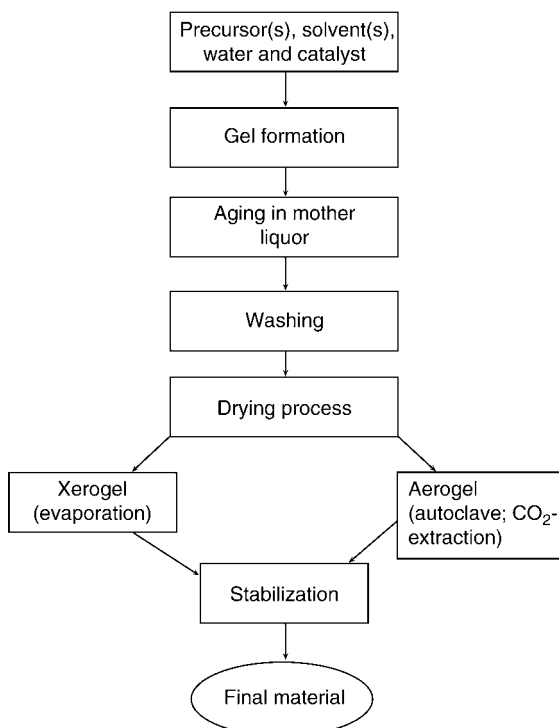


Figure 5.3 The sequence of steps involved in sol-gel processing for the synthesis of porous solid catalytic phases. (Adapted from [5].)

alcoholic solutions containing controlled amounts of water. The principles governing the reactivity of the hydrolysable metals are reviewed in detail by Livage *et al.* in [6, 7, 16] and the available experimental data for most transition metals in [1]. The hydrolysis equilibrium is shifted to the right with increasing solution pH, cation charge density, and temperature.

Besides addition of bases, hydrolysis of hydrated metal cations may be initiated by addition of another proton scavenger, like propylene oxide [18, 19]. Protonation of the epoxide oxygen by an acidic proton of a water ligand is followed by the epoxide ring opening through nucleophilic attack of the conjugated base.

Inorganic compounds with high positive charge on metal atoms (+IV–VI), present as anions of corresponding salts in aqueous solutions, like silicon, vanadium, molybdenum or tungsten, should be activated by acidification [2, 6, 7, 16]. This causes, for silicates, conversion of silicate anions to tetrahedrally coordinated precursors $[H_nSiO_4]^{(4-n)-}$ that do not contain coordinative water and can be further condensed by oxolation reactions. Here, the acidification extent n is controlled by the pH, being 2 under highly alkaline conditions and reaching 4 at $pH < 9$ [20].

Another kind of sol-gel precursors, metal alkoxides, the chemistry and peculiarities of which in sol-gel processing are well described in [2, 3, 21], react with water at rates depending on the metal's electronegativity, which determines the partial charge on the metal atoms (δ) [6]. Silica exhibits optimal electronegativity, so that for $Si(OC_2H_5)_4$ $\delta = +0.32$. This makes the hydrolysis rate slow, but tunable by catalyst addition. The hydrolysis of alkoxides proceeds in the presence of acid or base catalysts including strong Lewis bases, such as F^- ions via S_N2 nucleophilic substitution reactions with a transition state involving five-coordinated silica atoms. It passes a rate minimum at $pH = 7$ (Figure 5.4a).

Alkoxide sol-gel precursors can be converted to the same hydroxylated activated substances by nonhydrolytic routes. The thermal intermolecular hydroxylation was used as a first step for gelation of ZrO_2 at 200–300°C in a conventional reactor [23] or inside the channels of mesostructured SBA-15 silica [24]. Partially hydroxylated alkoxides can be synthesized by reactions between metal chlorides and alcohols with electron-donor substituents or reactions between basic alkoxides and carbonyl compounds like ketones [9].

5.2.2

Polycondensation

The activated species of the sol-gel precursors continue to react with each other to form colloidal solutions of oligomeric species. The precursors containing hydroxyl groups bonded to metal atoms condense according to olation, oxolation, and/or alcoxolation routes catalyzed under acidic and basic

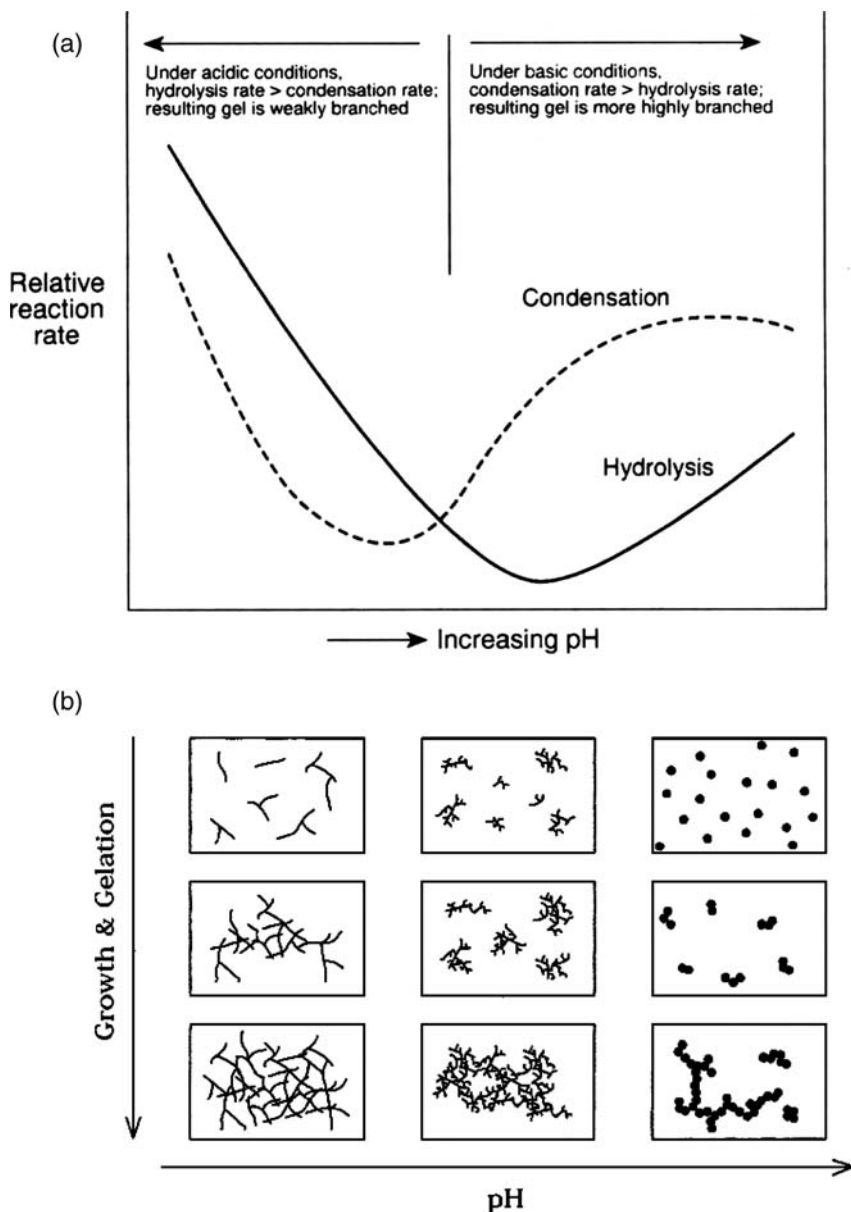


Figure 5.4 Dependence of hydrolysis and condensation rates of $\text{Si}(\text{OR})_4$ (a) and structure of the obtained gel (b) on pH. (a – Redrawn from [17], b – Redrawn from [22].)

conditions [6, 7, 16]. The partially hydrolyzed alkoxides of low reactivity, such as $\text{Si}(\text{OR})_4$, react under acidic conditions according to oxolation or alcoxolation reactions involving pentacoordinated silicon intermediates. Under basic conditions both $\text{Si}(\text{OR})_4$ and $\text{Si}(\text{OR})_3\text{OH}$ molecules are converted to negatively

charged oxo-intermediates evolving ROH or H₂O, respectively. These species act as nucleophiles in subsequent nucleophilic addition reactions with activated precursors forming Si—O—Si bridges. The salts formed during acidification of aqueous solutions containing high-valence metal anionic precursors, like silicates, decrease the electrostatic repulsion between ions that favors the corner sharing of [SiO₄]^{4−} tetrahedra and formation of cage polysilicates [16], increasing the condensation rates.

Another class of reactions leading to polycondensation of oxygen-containing metal precursors is the so-called “aprotic condensation” that proceeds during nonhydrolytic sol-gel processing where water is not required for precursor activation and not produced by condensation [9, 10]. It includes reactions between alkoxides of dissimilar metals differing in the polarity of M—O bonds, or of alkoxides with metal esters and metal chlorides. The condensation rate is strongly dependent on the OR/M ratio in mixed precursors, as well as on temperature, the presence of catalyst and structure of the R derivative.

The complexes of metal cations with polydentate chelating agents are condensed with polyalcohols like ethylene glycol according to acid-catalyzed polyesterification reactions. With increased degree of hydrolysis/polycondensation of metal cations they lose electron-donating water molecules and hydroxyl ligands and form more bonds, leading to a decrease in the nucleophilic power of OH groups. This, together with increasing positive charge on oligomeric clusters, stops polycondensation after formation of dimers, tetramers or oligomers containing more than 10 metal atoms like [Al₁₃O₄(OH)₂₄(OH₂)₁₂]⁷⁺ [6, 16].

5.2.3

Gelation/Aging/Washing

After a period of time called the “gelation time” the sol experiences a gelation transition, converting a liquid solution to a state where it can support a stress elastically [13]. It is a result of the formation of a network, which consists of condensed colloidal clusters entrapping the solution (Figure 5.1). In many cases gelation can be achieved by very slow, controlled base addition with a pump [25] or slow release of a base (OH[−]) by hydrolysis of urea added to aqueous salt solution [26]. The same effect is attained by addition of epoxide as proton scavenger (propylene oxide, 1,2-epoxybutane, glycidol, epichlorohydrin) to the organic solutions of hydrated metal salts, binding the acidic protons of hydrated ions under epoxide ring opening [27]. A similar effect is achieved by addition of chelating complexing agents to metal alkoxide solutions (carboxylic acids, β-diketonates) reducing the hydrolysis rate of metal precursors [6].

The gel structure is determined by the ionic character of the M—O bond, and the relationship between the activation/condensation rates. The relation

between hydrolysis and condensation rates of silicon alkoxides changes with increasing pH as shown in Figure 5.4a. It has a strong impact on the architecture of the forming network (Figure 5.4b). After visible gelation the sol-gel processing proceeds to the aging step where the structure and properties of the formed network continue to change up to the point that yields the target gel density. It includes four processes: polycondensation, syneresis, coarsening, and phase transformation [13, 17].

5.2.4

Gel Drying/Desolvation

The gel desolvation converts the hydro- or alcogel to a porous solid. It is generally done by solvent evaporation [13] or supercritical drying [4, 18]. Drying by evaporation, yielding xerogels, consists of three steps: (i) desolvation without pore opening accompanied with the network shrinkage caused by capillary forces, (ii) opening of the pores by liquid flow to the surface after the gel reaches a “leatherhard point” and resists the capillary forces due to greater packing density, and (iii) evaporation of the remaining liquid film in the last step. The shrinkage in the first step is caused by differential pressure across the pores that for a water-filled pore with a radius of 1 nm reaches 1.5×10^8 Pa [17]. It strongly reduces the pore volume and size in the xerogel compared to the texture of the corresponding wet gel (Figure 5.1). The surface area also drops by two to three times relative to this potential value.

A more efficient approach that in principle allows full conservation of the wet gel’s texture is supercritical drying, producing aerogels (Figure 5.1). The supercritical liquid has no meniscus in the wet gel pores and does not generate the structure-damaging capillary forces [28]. Two methods for producing the aerogels are widely used in practice: supercritical solvent release and supercritical extraction. The experimental setup of these techniques is well described in [4, 5].

5.2.5

Stabilization of Xero- and Aerogels

In order to ensure a steady operation of catalytic materials, the dried xero- or aerogels should be thermally transformed to a more active and stable solid phase. Heat treatment of a dried gel at increasing temperatures causes chemical modification of its surface, crystallographic transformations of the solid matter and reorganization of the pore geometry [13]. Nucleation and growth of stable crystalline phases accompanied with sintering and reduction of surface area and porosity proceed at higher temperatures.

5.3

Application of Sol-Gel Processing for the Preparation of Solid Catalysts

Sol-gel processing is widely used for the preparation of solid catalytic materials, which cover all the known applications of solid catalysts. Materials produced include bulk mono- or multimetallic monophasic oxide catalysts, mixed multiphasic catalysts prepared by entrapment of organic or inorganic catalytic materials in porous matrices, catalytic coatings, and membranes. The sol-gel technique is also employed for the production of preformed porous solids with well-controlled texture widely used as catalysts supports, like silica and alumina. This is due to the great flexibility of the sol-gel approach that permits fine tuning of pore and phase structure by adjusting a wide variety of precursor chemical properties and preparation parameters. But it also introduces complexity in the selection of the optimal chemical route and processing sequence/conditions, depending on the type of target catalytic material. In this section the peculiarities of sol-gel processing important for preparation of bulk monophasic catalysts, entrapped multiphasic composites, and catalytic coatings will be highlighted.

5.3.1

Bulk Catalytic Phase Materials: Xero- and Aerogels

5.3.1.1 Monometallic Catalytic Materials

The sol-gel processing chemistry discussed above allows the preparation of metal-oxide phases with controlled size, shape, and packing mode of primary particles, the structure of which (phase composition) is formed at the final thermolysis/crystallization steps. The requirements to reach maximal surface area and mesoporous structure with high pore volume are generally not compatible with the necessity to synthesize a catalytic material with a proper crystal structure formed at high temperatures, because that goes along with significant degradation of the gels texture. This is less important in the production of thermally stable but chemically inert porous silica for use as catalysts support [2, 20], but becomes critical in the preparation of thermally less stable transition-metal oxides [1]. Careful choice of molecular precursor and sol-gel chemical route combined with optimization of activation/condensation kinetics (hydrolysis ratio, catalysts, complexation agents), drying and crystallization conditions allowed preparation of many crystalline transition-metal oxides like TiO_2 , ZrO_2 , HfO_2 , Nb_2O_5 , CrO_x or Fe_2O_3 with the surface area exceeding $200 \text{ m}^2 \cdot \text{g}^{-1}$ [1, 29, 30]. Gelation conditions, structure, texture, and performance of many sol-gel derived monometallic catalytic phases are analyzed in a series of comprehensive reviews [1, 4, 31]. This is illustrated briefly below for the example of three

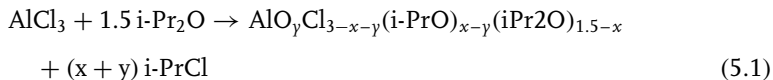
monometallic oxide phases – alumina and titania, widely used as solid catalysts and catalysts supports.

5.3.1.1.1 Alumina

Three main sol-gel strategies used for the preparation of porous alumina differ in the nature of molecular Al-precursors and chemical routes for their activation/condensation: hydrolysis-condensation of Al-alkoxides or salts, and nonhydrolytic condensation of Al-salt with alkoxide. Alumina xerogels were originally prepared from solutions of aluminum iso-propoxide, dissolving it in excess water ($\text{H}_2\text{O}/\text{Al} = 100$) with acid (HCl , HNO_3) addition to clear the sol, followed by heating the solution to the gelling point, and drying the gel in air at 353 K. The fast condensation under these conditions yields hydrated boehmite with a surface area of $300 \text{ m}^2 \text{ g}^{-1}$ [32]. Increasing the acid/Al molar ratio in the range 0.05–0.25 causes a steady decline of the surface area and pore volume. The very slow hydrolysis/condensation at room temperature, controlled by the humidity of the air above the Al-tert-butoxide – acetone solution in the absence of any catalyst, yielded crystalline γ -alumina with a surface area of $285 \text{ m}^2 \text{ g}^{-1}$ [33]. Use of a mediate hydrolysis ratio $\text{H}_2\text{O}/\text{Al}$ -alkoxide of 10 combined with addition of acid catalyst and acetylacetone as complexation agent, which controls the rate of Al-tert-butoxide hydrolysis, allowed to increase the surface area of γ -alumina xerogel fired at 773 K to $524 \text{ m}^2 \text{ g}^{-1}$ [34]. Addition of the nonionic copolymer surfactant Pluronic 123 to the sol formed in Al-tert-butoxide-EtOH- H_2O -HCl solution at hydrolysis ratios of 2–12 yielded a well-ordered hexagonal mesostructured alumina with a surface area of $410 \text{ m}^2 \text{ g}^{-1}$ after gelation/crystallization and burning out the organics [35]. The supercritical drying did not change the texture of alumina gels obtained under fast alkoxide hydrolysis conditions ($\text{H}_2\text{O}/\text{Al} = 100$, HCl) yielding a dry material with surface area of $350 \text{ m}^2 \text{ g}^{-1}$ [36]. Gellation under mild conditions in the absence of catalysts and $\text{H}_2\text{O}/\text{Al}$ -alkoxide ratios of 3–9 or at $\text{H}_2\text{O}/\text{Al} = 1.1$ in the presence of HNO_3 allowed preparation of aluminas with substantially higher pore volume of $1.35\text{--}9 \text{ cm}^3 \text{ g}^{-1}$ and surface area $456\text{--}680 \text{ m}^2 \text{ g}^{-1}$. Separation of the hydrolysis and condensation steps of Al-tert-butoxide, conducting it slowly at $\text{H}_2\text{O}/\text{Al} = 0.6$ with subsequent addition of HAc catalyst to a stable alumina sol, gave crystalline aerogels with very open texture and $>98\%$ porosity [37].

Slow basification of aqueous aluminum nitrate solution by hydrolysis of urea produced a material that was transformed at 573 K to γ -alumina xerogel with a surface area of $425 \text{ m}^2 \text{ g}^{-1}$ [38]. Gels obtained from aqueous solutions of inorganic aluminum salts, as a result of capturing the acidic protons of Al-water ligands by reaction with propylene oxide, displayed surface area of $660\text{--}709 \text{ m}^2 \text{ g}^{-1}$ after supercritical drying [39]. They retained high surface area after conversion to γ -alumina at 1073 K, and even as xerogels had surface areas of $325 \text{ m}^2 \text{ g}^{-1}$ and pore volumes of $1.2 \text{ cm}^3 \text{ g}^{-1}$ after calcination at 873 K.

An amorphous alumina xerogel is prepared by the nonhydrolytic method according to



where x denotes the extent of the condensation reaction of AlCl_3 with Pr_2O yielding the i-propoxy ligand and γ indicates condensation reaction between chloride and the i-PrO ligand forming Al–O–Al bridges [40].

The obtained amorphous hydrated aluminum oxide has a surface area of $640 \text{ m}^2 \text{ g}^{-1}$ [40]. It remained amorphous up to 973 K and crystallizes to η -alumina at 1123 K, resulting in a loss of surface to $230 \text{ m}^2 \text{ g}^{-1}$. Wetting of this xerogel with water decreases the crystallization temperature to 873 K [41].

5.3.1.1.2 Titania

Two sol-gel protocols were used for the preparation of titania xero- and aerogels: controlled hydrolysis/condensation of inorganic Ti-salts in aqueous solutions and of Ti-alkoxides in organic solvents. At low temperatures (ice addition) it is possible to stabilize the violently hydrolyzed TiCl_4 in aqueous solution as TiOCl_2 , forming a stable acidic sol that can be further converted to gel at elevated temperatures or by base addition [1]. Xerogels obtained in this way by basification of the sol with NH_4OH , NaOH or hexamethylenetetramine exhibited surface areas of 390–420, 320, and $470 \text{ m}^2 \text{ g}^{-1}$, respectively. Using amine as a base yielded a microporous material, while inorganic bases increased the pore volume by 50–70% and the pore diameter from 0.5 to 1.7 nm. Heating the xerogels results in a strong decrease of the surface area due to the glow transition caused by crystallization of amorphous material into the anatase structure [42]. Replacement of water for n-butanol followed by its supercritical release gave a crystalline (rutile + anatase) material with a surface area of $167 \text{ m}^2 \text{ g}^{-1}$ [43]. Another way to increase the surface area of crystalline titania aerogel to $262 \text{ m}^2 \text{ g}^{-1}$ is hydrothermal treatment of the hydrogel (reflux, autoclave), favoring titania crystallization at relatively low temperature [44].

In the preparation of titania from alkoxide precursors the main parameters affecting the xerogel texture are hydrolysis ratio ($\text{H}_2\text{O}/\text{Ti}$) and concentration of the acid catalyst. Optimization of these parameters, starting from $\text{Ti}(\text{n-BuO})_4$ – methanol solution, gave anatase aerogel with a surface area of $220 \text{ m}^2 \text{ g}^{-1}$ after calcination at 773 K [45]. The catalyst type used for hydrolysis/condensation of $\text{Ti}(\text{n-BuO})_4$ controls the structural evolution of xerogels at elevated temperatures: HCl-catalyzed gel crystallizes into anatase, while acetylacetone allows the rutile phase to be obtained more easily. The acetylacetone also inhibits the condensation process due to its chelating action that decreases the Ti-alkoxide hydrolysis rate. This prolongs the gelation time, favoring formation of less-dense structures and increases the crystallization temperature by 200 K. Hydrogen peroxide acts as a complexing agent in the opposite direction, strongly increasing the alkoxides hydrolysis/condensation

rates by the removal and conversion of terminal alkyl groups to hydroxyl groups, possibly with coordination change [46]. This causes gel shrinkage and gives a crystalline gel (anatase/rutile phases) already after drying of the gel at 423 K. Addition of polyethylene glycol to the gel obtained by hydrolysis/condensation of $\text{Ti}(\text{i-PrO})_4$ in ethanol in the presence of H_2O , HCl , and acetylacetone increased the surface area of the anatase phase fired at 793 K by a factor of 1.7 [47].

The xerogel prepared by hydrolysis/condensation of $\text{Ti}(\text{n-BuO})_4$ in i-PrOH consists of a pure anatase phase with a surface area of $122 \text{ m}^2 \text{ g}^{-1}$ [48]. Crystalline xerogel was obtained using the acidic hydrolysis of tetrabutyltitanate modified with acrylic acid in EtOH , where gelation was induced by subsequent basification with ammonia solution [49]. Drying and removal of bonded organics by photocatalytic oxidation yielded a titania xerogel being pure anatase and exhibiting a surface area of $359 \text{ m}^2 \text{ g}^{-1}$. The supercritical drying of wet gels allows the surface area of the aerogels to be increased to $769\text{--}840 \text{ m}^2 \text{ g}^{-1}$. A titania cryogel with a surface area of $511 \text{ m}^2 \text{ g}^{-1}$ was obtained by freeze drying [50]. Increasing the calcination temperature leads to a linear drop of the surface area of these materials due to sintering/crystallization with the lowest decline for materials dried by low-temperature CO_2 -solvent extraction.

5.3.1.2 Multimetallic Composite Catalytic Phases

Using the sol-gel strategy for the preparation of multimetallic crystalline catalytic phases with well-organized solid surfaces is based on its potential for mixing the cations at the precursor's molecular scale and thus on the potential for direct crystallization of composite phases. The principles of the sol-gel protocol for the preparation of multimetallic phases are discussed by Narendar and Messing in a comprehensive review [27].

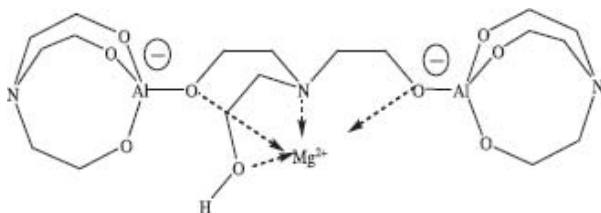
The main advantage of the sol-gel strategy is the possibility to achieve molecular homogenization and spatial fixation of metal cations of different chemical origin in aged gels that crystallize in the stabilization step via high-temperature solid-state reactions. In cases where the precursor activation is done by hydrolysis, the main reason for segregation of the metal cations at the colloidization-gelation steps is a wide difference of hydrolysis rates for metal atoms with different electrophilicity and ability to undergo coordinative expansion [6, 27]. This favors homocondensation ($\text{M}_1\text{--O--M}_1$, $\text{M}_2\text{--O--M}_2$) instead of heterocondensation ($\text{M}_1\text{--O--M}_2$), yielding separation of $\text{M}_1\text{O}_x(\text{OH})_y$ and $\text{M}_2\text{O}_z(\text{OH})_z$ phases in a gel. In such cases, the initial cation homogenization can be achieved by separating the steps of precursor hydrolysis and condensation.

When the activation of metal cations is done by their chelation with polydentate carboxylic acids the reasons for cation segregation in multimetallic systems are incomplete chelation, so that part of the metal precipitates as nitrates or hydroxides during the dehydration (condensation) step, and selective precipitation of some metal carboxylates occurs at corresponding pH

values. This can be avoided by controlling the carboxylate/metal ratio and pH during the activation step and by favoring the crosslinking reactions between uncomplexed carboxylate groups using citric acid and addition of ethylene glycol that leads to formation of ester bridges [10, 27]. The nonhydrolytic sol-gel route that does not require precursor activation and includes direct condensation reactions between alkoxides, esters or chlorides of dissimilar metals [9] yields highly homogeneous gels.

Homogeneous multimetallic gels after desolvation are amorphous solids that need further thermolysis-crystallization for production of catalytic materials with desired structure. This requires maintaining the homogeneous distribution of cations and directing the crystallization process to the formation of the required phases at the gel-stabilization steps. The measures that can be taken for improvement of the structure and texture of composite catalytic phases include reduction of the water or CO_2 pressure at the thermolysis step, rapid heating favoring fast crystallization before cation segregation that leads to formation of thermodynamically more stable phases, and optimizing the annealing temperature.

Spinel compounds have the general formula $\text{M(II)M(III)}_2\text{O}_4$ and a crystalline structure where trivalent metal ions occupy octahedral and divalent metal ions tetrahedral positions in a network formed by oxygen ions [51]. The traditional “ceramic route” for their preparation involves solid-state reaction between parent metal oxides that needs high temperatures of $>1400\text{ K}$ and yields materials with low surface area of $1\text{--}5\text{ m}^2\text{ g}^{-1}$. Homogenization of parent metal cations in solids prepared by the sol-gel synthetic protocol allows the crystallization temperature to be decreased to $<800\text{ K}$, maintaining the xero (aero-)gels texture that increases the spinels surface area to $>200\text{ m}^2\text{ g}^{-1}$. Mixing of aqueous $\text{MgAc}_2\text{--}(\text{C}_3\text{H}_7)_4\text{NOH}$ solution with $\text{Al}(\text{OC}_4\text{H}_9)_3\text{--}i\text{-PrOH}$ produced a gel that after calcination at 823 K yields only the crystalline MgO phase in the wide Mg/Al range of $0.15\text{--}6$ [52]. Synthesis of a double Mg--Al precursor as a complex containing triethanolamine derivative:



improves the metal homogenization in the gel formed by its hydrolysis under basic conditions yielding a mixture of MgO and MgAl_2O_4 spinel phases after calcination at $>873\text{ K}$ [53]. The pure spinel phase in this case was obtained only at 1473 K . Further improvement of Mg--Al homogenization in the gel

was achieved due to hydroxylation of Mg- and Al-ions in deionized water by addition of ammonia, followed by base-catalyzed condensation conducted in a closed vessel that excludes formation of carbonates [54]. It allowed the temperature needed for crystallization of a pure MgAl_2O_4 spinel phase to be decreased to 473 K. The nanocrystalline material prepared by this method retained the crystal size of <10 nm (XRD) up to 1073 K.

Similar results were obtained in the synthesis of CoAl_2O_4 [55] and NiAl_2O_4 [56] spinels using the commercial double-alkoxide precursors $\text{Co}(\text{Al}(\text{C}_3\text{H}_7)_2)_2$ and $\text{Ni}(\text{Al}(\text{C}_3\text{H}_7)_2)_2$ mixed with $\text{Al}(\text{OC}_3\text{H}_7)_3$ to adjust the $\text{Co}(\text{Ni})/\text{Al}$ ratio. After hydrolysis/gelation the air-dried gels were crystallized at 523 (Co) and 773 K (Ni) to the corresponding pure spinel phases with surface areas of 235 and $234 \text{ m}^2 \text{ g}^{-1}$, respectively. Reaction of CoCl_2 with preformed AlOOH sol gave a xerogel with lower metal homogenization, leading to an increase in the temperature of CoAl_2O_3 spinel crystallization to 673 K [57]. Gelation achieved by refluxing the mixed solution of CoAc_2 , Bi-, and Fe-nitrates in 2-methoxyethanol in the presence of water yielded a xerogel that was transformed at 523 K to the nanocrystalline $\text{CoFe}_{1.9}\text{Bi}_{0.1}\text{O}_4$ spinel phase and sintered at >923 K [58].

Hydrotalcites are layered double hydroxides of the general formula $[\text{M}(\text{II})_{1-x}\text{M}(\text{III})_x(\text{OH})_2]^{x+} [\text{A}^{n-}]_{x/n} z\text{H}_2\text{O}$, where A stands for anions, mainly carbonate and $x = 0.15 - 0.5$ ($\text{M}(\text{III})/\text{M}(\text{II}) = 1 - 6$) [59]. They have relatively low thermal stability, being converted to spinels at $>600-773$ K. Using the sol-gel synthesis protocol they should be crystallized at the gel-aging step. Reaction of aqueous AlOOH sol with MgCO_3 , $\text{Mg}(\text{OH})_2$, or MgO under basic conditions at 358 K [60] as well as reaction of prehydrolyzed $\text{Mg}(\text{OEt})_2$ with $\text{Al}(\text{sec-OBu})_3$ in $\text{BuOH-H}_2\text{O}$ solution at 343 K [61] yielded gels where only part of the material is present as the hydrotalcite phase. Combining the prehydrolysis of $\text{Mg}(\text{OEt})_2$, its subsequent mixing with $\text{Al}(\text{AcAc})_3$, and base catalysis at the condensation step prevented metal segregation during the following gelation step under reflux conditions [62]. It yielded a pure hydrotalcite xerogel with a surface area of $211 \text{ m}^2 \text{ g}^{-1}$, further improvement of the hydrotalcite texture characteristics was achieved by cogelation of $\text{Mg}(\text{OMe})_2$ and $\text{Al}(\text{i-OPr})_3$ in MeOH , adjusting the hydrolysis/condensation rate by controlled slow water addition [63]. This produced amorphous binary oxy/hydroxides that were converted to aerogel by supercritical methanol release, yielding a pure hydrotalcite phase with surface area of $>500 \text{ m}^2 \text{ g}^{-1}$ after ion exchange with carbonate anions. A pure Ni-Al phase with hydrotalcite-like crystalline structure and surface area of $127 \text{ m}^2 \text{ g}^{-1}$ was prepared by gelation from $\text{Ni}(\text{AcAc})_2 - \text{Al}(\text{i-PrO})_3$ solution under reflux conditions after addition of base catalyst [64]. Base catalysis (NaOH) for the condensation of mixtures containing prehydrolyzed $\text{Mg}(\text{OEt})_2 - \text{Cr-acetylacetonate}$ or Ni- and Cr-acetylacetonates in ethanol produced under reflux at 353 K pure Mg-Cr- and Ni-Cr- layered anionic clays with hydrotalcite structure and <20 nm crystal size [65].

Perovskites are mixed oxide compounds of the general formula ABO_3 containing a transition metal, such as Ti, Nb, Ta, in B position, Ca, Sr,

Co, Pb, Ce, or other RE-metals in A position and having the same basic structure with isometric symmetry, where A ions occupy voids between BO_6 octahedra [66]. The yttrium cobaltate phase YCoO_3 with perovskite structure was prepared by cogelation of Y and Co ions at 363 K in aqueous solution under slow basification conditions due to urea hydrolysis or by formation of a bimetallic carboxylate complex after addition of citric acid [67]. The xerogels obtained by these two methods demonstrated similar behavior – segregated Y_2O_3 and Co_3O_4 phases at temperatures up to 1073 K, and crystallization of a perovskite phase with a crystal size of 18 nm at 1173 K. Using partially hydroxylated basic Pb-acetate salt and $\text{Ti}(\text{n-OBu})_4$ in the presence of acetic acid that controls the rates of hydrolysis/polycondensation reactions, and conducting these reactions under slow $\text{i-PrOH-H}_2\text{O}$ addition yielded xerogel that formed ~ 50 nm nanocrystals with perovskite structure at 873 K [68].

The pure $\text{PbMg}_{0.33}\text{Nb}_{0.67}\text{O}_3$ perovskite phase was crystallized at 1253 K from xerogel obtained by cogelation of Pb-acetate, Mg- and Nb-ethoxides in methoxyethanol [69]. Its purity was controlled by addition of excess Pb and Mg components that prevented formation of the lead niobate pyrochlore phase. A pure perovskite phase with the composition $\text{SrBi}_2\text{Ta}_2\text{O}_9$ and a crystal size < 50 nm was formed at 1073 K from a xerogel precursor, obtained by gelation from $\text{Ta}(\text{EtO})_5$ and Sr-acetate and BiO-nitrate solution in methoxyethanol using an acetic acid catalyst [70]. Acetate ions act as bidentate ligands in this solution, equalizing the hydrolysis/condensation rates of Ta and other ions.

5.3.2

Catalytic Materials and Modifiers Entrapped in Porous Matrices

The sol-gel entrapment of guest entities in xero- or aerogels is a viable tool for the preparation of advanced catalytic materials [15]. From the viewpoint of phase composition the target here is opposite to that of the preparation of the multimetal monophasic gels. Entrapment should retain the structure of a guest phase as nanoparticles or isolated molecular substances in the well-defined matrix. Its aim is to add or change the chemical functionality, surface polarity or pore structure of the matrix gel, creating or altering its catalytic performance. These targets could be achieved by three main strategies:

- insertion of foreign atoms or molecular substances inside the primary micelles at the colloidalization stage of sol-gel processing by cocondensation with matrix precursors
- adsorption or sterical (physical) entrapment of molecular substances at the surface of primary particles or between them during the gelation/desolvation stages
- entrapment of preformed nanoparticles (> 1 nm) of catalytic phases.

Depending on the nature and the final state of entrapped guests this can produce composite catalytic phases appearing as xero- or aerogels (i.e.

by isomorphous substitution of silicon for aluminum or titanium atoms in the network of SiO_2 matrix particles), immobilize (heterogenize) the soluble molecular catalysts (functionalized chemicals, coordinative metal complexes, enzymes) in a porous matrix or stabilize the nanoparticles of catalytic phases (metals, metal oxides, mixed composites, polymers) in a porous matrix in a high dispersion state. In addition to these conventional applications of distribution of the catalysts in porous matrices, the sol-gel entrapment approach allows the surface polarity to be controlled, creating organic-inorganic hybrid materials, and tailoring of the pore structure by elimination of entrapped organic templates. This strongly affects the reagents/products adsorption and diffusion patterns. Cocondensation also permits spatial separation of different catalytic functionalities in porous matrices. This opens a wide range of possibilities for combining chemically noncompatible catalysts (i.e. acids and bases) for conducting one-pot processes including several reaction steps. Hundreds of publications reflect today the flexibility of the sol-gel entrapment technique, implementing a vast amount of reagents and chemical reactions for combining the components in composite catalytic materials. Since each of the three mentioned strategies require a special approach in handling the sol-gel processing, their peculiarities are considered below.

5.3.2.1 Atoms or Molecular Substances Entrapped by Cocondensation at the Colloidization Step

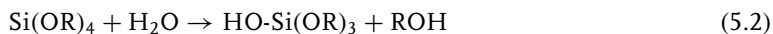
5.3.2.1.1 Mixed-Metal Oxide Xero- and Aerogels

Insertion of the foreign metal atoms in the inorganic network of metal oxides is widely used in the practice of catalyst preparation for the creation of active sites with different functionality, like acidic (Al in SiO_2) or redox functionality (Ti in SiO_2 , V in TiO_2). The foreign atoms can be entrapped in the main oxide (matrix) using sol-gel processing by two strategies: (i) mixing the separately prepared colloidal solutions of matrix and dopants, followed by cogelation of a composite sol and (ii) cocondensation of the matrix and dopants molecular precursors at the colloidization step. The second approach is much more flexible ensuring in principle molecular-scale homogeneity. But it requires special measures to avoid component segregation, as in the case of multimetallic phases preparation, especially when the reactivities of precursors in hydrolysis/condensation reactions are substantially different.

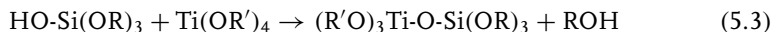
This problem can be solved by addition of the less-reactive precursor to the solution where the second, more-reactive precursor is partially prehydrolyzed, or equalization of the reactivity by selection of precursors with different molecular structure, or by using a complexing agent to control the hydrolysis rate. For preparation of aluminum silicates with acidic functionality created by entrapment of tetracoordinated aluminum ions in the silica matrix, the prehydrolysis of the less-reactive silicon alkoxide before addition of aluminum alkoxide suppresses the early formation of $\text{Al}-\text{OH}-\text{Al}$ bridges and subsequent

precipitation of pseudoboehmite or bayerite phases [71, 72]. The careful control of the hydrolysis ratio facilitates formation of an aluminosilicate precursor with tetrahedrally coordinated aluminum already at the colloidalization step [72]. The advantage of this synthesis protocol is the absence of cations, needed for incorporation of aluminum in the silica matrix by conventional cogelation of silicate and aluminate sols. This allows direct formation of acid sites without ion exchange or high-temperature calcination needed for removal of organic cations. The length of the alkyl chain in the aluminum alkoxide controlling its reactivity determines the relative amounts of tetrahedral, octahedral, or pentacoordinated aluminum in the silica matrix. Implementation of complexing agents that regulate the alkoxides hydrolysis rates increases the acidity of aluminosilicate gels to a much higher extent than could be achieved by conventional methods due to effective Al–O–Si bonds formation [73]. Cogelation after mixing the separately prepared sols causes segregation of silica and alumina phases after thermal treatment that yields materials with packing of interpenetrated alumina particles and polymeric clusters of silica.

A modified procedure was successfully used for entrapment of Ti [74] and Zr [75] molecular species into a silica matrix. It relies on three-step colloidalization, first producing partially hydrolyzed silicon alkoxide species:



followed by formation of mixed alkoxides after addition of the second reagent:



and the final hydrolysis/condensation of these substances. The fine tuning of the hydrolysis extent, utilizing at the second hydrolysis step the water released from the initial condensation, favors entrapment of titanium atoms into the silica network, and high activity/selectivity in partial organics oxidation with a peroxide.

If efficient active sites shall be created by stabilizing the molecular species at the surface of a well-defined phase, as in the case of VO_x/TiO_2 – anatase catalysts, the better activity in NO SCR was achieved by cocondensation of the dopant alkoxide with the surface groups of preformed colloidal particles of the matrix precursor, followed by gelation [76]. A similar approach of modifying the matrix precursor sol with dopant molecules yielded well-dispersed tantalum species at the silica surface, efficient in selective oxidation of pyrimidine thioether [77].

Addition of CoCl_2 to the reaction mixture in nonhydrolytic sol-gel processing of alumina according to the reaction $\text{AlCl}_3 + 1.5\text{Al(i-OPr)}_3 \rightarrow \text{AlO}_{1.5} + 3\text{iPrCl}$ caused efficient entrapment of Co (II) centers in alumina gels [78]. The material was leachproof and displays high activity in olefin epoxidation. Similar results were achieved by entrapment of Ti-ions in a silica matrix by reaction of SiCl_4 with Ti(i-PrO)_4 , forming a colorless composite sol.

5.3.2.1.2 Hybrid Organic-Inorganic Interphase Catalysts

Entrapment of organic molecules by sol-gel processing in inorganic xero- or aerogel matrices is possible by homo- and cocondensation of metal alkoxides modified with different functional groups (FGs). Various aspects of the preparation and handling of sol-gel cocondensed hybrid organic-inorganic catalytic materials are discussed in detail in several comprehensive reviews [79–81].

The general synthesis strategy for entrapment of organics by cocondensation at the colloidalization step is based on using organically modified monomeric precursors of the inorganic matrix. They contain at least two alkoxide (OR) groups that enable polymerization or copolymerization with corresponding metal alkoxides: $(\text{OR})_{n \geq 2}\text{A-X}$. Here, A is the matrix metal constituent and X the organic derivative, nonreactive (N) or containing reactive FGs. Depending on the chemical nature they can be synthesized by a variety of routes useful for the preparation of metal-binding ligands with silylated side chains [81]. The coordinated metal complexes (M), being efficient molecular catalysts for many organic reactions, can be attached or anchored to these monomeric precursors by complexation with silicon-tethered FGs, typically Lewis bases ($\text{FG} = -\text{NR}_2$, $-\text{Ph}$, $-\text{PPh}_2$, $-\text{P}(\text{CH}_3)_2$, etc. [80]), or by reaction of a terminal FG of the metal ligand with a corresponding alkoxide precursor: $\text{M-FG} + (\text{OR})_4\text{Ti} \rightarrow \text{M-FG-Ti}(\text{OR})_3$ where $\text{M} = \text{Co-phthalocyanine}$, $\text{FG} = \text{SO}_2\text{OH}$, SO_2Cl , both giving a compound $(\text{OR})_n\text{Ti-FG-M}$ [82].

The dialkoxo-derivatives $(\text{OR})_2\text{AFG}_2$, $(\text{OR})_2\text{AN}_2$, or $(\text{OR})_2\text{A}(\text{FG-M})_2$ cannot form a solid network, but chains resulting from their condensation can tune the flexibility of the oxide arrangement formed by cocondensation with metal alkoxides. Polycondensation of trialkoxy-derivatives (i.e. $(\text{OR})_3\text{-Si-FG-M}$) yields a 2D “pleated sheet” structure [2]. Creation of hard 3D structures requires cocondensation of organically modified and not modified metal alkoxides where the latter play the role of crosslinking agents. This is a common practice in the preparation of sol-gel entrapped catalysts with organically modified matrix precursors [79]. Cocondensation of two modified precursors, one with a catalytic function and the other containing nonreactive organic molecules, extends the potential for regulation of the catalysts performance [83]. Another possibility to obtain the 3D network is given by implementation of polysilylated organic molecules $[(\text{OR})_n\text{Si}]_z\text{N}$, $[(\text{OR})_n\text{Si}]_z\text{FG}$, or $[(\text{OR})_n\text{Si}]_z\text{FG-M}$. Their condensation results in formation of polysilsesquioxanes structures $[(\text{O}_{1.5}\text{Si})_z(\text{N}, \text{FG}, \text{FG-M})]_m$ with entrapped organic moieties [84]. The cocondensation of polysilylated organics with nonmodified metal alkoxides allows control of the density of organic molecules and network flexibility that also depends on the structure of organic molecules [79]. The density and texture of dried gels strongly dependent on the $\text{Si}(\text{OCH}_3)_4/\text{FG}-(\text{CH}_2)_n\text{Si}(\text{OR})_3$ ratio used in cocondensation, and do not depend on the kind of FG. Under acidic conditions the inductive effect of the organic modifier promotes the sol-gel reactions relative to nonmodified alkoxides, with a reverse situation in basic environments [81].

The selection of methods used for entrapment of organic catalysts and modifiers in porous solids by cocondensation depends on the chemical nature and reactivity of the immobilized catalysts. The nonreactive and functionalized organic molecules are inserted by cocondensation of preformed $(\text{OR})_3\text{Si}[\text{FG}(\text{N})]$ or $[(\text{OR})_3\text{Si}]_2\text{FG}(\text{N})$ with $\text{Si}(\text{OR})_4$ [85, 86]. The coordinated metal complexes can be inserted by two strategies, conducting their reactions with FGs before [87] or after the cocondensation of functionalized metal alkoxides $(\text{OR})_3\text{SiFG}$ or $[(\text{OR})_3\text{Si}]_2\text{FG}$ with $\text{Si}(\text{OR})_4$ [81]. The first approach (for metal complexes) gives more active and leachproof catalysts, if the accessibility of active species is not strongly reduced due to unfavorable gel structure [81].

Enhancement of the catalysts surface hydrophobicity, that favors adsorption of organic reagents, can be achieved by incorporation of nonreactive organics by means of cocondensation. The high effectiveness of this approach was demonstrated particularly in the preparation of Ti- and Zr-doped silica catalysts for selective oxidation of organics with peroxides in liquid phase [88–91]. The structure of the organic molecule entrapped by cocondensation in a Ti-Si aerogel strongly affected the epoxide yield in the oxidation of cyclohexene or cyclohexenol (Figure 5.5). The choice of modifier depends on the substrate

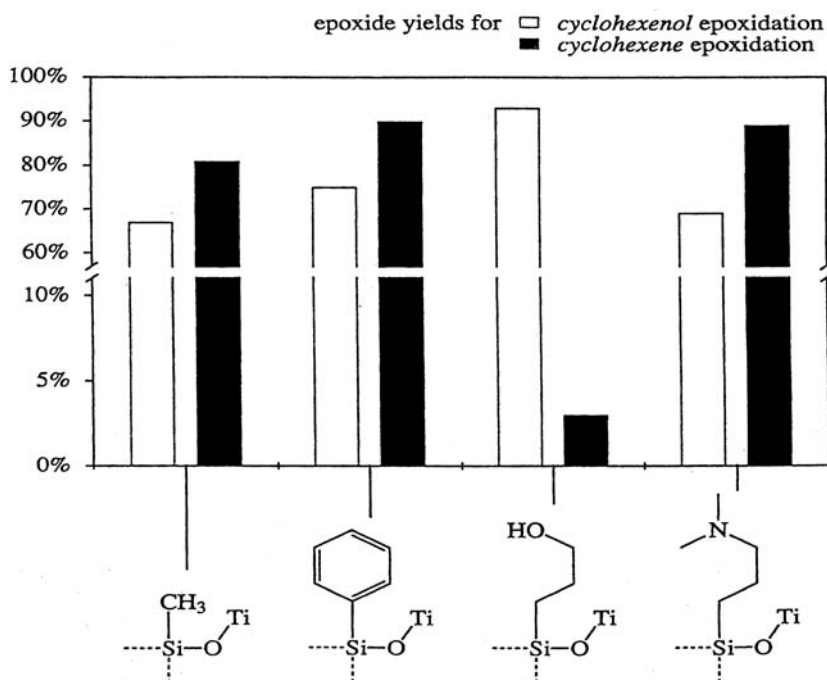


Figure 5.5 Epoxide yields in peroxide epoxidation of cyclohexenol and cyclohexene catalyzed by Ti-doped hydrophobic silica aerogels modified with different organic substances. (Reprinted from [89].)

nature: the hydroxypropyl-modified catalyst showed the best performance in alcohol oxidation, while in olefin oxidation the highest yield was obtained with phenyl-modified material. Increasing the surface methylation extent in Zr-doped silica up to 60% linearly raised the cyclohexene conversion and hydrogen peroxide efficiency up to a fourfold level due to improving the substrates adsorption capacity and decreasing the H_2O_2 decomposition [88]. Methylation of the Ti/SiO_2 surface also protects the entrapped Ti-species from leaching during the oxidation with aqueous H_2O_2 , reducing the water adsorption and probability for $\text{Ti}-\text{O}-\text{Si}$ bond hydrolysis. This improves the catalysts recovery/reuse performance, as was demonstrated in [90] for cyclooctene oxidation. Entrapment of organics with amine groups enhanced the selectivity in 3-methylcyclohexen-2-ol-1 up to 98% due to neutralization of the surface acidity of the $\text{Ti}-\text{SiO}_2$ catalyst reducing the rate of side reactions [91].

Entrapment of functionalized organics and coordinated metal complexes by cocondensation with precursors containing tethered reactive centers allows the preparation of so-called “interphase catalysts” (Figure 5.6) where the reactive centers (organic functional groups -FG or coordinated metal complexes -FG-M bound to the matrix) are located in the mobile liquid or gas phase. This overcomes the restricted accessibility of active sites to reacting molecules, and supplies the mobility required for formation of the transition state. Numerous examples of the successful preparation of such catalysts with high activity/selectivity patterns are classified in [79, 80]. In many cases, synergistic

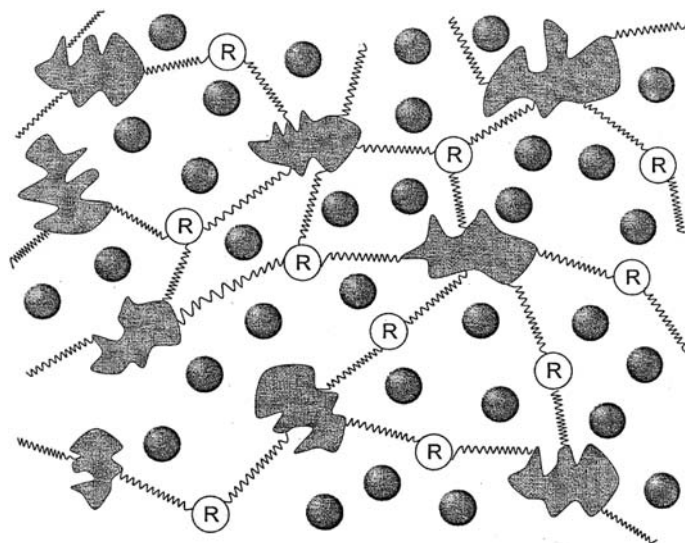


Figure 5.6 Representation of an interphase immobilized coordinative metal complex catalyst containing reactive groups (FG-M), – support/matrix, – spacer, – immobilized in an inorganic porous matrix: substrate/solvent. (Reprinted from [79].) R – functional reactive group (FG) or

effects were observed giving substantially higher turnover frequencies and product selectivities than those observed with homogeneous analogs of the entrapped catalysts.

5.3.2.2 Molecular Substances Adsorbed or Entrapped at the Gelation Step

In many instances it is possible to prepare efficient catalytic materials through encapsulation of the chemically functionalized molecules in a porous oxide matrix by physical or sterical entrapment at the gelation step of the sol-gel sequence (Figure 5.7). This implies the absence of a strong covalent bonding between entrapped species and the matrix precursor that excludes cocondensation and formation of mixed compounds at the colloidalization step. The entrapped molecular catalysts, if dissolved in the intermicellar liquid, become adsorbed at the surface of matrix pore walls after the drying step. This bonding is a result of “interfacial coordination chemistry” including the matrix surface groups in the inner sphere of coordinated metal complexes, electrostatic interactions of metal ions with surface SiO^- species that behave similarly to water at higher ligand field strength [20], hydrophobic interactions, H-bonding, acid–base or other interactions, depending on the entrapped matter and matrix precursor functionality [92]. It makes the immobilization of molecular catalysts more efficient, in addition to sterical hindrance, with respect to leaching, but can damage the performance. When the catalyst activity/selectivity is maintained the advantage of physical entrapment is the simplicity of the preparation, avoiding the difficulties associated with synthesis of tethered -F or -F-M substances.

5.3.2.2.1 Functionalized Organic Catalysts

The preparations and performance of molecular catalysts successfully heterogenized by physical entrapment for a wide range of reactions are reviewed in detail in [86, 93]. Two synthetic protocols were used, depending on the chemical properties of entrapped molecules: addition of dopant solution to prehydrolyzed $\text{Si}(\text{OR})_4$ at pH close to 7, or together with ammonium hydroxide to tetraalkoxysilane precondensed in acidic solution. Both, followed by gelation,

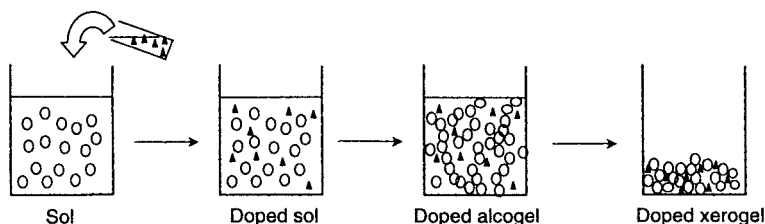


Figure 5.7 Steps in forming physically entrapped (adsorbed) molecular catalysts by sol-gel processing. (Adapted from [81].)

aging and drying yielded a variety of leachproof recyclable organoceramic catalysts with good activity/selectivity [86]. The main disadvantage of this approach is the need to direct the sol-gel procedure in a way to form microporous silica matrices with pore radius of 1–2 nm for efficient steric entrapment of dopants. This restricts the use of such catalysts to substrates that can penetrate the small pore openings, and reduces the overall reaction rates by diffusion limitations, since, in addition, part of the pore volume is occupied by dopants. As a result, the loading of entrapped catalysts is limited to dopant/Si ratios of <0.1 . As was demonstrated in [94], the catalyst surface area drops from 200 to $700 \text{ m}^2 \text{ g}^{-1}$ at $\text{Rh}(\text{CO})\text{Cl}(\text{L})_2/\text{Si}(\text{OEt})_4$ ratios of <0.1 to below $20 \text{ m}^2 \text{ g}^{-1}$ when this ratio exceeds 0.2. However, in some cases the accessibility of entrapped catalysts can be substantially improved at high loadings of reactive groups, using organically modified silica precursors and selected solvents, which favor swelling of the organic/inorganic hybrid matrix [79]. Another approach is physical sol-gel entrapment of metal complexes dissolved in an ionic liquid that after extraction leaves a more open xerogel structure with only strongly adsorbed, accessible catalyst molecules [95]. Careful comparison of cocondensation and physical entrapment strategies applied to immobilization of the same reactive molecule in a silica matrix shows that cocondensation gives more active and leachproof catalysts. In some cases better immobilization of the molecular catalyst is achieved by physical entrapment in an alumina matrix obtained by the nonhydrolytic sol-gel route [96].

5.3.2.2.2 Inorganic Molecular Catalysts

The bulky molecules of the Keggin-type dodecaheteropolyacids ($\text{H}_n[\text{XM}_{12}\text{O}_{40}]$, $n = 3, 4$; $\text{X} = \text{Si}, \text{P}$, $\text{M} = \text{Mo}, \text{W}$) of about 1 nm in size could be efficiently immobilized in a silica matrix by physical entrapment using the sol-gel method [97, 98]. They demonstrated higher activity and recyclability in many acid-catalyzed reactions compared with the silica-supported analogs. However, small inorganic molecules like the $\text{PtCl}_4\text{--CO}$ complex, only weakly adsorbed at the surface of the matrix pores, are easily leached out in catalytic runs, even if they had been entrapped in the silica matrix by sol-gel processing [99]. As was shown recently by several groups, strong adsorption at the surface of the porous matrix is critical for successful immobilization of inorganic molecular catalysts by sol-gel entrapment. Steric factors and matrix microporosity are of secondary importance. Addition of CrCl_3 salt to the prehydrolyzed sol of Si- or Zr-alkoxides caused entrapment of Cr-ions in the resulting gels, so that they became immobilized at the silica surface as molecular Cr(VI)-oxide species after oxidation with ozone due to reactions with surface hydroxyls [48]. Analogously, a Cu/SiO₂ catalyst containing adsorbed Cu ions was prepared by addition of CuSO_4 salt to acidified $\text{Si}(\text{OEt})_4$ solution, followed by decomposition of the salt in the obtained gel at 773 K [100]. Both catalysts displayed high activity in oxidation of alcohols and CO and good recyclability. Interaction of $\text{Ru}(\text{CO})_{12}$ and $\text{Os}(\text{CO})_{12}$ -carbonyls with an alumina surface, after sol-gel

entrapment using $\text{Al}(\text{i-OPr})_3$ precursor, immobilized them in the form of coordinatively unsaturated complexes $= \text{Al-O-C-Ru}(\text{Os})(\text{CO})_{10}$ that are stable against leaching and metal-cluster formation [101]. These surface species in a mesoporous matrix displayed substantially higher activity in hydrogen-transfer reactions compared with homogeneous carbonyls and excellent leachproof and recycling performance.

5.3.2.2.3 Enzymes

Bioceramics – porous inorganic matrices with entrapped enzymes, catalytic antibodies, and whole cells – are a viable catalytic tool for the improvement of biotechnological and chemical processes, and were extensively studied in the last decade. The details of their preparation by the sol-gel entrapment strategy, properties, and performance are reviewed in several papers [102–106]. All biological catalysts are bulky polymeric molecules with molecular weights of 5000–400 000 and sizes in the range of 1–6 nm for globular conformations. Therefore, the main sol-gel encapsulation strategy in this case is physical or steric entrapment. The sol-gel entrapment protocol for bioencapsulation should be modified to ensure that condensation of the silica matrix precursors and subsequent processing can be done in the biocompatible pH range of 5–9, compatible redox conditions, and temperatures of <333 K, minimizing the use of solvents and toxic organic species. The main problems here are the decomposition of biocatalysts by reactions with alcohols evolved from hydrolysis of Si-OR groups, deactivation as a result of reactions of silica precursors with reactive centers of enzymes, and gel shrinkage, pressurizing the entrapped molecules. The optimized entrapment protocol [105] involves 5–100% prehydrolysis of alkoxysilane precursors, removal of the alcohols by evaporation, mixing with buffered biological catalyst containing fluoride or amine condensation catalysts, drying control additives as formamide and polyols, and structure modifiers like PVA or PEG, directing the silicate/siloxane oligomer growth via protein topology. After aging for 12–72 hours and washing, controlled desiccation allows extreme shrinkage of the catalyst gel to be avoided.

This procedure, using $\text{Si}(\text{OR})_4$ precursors, allowed preparation of a series of entrapped biological catalysts that included phosphatase, aspartase, glucose oxidase, trypsin, and other enzymes [102, 107]. Being optimized, they expressed 100% activities relative to the natural forms. However, for other enzymes like lipases, which have versatile biocatalytic activity in synthetic organic chemistry, food, and oil processing, it was necessary to use silica gels modified with alkyl groups in order to get similar results [103]. The highest activity was observed for catalysts that had been prepared starting from $\text{CH}_3\text{-Si}(\text{OCH}_3)_3$ and $n\text{-C}_3\text{H}_7\text{-Si}(\text{OCH}_3)_3$ precursors mixed with $\text{Si}(\text{OR})_4$ at stoichiometric water to silane ratio. This provides a lipophilic environment for the enzyme, which is inactive in the absence of an aqueous/lipid interface, and favors the transport of organic substrate inside the matrix pores. Further improvement

of the entrapment efficiency, that avoided reactions of the biomolecules with evolved alcohols and allowed the enzyme loading to be increased to 20–30 wt.%, was achieved by changing polyalkoxysilanes as gel precursors to water-soluble polyglyceroxysilanes. This was done by transesterification of partially hydrolyzed alkoxysilanes with glycerol before enzyme addition [104, 108]. The glycerol evolved during synthesis of bioceramics is biocompatible and acts as an additional drying control additive.

5.4

Summary

Sol-gel processing, originally developed as a tool for controlling the texture of pure metal-oxide phases, has become a universal technique for the preparation of the full spectrum of modern catalytic materials from multimetallic composite oxide phases to organic–inorganic hybrid interphase catalysts, heterogenized enzymes, and catalytic coatings and films. This universality results from the combination of soft and hard matter chemistry and technology during sol-gel processing. It opens up a wide range of opportunities for chemical functionalization of porous materials and careful control of their texture. The possibility to handle the material as a viscous liquid before its gelation/solidification brings an added value to this emerging technology – the opportunity to control the shape of catalytic materials at the nanoscale by its insertion into the mesoporous matrices or by formation of thin films. Sol-gel processing is developing in line with progress in soft/hard matter chemistry and catalytic functionalization of materials, and it is one of the important tools for the preparation of advanced catalysts.

References

1. Landau, M.V. (2002) in *Handbook of Porous Solids* (eds F. Schüth, K.S.W. Sing and J. Weitkamp), Wiley-VCH Verlag GmbH, Weinheim, Vol. 7, p. 1677.
2. Brinker, C.J. and Scherer, G.W. (1990) *Sol-Gel Science. The Physics and Chemistry of Sol-Gel Processing*, Academic Press, Boston, p. 908.
3. Hench, L.L. (2007) *Kirk-Othmer Encyclopedia of Chemical Technology*, 5th edn, John Wiley & Sons, Inc., New York, Vol. 23, pp. 53–84.
4. Schneider, M. and Baiker, A. (1995) *Catal. Rev. Sci. Eng.*, **37**, 15.
5. Piere, A.C. and Pajonk, G.M. (2002) *Chem. Rev.*, **102**, 4243.
6. Livage, J., Henry, M. and Sanchez, C. (1988) *Prog. Solid State Chem.*, **18**, 259.
7. Jolivet, J.P., Henry, M. and Livage, J. (2000) *Metal Oxide Chemistry and Synthesis – From Solution to Solid State*, John Wiley & Sons, Ltd, Chichester, John Wiley & Sons, Inc., New York, Wiley-VCH Verlag GmbH, Weinheim, p. 321.
8. Lessing, P.A. (1989) *Am. Ceram. Soc. Bull.*, **68**, 1002.
9. Vioux, A. (1997) *Chem. Mater.*, **9**, 2292.
10. Predieri, G. and Cauzzi, D. (2000) *Chim. Ind.*, **1**.

11. Vioux, A. and Leclercq, D. (1996) *Heterogen. Chem. Rev.*, **3**, 65.
12. Mackenzie, J.D. and Bescher, E.P. (2007) *Acc. Chem. Res.*, **40**, 810.
13. Hench, L.L. and West, J.K. (1990) *Chem. Rev.*, **90**, 33.
14. Hector, A.L. (2007) *Chem. Soc. Rev.*, **36**, 1745.
15. Pagliaro, M., Ciriminna, R. and Palmisano, G. (2007) *Chem. Soc. Rev.*, **36**, 932.
16. Livage, J. (1998) *Catal. Today*, (41), 3.
17. Ko, E.I. (1999) in *Preparation of Solid Catalysts* (eds G. Ertl, H. Knözinger and J. Weitkamp), Wiley-VCH Verlag GmbH, Weinheim, p. 85.
18. Baumann, T.F., Gash, A.E., Fox, G.A., Satcher, J.H. and Hrubesh, L.W. (2002) in *Handbook of Porous Solids* (eds F. Schüth, K.S.W. Sing and J. Weitkamp), Wiley-VCH Verlag GmbH, Weinheim, Vol. 3, p. 2014.
19. Gash, A.E., Tillotson, T.M., Satcher, J.H., Poco, J.F., Urubesh, L.W. and Simpson, R.L. (2001) *Chem. Mater.*, **13**, 999.
20. Iller, R.K. (1979) *The Chemistry of Silica*, John Wiley & Sons, Inc., New York, p. 866.
21. Singh, A., Bradley, D.C., Mehrotra, R.C. and Rothwell, I. (2001) *Alcovo and Aryloxo Derivatives of Metals*, Academic Press, New York, p. 704.
22. Cushing, B.L., Kolesnichenko, V.L. and O'Connor, C.J. (2004) *Chem. Rev.*, **104**, 3893.
23. Inoue, M., Kominami, H. and Inui, T. (1993) *Appl. Catal.*, **97**, L25.
24. Landau, M.V., Titelman, L., Vradman, V. and Wilson, P. (2003) *Chem. Commun.*, 594.
25. Sonnemans, J., de Keijer, H. and Mars, P. (1975) *J. Colloid Interface Sci.*, **51**, 335.
26. Abecassis-Wolfowich, M., Rotter, H., Landau, M.V., Korin, E., Erenburg, A.I., Mogilyansky, D. and Gartstein, E. (2003) *J. Non-Cryst. Solids*, **318**, 95.
27. Narendar, Y. and Messing, G.L. (1997) *Catal. Today*, **35**, 247.
28. Bunker, C.E., Rollins, H.W. and Sun, Y.-P. (2002) in *Supercritical Fluid Technology in Material Science and Engineering: Synthesis, Properties and Applications* (ed. Y.-P. Sun), Marcel Dekker, New York, p. 1.
29. Erenburg, A., Gartstein, E. and Landau, M.V. (2005) *J. Phys. Chem. Solids*, **66**, 81.
30. Rotter, H., Landau, M.V., Carrera, M., Goldfarb, D. and Herskowitz, M. (2004) *Appl. Catal.*, **47**, 104.
31. Pajonk, G.M. (2007) in *Catalysts Preparation* (ed. J. Regalbuto), CRS Press LLC, Boca Raton, p. 31.
32. Nguefack, M., Popa, A.F., Rossignol, S. and Kappenstein, C. (2003) *Phys. Chem. Chem. Phys.*, **5**, 4279.
33. Kureti, S. and Weisweiler, W. (2002) *J. Non-Cryst. Solids*, **303**, 253.
34. Le Bihan, L., Dumeignil, F., Payen, E. and Grimblot, J. (2002) *J. Sol-Gel Sci. Technol.*, **24**, 113.
35. Niesz, K., Yang, P. and Somorjai, G.A. (2005) *Chem. Commun.*, 1986.
36. Keysar, S., Cohen, Y., Shagal, S., Slobodiansky, S. and Grader, G.S. (1999) *J. Sol-Gel Sci. Technol.*, **14**, 131.
37. Poco, J.F., Satcher, J.H. and Hrubesh, L.W. (2001) *J. Non-Cryst. Solids*, **285**, 57.
38. Macedo, M.I.F., Osawa, C.C. and Bertran, C.A. (2004) *J. Sol-Gel Sci. Technol.*, **30**, 135.
39. Baumann, T.F., Gash, A.E., Chinn, S.C., Sawvel, A.M., Maxwell, R.S. and Satcher, J.H. (2005) *Chem. Mater.*, **17**, 395.
40. Grader, G.S., De Hazan, Y., Bravo-Zhivotovskii, D. and Shter, G.E. (1997) *J. Sol-Gel Sci. Technol.*, **10**, 127.
41. Grader, G.S., Shter, G.E., Avnir, D., Frenkel, H., Sclar, D. and Dolev, A. (2001) *J. Sol-Gel Sci. Technol.*, **21**, 157.
42. Gavrilov, V.Yu. and Zenkovetz, G.A. (1993) *Kinet. Katal.*, **34**, 357.
43. Hu, Z.S., Dong, J.X. and Chen, G.X. (1999) *Powder Technol.*, **101**, 205.
44. Iwasaki, M., Hara, M. and Ito, S. (1998) *J. Mater. Sci. Lett.*, **17**, 1769.

45. Campbell, L.K., Na, B.K. and Ko, E.I. (1992) *Chem. Mater.*, **4**, 1329.
46. Yoldas, B.E. (1986) *J. Mater. Sci. Lett.*, **21**, 1087.
47. Magalhaes, A.A.C., Nunes, D.L., Robles-Dutenhefner, P.A. and de Sousa, E.M.B. (2004) *J. Non-Cryst. Solids*, **348**, 185.
48. Gruttadauria, M., Liotta, L.F., Deganello, G. and Noto, R. (2003) *Tetrahedron*, **59**, 4997.
49. Mao, L., Li, Q., Dang, H. and Zhang, Z. (2005) *Mater. Res. Bull.*, **40**, 201.
50. Boiadjieva, T., Cappelletti, G., Ardizzone, S., Rondinini, S. and Vertova, A. (2003) *Phys. Chem. Chem. Phys.*, **5**, 1689.
51. Sickafus, K.E., Wills, S.M. and Grimes, N.W. (1999) *J. Am. Ceram. Soc.*, **82**, 3279.
52. Bolognini, M., Cavani, F., Scagliarini, D., Flego, C., Perego, C. and Saba, M. (2003) *Microporous Mesoporous Mater.*, **66**, 77.
53. Thanabodeekij, N., Sathupunya, M., Jamieson, A.M. and Wongkasemjit, S. (2003) *Mater. Charact.*, **50**, 325.
54. Naskar, M.K. and Chatterjee, M. (2005) *J. Am. Ceram. Soc.*, **88**, 38.
55. Arean, C.O., Mentrui, M.P., Platero, E.E., Llabres, F.X., Xamena, I. and Parra, J.B. (1999) *Mater. Lett.*, **59**, 22.
56. Arean, C.O., Mentrui, M.P., Lopez Lopez, A.J. and Parra, J.B. (2001) *Colloids Surf., A*, **180**, 253.
57. Chemlal, S., Larbot, A., Persin, M., Sarrazin, J., Sghyar, M. and Rafiq, M. (2000) *Mater. Res. Bull.*, **35**, 2515.
58. Kim, W.C., Lee, S.W., Kim, S.J., Yoon, S.H. and Kim, C.S. (2000) *J. Magn. Magn. Mater.*, **215–216**, 217.
59. Allmann, R. (1986) *Acta Crystallogr., Sect. A*, **24**, 972.
60. Stamiros, D., O'Connor, P., Jones, W. and Brady, M. (2003) US Patent 6,555,496, assigned to Akzo Nobel.
61. Wang, J.A., Morales, A., Bokhimi, X., Novaro, O., Lopez, T. and Gomez, R. (1999) *Chem. Mater.*, **11**, 308.
62. Lopez, T., Bosch, P., Ramos, E., Gomez, R., Novaro, O., Acosta, D. and Figueras, F. (1996) *Langmuir*, **12**, 189.
63. Choudary, B.M., Jaya, V.S., Reddy, B.R., Kantam, M.L., Rao, M.M. and Madhavendra, S.S. (2005) *Chem. Mater.*, **17**, 2740.
64. Jitanu, M., Balasoio, M., Zaharescu, M., Jitanu, A. and Ivanov, A. (2000) *J. Sol-Gel Sci. Technol.*, **19**, 453.
65. Jitanu, M., Zaharescu, M., Balasoio, M. and Jitanu, A. (2003) *J. Sol-Gel Sci. Technol.*, **26**, 217.
66. Rao, C.N.R. and Raveau, B. (1995) *Transition-metal oxides*, VCH Publishers, New York, p. 373.
67. Buassi-Monroy, O.S., Luhrs, C.C., Shavez-Chavez, A. and Michel, C.R. (2004) *Mater. Lett.*, **58**, 716.
68. Umar, V., Marimuthu, R., Patil, S.S., Ohya, Y. and Takahashi, Y. (1996) *J. Am. Ceram. Soc.*, **79**, 2775.
69. Su, W.-F.A. (2000) *Mater. Chem. Phys.*, **62**, 18.
70. Wang, W., Jia, D., Zhou, Y. and Ye, F. (2002) *Mater. Res. Bull.*, **37**, 2517.
71. Yoldas, B.E. (1984) *J. Non-Cryst. Solids*, **63**, 150.
72. Pozarnsky, G.A. and McCormick, A.V. (1995) *J. Non-Cryst. Solids*, **190**, 212.
73. Toba, M., Mizukami, F., Niwa, S., Sano, T., Maeda, K. and Shoji, H. (1994) *J. Mater. Chem.*, **4**, 1131.
74. Talmon, H., Sone, T., Mikami, M. and Okazaki, M. (1997) *J. Colloid Interface Sci.*, **188**, 493.
75. Nogami, M. and Nagasaka, K. (1989) *J. Non-Cryst. Solids*, **109**, 79.
76. Schneider, M., Maciejewski, M., Tschudin, S., Wokaun, A. and Baiker, A. (1994) *J. Catal.*, **149**, 326.
77. Cimpeanu, V., Parvulescu, V., Parvulescu, V.I., Capron, M., Grange, P., Thompson, J.M. and Hardacre, C. (2005) *J. Catal.*, **235**, 184.
78. de Lima, O.J., Papacidero, A.T., Rocha, L.A., Sacco, H.C., Nassar, E.J., Giuffi, K.J., Bueno, L.A.,

- Messaddeq, Y. and Ribeiro, S.J.L. (2003) *Mater. Charact.*, **50**, 101.
79. Linder, E., Schneller, T., Auer, F. and Mayer, H.A. (1999) *Angew. Chem. Int. Ed. Engl.*, **38**, 2154.
 80. Lu, Z., Linder, E. and Mayer, H.A. (2002) *Chem. Rev.*, **102**, 3543.
 81. Watton, S.P., Taylor, C.M., Kloster, G.M. and Bowman, S.C. (2003) *Prog. Inorg. Biochem. Biophys.*, **51**, 333.
 82. Stuchinskaya, T., Kundo, N., Gogina, L., Schubert, U., Lorenz, A. and Maizlish, V. (1999) *J. Mol. Catal., A*, **140**, 235.
 83. Linder, E., Schneller, T., Auer, F., Wegner, P. and Mayer, H.A. (1997) *Chem. Eur. J.*, **3**, 1833.
 84. Corriu, R. and Leclercq, D. (1996) *Angew. Chem., Int. Ed. Engl.*, **35**, 1420.
 85. Schubert, U. (1994) *New J. Chem.*, **18**, 1049.
 86. Blum, J., Avnir, D. and Schumann, H. (1999) *Chem. Tech.*, **29**(2), 32.
 87. Jin, W. and Brennan, J.D. (2002) *Anal. Chim. Acta*, **461**, 1.
 88. Morandin, M., Gavagnin, R., Pinna, F. and Strukul, G. (2002) *J. Catal.*, **212**, 193.
 89. Baiker, A., Grunwaldt, J.-D., Müller, C.A. and Schmidt, L. (1998) *Chimia*, **52**, 517.
 90. Buechler-Skoda, M., Gill, R., Wu, D., Nguen, C. and Larsen, G. (1999) *Appl. Catal.*, **185**, 301.
 91. Dusi, M., Mueller, C.A., Mallat, T. and Baiker, A. (1999) *Chem. Commun.*, 197.
 92. Dunn, B. and Zink, J.I. (1997) *Chem. Mater.*, **9**, 2280.
 93. Avnir, D., Klein, L.C., Levy, D., Schubert, U. and Wojcik, A.B. (1998) in *The Chemistry of Organosilicon Compounds* (eds Y. Apeloig and Z. Rapoport), Wiley, Chichester, UK, Vol. 2, p. 2317.
 94. Schubert, U., Rose, K. and Schmidt, H. (1988) *J. Non-Cryst. Solids*, **105**, 165.
 95. Craythorne, S.J., Crozier, A.R., Lorenzini, F., Marr, A.C. and Marr, P.C. (2005) *J. Organomet. Chem.*, **690**, 3518.
 96. Caiut, M.A., Nakagaki, S., De Lima, O.J., Mello, C. and Leite, C.A.P. (2003) *J. Sol-Gel Sci. Technol.*, **28**, 57.
 97. Molnar, A., Keresszegi, C. and Török, B. (1999) *Appl. Catal.*, **189**, 217.
 98. Izumi, Y. (2001) in *Fine Chemicals through Heterogeneous Catalysis* (eds R.A. Sheldon and H. van Bekkum), Wiley-VCH Verlag GmbH, Weinheim, p. 100.
 99. Israelsohn, O., Volhardt, K.P. and Blum, J. (2002) *J. Mol. Catal., A*, **184**, 1.
 100. de Sousa, E.M.B., Guimaraes, A.P., Mohallem, N.D.S. and Lago, R.M. (2001) *Appl. Surf. Sci.*, **183**, 216.
 101. Eliau, N., Avnir, D., Eisen, M.S. and Blum, J. (2005) *J. Sol-Gel Sci. Technol.*, **35**, 159.
 102. Avnir, D., Braun, S., Lev, O. and Ottolenghi, M. (1994) *Chem. Mater.*, **6**, 1605.
 103. Reetz, M.T. (1997) *Adv. Mater. (Weinheim, Germany)*, **9**, 943.
 104. Gill, I. and Ballesteros, A. (2000) *Trends Biotechnol.*, **18**, 282.
 105. Gill, I. (2001) *Chem. Mater.*, **13**, 3404.
 106. Jin, W. and Brennan, J.D. (2002) *Anal. Chim. Acta*, **461**, 1.
 107. Braun, S., Shtelzer, S., Rappoport, S., Avnir, D. and Ottolenghi, M. (1992) *J. Non-Cryst. Solids*, **147–148**, 739.
 108. Gil, I. and Ballesteros, A. (1998) *J. Am. Chem. Soc.*, **120**, 8587.

6

Deposition Precipitation

Krijn P. de Jong

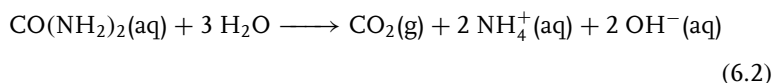
6.1

Introduction

A number of different methods for the preparation of supported metal (oxide) catalysts are dealt with in this book. In this chapter we discuss deposition precipitation as a generic method to emplace metals, metal oxides, metal sulfides, or metal hydroxides as small particles onto an existing support material. The deposition of the metal (compound) is brought about by a chemical reaction in the liquid phase. This chemical reaction leads to formation of a metal compound with low solubility in the solvent in question. The precipitation that follows is steered to take place exclusively at the surface of a suspended support material. The precipitation of metal hydroxides from an aqueous solution, such as



is widely used in this respect. The introduction of hydroxyl ions can be brought about by the injection of an alkaline solution or by the hydrolysis of urea,



The increase of pH of a metal salt solution using urea to bring about the deposition of the metal hydroxide onto a suspended support material has often been used. In fact, three methods to bring about precipitation are most used:

- pH increase
- reduction
- ligand removal.

In this chapter these methods will be discussed in detail.

Deposition precipitation (DP) was patented in 1943, reporting Stöwenert as the inventor working at IG Farben [1]. Geus and coworkers explored this method further while working at DSM in the 1960s [2]. After moving to Utrecht

Table 6.1 History of deposition precipitation.

Year	Assignee/author	Remarks	Reference
1943	IG Farben	Precipitation of (hydro)oxides, sulfides, selenides using urea and analogs	1
1967	Stamicarbon	Precipitation with urea from homogeneous solution; powder support	2
1970	Unilever	Precipitation with urea from concentrated solutions; prevention of solvent evaporation	11
1983	Geus <i>et al.</i>	Fundamental studies – urea method, powder supports	3, 4
1988	De Jong	Use of support bodies; controlled nonuniform metal distributions	9
1990	Che/Louis	Molecular details of urea method	5–8
2005	De Jong <i>et al.</i>	DP using carbon supports	10

University and working with Van Dillen he continued to study the fundamental aspects of DP [3, 4]. Che and Louis [5–8] revealed the molecular details of the urea method for silica powder, while De Jong [9] studied DP using support bodies (mm sized) rather than support powder (μm -sized agglomerates). More recently, DP with carbon supports has been explored [10]. For an overview of the history of DP we refer to Table 6.1 [1–11]. The general advantages acclaimed for DP are that high metal loadings can be combined with small particles and narrow particle-size distributions. Furthermore, the method in principle can be much more reproducible from one laboratory to another than some other methods of catalyst preparation. Finally, enhanced metal–support interaction of the reduced catalyst leads to improved thermal stability, as has been claimed by several workers (details in Section 6.4.1).

Geus and coworkers [12, 13], De Jong [9], and most recently Louis [14] have written reviews that cover the principles and developments of DP. This chapter deals first with some general principles, both theoretically and practically, followed by a description of mechanistic studies. Subsequently, case studies that provide interesting results are reviewed in a more encyclopedic manner. These case studies have been organized according to the principle of precipitation, that is, pH increase, reduction, and ligand removal. Finally, summary, conclusions, and outlook are presented. DP of gold is not dealt with in this chapter as this important topic is presented separately in Chapter 17.

6.2 Theory and Practice

Nucleation and growth theory is at the heart of the DP method. For a general introduction to this theory we refer to the literature [15, 16]. In summary, the

thermodynamic stability of the bulk solid versus the dissolved components dictates the solubility of the solid in question. In the case of a poorly soluble compound and a supersaturated solution precipitation can be inhibited by the unfavorably high surface energy of small particles. The balanced factors of bulk and surface free energy terms are represented by the overall Gibbs free energy change, ΔG_{tot} :

$$\Delta G_{\text{tot}} = 3/4\pi r^3 \cdot \Delta\mu_{\text{sl}} + 4\pi r^2 \cdot \gamma \quad (6.3)$$

In this formula

r = radius of the particle

$\Delta\mu_{\text{sl}}$ = difference in thermodynamic potential of solid and solute

γ = surface free energy of the solid in contact with solution or support.

A plot of ΔG_{tot} as a function of r for a number of scenarios is shown in Figure 6.1. In the absence of a support the solid line may be representative, that is the solubility is relatively high, as is the surface free energy. In the case of a support being present the nucleation may be favored over the bulk liquid either because of a lower solubility of the compound (dashed line) or because of a lower surface free energy (broken line). In many cases it has been suggested that DP is possible because of an interaction of the precipitate with the support, that is an effective lowering of γ . However, we present evidence (Section 6.3.2) that in fact with silica supports the stabilization of the precipitate (lowering of $\Delta\mu_{\text{sl}}$) is at least as important as the lowering of the surface free energy. Anyway, the facilitated nucleation of the precipitate by the presence of the support plays a key role. One should realize, however, that the experimental details of the precipitation process are essential too. Therefore, we now turn to the practical aspects of DP.

DP at the laboratory scale is advantageously carried out in the equipment shown in Figure 6.2 [17]. A double-walled, thermostatted, and baffled vessel (typically 250–1000 ml) is equipped with stirrer, pH-electrode, and two injection points for gas and liquid. The vessel is filled at room temperature with an aqueous solution of the metal salt in question followed by addition of the support (typically 20 g/l) and stirring. Precipitation can be either brought about by injection of the precipitant (e.g. alkaline solution) or by addition of a compound that slowly enhances the pH (e.g. urea). In the case of injection the challenge is to restrict concentration gradients in the solution. Close to the point of the liquid injection inevitably the local concentration of alkaline will exceed that of the bulk suspension. For that reason, nucleation in the bulk liquid may take place in the vicinity of the injection point. For that reason, when injection is being applied vigorous stirring is mandatory to bring about large shear forces and reduce concentration gradients. In the case of urea, hydrolysis is slow at the prevailing temperature (typically 90 °C) and concentration gradients will be minimal even when stirring at moderate rates is applied. The pH electrode

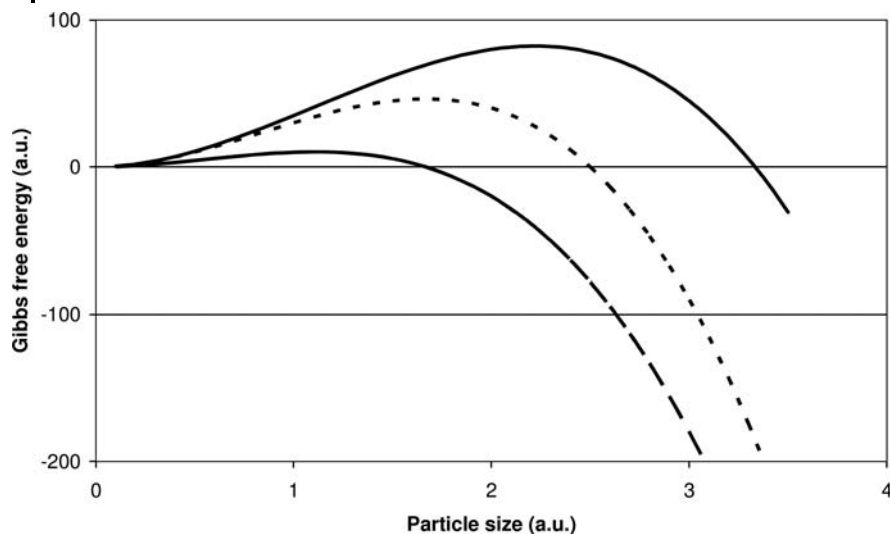


Figure 6.1 Gibbs free energy as a function of particle size for (top – solid line) high solubility + high surface energy, (middle – dashed line) low solubility + high surface energy, and (bottom – broken line) high solubility + low surface energy.

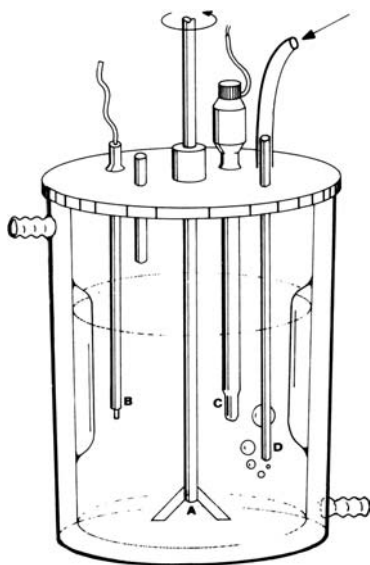


Figure 6.2 Schematic presentation of a setup for deposition precipitation at the laboratory scale [17]. The baffled vessel is double walled to allow temperature control and details comprise stirrer (a), liquid injection tube (b), pH electrode (c), and gas injection tube (d). (Reproduced from I.I.M. Tijburg, PhD Thesis, Utrecht University (1989).)

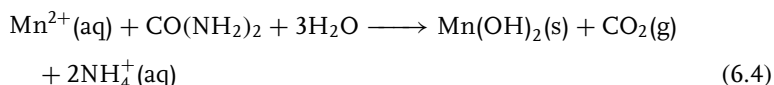
is used to study the precipitation process as will be shown and discussed in Section 6.3. Gas injection is sometimes needed to prevent oxidation by air.

The equipment described above, in principle, can also be used with support bodies (millimeter sized) instead of support powder (micrometer sized). However, attrition of support bodies may be severe under the conditions of stirring. Using support bodies one can either accept some attrition (often acceptable at the laboratory scale) or work in a different way. For example, one can work with concentrated solutions of, for example, metal salt and urea in water and just fill the pores of the support bodies with this solution. The hydrolysis of urea, typically at 90 °C, should subsequently be carried out with limited or no evaporation of water. Since CO₂ is formed a fully closed vessel is not an option; a system that restricts evaporation such as a lid on a vessel can be used. The vessel can be rotated to prevent temperature and concentration gradients during DP.

6.3 Mechanistic Studies

6.3.1 Kinetics

The deposition of manganese hydroxide onto silica powder and silica granules (0.6–1.4 mm) using urea hydrolysis has been studied in detail by De Jong [9]. Manganese nitrate had been dissolved in water and deposition took place according to the overall reaction.



An overview of the experiments can be found in Table 6.2, while pH records for two experiments are shown in Figure 6.3. The initial pH just below 2 had been realized by acidification of the solution prior to urea hydrolysis. In

Table 6.2 Details and kinetic constants of precipitation of manganese hydroxide onto silica support.

Experiment	Support	Temperature (°C)	Mn ²⁺ concentration (mmol.l ⁻¹)	Urea concentration (mmol l ⁻¹)	k _U (h ⁻¹)	k _{Mn} (h ⁻¹)
U30	Granules	90.5	9.1	46	n.d.	0.12
U31	Powder	90.5	9.1	46	0.14	0.12
U33	—	88.5	36	182	0.10	0.04
U34	Granules	88.5	36	182	0.10	0.10

k_U is the first-order rate constant for urea hydrolysis and k_{Mn} is the first-order rate constant for manganese removal from solution.

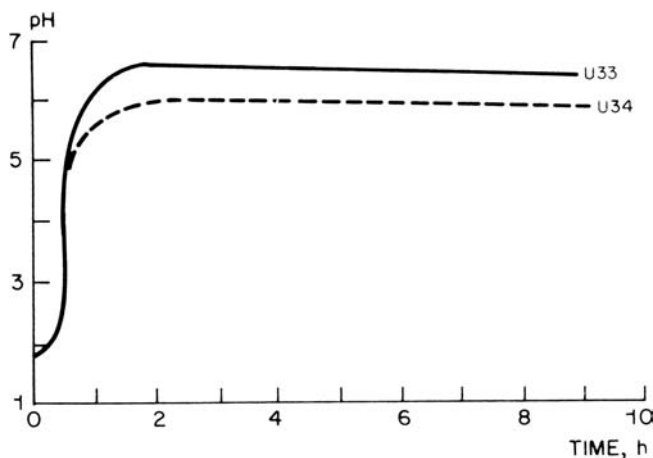
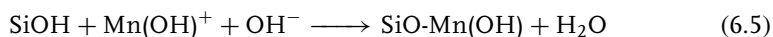


Figure 6.3 Records of pH as a function of time for deposition of manganese hydroxide; experiment U33 (no support) and U34 (silica granules). Hydrolysis of urea started at time zero. (Reproduced with permission from Elsevier [9].)

these experiments the rate of hydrolysis of urea and the rate of removal of manganese from solution have been measured independently. Removal of manganese from solution started to occur 1–2 hours after hydrolysis of urea. Both the rate of hydrolysis of urea and the rate of removal of manganese from solution could be described well by first-order kinetics and the related rate constants have been summarized in Table 6.2. Please note that the kinetics of the hydrolysis of urea is not affected by pH [18] and the kinetic constants, therefore, are valid throughout the experiment. From the data in Table 6.2 it appears that urea hydrolysis, furthermore, is not affected by the presence of the support and that the absolute rate (the product of rate constant and concentration) is typically five times higher for urea hydrolysis than for Mn deposition. From the latter observation it was concluded that urea hydrolysis leads predominantly to formation of $\text{NH}_3(\text{g})$ and that only 20% is used effectively for precipitation. The use of a 5–10-fold excess of urea in DP is in line with this observation.

The pH records shown in Figure 6.3 reveal some general features of DP using urea. In the absence of a support a minor but significant overshoot is apparent after 1.5–2 hours. This overshoot is characteristic of the precipitation process being activated due to the required formation of small solid nuclei that call for a supersaturated solution (cf. Figure 6.1). Following the overshoot at pH = 6.6 the pH drops slightly due to growth of nuclei and a pseudo-steady state is apparent for several hours at pH = 6.3. In the presence of a silica support an overshoot is not apparent and the pseudo-steady state pH is lowered to 5.3. The latter lowering points to the (thermodynamic) stabilization of the $\text{Mn}(\text{OH})_2$ phase due to the interaction with silica.

From the kinetic data in Table 6.2 it appears that the rates of Mn removal from solution were similar for silica powder and for silica granules. Mass-transfer effects, therefore, did not affect the overall rate of Mn deposition. For the silica granules the distribution of the Mn concentration as a function of position (Figure 6.4), however, clearly reveals a diffusion limitation for the final deposition reaction. From a kinetic analysis in combination with diffusion (Thiele modulus, ϕ) De Jong has concluded that the rate constant for the final deposition reaction greatly exceeded the rate constants shown in Table 6.2. An analysis was proposed that involved as the final deposition reaction



with an associated first-order rate constant k_D . From the values of ϕ one can easily estimate values of k_D that turned out to be orders of magnitude larger than k_{Mn} . In other words, diffusion limitation in DP is not caused by the rate-determining step of urea hydrolysis but by the fast secondary deposition reactions with the support. The rate constant for Ni and Rh deposition turned out to be smaller than that for Mn deposition. These kinetic data are important for understanding the process of DP in more depth and to enable the use of support bodies.

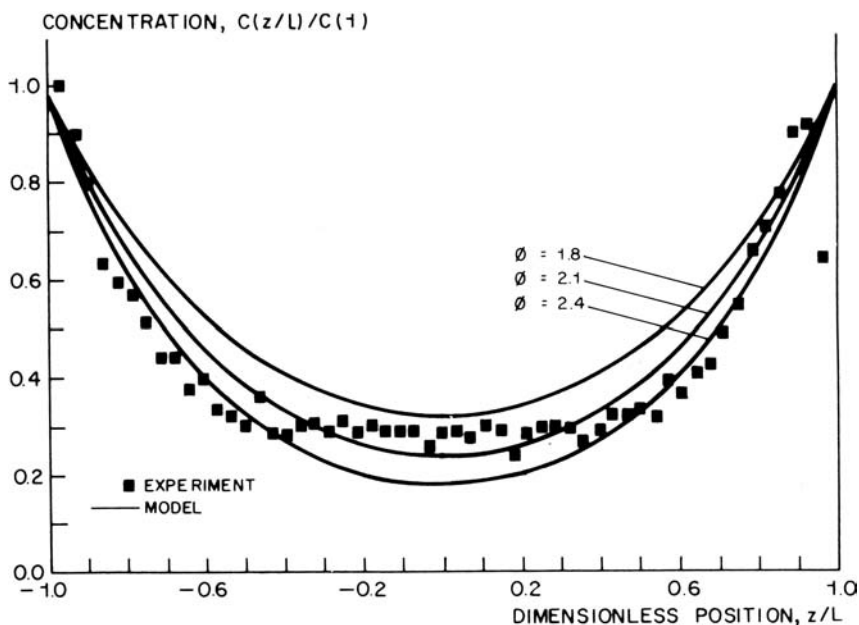


Figure 6.4 Distribution of manganese over a representative silica granule (~ 1 mm size) from experiment U34. The drawn lines have been calculated for different values of the Thiele modulus (ϕ). (Reproduced with permission from Elsevier [9].)

6.3.2

Molecular Details

In an excellent series of papers Burattin, Che and Louis [5–8] have proposed the molecular details of DP with urea studying the important system of nickel on silica. By variation of the silica specific surface area, nickel concentration and DP time, the authors concluded that turbostratic nickel hydroxide is the main phase deposited when short reaction times and low silica surface area are applied. Longer reaction times and higher silica surface area led to 1 : 1 nickel phyllosilicate of increasing crystallinity. The overall reaction mechanism is depicted in Figure 6.5 and is now discussed in some detail. Following the papers mentioned, the authors describe the key steps of the mechanism as follows.

1. Electrostatic adsorption of $\text{Ni}(\text{OH}_2)_6^{2+}$ onto silica (step 1 in Figure 6.5).
2. With increasing pH the nickel hexa-aqua complex is hydrolyzed to form $\text{Ni}(\text{OH})(\text{OH}_2)_5^+$ and $\text{Ni}(\text{OH})_2(\text{OH}_2)_4$.
3. Hydrolytic adsorption of all of these nickel species onto silica, which involves reactions such as $\text{Ni}(\text{OH})(\text{OH}_2)_5^+ + \text{Si-OH} \longrightarrow \text{Si-O-Ni}(\text{OH}_2)_5^+ + \text{H}_2\text{O}$.
4. Several routes from solution and from surface reactions to form nickel hydroxide and/or 1 : 1 nickel phyllosilicate (Figure 6.5).

Although 2:1 phyllosilicate is thermodynamically more stable than 1:1 phyllosilicate, the authors provide evidence that kinetic barriers exist to form the former compound under the conditions prevailing during DP. The authors discuss in detail the possible contributions from reactions in the liquid phase involving dissolved silica (top line in Figure 6.5) versus reactions on nickel species with surface silanol groups (bottom line in Figure 6.5). No data for the relative contributions of both routes for the DP reactions have been presented.

Van der Lee and coworkers [10] have carried out a somewhat similar study with silica that was extended into the application of a carbon support for the

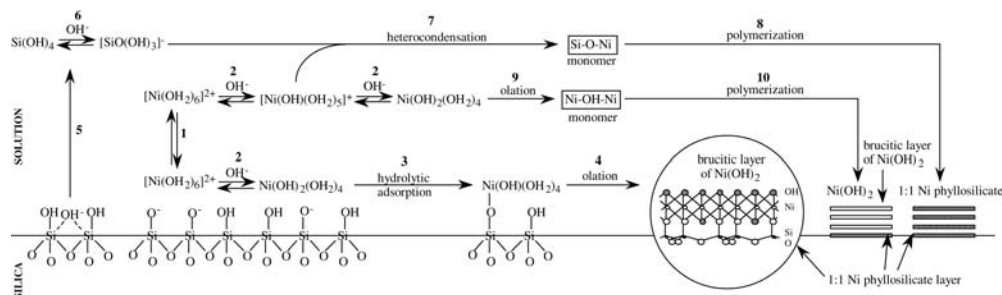


Figure 6.5 Proposed mechanism for the deposition of nickel hydroxide onto silica. (Reproduced with permission from the American Chemical Society [6].)

urea DP of nickel from an aqueous suspension. Earlier, Wigmans and Moulijn [19], on the one hand, and Van Steen and Prinsloo [20], on the other hand, had reported on DP of nickel and iron onto carbon supports. For activated carbons nonuniform nickel distributions were reported, while large iron particles were obtained with carbon nanotube supports. In a comprehensive study using well-defined and nonmicroporous carbon nanofiber (CNF) supports, it was found by Van der Lee *et al.* [10] that excellent results for DP of nickel using urea could be obtained. Nickel loadings up to 50 wt% and particle sizes for metallic Ni of 6–8 nm have been reported. Before use in DP experiments the CNF were surface oxidized using nitric acid (reflux, 2 hour) that led to typical densities of ~ 1 carboxylic acid groups per nm^2 . DP could only be successfully carried out when these acid sites were present. Phenol-type groups as well as other oxygen-containing groups did not suffice and their exclusive presence led to precipitation of nickel hydroxide in the bulk solution, thus separate from the support.

Using surface-oxidized CNF (CNF-O) pH and nickel deposition as a function of time was measured and compared to silica. These data are shown in Figure 6.6. With silica, deposition of nickel did not occur prior to nucleation of a solid phase as inferred from the pH overshoot at $t = 40$ min. This result does not indicate the electrostatic adsorption of nickel cations onto silica but rather suggests hydrolytic deposition as described above. With the CNF-O support, however, deposition of nickel is apparent right from the start of the experiment. The lower slope of the pH–time curve points to more extensive consumption of hydroxyl ions and related hydrolysis of adsorbed nickel species. The initial adsorption process is ascribed to electrostatic adsorption of Ni^{2+} (aq) onto the COO^- surface groups. The subsequent smooth nucleation of nickel hydroxide results in almost no overshoot of pH being observed with carbon. The final product obtained from DP clearly shows the plate-like nickel hydroxide features on the support (Figure 6.7). It was concluded by the authors that nickel ion adsorption (IA) sufficed for facilitating nucleation of nickel hydroxide onto the carbon support. Please note that this mechanism differs fundamentally from that of nickel onto silica. For the latter system the stability of the deposited phase is enhanced versus that of unsupported nickel hydroxide. From the pH curves (Figure 6.6) it is apparent that the plateaus of pH (>4 h) are different in level, pointing to stabilization by silica and not by carbon. This purely kinetic basis for DP on carbon makes the process less robust and nonuniform or poorly dispersed phases can be more easily obtained. For example, the Chen–Holmen group [21, 22] has obtained less favorable results for Cu and Ni onto CNF-O, probably because of a shorter time (10 min versus 2 h) for surface oxidation of the support prior to DP. A second example involves the DP of cobalt with urea onto CNF-O reported by Bezemer *et al.* [23] and showing very poor dispersions. From detailed analysis it turned out that most likely with Co^{2+} (aq) the extent of IA is less than with Ni^{2+} (aq) and not sufficient to induce nucleation of the cobalt hydroxide onto the support.

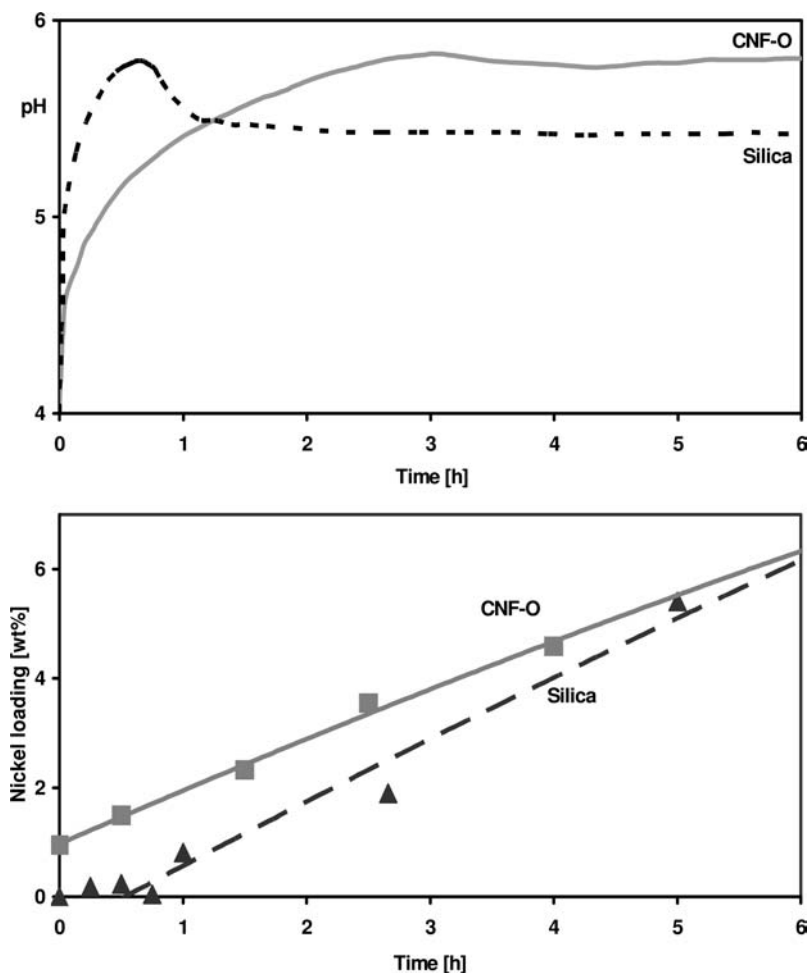


Figure 6.6 Development of pH and nickel loading with silica (broken lines) and carbon nanofiber support (full lines) as a function of time. (Reproduced with permission from the American Chemical Society [10].)

6.4 Case Studies

6.4.1 pH Increase

As mentioned before, the urea method for nickel has been used and studied most widely. Here, we focus on a broader range of metals that have been deposited as well as on studies that reveal details not discussed before.

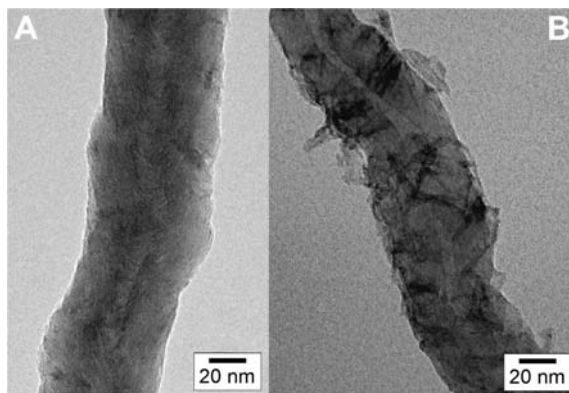


Figure 6.7 Transmission electron micrographs of bare carbon nanofiber (a) and one loaded with nickel hydroxide platelets (b). (Reproduced with permission from the American Chemical Society [10].)

Several groups have shown the remarkable thermal stability of finished, supported metal catalysts prepared by DP. Both the local curvature of the silica in interaction with metallic nickel particles and the extent of reduction play a key role in this respect. Montes and coworkers [24] have exposed Ni/SiO₂ prepared via urea DP to reduction–oxidation cycles and shown that these catalysts were much more stable than their impregnation counterparts. Chang and coworkers [25] have shed another light on the robustness of urea DP by using silica from a natural source, that is from rice husk ash ($\sim 130 \text{ m}^2 \text{ g}^{-1}$), as support and obtaining excellent metal dispersions at $\sim 25 \text{ wt\%}$ Ni loading. Gómez-Reynoso and colleagues [26] used DP of nickel hydroxide onto SBA-15, an ordered mesoporous silica support. Although nickel phyllosilicates had been formed the cylindrical mesoporous were still intact and 2–4 nm metallic nickel particles were obtained at metal loadings of 10–13 wt%.

Next to nickel a range of other metals has been deposited onto supports using DP techniques. A special challenge provided copper onto silica using urea. The Geus group [3, 13, 27] has published a series of papers on this topic that reveal some intricate details. The special case of copper nitrate as precursor posed some challenges as basic copper nitrate, $\text{Cu}_2(\text{NO}_3)(\text{OH})_3$, precipitates typically at $\text{pH} = 5$ where the interaction with silica is quite limited and thus deposits separate from the support. Prolonged precipitation ($> 20 \text{ h}$) is needed to dissolve the basic copper nitrate and to precipitate another copper compound at more elevated pH where good interaction prevails and copper hydrosilicate is formed. The pH curve shown in Figure 6.8 reveals nicely the phenomena mentioned. The plateau for $t = 3\text{--}6 \text{ h}$ points to intermediate precipitation of $\text{Cu}_2(\text{NO}_3)(\text{OH})_3$. After prolonged hydrolysis of urea and subsequent reduction, metallic copper particles ranging from 3–8 nm at Cu loadings of 5–35 wt% were obtained on the silica support.

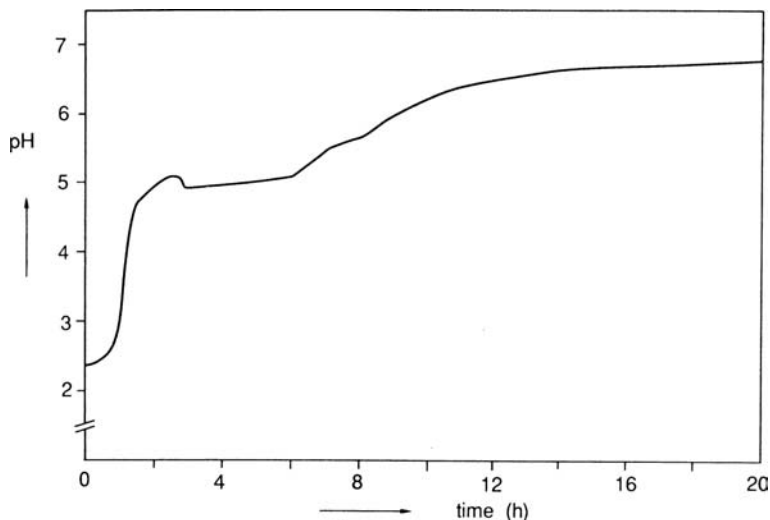


Figure 6.8 pH curve recorded during precipitation of 20 wt% copper onto silica using urea; the pH plateau for $t = 3\text{--}6$ hour points to intermediate precipitation of bulk $\text{Cu}_2(\text{NO}_3)(\text{OH})_3$. (Reproduced with permission from Elsevier [27].)

In general, divalent transition-metal ions can be applied using urea DP. For trivalent ions hydrolysis may take place at pH values that are too low, thus preventing the interaction with silica that typically is favored at $\text{pH} > 5$. Mul and Hirschon [28], however, successfully applied La(III)oxide onto silica by injection of a NH_4OH solution starting at $\text{pH} = 4$ and ending at $\text{pH} = 10$. From the pH measurements an interaction between $\text{La}(\text{OH})_3$ and SiO_2 could be inferred, while XRD showed the La phase to be amorphous.

Bimetallic catalysts can in principle be obtained using the urea method to arrive at codeposition precipitation. De Jong and coworkers [29] have applied this method for Rh/MnO/SiO₂ catalysts starting from an aqueous solution of Rh(III) and Mn(II) nitrates. From detailed characterization of this catalyst, though, it followed that the MnO phase had been dispersed over and in the silica support, thereby limiting the interaction with the 1-nm metallic Rh particles. Wielers *et al.* [30] followed a different strategy to arrive at bimetallic FeCu/SiO₂ catalysts. First, Cu was deposited onto silica using urea (*vide supra*) followed by redispersion of the solid in an iron(III) nitrate solution and subsequent injection of NH_4OH solution to precipitate Fe-hydroxide onto the copper-loaded silica. Also, in this system a range of iron species was apparent and the extent of copper–iron interaction varied quite widely in this system. For this reason bimetallic catalysts are advantageously prepared using reduction techniques discussed in Section 6.4.2.

For the deposition of noble metals onto supports the urea method has not been used extensively. For the preparation of Ru and Pt supported on CNF,

Toebe and coworkers [31] have compared DP with IA. For Pt they started from $\text{Pt}(\text{NH}_3)_4(\text{NO}_3)_2$ dissolved in an acidified ($\text{pH} = 3$) suspension of CNF in water followed by DP using urea at 90°C (final $\text{pH} = 6$). For comparison IA at $\text{pH} = 6$ was performed with the same precursor at temperatures of 25 or 90°C . With both preparation techniques, homogeneously distributed, highly dispersed and thermally stable metal particles were obtained with an average size of 1–2 nm. Starting with an intake of Pt of 5 wt%, with DP loadings of ~ 4 wt% could be achieved, whereas IA at the prevailing conditions led to ~ 2 wt% for reasons that were not fully understood. For Ru excellent results (1–2 nm particles at 5 wt% loading) using urea were obtained when $\text{Ru}(\text{NO})(\text{NO}_3)_3(\text{H}_2\text{O})_2$ was used as a precursor. With RuCl_3 next to small particles also large lumps of RuO_x were found, probably originating from the precursor salt. In all cases (DP and IA, Pt and Ru) it was concluded that the carboxylic acid groups on the surface-oxidized CNF were key anchoring points for deposition. Furthermore, it was apparent with Pt that quantitative deposition of the metal using urea could not be achieved. For that reason, many workers prefer DP by alkaline injection to arrive at more elevated $\text{pH} > 6$ to approach quantitative deposition. In the next paragraph we summarize a few of these studies.

With noble metals (Pd, Ir, Pt, Au) DP by means of pH increase has been practiced many times by addition of the metal precursor solution to a suspension of the support in an aqueous alkaline solution. For example, Augustine and Leary [32] have prepared in this way 1 wt% Pd/MgO with a final Pd dispersion of 40%. Deposition of Ir-precursor onto TiO_2 was realized [33] by dispersion of the support in an aqueous solution of IrCl_4 the pH of which was adjusted to 8 by addition of NaOH solution. After work-up and calcination in air at 400°C it was found that Ir or IrO_2 had been deposited as a thin layer of about 2 nm thick onto the TiO_2 support. Kim and coworkers [34] have prepared Pd/ZnO by addition of sodium carbonate solution (final $\text{pH} = 8$) to a suspension of ZnO in palladium nitrate solution. Comparison of the DP catalysts with those prepared by impregnation or coprecipitation revealed favorable performance of the former for the methanol synthesis. Gopinath *et al.* [35] have prepared Pd/ ZrO_2 catalysts by addition of Na_2CO_3 solution to $\text{PdCl}_2(\text{aq})/\text{ZrO}_2$ suspension. The ~ 1 –nm Pd particles dispersed on ZrO_2 thus obtained performed favorably for the hydrodechlorination of chlorobenzene when compared to catalysts obtained via impregnation.

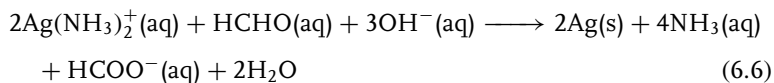
The injection method of DP has been also applied many times for the preparation of carbon-supported noble-metal catalysts. Jin *et al.* [36] have deposited 5 wt% Pd on activated carbon fibers by alkaline hydrolysis of palladium chloride and obtained metal dispersions of 55–77%. Dispersions of 40–50% have been reported by Farkas *et al.* [37] who prepared Pd/C by fast addition of NaOH solution to a suspension of carbon in an aqueous solution of K_2PdCl_4 . More highly loaded Pd and Pt catalysts (10 wt%) have been prepared by drop-wise addition of the metal salt solution to the suspension of carbon in Na_2CO_3 solution. In this case [38] a Pt particle size of 10 nm and a Pd particle

size of 17 nm were reported. Ion adsorption led to much smaller particle sizes. By quick addition of NaOH solution to a suspension of carbon support in PdCl₂ solution, Cabiatic *et al.* [39] obtained 5–10 nm Pd particles at a loading of ~4 wt%. Clearly, details of support, metal loading, and the method of mixing of reactants all play a vital role in the dispersion and distribution of the metal in the finished catalyst.

6.4.2

Reduction Deposition Precipitation

Precipitation can also be brought about by reduction of solvated metal ions to the metal. This method is sometimes referred to as electroless plating. We prefer the name reduction deposition precipitation (RDP) for this method. RDP has been explored with the aim of catalyst preparation using oxidic supports by De Jong and Geus [40] and by Barbier and coworkers [41]. Typically, the support is suspended in a solution of the metal precursor and a reducing agent such as formaldehyde is added to bring about deposition of the metal as shown for silver.

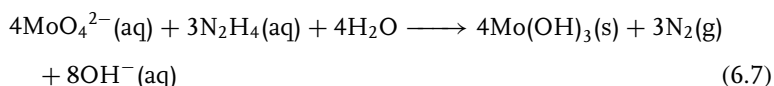


One of the fundamental problems of using chemistry such as this one, is the thermodynamic instability of the solution. In other words, if both the silver–ammonia complex and the reducing agent are present in solution the reaction may proceed irreversibly. In practical terms this means that the mixed solution is unstable and the details of the procedures do matter. In fact, one of the roles of the ammonia is to stabilize the silver ions, as “unprotected” silver nitrate solutions will be reduced by formaldehyde spontaneously under a wide range of conditions.

First, we discuss the detailed study of De Jong and Geus [40] using RDP, for the preparation of Ag/SiO₂ catalysts, which reveals some of the basic principles of the technique. The preparation of 10–15 wt% Ag onto silica was brought about by the reduction of silver ions using HCHO. Typically, HCHO was added at 5 °C (to prevent premature reaction) to a suspension of silica in an aqueous solution of silver nitrate and ammonia that was subsequently heated to 50 °C. At the latter temperature, reaction (6.6) proceeded smoothly. In view of the elevated pH = 9–10 of the suspension an appreciable interaction of the Ag(NH₃)₂⁺ ions with the positively charged silica particles (PZC ≅ 2) may be expected. This interaction turned out to be key for obtaining highly dispersed Ag/SiO₂ catalysts. The authors provided evidence for this by comparison with the reduction of an Ag-EDTA complex that is negatively charged at the prevailing pH. Although Ag–NH₃ and Ag–EDTA complexes have very similar thermodynamic stability, it was observed that the reduction temperature

needed for the latter complex turned out to be higher than for the former complex. Furthermore, the silver dispersion observed from the two complexes differed largely, as can be inferred from the TEM images shown in Figure 6.9. In all cases, though, the silver particle-size distribution turned out to be a bimodal one. It was suggested that next to nucleation at the support (leading to Ag particles ~ 5 nm) nucleation in the bulk liquid (leading to Ag particles of 20–40 nm) also played a role.

Of course, RDP is very suitable to deposit noble metals in view of their facile reduction from aqueous solutions. A number of studies have shown that attractive results can also be obtained with non-noble metals and with metal oxides and metal sulfides. De Jong [9, 42] has studied the deposition of molybdenum (hydr)oxide by reduction of ammonium molybdate with hydrazine according to the reaction



Deposition of molybdenum(III)oxide onto a silica support was realized at pH = 8.7 at temperatures of 0–60 °C over a wide range of loadings of 1–20 wt% Mo. As can be inferred from Equation 6.7 it is to be expected that a lower pH will favor this redox reaction. Based on this fact a very peculiar phenomenon was noted and exploited. Using silica spheres of 1.5 mm size an impregnation with the aqueous molybdate/hydrazine solution was carried out. It was observed that under certain conditions of concentrations and temperature the deposition of the (brown) Mo compound took place

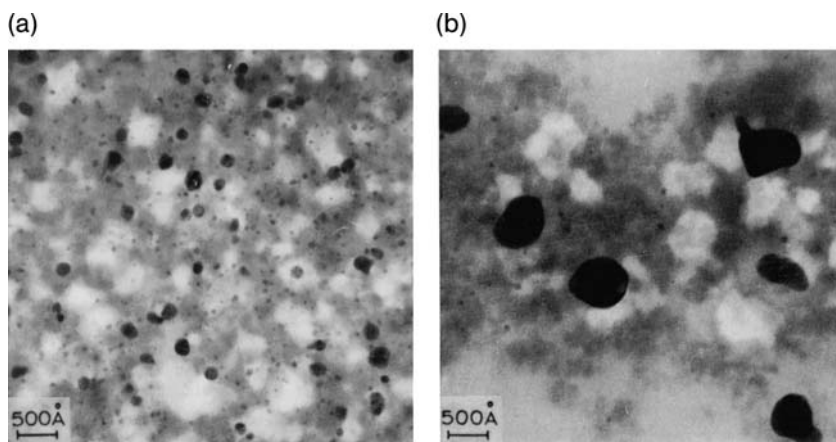


Figure 6.9 TEM images of 10 wt% Ag/SiO₂ catalysts obtained by (a) reduction of $\text{Ag}(\text{NH}_3)_2^+(\text{aq})$ by formaldehyde at 5–50 °C and (b) by reduction of Ag-EDTA(aq) complex by formaldehyde at 60 °C. (Reproduced with permission from Elsevier [40].)

exclusively in the center of the silica spheres. Working at low Mo loadings the RDP conditions could be selected, such that the reaction stopped after some time and Mo had been only deposited at the center of the spheres. At more elevated Mo loadings the egg-yolk-type distribution was still apparent, while the highest loadings led to enrichment at the edge related to mass-transfer limitation. The line scans obtained via EDX for Mo over the silica spheres as a function of Mo loading are displayed in Figure 6.10. In particular, the method using transient RDP, that is, short reaction times that did not deplete the solution, was successful to realize egg-yolk distributions. The method proposed has been generalized to involve redox reactions that produce H^+ or OH^- ions. Egg-yolk distributions for $Ag/\gamma-Al_2O_3$ and $Cu/\gamma-Al_2O_3$ have been obtained using similar chemistry [9, 42].

Recently, Barrio and coworkers [43] prepared coatings of MnO_2 on alumina by RDP using acetone as solvent. $KMnO_4$ dissolved in acetone was reduced by ethanol to give MnO_2 . As the Lewis-acid sites of the alumina catalyzed the RDP, preferential deposition on the support was obtained. The resulting catalysts appeared to be very active in VOC complete oxidation.

Bezverkhy and coworkers [44] from the IRC in Lyon have studied the preparation of alumina-supported MoS_2 via RDP. Starting from an aqueous solution of ammonium tetrathiomolybdate, $(NH_4)_2MoS_4$, reduction to deposit MoS_2 onto the suspended alumina was brought about by hydrazine, N_2H_4 .

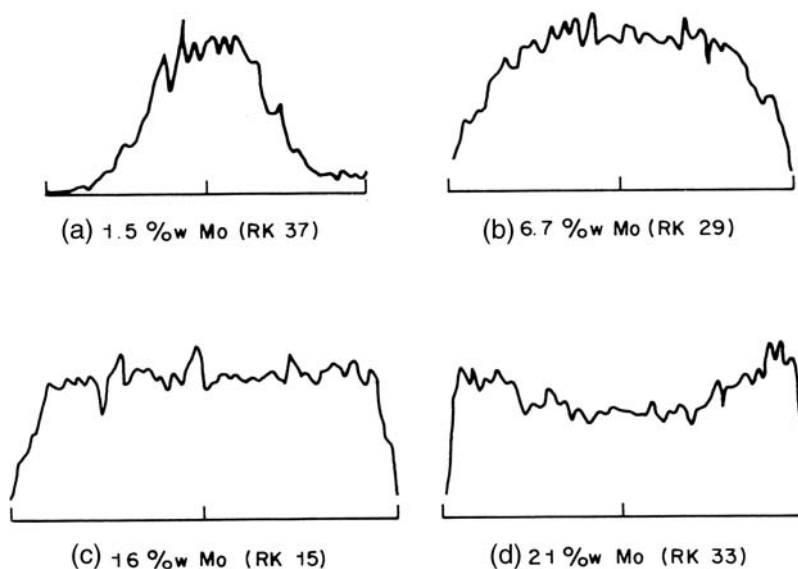


Figure 6.10 EDX line scans for the Mo concentration (vertical axis) versus the position (horizontal axis) over 1.5-mm spheres for different Mo loadings; the Mo had been deposited via RDP (see text). (Reproduced with permission from Elsevier [9].)

MoS₂ nanocrystals with an average stacking number of 3 and an average length along the basal planes of 3 nm were obtained. The HDS activity of the catalysts increased linearly with the Mo loading until and including 22 wt% of Mo, which is well above the monolayer capacity of the alumina. In a subsequent study [45] these workers found that some remaining carbon on the catalysts was very beneficial for catalyst stability under sulfiding and reaction conditions. Moreover, promotion of the HDS catalyst by addition of cobalt appeared to be facile by using reflux with Co(acac)₂ solution. The Co-promoted C-MoS₂/Al₂O₃ catalysts were shown to be two to three times more active than a commercial counterpart.

With carbon supports RDP has been used often for deposition of Pd using an organic reductant such as formaldehyde. Typical examples are the work of Hoogenraad *et al.* [46], Heal and McKayala [47], and Yang *et al.* [48]. Platinum has been deposited onto single-wall nanotubes by reduction of K₂PtCl₄ by ethylene glycol at 120–130 °C [49]. Copper and nickel deposition onto surface-oxidized multiwall carbon nanotubes sensitized with PdSn has been studied by Ang *et al.* [50]. Reduction by hydrazine has also been carried out for Ni²⁺(aq) to deposit metallic nickel onto a graphitic support [51]. From the characterization it turned out that the surface of the particles was partially oxidized in line with the relatively low reduction potential of Ni²⁺(aq)/Ni. Please note that in a number of cases it has been demonstrated that surface oxidation of the carbon support plays an important role in RDP to arrive at selective deposition of the metal onto the support and to realize high dispersions.

Reduction deposition precipitation provides excellent opportunities to prepare bimetallic catalysts with enhanced precision. Bimetallic catalysts have been advantageously prepared using RDP in which the first metal already present on the support catalyzed the redox reaction to deposit the second metal exclusively onto the first one. De Jong and Geus [40] have explored this procedure for AgPt/SiO₂ catalysts by RDP of silver onto Pt/SiO₂. Using the chemistry of Equation 6.6 under carefully chosen conditions, exclusive deposition of Ag onto existing Pt particles could be realized. This exclusiveness was demonstrated in several ways. From TEM (Figure 6.11) it appeared that the 2-nm Pt particles had grown to 3-nm AgPt bimetallic particles. The fact that the Pt could be fully covered was further supported by CO adsorption using IR spectroscopy [52]. The C–O stretch vibration on Pt at 2090 cm⁻¹ had almost fully disappeared for the system with 64 at% Ag/36 at% Pt. Similar results for this system were obtained using NO and N₂ adsorption in combination with IR [51]. Schaal and coworkers [53] have deposited similarly Cu onto Pd/SiO₂ and Ag onto Pt/SiO₂ via RDP (referred to as electroless plating by the authors). Next to selective deposition of Cu onto existing Pd particles, autocatalytic reduction of copper on copper also took place.

Barbier and coworkers [41] have proposed and developed a very elegant method to steer the deposition of the second metal to the first one using RDP. When the first metal is a noble metal, hydrogen chemisorption could be used to deposit the second metal via local chemical reduction. Bachir *et al.*

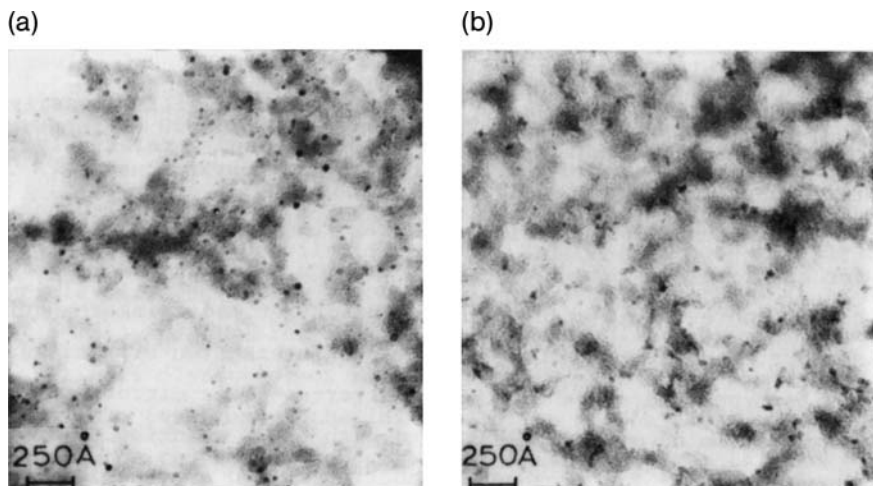


Figure 6.11 TEM images of Pt/SiO₂ and AgPt/SiO₂; the latter has been obtained via RDP. (Reproduced with permission from Elsevier [40].)

[41] have deposited Fe onto supported Pd/Al₂O₃ by exposing a suspended catalyst to Fe³⁺/H₂. Deposition of a monolayer of Fe onto the Pd particles was claimed. Similarly, Micheaud *et al.* [41] started from parent Pd/Al₂O₃ with preadsorbed hydrogen atoms. Pt²⁺ ions in acetone were reduced onto metallic Pd by adsorbed H atoms. Using EXAFS and IR of adsorbed CO, evidence was provided that Pt atoms were preferentially deposited on the low-coordination sites of the Pd particles.

6.4.3

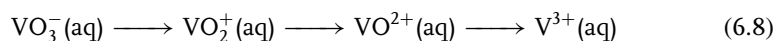
Ligand Removal

At elevated pH ligands such as ammonia and EDTA can be used to stabilize transition-metal ions in water. Removal of these ligands via evaporation or oxidation has been used in the past to bring about deposition onto an oxidic support material [13, 54]. In particular, Lok *et al.* [54] have explored deposition of cobalt onto alumina starting from a cobalt ammine complex at elevated pH by removing slowly the ammonia from the solution by heating to 90 °C and flushing with N₂. Highly loaded and highly dispersed Co/Al₂O₃ active for the Fischer–Tropsch synthesis were thus obtained. Bezemer *et al.* [23] have used the same method to deposit 15 wt% Co onto a CNF support. In Figure 6.12 TEM images of a reduced and passivated sample of Co/CNF are shown; they display 8-nm Co particles quite uniformly dispersed over the CNF support.

6.4.4

Miscellaneous Methods

The deposition of catalytically important elements from groups 4–6 can be dealt with in a number of ways. Geus and coworkers [55–57] have developed a method that is not so well known but can be advantageously applied to deposit, in particular, Ti, V, and Mo. The challenge in the deposition of the metal oxides mentioned refers to the incompatibility of their aqueous chemistry and the oxide surface chemistry. In particular, anions such as VO_4^{3-} do not interact significantly with silica at relevant pH values. The proposed method involves reduction of these oxo-anions to lower valence cations that do interact with silica. For example, Vogt and Geus [54] proposed the electrochemical reduction of ammonium metavanadate in formic acid solution according to the scheme shown.



Subsequently, silica was suspended in the V(III) solution at $\text{pH} = 2.3$. Under an N_2 atmosphere $\text{NaOH}(\text{aq})$ was injected at 25°C until $\text{pH} = 6$. Highly dispersed $\text{V}_2\text{O}_5/\text{SiO}_2$ was obtained after filtration, drying and calcination. Loadings below 20 wt% V_2O_5 led to 1.5-nm crystals (TEM), while above 20 wt% larger crystals not adhering to the support were observed. Similar reduction and injection methods have been used to deposit Ti(III) [56] and Mo(III) [57] onto silica. These methods can be considered as alternatives to RDP as represented by Equation 6.7 for Mo.

Bimetallic catalysts can be prepared advantageously using RDP when noble metals are involved. Geus [58, 59] proposed a new method for obtaining bimetallic catalysts of well-defined composition for non-noble metals. To this end they used DP of salts of cyano-complexes. For example, $\text{CuFe}/\gamma\text{-Al}_2\text{O}_3$ catalysts were obtained [59] by injection of an aqueous solution of $\text{K}_3\text{Fe}(\text{CN})_6$

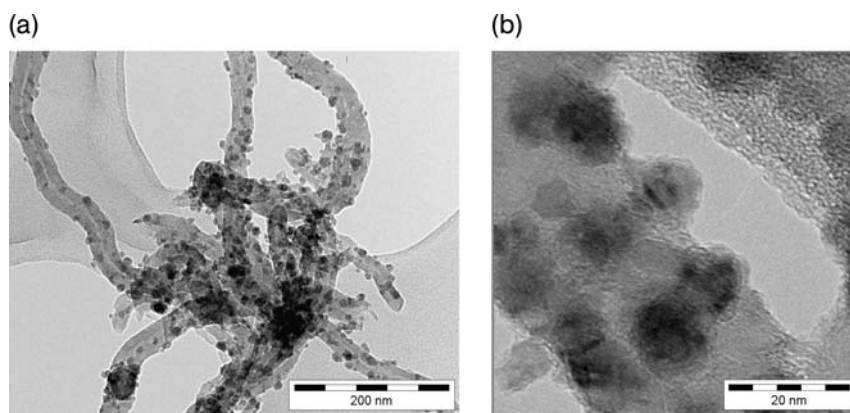


Figure 6.12 TEM images of reduced and passivated Co/CNF at medium (a) and high (b) resolution. (Reproduced with permission from Elsevier [23].)

into a suspension of the support in a solution of $\text{Cu}(\text{NO}_3)_2$ that gives rise to precipitation of $\text{Cu}_3[\text{Fe}(\text{CN})_6]_2$. Provided there is sufficient interaction between the support and the negatively charged complex cyano particles, a good dispersion can be obtained. The thermal treatment of these precursors turned out to be critical as oxidation to mixed oxides had to precede reduction in hydrogen to promote formation of alloy particles and to restrict formation of HCN. One of the key advantages of this method is the option to control the metal ratio in, for example, CuFe alloy particles by using a range of cyano salts such as $\text{Cu}_2\text{Fe}[\text{CN}]_6$, $\text{Cu}_3[\text{Fe}(\text{CN})_6]_2$ and $\text{CuFe}(\text{NO})(\text{CN})_5$.

Based on detailed insight into the nature of the interaction of aqueous metal ions with oxidic surfaces (see Chapter 2) Lycourghiotis and coworkers [60–63] have proposed equilibrium deposition filtration (EDF) to arrive at the controlled preparation of supported metal-oxide catalysts. The unique feature of EDF involves control of pH, concentration and equilibration time to arrive at well-defined catalysts. The equipment used in combination with the variables mentioned gives potential advantages of EDF over DP although both methodologies have aspects in common. To illustrate the features of the EDF technique we describe the preparation of a series of Co-oxide/ $\gamma\text{-Al}_2\text{O}_3$ catalysts used for VOC oxidation [62]. Starting from 5.0 l of $1.0 \times 10^{-3} - 25 \times 10^{-3}$ M cobalt nitrate solutions in water, 10 g of $\gamma\text{-Al}_2\text{O}_3$ powder was added. A pH control system was used to inject NH_4OH solution to arrive at pH = 7. By variation of both cobalt nitrate concentration and the equilibration time (1–384 hours) the Co loading could be varied from 5–16 wt%. Most importantly, EDF enables one to control the ratio of Co(II) surface precipitates over Co(II) inner-sphere complexes on the support. The ratio of these two phases, R_{DRS} , could be deduced from diffuse reflection spectra of the dried samples. For an extensive description of the EDF methodology we refer to the review by Bourikas and Lycourghiotis [63].

Work at Chiba University [64] has involved DP in wet silica gel. Starting from acidified TEOS, nickel nitrate, and urea, hydrolysis of TEOS was carried out at 50 °C to provide the silica support *in situ*. Subsequently, from the same reaction mixture, nickel (20 wt% NiO) was deposited by urea hydrolysis at 80 °C. Due to the intimate interaction between Ni(II) and silica high reduction temperatures were needed, though high Ni dispersions were still obtained.

Finally, we summarize studies that make use of special circumstance to initiate or to facilitate DP onto support materials. Following earlier work of Arul Dhas and Gedanken, Landau and coworkers [65] have used ultrasound to induce precipitation of Mo-oxide starting from $\text{Mo}(\text{CO})_6$ dissolved in decalin. Working under air at room temperature and using Al-MCM-41 as support, loadings as high as 45 wt% MoO_3 have been obtained. Bianchi and coworkers [66] provided evidence that sonication prior to RDP assisted in obtaining a more uniform Pd metal distribution over 2-mm carbon grains.

Crisafulli *et al.* [67] have carried out liquid-phase photodeposition (LPPD) for the preparation of Pt/ $\gamma\text{-Al}_2\text{O}_3$. LPPD involved irradiation of an ethanol suspension of $\text{Pt}(\text{acac})_2$ containing the $\gamma\text{-Al}_2\text{O}_3$ support. Using different

wavelengths (254, 350, or 400 nm) at room temperature in a quartz or glass reactor, photodegradation of $\text{Pt}(\text{acac})_2$ was brought about and followed spectrophotometrically at 350 nm. At ~ 1 wt% of Pt particles of 1.6–1.8 nm were obtained with a particle-size distribution shown, importantly, to be narrower than a catalyst prepared by impregnation of $\gamma\text{-Al}_2\text{O}_3$ with an aqueous solution of H_2PtCl_6 .

6.5

Summary, Conclusions, and Outlook

The urea method for DP has been studied now in great detail and provided fundamental insight into the phenomena that take place. With silica supports the deposition of group 8–12 metals has been studied particularly well. Here, it has been proposed, based on results for nickel-on-silica, the thermodynamic driving force, originating from condensation reactions that ultimately may lead to nickel phyllosilicate formation, is probably more important than the kinetic effects. With DP of nickel(II) on CNF supports, however, the more acidic surface groups cause nickel ion adsorption that precedes precipitation and provides a kinetic pathway to nucleation of nickel hydroxides. We feel that kinetic pathways for DP, although elegant, are less robust than thermodynamic pathways.

RDP has been studied in much less depth. Interesting studies continue to appear, however, such as direct deposition of MoS_2 onto $\gamma\text{-Al}_2\text{O}_3$. Bimetallic catalysts, in particular those based on noble metals, can be advantageously prepared using RDP techniques.

DP based on ligand removal has gained renewed attention recently as preparation of cobalt-based Fischer–Tropsch catalysts was successfully done for several support materials.

Miscellaneous results for DP have been described with a variety of methods based on injection of complex salts, sonication and light-induced deposition.

Future research on DP might involve *in-situ* spectroscopy studies, somewhat similar to those described for extrudates and pellets (Chapter 10). In fact, the use of diluted suspensions facilitates study of both solution and solid under the actual conditions of DP.

Acknowledgments

The author is indebted to Prof. John Geus and Dr. Jos van Dillen for early exposure to this catalyst preparation method. Furthermore, ongoing cooperation with Dr. Harry Bitter and Dr. Petra de Jongh is acknowledged as well as important comments on the manuscript from Dr. Catherine Louis. Financial support for this work from Utrecht University, NWO-CW, STW, and NRSCC is appreciated.

References

1. Stöwenert, F. IG Farben (1943) German Patent 740,634.
2. Geus, J.W. (1967) Netherlands Patent Applications 67,05259 and (1970) Netherlands Patent Applications 68,16777; Netherlands Patent 16,777 (1968); German Patent 1,963,827 (1970); to Stamicarbon.
3. van Dillen, A.J., Geus, J.W., Hermans, L.A.M. and van der Meijden, J. (1976) Proceedings 6th International Congress on Catalysis, London, p. 677.
4. Hermans, L.A.M. and Geus, J.W. (1979) *Stud. Surf. Sci. Catal.*, **3**, 113.
5. Burattin, P., Che, M. and Louis, C. (1997) *J. Phys. Chem. B*, **101**, 7060.
6. Burattin, P., Che, M. and Louis, C. (1998) *J. Phys. Chem. B*, **102**, 2722.
7. Burattin, P., Che, M. and Louis, C. (1999) *J. Phys. Chem. B*, **103**, 6171.
8. Burattin, P., Che, M. and Louis, C. (2000) *J. Phys. Chem. B*, **104**, 10482.
9. de Jong, K.P. (1991) *Stud. Surf. Sci. Catal.*, **63**, 19.
10. (a) Bitter, J.H., van der Lee, M.K., Slotboom, A.G.T., van Dillen, A.J. and de Jong, K.P. (2003) *Catal. Lett.* **89**, 139; (b) van der Lee, M.K., van Dillen, A.J., Bitter, J.H. and de Jong, K.P. (2005) *J. Am. Chem. Soc.*, **127**, 1357382.
11. Lever Brothers Company (1970) US Patent 3,668,148.
12. Geus, J.W. (1983) *Stud. Surf. Sci. Catal.*, **16**, 1.
13. Geus, J.W. and van Dillen, A.J. (1999) in *Preparation of Solid Catalysts* (eds G. Ert *et al.*), Wiley-VCH Verlag GmbH, Weinheim, pp. 460–87.
14. Louis, C. (2007) in *Catalyst Preparation. Science and Engineering* (ed. J. Regalbuto), CRC Press, New York, pp. 319–39.
15. Evans, D.F. and Wennerström, H. (1994) *The Colloidal Domain*, Wiley-VCH, New York.
16. Roduner, E. (2006) *Nanoscopic Materials. Size-Dependent Phenomena*, RSC Publishing, Cambridge.
17. Tijburg, I.I.M. (1989) PhD Thesis, Utrecht University, Utrecht.
18. Warner, R.C. (1942) *J. Biol. Chem.*, **142**, 706.
19. Wigmans, T., van Doorn, J. and Moulijn, J.A. (1983) *Surf. Sci.*, **135**, 532.
20. van Steen, E. and Prinsloo, F.F. (2002) *Catal. Today*, **71**, 327.
21. Ochoa-Fernández, E., Chen, D., Yu, Z., Tøtdal, B., Rønning, M. and Holmen, A. (2005) *Catal. Today*, **102–103**, 45.
22. Kvande, I., Chen, D., Rønning, M., Venvik, H.J. and Holmen, A. (2005) *Catal. Today*, **100**, 391.
23. Bezemer, G.L., Radstake, P.B., Koot, V., van Dillen, A.J., Geus, J.W. and de Jong, K.P. (2006) *J. Catal.*, **237**, 291.
24. Montes, M., Soupart, J.B., de Saedeleer, M., Hodnett, B.K. and Delmon, B. (1984) *J. Chem. Soc., Faraday Trans. 1*, **80**, 3209.
25. Chang, F.W., Hsiao, T.J. and Shih, J.D. (1998) *Ind. Eng. Chem. Res.*, **37**, 3838.
26. Gómez-Reynoso, R., Ramírez, J., Nares, R., Luna, R. and Murrieta, F. (2005) *Catal. Today*, **107–108**, 926.
27. van der Grift, C.J.G., Elberse, P.A., Mulder, A. and Geus, J.W. (1990) *Appl. Catal.*, **59**, 275.
28. Mul, G. and Hirschon, A.S. (2001) *Catal. Today*, **65**, 69.
29. de Jong, K.P., Glezer, J.H.E., Kuipers, H.P.C.E., Knoester, A. and Emeis, C.A. (1990) *J. Catal.*, **124**, 520.
30. Wielers, A.F.H., Hop, C.E.C.A., van Beijnum, J., van der Kraan, A.M. and Geus, J.W. (1990) *J. Catal.*, **121**, 364.
31. Toebe, M.L., van der Lee, M.K., Tang, L.M., Huis in 't Veld, M.H., Bitter, J.H., van Dillen, A.J. and de Jong, K.P. (2004) *J. Phys. Chem. B*, **108**, 11611.
32. Augustine, R.L. and O'Leary, S.T. (1995) *J. Mol. Catal. A*, **95**, 277.
33. Okumura, M., Masuyama, N., Konishi, E., Ichikawa, S. and Akita, T. (2002) *J. Catal.*, **208**, 485.
34. Kim, C.-H., Lee, J.S. and Trimm, D.L. (2003) *Top. Catal.*, **22**, 319.
35. Gopinath, R., Lingaiah, N., Seshu Babu, N., Suryanarayana, I., Sai Prasad, P.S. and Obuchi, A. (2004) *J. Mol. Catal. A*, **223**, 289.

36. Jin, H., Park, S.-E., Lee, J.M. and Ryu, S.K. (1996) *Carbon*, **34**, 429.
37. Farkas, G., Hegedus, L., Tungler, A., Mathe, T., Figueiredo, J.L. and Freitas, M. (2000) *J. Mol. Catal. A: Chem.*, **153**, 215.
38. Jhung, S.H., Lee, J.-H., Lee, J.-M., Lee, J.H., Hong, D.-Y., Kim, M.W. and Chang, J.-S. (2005) *Bull. Korean Chem. Soc.*, **26**, 56368.
39. Cabiacc, A., Delahay, G., Durand, R., Trens, P., Plée, D., Medevielle, A. and Coq, B. (2007) *Appl. Catal. A*, **318**, 17–21.
40. (a) de Jong, K.P. and Geus, J.W. (1982) *Appl. Catal.*, **4**, 41; (b) de Jong, K.P. and Geus, J.W. (1983) *Stud. Surf. Sci. Catal.*, **16**, 111; (c) de Jong, K.P. (1999) *Curr. Opin. Solid State Mater. Sci.*, **4**, 55.
41. (a) Bachir, R., Lafitte, E., Marécot, P., Didillon, B. and Barbier, J. (1997) *J. Chem. Phys.*, **94**, 1906; (b) Bachir, R., Marécot, P., Didillon, B., Barbier, J. (1997) *Appl. Catal. A*, **164**, 313; (c) Micheaud, C., Marécot, P., Guérin, M., Barbier, J. (1997) *J. Chim. Phys.*, **94**, 1897.
42. de Jong, K.P. (1993) European Patent 0,258,942,B1 to Shell.
43. Barrio, I., Legórburu, I., Montes, M., Domínguez, M.I., Centeno, M.A. and Odriozola, J.A. (2005) *Catal. Lett.*, **101**, 151.
44. Bezverkhyy, I., Afanasiev, P., Geantet, C. and Lacroix, M. (2001) *J. Catal.*, **204**, 495.
45. Bezverkhyy, I., Afanasiev, P. and Lacroix, M. (2005) *J. Catal.*, **230**, 133.
46. Hoogenraad, M.S., van Leeuwarden, R.A.G.M.M., van Breda Vriesman, G.J.B., Broersma, A., van Dillen, A.J. and Geus, J.W. (1995) *Stud. Surf. Sci. Catal.*, **91**, 263.
47. Heal, G.R. and McKay, L.L. (1988) *Carbon*, **26**, 815.
48. Yang, Y., Zhou, Y., Cha, C. and Carroll, W.M. (1993) *Electrochim. Acta*, **38**, 2333.
49. Lordi, V., Yao, N. and Wei, J. (2001) *Chem. Mater.*, **13**, 733–37.
50. Ang, L.M., Hor, T.S.A., Xu, G.Q., Tung, C.H., Zhao, S.P. and Wang, J.L.S. (2000) *Carbon*, **38**, 363–72.
51. Cerro-Alarcón, M., Bachiller-Baeza, B., Guerrero-Ruiz, A. and Rodríguez-Ramos, I. (2006) *J. Mol. Catal. A*, **258**, 221.
52. (a) de Jong, K.P., Bongenaar-Schlenter, B.E., Meima, G.R., Verkerk, R.C., Lammers, M.J.J. and Geus, J.W. (1983) *J. Catal.*, **81**, 67; (b) de Jong, K.P., Meima, G.R. and Geus, J.W. (1982–1983) *Appl. Surf. Sci.*, **14**, 73.
53. (a) Schaal, M.T., Metcalf, A.Y., Montoya, J.H., Wilkinson, J.P., Stork, C.C., Williams, C.T. and Monnier, J.R. (2007) *Catal. Today*, **123**, 142; (b) Schaal, M.T., Pickerell, A.C., Williams, C.T. and Monnier, J.R. (2008) *J. Catal.*, **254**, 131.
54. (a) Bonne, R.L.C. and Lok, C.M. (1996) WO Patent 9604072; (b) Lok, C.M. (2004) *Stud. Surf. Sci. Catal.*, **147**, 283.
55. Vogt, E.T.C., de Boer, M., van Dillen, A.J. and Geus, J.W. (1988) *Appl. Catal.*, **40**, 255.
56. Vogt, E.T.C., Boot, A., van Dillen, A.J., Geus, J.W., Janssen, F.J.J.G. and Kerkhof, F.M.G. (1988) *J. Catal.*, **114**, 313.
57. Biermann, J.J.P., Janssen, F.J.J.G., de Boer, M., van Dillen, A.J., Geus, J.W. and Vogt, E.T.C. (1990) *J. Mol. Catal. A*, **60**, 229; (b) de Boer, M., van Dillen, A.J., Koningsberger, D.C., Geus, J.W., Vuurman, M.A. and Wachs, I.E. (1991) *Catal. Lett.*, **11**, 227.
58. van de Loosdrecht, J., van Dillen, A.J., van der Horst, A.A., van der Kraan, A.M. and Geus, J.W. (1995) *Top. Catal.*, **2**, 29.
59. Boellaard, E., van der Kraan, A.M., Sommen, A.B.P., Hoebink, J.H.B.J., Marin, G.B. and Geus, J.W. (1999) *Appl. Catal. A*, **179**, 175.
60. Bourikas, K., Hiemstra, T. and van Riemsdijk, W.H. (2001) *J. Phys. Chem. B*, **105**, 2393–403.
61. Bourikas, K., Kordulis, C., Vakros, J. and Lycourghiotis, A. (2004) *Adv. Colloid Interface Sci.*, **110**, 97–120.
62. Ataloglou, T., Fountzoula, C., Bourikas, K., Vakros, J., Lycourghiotis, A. and Kordulis, C. (2005) *Appl. Catal. A*, **288**, 1.

63. Bourikas, K., Kordulis, C. and Lycourghiotis, A. (2006) *Catal. Rev.*, **48**, 363–444.
64. Takahashi, R., Sato, S., Sodesawa, T., Nakamura, N., Tomiyama, S., Kosugi, T. and Yoshida, S. (2001) *J. Nanosci. Nanotech.*, **1**, 169.
65. (a) Vradman, L., Landau, M.V., Herskowitz, M., Ezersky, V., Talianker, M., Nikitenko, S., Koltypin, Y. and Gedanken, A. (2003) *J. Catal.*, **213**, 163; (b) Vradman, L., Landau, M.V., Herskowitz, M., Ezersky, V., Talianker, M., Nikitenko, S., Koltypin, Y. and Gedanken, A. (2003) *Stud. Surf. Sci. Catal.*, **146**, 721.
66. Bianchi, C.L., Gotti, E., Toscana, L. and Ragaini, V. (1997) *Ultrason. Sonochem.*, **4**, 317.
67. Crisafulli, C., Scirè, S., Giuffrida, S., Ventimiglia, G. and Lo Nigro, R. (2006) *Appl. Catal. A*, **306**, 51.

7

Coprecipitation

Martin Lok

7.1

Introduction

For the preparation of heterogeneous catalysts two principal methods exist, viz. the impregnation of preformed supports with a solution of precursors of the active metal(s), and the so-called coprecipitation where one or more metals are precipitated together with the support or its precursor. The first method is not only used at lab scale, but is also widely applied industrially. It is relatively easy to perform and does not require complicated or expensive equipment. In addition, metal gradients across the catalyst pellet from eggshell to a uniform distribution can be realized (Chapters 4 and 10). However, for a number of catalysts, and especially at large scale, coprecipitation can be very attractive and indeed a large number of commercial catalysts, for example, for methanol production, hydrogenation, steam reforming, water gas shift reaction, and butane oxidation are produced in this way [1, 2]. This method is often considered to be more difficult and indeed requires an accurate control of conditions and hence the use of more complicated equipment. During this coprecipitation, in a single process, not only the chemical phase(s), but also the dispersion, and hence the surface area of the active phase, are created and by controlled agglomeration of primary and secondary units, the porous structure, and, moreover, particle size and shape. All these features are strongly dependent on the process conditions like the nature and method of dosing of ingredients, mixing and stirring. Therefore, these conditions have to be accurately controlled throughout the precipitation process. A complication is that probably no single condition exists that is optimal for all of the above processes. In view of these difficulties, it is understandable that sometimes, and especially at smaller scale, it is easier to export all these problems of creating porous structure and particle size and shape to the support manufacturer and start off with a well-defined preformed support with the right physical properties.

A benefit of coprecipitation over impregnation is the high attainable metal loading of up to 60%, sometimes up to 80% or even higher, compared to

typically <30% metal loading for impregnation. Because of these high metal loadings, coprecipitated catalysts are often referred to as “bulk” catalysts or “self-supporting” catalysts. Another benefit is the relatively high metal dispersion. As a result the weight and volume activities, which are a function of the product of both metal loading and dispersion, are generally higher than for an impregnated catalyst. Not only different metals and support (precursors) may be deposited in a single process, but also mixtures of metallic and/or even nonmetallic promoters, for example, sulfur, making coprecipitation a highly versatile process.

A drawback of the coprecipitation process is the generation of large quantities of salt solutions and the fact that after precipitation the product has to be separated, which is mostly done by filtration. In addition, the catalyst (precursor) will be in powder form, often with a particle size of 5–30 μm , while for many applications a shaped product like a tablet, extrudate, or fluid-bed particle is required. Coprecipitated powders can be shaped, but if after shaping a calcination has to be applied, for example, to achieve mechanical strength, this has to be performed at almost always milder conditions than those for preformed supports that may easily be heated to 700 °C or even higher. To achieve a high weight or volume activity, a high metal loading is often quite important for base-metal catalysts, but this is less so for the more expensive and often much more active platinum-group metals. For these metals, impregnation, or hybrid methods like deposition-precipitation, are mostly the methods of choice and coprecipitation is rarely used. The final choice of a production route will be determined by an often complex interplay between a number of different factors.

In general, the fundamentals of coprecipitation are difficult to study. The very high supersaturation levels, the low stability of supersaturated solutions, secondary changes in the solid phase formed and chemical changes during the aging of precipitates are reasons why our knowledge about precipitation is far more limited compared to mass crystallization of readily soluble substances. Another problem is that much information is published in specialist papers on, for example, reactor design and mixing, which, though highly relevant, are not always accessible to, or widely read by, catalytic scientists. In addition, much useful information is “hidden” in patents. Nevertheless, some excellent reviews in the open literature are available [3] and the background sections of patents usually provide very relevant concise literature surveys.

7.2

Basic Principles of Precipitation and Nucleation

Though the preparation of coprecipitated catalysts comprises a number of steps, for example, precipitation, filtration, washing, shaping, drying, calcination, and sometimes activation, precipitation is most important, as during that step the basic properties of the catalyst are established. Indeed,

catalyst performance can be significantly influenced by just changing the precipitation conditions. This chapter exclusively focuses on the precipitation step. The subject of precipitation is vast and can only be dealt with here in brief. In addition, different materials may be formed by different mechanisms. For more information on precipitation fundamentals we refer to the various textbooks [4–8].

Precipitation comprises three major steps, that is, liquid mixing, nucleation and crystal growth to form primary particles, and aggregation of the primary particles. Though nucleation and crystal growth usually proceed simultaneously, it is possible to treat them separately. It is generally agreed that for the formation of monodisperse crystal separation of the nucleation and growth events is key [9]. Especially for multicomponent systems, nucleation is a complex process. It mostly starts with the formation of clusters, which are capable of spontaneous growth by the subsequent addition of monomers until a critical size is reached. Clusters smaller than this size tend to redissolve, while larger clusters will continue to grow. Nucleation has been compared to a chemical reaction and similar to a chemical reaction an energy barrier must be surmounted. Therefore, it is necessary to create some degree of supersaturation before spontaneous crystallization will occur [4, 9]. The nucleation rate can be described as in Equation 7.1, as one of the several equations proposed for nucleation rate [9, 10]:

$$\frac{dN}{dt} = \beta \exp \left[\frac{-16\pi\sigma^3 v^2}{3(kT)^3 \ln^2 s} \right] \quad (7.1)$$

in which β is a pre-exponential term, σ the solid/fluid interfacial energy, v the solid molecular volume, T is temperature, and s the supersaturation.

This equation is usually simplified as

$$\frac{dN}{dt} = \beta \exp \left(\frac{-A}{\ln^2 s} \right) \quad (7.2)$$

in which A is the interfacial energy parameter.

It is evident that nucleation strongly depends on both concentration and temperature. If the nucleation rate is plotted as a function of supersaturation a curve like that in Figure 7.1 is produced.

Thus, there is in essence a critical supersaturation concentration below which nucleation is very slow and above which nucleation is very fast. The range between this critical supersaturation concentration and the solubility concentration is the domain of deposition-precipitation discussed elsewhere (Chapter 6), while impregnation (Chapter 4) is performed in the concentration range below the solubility limit. Especially for multicomponent systems, it is important to operate at high supersaturation levels so that the solubility product of all products is simultaneously exceeded, otherwise a possibly undesired sequential precipitation may occur.

Supersaturation can be produced in a variety of ways both by physical and chemical methods: cooling of the reaction mixture, evaporation of solvents,

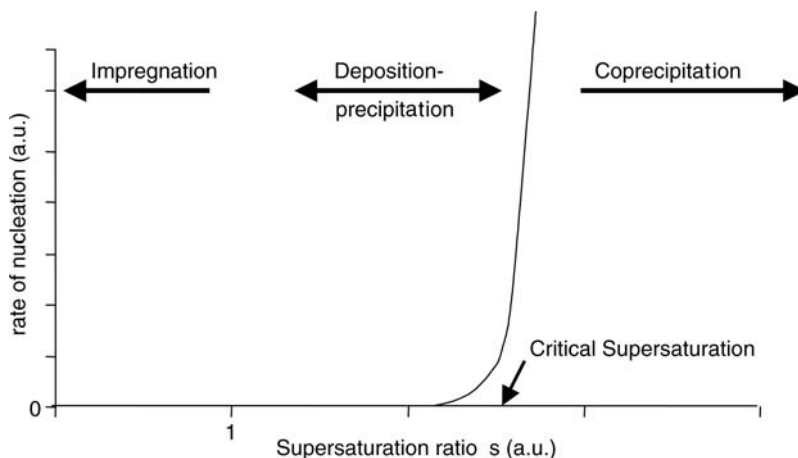


Figure 7.1 The relation between the homogeneous nucleation rate (nuclei per ml/second) and the degree of supersaturation. (Modified after [4].) s = actual concentration/solubility.

direct reaction of ions, redox reaction, hydrolysis, and so on, but reaction of ions in aqueous media, by which the solubility product is exceeded, is most commonly practiced. Water is chosen as solvent not only for economic reasons but mainly because solubility for most metal salts is much higher in water than in organic solvents.

There are several mechanisms for crystal growth, but most of them lead to the simplified equation for the growth rate as shown in Equation 7.3 [9, 10].

$$k_g = a(c - c_{eq})^n \quad (7.3)$$

in which a is the growth rate constant, c = concentration, and c_{eq} = solubility concentration (close to zero for most hydroxides and carbonates).

The exponent n is usually only 1–2 and often close to 1. Thus, while nucleation rate increases exponentially with (supersaturation) concentration, the dependency of the crystallite growth rate is closer to a linear function. Therefore, high supersaturation levels promote nucleation rather than crystal growth and favor the precipitation of highly dispersed materials. In contrast, precipitation from more dilute solutions tends to produce fewer, but larger crystals. Especially for those catalysts where the final dispersion and activity reflects the initial dispersion of the precipitate, like silica-supported nickel, a high initial dispersion is highly desirable. Monodisperse crystals are produced when a burst of nucleation, which enables separation of the nucleation and growth processes, is combined with the subsequent diffusion-controlled growth process through which the crystal size is determined [11].

Apart from nucleation and crystal growth, aggregation is an important process. Aggregation leads to fewer and larger, but yet porous particles.

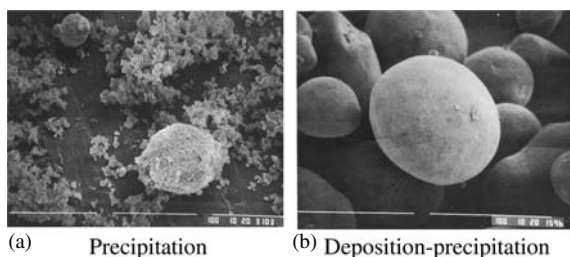


Figure 7.2 (a) 20% Ni/alumina catalyst prepared by coprecipitation in the presence of preformed alumina support showing precipitate separate from carrier. (b) Catalyst having the same composition but prepared by deposition precipitation.

Aggregation is the formation of clusters of nanoscale primary particles into micrometer-scale secondary particles. Physical or chemical forces, such as crystal bridges, can hold these aggregates together. Porosity is then determined by how the primary particles are stacked, and pores can be considered as voids between the primary particles. Porosity can be manipulated by influencing the stacking, as will be shown later. Other processes, apart from aggregation, which could take place during precipitation are recrystallization (Ostwald ripening) and a change in chemical composition or a change in phase composition.

Because of the very high supersaturation during the precipitation of most base metal hydroxides or carbonates, nucleation will be spontaneous, that is, homogeneous, which therefore explains why only limited deposition onto a preformed carrier occurs. Nucleation such as this by rapid mixing is generally much too fast for all the nuclei to diffuse into the pores and to deposit onto the internal surface of a preformed support. Therefore, significant amounts of precipitate may be formed separate from the support or on the external surface (Figure 7.2).

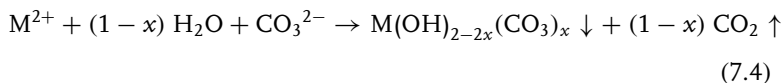
If complete deposition onto a preformed support is important, different deposition methods like impregnation or deposition-precipitation should be considered (Chapters 4 and 6).

7.3

Raw Materials

A high supersaturation, as required for highly dispersed coprecipitates, can be realized by a rapid mixing of concentrated solutions to form insoluble materials. Suitable precursors are highly soluble inorganic metal precursors like metal nitrates, chlorides, sulfates, and highly soluble basic reagents like sodium carbonate, sodium hydroxide, or mixtures thereof. Organic precursors, like acetates, may be suitable too but are often less soluble than the corresponding inorganic salts. An additional benefit of using high

concentrations is the increased space-time yields by increasing throughput or decreasing reactor volume. Metal hydroxides or carbonates are often preferred as precipitates because of their very low solubility, for example, the solubility products for nickel hydroxide and nickel carbonate at 25 °C are $[\text{Ni}][\text{OH}]^2 = 5.47 \times 10^{-16} \text{ mol}^3 \text{ l}^{-3}$ and $[\text{Ni}][\text{CO}_3] = 1.42 \times 10^{-7} \text{ mol}^2 \text{ l}^{-2}$, respectively [12]. The resulting mixed hydroxides or hydroxycarbonates typically have surface areas of several hundred m^2/g and thus consist of primary particles of nanometer dimensions. When using sodium carbonate as a reagent, substantial amounts of CO_2 may be released:



Preferably both raw materials and process conditions should be selected in a way to minimize incorporation of counterions of the metal precursor salts. In addition, any remaining counterions should be easily removable by calcination or by reduction. Suitable ions are nitrates, hydroxides, and carbonates.

The precipitation of certain crystalline phases allows two or more metals to engage in intimate contact, for example, in hydrotalcites like $\text{Ni}_6\text{Al}_2(\text{OH})_{16}\text{CO}_3$ and $\text{MgNi}_5\text{Al}_2(\text{OH})_{16}\text{CO}_3$, or in various $(\text{Cu,Zn})_2(\text{OH})_2\text{CO}_3$ phases [13–16]. This mixing of two or more metals at the atomic scale makes coprecipitation highly attractive.

Coprecipitation often results in amorphous material as a first phase. During subsequent aging, the amorphous phase may convert to a crystalline phase via a solution species. The resulting mixed-metal carbonates can easily be decomposed by calcination and/or reduction yielding benign by-products like water and carbon dioxide.

The support is often coprecipitated simultaneously with the active metals in a single process step. This can be done by mixing in basic precursors of the support, such as sodium silicate, sodium aluminate, or mixtures thereof, with the base precipitant. These can alternatively be added separately. Also, more acidic compounds like aluminum nitrate can be used as support precursors and, optionally, mixed in with the metal precursor. Compared to preformed supports, the amount of support precursor can be quite low and this is why coprecipitates may contain very high metal levels up to 80–90%, a level not attainable by impregnation. 20–30 mol% of silicate or aluminate relative to the metal is usually sufficient to obtain a high metal surface area after reduction. It may be debated whether the resulting metal silicate, aluminate, or alumina, are real supports or that names like “stabilizer” or “spacer” are more appropriate.

Apart from soluble support precursors, preformed solid supports can be introduced during coprecipitation. As discussed in Section 7.2 coprecipitation is too fast for quantitatively depositing metals onto the internal surface area of a support. Nevertheless, preformed supports are being used, mostly because via a support dissolution/redeposition mechanism, catalysts are obtained quite similar in catalytic performance to those based on soluble support precursors,

despite having different physical properties. In this case, often an extensive aging process is required to allow this dissolution/redeposition to take place.

Coprecipitation is typically carried out in aqueous media. Organic solvents are mostly used for special reasons, for example, alcohols are applied in the precipitation of VPO oxidation catalysts because of their reducing properties [17].

7.4

Precipitation Conditions

The primary precipitation products are not necessarily the thermodynamically most stable products and usually, depending on the process conditions, counterions like carbonate, sulfate, nitrate, or chloride initially incorporated, are later partially or largely displaced by hydroxide. This displacement process is promoted by high pH and temperature, or by prolonged aging. Thus, when precipitating nickel nitrate with sodium carbonate, for example, at ambient temperature and a pH close to neutral, the kinetics dictate the formation of a nickel precipitate with high levels of nitrate and carbonate incorporation, while the thermodynamics favor a product closer to the hydroxide. Therefore, during aging this product is gradually transformed into a nickel-hydroxide-like product while releasing CO_2 (and nitrate). At higher pH and temperatures this process may, in principle, proceed to a high degree of completion. The final product, however, may still contain some carbonate, and less so nitrate, because eventually in the equilibrium situation, the stability of the products, and the concentration of reactants present, may determine the end product composition.

7.5

Process Operation

The above chemical transformations are of importance to the way the coprecipitation is carried out. In principle, there are several modes of operation. In a batch-wise operation, the base can be added to the acidic metal solution, or vice versa (forward and reverse coprecipitation, respectively), or both solutions can be added simultaneously.

In a batch-wise operation, the product formed at the beginning of the precipitation is different from that formed at the end of the process and the final product is expected to be a mixture that is mostly suboptimal. Thus, in forward precipitation the pH rises gradually and, as expected for a product produced under acidic or neutral conditions, the material is rich in counterions like carbonate, nitrate, chloride, and sulfate. Extensive aging at higher pH is required to convert the material to a hydroxide-like precipitate. In addition, the least-soluble product will precipitate first leading to a sometimes undesirable

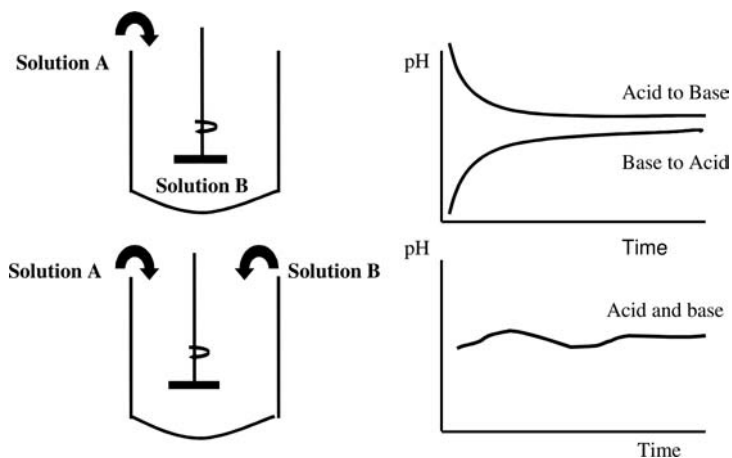


Figure 7.3 Precipitation processing routes: forward (base to acid) and reverse (acid to base) precipitation, continuous precipitation, and corresponding pH profiles.

sequential precipitation of ingredients. Based on the solubility constants of the hydroxides the following order of precipitation is expected: Fe^{3+} , Cr^{3+} , Cu^{2+} , Zn^{2+} , Ni^{2+} . Often, this method of forward precipitation leads to voluminous precipitates, possibly because the presence of bulky counterions and/or the low pH prevents a good stacking of hydroxide platelets, and hence may lead to a highly porous catalyst. When starting the precipitation in the high pH range, sequential precipitation of metals is less of a problem because the excess base present guarantees that the solubility products of all the precipitate components are exceeded. Initially, products rich in hydroxides are produced, and when pH is lowered other counterions may gradually be incorporated, at least if neutrality is approached. Thus, both methods lead to mixtures of products not only differing in chemical compositions but also with different structural and textural properties.

To avoid or minimize the formation of mixed products, the preferred method is to operate at constant pH by using a simultaneous addition of reactants (semibatch process). However, even using this mode, mixtures are produced, albeit to a lesser degree, because the change in liquid volume in the reactor alters both the concentration of the reactants and the hydrodynamics. A further improvement, therefore, is to perform the process continuously rather than batch-wise. Even then it is important to minimize concentration gradients in the reactor through good process control.

A good illustration of the importance of the order in which reactants are mixed is given in Figure 7.4, which shows the differences in XRD for aluminum hydroxide precipitation at pH 9 [18]. Each procedure led to a different compound: microporous boehmite (aluminum nitrate added to sodium carbonate), bayerite (sodium carbonate added to aluminum nitrate), or fibrillar boehmite (simultaneous addition).

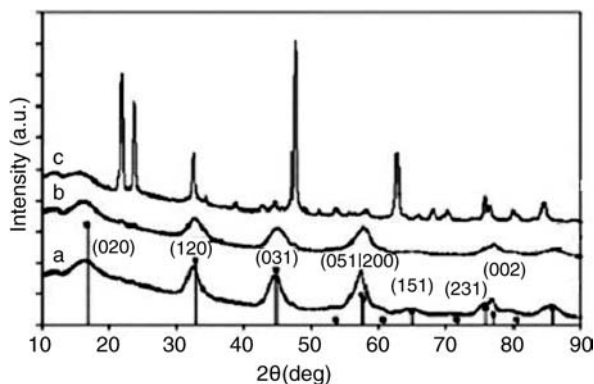


Figure 7.4 Effect of order of addition on alumina composition; XRD patterns of alumina obtained by (a) 2-jet precipitation at constant pH, (b) acid to base addition, and (c) base to acid addition [18].

By using sodium hydroxide as reagent it is more difficult to maintain a constant pH than with sodium carbonate. This is particularly a problem when operating close to pH 7 when small amounts of NaOH may cause large shifts in pH. At higher pHs dense cakes of low porosity may be produced, possibly because the pure hydroxides stack more easily. Because of its buffering action, the use of sodium carbonate, or mixtures with sodium hydroxide, rather than sodium hydroxide on its own helps to perform a stable operation.

As discussed above, during coprecipitation several processes occur like nucleation, crystal growth, aggregation and metal–support interaction. Though these processes are mostly performed in a single reactor, the applied conditions are not necessary optimal for each process step. It can be beneficial to separate these and thus create more freedom to optimize the various processes independently. Thus, in the so-called sequential coprecipitation the conditions in a first precipitation reactor can be adapted to favor a high dispersion (low-temperature, high-power input), while in a subsequent reactor the reaction with the support precursor/stabilizer is performed under different conditions chosen to favor a certain pore and aggregate size [19–21]. This principle has been shown for Ni/SiO₂ catalysts where nickel hydroxycarbonate is prepared by low-temperature precipitation of nickel with soda. In a second reactor the precipitate is then reacted with sodium silicate at higher temperatures. By changing the temperature of the silicate-dosing step by only a few degrees C, the pore size can be significantly changed. This is thought most likely to be caused by influencing the stacking of platelets (Figure 7.5).

In precipitation, mixing of liquid flows occurs before nucleation and aggregation start and this interspersing of component solutions has an

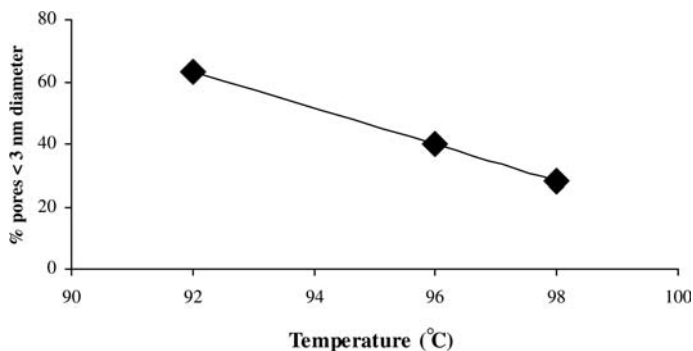


Figure 7.5 Effect of silicate addition temperature on pore size in nickel/silica catalyst made by sequential precipitation [21].

extremely pronounced effect on precipitation. Three discrete steps are distinguished:

- Distributive mixing where one component is distributed in large eddies into the second component resulting in a nonuniform mixture.
- Dispersive mixing where large regions of these solutions are split into smaller ones as a result of turbulence. The reaction begins at the boundary of the regions.
- Diffusive mixing where the eddy size decreases, depending on the dissipated energy, and diffusion starts to mix the components at the molecular scale.

A closer analysis shows that the rate of stirring, or power per unit volume, primarily affects the nucleation, as does the concentration of reactants whereas, the growth rate is much less influenced by these factors [10]. Similar to nucleation, aggregation is diffusion controlled, and thus aggregate size and distribution are strongly influenced by the reactor hydrodynamics. Aggregate size can be influenced by changing the stirring rate and the manner of mixing (Figure 7.6, see also [22]).

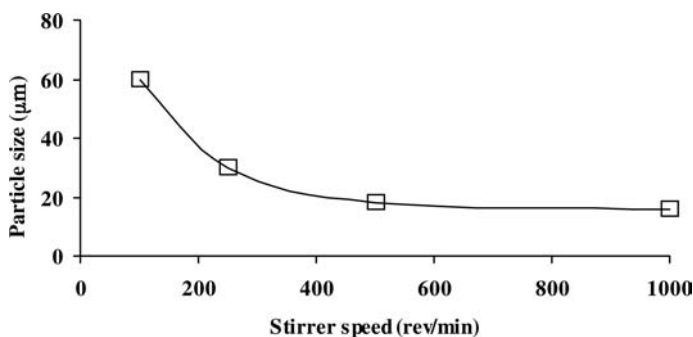


Figure 7.6 Relation particle size and stirring speed for nickel/guhr catalysts.

This means that the aggregate size distribution mirrors the turbulence spectrum of the reactor. Variables that determine mixing are reactor design, number and design of baffles, impeller design, power input, feed concentration, feed rate, location and number of inlet tubes, and so on. The position of the inlet tube(s) and the conditions near these feed points are also important and generally the solutions should be introduced close to the agitator [23, 24].

7.6 Examples

The principles discussed above will be illustrated by a few selected examples.

7.6.1 High Metal Nickel/Alumina Catalysts

Coprecipitated nickel/alumina catalysts with high nickel loadings are widely used in hydrogenation, steam reforming, and methanation. The information on precipitated nickel alumina catalysts is massive and the first papers originated from as early as 1924 [25]. Much information on the effect of precipitation conditions and composition can be found in a single, often neglected Russian paper [26], see also [27]. In this, a range of catalysts was prepared by simultaneous addition of quite concentrated solutions of nickel nitrates (Ni 120 g/l) and sodium carbonate (150 g/l) at 75 °C and at a constant pH of 7–7.2. The results show that using a low support/stabilizer level (Al/Ni molar ratio 0.125–0.5), coprecipitation of Ni and Al can yield very high nickel surface areas (NiSA) per g catalyst (Figure 7.7). Catalysts with these low Al levels can be reduced at moderate reduction temperatures of 325–400 °C, and NiSA starts to decline only for much higher reduction temperature like 600 °C. For these higher reduction temperatures a higher stabilizer level was required. Because of the high dispersion (Ni crystallite size was 3 nm at a reduction temperature of 400 °C), the high nickel content, and a high degree of reduction (DR), these catalysts with a low stabilizer level showed a high NiSA per g catalyst and thus a high activity can be expected. Based on temperature-programmed reduction and X-ray diffraction studies it was suggested that the calcined phase did not consist of a mixture of pure oxidic phases, but was continuously variable, that is, a solid solution of aluminum oxide in nickel oxide [16].

In a BASF patent, mixing of Ni and Al at the atomic scale by crystallizing takovite $\text{Ni}_6\text{Al}_2(\text{OH})_{16}\text{CO}_3 \cdot 4 \text{H}_2\text{O}$ is claimed [13], but as shown above [26], the composition is not always truly stoichiometric and the composition (Ni/Al ratio) may vary and still produce good catalysts. For $2 < \text{Ni/Al} < 3$, the precipitate has a layer structure with nickel and aluminum occupying interchangeable positions in the “brucite-type” layers, while various anions are found as

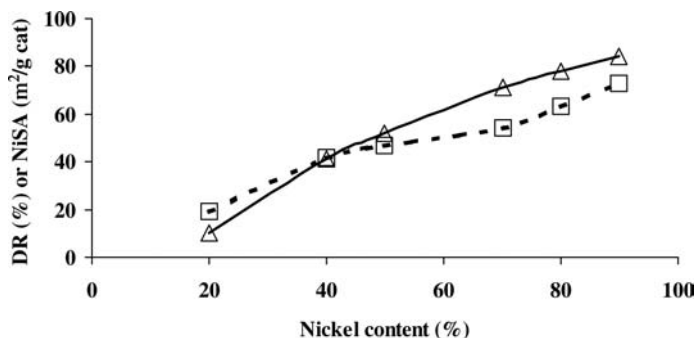


Figure 7.7 Coprecipitated nickel-alumina catalysts: Nickel surface area (NiSA, triangles) and degree of reduction (DR, squares) as a function of nickel content. (After [26].)

compensating charges in the interlayer [15]. Outside this Ni/Al range, the Ni or Al forms a separate phase of $\text{Ni}(\text{OH})_2$ or $\text{Al}(\text{OH})_3$, deposited next to the takovite [15, 16]. The above patent describes mixing of concentrated solutions of metal (Ni, Al) and sodium carbonate (2 mol/l each) at 80 °C and pH 4.5–5.5. Thereafter, the pH is raised to 6.5 and stirred for a further 15 min. After filtration, washing, drying, and activation in hydrogen, the catalyst proved to be more active and selective in fat hydrogenation than a prior art nickel catalyst based on a kieselguhr support.

7.6.2

Single-Step Sulfur-Promoted Nickel/Alumina Catalyst

Fats and oils can be hydrogenated with a nickel catalyst that has been partially poisoned (promoted) with sulfur. Utilizing this process, steep melting hardened fats are produced that are suitable for use as cocoa butter substitutes [28, 29]. Bouwman *et al.* [30] describe an elegant process of precipitating in a single process not only the metal and the support/stabilizer, but also the sulfiding agent. In this process, the principle of constant pH is applied by simultaneous dosing of both the basic and the acidic precursor: 800 ml of nickel chloride in water (Ni 100 g/l), 800 ml of a solution containing sodium carbonate (200 g/l), sodium aluminate (33 g/l), and sodium sulfide (18 g/l) were added simultaneously at the same rate pumped into a well-stirred 4-l precipitation vessel at 80 °C. The high concentration of the reactants is in line with our discussions in Section 7.2, that concentrated solutions of highly soluble precursors like metal nitrate or chlorides should be used to achieve both a high supersaturation and a high reactor throughput. The pH of the slurry formed was 7.8 and after 1 h the precipitation was completed. The catalyst was washed, filtered, dried, and activated in hydrogen at 400 °C. The product was a partially sulfided high nickel catalyst suitable for selective hydrogenation of vegetable oils.

7.6.3

Copper/Zinc Methanol Catalysts

Mixed copper/zinc catalysts with high copper-to-zinc ratios are widely used as catalysts for low-pressure methanol production and for low-temperature shift reaction [2, 31], see also Chapter 15. These catalysts are commonly made by coprecipitating mixed-metal nitrate solutions by addition of alkali. Li and Inui [32] showed that apart from chemical composition, pH and temperature are key process parameters. Catalyst precursors were prepared by mixing aqueous solutions of copper, zinc, and aluminum nitrates (total concentration 1 mol/l) and a solution of sodium carbonate (1 mol/l). pH was kept at the desired level by adjusting the relative flow rate of the two liquids. After precipitation was complete, the slurry was aged for at least 0.5 h. When the precipitation was conducted at pH 7.0, the precipitate consisted of a malachite-like phase $(\text{Cu,Zn})\text{CO}_3(\text{OH})_2$ and the resulting catalysts were very active, while at pH < 6 the formation of hydroxynitrates was favored, which led to catalysts less active than those prepared at pH 7.0 (Figure 7.8).

Aging temperature was also an important parameter with catalysts prepared at 70 °C being more active than those prepared at 50 °C. It was concluded that where pH exerted its effect through modification of the chemical composition, temperature mainly affects the precipitation kinetics. In general, the presence of basic nitrate in the precipitate was detrimental, whereas malachite was beneficial [32].

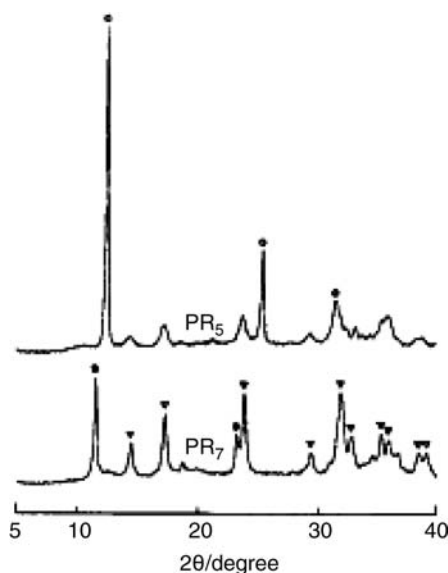


Figure 7.8 XRD patterns of copper/zinc catalysts coprecipitated at pH 5 (PR_5) and at pH 7 (PR_7) from [32].

7.6.4

Iron-Based Fischer–Tropsch Catalysts

Coprecipitated iron catalysts have been utilized for many years in the Fischer–Tropsch process for conversion of carbon-containing feedstocks to transportation fuels and chemicals. The use of iron catalysts is attractive due to their low costs and water gas shift activity, allowing the use of synthesis gas with a low H_2/CO ratio, as is the case for synthesis gas produced from coal or biomass. Unsupported iron catalysts sinter readily upon reduction in hydrogen and it was found that incorporation of silica at a level of 6–10% stabilized the surface area upon reduction. Copper as a reduction promoter was coprecipitated with the iron. A typical composition is $100Fe/5Cu/4.2 K/xSiO_2$ [33–35]. Other promoters like manganese may be coprecipitated with the iron by mixing manganese nitrate with the iron nitrate feed [36]. Typically, concentrated solutions of ferric nitrate, copper nitrate, and optionally promoter metal nitrates are added to soda at high temperature, thus ensuring that all metals are codeposited, rather than sequentially, as would be the case if the reverse order is used. Silica and potassium can be incorporated at various stages of the process.

7.6.5

Unsupported Metal Sulfide Catalysts for Hydrotreating

Traditionally, hydrotreating catalysts are prepared by impregnation of mostly alumina supports with a solution containing a group 6 (often Mo) precursor and a salt of group 9–10 metal (Ni or Co), see Chapter 14. Recently, high-metal catalysts based on coprecipitation have been claimed to have unprecedented activity for hydrodesulfurization, hydrodenitrogenation, and aromatics saturation [37]. The high activity has been attributed to the higher number of active sites in the unsupported catalysts and the absence of metal–support interaction. The preparation could involve either precipitation of the oxidic catalyst followed by sulfidation of the precipitate, or the direct precipitation of the mixed sulfide (see also the example in Section 7.6.2). In a recent patent, a group 9–10 metal precursor is coprecipitated with at least two group 6 metal precursors [38]. In an example, a concentrated solution of cobalt nitrate (58 g in 50 ml water) was reacted that a solution of ammonium heptamolybdate and ammonium metatungstate which was previously basified with ammonia to pH 9.8. The resulting catalyst was filtered, washed, dried, and sulfided before use.

7.7

New Developments in Process Monitoring

A key factor controlling the quality of the precipitate is the uniformity of mixing of reactants, which influences the chemical and physical properties of the

precipitate, for example, the phase composition, the porosity, and the particle size and form. Traditionally the coprecipitation process is monitored *in situ* just by pH, or sometimes by conductivity measurements, but nowadays more modern methods like flow visualization and tomography by noninvasive *in-situ* techniques such as positron-emission particle tracking (PEPT) and electrical resistance tomography (ERT) have become available [39, 40]. Application of these techniques is expected to provide a better understanding of the effect of mixing variables on vessel hydrodynamics and hence of factors determining the quality of the precipitate. PEPT is a flow visualization technique that uses positron-emitting tracer particles. The vessel is located between the positron cameras and the tracer position can be determined by triangulation. ERT uses electrodes to measure voltages around the vessel to give a conductivity map, thus yielding information on the spatial and temporal distribution of the fed ionic species. This allows a 3D image of the process to be constructed and inhomogeneities can be seen through regions of different conductivity. Based on this information, the quality of mixing can be improved that should lead to the production of more uniform and hence better catalysts. The most recent developments in this area are now providing deeper insights into the influence of mixing conditions on coprecipitated materials made through the combination, for the first time, of ERT and PEPT [41].

Because of its versatility coprecipitation will remain a major route to high-metal catalysts in the future. A challenge will be to reduce the environmental impact by minimizing water consumption and by reducing the amount of salt-containing effluents in addition to improving the catalysts by an improved quality of mixing.

Acknowledgments

The author thanks S. Axon, J. Casci and A. Zwijnenburg for suggestions and comments and Johnson Matthey for permission to publish.

References

1. Andrew, S.P.S. (1976) in *Preparation of Catalysts I, Scientific Bases for the Preparation of Heterogeneous Catalysts* (eds B. Delmon, P.A. Jacobs and G. Poncelet), Elsevier, Amsterdam, p. 429.
2. Twigg, M.V. (1996) *Catalyst Handbook*, Manson Publishing Ltd, London.
3. Schüth, F. and Unger, K. (1997) in *Precipitation and Coprecipitation, Handbook of Heterogeneous Catalysis* (eds G. Ertl, H. Knozinger and J. Weitkamp), Wiley-VCH Verlag GmbH, Weinheim, pp. 72–86.
4. Walton, A.G. (1967) *The Formation and Properties of Precipitates*, InterScience Publishers, New York/London/Sydney.
5. Mullin, J.W. (2001) *Crystallization*, Butterworth-Heinemann (Elsevier), Oxford.
6. Brice, J.C. (1986) *Crystal Growth Processes*, Blackie & Son, Glasgow.

7. Strickland-Constable, R.F. (1968) *Kinetics and Mechanism of Crystallization*, Academic Press, London and New York.
8. Stiles, A.B. and Koch, T. (eds) (1995) *Catalyst Manufacture*, Marcel Dekker, New York.
9. den Ouden, C.J.J. and Thompson, R.W. (1991) *J. Colloid Interface Sci.*, **143**, 77.
10. Nývlt, J. (1995) *Cryst. Res. Technol.*, **30**, 737.
11. Park, J., Joo, J., Kwon, S.G., Jang, Y. and Hyeon, T. (2007) *Angew. Chem. Int. Ed.*, **46**, 4630.
12. Martell, A.E. and Smith, R.M. (1977) *Critical Stability Constants*, Vol. 3. Plenum Press, New York.
13. Broecker, F.J., Kaempfer, K., Marosi, L., Schwarzmamm, M. and Triebkorn, B. (1975) Process for the Preparation of a Nickel Magnesium Aluminium Catalyst. US patent 3865753.
14. Broecker, F.J., Heners, J., Marosi, L., Schwarzmamm, M. and Laurer, P.R. (1975) Nickel Containing Hydrogenation Catalysts for the Selective Hydrogenation of Fats and Oils. US patent 3896053.
15. Kruissink, E.C., Alzamora, L.E., Orr, S., Doesburg, E.B.M., van Reijen, L.L., Ross, J.R.H. and van Veen, G. (1979) *Preparation of Catalysts II, Scientific Bases for the Preparation of Heterogeneous Catalysts*, Studies in Surface Science and Catalysis, Vol. 3 (eds B. Delmon, P. Grange, P. Jacobs and G. Poncelet), Elsevier, Amsterdam, p. 143.
16. Puxley, D.C., Kitchener, I.J., Komodromos, C. and Parkyns, N.D. (1983) *Preparation of Catalysts III, Scientific Bases for the Preparation of Heterogeneous Catalysts*, Studies in Surface Science and Catalysis, Vol. 16 (eds G. Poncelet, P. Grange and P.A. Jacobs), Elsevier, Amsterdam, p. 237.
17. Cavani, F. and Trifiro, F. (1995) *Preparation of Catalysts VI, Scientific Bases for the Preparation of Heterogeneous Catalysts*, Studies in Surface Science and Catalysis, Vol. 91 (eds G. Poncelet, P. Grange, J. Martens, B. Delmon, P.A. Jacobs and P. Grange), Elsevier, Amsterdam, p. 1.
18. Hocheplid, J.-F., Ilioukhina, O. and Berger, M.-H. (2003) *Mater. Lett.*, **57**, 2817.
19. Lok, C.M. and Ganguli, K.L. (1986) Process for Preparing a Transition Metal-Silicate Catalyst. U.S. patent 4,591,597.
20. Ganguli, K.L. Nootenboom, P. and Lok, C.M. (1987) Nickel/Alumina Catalyst and Process for its Preparation. U.S. patent 4,657,889.
21. Lok, C.M. (1992) Nickel/Silica Hydrogenation Catalysts and the Preparation and Their Use in Hydrogenating Unsaturated Fatty Acids. U.S. patent 5112792.
22. Pohorecki, R. and Baldyga, J. (1983) *Chem. Eng. Sci.*, **38**, 79.
23. Peleka, F., Mavros, P. and Zamboulis, D. (2004) Proceedings 5th International Symposium on Mixing in Industrial Processes, Seville, Spain.
24. Harnby, N., Nienow, A.W. and Edwards, M.F. (2000) *Mixing in the Process Industries*, Butterworth-Heinemann, London.
25. Zelinsky, N. and Kommarewski, W. (1924) *Chem. Ber.*, **57**, 667.
26. Borisova, M.S., Dzis'ko, V.A. and Simonova, L.G. (1974) *Kinet. Catal.*, **13**, 425.
27. Dzis'ko, V.A., Noskova, S.P., Borisova, M.S., Bolgova, V.D. and Karakchiev, L.G. (1976) *Kinet. Catal.*, **15**, 667.
28. Patterson, H.B.W. (1994) *Hydrogenation of Fats and Oils: Theory and Practice*, AOCS Press, Champaign.
29. Tateishi, T., Murase, K. and Iwanaga, Y. (1974) Process for Preparing Hard Butter. US patent 3,856,831.
30. Bouwman, H. and Blom, P.J.W. (1995) Sulphur Promoted Nickel Catalyst and Preparation Thereof. US patent 5,223,470.
31. Chinchin, G.C., Denny, P.J., Jennings, J.R., Spencer, M.S. and Waugh, K.C. (1988) *Appl. Catal.*, **36**, 1.
32. Li, J.-L. and Inui, T. (1996) *Appl. Catal. A*, **137**, 105.

33. Dry, E. (1981) in *The Fischer–Tropsch Synthesis, Catalysis Science and Technology* (eds J.R. Anderson and M. Boudart), Springer-Verlag, Vol. 1.
34. Davis, B.H. (2003) *Catal. Today*, **84**, 83.
35. Sudsakorn, K., Goodwin, J.G. Jr., Jothimurugesan, K. and Adeyiga, A.A. (2001) *Ind. Eng. Chem. Res.*, **40**, 4778.
36. Yang, Y., Xiang, H.W., Tian, L., Wang, H., Zhang, C.H., Tao, Z.C., Xu, Y.M.Y., Zhong, B. and Li, Y.W. (2005) *Appl. Catal. A*, **284**, 105.
37. Eijssbouts, S., Mayo, S.W. and Fujita, K. (2007) *Appl. Catal. A*, **322**, 58.
38. Sabato, M., Soled, S.L., Riley, K.L., Cerfontein, M.B., Free, H.W.H., Oogjen, B.G. and Eijssbouts, S. (2003) A Novel Mixed Metal Catalyst, its Preparation by Co-Precipitation, and its Use. AU patent 2003242446.
39. Fishwick, R.P., Winterbottom, J.M. and Stitt, E.H. (2003) *Catal. Today*, **70–80**, 195.
40. Fishwick, R., Winterbottom, M., Parker, D., Fan, X. and Stitt, H. (2005) *Can. J. Chem. Eng.*, **83**, 97.
41. Edwards, I., Axon, S.A., Barigou, M., Mann, R., Stephenson, D.R. and Stitt, E.H. (2007) The Use of Multimodal Tomography in the Study of Boehmite Precipitation. Proceedings 5th World Congress on Industrial Process Tomography, Bergen.

8

Clusters and Immobilization

Sophie Hermans

8.1

Introduction

In this chapter, concepts of organometallic chemistry are used to describe original preparation procedures that lead ideally to the so-called “single-site” catalysts. This is a common goal amongst scientists in the field of heterogeneous catalysis, as catalysts characterized by only one type of surface structure are believed to be more active or selective and to allow precise mechanistic studies. However, determining the type of active site that is required by a particular catalytic reaction remains tricky, as most industrially relevant catalysts are often complex and not fully characterized. The complexity of solid catalysts is brought about by the intrinsic variations of the composition and structure of their surfaces and concomitant active sites. It is a general statement in heterogeneous catalysis that characterizing the active sites is a challenge. First, because most heterogeneous catalysts are solid materials, which are more difficult to analyze than molecules in solution. Second, because they are very often supported, hence the active phase is present as only a few weight per cent of the total material, rendering characterizations even more difficult. Third, because the catalytic reaction occurs at the interface, so it is in fact only the outermost layer of the material that is important. And finally, because heterogeneous catalysts are dynamical systems that undergo transformations during their use, suggesting that the true active site is maybe only created under reaction conditions by restructuration of the prepared material. All this having been said, considerable insight into active structures has been gained over the years by very elegant structure–activity studies, sometimes with model catalysts in ultrahigh vacuum or more realistic one under *in situ*/operando mode. It is thus worth trying to build nanostructured solid materials, which are well defined at the atomic level, and that should function optimally for the desired process. The aim of this chapter is to show how clusters and immobilization techniques can help to approach such a goal. Clusters are understood here in the sense of multinuclear metal complexes, consisting of a core of metallic atoms

bonded to each other and surrounded by a sheath of protective organic ligands (Figure 8.1). Immobilization refers to various reactions between organic or organometallic moieties and the surface of the support in order to graft the active phase or its precursor to it. As a consequence, these concepts do not apply to unsupported (“bulk”) catalysts. The literature within the field covered in this chapter is really vast, hence mainly review papers are cited, which can be consulted for individual references.

8.2

The Surface of Common Supports

Solid materials that are commonly used as supports in heterogeneous catalysis can be classified into three broad categories: (i) inorganic oxides such as silica and alumina, (ii) carbonaceous materials, and (iii) polymers. This latter type of supports will not be treated in the present chapter as it involves a very different kind of chemistry and specific methods of characterization. However, it must be remembered that some of the concepts developed here have been applied to polymers too. Regarding the other two, they are very different in terms of surface properties but involve roughly similar methodologies. Inorganic oxides are by far the most frequently encountered for immobilization or as supports for clusters. Before going into further details on how to build single-site

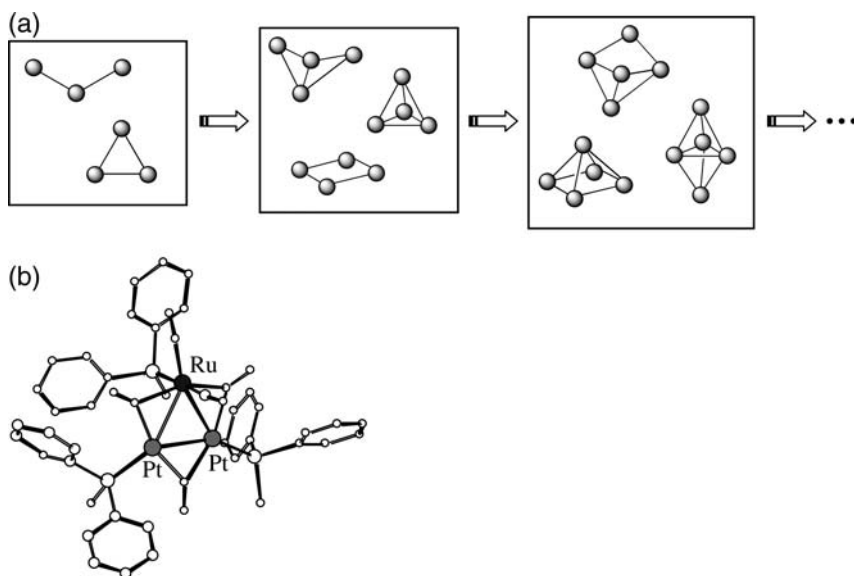


Figure 8.1 What is a cluster? (a) Examples of cluster cores without layer of ligands and (b) example of triangular mixed-metal cluster with ligands.

catalysts on such solids, one must first spend some time to get to know the very nature of their surface.

Inorganic oxides, of general formula M_xO_y , where $M = \text{Si, Al, Ti}$, and so forth, are usually made of corner-, edge-, or face-sharing polyhedra consisting of a central M atom surrounded by bridging oxygen atoms that form a covalent network structure. At the surface, the unconnected O atoms are usually protonated, giving surface hydroxyl groups. In the case of silica (SiO_2), which is a most frequently used support, these are called silanols [1]. They make the surface hydrophilic and can easily form H-bonds with adsorbates, such as water, or metallic species. Rather than an exclusive presence of terminal silanols, a number of different oxygenated groups are present at the surface of amorphous silica, for instance: (i) isolated or vicinal silanols ($\equiv \text{SiOH}$), (ii) geminal silanols, also called silanediols, ($= \text{Si}(\text{OH})_2$), (iii) surface siloxane groups ($\equiv \text{Si}-\text{O}-\text{Si} \equiv$ bridges) (Figure 8.2a). The vicinal silanols are bridged through hydrogen bonds. Geminal silanols might also be H-bonded. The chemistry that can be done at the surface of silica (and by analogy at the surface of the other inorganic oxides) depends on the concentration and distribution of the different types of such groups [1]. These can be modulated by various treatments, the most common being heating under vacuum. The three main processes that can happen to the surface are (i) dehydration, the

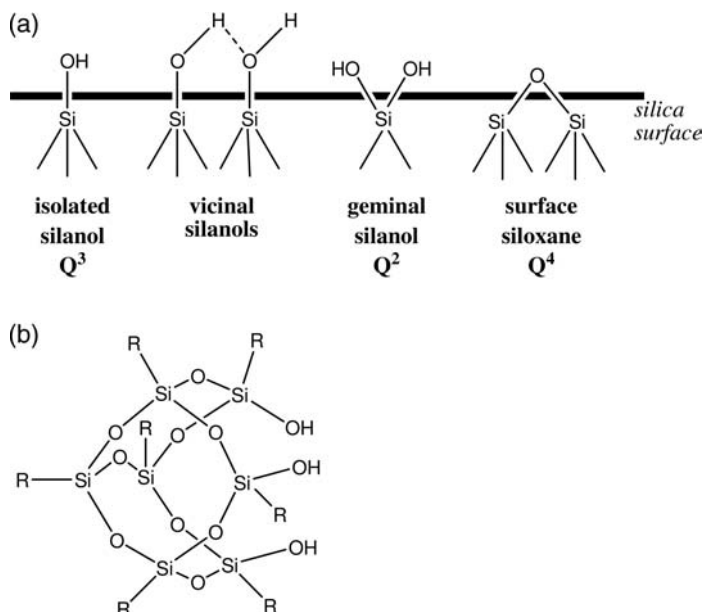


Figure 8.2 (a) Type of groups at the silica surface (the Q^n terminology stems from NMR, and is used to describe the number of O-bridges around the central Si atom) and (b) the trisilanol silsesquioxane ($\text{R}_7\text{Si}_7\text{O}_9(\text{OH})_3$) as a model for silica surfaces.

removal of physically adsorbed water, (ii) dehydroxylation, the removal of silanol groups, and (iii) rehydroxylation, the restoration of the hydroxyl groups by water adsorption [1]. The number of OH groups per unit surface area, α_{OH} (OH/nm²), can be determined by isotopic exchange between D₂O and the surface OH groups or temperature-programmed desorption (TPD) [1]. This value can reach a maximum of 4–6 OH/nm². When a silica sample is heated in vacuum in order to remove the hydroxyl groups, the value of α_{OH} decreases markedly between 200 and 400 °C, and then more slowly to approach zero at about 1200 °C. Below 200 °C, it is mainly dehydration that occurs. The type of groups present (Figure 8.2a) can also be determined by a combination of TPD and MAS-NMR (magic-angle spinning nuclear magnetic resonance, for the characterization of solids). The acido–basic character of the surface can also be determined by adsorption of probe molecules and characterization by infrared spectroscopy [2]. Basic probes include pyridine, ammonia, and carbon monoxide. Obviously, the treatment temperature will have an influence on the nature of groups at the surface. When nontreated, silica presents mainly terminal, vicinal, and geminal silanols. When heated under vacuum, the number of vicinal silanols will decrease first to become terminal silanols and then siloxanes at higher temperatures [1]. In order to model the reactivity of silica surfaces, researchers have used polyhedral oligomeric silsesquioxanes (POSS), which are a family of polycyclic compounds consisting of silicon and oxygen [3]. Figure 8.2b shows an example of silsesquioxane with three OH groups, but synthetic modifications can give POSS that are suitable models for isolated, vicinal, or geminal silanol groups, and allow reactivity or structural studies to be carried out more easily than with the bulk silica, because they can be characterized in solution or even by X-ray diffraction (XRD) crystallography.

Carbon is more hydrophobic, consisting of C₆-aromatic rings arranged into sheets (called graphene), which can be organized variously leading to different substructures: in parallel stacks for graphite, in less perfect arrangements in the case of activated or amorphous carbon and as concentric rolled tubes in nanotubes. Due to its high specific surface area ($S_{\text{BET}} > 1000 \text{ m}^2/\text{g}$) and low cost, activated carbon is the most commonly used carbonaceous support [4]. It is produced from carbon-rich feedstock (coal, wood or waste material such as coconut shells, fruit stones) by chemical activation with reactants such as zinc chloride, phosphoric acid, or potassium hydroxide, or by carbonization brought about by high-temperature treatment followed by oxidative activation (which increases the specific surface area by creating pores) [4–6]. Heteroatoms, such as O, N, or S, remaining from the source material, or introduced during the activation step, are present at the surface as functional groups. The oxygenated functions are by far the most numerous, but with a surface density well below that of the OH groups on inorganic oxides. They can be removed by thermal treatment at high temperature [7], or – in order to enhance the surface reactivity – increased by further oxidation in the gas or liquid phase [8]. The gas-phase treatments involve, for example, oxygen or ozone, while liquid-phase

oxidants are nitric acid, hydrogen peroxide, perchlorate or permanganate. The nature of the surface O-groups of activated carbon has been determined to be mainly carboxylic acids, lactones, phenols, and carbonyls (Figure 8.3). They can be quantified by the so-called Boehm's titration method [7–9], but also by FTIR or DRIFTS, TPD, XPS, or TGA/MS. However, carbon has been far less used than silica for immobilization because it is less easily amenable to surface modifications and reactions, and less easily characterized by spectroscopy: its high absorbing power renders infrared spectra of high quality very difficult to obtain.

8.3 Clusters in Catalysis

The first chronological appearance of clusters in catalysis is their use as *models* for heterogeneous catalysts. More precisely, it was found that polynuclear metal complexes such as transition-metal clusters can act as soluble models for supported metallic particles, that are much more complicated to study. Clusters can be isolated and characterized by the “classical” methods of preparative chemistry. They show typical characteristics of metal surfaces, such as polycentric ligand–metal bonds and delocalized metal–metal bonds. The use of metal clusters as models for the surface of catalysts was named by Muetterties the *cluster-surface analogy* [10]. The first development in this area of research was mainly structural, and consisted in investigating the interaction

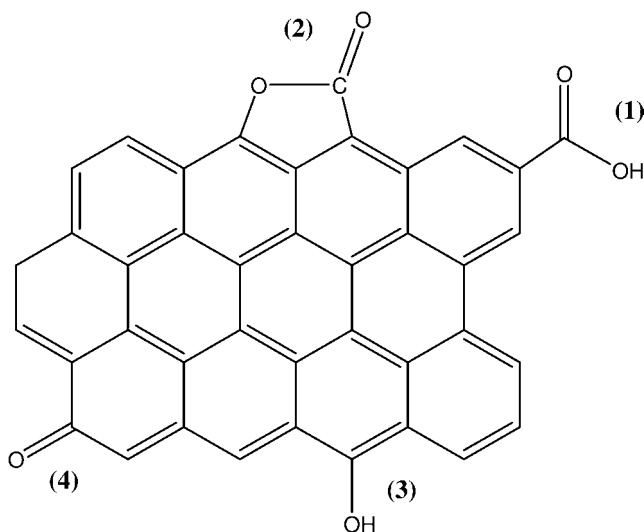


Figure 8.3 Oxygen surface functions most commonly found at the surface of activated carbons: (1) carboxylic acid, (2) lactone, (3) phenol and (4) carbonyl.

of various ligands with clusters, and determining precisely their bonding modes, as an approximation of what can happen when an organic molecule adsorbs on a metal surface [11]. It followed quickly that the organic moieties bound to a metal core can undergo transformations that parallel not only the structure but also the reactivity of molecules on surfaces. Some elementary steps of complicated mechanisms occurring in heterogeneous catalysis have been elucidated thanks to cluster models.

Molecular clusters have then been investigated as homogeneous catalysts by themselves [11, 12]. It was hoped that cooperative effects between several metallic atoms, hence the possibility of multicenter activation and multielectron processes, would be highly beneficial. In addition, selectivity and activity could still be finely tuned by ligand design. Even enantioselective catalysis is a possibility with chiral ligands. Many species (mainly homometallic and of low nuclearity, but sometimes heterometallic clusters too) have been used successfully in homogeneous catalysis [11–14]. With the vast majority of transition-metal clusters bearing CO ligands, the type of reaction catalyzed usually involves C_1 chemistry [15]. However, few of these processes have become economically viable because the reactive clusters are usually unstable and the more stable ones are usually less active. The main challenge for scientists working in this area has been to prove that the activity is really due to the action of the intact cluster and not to mononuclear complexes formed by fragmentation or colloidal particles formed by aggregation. The use of very large soluble clusters as nanostructured defined species for use as quasihomogeneous catalysts has also been investigated and shown to give promising results [16].

Subsequently, metal clusters have been immobilized on solid supports such as inorganic oxides or polymers to be used as heterogeneous catalysts without losing the benefits of homogeneous catalysts [11, 13]. This approach will be treated in the following sections, together with mononuclear metal complexes. The problem here again arises from fragmentation or agglomeration during catalysis.

Finally, metal clusters have been used as precursors for well-defined metallic particles deposited on various supports [14]. This is probably the aspect of the usage of clusters in catalysis that could be of the most practical importance. By an appropriate choice of molecular precursor, one can control at the microscopic level the size and composition of the final particles. This is most useful for bimetallic entities, as it is very difficult to prepare by the traditional methods a heterogeneous catalyst with a perfect homogeneity of composition, meaning the same molar ratio of the two metals at each point of the surface. The principle of the method is outlined in Figure 8.4. It consists in first depositing the metal cluster on the support. This can happen by simple physisorption during an impregnation procedure by bringing into contact the solid support with a concentrated solution of the cluster. Alternatively, the cluster can react with the surface and become chemisorbed: this will

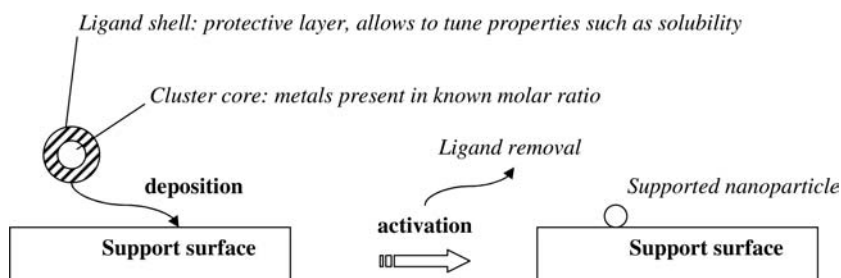


Figure 8.4 Clusters as precursors of supported nanoparticles.

be treated in more detail in the following section. After this first step, the solid is recovered by filtration and dried, then activated by gentle heating, usually under vacuum or under a stream of inert gas. This step is crucial as it should remove selectively the ligands shell, to leave on the surface activated naked nanoparticles. The metals being already in a low oxidation state in the starting cluster, low activation temperatures are sufficient when compared to the usual mononuclear complexes or metal salts used as catalyst precursors. In addition, the ligands being usually carbonyls, this step can be conveniently followed by *in-situ* infrared spectroscopy (by following the disappearance of the ν_{CO} bands) or by extended X-ray absorption fine structure spectroscopy (EXAFS) [17]. The obtained supported particles in an ideal case retain the shape and stoichiometry of the parent compound, allowing a very precise control of the surface structures that have been built at the nanoscale. In short, single-site catalysts must be obtained. However, it is very difficult to control the degree of ligand removal and/or aggregation on the surface, hence this ideal case is seldom the reality. Nevertheless, very nice examples of supported nanoparticles active in various catalytic processes have been reported following this general strategy [18–20]. For example, Pt, Pt-Sn, and Ru–Se carbonyl clusters have been synthesized, then adsorbed on carbon, in order to prepare electrocatalysts for fuel-cell reactions [21]. Indeed, it is known that very small, and preferably bimetallic, noble-metal particles are needed for this application. A homogeneous distribution of particles, whose sizes were about 1.5, 2.4, and 2 nm, respectively, was observed by TEM. Within the same context, Frenkel, Nuzzo *et al.* [22, 23] studied the incorporation of a Ru–Pt mixed-metal carbonyl cluster $\text{PtRu}_5\text{C}(\text{CO})_{16}$ on carbon, followed by activation in hydrogen to give naked bimetallic nanoparticles. These were characterized in detail by a combination of *in-situ* EXAFS, scanning transmission electron microscopy, microprobe energy-dispersive X-ray analysis, electron microdiffraction, and TPD, in order to propose a structural model for the surface nanosized entities. It was found that the initial Pt1:Ru5 ratio was retained and that the metal particles had an average diameter of 1.5 nm. Mesoporous silica such as MCM-41 has also been extensively used as support for cluster-derived bimetallic nanoparticles [24–30]. We have shown that truly bimetallic

nanoparticles are formed within the 30 Å channels of MCM-41, which are highly active for various selective hydrogenation reactions, such as the solvent-free transformation of cyclic poly-enes into their corresponding mono-enes. Obviously, many other cluster-derived catalysts supported on various materials such as amorphous silica [31] and alumina [32] have appeared over the years, and proven again and again the advantage of using single-source metallic precursors for the preparation of supported particles of controlled size and composition. For example, Au catalysts supported on various inorganic oxides have been prepared from cluster precursors and shown to be highly active for low-temperature CO oxidation, a reaction where particle size is really important [33]. The key to success apparently lies in the choice of cationic gold precursors such as $[\text{Au}_9(\text{PPh}_3)_8]^{3+}$, which interact directly with unprotonated surface hydroxyl groups (O^- sites), enabling the preparation of stabilized small Au particles.

8.4

Reaction with Unmodified Surface

In this section, we will describe some examples of surface reactivity, where a metal complex (being mononuclear or cluster) reacts in a chemical sense with some of the functionalities that are present on the solid used as support. The reactions involving grafted organic fragments introduced beforehand in order to play the role of ligands for the metallic entities will be treated in the last section of this chapter.

As mentioned above, the surface of common supports presents oxygenated functions that can be used as anchors for metallic moieties. This entire field of study has been called “surface organometallic chemistry” [34]. The nature of the product formed after reacting a complex with a given solid has been mainly investigated spectroscopically, by infrared and EXAFS above all, but also by solid-state NMR, XPS, and Mössbauer [35]. It must be noted that the interpretation of spectra usually relies on comparisons with data obtained with reference compounds (especially for EXAFS) and theoretical calculations. Temperature-programmed methods and simple elemental analyses have also given invaluable insight. The oxidation state of a metal center might be determined by XANES or XPS. The use of solvent extraction of the surface species has been suggested as an alternative, because the eventual extracted species can be more easily characterized by the “classical” chemical methods such as elemental analysis, NMR and crystallography [36]. When the molecules are loosely deposited on the surface, a direct solvent extraction is sufficient. However, when the complex has reacted with the support, more complicated procedures have to be applied, involving usually first a selective surface reaction to be able to desorb the grafted species. The nature of the surface species can also be assessed by using organometallic models with ligands that mimic

surface functions, such as silsesquioxanes for silanols, and investigating their structure and reactivity.

The various possible surface reactions are (i) ion pairing usually with surface cationic centers such as Al^{3+} in alumina or zeolites, (ii) weak interaction with surface hydroxyl ($\text{M}-\text{OH}$) or oxo ($\text{M}=\text{O}$) groups via H-bonds, for example, (iii) ligand exchange for surface oxy ($\text{M}-\text{O}^-$) groups, (iv) oxidative addition into an O-H bond giving surface hydride species, (v) nucleophilic or electrophilic attack on a ligand of the complex by surface OH groups, (vi) electrophilic cleavage of M-C bonds of the complex by surface groups (Figure 8.5a), (vii) abstraction by surface groups of H atoms bonded to the metal [34–38]. The highly strained $\equiv\text{M}-\text{O}-\text{M}\equiv$ bridges are highly reactive and can be opened by reaction with organometallic complexes (Figure 8.5b). As can be seen, the role of the support as a coordinating ligand stabilizing the surface species is a key factor of this chemistry. The group of J.-M. Basset has been a major actor in the field, and elucidated many mechanisms by careful analysis of the gaseous side-products formed during surface reactions or isotopic labeling experiments using ^2H - or ^{18}O -enriched silica [34]. Moreover, they have studied the reactivity of the grafted complexes, which can undergo subsequent reactions with the support or other molecules. The reactivity of surface-bound complexes is usually very similar to that of molecular analogs, they are thus still amenable to further modifications, for example, replacement of the ligands by others more adapted to the targeted catalytic reaction [38]. By careful heating under vacuum, multigrafted species are obtained. Under reductive conditions (for example in the presence of H_2), they are transformed into supported metallic particles.

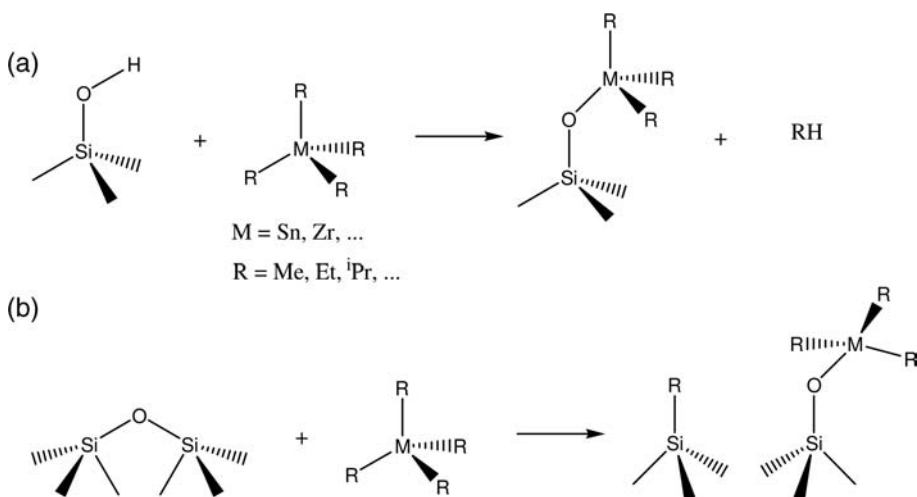


Figure 8.5 Surface reactions: (a) electrophilic cleavage of a M-C bond of the complex by a surface hydroxyl group and (b) opening of surface $\equiv\text{M}-\text{O}-\text{M}\equiv$ bridge.

The catalytic activity of grafted molecular fragments might be similar or modified when compared to the original complex. The presence of the support, via electronic or steric effects, might affect positively the selectivity. Moreover, it will favor site isolation and hinder dimerization of the complex bound to the surface. These well-defined materials allow the establishment of structure–activity relationships at the molecular level [37, 39]. The limitation of such systems is that the number of OH groups on the surface controls the number of chemisorbed species, hence the loading of active phase.

Different groups have also investigated the reactivity of molecular clusters with various supports with the goal of preparing tailored heterogeneous catalysts [18–20, 40, 41]. Metal clusters have interesting reactions at the surface of oxide materials, ranging from simple physisorption, to electrostatic interactions after electron transfer/deprotonation by the surface, to covalent bonds, for example, by oxidative addition to M–OH surface groups (Figure 8.6). Some clusters are easily broken down to oxidized mononuclear surface species, but it has also been shown that the oxide surface is actually a good medium for the *formation* of metal clusters from mononuclear precursors, which is called “surface-mediated synthesis” [17, 37, 40, 42]. It allowed the clean preparation, with better yields, under milder conditions, of some clusters that were difficult to obtain in a pure form by solution reactions. Usually, neutral clusters are obtained on silica, while anionic clusters are obtained on silica in the presence of a base such as Na_2CO_3 or K_2CO_3 or on a basic support such as MgO [42]. The nuclearity increases when the temperature is raised. The anionic clusters formed interact with Mg^{2+} or Al^{3+} in the case of alumina and so ion exchange with a counteranion is needed to recover the cluster if needed. The species obtained are first elucidated thanks to infrared spectroscopy, by examination of the ν_{CO} bands of the cluster and the ν_{OH} bands of the support, and by comparison with molecular analogs. The presence of edge- or face-bridging carbonyl ligands, for example, is a good indication of metal–metal bonding. The set of methods described above for mononuclear complexes also apply for clusters on surfaces [35]. EXAFS in particular is especially powerful [43], as it gives information pertaining to the metal but also the ligand’s shell, and can be carried out in reactive atmospheres and at high temperature to study catalysts as they function. In addition, TEM might give some information regarding nuclearities and theory will help data interpretation. It has been shown, for example, that with mixed-metal clusters, the more oxophilic metal will interact

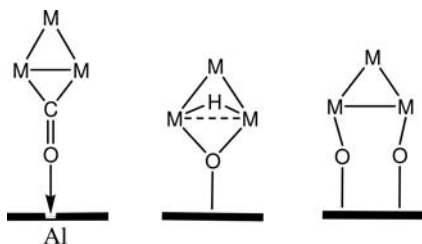


Figure 8.6 Some examples of possible bonding modes for clusters on inorganic oxides surfaces (auxiliary ligands are omitted for clarity).

with the surface, thus acting as a “glue” for the other metal that remains at a low oxidation state, providing a route towards highly dispersed noble metals [43, 44].

Once anchored, the clusters can be used as heterogenized catalysts [45]. The grafted clusters are also good precursors for small metallic particles. If the ligand-removal step, usually decarbonylation, is carried out with great care, the formed “naked” metallic entities might consist of the intact metal frame of the original cluster [40, 43, 44]. Recent results, however, seem to indicate that some fragments of the ligands might remain on the metallic core such as the C atom of a CO molecule [35], bringing the attention to the choice of ligands in the original complex, which must be exempt of heteroatoms potentially deleterious for the catalytic activity. These pseudomolecular species are bonded to the surface by metal–oxygen bonds, and the metal atoms at the interface are formally oxidized. The catalytic activity will differ from that of the intact cluster in the homogeneous phase or supported nanoparticles prepared by more traditional methods. The present structures might act as catalysts through coordinative unsaturations for bonding of reactants as ligands. The support is obviously necessary to stabilize such coordinatively unsaturated fragments. Indeed, one major drawback is fragmentation and/or agglomeration of supported clusters or cluster-derived structures.

8.5 “Ship-in-a-Bottle” Synthesis

The so-called “ship-in-a-bottle” concept is intimately linked to zeolites used as support materials [46]. Zeolites are crystalline aluminosilicates with high surface area due to an array of interconnected micropores that are open to the exterior. These pores can be uni-, bi-, or tridirectional, leading to more or less hindered diffusion. In the case of tridirectional zeolites (in particular, faujasite X and Y), the shape of these micropores is not cylindrical, but consists of internal voids, called “supercages,” connected via smaller diameter cavities whose entrance is usually termed an “aperture” and consist of $-(O-Si(Al)-O)-$ rings made of 8, 10, or 12 atoms usually, corresponding to a diameter of 3, 5, or 7 Å. The concept of “ship-in-a-bottle” synthesis, first used by Herron [47], is to introduce reactants within the zeolite framework, which are small enough to diffuse through the apertures, that will react inside the supercages to give products that are too big to diffuse out. These new structures are thus physically entrapped inside the rigid host of the crystalline zeolite, like a miniature ship built in a thin-necked glass bottle. This procedure is a method of immobilization for species that can act as catalysts, without the need for developing specific interactions with the support surface.

Within the context of the present chapter, this strategy can be used to build metal complexes that will be stabilized inside zeolites pores and too voluminous to leach out (Figure 8.7a). The obtained materials will be used as

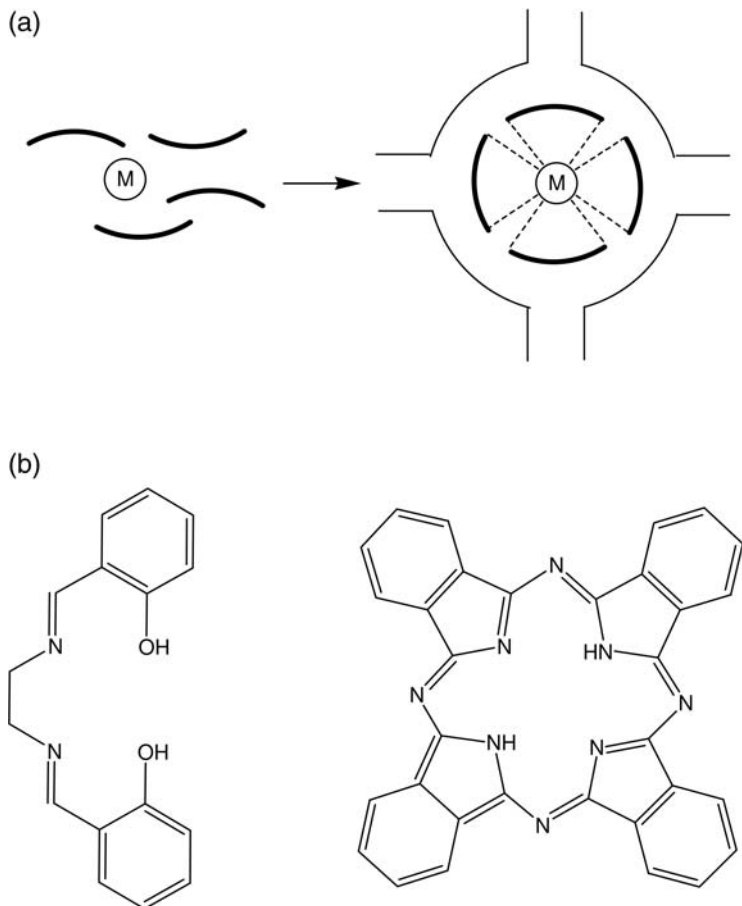


Figure 8.7 (a) The “ship-in-a-bottle” concept and (b) examples of ligands used to synthesize zeolite-entrapped metal complexes.

very selective heterogeneous catalysts because the substrate to be catalytically transformed will still be able to diffuse inside the micropores through to the metal complexes where it will react. This concept is particularly powerful for enantioselective catalysis with chiral complexes, because they are thus heterogenized without the risk of losing the chiral information by grafting them to a solid support. The advantage is that there is no covalent bond between the entrapped species and the support, which should make them very similar to their homogeneous counterparts in terms of structure, hence activity and/or selectivity.

Confinement inside a protected environment might contribute to complex stabilization, because the effect of the atmosphere (air, moisture, solvents, other reactants) will be minimized. This is particularly true for liquid-phase

oxidation catalysis, where conditions are very demanding. Several examples have appeared of complexes that, when encapsulated, display an activity with peroxides as oxidants without being degraded [48, 49]. Encapsulation can also be considered to be the most elegant form of site isolation, hindering completely active-site dimerization and agglomeration. Moreover, the immobilized species are still amenable to postsynthetic modifications. Drawbacks are related to diffusion hindrance for bulky substrates and low loadings compared to commercially available catalysts. The term “zeozymes” (acronym for zeolite mimics of enzymes) has been used to describe these materials, as they bear a resemblance to enzymatic systems where the active groups are located within protected pockets inside a folded protein, which provides stabilization and steric constraints, hence increased selectivity. The group of P. A. Jacobs has been very active in the field of enzymes mimicry using ship-in-a-bottle strategies [50].

In practice, reactants are usually driven inside the zeolite pores by impregnation. This synthetic procedure consists in dissolving the building blocks of the “ship” in an appropriate solvent and suspending the solid zeolite into this solution for a certain amount of time, allowing diffusion to proceed. Gentle heating might speed up the process. The choice of solvent is obviously important as it cannot compete for adsorption inside the pores. The zeolite is also dehydrated before use to empty the micropore volume. An alternative is chemical vapor deposition when the reactants are sufficiently volatile. This removes the problem of choosing the appropriate solvent for impregnation. The presence of Al replacing part of the Si in the O-bonded structure of the zeolite leads to negative charges that need to be counterbalanced by extra-framework cations. Metallic cations can thus be relatively easily introduced inside zeolites by ion exchange for these charge-balancing species. Ligands can then be introduced in a second step. The major drawback of these preparations is that the selectivity of the complex formation inside the pores needs to be close to 100%, as by-products or unreacted species can only be removed with great difficulty by solid–liquid extraction. Going one step further, one can also consider intrazeolite ligands synthesis. Alternatively, zeolites can be crystallized around a preformed structure that will be entrapped in the final material. The problems here stem from degradation of the complex during zeolite synthesis under hydrothermal conditions or lack of zeolite crystallization in the presence of a guest molecule.

Once synthesized, the nature of the encaged complex needs to be confirmed by a combination of characterization techniques. Spectroscopies such as UV-vis, IR, and Raman can be very useful as the zeolite matrix does not usually obstruct the interesting zones of the spectra. The former is used to probe the metal, while the latter two are more ligand-based techniques. Results are usually compared to the pure, unsupported, complex. Solid-state NMR can also give precious information but with enriched samples or analyses of heteroatoms. electron paramagnetic resonance (EPR) spectroscopy has also been used, especially with Co(II) complexes. X-ray photoelectron spectroscopy

can assist identification of the complex location: on the external surface or within the cages of the zeolite, which obviously is a crucial point to be determined.

Classical examples of species immobilized via the ship-in-a-bottle strategy include Co, V, Fe, Ru, or Rh complexes with ligands such as Schiff bases (for instance Salen) or phthalocyanine (Pc) (Figure 8.7b). In the first case, the free ligand is sufficiently flexible due to the central C–C bond to enter the mouth openings of the zeolite supercages, while Salen complexes become rigid because of a square-planar configuration and too voluminous to come out [47]. This is now called the “flexible ligand method,” and involves first preparing an ion-exchanged zeolite, and then bringing it into contact with the Salen ligand in a melted form. The solid formed is purified by Soxhlet extraction. It should be noted that the ligand releases two protons that take up the position of charge-balancing species given up by the metal ion that is now complexed: this confers Brønsted acidity to the final material, unless a neutralization procedure is applied. In the second case, for the entrapment of metallophthalocyanines, the metal center is introduced via ion exchange or adsorption of a labile metal complex such as metallocene or carbonyl, followed by synthesis of the ligand from smaller building blocks, such as 1,2-dicyanobenzene (*o*-phthalodinitrile), inside the zeolite cavities [51]. Alternatively, a build-the-bottle-around-the-ship strategy can be used, meaning crystallizing the zeolite around the preformed metal complex.

Recent examples of ship-in-a-bottle catalysts include the formation of a chiral Salen complex of cobalt inside the pores of the ordered mesoporous silica SBA-16 [52]. The support was first silylated with phenyltrimethoxysilane to tailor the pore entrance size. The complex was then synthesized using the molecular fragments 3,5,3',5'-tetra-*tert*-butyl-SalenH₂ and Co(OAc)₂. The entrapped catalyst exhibited comparable enantioselectivity to its homogeneous counterpart in the asymmetric ring opening of terminal epoxides, and could be reused 10 times without loss of efficiency. The incorporation of various Schiff-base complexes inside zeolites X or Y is still a field of intense study [53–56]. The complex [Mn(X₂-haacac)Cl] (haacac = bis(2-hydroxyanil)acetylacetone; X = H, CH₃, Cl, or NO₂) has been encapsulated in the pores of zeolite Y by the flexible ligand method, by template condensation between pre-entrapped [Mn(X-C₆H₄NO₂)₂]²⁺ complexes and acetylacetone [57]. This catalyst was much more active and stable than its homogeneous counterpart in the aerobic oxidation of styrene. Nickel(II) complexes with tetraaza[14]annulene ligands have been encapsulated inside the pores of zeolites Y by reaction of substituted-1,2-phenylenediamine with Ni(II) ion-exchanged zeolites, followed by treatment with 2,4-pentanedione, to give [Ni(Me₄R₂-Bzo[14]tetraeneN₄)] (R = H, CH₃, Cl, and NO₂) [58]. The obtained materials were tested in the oxidation of phenol to a mixture of catechol and hydroquinone using hydrogen peroxide as oxidant. Within a completely different context, efforts have been directed toward the encapsulation in zeolite Y of Keggin-type heteropolyacids (HPAs) such as 12-molybdophosphoric acid, starting from MoO₃ and H₃PO₄ as the

Mo and P sources, respectively [59]. This gives rise to a supported acidic species that can act as solid acid catalyst, much more environmentally friendly than homogeneous acids.

Molecular clusters have also been built inside zeolite cavities [42, 46, 60–63]. The synthetic procedure involves here preparing first an ion-exchanged zeolite, usually by adsorbing a small metal complex such as $[\text{Pd}(\text{NH}_3)_4]^{2+}$ or $[\text{Pt}(\text{NH}_3)_4]^{2+}$ as precursor inside the pores. In a second step, the cluster is formed by calcination, reduction and then heating in the presence of carbon monoxide (providing the needed ligands) and sometimes water or H_2 . In general, neutral carbonyl clusters are formed in the less-basic zeolites (such as NaY), whereas anionic species are formed in the more-basic zeolites (such as NaX). Characterization is usually carried out by NMR and IR spectroscopies to determine the ligand shell, and by EXAFS to prove the existence of metal–metal bonds and the average structure obtained. For example, the $[\text{Rh}_6(\text{CO})_{15}]^{2-}$ cluster was formed inside the cages of zeolite X by carbonylation of sorbed $[\text{Rh}(\text{CO})_2(\text{acac})]$ at 125 °C [64]. Mixed-metal clusters can be obtained by coadsorption of two different metal salts [65]. Once formed inside the zeolitic cavities, the cluster species can be decarbonylated, giving encapsulated very small metal particles (smaller than about 1 nm in diameter) with various possible catalytic activities [64, 66].

8.6

Tethering

In this final section, we will describe a last concept related to immobilization, that is the covalent grafting of metallic complexes onto *modified* inorganic supports. This is usually called “tethering,” and involves the use of a “spacer” molecule between the original surface of the solid used as support and the metallic entities. We are here situated at the boundary between homogeneous and heterogeneous catalysis. The support is expected to provide extra stabilization and enhanced selectivity to the grafted complex, and to allow its easier recovery at the end of the catalytic process. The spacer molecule can be introduced before bringing in the complex, and might involve more or less sophisticated surface reactions. One possibility is to build on the surface an organic moiety capable of playing the role of a ligand [38]. The metal complex will thus be grafted by ligand exchange. This is a very elegant procedure, and a highly controllable one. However, it suffers one major drawback: if the tethered complex is to be used as an immobilized homogeneous catalyst, the necessary step of ligand exchange might markedly alter its structure hence its reactivity or selectivity [37]. In the case of asymmetric catalysis, the chiral information might even be lost. Another possibility is thus to prepare a useful complex containing a ligand that is capable of reacting with the surface and that will play the role of anchor [38]. The involvement of spacer molecules has two

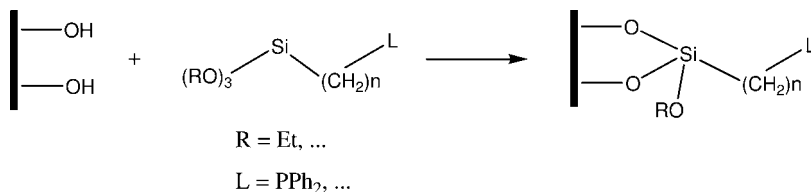


Figure 8.8 Building of a surface ligand on silica using a tri-alkoxysilane.

advantages: (i) it extends the range of available surface groups beyond oxygen-donating ligands and (ii) it brings some flexibility to the anchored complex. This type of material is often termed a “hybrid organic-inorganic catalyst” [67].

On silica, silanol groups are ideal anchoring sites: chlorosilanes, alkoxy-silanes, and disilylazanes have been used extensively to graft metal species (Figure 8.8). The Si atom of the silane might be bonded to the surface via one, two, or three Si–O–Si bonds, the tripodal grafting being of course most desirable because of the expected improved stability. Another approach involves cocondensation of the silica (or other inorganic oxide) precursor with an organoalkoxysilane during the support preparation. Using one approach or the other, these oxides-tethered complexes have found a realm of catalytic applications [67]. The recent examples are numerous [68]. Metallic complexes have also been extensively grafted or tethered to the inner walls of zeolites or mesoporous silicas such as MCM-41 [48, 49, 69]. Polymers are more amenable to synthetic modifications in order to introduce potential ligands such as phosphines or amines as side arms, hence they have been used widely as immobilizers for homogeneous catalysts, but this is beyond the scope of this chapter. Metal complexes tethered onto active carbon are far less numerous. However, Silva *et al.*, for example, successfully immobilized on a modified carbon support complexes that could even be chiral [70–73], such as manganese(III) *salen* species, for applications in (enantioselective) epoxidation. The synthetic strategy involved first increasing the number of oxygenated surface groups by oxidation, then building a pendant ligand by grafting of organic fragments onto it, and introducing the metallic moiety on its dangling end in a last step. Finally, examples of tethered clusters are also very scarce. A recent example involves the anchoring of $[\text{Co}_4(\text{CO})_{10}(\text{dppa})]$ ($\text{dppa} = (\text{Ph}_2\text{P})_2\text{NH}$) onto the mesoporous silica SBA-15 modified with the chelating phosphine ligand $(\text{Ph}_2\text{P})_2\text{N}(\text{CH}_2)_3\text{Si}(\text{OMe})_3$ [74].

8.7

Concluding Remarks

In this chapter, we have shown that by using concepts of organometallic chemistry applied to the reactivity of surfaces, it is possible to build supported metal-containing species in a controlled manner. These range

from mononuclear complexes to molecular clusters, and can be immobilized onto the support by simple physisorption, by direct reaction with oxygenated surface groups, by entrapment within the pores, or by tethering to dangling organic groups. Moreover, they are still amenable to further modifications, such as ligand fine tuning, or a set of thermal treatments in order to produce well-defined supported nanoparticles of known composition. The obtained nanostructured catalysts find a variety of applications in oxidation as well as in hydrogenation catalysis. However, few of these materials are industrially viable yet, for economical or environmental reasons. Their stability is often an issue and major leaching problems have been reported. This has been addressed by various authors recently, and very stable grafted species, even in oxidative conditions, have appeared. In addition, the sophisticated synthetic procedures are long and tedious, and the degree of perfection of the obtained materials has sometimes been overestimated. Characterization relies heavily on EXAFS, which only gives an average picture. It is very likely that in most cases there is not a single type of structure on the surface, and it is not possible to purify if several different complexes are present. The expected higher costs of catalysts based on organometallic compounds will be accepted if improved performance in prolonged use is demonstrated. To reach this goal further research in this promising area is needed.

References

1. Zhuravlev, L.T. (2000) *Colloids Surf. A: Physicochem. Eng. Aspects*, **173**, 1.
2. Busca, G. (1999) *Phys. Chem. Chem. Phys.*, **1**, 723.
3. Hanssen, R.W.J.M., van Santen, R.A. and Abbenhuis, H.C.L. (2004) *Eur. J. Inorg. Chem.*, 675.
4. Auer, E., Freund, A., Pietsch, J. and Tacke, T. (1998) *Appl. Catal., A*, **173**, 259.
5. Ahmadpour, A. and Do, D.D. (1996) *Carbon*, **34**, 471.
6. Moreno-Castilla, C. and Rivera-Utrilla, J. (2001) *MRS Bull.*, **26**, 890.
7. Polania, A., Papirer, E., Donnet, J.B. and Dagois, G. (1993) *Carbon*, **31**, 473.
8. Boehm, H.P. (1994) *Carbon*, **32**, 759.
9. Boehm, H.-P. (1966) *Angew. Chem. Int. Ed.*, **5**, 533.
10. Muettterties, E.L. (1977) *Science*, **196**, 839.
11. Dyson, P.J. (2004) *Coord. Chem. Rev.*, **248**, 2443.
12. Süß-Fink, G. and Meister, G. (1993) *Adv. Organomet. Chem.*, **35**, 41.
13. Braunstein, P. and Rosé, J. (1995) in *Comprehensive Organometallic Chemistry II* (eds E.W. Abel, F.G.A. Stone and G. Wilkinson), Elsevier, Amsterdam, Chapter 7, 10, p. 351.
14. Braunstein, P. and Rosé, J. (1999) in *Metal Clusters in Chemistry* (eds P. Braunstein, L.A. Oro and P.R. Raithby), Wiley-VCH Verlag GmbH, Weinheim, Vol. 2, p. 616.
15. Ugo, R. and Psaro, R. (1983) *J. Mol. Catal.*, **20**, 53.
16. Lewis, L.N. (1993) *Chem. Rev.*, **93**, 2693.
17. Gates, B.C. (1995) *Chem. Rev.*, **95**, 511.
18. Ichikawa, M. (1992) *Adv. Catal.*, **38**, 283.
19. White, M.G. (1993) *Catal. Today*, **18**, 1.
20. Gates, B.C., Guzzi, L. and Knözinger, H. (1986) *Stud. Surf. Sci. Catal.*, **29**, 1.
21. Alonso-Vante, N. (2006) *Fuel Cells*, **6**, 182.

22. Nashner, M.S., Frenkel, A.I., Adler, D.L., Shapley, J.R. and Nuzzo, R.G. (1997) *J. Am. Chem. Soc.*, **119**, 7760.
23. Nashner, M.S., Frenkel, A.I., Somerville, D., Hills, C.W., Shapley, J.R. and Nuzzo, R.G. (1998) *J. Am. Chem. Soc.*, **120**, 8093.
24. Schweyer-Tihay, F., Estournès, C., Braunstein, P., Guille, J., Paillaud, J.-L., Richard-Plouet, M. and Rosé, J. (2006) *Phys. Chem. Chem. Phys.*, **8**, 4018.
25. Behrens, S. and Spittel, G. (2005) *Dalton Trans.*, 868.
26. Ozkaya, D., Zhou, W., Thomas, J.M., Midgley, P., Keast, V.J. and Hermans, S. (1999) *Catal. Lett.*, **60**, 113.
27. Raja, R., Sankar, G., Hermans, S., Shephard, D.S., Bromley, S., Thomas, J.M., Johnson, B.F.G. and Maschmeyer, T. (1999) *Chem. Commun.*, 1571.
28. Hermans, S., Raja, R., Thomas, J.M., Johnson, B.F.G., Sankar, G. and Gleeson, D. (2001) *Angew. Chem. Int. Ed.*, **40**, 1211.
29. Raja, R., Khimyak, T., Thomas, J.M., Hermans, S. and Johnson, B.F.G. (2001) *Angew. Chem. Int. Ed.*, **40**, 4638.
30. Jones, M.D., Duer, M.J., Hermans, S., Khimyak, Y.Z., Johnson, B.F.G. and Thomas, J.M. (2002) *Angew. Chem. Int. Ed.*, **41**, 4726.
31. Chandler, B.D., Schabel, A.B. and Pignolet, L.H. (2000) *J. Catal.*, **193**, 186.
32. Nashner, M.S., Somerville, D.M., Lane, P.D., Adler, D.L., Shapley, J.R. and Nuzzo, R.G. (1996) *J. Am. Chem. Soc.*, **118**, 12964.
33. Kozlov, A.I., Kozlova, A.P., Liu, H. and Iwasawa, Y. (1999) *Appl. Catal., A: Gen.*, **182**, 9.
34. Basset, J.-M., Lefebvre, F. and Santini, C. (1998) *Coord. Chem. Rev.*, **178–180**, 1703.
35. Fierro-Gonzalez, J.C., Kuba, S., Hao, Y. and Gates, B.C. (2006) *J. Phys. Chem. B*, **110**, 13326.
36. Roberto, D., Cariati, E., Pizzotti, M. and Psaro, R. (1996) *J. Mol. Catal. A: Chem.*, **111**, 97.
37. Tada, M. and Iwasawa, Y. (2003) *J. Mol. Catal. A: Chem.*, **204–205**, 27.
38. Choplin, A. and Quignard, F. (1998) *Coord. Chem. Rev.*, **178–180**, 1679.
39. Iwasawa, Y. (1997) *Acc. Chem. Res.*, **30**, 103.
40. Guzman, J. and Gates, B.C. (2003) *Dalton Trans.*, 3303.
41. Psaro, R. and Recchia, S. (1998) *Catal. Today*, **41**, 139.
42. Cariati, E., Roberto, D., Ugo, R. and Lucenti, E. (2003) *Chem. Rev.*, **103**, 3707.
43. Alexeev, O. and Gates, B.C. (2000) *Top. Catal.*, **10**, 273.
44. Gates, B.C. (2000) *J. Mol. Catal. A: Chem.*, **163**, 55.
45. Ugo, R., Dossi, C. and Psaro, R. (1996) *J. Mol. Catal. A: Chem.*, **107**, 13.
46. Corma, A. and Garcia, H. (2004) *Eur. J. Inorg. Chem.*, 1143.
47. Herron, N. (1986) *Inorg. Chem.*, **25**, 4714.
48. Arends, I.W.C.E. and Sheldon, R.A. (2001) *Appl. Catal., A: Gen.*, **212**, 175.
49. Sheldon, R.A., Arends, I.W.C.E. and Lempers, H.E.B. (1998) *Catal. Today*, **41**, 387.
50. Parton, R.F., Vankelecom, I.F.J., Casselman, M.J.A., Bezoukhanova, C.P., Uytterhoeven, J.B. and Jacobs, P.A. (1994) *Nature*, **370**, 541.
51. Balkus, K.J. Jr., Khanamedova, A.K., Dixon, K.M. and Bedioui, F. (1996) *Appl. Catal., A: Gen.*, **143**, 159.
52. Yang, H., Zhang, L., Su, W., Yang, Q. and Li, C. (2007) *J. Catal.*, **248**, 204.
53. Jin, C., Fan, W., Jia, Y., Fan, B., Ma, J. and Li, R. (2006) *J. Mol. Catal. A: Chem.*, **249**, 23.
54. Salama, T.M., Ahmed, A.H. and El-Bahy, Z.M. (2006) *Microporous Mesoporous Mater.*, **89**, 251.
55. Połtowicz, J., Pamin, K., Tabor, E., Haber, J., Adamski, A. and Sojka, Z. (2006) *Appl. Catal., A: Gen.*, **299**, 235.
56. Ferreira, R., García, H., de Castro, B. and Freire, C. (2005) *Eur. J. Inorg. Chem.*, 4272.
57. Salavati-Niasari, M. (2006) *Microporous Mesoporous Mater.*, **95**, 248.
58. Salavati-Niasari, M. and Bazarganipour, M. (2006) *Catal. Commun.*, **7**, 336.

59. Mukai, S.R., Shimoda, M., Lin, L., Tamon, H. and Masuda, T. (2003) *Appl. Catal., A: Gen.*, **256**, 107.
60. Sheu, L.L., Knozinger, H. and Sachtler, W.M.H. (1989) *Catal. Lett.*, **2**, 129.
61. Zhang, Z.C. and Sachtler, W.M.H. (1991) *Polyhedron*, **10**, 673.
62. Xiao, F.S., Xu, R.R.X. and He, Y.N. (1997) *React. Kinet. Catal. Lett.*, **61**, 383.
63. Brabec, L. and Nováková, J. (2001) *J. Mol. Catal. A: Chem.*, **166**, 283.
64. Weber, W.A., Phillips, B.L. and Gates, B.C. (1999) *Chem. Eur. J.*, **5**, 2899.
65. Brabec, L. (2001) *J. Mol. Catal. A: Chem.*, **169**, 127.
66. Gates, B.C. (1996) *Stud. Surf. Sci. Catal.*, **100**, 49.
67. Valkenberg, M.H. and Hölderich, W.F. (2002) *Catal. Rev.*, **44**, 321.
68. Likhar, P.R., Roy, S., Roy, M., Kantam, M.L. and De, R.L. (2007) *J. Mol. Catal. A: Chem.*, **271**, 57.
69. Anwender, R. (2001) *Chem. Mater.*, **13**, 4419.
70. Silva, A.R., Martins, M., Freitas, M.M.A., Figueiredo, J.L., Freire, C. and de Castro, B. (2004) *Eur. J. Inorg. Chem.*, 2027.
71. Silva, A.R., Figueiredo, J.L., Freire, C. and de Castro, B. (2005) *Catal. Today*, **102**, 154.
72. Jarrais, B., Silva, A.R. and Freire, C. (2005) *Eur. J. Inorg. Chem.*, 4582.
73. Silva, A.R., Budarin, V., Clark, J.H., de Castro, B. and Freire, C. (2005) *Carbon*, **43**, 2096.
74. Schweyer-Tihay, F., Braunstein, P., Estournès, C., Guille, J.L., Lebeau, B., Paillaud, J.-L., Richard-Plouet, M. and Rosé, J. (2003) *Chem. Mater.*, **15**, 57.

9

Shaping of Solid Catalysts*Bettina Kraushaar-Czarnetzki and Steffen Peter Müller*

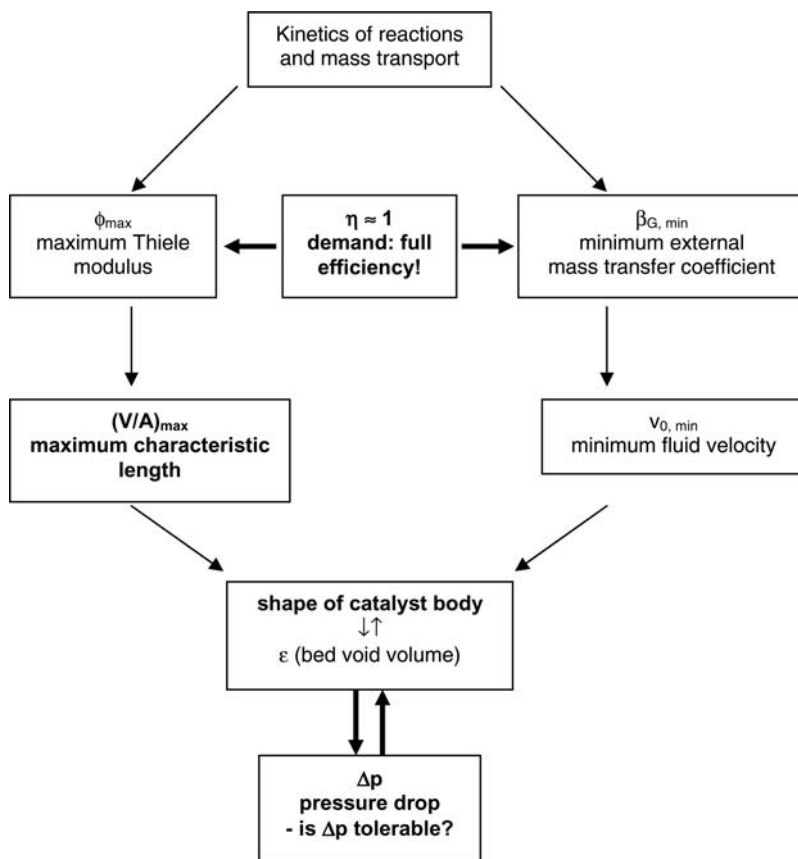
9.1

Objectives of Catalyst Shaping

What makes the difference between a research catalyst sample and an industrial catalyst? Obviously, industrial catalysts are shaped bodies with appearances varying from tiny, fluidizable spheres up to large monolithic blocks, and they are manufactured on a large scale. We assume that the essential ingredients and the related nature of the catalytically active surfaces are identical in research catalysts and industrial catalysts. However, this is not entirely true as can be illustrated by the comparison of, for instance, pips with fruit (engineered by nature), or of starch with noodles (engineered by human): the superimposed macrostructure contains additional substances or phases and serves for preservation, stabilization, easy handling, and transportation of the essential ingredient.

Shaping of catalysts has similar purposes and is, of course, linked to the desired functions of a specific catalyst that, in turn, unfold in a chemical reactor, only. This is why this chapter is primarily organized along the intended reactor operation and the corresponding catalyst requirements rather than by a systematic treatment of the various shaping technologies. We distinguish between fixed-bed, moving-bed, and fluidized-bed reactors, whereby the latter include slurry- and ebullated-bed reactors for (G)/L/S (S = catalyst) processes.

Fixed-bed reactors are most convenient with respect to design and operation, but their applicability is limited by the pressure drop along the catalyst packing, and by the efficiency of radial heat removal or supply, both of which are properties strongly influenced by the structure of the catalyst bed. Size and shape of a catalyst are also decisive for the avoidance of internal (in porous catalysts) and external mass transport limitations, and for heat transfer. Actually, aiming for a catalyst efficiency of $\eta \approx 1$ should be a primary demand in catalyst design because conversion, selectivity, and thermal stability are strongly affected by transport resistances. The internal mass transport, that is, the diffusion in porous catalysts, can be enhanced by furnishing the catalyst with larger pores. However, this is possible to a limited extent, only, since



Scheme 9.1 Scheme for the estimation of size and shape of fixed-bed catalysts.

increasing pore sizes negatively affect the mechanical stability. A stronger tool represents the choice of the characteristic length of the active material in terms of V/A (V = pellet volume, and A = external surface area). As indicated in Scheme 9.1, the demand for $\eta \approx 1$ also implies a minimum fluid velocity to avoid external transport resistances. Finally, the shape of the catalyst, which influences the bed porosity ε , should be designed such that the pressure drop along the catalyst bed is tolerable at the characteristic length V/A and the fluid velocity v_0 required for the exclusion of mass-transfer resistances. Sometimes, these requirements cannot be met with bulk catalysts. In such cases, the option of fixed-bed operation can be maintained only, if the catalytically active material is employed as a thin layer on large, inert, and nonporous particles (egg-shell catalysts), or on monolithic carriers such as honeycombs or foams. The even distribution of the catalyst coating and its integrity under thermal and mechanical stress represents a major challenge in these systems. In any case, fixed-bed catalysts have to resist the static and dynamic pressure in the reactor, and

attrition during loading, discharge, and possible vibrations upon operation of the reactor. The crush and attrition strengths are linked to the porosity of the catalyst body and to the materials employed, that is, the strength of adhesive forces and/or the degree of crosslinking between the particles forming the body.

The requirements for moving-bed catalysts are basically the same as those for fixed-bed systems. However, there is no choice of the shape because moving-bed particles must be spherical. In addition, crush and attrition strengths need to be higher.

Catalysts for fluidized-bed reactors have to be spherical as well. The appropriate particle size fraction for gas–solid systems can be estimated after Geldart [1] from the density difference between solid and gas. Most widely used catalysts for fluidized beds and risers are Geldart-type B powders with particle diameters ranging from 40 to 500 μm or solid densities between 1.4×10^3 and $4 \times 10^3 \text{ kg/m}^3$, respectively. When fluidization is provided by a liquid as in ebullated-bed reactors, the particle sizes may be substantially larger because of the higher buoyancy in these systems. However, all types of fluidized-bed catalysts must exhibit high mechanical stability because they are exposed to abrasion on reactor walls and internals, collisions between particles and shear forces exerted by the surrounding fluid.

In summary, the following aspects have to be taken into account upon formulation and shaping of solid catalysts through appropriate choice of materials, catalyst size, and shape, and by applying a suitable manufacturing technique:

- avoidance of negative effects of materials used (carriers, binders, solvents, or formulation additives) on the intrinsic activity, selectivity, and stability of the active material;
- provision of sufficient active surface area;
- avoidance of external and, in case of porous catalysts, internal mass-transfer resistances;
- avoidance of high pressure drops (in fixed and moving beds);
- realization of thermal resistance against, for instance, fracture, sintering, phase transition;
- adjustment of mechanical resistance against crushing and attrition;
- ensuring high effective heat conductivity in fixed and moving beds used for strongly exo- or endothermic reactions.

The first point in the list above does not mean that carriers, binders, or formulation aids must be nonreactive. Rather, there are applications in which a self-activity of these materials is desired. For instance, in hydrocracking and fluidized catalytic cracking, mesoporous matrices with acidic properties are employed to promote bottom cracking of heavy feed components that cannot penetrate the small pores of the embedded zeolite. It is important to find out whether the chemical nature of additives and materials used to shape active sites is beneficial or detrimental for the overall performance of the final catalyst body at the conditions of the catalyzed process.

Obviously, the purposeful design of a technical catalyst requires not only experience in the area of catalysis, but also knowledge about reactor and process, kinetics of reactions and transport processes, and about hydrodynamics. Finally, the realization of a design concept needs support from various disciplines in thermal and mechanical process engineering. It is said that there is a lot of art in catalyst shaping. This statement ignores the fact that the underlying principles and mechanisms, for instance in the areas of agglomeration, rheology, drying, and sintering have been investigated for decades, albeit in different contexts. We anticipate that significant progress will be made in catalytic processing, if the shaping of catalysts were to become – more than it is currently – a topic of interdisciplinary effort.

Sections 9.2 and 9.3 deal first with the shaping of fixed-bed catalysts. In industrial practice, three types of catalytic fixed beds are applied: particle beds, monolithic packings, and layers of gauzes. Gauzes consist of highly active alloys of precious metals and are employed in extremely rapid and exothermic reactions like the Ostwald and Andrussow processes. They are manufactured through knitting or weaving of metal wires, both of which are techniques that need no further explanation. The following sections will focus on the shaping of particles (Section 9.2) and monolithic packings (Section 9.3). Figure 9.1 shows a small selection comprising spheres, foams, and a honeycomb. Monolithic honeycombs and foams are mostly employed as nonreactive carriers that are furnished with a coating of the catalytic material. In particles, however, the catalyst typically is distributed over the entire, porous bulk. Catalytic coatings or shells are generated only, if diffusional transport resistances need to be avoided. Finally, in Sections 9.4 and 9.5 we present shaping for moving-bed and fluidized-bed catalysts, respectively.

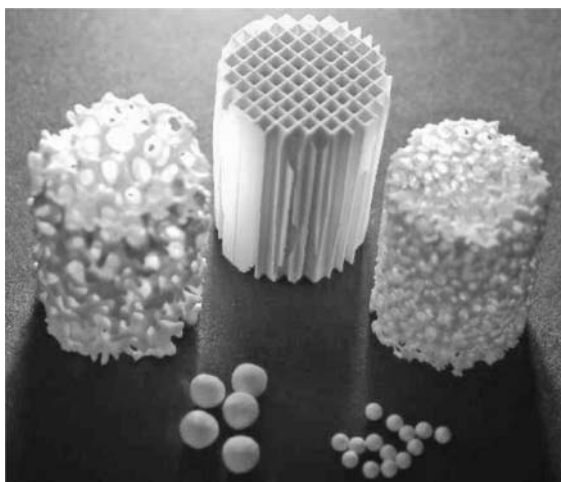


Figure 9.1 Shapes of fixed-bed catalysts and carriers: foams with 20 and 45 ppi, a 400-psi honeycomb, and spheres with diameters of 3.3 and 1.5 mm.

9.2

Fixed-Bed Reactors – Particle Beds

Most catalytic reactors in refining and chemical processes comprise of fixed beds filled with granular catalysts. As a rule of thumb, the diameters of the particles in fixed beds should not be smaller than 1–2 mm to avoid high pressure drops. In addition to the size, the shape is important because it affects the bed porosity ε . Packings of uniform spheres exhibit a voidage between 0.35 and 0.4, but the value will be substantially lower, if the bed consists of mixed particles with different diameters. Beds of Raschig rings have voidages from 0.5 to 0.8 depending on the wall thickness, and cylindrical particles yield bed porosities of 0.3 to 0.35 [2]. By means of extrusion it is possible to produce many other shapes, for instance, helices of two or three adjacent strings, which yield considerably higher bed porosities and, hence, smaller pressure gradients than conventional cylinders of the same size. Other techniques allow little variation in the shapes produced.

9.2.1

Pelleting

Pelleting is a high-pressure agglomeration technique producing particles, usually short cylinders, with high shape accuracy. Typically, the dry catalyst powder is compressed in a die by applying forces between 50 and 80 kN with a punching tool. Both the controlled charging of the die and the subsequent compaction are best accomplished with fluidizable, weakly preagglomerated powder particles. Sometimes, small amounts of liquid or solid additives are used to prevent dust formation and to promote compaction by lubrication; such additives are, for example, water, graphite, talc, stearic acid, waxes, and greases [3, 4]. Furthermore, binders may be added to enhance the mechanical stability after compression. For instance, starch is used as a binder to stabilize active carbon pellets.

For research purposes, pelleting is usually carried out batchwise in so-called reciprocating single punch-and-die presses. In large-scale production, however, continuously runned rotary machines are employed. High outputs are realized by a series of dies with upper and lower punches. Figure 9.2 shows such a rotary press together with an upper and a lower punch. After filling of the die with powder, the punches are moved together. If needed, the punches remain in the closed position for a certain time (dwell time) to achieve maximum compaction. Finally, one punch is withdrawn, and the other ejects the pellet.

Important processing parameters are the maximum pressure and the rate of the pressure rise, both of which influence not only the hardness of the pellet produced, but also the integrity of the compacted particles inside. It is intended that agglomerates undergo deformation, breakdown,

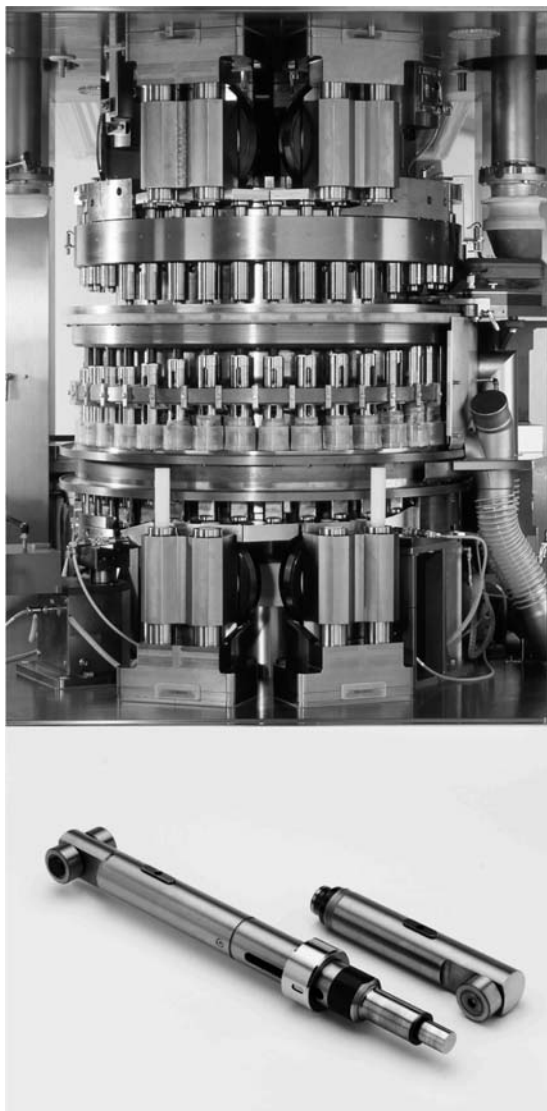


Figure 9.2 Rotary press (top) and punches (bottom) for pelleting. (Courtesy of FETTE GmbH.)

and compaction. However, the process may also cause crushing of crystals, shifting of crystal planes, and other effects of high mechanical stress. A further disadvantage of pelleting, and, actually a consequence of the foregoing, comprises the fact that porosity and pore texture of the final products can hardly be controlled as these properties depend on the pressure required to form stable bodies. Porosities can be as low as 5%, and it is difficult to



Figure 9.3 Examples of catalyst particles shaped by means of pelleting. (Courtesy of FETTE GmbH.)

maintain values above 30% [3]. Figure 9.3 shows, however, that it is possible to press catalyst pellets with structured perforations such that mass transfer of reactants can proceed over an enlarged external surface.

9.2.2 Granulation

Granulation is size enlargement by wet tumbling-growth agglomeration. A cohesive liquid is sprayed onto the catalyst powder such that the wetted particles stick together. The granules grow by contacting further particles like a rolling snowball. In the first instance, adhesion between the particles in the granules is caused by capillary forces only. If the sprayed liquid contains substances that can undergo hydrolysis and condensation reactions (e.g. alkoxides) or gelation (destabilized sols, macromolecular organics), the granules can be stabilized through crosslinking of these binders. Inorganic binders provide more sustainable mechanical strength, but typically reduce the pore size of the granules. Organic binders, on the other hand, have to be burned out after shaping, and the resulting granules are mechanically weak.

An early granulation technique for catalysts is pan granulation, yielding beads of nearly spherical shape with diameters between 2 and 20 mm (Figure 9.4). A pan granulator consists of a round dish with a rim rotating around an inclined axis, equipped with a device for feeding catalyst powder onto the dish, and a device for spraying the liquid. Rotation of the inclined pan enforces rolling of the wetted particles on the surface. The granules grow layer by layer through take-up of other particles. However, collisions with the scraper, the rim, or with other agglomerates may also cause deformation or disintegration. The “green” granules are discharged continuously by centrifugal forces and exhibit a broad size distribution that depends on the



Figure 9.4 Examples of catalyst particles shaped by means of pan granulation. (Courtesy of CeramTec AG.)

residence-time distribution. The latter, in turn, is varied through the rotation speed and the inclination angle of the dish. The green bodies still contain all the moisture and need to be dried and calcined in separate devices.

Today, most granules are produced in so-called mixer agglomerators [3]. These devices are usually operated batchwise. The underlying principle is the same as in pan granulation, however, movement of the moist particles is forced by a mixing tool. In addition, the vessel may rotate in the opposite direction as shown in Figure 9.5. The application of blades or scrapers not only avoids clagging of moist material at the walls of the vessel, but also ensures that weak granules are destroyed by attrition.

Some granulators enable combined agglomeration and drying. An example is shown in Figure 9.6. Here, the granules are moved by a rotating disc at the bottom and a hot gas flow coming up along the walls of the chamber. Some granulators are more suitable for the production of small spheres for

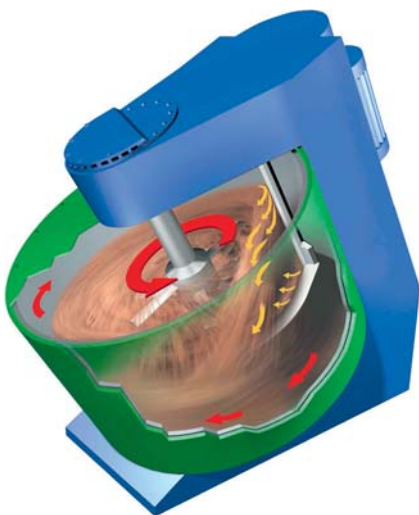


Figure 9.5 Mixer agglomerator. (Courtesy of Maschinenfabrik Gustav Eirich GmbH & Co. KG.)

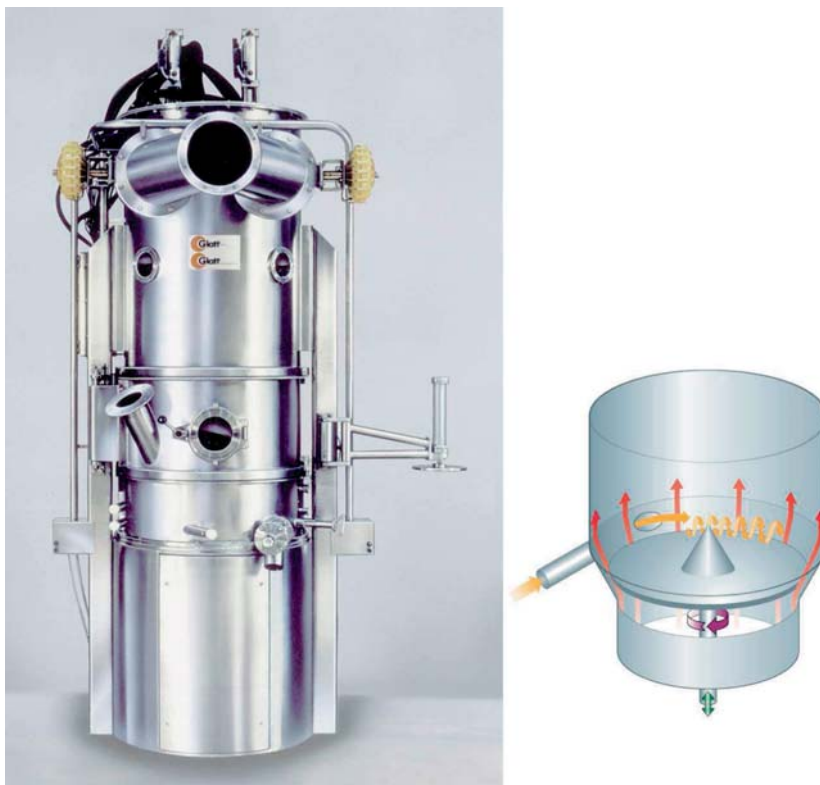


Figure 9.6 Hot-gas granulator. (left) view of the apparatus and (right) scheme of solids movement and gas flow. (Courtesy of Glatt GmbH.)

fluidized catalysts, others for fixed or moving-bed particles of a few millimeters diameter, or for the coating of bodies to produce egg-shell catalysts.

9.2.3

Extrusion

Extrusion is the most widely used technique for the shaping of fixed-bed catalysts or carriers. The principle looks simple: a highly filled suspension or paste is passed through a profiled die that determines the shape of the green body. High pressures may be required for transport and deformation of the viscous paste in the die. Other than in pelleting, however, the effect of the extrusion pressure on the compaction is small because the particles are suspended in a liquid. Indeed, one of the great advantages of extrusion is the flexibility with respect to the porosity of the finished product. For instance,

through adjustment of the liquid/solid ratio in the extrusion paste, it is possible to vary the porosity between about 30 and 60% [3, 5–7].

The complete process includes the following steps: (1) mixing and kneading of the solid precursors with liquid (usually water), and, if applicable, with additives (e.g. plasticizers, peptizing agents), (2) degassing and extrusion to strings that are cut into suitable lengths by a cutting device mounted at the extruder, (3) drying of the green bodies, and (4) firing.

Step (2) is realized in either screw (= auger) or piston extruders. Screw extruders can be run continuously. The paste is transported along the axis of a so-called barrel by one (single-shaft), two (twin-shaft), or more (multiple-shaft) screws that, in the latter cases, are operated in counter-rotating or corotating mode. Figure 9.7 shows a cutaway view of a single-shaft auger extruder with a die suitable to produce a bunch of cylindrical extrudates. Some screw extruders are additionally equipped with a mixer shaft upflow to the auger, such that mixing of the ceramic paste and its transport to the die can be realized in a single machine [8, 9]. Piston extruders, in contrast, are charged batchwise. The feed has to be prekneaded in a separate mixer device. Nevertheless, piston extrusion has several advantages. For instance, very high press forces can be generated, allowing for extrusion of pastes with low moisture content and high compaction. Furthermore, laminations caused by the auger rotation in screw extruders can be avoided. For catalyst and carrier extrusion, in particular, an important advantage of piston extrusion comprises the much lower shear stress. This has two consequences: (i) the degree of contamination through abrasion of material from the barrel and die is negligible and (ii) the size distribution of the ceramic particles in the paste, once adjusted in the separate kneading device, remains unchanged upon extrusion.

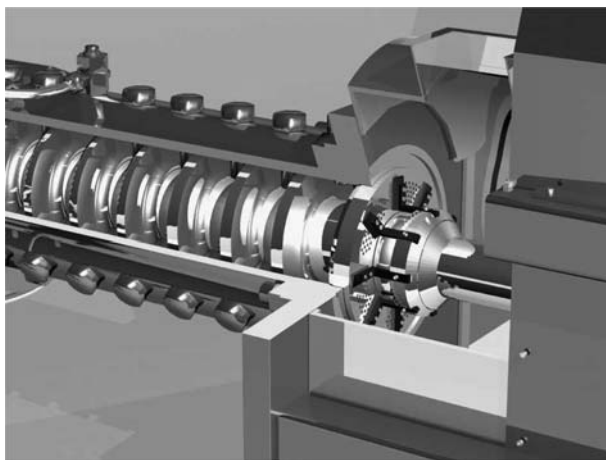


Figure 9.7 Single-screw extruder. (Courtesy of Amandus Kahl GmbH & Co. KG.)

The latter aspect brings us back to step 1 of the extrusion process. Mixing should not be taken laxly because it is the most important stage of conditioning in extrusion [10, 11]. The transformation of solid and liquid ingredients into a paste with suitable rheological properties is usually accompanied by mechanical and surface-chemical changes. The size of the powder particles may be reduced substantially under the action of shear forces, which results in smaller pore sizes of the finished product (see also Section 9.2.4). Deagglomeration is also induced by change of the paste's pH to values far from the isoelectric point (peptization) [12]. Adsorbed protons or hydroxyl ions, respectively, furnish the particles with surface charges that, in turn, cause electrostatic repulsion. Size, shape, and electrokinetic properties of the solids definitely have a strong effect on plasticity and flow behavior. Of course, these crucial rheological properties can also be altered on purpose to some extent. The apparent viscosity, for instance, strongly decreases with increasing volumetric ratio liquid/solid in the paste, and the plasticity can be improved by addition of so-called plasticizers, which are typically organic network-forming polymers, for example, derivatives of cellulose or polyalcohols [5, 11, 13]. Nevertheless, flow of suspensions is characterized by strong non-Newtonian shear-rate- and time-dependent deviations of the viscosity. In addition, wall slip behavior or effects of gelation and aging of paste ingredients may play a role [8–12, 14]. The present understanding of the flow of suspensions is not yet sufficient to predict extrusion behavior from rheological data, or to advise on exact and quantitative measures to improve the extrusion process.

After passing the die, the extruded strings are cut into bodies of specified lengths with a rotating blade or a fine wire. Green extrudates are fragile because the precursor particles stick together by adhesive and capillary forces only, like in a sand castle. Mechanical strength is provided during calcination or firing (step 4) through formation of solid-state bridges between the particles in the extrudate. Crosslinking between particles can be achieved either by condensation of surface hydroxyls, yielding oxygen bridges, or by sintering. However, many catalysts or catalyst precursors do not exhibit suitable surface hydroxyl groups, or they are sensitive toward thermally induced structural changes. Therefore, extrusion as well as many other shaping processes requires the addition of inorganic binders that can undergo interparticle crosslinking at temperatures sufficiently low to avoid damage of the catalytically active material. Most widely used binders in industrial catalyst extrusion are hydrated or hydroxide forms of alumina and of silica-alumina [3, 5, 10–12, 14, 15]. Upon calcination at 500–600 °C, these binders transform into strong, porous matrices of interconnected oxidic particles embedding the catalyst particles. Of course, calcination in air also results in the burnout of organic additives like plasticizers.

9.2.4

Tailoring of the Pore-Size Distribution

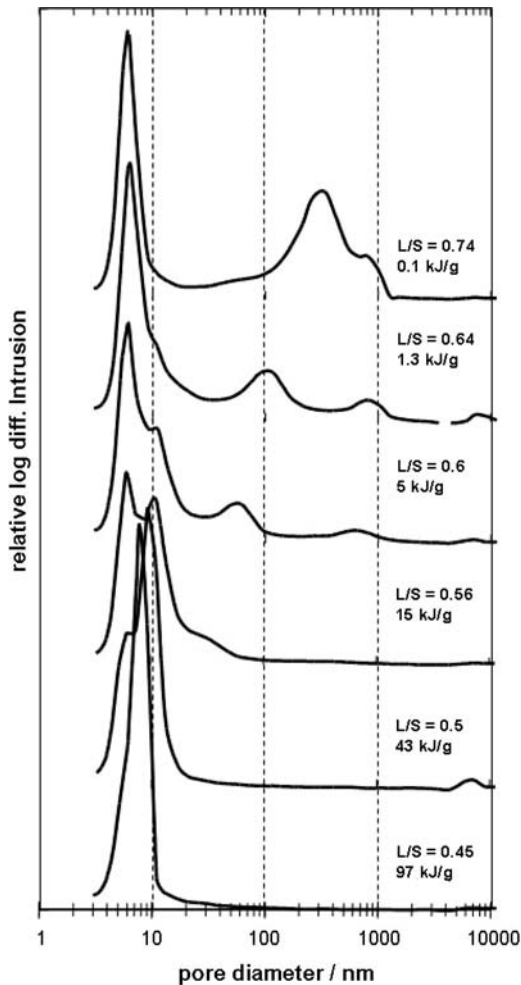
The foregoing sections have shown that all catalyst-shaping technologies are based on size enlargement through dry or wet agglomeration of small particles. Unless complete compaction has been carried out, for example, by means of sintering or recrystallization, the small particles are connected by distinct points of contact to next neighbors and form a porous packing. For a dense packing of spherical particles of equal size (D_{sphere}), the hydraulic diameter of the voids can be calculated according to Equation 9.1:

$$D_{\text{hydraulic}} = \frac{2}{3} \cdot \frac{\varepsilon}{1 - \varepsilon} \cdot D_{\text{sphere}} \quad (9.1)$$

With a typical value of the porosity (ε) of $\varepsilon = 0.363$, the resulting hydraulic diameter becomes $0.38 \times D_{\text{sphere}}$. In shaped catalyst or carrier bodies, porosities may be substantially higher because of lower packing densities and/or diverging particle morphologies. Nevertheless, it is obvious that the use of small particles generates small voids, whereas the formation of large mesopores ($2 \text{ nm} < d < 50 \text{ nm}$) or macropores ($d > 50 \text{ nm}$) requires agglomeration of at least a major portion of large particles.

Mostly, large catalyst or binder particles are agglomerates by themselves. Many alumina-based binders, for instance, are purchased in the form of spray-dried powders. An example is Pural SB (Sasol), a widely used pseudo-boehmite ($\text{AlO}(\text{OH}) \cdot x \text{H}_2\text{O}$) powder. The agglomerates have a mean diameter of $45 \mu\text{m}$ and consist of particles with 50 nm diameter. A controlled breakdown of the agglomerates allows for the adjustment of the pore-size distribution. In extrusion, for instance, the breakdown of agglomerates can be achieved during kneading of the paste. If the mixer is equipped with a device for monitoring the mechanical energy input (e.g. measurement of the torque at the rotors), it is possible to adjust in a reproducible way the particle size of the binder and, hence the pore-size distribution in the finished extrudates [5, 6]. Figure 9.8 shows mercury intrusion plots of calcined extrudates produced with Pural SB. At a low energy input during mixing (top) it is possible to preserve many large agglomerates, and a bimodal pore-size distribution with meso- and macropores is obtained. With increasing input of mechanical energy, the size of the agglomerates is reduced until only primary particles with $\varnothing = 50 \text{ nm}$ are left, which give rise to a mean pore diameter of 8 nm (Figure 9.8, bottom plot) in the finished extrudates.

Recently, a novel type of binder for catalyst shaping has been identified that allows for tailoring of the pore-size distribution in a different way. The material is an amorphous aluminum phosphate hydrate (APH) available as a powder, which is employed like conventional binders, for instance, in extrusion. In contrast to conventional particulate binders, however, calcination at 500°C transforms APH via water evaporation, viscous sintering, and a phase transition into a dense, crystalline phase with the structure of tridymite.

**Figure 9.8**

Mercury-intrusion plots of calcined alumina extrudates; from the top to the bottom, the specific mechanical energy input during mixing of the pastes was increased; L/S is the ratio liquid to solid in the extrusion paste.

If zeolite crystals or other refractory particles are present, a pore structure evolves, formed by the embedded particles and the sinter necks of the AlPO_4 matrix in between. Here, the pore-size distribution can be tailored through choice of both, the size of the embedded particles and their relative amount in the shaped bodies. Other than with particulate binders, the coformation of small mesopores can be avoided, and macropores in a narrow, monomodal size distribution can be realized [7].

For many catalytic applications, it may be desirable to furnish catalysts or carriers with a high portion of macropores to enhance diffusional transport of reactants. Unfortunately, the mechanical strength of the bodies decreases with increasing porosity and with increasing size of the powder particles employed [5, 7]. For an agglomerated body composed

of equal-sized spheres, Rumpf [16] showed that the tensile strength σ amounts to

$$\sigma = \frac{9}{8} \left(\frac{1 - \varepsilon}{\pi D_{\text{sphere}}^2} \right) N \cdot F \quad (9.2)$$

where ε is the agglomerate porosity, F is the bonding force per point of contact, and N is the average number of points of contact between one sphere and its neighbors.

As an approximation, the coordination number is $N = \pi/\varepsilon$. The magnitude of F depends on the bonding mechanism. Van der Waals and attractive electrostatic forces are much weaker than chemical bonds, for example, formed by dehydroxylation. Most stable are agglomerates bound by solid bridges between the particles. For instance, agglomerates composed of spheres with 100 nm diameter exhibit tensile strengths between 0.1 and 100 N/cm², if these spheres are bound by van der Waals forces, but tensile strengths higher than 10 kN/cm² when the spheres are connected by solid bridges, for example, sinter necks [16]. If larger particles are used in order to obtain larger pores, the tensile strength is greatly reduced, for example, by two orders of magnitude, if the agglomerates consist of 1- μ m instead of 100-nm spheres. So, even if relatively strong bonding forces can be realized in a catalyst body, Equation 9.2 still holds, meaning that a compromise should be found between the requirements of low diffusional transport resistance of reactants and high mechanical strength. If this is not possible, the diffusional pathway can be reduced either by shaping smaller catalyst bodies or by producing egg-shell structures.

9.2.5

Fixed-Bed Egg-Shell Catalysts

It is possible to shape catalyst bodies, in which the catalytically active substances are not distributed over the complete bulk, but rather located in concentric areas. Many fluidized-bed catalysts, for instance, are spheres in which the active phase represents the core, and the shell is a porous, protective layer to prevent attrition. Bodies exhibiting the active phase in the core are denoted as egg-yolk catalysts. For fixed-bed applications, so-called egg-shell structures are more convenient, in which the catalytic material is located at the external surface, whereas the core is nonreactive.

The production of egg-shell structures for fixed-bed reactors follows two principles. As shown in Figure 9.9, one method comprises coating of a nonporous carrier, a preshaped ceramic body, with a catalyst powder by means of granulation (see Section 9.2.2). Coated carriers are generally more fragile than bulk catalysts. In particular, egg-shell catalysts granulated with organic binders can be used only once. After removal of the organic binder by burnout, collisions with other granules or with reactor internals cause cracking and

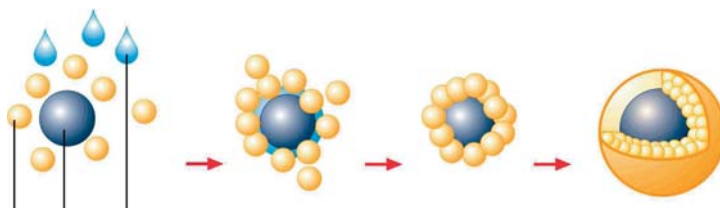


Figure 9.9 Formation of an egg-shell catalyst by means of granulation. (Drawing courtesy of Glatt GmbH.)

scale off of the shell. Therefore, such catalysts are calcined *in situ*, that is, in the catalytic reactor rather than prior to charging. Unloading of the spent catalyst bed, finally, will most likely destroy many of the egg-shell bodies.

Whenever catalysts are produced by impregnation of porous supports, it is possible to generate egg-shell, egg-yolk, or egg-white distributions of the active material through dynamic instead of equilibrium impregnation. Contact time, viscosity, surface tension, and concentration of the solution used for impregnation are adjusted to the size, porosity, and pore-size distribution of the catalyst body to achieve a gradient in penetration. Catalyst manufacturers have disclosed numerous patents on this topic that will not be cited here. Rather, we refer to a nice study including both systematic experiments and a theoretical model of impregnation reported by Galarraga *et al.* [17]. Gradients in the local distribution of active material on a porous support are also generated upon drying of the impregnated bodies [18] or by means of homogeneous deposition-precipitation [19]. Particularly sharp boundaries between the covered external support area and the uncovered core of a body can be realized by employing partial wetness impregnation with a hydrophobic liquid prior to impregnation with the aqueous precursor solution [20].

9.3 Fixed-Bed Reactors – Monoliths

9.3.1 Honeycombs

Honeycombs are monoliths with a multiplicity of parallel, straight channels. Like in natural honeycombs, the shape of the channel cross-sections, the so-called cells, may be hexagonal, but square, triangular, and sinusoidal cell shapes are more common in fabricated materials. Geometric features used to characterize honeycombs are the cell density expressed as cells per square inch (cps_i, in.⁻²), and the wall thickness (mm).

Honeycombs have been developed for catalytic treatment of exhaust gases from automotive and stationary sources. These catalysts must exhibit a low

pressure drop because they are exposed to high volumetric gas flows at low inlet pressures. In conventional honeycombs, the walls of the channels are smooth, and the flow along is laminar. Hence, diffusion is the governing mechanism of mass transport of reactants to the catalyst surface. The means to increase conversion is a greater specific surface area. This is achieved by increasing the cell densities. To overcome the concomitant rise in pressure drop, manufacturing techniques have been confined to reduce the wall thicknesses. Today, honeycombs can be produced with up to 1200 cpsi and wall thicknesses as low as 0.03 mm. However, typical substrates for autocatalysts exhibit 400 to 500 cpsi. The wall thicknesses in such substrates amount to about 0.15 mm in the case of ceramic and between 0.03 and 0.110 mm in metallic substrates [21–23]. The term substrate has been chosen on purpose because honeycombs have the function of carriers in car exhaust catalysts. Their channel walls have to be coated with a thin, porous support layer that is, finally, impregnated with the Pt catalyst and promoters.

Bulk honeycomb catalysts are used in stationary applications. An example is the selective catalytic reduction (SCR) of NO_x in exhaust gases of power plants and gas turbines. Stationary SCR catalysts are honeycombs consisting of porous V_2O_5 /anatase promoted by WO_3 or MoO_3 [24, 25]. Typical dimensions of a single SCR-honeycomb are a length of 0.85 m and a cross-section of $0.2 \text{ m} \times 0.2 \text{ m}$. Depending on the particulate concentration in the exhaust gas to be treated, cell densities are used between about 10 and 45 cpsi at wall thicknesses around 1 mm. Several honeycombs are combined in modules (Figure 9.10) that, in turn, are arranged in layers. Typically, three layers of modules are stacked on top of each other in one SCR reactor, arranged with an empty space in between to allow for flow redistribution.

9.3.1.1 Ceramic Honeycombs

The first thin-wall ceramic honeycombs were manufactured by wrapping of alternate layers of flat and corrugated sheets of a porous paper that were coated with small glass particles. Upon subsequent calcination in air, the paper preform burned off, and the glass particles were exposed to sintering and crystallization [26].

Nowadays, industrial manufacturing of ceramic honeycomb structures occurs exclusively by means of extrusion. Decisive for the discharge geometry is the design of the pressure head and die assembly in the extruder. Strings without channels can be formed with a simple die plate equipped with channels of the desired geometry. However, the shaping of multichannel extrudates such as honeycombs requires a more complicated pressure head to equalize the velocity profile in the paste before reaching the die inlet, and the die itself is a combination of core plate and exit frame. Here, the paste is first forced into a certain pattern, for example, rectangular, of holes in the core plate. At the end of the small channels in the core plate, the paste filaments reach the bottom of a slot array where they are spread sideways to fill the whole of the

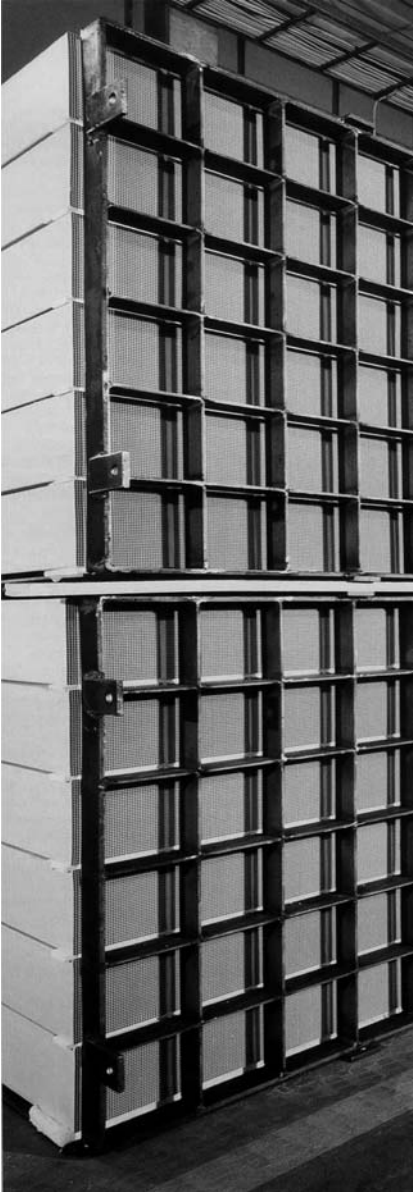


Figure 9.10 Stack of SCR honeycombs.

available slot area. The slots are arranged like the channel walls needed in the green body, and they have the same thickness. Finally, the green product leaves from the other side of the die and is cut into the suitable length. For a more comprehensive overview on extrusion equipment we refer to a recent monograph edited by Händle [9].

Extrusion is applicable to a broad variety of oxidic compounds, carbides, nitrides, and other materials. However, the vast majority of ceramic honeycombs is produced for automotive applications. These honeycombs are generally made of cordierite ($2 \text{ MgO} \cdot 2 \text{ Al}_2\text{O}_3 \cdot 5 \text{ SiO}_2$), a low-cost ceramic with a low coefficient of thermal expansion and a high melting temperature (1723 K). Honeycombs made of extruded cordierite were first introduced by Corning Inc. [27]. The typical precursor is a mixture of clay (kaolin), talc, and alumina. Viscous sintering of cordierite precursors starts at 1628 K with the melting of talc, which undergoes capillary drainage into the gaps between the surrounding particles. Cordierite is formed above 1673 K [28]. Sintering results in shrinkage and densification of the material. The resulting channel walls are no longer permeable although they still exhibit porosities typically between 35 and 40%. Since the stability of honeycombs toward thermomechanical stress is strongly reduced with decreasing extent of wall densification, it is desirable to further reduce porosities and to promote a high degree of pore shrinkage and microstructural evolution. Modern sintering technology may provide several tools to reach this goal. Important factors are, for instance, a high degree of compaction of the green preform and a good quality of the precursor particles, that is, the particles should be as small as possible in a narrow size distribution, and agglomeration should be avoided through adjustment of the pH value [29].

9.3.1.2 Metallic Honeycombs

The manufacturing of metallic honeycombs follows the same concept of wrapping of corrugated and flat strips as applied to the earliest ceramic honeycombs. Here, the strips are made of metal foil. The corrugated foils are formed by passing a pair of gearwheels; the shape of the teeth is usually sinusoidal or triangular. Figure 9.11 shows segments of four honeycombs with different cell densities, all of which are manufactured by winding around a single spindle. The substrate for preturbocharger applications depicted in

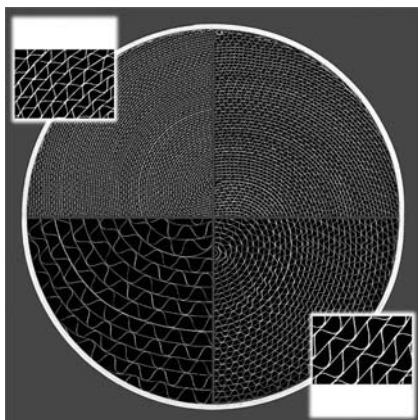


Figure 9.11 Segments of metallic honeycombs with 400–1200 cpsi. (Courtesy of EMITEC GmbH.)



Figure 9.12 S-shaped design of a metallic honeycomb used as a turbocharger. (Courtesy of EMITEC GmbH.)

Figure 9.12 is an example for an S-shaped design that is formed by wrapping the foils around two mandrels. These honeycombs are more robust toward thermal expansion, deformation and, in particular toward “telescoping,” the latter describing the axial displacement, that is, pushing out, of foil layers in the center of the honeycomb.

Many other modifications of the wrapping concept have been introduced, be it to reduce the consumption of metal foil by omitting the flat strips or to improve the distribution of the gas flow over the front face of the monolith by a radial increase in the cell densities. Recent developments aim at the generation of local turbulence in the channels and at the realization of radial flow. Both measures are intended to improve the utilization of the supported catalyst. Local turbulence should enhance the mass transfer between gas and catalyst surface and, hence, the catalyst effectiveness. Radial permeability of the channels should enable the equalization of flow maldistributions and, hence, of the mean residence times within the channels that results in a higher overall conversion. An example of such a design is depicted in Figure 9.13. In this structure, radial mixing is possible because the flat foil is perforated. In addition, the corrugated foil is equipped with blades that not only promote the longitudinal split and recombination of the flow paths between the next-neighbor channels but also should enhance local turbulence. Such a design requires a more complex manufacturing technology and causes a higher pressure drop than a smooth-channel monolith with comparable cell density. Provided that the gain in catalyst efficiency is sufficiently high in microstructured monoliths to offset the loss of catalyst surface area, it is possible to compensate for the higher pressure drop by reducing the cell density and/or the length of the channels. These measures would also be suited to reduce the weight of the converters and to save raw materials.

Generally, all types of metal foils can be used to form a monolith. However, ferritic steels, that is, alloys containing iron, chromium, and aluminum are preferred because these develop a passivating oxide layer upon heating in air. Particularly desirable is an alumina-rich surface that is formed at temperatures above 1073 K by oxidation of bulk aluminum and migration to the surface.

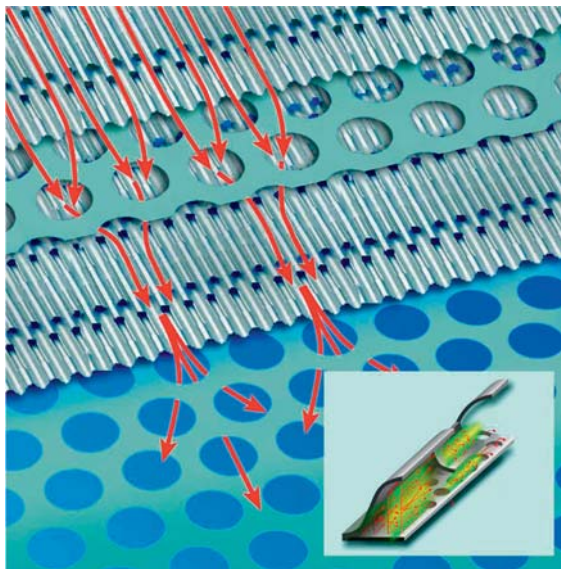


Figure 9.13 LS-PE structure of the foils for a metallic honeycomb used to generate radial permeability and to enhance local turbulence. (Drawing courtesy of EMITEC GmbH.)

Alumina layers are strongly adhering, self-healing, and represent a perfect, compatible grounding for the washcoated layer of alumina particles that, finally, serves as the actual support for the catalyst [23].

9.3.2

Open-Cell Foams

By definition, foams consist of dispersed, closed bubbles, or cells, respectively, embedded in a continuous liquid or solid phase. Unfortunately, the term foam has been adopted also for solid monoliths with cells being interconnected such that the void space becomes continuous within a network of struts as shown in Figure 9.1. To distinguish these monoliths from real foams, it is custom to add the attributes “open-cell” or “reticulated” although the denotation sponge would be correct and less cumbersome. Solid foams with closed cells like, for example, cellular concrete play an important role as thermal-insulation and sound-barrier materials and in the construction of buildings. In the context of catalysis, however, only the reticulated foams are of interest because their open, irregular network allows for flow through of gaseous or liquid reactants in all directions.

Foam monoliths can be produced from a broad variety of materials. Commercially available are ceramic foams made of alumina, mullite, cordierite, silicon carbide, or zirconia, but numerous other oxides, carbides, nitrides, and

composites have been used as well. Metallic foams have been prepared consisting of aluminum, nickel, and various alloys, like ferritic steels. In any case, the solid framework is mechanically stable only if it underwent at least a partial sintering. Because most catalytic materials would be damaged under sintering conditions, foams are used as carriers rather than as bulk catalysts.

Depending on the mean cell sizes and strut thicknesses, foam packings exhibit bed porosities between 75 and 95%. Pressure drop, when compared between fixed beds of the same specific external surface area, is somewhat greater over foams than over honeycombs, but considerably lower than over particle beds. The low pressure drop together with the excellent mass and, in particular, heat-transfer properties of foam packings render them particularly useful for rapid reactions of high exo- or endothermicity, when the realization of high fluid flow, efficient mass transfer, and/or efficient heat removal or supply, respectively, is mandatory [30, 31].

Foam manufacturing follows two alternative principles: replication or foaming. The replication method was already invented in 1963 by Schwarzwald and Somers [32], but it is still the most common technique used in industry. Schwarzwald and Somers already addressed the potential of foams as catalysts and catalyst carriers in their patent. They gave an example of the preparation of a bulk catalyst containing vanadia that was used in volatile organic compound (VOC) oxidation.

The replication method involves coating of an elastic polymer sponge with a slip containing the precursors of the ceramic or metallic material, a liquid (usually water) and additives to adjust the rheological properties and adhesion of the slip, or to promote sintering. The polymer sponges employed consist of polyurethane or polyester, but many other materials can be used as well. In practice, coating is achieved by immersing the polymer sponge in the slurry, followed by squeezing to remove air and excess slip, and to prevent drainage. This procedure may be repeated to achieve thicker layers. After drying, the final step is a heat treatment to burn out or to decompose the polymer and to sinter the precursor particles. In the case of oxidic ceramics, this procedure is carried out in air. Carbides, nitrides, and borides are sintered in protective atmospheres (e.g. Ar), metals in reducing atmospheres. The resulting monoliths have the same shape as the polymer used for replication. Drying and sintering, however, result in a shrinkage of up to 25%, the precise extent being dependent on the particle-size distribution of the precursors.

Most demanding in the replication process is the uniform infiltration of the polymer. This step requires a careful adjustment of the slip rheology. Preferably, the slip should exhibit viscoelastic and thixotropic properties [33]. In addition, there exists an optimum apparent viscosity range for every cell size that allows for complete and regular coverage of the polymer without blocking of windows between the cells [34]. The problems of wet coating can be circumvented by applying electrospraying [35] or chemical vapor deposition [36, 37]. These techniques, however, are expensive, require longer processing

times to deposit layers of substantial thickness, and their applicability is limited to small preforms of simple geometries.

The alternative to foam replication is manufacturing by foaming of slurries or gels. The foaming agent may be either gas supplied from external sources or gas produced *in situ* through reaction. In catalytic applications, foamed monoliths are less useful than replication products because, at least in the present state of the art, they have lower porosities and contain considerably more closed cells. Therefore, these techniques are not treated here, but reference is made to a review by Binner [38].

9.3.3

Coating of Monoliths

Preparation and characterization of coatings of porous support layers or catalysts is the subject of numerous patents and publications. This chapter has to be restrictive and will focus on some aspects of washcoating as this technique is widely used in industry and can be applied to a broad variety of materials to be deposited. However, typical problems encountered in washcoating are drainage or entrainment loss, blockage of channels or pores, poor adhesion, and cracking during drying due to capillary forces. The coating of complex surface geometries like foams, structured packings, or microreactors is even more challenging. The increasing interest in these novel carrier types may trigger development and scale-up of technologies that presently appear exotic. Here, we mention only three examples of coating methods that avoid the typical drawbacks of washcoating. (i) Metallic or oxidic nanoparticles can be uniformly deposited on complex geometric structures like foams by reactive adsorption of precursor-complexes from supercritical CO₂ solutions. This process is known as supercritical fluid reactive deposition (SFRD) [39, 40]. (ii) Janssen *et al.* described the growth of highly stable, closed zeolite layers on monolithic substrates, thereby using the carrier itself as a source of silicon or aluminum for the crystallization [41]; many other groups have adopted this method. (iii) The deposition of oxides and mixed oxides can be achieved “dry” from the gas phase. For instance, foams have been coated with porous layers of V₂O₅/TiO₂ nanoparticles by means of flame spray pyrolysis (FSP) to produce highly active catalysts for the oxidation of o-xylene to phthalic anhydride [42, 43]. Several reviews have been published, in which other methods for monolith coating are included [44–47].

Washcoating is the conventional method for furnishing monoliths with a porous layer of particles. The procedure as such is simple, comprising (i) dipping of the monolith into a suspension or sol, (ii) pulling the piece out after a while, (iii) removing excess slurry by blowing off or centrifugation, and (iv) drying and, optionally, calcination. However, the quality of a washcoat depends on numerous factors among which is the particle-size distribution of the precursors. Large particles (diameter $\varnothing < 10\ \mu\text{m}$) usually show poor

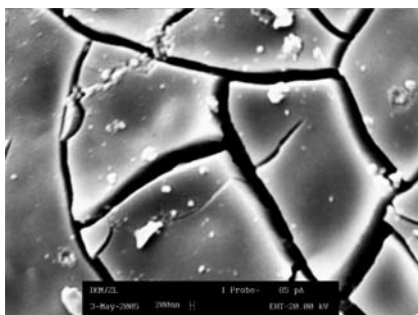


Figure 9.14 Cracks of a sol-gel washcoat of SnO_2 on a ceramic foam; the cracking occurs during drying, when high capillary pressure compress the particles.

adhesion to the substrate whereas layers of colloidal particles (diameter $\varnothing < 500$ nm) as generated by sol-gel washcoating typically undergo fracture upon drying (Figure 9.14). Adhesion is greatly influenced by attractive London–van der Waals forces and electrostatic forces. Electrostatic forces are created by adsorbed ions and can be adjusted through the pH value of the liquid. It is desirable to install net repulsive forces between the particles in the slurry and attractive forces between particles and substrate. Other important factors influencing the washcoat quality are the viscosity of the slurry and the surface tension of the liquid used. These properties can be altered by choice of the liquid itself and by using additives. Thickeners are, for instance, polymeric alcohols and cellulose derivatives. Wetting agents are anionic, cationic or nonionic surfactants [45, 47].

Washcoats can, in principle, be made with all types of particles. The washcoat itself may be the catalyst, or it serves as a support. In the latter case, a further step in the manufacturing is the deposition of the actual catalyst or catalyst precursor in the porous washcoat by, for instance, impregnation, adsorption, or grafting. Indeed, most washcoats are used as supports in order to boost the surface area and to provide a strong, stabilizing interaction with the deposited catalyst. In this context, washcoats of alumina, silica, zirconia, and titania are most widely used. The particles in the suspensions or sols used typically consist of the corresponding hydrated oxide or hydroxide. They are prepared either by mechanical (milling) and chemical (peptization) deagglomeration of the oxidic bulk material, or by hydrolysis and condensation of alkoxides or soluble salts. In the case of alumina washcoats on automotive converters, the precursor is boehmite ($\text{AlO}(\text{OH}) \cdot x\text{H}_2\text{O}$). The boehmite layer is transformed into $\gamma\text{-Al}_2\text{O}_3$ by heating the coated monolith to about 770 K.

9.4

Catalysts for Moving-Bed Reactors

Moving beds are prone to the same pressure-drop constraints as fixed beds and require, therefore, particles with diameters greater than about 3 mm.

Mechanically strong spheres of this size are produced by extrusion, granulation, or drip coagulation.

Extrusion (see Section 9.2.3) produces strings. It is possible to obtain spheres by cutting cylindrical “green” strings into pieces at lengths equal to their diameter, and subsequent rolling of the pieces on a rotating wheel. Drying and calcination are carried out after this transformation of the shape.

As mentioned in Section 9.2.2, spherical bodies can be produced directly by means of granulation, but the mechanical strength of granules strongly depends on the type and amount of binder applied with the spray.

Drip coagulation yields very strong, porous spheres, but this technique is expensive. The principle was already disclosed in 1952 in a patent on the manufacturing of alumina spheres [48]. According to this first description, droplets of an alumina sol fall down into a liquid-filled container, first passing an aqueous phase and then reaching a heavy, hydrophobic phase on the bottom, kept at a higher temperature. The aqueous solution contains a weak organic base that stabilizes the sol. The solidification through gelation and aging of the droplets occurs in the oil bath and is promoted by the elevated temperature there. This process may take several hours. Finally, the spheres are discharged, dried, and calcined. Drip coagulation can be applied to many materials other than alumina, provided that a suitable sol can be prepared. The sol may be used as such, or as a binder for suspended catalyst particles like zeolite crystals. Today, most drip coagulation processes run with a light oil phase on top of a heavier aqueous phase where gelation is triggered by a change of the pH value [49]. In any case, the question may arise why the droplets first have to pass a liquid in which gelation is largely suppressed or slowed down. Indeed, this is an essential feature of the technique: immediately after leaving the nozzle, the droplets are deformed. First passing through a liquid at low gelation rate allows for assuming the ideal spherical shape before the external surface becomes rigid.

Simpler dripping methods have been reported where the solidification starts immediately after contact of the drops with the liquid. An example represents freezing of slurry droplets in liquid nitrogen and subsequent freeze-drying and calcination of the bodies [50]. However, such methods produce particles of anisotropic shape, and the size distributions are broad because many droplets break apart upon bouncing against the liquid surface.

9.5

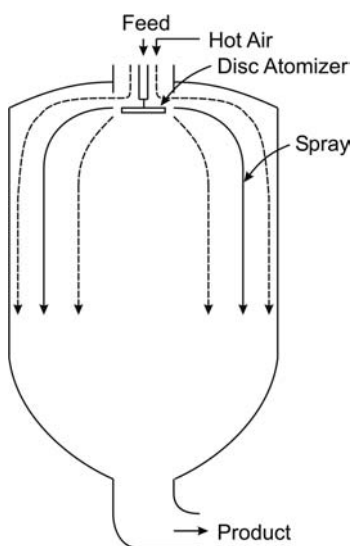
Catalysts for Fluidized Beds

Attrition-resistant microspheroidal catalyst particles for fluidized beds are manufactured by means of spray drying. The catalyst particles, for instance zeolite crystals, are suspended in an aqueous sol or hydrogel of binder particles that, after processing, serve as a mechanically strong and porous matrix. Typical binders are silica-alumina and alumina gels, clays (e.g. kaolin, bentonite), and

combinations thereof. In the spray dryer, this slurry is sprayed into a hot gas flow. While passing the drying chamber, the binder particles undergo gelation, and the liquid evaporates. As a result, the catalyst particles are embedded in a matrix of crosslinked matrix particles. This process can be repeated, that is, spray-dried particles can be processed a second time, to furnish them with a protective shell.

Spray drying is wet agglomeration, however, other than in granulation, it is undesired that droplets or moist particles grow by coalescence or take up of fines. Rather, the ideal spray-dried particle has the same solids content as the original droplet when leaving the spraying device. This also implies that breakdown of particles by collisions with internals has to be avoided. The mean free trajectory of the drying droplets and, hence, the size of the spray drier is one of the decisive factors influencing the final particle-size distribution. Other important process parameters are solids content and viscosity of the slurry as well as temperature and flow velocity of the hot gas.

Diameter and size distribution of the droplets strongly depend on the design of the spraying device, the so-called “atomizer.” Typical devices are high-pressure nozzles, gas–liquid nozzles, and high-speed centrifugal disks. The latter are most convenient for slurries that erode and plug nozzles. Furthermore, disk atomization allows for a good control of drop diameters in narrow size distributions through choice of the disk diameter and the rotation speed. Anyway, the largest drop sizes rarely exceed 500 μm . There are also different designs of drying chambers. Typically, this is a vertical, large-diameter cylinder with a settling cone at the bottom. The atomizer is usually placed at the top of the chamber as shown in Scheme 9.2. The hot gas may be employed either in cocurrent or countercurrent mode, but cocurrent flow is preferred



Scheme 9.2 Scheme of a spray dryer with cocurrent disc atomizer.

to control the residence time and to avoid collisions between particles during their passage through the drying chamber [51].

References

- Geldart, D. (1973) *Powder Technol.*, **7**, 285.
- Leva, M. (1959) *Fluidisation*, McGraw-Hill, New York.
- Pietsch, W. (2002) *Agglomeration Processes*, Wiley-VCH Verlag GmbH, Weinheim.
- Bartholomew, C.H. and Farrauto, R.J. (2006) *Fundamentals of Industrial Catalytic Processes*, Wiley-VCH Verlag GmbH.
- Mäurer, T. (2004) Investigation of Mass Transport Phenomena in the Conversion of Methanol to Olefins over Technical Alumina/ZSM-5 Catalysts. Dissertation, Shaker, Aachen, University of Karlsruhe.
- Müller, S.P., Kucher, M., Ohlinger, C. and Kraushaar-Czarnetzki, B. (2003) *J. Catal.*, **218**, 419.
- Freiding, J., Patcas, F.-C. and Kraushaar-Czarnetzki, B. (2007) *Appl. Catal., A*, **328**, 210.
- Benbow, J.J. and Bridgewater, J. (1993) *Paste Flow and Extrusion*, Clarendon Press, Oxford.
- Händle, F. (ed.) (2007) *Extrusion in Ceramics*, Springer, Heidelberg.
- Benbow, J.J. and Bridgewater, J. (1987) *Chem. Eng. Sci.*, **42**, 753.
- Danner, A. and Unger, K.K. (1987) *Stud. Surf. Sci. Catal.*, **31**, 343.
- JirátoVá, K., Janáček, L. and Schneider, P. (1983) *Stud. Surf. Sci. Catal.*, **16**, 653.
- Moreno, R. (1992) *Am. Ceram. Soc. Bull.*, **71**(11), 1647.
- Graczyk, J., Gleißle, W., Roth, A. and Kotter, M. (1990) *Erdöl Kohle Gas Petrochemie*, **43**, 27.
- Li, Y.Y., Perera, S.P., Crittenden, B.D. and Bridgewater, J. (2001) *Powder Technol.*, **116**, 85.
- Rumpf, H. (1962) in *Agglomeration* (ed. W.A. Knepper), Interscience Publishers, New York, p. 379.
- Galarraga, G., Peluso, E. and de Lasa, H. (2001) *Chem. Eng. J.*, **82**, 13.
- Lekhal, A., Glasser, B.J. and Khinast, J.G. (2001) *Chem. Eng. Sci.*, **56**, 4473.
- de Jong, K.P. (1991) *Stud. Surf. Sci. Catal.*, **63**, 19.
- Zhuang, Y.Q., Claeys, M. and van Steen, E. (2006) *Appl. Catal., A*, **301**, 138.
- Gulati, S.T. (2006) in *Structured Catalysts and Reactors* (eds A. Cybulski and J.A. Moulijn), CRC Press, Boca Raton, p. 21.
- Twigg, M.V. and Wilkins, A.J.J. (2006) in *Structured Catalysts and Reactors* (eds A., Cybulski and J.A., Moulijn), CRC Press, Boca Raton, p. 109.
- Twigg, M.V. and Webster, D.E. (2006) in *Structured Catalysts and Reactors* (eds A., Cybulski and J.A. Moulijn), CRC Press, Boca Raton, p. 71.
- Bosch, H. and Janssen, F. (1988) *Catal. Today*, **2**, 369.
- Forzatti, P. and Lietti, L. (1996) *Heterogen. Chem. Rev.*, **3**, 33.
- Hollenbach, R.Z. (1963) Method for making ceramic articles. US Patent 3,112,184.
- Bagley, R.D. (1974) Extrusion method for forming thin-walled honeycomb structures. US Patent 3,790,654.
- Lackman, I.M. (1984) *Advances in Ceramics*, Vol. 9, *Forming of Ceramics*, The American Ceramic Society, Columbus, p. 201.
- Rahaman, M.N. (2008) *Sintering of Ceramics*, CRC Press, Boca Raton.
- Reitzmann, A., Patcas, F.C. and Kraushaar-Czarnetzki, B. (2006) *Chem. Eng. Technol.*, **78**, 885.
- Twigg, M.V. and Richardson, J.T. (2007) *Ind. Eng. Chem. Res.*, **46**, 4166.
- Schwarzwalder, K. and Somers, A.V. (1963) Method for making porous ceramic articles. US Patent 3,090,094.

33. Montanaro, L., Jorand, Y., Fantozzi, G. and Negro, A. (1998) *J. Eur. Ceram. Soc.*, **18**, 1339.
34. Buciuman, F.C. and Kraushaar-Czarnetzki, B. (2003) *Ind. Eng. Chem. Res.*, **42**, 1863.
35. Jayasinghe, S.N. and Edrisinghe, M.J. (2002) *J. Porous Mater.*, **9**, 265.
36. Sherman, A.J., Tuffias, R.H. and Kaplan, R.B. (1991) *Am. Ceram. Soc. Bull.*, **70**, 1025.
37. Lin, Y.S. and Burggraaf, A.J. (1992) *AIChE J.*, **38**, 445.
38. Binner, J. (2005) in *Cellular Ceramics* (eds M. Scheffler and P. Colombo), Wiley-VCH Verlag GmbH, Weinheim, p. 33.
39. Patcas, F.C., Incera Garrido, G. and Kraushaar-Czarnetzki, B. (2007) *Chem. Eng. Sci.*, **62**, 3984.
40. Incera Garrido, G., Patcas, F.C., Upper, G., Türk, M., Yilmaz, S. and Kraushaar-Czarnetzki, B. (2008) *Appl. Catal., A*, **338**, 58.
41. Janssen, J., Koegler, J., van Bekkum, H., Calis, H., van den Bleek, C., Kaptijn, F., Moulijn, J.A., Geus, E. and van der Puil, N. (1998) *Microporous Mesoporous Mater.*, **21**, 213.
42. Schimmoeller, B., Schulz, H., Pratsinis, S.E., Bareiss, A., Reitzmann, A. and Kraushaar-Czarnetzki, B. (2006) *J. Catal.*, **243**, 82.
43. Bareiss, A., Reitzmann, A., Schimmoeller, B., Schulz, H. and Pratsinis, S.E. (2007) Manufacturing Process for Catalytically Active Material. WO 2007/000068.
44. Nijhuis, T.A., Beers, A.E.W., Vergunst, T., Hoek, I., Kaptijn, F. and Moulijn, J.A. (2001) *Catal. Rev. Sci. Eng.*, **43**, 345.
45. Avila, P., Montes, M. and Miro, E.E. (2005) *Chem. Eng. J.*, **109**, 11.
46. Meille, V. (2006) *Appl. Catal., A*, **315**, 1.
47. Agrafiotis, C. and Tsetsekou, A. (2000) *J. Mater. Sci.*, **35**, 951.
48. Hoekstra, J. (1952) Spheroidal Alumina. US Patent 2,620,314.
49. Barton, H. (1987) *Stud. Surf. Sci. Catal.*, **32**, 103.
50. Haas, A. (2003) Production and Shaping of Shaped Bodies by Means of Low-Temperature Cooling and Drying Process. WO 03/049849.
51. Masters, K. (1985) *Spray Drying*, John Wiley & Sons, Inc., New York.

10

Space and Time-Resolved Spectroscopy of Catalyst Bodies

Bert M. Weckhuysen

10.1

Introduction

Heterogeneous catalyst materials are often employed in fixed-bed reactors and mm-sized catalyst bodies of various shapes and sizes are used in order to minimize pressure drop across the reactor (Chapter 9). Since the efficiency of the final catalytic system depends on both the nature and distribution of the active phase sufficient control over the preparation process is crucial. The classical unit operations of industrial catalyst preparation include impregnation and drying followed by calcination. In the steps of impregnation and drying the chemical processes taking place in the impregnation solution and at the solid/liquid interface are important, whereas gas/solid interface and solid–solid reactions are key in the calcination step [1–6].

These physicochemical processes at the liquid/solid, gas/solid, and solid/solid interfaces during catalyst preparation and their related consequences for catalyst performance underline the importance to (i) fundamentally understand the distribution of metal-ion complexes in three dimensions within catalyst bodies and (ii) have molecular information on the nature of metal-ion complexes formed as a function of time and space during the elementary steps of catalyst preparation. This can be done by applying spectroscopy during the preparation of mm-sized catalyst bodies. In this way, the genesis of the active phase can be monitored and better understood. This chapter discusses the potential of different methods to provide these space- and time-resolved physicochemical insights. In a first part, an overview of both invasive and noninvasive methods will be presented. The second part deals with two showcases to illustrate the advantages of this approach. The chapter closes with a look into the future.

10.2

Space- and Time-Resolved Methods Applied to Catalyst Bodies

The methods explored so far for studying impregnation, drying, and calcination processes of mm-sized catalyst bodies are Raman microspectroscopy [7–11],

IR microspectroscopy [12], and UV-Vis-NIR DR microspectroscopy [9, 12–15] as invasive techniques and tomographic energy-dispersive diffraction imaging (TEDDI) [16] and magnetic resonance imaging (MRI) [17–25] as noninvasive techniques. In what follows, we will discuss the application of these methods for catalyst preparation studies, illustrating their possibilities and limitations.

10.2.1

Invasive Methods

The general strategy to apply invasive microspectroscopic methods to catalyst preparation processes is schematically illustrated in Figure 10.1 for the impregnation of catalyst bodies with an ammonium-hexamolybdate (AHM)-citrate solution at a pH of 0.5 [9]. The technique of choice here is Raman microspectroscopy since molybdenum oxide complexes possess characteristic Raman spectroscopic fingerprints enabling their identification. The approach consists of taking, after several points in time during catalyst impregnation, one or more catalyst bodies from the synthesis vessel [8, 9]. This is followed by cleaving them in the middle, perpendicular to their z -axis, using, for example, a razor blade. By making cross-sectional scans one can record spatially resolved Raman spectra at different positions inside the individual bisected catalyst

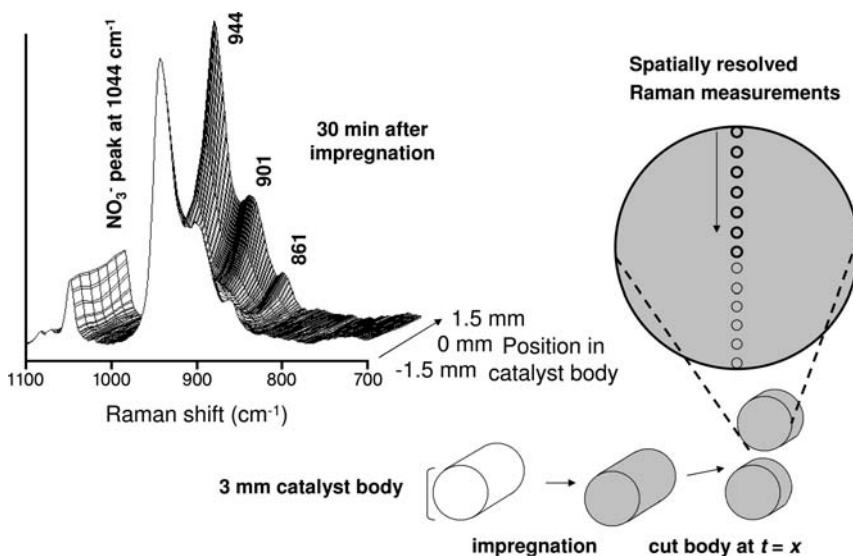


Figure 10.1 Layout of the experimental procedure used for measuring time- and space-resolved Raman spectra on bisected Al₂O₃ catalyst bodies after impregnation with an aqueous ammonium

heptamolybdate (AHM)-citrate solution. The Raman spectra shown are obtained after 30 minutes of impregnation.

bodies. Due to the advancements in modern Raman instrumentation spinning of the catalyst bodies, as was required in the first study of Knözinger and coworkers on catalyst bodies [7], is not necessary. This offers the possibility to map with a spatial resolution of the order of a few micrometers the speciation of, for example, molybdenum oxide complexes at each point of the cross-sections of the catalyst bodies under study.

Figure 10.1 shows a typical set of Raman spectra as a function of the position in the bisected catalyst body, indicating that after 30 minutes of impregnation an egg-shell distribution of the molybdenum complexes is formed within the catalyst body [9]. This is evidenced by comparing the intensity of the Raman bands at around 944, 901, and 861 cm^{-1} of the AHM–citrate complex with the intensity of the Raman NO_3^- internal standard at around 1044 cm^{-1} . It is important to notice that a homogeneous distribution of the NO_3^- compound was found almost instantly after impregnation, guaranteeing its use as an internal standard and making relative quantification of molybdenum oxide species within the catalyst bodies possible. Another observation is that the Raman bands of the AHM–citrate complex present in the pores of the alumina catalyst body are almost identical to that of the impregnation solution, indicating the weak interaction between this complex and the alumina surface.

It is obvious that the above-described strategy is not limited to Raman microspectroscopy alone, but can be applied to any spectroscopic technique that can be performed in a space- and time-resolved manner. The most logical extension is then IR microspectroscopy, which is commercially available and can be used to study the vibrational signatures of organic additives, such as amines [12]. Practical spatial resolutions of IR microscopes are in the order of 20 μm , but by making use of synchrotron IR light the diffraction-limited spatial resolution of a few micrometers can be reached. However, it is important to stress that due to the low Raman scattering properties of water Raman microspectroscopy is still preferred over IR microspectroscopy when aqueous impregnation solutions are applied for catalyst preparation processes. The situation becomes more promising for IR microspectroscopy when dried catalyst bodies are under investigation. This is illustrated in Figure 10.2a, which shows space-resolved IR spectra in the region between 3500 and 2500 cm^{-1} measured from the edge to the center of $\text{Ni}(\text{en})_3^{2+}$ (with *en* = ethylene diamine) complexes impregnated onto an Al_2O_3 catalyst body [12]. These spectra were obtained after drying the catalyst bodies for 8 hours at 100 °C. In the spectral region under consideration, several absorption bands can be noticed; that is, a doublet at around 2936 and 2892 cm^{-1} typical of C–H stretching vibrations and two bands at around 3338 and 3282 cm^{-1} characteristic of N–H stretching vibrations from the *en* ligands coordinating the Ni^{2+} ion in an octahedral symmetry. From the spectra in Figure 10.2a one can conclude that the dried catalyst body containing the $\text{Ni}(\text{en})_3^{2+}$ complexes exhibited an egg-shell distribution of the *en* ligands since the C–H and NH-stretching vibrations are more intense in the edges than toward the center of the catalyst body.

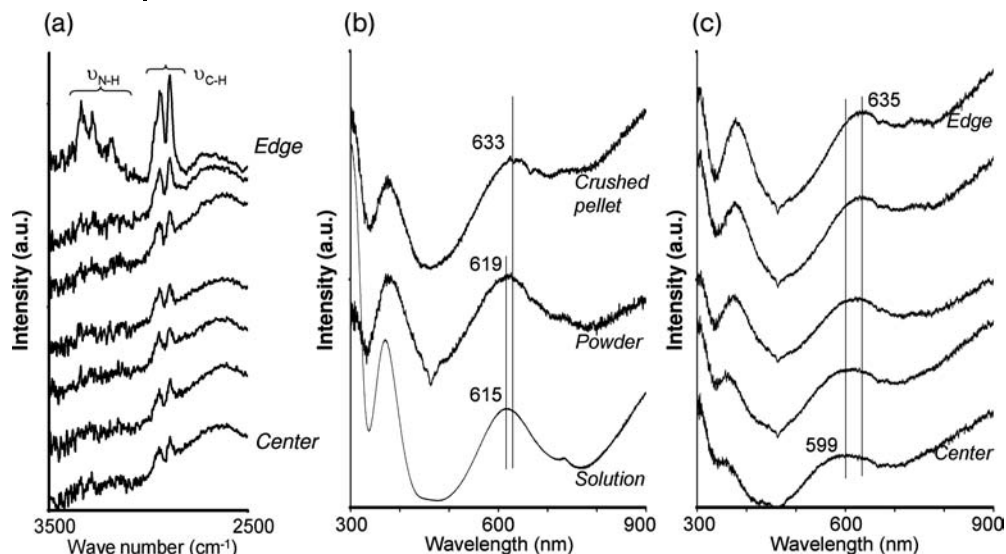


Figure 10.2 (a) Space-resolved IR spectra of a bisected Al_2O_3 catalyst body impregnated with a $\text{Ni}(\text{en})_3^{2+}$ solution after drying for 8 hours at 100°C ; (b) UV-Vis-NIR spectrum of an aqueous solution containing $\text{Ni}(\text{en})(\text{H}_2\text{O})_4^{2+}$ complexes, together with the corresponding UV-Vis-NIR DR spectra obtained after impregnating Al_2O_3 powder or an Al_2O_3 catalyst body with the Ni -containing solution. The latter spectrum is obtained after crushing the catalyst body; and (c) Space-resolved UV-Vis-NIR DR spectra of an Al_2O_3 catalyst body impregnated with an aqueous solution containing $\text{Ni}(\text{en})(\text{H}_2\text{O})_4^{2+}$ complexes.

Another promising method for studying catalyst preparation processes is UV-Vis-NIR DR microspectroscopy, which allows measuring the d–d and charge-transfer (CT) transitions of various coordination geometries and oxidation states of transition metal-ion complexes as well as the $n \rightarrow \pi$ and $\pi \rightarrow \pi$ transitions of organic and inorganic additives present in the impregnation solutions [13]. The spatial resolution of the currently used experimental setup is of the order of about $50\text{--}100\ \mu\text{m}$, but can be brought near the diffraction limit by making some experimental modifications. As an example we illustrate the use of this UV-Vis-NIR DR microspectroscopy setup by monitoring the impregnation of an aqueous solution containing $\text{Ni}(\text{en})(\text{H}_2\text{O})_4^{2+}$ complexes onto a powdered Al_2O_3 support as well as a related catalyst body and crushed catalyst body [12]. The obtained spectra are given in Figures 10.2b and c. The aqueous solution containing the $\text{Ni}(\text{en})(\text{H}_2\text{O})_4^{2+}$ complex is characterized by a d–d transition at around $615\ \text{nm}$ (Figure 10.2b). The corresponding UV-Vis-NIR DR spectrum of the impregnated Al_2O_3 powder is included in Figure 10.2b and it can be seen that this powdered sample exclusively contains $\text{Ni}(\text{en})(\text{H}_2\text{O})_4^{2+}$ complexes. However, when the same solution is used for the impregnation of an Al_2O_3 -catalyst body the

UV-Vis-NIR DR spectra do change along the cross-section of the catalyst body. This can be proven by cleaving the catalyst bodies after impregnation and measuring the corresponding UV-Vis-NIR DR spectra, which are shown in Figure 10.2c. The spectrum at the edge reveals the presence of $\text{Ni(en)(H}_2\text{O)}_4^{2+}$, whereas in the center of the catalyst body a new absorption band appears. This absorption band at around 599 nm is a d–d transition of a $\text{Ni(en)}_2(\text{H}_2\text{O})_2^{2+}$ complex. The increasing amount of *en* in the first coordination sphere of the Ni^{2+} ion explains the blue shift of the d–d transition. Finally, one can crush this $\text{Ni(en)(H}_2\text{O)}_4^{2+}$ -impregnated catalyst body and measure a UV-Vis-NIR DR spectrum of this crushed body (Figure 10.2b). It can be seen that this spectrum is very similar to that of the edge of the $\text{Ni(en)(H}_2\text{O)}_4^{2+}$ -impregnated catalyst body (Figure 10.2c), illustrating the effect a catalyst body may exert in the speciation of supported metal-ion complexes.

10.2.2

Noninvasive Methods

The MRI technique exploits the interaction of magnetic properties of nuclei present in an object with external static high magnetic fields [17–23]. This leads to resonance phenomena with oscillating magnetic fields in the radiofrequency regime. By applying simultaneously specific radiofrequency and phase-encoding routines information on the distribution of nuclei in the *X–Y* plane of a catalyst body, perpendicular to its *Z*-axis, can be obtained in a noninvasive manner. This can be done by placing the catalyst body in the center of the radiofrequency coil. Two different MRI measuring strategies can now be applied to study impregnation processes within catalyst bodies in a space- and time-resolved manner.

The first promising and most straightforward MRI approach concerns the imaging of NMR-sensitive nuclei, such as ^1H , ^{13}C , and ^{31}P . The first characterization studies in which ^1H NMR imaging has been used for studying catalyst preparation processes originates from Koptug *et al.* [17] and Gladden *et al.* [25]. For example, the research team of Koptug has been studying the process of drying of different Al_2O_3 and TiO_2 bodies impregnated with various liquids. Despite the short spin-spin relaxation times usually exhibited by liquids that permeate porous solids, the possibility to monitor their evaporation in real time by detecting one-dimensional liquid concentration profiles along the diameter of a cylindrical sample could be demonstrated. ^{13}C can also be used for monitoring, for example, citrate as organic additive although the small gyromagnetic ratio as well as the low natural abundance of ^{13}C leads to a relatively low sensitivity of the MRI method. In contrast, ^{31}P MRI images enable imaging of the transport of phosphate in a relatively easy manner as an inorganic additive to impregnation solutions when contacted with an Al_2O_3 catalyst body [21]. Since the ^{31}P nuclei contained in the alumina pores have

spin lattice relaxation times much faster than in the impregnation solution one can distinguish between these two ^{31}P contributions.

The second MRI approach makes use of the large gyromagnetic ratio of ^1H nuclei and their inherent high concentration in the catalyst bodies impregnated with an aqueous solution containing a metal-ion salt [22, 23]. As a consequence, ^1H MRI can be carried out with great sensitivity on these systems. Unpaired electrons, creating their own magnetic field paramagnetic nuclei in an impregnation solution occluded in the pores of a catalyst body, will induce a decrease in the relaxation time of the ^1H nuclei. By using a specific pulse sequence it is possible to distinguish between perturbed and unperturbed ^1H nuclei of the impregnated solution occluded in the pores of a catalyst body. In other words, the amount of paramagnetic nuclei can be monitored in space and time within a catalyst body by monitoring the quenching of the ^1H MRI signal. This indirect but powerful method is illustrated in Figure 10.3 for the impregnation of an Al_2O_3 catalyst body with a 0.2 M $\text{Co}(\text{NO}_3)_2$ solution [22]. Figure 10.3 shows two-dimensional (2D) ^1H MRI images of an Al_2O_3 catalyst body at several times after impregnation, together with a quantitative Co^{2+} -ion distribution plot, derived from the 2D images. It can be concluded that the transport of Co^{2+} -ions after pore-volume impregnation takes place in two distinct steps. In a first step, Co^{2+} complexes are transported into the catalyst body as they travel with the capillary flow of the water solvent. Adsorption of Co^{2+} complexes on the alumina surface takes place as coordinating water molecules are exchanged for support oxygen atoms and a Co^{2+} concentration gradient is instantly established after impregnation. Since the impregnation method was carried out without excess solution the total amount of Co^{2+} inside the catalyst body remained constant as a function of time after impregnation. Initially, the Co^{2+} concentration near the outer surface of the catalyst body was therefore higher than 0.2 M. The concentration gradient over the catalyst body resulted in diffusion of Co^{2+} complexes toward the center. The Co^{2+} front travels into the catalyst body and eventually after 4 hours a homogeneous distribution of the metal-ion complexes and an average Co^{2+} concentration of 0.2 M were observed. One could wonder if this indirect MRI method merely provides quantitative insight into the dynamics of the impregnation processes of paramagnetic metal ions. Interestingly, this is not the case and the MRI approach also allows distinguishing between different forms of metal-ion complexes (e.g. coordination environments) simultaneously present in the support oxide pore system provided the differences in the relaxation times (T_1 and T_2) of these complexes are sufficiently large.

A second noninvasive method, denoted as TEDDI, allows nondestructively probing of both the structural and chemical content of individual volume elements within catalyst bodies by using an intense hard white X-ray beam produced by synchrotron wiggler devices [16]. The volume element is defined by the intersection of the incident X-ray beam with the diffracted beam that passes through the postsample collimator into the detector. Many such volume-element locations can be visited by scanning the catalyst body through

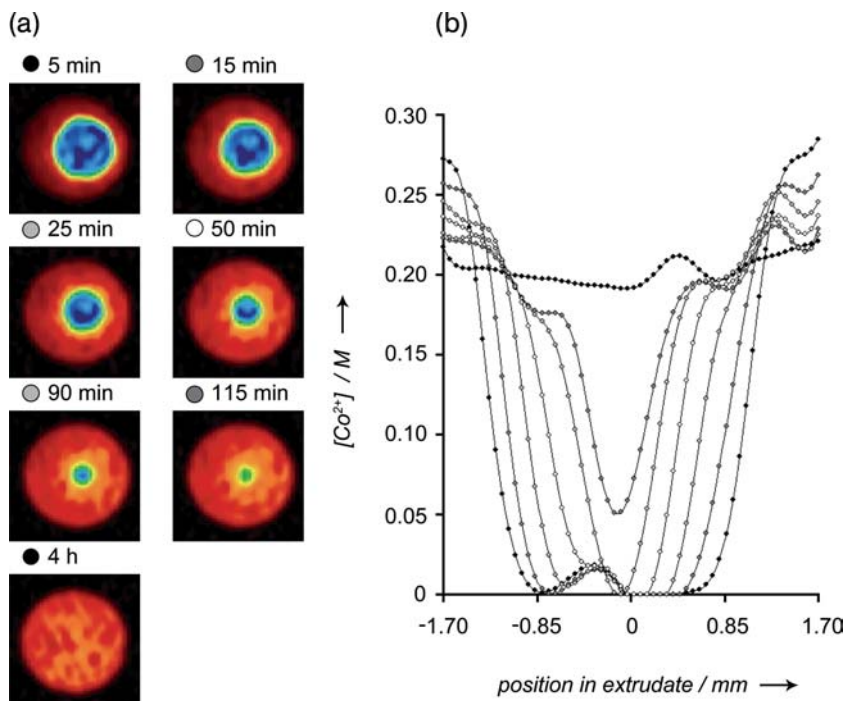


Figure 10.3 (a) 2D ^1H MRI images of an Al_2O_3 catalyst body at several times after impregnation with a $0.2\text{ M Co}(\text{NO}_3)_2$ solution. Blue: high ^1H NMR signal (a low Co^{2+} concentration); red: low ^1H NMR signal (a high Co^{2+} concentration) and

(b) Quantitative Co^{2+} -ion distribution plots, derived from the 2D images shown in (a), as a function of time after impregnation with a $0.2\text{ M Co}(\text{NO}_3)_2$ solution.

the X-ray beam and collecting the X-ray signal from each location by means of an energy-dispersive detector. This signal contains both the diffraction pattern and a fluorescence peak from the defined volume element in the catalyst body. Therefore, a full scan gives rise to a complete diffraction and fluorescence record of the whole sample region of interest. With the X-ray diffraction method, provided at least one diagnostic diffraction peak can be identified for each phase, it is possible to obtain concentration maps for crystalline phases within a catalyst body in a time- and space-resolved manner. In a similar fashion, the fluorescence mapping allows identification of the chemical composition of a catalyst body in a time- and space-resolved manner. Figure 10.4a illustrates the application of the TEDDI methodology to the calcination process of a single $\text{Mo}/\text{Al}_2\text{O}_3$ catalyst body after drying and calcination in air [16]. By scanning over the whole $y-z$ area of the catalyst body, concentration maps can be obtained from the $\text{Mo}_{\text{K}\alpha 1,2}$ fluorescence as well as from the (311) $\gamma\text{-Al}_2\text{O}_3$ and (210) MoO_3 diffraction peaks. A typical

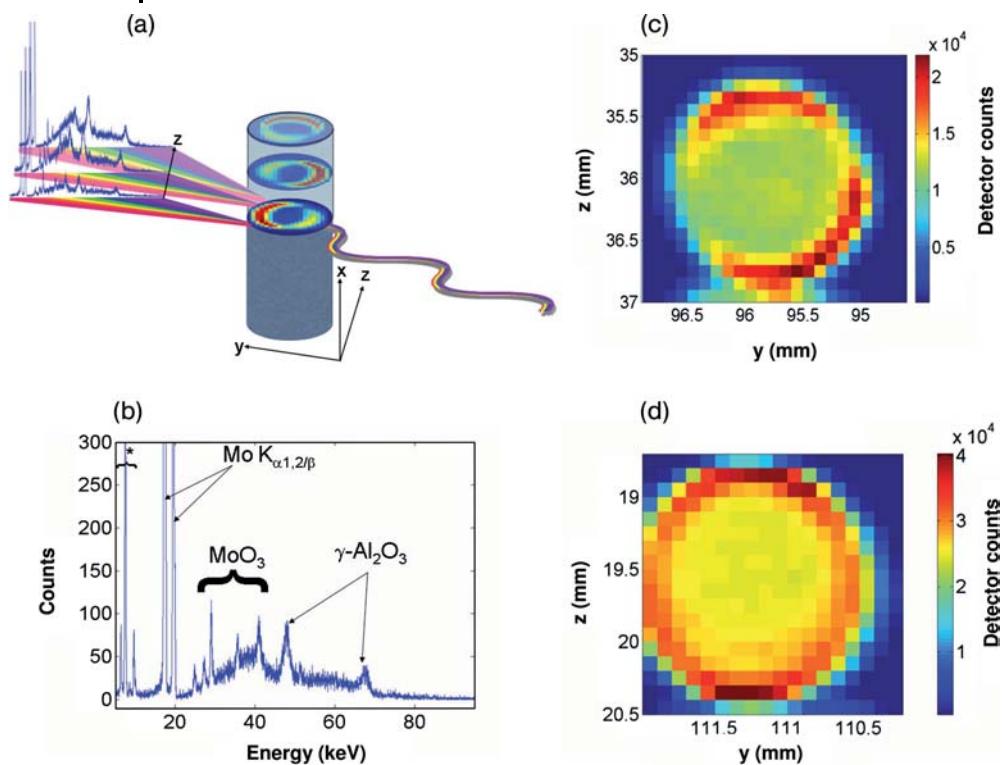


Figure 10.4 (a) Layout of the experimental procedure used for measuring time- and space-resolved fluorescence and diffraction patterns from a specific volume within a catalyst body making use of the TEDDI technique; (b) Detector signal from a Mo/Al₂O₃ catalyst body after calcination at 500 °C; (c) Typical $\gamma - z$ map of the MoK_{α1,2} fluorescence signals from a Mo/Al₂O₃ catalyst body after drying at 120 °C; and (d) Typical $\gamma - z$ diffraction map, based on the (210) reflection of MoO₃ crystals, from the Mo/Al₂O₃ catalyst body after calcination at 500 °C.

TEDDI detector signal from a specific region within the Mo/Al₂O₃ catalyst body after calcination at 500 °C is given in Figure 10.4b. Based on such detector signals concentration maps can be constructed. As an example, Figures 10.4c and d show, respectively, a specific $\gamma - z$ MoK_{α1,2} fluorescence map and a $\gamma - z$ MoO₃ diffraction map. From the latter 2D image it can be seen that during calcination crystalline MoO₃ is formed and that there exists an egg-shell distribution of these MoO₃ crystallites within the catalyst body. The advantage of the TEDDI technique compared to the MRI technique is that no water phase is needed to visualize metal-oxide distributions, making it possible to study catalyst bodies after drying, calcination as well as activation. Finally, it is fair to say that the measuring time to collect a full map with the TEDDI method is still of the orders of hours and improved detector technology is

required to enable the study of the different catalyst preparation steps in a dynamic fashion. Work is underway to improve the time resolution of TEDDI experiments.

10.3

Case Studies

10.3.1

Keggin-Type Co-Mo Complexes in Catalyst Bodies

Co-MoS₂/Al₂O₃ catalysts are used in hydrotreating processes and are prepared by the impregnation of Al₂O₃-based catalyst bodies with a solution containing suitable Mo and Co complexes, followed by aging, drying, and sulfidation. Co atoms are located at the edges of the alumina-supported MoS₂ slabs and constitute the active sites in these promoted catalysts. To enable maximal catalytic activity it is of crucial importance that Co and Mo are in close contact with each other during catalyst preparation. A strategy to achieve this is to use suitable heteropolyanion compounds containing both Mo and Co as precursors. An example is H₂PMo₁₁CoO₄₀⁵⁻. However, the stability of this heteropolyanion compound during catalyst preparation was found to be a problem and phosphate-containing complexes are reported to decompose upon adsorption onto the Al₂O₃ surface [9].

By making use of combination of Raman and UV-Vis-NIR DR microspectroscopic methods it is possible to monitor the disintegration and formation of H₂PMo₁₁CoO₄₀⁵⁻ complexes inside the pores of Al₂O₃ catalyst bodies and rationalize the distribution of this complex after impregnation in terms of the surface chemistry of the alumina support [9]. The general strategy of this approach has already been explained above. Figure 10.5 presents the Raman and UV-Vis-NIR DR spectra recorded at different positions inside the Al₂O₃ catalyst bodies after 15 and 180 minutes of impregnation with an aqueous H₂PMo₁₁CoO₄₀⁵⁻ solution. The presence of the H₂PMo₁₁CoO₄₀⁵⁻ complex inside the Al₂O₃ pores, as evidenced by the characteristic Raman band at 971 cm⁻¹ is observed 15 minutes after impregnation only in the outer shell of the bodies. More toward the center of the alumina bodies Mo is present as a H_xMo₇O₂₄^{(6-x)-} species as can be concluded from the position of the main Mo—O stretch vibration at 947 cm⁻¹. However, near the core of the catalyst body, the absence of any Mo—O vibration peak indicates that no Mo⁶⁺ complex are present.

These Raman microspectroscopy observations are in full agreement with the UV-Vis-NIR DR measurements recorded at the same points of the bisected pellet after 15 minutes after impregnation [9]. Indeed, a clear shoulder is observed at 17 600 cm⁻¹ and the onset of the O → Mo⁶⁺ charge-transfer absorption band is shifted into the visible region of the spectrum. This confirms the presence of the H₂PMo₁₁CoO₄₀⁵⁻ complex in the outer shell of the support bodies after 15 minutes. On the other hand, toward the core of the pellets all

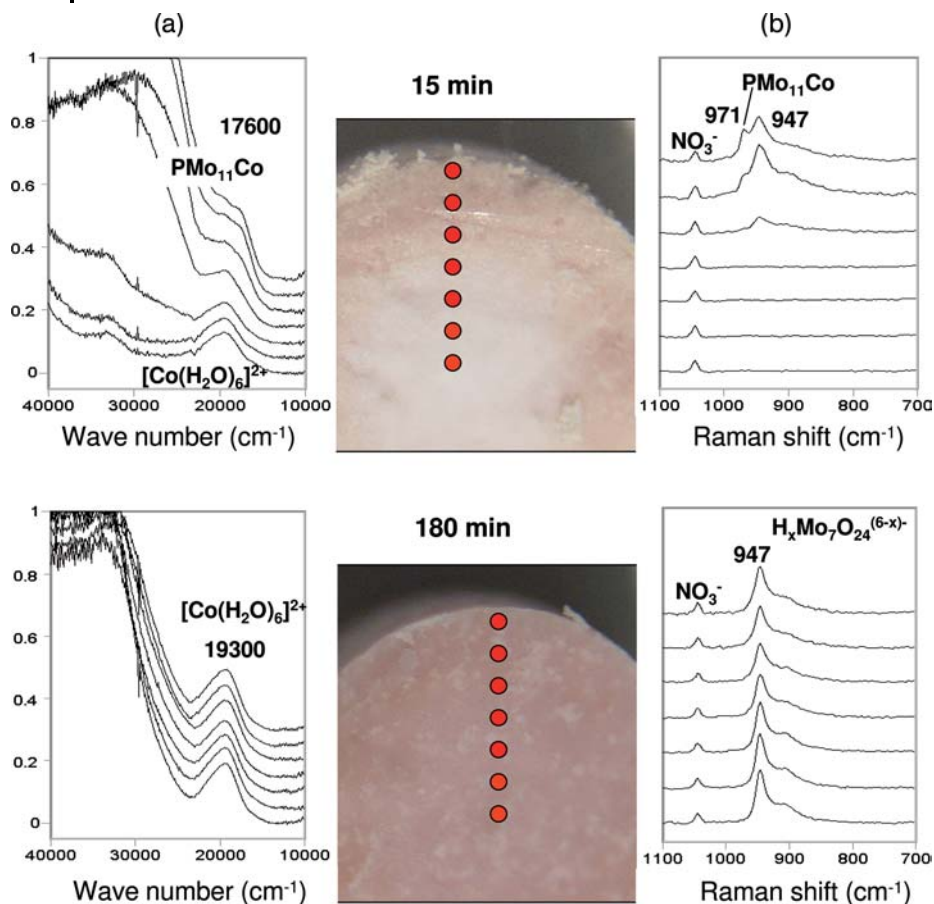
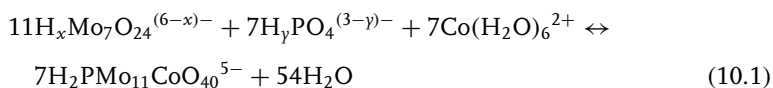


Figure 10.5 Space- and time-resolved UV-Vis-NIR DR (a) and Raman (b) spectra recorded of a bisected Al_2O_3 catalyst body after 15 and 180 minutes of impregnation with an aqueous solution containing $\text{H}_2\text{PMo}_{11}\text{Co}_{40}^{5-}$ complexes.

Co^{2+} seems to be present as $\text{Co}(\text{H}_2\text{O})_6^{2+}$ and the $\text{O} \rightarrow \text{Mo}^{6+}$ charge-transfer absorption band is absent, validating the Mo concentration gradient observed in the Raman microspectroscopy measurements. 180 minutes after impregnation a homogeneous distribution of the $\text{H}_x\text{Mo}_7\text{O}_{24}^{(6-x)-}$ complex is observed throughout the catalyst bodies and the intensity of the Raman 947 cm^{-1} peak relative to that of the NO_3^- internal standard is identical for all positions inside the Al_2O_3 bodies. This is in line with the observation that the $\text{O} \rightarrow \text{Mo}^{6+}$ charge-transfer absorption band is observed for all positions along the cross-section. In addition, a homogeneous distribution of the $\text{Co}(\text{H}_2\text{O})_6^{2+}$ is already obtained as the intensity of the Co^{2+} d–d transition with its maximum at 19 300 cm^{-1} is the same for all positions along the cross-section of the catalyst bodies.

The above-described observations can be rationalized as follows. Phosphate is known to react with the Al_2O_3 surface in an acidic environment to form a surface AlPO_4 phase. In this way, phosphate is withdrawn from the solution inside the Al_2O_3 pores. Hence, a decreasing phosphate gradient can be expected toward the center of the catalyst body. As the impregnation solution containing $\text{H}_2\text{PMo}_{11}\text{CoO}_{40}^{5-}$ complexes penetrates the alumina pellets, reaction of phosphate with the Al_2O_3 surface results in a lower phosphate concentration in the solution inside the pores of the support body. As a consequence, the equilibrium of the reaction equation:



shifts to the left and $\text{H}_x\text{Mo}_7\text{O}_{24}^{(6-x)-}$ and $\text{Co}(\text{H}_2\text{O})_6^{2+}$ are being formed, which follow their way toward the core of the bodies, each at their own rate.

Experimental evidence for this surface reaction between the Al_2O_3 surface and phosphate could be obtained with ^{31}P MRI experiments in which the dynamics of the impregnation of an Al_2O_3 catalyst body in the presence of a H_3PO_4 solution was monitored [21]. Based on an analysis of the 2D ^{31}P MRI images detected during catalyst impregnation it was found that the transport of phosphate throughout the catalyst body is very slow compared to water and takes almost 20 hours before the phosphate reaches the center of the catalyst body. This observation points to a strong interaction between phosphate and the alumina support. To strengthen this conclusion Figure 10.6 shows 2D ^{31}P MRI images of dried Al_2O_3 catalyst bodies after 18.5 hours and 95 minutes of impregnation with a phosphate-containing aqueous solution [21]. It is clear that adsorbed phosphate is present in the entire catalyst body up to 18.5 hours after the start of the impregnation process. However, termination of the impregnation process after 95 minutes, followed by drying, clearly indicated the formation of an egg-shell-type distribution of phosphate over the catalyst body due to the surface reaction of phosphate with the alumina support. The amount of free phosphate is therefore a crucial factor in the formation of specific Co–Mo complexes within the pores of the alumina catalyst bodies. With this knowledge in mind we could prove that the $\text{H}_2\text{PMo}_{11}\text{CoO}_{40}^{5-}$ complexes can be formed inside Al_2O_3 catalyst bodies by increasing the amount of free phosphate to the initial impregnation solution [9]. In this manner, the reaction of free phosphate with the support results in a lower phosphate concentration inside the pores creating the optimal conditions for the formation of the $\text{H}_2\text{PMo}_{11}\text{CoO}_{40}^{5-}$ complex. Summarizing, the strong interaction between phosphate and the alumina surface leads to strong concentration gradients of this component within the support bodies in the first hours after impregnation, which may be of use when preparing catalyst bodies with different $\text{H}_2\text{PMo}_{11}\text{CoO}_{40}^{5-}$ distributions.

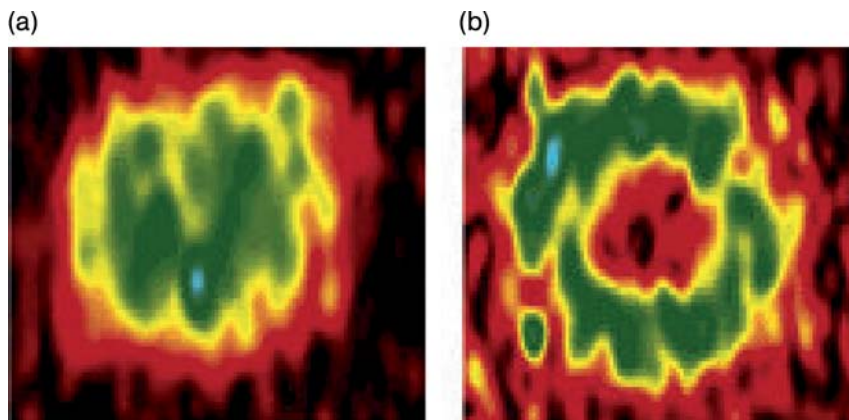


Figure 10.6 2D ^{31}P images showing phosphate distributions in dried Al_2O_3 catalyst bodies after impregnation for 18.5 hours (a) and 95 minutes (b) Green color indicates presence of phosphorus.

10.3.2

Speciation of Co Complexes in Catalyst Bodies

Impregnation solutions used in industrial catalyst preparation processes usually contain a variety of components, each with their own interaction with the support surface. Besides metal-precursor salts, organic complexing agents, such as citrate, are often added to impregnation solutions. As a consequence, different metal-chelate complexes can be formed in the impregnation solution as a function of pH and metal-ion concentration. Since it is known that pH gradients may occur inside catalyst bodies after impregnation different interactions between the metal-ion complexes and the support surface are expected, which may lead to different transport rates of these compounds through the support bodies. Such processes can be best illustrated by a recent characterization study in which the transport phenomena and related macrodistribution of different types of Co^{2+} -complexes inside $\text{Co}/\text{Al}_2\text{O}_3$ catalyst bodies have been investigated by a combination of MRI and UV-Vis-NIR DR microspectroscopy [23]. While UV-Vis-NIR DR microspectroscopy provided molecular information on the Co^{2+} complexes inside the Al_2O_3 matrix obtained after bisecting catalyst bodies at specific times during impregnation, the macrodistribution of Co^{2+} complexes inside the catalyst bodies and the dynamics of the impregnation processes could be determined by the MRI method in a noninvasive manner.

As an example we discuss here the impregnation of Al_2O_3 catalyst bodies with an aqueous Co-citrate solution at a pH of 5 for a Co : citrate ratio of 1. Figure 10.7a shows the 2D ^1H MRI image obtained from the catalyst bodies after 15 hours of impregnation [23]. It can be observed that a sharp

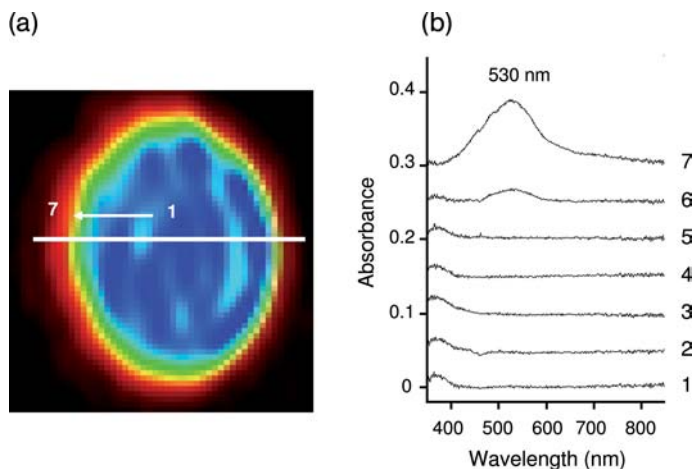


Figure 10.7 (a) 2D ^1H MRI image of an Al_2O_3 catalyst body after 15 hours of impregnation with a 0.2 M $\text{Co}(\text{NO}_3)_2$ solution containing 0.2 M citrate at a pH of 5. Blue: high ^1H NMR signal (a low Co^{2+} concentration); red: low ^1H NMR signal (a high Co^{2+} concentration) and

(b) corresponding UV-Vis-NIR DR spectra recorded on the corresponding bisected Al_2O_3 catalyst body. The locations of the measurement spots are indicated in the 2D ^1H MRI image.

ring of low ^1H NMR signal intensity near the external surface of the catalyst bodies is present even after 15 hours. Since the red regions of the MRI image corresponds to a high amount of Co^{2+} complexes, whereas the blue regions indicate low amounts of Co^{2+} complexes the image clearly points toward a sharp egg-shell distribution of the Co^{2+} complexes. The UV-Vis-NIR DR spectra recorded on the corresponding bisected catalyst body, given in Figure 10.7b, show an absorption band located at around 530 nm, which is due to Co^{2+} d–d transitions. This band is only clearly observed in the spectrum recorded near the external surface of the catalyst body, confirming the sharp egg-shell profile for this catalyst body as proposed from the 2D ^1H MRI image.

By a systematic variation of the Co : citrate ratio and pH of the impregnation solution the macrodistribution of the Co^{2+} -complexes in the impregnated catalyst bodies could be varied from egg-shell, through egg-white and egg-yolk to uniform. This is illustrated by the related 2D ^1H MRI images in Figure 10.8 [23]. In the absence of citrate aqueous Co^{2+} complexes are slowly transported toward the center of the catalyst body and at a pH of 1 and 160 minutes of aging a homogeneous distribution of Co^{2+} can be observed. 2D ^1H MRI image of this sample is shown in Figure 10.8a. In contrast, the addition of citrate to the Co^{2+} -containing solutions had profound effects on the impregnation process and the final macrodistribution of Co^{2+} complexes. First, the coordination of Co^{2+} to citrate resulted in a considerable increase in the interaction between the Co^{2+} complex and the alumina support. As a

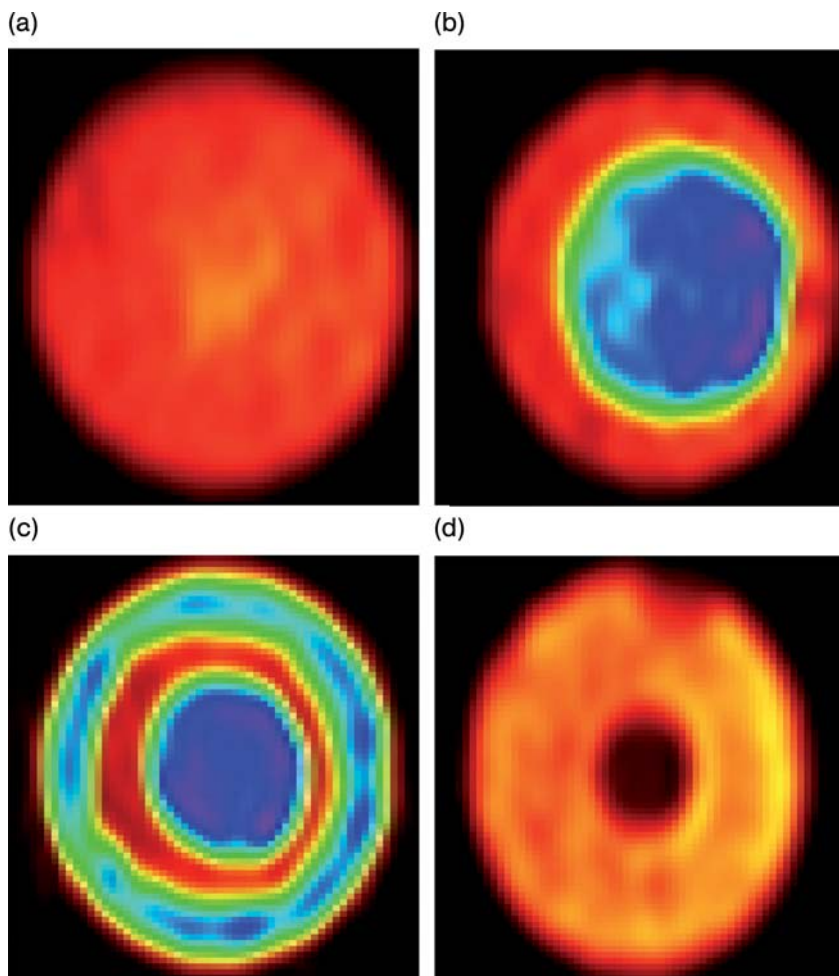


Figure 10.8 2D ^1H MRI images of Al_2O_3 catalyst bodies obtained after impregnation with a $\text{Co}(\text{NO}_3)_2$ solution containing different amounts of citrate at various pH values: (a) Uniform Co^{2+} profile (pH = 1; Co : Citrate ratio of 1 and impregnation time of 160 minutes); (b) Egg-shell Co^{2+} profile (pH = 5; Co : Citrate ratio of 0.5 and impregnation time of 50 minutes); (c) Egg-white Co^{2+} profile (pH = 9; Co : Citrate ratio of 0.66 and impregnation time of 145 minutes); and (d) Egg-yolk Co^{2+} profile (pH = 1; Co : Citrate ratio of 0.2 and impregnation time of 90 minutes).

result, a sharp egg-shell Co^{2+} distribution was established immediately after impregnation with a Co^{2+} citrate complexes at a pH of 5 (Figure 10.8b). Second, competitive adsorption between free citrate and Co^{2+} complexes resulted in a faster transport of Co^{2+} complexes toward the center of the catalyst bodies as compared to impregnation solutions containing only Co^{2+} ions. This strong

interaction between free citrate and the alumina surface may even lead to the establishment of an egg-yolk distribution after impregnation and aging as shown in Figure 10.8d. Near the exterior surface of the catalyst bodies, fewer sites are now available for adsorption of the Co^{2+} complexes, and the Co^{2+} complexes were found to diffuse to the center of the catalyst bodies. As an intermediate situation egg-white distributions of Co^{2+} complexes can be formed within catalyst bodies and visualized with the MRI technique as illustrated in Figure 10.8c.

10.4 Future Prospects

The two showcases discussed illustrate the great potential for studying the fundamental aspects of catalyst preparation in a space- and time-resolved manner. By applying this approach the dynamics of the processes taking place in catalyst bodies during impregnation, drying, and calcination can be established. This information can be related to experimental factors, allowing the improvement of current catalyst formulations as well as the development of new preparation recipes. It should be clear that space- and time-resolved characterization is not limited to, for example, impregnation processes, but can also be applied to ion exchange and chemical vapor deposition processes. This also implies that the approach can be applied to other macroscopic bodies composed of, for example, zeolites or other ion-exchange materials. Equally important to notice is that the data obtained could be used to start further theoretical modeling of transport behavior of metal ions within catalyst bodies. Finally, technological developments in techniques are making it possible to start studying preparation processes with a higher space and time resolution allowing that more chemical information could be revealed. The advent of proper *in-situ* capabilities undoubtedly allows extending these studies to other important steps in catalyst-preparation processes, such as reduction and sulfidation.

Acknowledgments

B.M.W. acknowledges financial support by NWO-CW (Van der Leeuw and VICI grants), NRSC-Catalysis and Albemarle Catalysts BV. The research described in this chapter would have been impossible without the dedication and inspiration of a lot of people. The following people at Utrecht University have contributed to this research work: J. Bergwerff, L. Espinosa Alonso, L. van de Water, A. Beale, X. Nijhuis, T. Visser and K. de Jong. The MRI work has been done in collaboration with A. Lysova and I. Koptug of the Boreskov Institute of Catalysis and International Tomography Center in Novosibirsk, Russia. The TEDDI experiments have been performed in collaboration with S. Jacques and P. Barnes of the University College London, UK.

References

- Regalbuto, J. (ed.) (2007) *Catalyst Preparation: Science and Engineering*, CRC Press LCC, Boca Raton.
- Bourikas, K., Kordulis, C. and Lycourghiotis, A. (2006) *Catal. Rev. Sci. Eng.*, **48**, 363.
- Ertl, G., Knozinger, H. and Weitkamp J. (eds) (1999) *Preparation of Solid Catalysts*, Wiley-VCH Verlag GmbH, Weinheim.
- de Jong, K.P. (1999) *Curr. Opin. Solid State Mater. Sci.*, **4**, 55.
- de Jong, K.P. (1998) *CatTech*, **3**, 87.
- Neimark, A.V., Kheifez, L.I. and Fenelonov, V.B. (1981) *Ind. Eng. Chem. Prod. Res. Dev.*, **20**, 439.
- Mang, T., Breitscheidel, B., Polanek, P. and Knözinger, H. (1993) *Appl. Catal. A.*, **106**, 239.
- Bergwerff, J.A., Visser, T., Leliveld, R.G., Rossenaar, B.A., de Jong, K.P. and Weckhuysen, B.M. (2004) *J. Am. Chem. Soc.*, **126**, 14548.
- Bergwerff, J.A., van de Water, L.G.A., Visser, T., de Peinder, P., Leliveld, B.R.G., de Jong, K.P. and Weckhuysen, B.M. (2005) *Chem. Eur. J.*, **11**, 4591.
- Bergwerff, J.A., Jansen, M., Leliveld, B.R.G., Visser, T., de Jong, K.P. and Weckhuysen, B.M. (2006) *J. Catal.*, **243**, 292.
- Bergwerff, J.A., Visser, T. and Weckhuysen, B.M. (2008) *Catal. Today*, **130**, 117.
- Espinosa Alonso, L., de Jong, K.P. and Weckhuysen, B.M. (2008) *J. Phys. Chem., C*, **112**, 7201.
- van de Water, L.G.A., Bergwerff, J.A., Nijhuis, T.A., de Jong, K.P. and Weckhuysen, B.M. (2005) *J. Am. Chem. Soc.*, **127**, 5024.
- van de Water, L.G.A., Bezemer, G.L., Bergwerff, J.A., Versluijs-Helder, M., Weckhuysen, B.M. and de Jong, K.P. (2006) *J. Catal.*, **242**, 287.
- van de Water, L.G.A., Bergwerff, J.A., Leliveld, B.R.G., Weckhuysen, B.M. and de Jong, K.P. (2005) *J. Phys. Chem., B*, **109**, 14513.
- Beale, A.M., Jacques, S.D.M., Bergwerff, J.A., Barnes, P. and Weckhuysen, B.M. (2007) *Angew. Chem. Int. Ed.*, **46**, 8832.
- Koptyug, I.V., Fenelonov, V.B., Khitrina, L.Y., Sagdeev, R.Z. and Parmon, V.N. (1998) *J. Phys. Chem., B*, **102**, 3090.
- Koptyug, I.V., Kabanikhin, S.I., Iskakov, K.T., Fenelonov, V.B., Khitrina, L.Y., Sagdeev, R.Z. and Parmon, V.N. (2000) *Chem. Eng. Sci.*, **55**, 1559.
- Koptyug, I.V., Khitrina, L.Y., Aristov, Y.I., Tokarev, M.M., Iskakov, K.T., Parmon, V.N. and Sagdeev, R.Z. (2000) *J. Phys. Chem., B*, **104**, 1965.
- Khitrina, L.Y., Koptyug, I.V., Pakhomov, N.A., Sagdeev, R.Z. and Parmon, V.N. (2000) *J. Phys. Chem., B*, **104**, 1966.
- Lysova, A.A., Koptyug, I.V., Sagdeev, R.Z., Parmon, V.N., Bergwerff, J.A. and Weckhuysen, B.M. (2005) *J. Am. Chem. Soc.*, **127**, 11916.
- Bergwerff, J.A., Lysova, A.A., Espinosa Alonso, L., Koptyug, I.V. and Weckhuysen, B.M. (2007) *Angew. Chem. Int. Ed.*, **46**, 7224.
- Bergwerff, J.A., Lysova, A.A., Espinosa Alonso, L., Koptyug, I.V. and Weckhuysen, B.M. (2008) *Chem. Eur. J.*, **14**, 2363.
- Gladden, L.F., Mantle, M.D. and Sederman, A.J. (2006) *Adv. Catal.*, **50**, 1.
- Hollewand, M.P. and Gladden, L.F. (1994) *Magn. Res. Imag.*, **12**, 291.

11

High-Throughput Experimentation

Uwe Rodemerck and David Linke

11.1

Introduction

About 10 years after the application of combinatorial methods to organic chemistry, especially in the development of new drugs in the pharmaceutical industry, combinatorial and high-throughput methods were also applied in searching for new inorganic materials and heterogeneous catalysts. The first examples in catalysis were rather simple reactions like, for example, the oxidation of hydrogen [1]. The catalysts were prepared as small spots on a wafer substrate by a sputtering technology and tested for their activity by observing the heat generated by the exothermic reactions via IR thermography. Although these first applications showed the principal possibility of making parallel experiments in catalysis, the preparation of the catalysts as well as the testing conditions were far from the standard laboratory or technical procedures. The use of nonstandard preparation procedures may lead to significant difficulties in scaling-up the production of successful candidates. However, high numbers of catalysts can be prepared and tested by these so-called stage I or primary screening methods. To overcome this limitation, so-called stage II or secondary screening methods were soon developed that are based on more conventional laboratory techniques for both catalyst preparation and testing but still use the advantage of parallelization and automation of the experiments. The choice of using stage I or stage II screening depends on the task of catalyst development. If a catalyst is searched for a reaction for which up to now no catalyst is known, stage I methods are best suited since very high numbers of catalysts can be prepared and tested, which maximizes the chance of finding good candidates. If, however, known catalytic systems should be improved or candidates from stage I need to be optimized, stage II methods are required in order to be able to detect the sometimes small improvements in catalyst performance. Accordingly, stage II methods are often applied in industry since even small improvements of the catalysts can significantly improve the process economics. Here, catalyst preparation techniques should reflect the complete industrial preparation

route including the additives given to the catalyst in order to minimize the risk of failure in scale-up of the preparation (Figure 11.1 and Table 11.1).

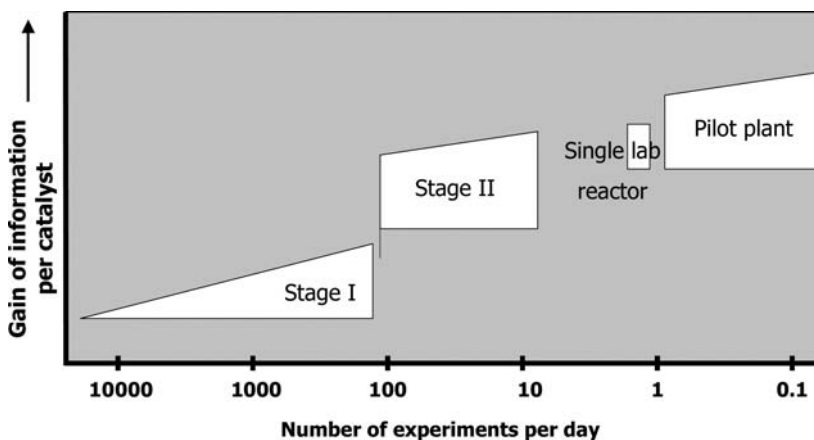


Figure 11.1 Number of experiments per day and gain of information on catalysts with high-throughput and conventional method.

Table 11.1 Comparison of stage I and stage II methods in high-throughput catalysis.

	Stage I	Stage II
Integration	Very high (100–10 000 experiments/day)	Moderate (10–100 experiments/day)
Preparation	Methods adapted from inorganic materials preparation, spots on wafer substrates, μg amounts of powder	Methods adapted from lab or industrial preparation (impregnation, precipitation, crystallization, calcination, reduction), 0.5–20 g
Testing conditions	Gas-flow regime, mass and heat transfer are not comparable to lab reactors, fast testing (seconds, nonsteady state)	Follows the rules of chemical engineering, catalysts are tested in steady state
Product analytics	Parallel or very fast sequential analysis methods, for example, IR thermography, REMPI, qualitative or semiquantitative measure (is the desired product formed or not?), special design for one reaction	Sequential analysis methods, fast (multidimensional) gas chromatography, GC-MS quantitative measure (conversion, selectivity, space-time yield, kinetic constants), universally usable
Application	To discover new catalytic materials	To improve known catalytic systems, to study influence of dopants and modifiers, to study deactivation, to measure kinetics

Since the first applications in the mid-1990s combinatorial catalysis has been developed into a standard tool for catalyst development. Whereas before the year 2000 only limited publications dealt with high-throughput preparation and testing of catalysts the number of publications strongly increased since then and reached a level of about 150 publications per year, about 30% of them are dealing with preparation of catalysts.

This review puts its focus on high-throughput preparation of heterogeneous catalysts, that is, solid-state materials that are applied in fixed-bed reactors for gas-phase reactions and in trickle-bed or stirred-tank reactors for liquid or gas–liquid reactions, respectively. Other fields of catalysis are not discussed since very different catalytic systems are used. We refer to the following reviews for homogeneous catalysis [2, 3], where combinatorial catalysis deals mainly with variation of ligands and for electrochemical catalysis [4, 5], where catalysts are prepared as arrays of thin films in electrochemical cells.

11.2 Synthesis Strategies

The often used synonym combinatorial catalysis instead of high-throughput catalysis implies that all possible combinations of all parameters that can affect catalyst performance (precursor compounds, chemical composition, synthesis protocol, calcination, . . .) will be screened to find the best suited catalyst for the reaction. Although such strategies are used in combinatorial chemistry, it is almost impossible to adapt them to heterogeneous catalysis.

Let us assume that about 50 elements from the periodic table can be part of solid catalysts. Then, 1225 combinations are possible for binary compositions, 19 600 for ternary, 230 000 for quaternary and about 10^{10} compositions can be created for a catalyst containing 10 elements according to the formula below [6, 7].

$$N = \frac{n_E!}{(n_R!(n_E - n_R)!)} \quad (11.1)$$

n_E , n_R – numbers of elements in the pool and in the catalyst.

In fact, the number of possible catalyst compositions is much higher since the previous calculation neglects that the catalysts can have different stoichiometry for the same elements. Taking into account that besides the chemical composition also parameters of preparation, calcination and testing could be varied, a huge number of experiments results (so-called combinatorial explosion). To overcome this problem three principle strategies can be used: (i) restricting the number of experiments by using previous knowledge (elimination of parameters), (ii) using experimental methods that allow screening of thousands to millions of catalysts (stage I screening), and (iii) use intelligent experimental design to restrict the number of experiments.

11.2.1

Combinatorial Strategies

True combinatorial strategies mean that all combinations of relevant parameters are screened. Even if fast stage I screening methods are applied the number of parameters has to be restricted to keep the number of experiments within practical limits.

In most reported applications, the array concept was applied in the syntheses, that is, all catalysts were synthesized in spatially addressable arrays of synthesis vials. By the help of synthesis robots, the precursor solutions were dosed to the vials sequentially followed by filtration of the precipitates or by simple drying of the resulting slurries.

In combinatorial chemistry several methods were developed that can produce a large number of highly diverse organic compounds by sequential creation of large molecules from synthesis blocks. One of these, the split-and-pool method (also called combine-and-mix) that creates mixtures of thousands to millions of substances has been adapted to heterogeneous catalysis [8–11]. In contrast to the synthesis of parallel libraries (arrays), this procedure that was originally developed for preparation of organic combinatorial libraries [12] is rather simple and can even be done manually. Figure 11.2 demonstrates the principle: A large number of inorganic beads (catalyst support, e.g. alumina) are divided into n beakers to which different solutions of catalyst precursors were added. The precursors are fixed to the support surface by drying or calcination. In a second step, all beads were mixed together and divided again to the beakers where again different compounds were fixed on the beads. In the following, mixing and dividing is repeated several times and very large numbers of combinations of the different precursors are synthesized by a limited number of syntheses steps. However, the split-and-pool method has the disadvantage that, due to the mixing, the composition of the individual beads is unknown. This problem is overcome by analyzing the composition of catalysts that show good performance by X-ray fluorescence analysis.

11.2.2

Methods to Reduce Experiments

Here, we limit our summary to the most common optimization methods. An extended review of this topic has recently been given by Holena and Baerns [13].

Statistical methods have been used for a long time, especially in chemical industry, to reduce the number of experiments when a multiparameter problem has to be solved. Design of experiments (DoEs) or factorial design is the most frequently used method in high-throughput catalysis. Examples are:

- NO oxidation over supported Pt: influence of synthesis variables (Pt precursor, support, loading, calcination gas and temperature; two levels each) [14]

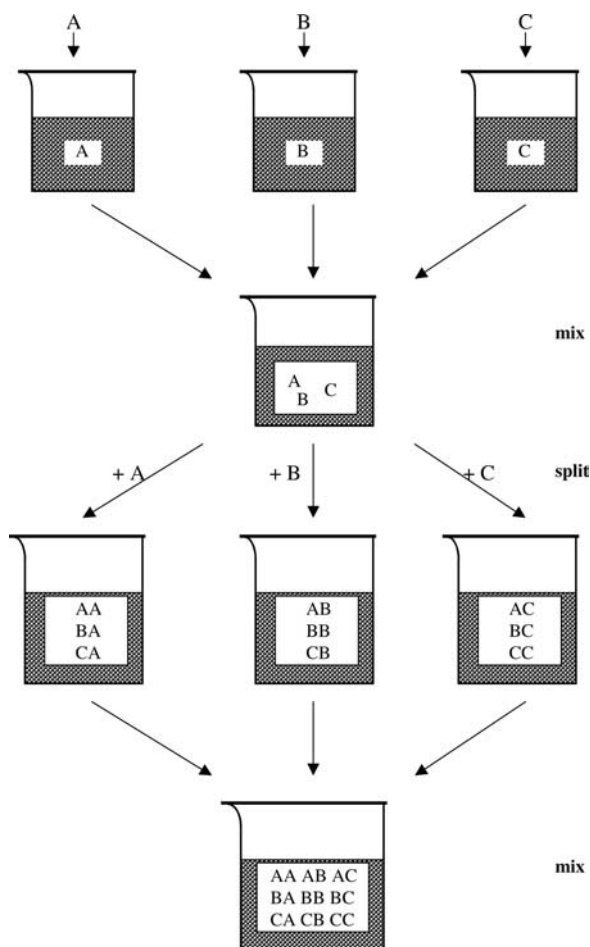


Figure 11.2 Principle of split-and-pool synthesis of catalysts.

- development of transition-metal-free heterogeneous epoxidation catalysts (full factorial approach: three synthesis methods, composition) [15]
- oil-soluble molybdenum catalyst precursors for hydrotreatment of heavy petroleum residues [16]
- K-promoted Co–Mo catalysts for Fischer–Tropsch synthesis of hydrocarbons (composition, calcination time and temperature) [17]
- hydrothermal zeolite synthesis [18, 19]
- elucidation of significance of parameters in the preparation of supported noble-metal catalysts [20].

DoE methods are well suited when the number of parameters is low. However, if a multidimensional optimization (more than 10 parameters)

should be done, even reduced factorial plans require too many experiments.

For catalyst optimization using high-throughput experimentation, evolutionary strategies have been shown to be very effective if vast parameter spaces (many nominal catalyst components) have to be searched for the optimal catalyst composition. The concept of the algorithm has been described in detail by Wolf *et al.* [21], some application examples are discussed by Rodemerck *et al.* [22] and Holena [23].

The following features make these strategies valuable:

- no *a-priori* information on the topology of the parameter space is required
- discrete (e.g. preparation method or calcinations atmosphere) and continuous parameters (e.g. molar fractions of elements) can be optimized simultaneously
- the global optimum is searched
- due to their population concept evolutionary strategies are compatible with the array concept of parallel catalyst preparation and testing.

The evolutionary strategy applied in catalyst optimization is, as in biological systems, based on the operators “mutation” and “crossover” as well as selection of the fittest individuals. Applied to catalyst composition, new catalysts are created from the best catalysts of the former generation by qualitative mutation (one or more chemical elements or compounds are replaced by others), quantitative mutation (the concentration of one or more compounds is changed), and crossover (components are exchanged between two materials of the former generation generating two new materials). The “survival of the fittest” is implemented by using a selection criteria based on ranking by quality, which is derived from the high-throughput testing results of a generation of catalysts. Catalysts with a higher position in the ranking have a higher probability to be selected as “parents” for the next generation.

The methodological basis of the evolutionary approach, which is implemented in a software package developed at the authors’ institute is described in Figure 11.3 and consists of the following steps:

1. Random definition of the first generation of catalytic materials based on the components and preparation methods selected. In order to adjust parameters concerning the catalyst composition or preparation in a meaningful way, parameters can be assigned to groups of components.
2. Preparation and catalytic performance test of all samples in the generation.
3. Creation of a new library (the next generation) by means of evolutionary operators (crossover and mutation) from the best catalysts (identified by their catalytic performance) of all materials of all previous generations.
4. Preparation and testing of the materials of the next generation.

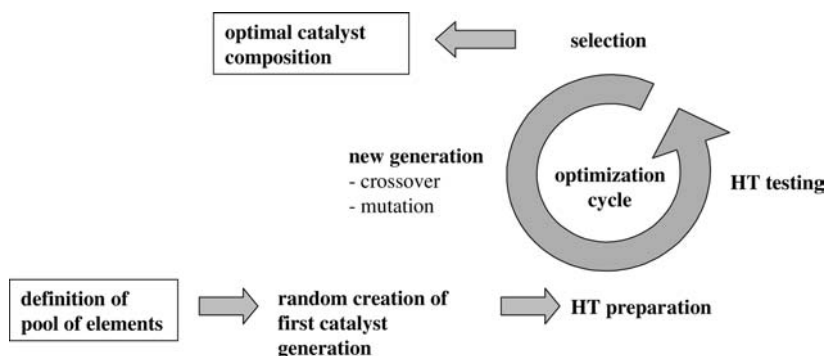


Figure 11.3 Optimization of catalyst composition using an evolutionary strategy.

Steps 3 and 4 are repeated, until a given performance target is met or until no significant progress is observed when going from one generation to the next.

An improved software code that creates tailor-made genetic algorithms according to a user-defined problem has been published by Holena *et al.* [24]. The software allows the user to describe the problem by a catalyst description language and then creates a case-specific genetic algorithm for finding the optimal catalyst. The new software gives the user a powerful tool to include former knowledge that restricts the parameter space to reasonable areas, that is, all catalyst compositions or preparation methods that are thought to be useless can be excluded.

Nowadays, evolutionary strategies using genetic algorithms are the most applied optimization tools in high-throughput development of heterogeneous catalysts. Besides the above-cited publications, they have been, for example, used for developing mixed-metal oxides for oxidative dehydrogenation of ethane [25–29] and propane [21, 25, 27, 28, 30–32], low-temperature oxidation of propane traces in air [33], light-paraffin isomerization [34], partial oxidation of isobutane to methacrolein [35], alkene epoxidation [36], CO oxidation [37], and methane oxidation [32, 38].

11.3 Catalyst Libraries for Primary Screening

11.3.1 Wafer-Based Preparation

The idea to prepare solid catalysts as thin-film spots on the surface of wafer substrates had been inspired by technologies that were developed for high-throughput discovery of materials by Hanak [39], by Symyx [40–44] and others [45, 46]. Hundreds to thousands of small spots of differently composed

materials are deposited on a support material (silicon wafers are often used). The materials are prepared by a sputtering technology with the help of masks that allows depositing gradients of amounts of a component at the support surface. After depositing different components using differently shaped masks a high number of compositions can be created using only limited preparation steps [40–43, 46]. Another method uses a solution-based process that also creates gradients [45]. Both methods are well suited to prepare thin films of solid catalysts on a wafer. Especially at Symyx the method has been used frequently (see review [47]). The gradient sputtering is well suited when very high numbers of compositions are to be prepared as it is necessary when using true combinatorial strategies (see Section 11.2.1). However, the method has some disadvantages: First, it is not certain that thus prepared catalysts have the same structure as bulk catalysts of the same composition due to the small amount and the possible interaction with the support material. Second, from an engineering point of view the catalytic test is problematic since gas flow as well as mass and heat transfer are not comparable to a standard fixed-bed lab reactor. Moreover, when the catalysts are only heated and tested for seconds [48] it is questionable if the catalyst is already in a steady state (industrial catalysts often need an activation phase from several hours to some days to reach their final activity and selectivity). However, the advantage of preparation of high numbers of catalysts in a short time makes the wafer-based preparation method essential for discovering new catalytic materials. For improving of known catalysts, however, it is less suited due to generating only semiquantitative results and scale-up problems. Here, stage II methods can deliver more reliable and detailed information.

11.3.2

Single Pellets

The idea behind using single pellets in high-throughput catalysis is that one single pellet should behave like the pellets in an industrial catalyst bed and therefore, scale-up should not be a problem. However, this is only true when both preparation and test are comparable to industrial procedures, which is not the case in most applications. Therefore, we discuss it here in the stage I section. The single-pellet technology has been described first by the group of Senkan [49, 50]. A 66-member ternary Pt/Pd/In library was prepared by coimpregnation of cylindrical-shaped alumina pellets. With the help of a liquid delivery system, precursor solutions of Pt, Pd, and In were mixed together and the alumina pellets were added to the solution. Afterwards, the water was evaporated and the pellets were calcined at 500 °C for 2 hours. The calcined pellets were tested in an array microreactor consisting of a ceramic plate having wells for the pellets and small channels for gas supply and reaction gas outlet for cyclohexane dehydrogenation to benzene. The same technology was used for preparation and testing of a quaternary Pt/Pd/In/Na library for

selective NO reduction by propene [51], the discovery of new catalysts for low-temperature combustion of propane [33], and the direct oxidation of propene to propene oxide [52].

11.3.3

Single Beads

The single-bead technology has been developed by hte AG to use the split-and-pool method for combinatorial generation of high numbers of differently composed catalysts (see Section 11.2.1). Similar to the single pellets discussed in the previous section between 96 and 625 single catalyst beads can be tested in specially designed reactors in parallel [11, 53]. Each bead is placed inside a pyramidal-shaped hole and has contact to the wall only at four points so that there is enough space for the gas to flow around the bead without significant pressure drop. Thus, this arrangement can be considered a part of a catalyst bed of a standard laboratory fixed-bed reactor and it is assumed that the data derived from this reactor are more reliable compared to others where the gas flow is rather undefined. Moreover, the catalyst beads themselves are prepared similar to supported catalysts used in larger reactors and, in contrast to thin-film catalysts used in stage I screening, upscaling will generate fewer problems.

Recently, Schüth *et al.* presented a new preparation route that allows preparation of beads of nonsupported mixed-metal oxides [54, 55]. The method is based on the so-called activated-carbon route developed earlier for preparation of high surface area oxides and mixed-metal oxide catalysts [56, 57]. Small beads of activated carbon are impregnated by precursor solutions of high concentration. Nitrates are well suited due to their high solubility in water but also other inorganic or organometallic precursor compounds dissolved in water or organic solvents can be used. After impregnation the beads are dried, subsequently the carbon is burnt and often oxidic catalysts in the form of small spheres result that are suggested to be tested directly in parallel single-bead reactors [54].

11.4

Catalyst Libraries for Secondary Screening

High-throughput preparation and testing techniques that are similar to standard lab procedures and deliver reliable data even for kinetic analysis are called stage II screening or secondary screening. The spectrum of parallel reactors comprises reactors with individual feed supply and heating where only the product analysis is shared [58, 59] as well as reactors with joint gas supply and heating (see, for instance, [60–62]). The individual reactors themselves are fixed-bed reactors similar to standard lab reactors and the same demands

are made on the catalyst from an engineering point of view. If properly carried out even kinetic data can be derived from such reactors and upscaling of the catalysts should not be a problem.

For catalyst preparation all techniques are available that are used in standard lab preparation of inorganic materials. Most of the preparation steps can be automated and can be done in parallel using synthesis robots. In the next sections, the most frequently used preparation routes are discussed. Postsynthesis treatment steps common to many different preparation routes are discussed separately at the end of the section.

11.4.1

Impregnation Techniques

Impregnation (see Chapter 4 for background) is the most frequently used technique in high-throughput preparation due to its apparent simplicity. Table 11.2 summarizes examples of high-throughput impregnation preparation of catalysts.

11.4.2

Precipitation

Hoffmann *et al.* have studied the high-throughput preparation of demanding catalysts, that is, Au/Co₃O₄ by coprecipitation (Chapter 7) and Au/TiO₂ by deposition-precipitation (Chapters 6 and 17) already in the early years of high-throughput catalysis [60]. They used a GILSON-XL-232 robot and varied the concentrations and pH values during precipitation. The reproducibility of the syntheses measured by testing the catalysts in low-temperature CO oxidation was much better compared to manual preparation.

Several research groups studied the influence of preparation conditions of Cu/ZnO catalysts on their catalytic properties in high-pressure methanol synthesis [82–84]. Researchers from Symyx Technologies showed for the oxidative dehydrogenation of ethane that upscaling of a mixed-metal oxide catalyst is possible even if different preparation methods are used [85]. They prepared tens of thousands of different compositions of mixed-metal oxides as thin films on a wafer substrate in a primary screening by sol-gel or evaporation method. The best catalysts identified in this screening were scaled-up to the secondary screening stage (50 mg level) by a coprecipitation method. At the last stage, the best catalysts were prepared on the 20 g scale under identical precipitation conditions and tested in a conventional reactor. Nearly the same conversion and selectivity in ethane dehydrogenation was measured for the 50 mg and 20 g scale catalysts.

A new method that may overcome the drawbacks of traditional precipitation methods is the use of micromixers, which combine excellent mixing (to

Table 11.2 Catalyst libraries prepared by impregnation techniques.

Catalyst library	Catalyzed reaction	Preparation details	References
Bi, Cr, Co, Er, Gd, Fe, Ni, Pd, Ag, Ti, V, Zn, Pt, Rh on γ -Al ₂ O ₃ pellets	H ₂ oxidation		[1]
66 ternary Pt-Pd-In catalysts on γ -Al ₂ O ₃ pellets	Dehydrogenation of cyclohexane	Mixing of solutions, adding one alumina pellet, evaporation of water	[63, 64]
56 quaternary Pt-Pd-In-Na catalysts on γ -Al ₂ O ₃ pellets	NO reduction by propene	Mixing of solutions, adding one alumina pellet, evaporation of water	[51]
30 binary Mn-NaWO ₄ /SiO ₂ catalysts	Oxidative coupling of methane		[61]
36 ternary Pt-Zr-V/ γ -Al ₂ O ₃ catalysts	Methane oxidation	Impregnation of support placed in channels of a monolith	[65, 66]
210 catalysts containing three to five elements from Pt, Pd, Rh, Ru, Au, Cu, Ag, Mn on TiO ₂ or Fe ₂ O ₃	Low temperature combustion of propane	i.w. (incipient wetness) impregnation in three steps, components that do not precipitate were mixed together	[33]
ternary catalysts from Cu, Ni, Ba, Zr, Mn, Fe, La, Cr, Ag, Pt, Co, Cs, Sr, Ce, W, Mo on SiO ₂ and TiO ₂	Methane oxidation	i.w. impregnation	[62]
140 bimetallic Pt on activated carbon catalysts, second metals: Co, Y, Ni, Pr, Nd, Cr, Ga, Pb, Mn, Ba, Cu, La, Sn, V	Hydrogenation of crotonaldehyde	i.w. impregnation of commercial Pt/C catalyst	[67]
Ag, Ca, Co, Cr, Cu, Fe, Ga, La, Mg, Mn, Ni, Zr on α -Al ₂ O ₃	Oxidative dehydrogenation of ethane and propane	Preparation of a thick shell (20 wt%) of active components on inert α -Al ₂ O ₃ beads by sequential wet impregnation	[68]

(continued overleaf)

Table 11.2 (continued).

Catalyst library	Catalyzed reaction	Preparation details	References
Different supported catalysts	Propene oxidation; butadiene hydrogenation	192 catalysts with five components can be completed in 2 h; impregnation of activated carbons leads to high surface area oxides	[69]
V-free mixed-metal oxides supported on α -Al ₂ O ₃	Oxidative dehydrogenation of ethane	Preparation of a eggshell (20 wt%) of active components on inert α -Al ₂ O ₃ beads by impregnation	[29]
Quaternary Mo-V-Nb-W mixed-metal oxides on Al ₂ O ₃	Selective oxidation of propane	Wet and dry impregnation, care was taken to obtain homogeneous distribution over the support	[70]
Doped V-Mg mixed-metal oxides	Oxidative dehydrogenation of ethylbenzene	Wet impregnation of freshly precipitated MgO	[71]
Catalysts containing metal oxides (ZrO ₂ , TiO ₂), acidity enhancer (SO ₄ ²⁻ , BO ₄ ³⁻ , PO ₄ ³⁻ , WO _x), and promoters (Pt, Ce, Pd, Sn, Ni, Mn, Nb)	Light-paraffin isomerization	i.w. impregnation	[72]
Catalysts containing metal oxides (γ -Al ₂ O ₃ , ZrO ₂ , TiO ₂), acidity enhancer (SO ₄ ²⁻ , BO ₄ ³⁻ , PO ₄ ³⁻ , WO _x), and promoters (Pt, Ce, Pd, Sn, Ni, Mn, Nb)	Paraffin isomerization	i.w. impregnation with the acidity enhancer, drying, i.w. impregnation with the promoter, drying, i.w. impregnation with Pt	[73]
Single and binary metal catalysts (35 metals) on γ -Al ₂ O ₃	Propene oxidation to propene oxide	i.w. impregnation of γ -Al ₂ O ₃ single pellets	[52]

43 elements supported on SiO ₂ (0.1, 1, and 5 mol%)	Selective oxidation of methane	i.w. impregnation	[74]
24 carbon-supported noble metal catalysts	Reductive amination of benzaldehyde	i.w. impregnation of carbon, drying, reducing in H ₂ /N ₂ flow	[75]
Quaternary Mo-Nb-Sb-V mixed oxides supported on SiO ₂	Oxidation of propane to acrylic acid	Comparison of solution-based automated impregnation to standard slurry method	[76]
K _x La _{1-x} FeO ₃ , A _{2x} Cu _{1-x} Fe ₂ O ₄ and A _{2x} Co _{1-x} Fe ₂ O ₄ (A = Li, Na, K, Cs)	Diesel soot combustion	Catalysts and soot prepared by ink jet technology directly in crucibles used for thermogravimetric study	[77]
Pt on Ce _{0.9} Mo _{0.1} O _x (M = Pb, Bi, Zr, V, W, Mo, Y, La, In, Sn, Zr/Bi)	(Reverse) water gas shift reaction	Catalysts prepared manual, Pt was loaded on the catalysts by robot via i.w. impregnation	[78]
33 elements supported on HZSM-5	CH ₄ + CO → benzene	wet impregnation	[79]
Supports (α-Al ₂ O ₃ , γ-Al ₂ O ₃ , ZrO ₂ , Cu/Zn/Al), main metals (Fe, Cr, Cu, Zn, Ni, Mn, Co, Mo, La, Sm, Ce), precious metals (Au, Pt, Pd, Ru), promoters (Ca, K, Li, Cs)	Water gas shift reaction	Sequential impregnation of support, optimization of composition by genetic algorithm	[80]
Pt and 11 additives (Y, La, Zr, Mo, Re, Ir, Ni, Pt, Zn, Ag, Au) loaded on 12 supports (oxides, carbides, nitrides, borides)	HCN synthesis	Impregnation on low-surface supports, optimization of composition by genetic algorithm	[81]

minimize pH gradients) with adjustable residence time. It was shown for hydrotalcites syntheses [86] and for precipitation of metal-substituted dawsonites [87] that mixed-metal oxide nanomaterials with tuneable properties can be prepared. Although the method has been used by the authors for single-material preparation it seems straightforward to adapt it to high-throughput preparation of catalysts either by parallel working micromixers or by preparing differently composed precipitates sequentially by changing the precursor solution.

11.4.3

Hydrothermal Synthesis

Preparation under hydrothermal conditions (temperatures above 100 °C and the presence of water) can be used to enhance crystallization and it is therefore the method of choice for zeolite synthesis (Chapter 12) but is used for making mixed-metal oxides, too.

Akporiae *et al.* [88] developed a multiautoclave system consisting of Teflon blocks each of them containing 100 reaction chambers. By stacking the blocks, up to 1000 hydrothermal syntheses can be done in one experiment. The authors used the multiautoclave in combination with automated X-ray powder diffraction to explore ternary and quaternary phase diagrams in the $\text{Na}_2\text{O}-\text{SiO}_2-\text{Al}_2\text{O}_3$ and the $\text{Na}_2\text{O}-\text{Li}_2\text{O}-\text{Cs}_2\text{O}-\text{tetramethylammonium}_2\text{O}$ system. Areas in the multicomponent parameter spaces where the different crystalline structures of zeolites are formed could be identified in a single experiment. This is an impressive example showing the drastic decrease in time and costs by applying high-throughput experimentation. Using similar multiautoclaves, Choi *et al.* studied phase diagrams of alumophosphate molecular sieves [89]. Pescarmona *et al.* determined the optimal synthesis conditions for zeolite beta with different Si/Al ratios by variation of silica and alumina sources, nature and concentration of template, alkali type and concentration, water content, pH, temperature, and reaction time [90]. The same group studied Ti-containing silsesquioxanes (small discrete siloxane cages) used both as homogeneous catalysts and as model structures for identifying active centers in Ti-containing epoxidation catalysts [90, 91]. By applying high-throughput experimentation in synthesis, X-ray diffraction characterization, and data-mining techniques, Corma *et al.* discovered a new type of zeolite ITQ-30 in a wide range of Si/Al ratios that belongs to the MWW family [19] and a new silicogermanate zeolite ITQ-33 having 18-ring large pores [92].

Hydrothermal synthesis has also been used to prepare mixed-metal oxide catalysts. The group of Maier presented already in 1998 the first hydrothermal high-throughput preparation method for such catalytic materials [93]. Corma *et al.* used a hydrothermal treatment of sol-gel synthesized Ti-silicalite catalyst precursors to accelerate the crystallization [94].

11.4.4

Sol-Gel Chemistry

Sol-gel chemistry (Chapter 5) is a preparation method, which can easily be adapted to synthesis robots. The application of this method to high-throughput catalysis was first described by the group of Maier, who prepared amorphous microporous mixed-metal oxides in small cavities of a carrier slate plate [95, 96]. Libraries of doped TiO_2 , SnO_2 , and WO_3 have been prepared in larger amounts in sets of HPLC flasks [97]. The robot-assisted sol-gel preparation has been applied to mixed-metal oxide catalysts of various composition and the catalysts have been tested for several reactions in gas phases as well as in liquid phase (see Table 11.3).

Improvements or supplements to the sol-gel method have been reported by several groups: Dai *et al.* prepared a library of doped- TiO_2 photodegradation catalysts by precipitation the active compounds onto SiO_2 as a mechanical support [103]. Corma *et al.* reported the sol formation by use of a synthesis robot and the crystallization under hydrothermal conditions in autoclaves [94]. Pescarmona *et al.* presented a detailed study of the preparation conditions (precursor concentration, type and amount of hydrolyzing agent, amount of alcohol) for the preparation of transition-metal-free B-Al-Ga mixed oxides using a full-factorial library design [106].

11.4.5

Drying, Calcination, and Shaping

In most cases catalyst precursors need a pretreatment before they can be used: Besides drying normally a calcination step follows in which a solid-state reaction at elevated temperature yields the active catalyst. In this reaction, anions (nitrates, oxalates, acetates, chlorides), as well as additives are decomposed or burnt and thereby removed from the catalysts.

In industrial preparation, catalyst precursor solutions or slurries are often spray dried. This method leads to a uniform distribution of the components in the particles. Typical lab spray dryers operate with a minimal catalyst mass of about 10 g, which is much higher than the amounts that are prepared in most high-throughput experiments. Recently, a freeze-drying method has been presented that produces as uniform catalyst particles as spray drying, but can operate with small amounts and can easily be done in parallel for many samples [107–109]. According to the freeze-drying method the suspension is first frozen, afterwards the solvent (in most cases water) is sublimed in vacuum. Like in spray dryers the precipitates have the possibility to precipitate but crystal growth is hindered due to lack of time in the case of spray drying or due to hindered diffusion in the case of freeze drying.

A parallel calcination apparatus that corresponds to the industrial used rotary kiln has been developed by Mayer *et al.* [109,]. Several tubes are arranged in a

Table 11.3 Catalyst libraries prepared by sol-gel techniques.

Catalyst library	Catalyzed reaction	Preparation details	References
37 mixed-metal oxides based on SiO ₂ and TiO ₂	Hydrogenation of 1-hexene, oxidation of isooctane	1–3 mol% of active transition-metal oxide in a matrix of base-metal oxide (TiO ₂ , SiO ₂)	[95]
33 mixed-metal oxides based on SiO ₂ , ZrO ₂ , and TiO ₂	Oxidation of propene	2–5 mol% of active transition-metal oxide in a matrix of base-metal oxide	[98]
32 mixed-metal oxides based on SiO ₂ and TiO ₂	Oxidation of toluene	1–3 mol% of active transition-metal oxide in a matrix of base-metal oxide	[99]
About 200 mixed-metal oxides based on TiO ₂ , SnO ₂ , and WO ₃	Photocatalysis using visible light for wastewater treatment	Change of electronic properties of base-metal oxides by dopants	[97]
Three 207-member libraries of Sb-rich Mo-V-Sb mixed-metal oxides	Selective oxidation of isobutane to methacrolein	Alkoxide precursors, hydrolysis with acetic acid, gel formation overnight	[100]
Doped V-Mg mixed-metal oxides	Oxidative dehydrogenation of ethylbenzene	Low-temperature hydrolysis of Mg(OR) ₂ and VO(OR) ₃	[71]
Mixed-metal oxides based on CoO _x , MnO _x , and NiO _x doped by 56 different metal centers	Room-temperature CO oxidation	Alkoxide precursors, 5 days gel formation and drying at room temperature	[101]
Mixed-metal oxides containing V, Fe, Mo, Cr, Ta, Nb, Mn, Sb and Bi	Selective oxidation of isobutane to methacrolein	Alkoxide precursors + complexing agent (4-hydroxy-4-methyl-pentanone) + acid	[102]
Ti-silicates	Epoxidation of cyclohexene, 1-hexene, 1-decene, 1-dodecene	Crystallization under hydrothermal conditions, variation of preparation parameters	[94]

Mixed-metal oxides	Photodegradation of 1,6-hexamethylenediamine	Catalysts supported on SiO ₂ , starting compounds are chlorides, bromides, nitrates, hydroxides, acetates, vanadate, tungstate; partly addition of block copolymer	[103]
Optimization of doped Mo-V-Sb mixed-metal oxide system	Partial oxidation of isobutane to methacrolein	Alkoxide hydrolysis by HCl in propanol solution; use of genetic algorithms for optimization of catalyst composition; best catalysts have been scaled-up	[35]
> 5000 mixed-metal oxides	CO ₂ reforming of methane	Preparation in 10 ml vials, 3 different preparation methods (matrix metal precursors alkoxide, propionate, or nitrate); best catalysts confirmed by conventional synthesis and testing	[104]
Mixed-metal oxides	Low-temperature soot oxidation	Two different recipes for Ce-based and Co- or Mn-based catalysts, 4-hydroxy-4-methyl-pentanone as complexing agent	[105]
Transition-metal-free B-Al-Ga mixed oxides	Epoxidation of cyclooctene with H ₂ O ₂	Full factorial library design; study of the composition of the sol (concentration of precursor, type and amount of hydrolyzing agent and amount of alcohol) for Al ₂ O ₃ - and Ga ₂ O ₃ -based mixed oxides	[15]

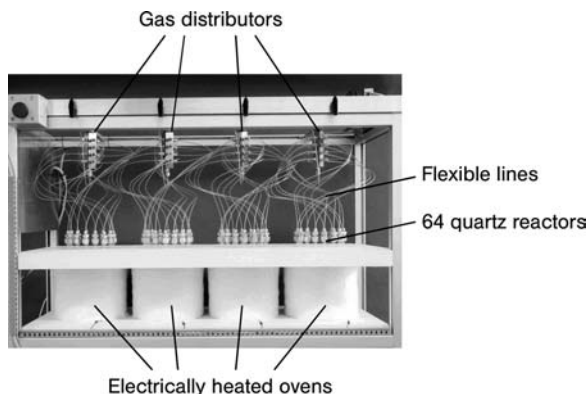


Figure 11.4 Apparatus for parallel calcination of 64 catalysts developed at Leibniz Institute for Catalysis Berlin, Germany.

drum that is rotated. By this, the catalyst powders in each of the tubes are mixed well during the calcination and inhomogeneity and plugging is prevented.

A fixed-bed setup for calcination has been realized at the authors' institute (Figure 11.4): 64 fixed-bed reactors are placed inside four ovens. The reactor inlets are connected by flexible lines with four gas supplies. Solid and liquid reaction products are condensed after the reactor outlets and the gases are led to the exhaust. By combination of four different gas compositions and four heating regimes (calcination temperatures, heating ramps, times) one can easily study the influence of calcination conditions on catalyst structure and performance. Moreover, gas composition can also be changed during the calcination procedure, which allows multistep calcination protocols.

An important aspect of industrial catalyst preparation is shaping to obtain granulates, beads or pellets for the use in fixed-bed reactors (Chapter 9). However, parallel shaping of catalyst powders is not yet available on commercial synthesis platforms although ideas for parallel pressing, crushing and sieving have been published [111].

11.5

Catalyst Libraries for Special Reactor Types

For special reactor types such as monoliths [65, 112] and coating of microreactors [113–116] we refer to the literature.

11.6

An Industrial Point of View

The chemical industry has been interested in high-throughput catalysis since it started in the mid-1990s. Companies specialized in high-throughput like

Symyx in the United States, hte AG in Germany, and Avantium in the Netherlands were the initial industrial drivers. Meanwhile, many of the big chemical companies operate their own high-throughput laboratories. The driving force for using HT technologies in industry is an economic one: Changing feedstock for chemical industry requires the development of new processes with new catalysts. Thousands of catalytically materials have to be prepared and tested until a new catalytic process can be put into operation. High-throughput experimentation can significantly speed up this process.

Although nowadays most of the bigger chemical companies are using high-throughput technology, publications from an industrial point of view are rare. Recently, a short summary of the main differences between laboratory and industrial preparation of catalysts and how to approach industrial demands by high-throughput experimentation was given by Dingerdissen and Linke [117]. The main difference from academic catalyst preparation is that in industry only a limited number of unit operations are used and therefore, several highly sophisticated lab preparation techniques, unless they result in extraordinary catalysts, cannot be applied in industry. Moreover, economic factors (costs of precursor materials) and ecological demands (avoid toxic and environmentally harmful waste) have to be considered. In fact, most catalysts in industry are manufactured by impregnation, precipitation, or ion-exchange techniques. Recently, Degussa has published some features of their high-throughput synthesis equipment illustrated by preparation of an advanced Pd-based vinyl acetate catalysts [109, 118].

11.7 Conclusions

Catalyst preparation by high-throughput technologies has become well adapted over the last decade. All unit operation with the exception of some solid handling operations can now be carried out on robotic platforms. Nevertheless, increasing the speed and throughput of preparation will remain an important topic.

Wide varieties of methods for planning and optimizing high-throughput catalyst libraries have been explored. True combinatorial approaches have been nearly completely replaced by statistical design of experiments or (stochastic) optimization methods. Future improvements may be gained from better integrating chemical knowledge into the library design, that is, by reducing the fraction of experiments in regions of the parameter space where the chance of success is essentially zero. This idea requires joint efforts from informatics as well as from chemists in order to better represent the chemical knowledge, for example, in the form of databases or expert systems, and to integrate that knowledge into optimization strategies.

Another, only recently addressed, aspect is to use high-throughput technologies, specifically stage II methods, in order to find out which

parameters influence the catalyst synthesis steps and to what degree [20]. Such studies can offer more insight into the preparation process itself and can therefore ease upscaling if this knowledge is used to identify preparation routes that are more robust against variation of parameters.

References

1. Moates, F.C., Somani, M., Annamalai, J., Richardson, J.T., Luss, D. and Willson, R.C. (1996) *Ind. Eng. Chem. Res.*, **35**, 4801–3.
2. Burello, E. and Rothenberg, G. (2006) *Int. J. Mol. Sci.*, **7**, 375–404.
3. de Vries, J.G. and de Vries, A.H.M. (2003) *Eur. J. Org. Chem.*, **2003**, 799–811.
4. Strasser, P., Gorer, S., Fan, Q., Chondroudis, K., Cendak, K., Giaquinta, D. and Devenney, M. (2004) Combinatorial synthesis and high-throughput screening of fuel cell electrocatalysts, in *High-Throughput Screening in Chemical Catalysis* (eds A. Hagemeyer, P. Strasser and J.A.F. Volpe), Wiley-VCH Verlag GmbH, Weinheim, pp. 271–98.
5. Liu, J.H., Jeon, M.K., Mahmood, A. and Woo, S.I. (2006) High-throughput screening for fuel cell technology, in *Combinatorial and High-Throughput Discovery and Optimization of Catalysts and Materials* (eds R.A. Potyrailo and W.F. Maier), CRC Press, Boca Raton, pp. 259–78.
6. Senkan, S. (2001) *Angew. Chem. Int. Ed.*, **40**, 312–29.
7. Duff, D.G., Ohrenberg, A., Voelkening, S. and Boll, M. (2004) *Macromol. Rapid Commun.*, **25**, 169–77.
8. Newsam, J.M., Schunk, S.A. and Klein, J. (2000) DE 100059890 A1.
9. Newsam, J.M. (2000) Design of catalysts and catalyst libraries, in *Combinatorial Catalysis and High Throughput Catalyst Design and Testing* (eds E.G. Derouane, F. Lemos, A. Corma and F.R. Ribeiro), Kluwer Academic Publishers, Dordrecht, pp. 301–35.
10. Sun, Y., Chan, B.C., Ramnarayanan, R., Leventry, W.M., Mallouk, T.E., Bare, S.R. and Willis, R.R. (2002) *J. Comb. Chem.*, **4**, 569–75.
11. Klein, J., Zech, T., Newsam, J.M. and Schunk, S.A. (2003) *Appl. Catal. A: Gen.*, **254**, 121–31.
12. Lam, K.S., Lebl, M. and Krchnak, V. (1997) *Chem. Rev.*, **97**, 411–48.
13. Holena, M. and Baerns, M. (2008) Computer aided design of solid catalysts, in *Handbook of Heterogeneous Catalysis* (eds G. Ertl, H. Knözinger, F. Schüth and J. Weitkamp), Wiley-VCH Verlag GmbH, Weinheim, pp. 66–81.
14. Schmitz, P.J., Kudla, R.J., Drews, A.R., Chen, A.E., Lowe-Ma, C.K., McCabe, R.W., Schneider, W.F. and Goralski, C.T. Jr. (2006) *Appl. Catal. B: Environm.*, **67**, 246–56.
15. Pescarmona, P.P., Janssen, K.P.F. and Jacobs, P.A. (2007) *Chem. Eur. J.*, **13**, 6562–72.
16. Rueda, N., Bacaud, R., Lanteri, P. and Vrinat, M. (2001) *Appl. Catal. A: Gen.*, **215**, 81–89.
17. Chen, H. and Adesina, A.A. (1997) *Appl. Catal. A: Gen.*, **162**, 47–56.
18. Tagliabue, M., Carluccio, L.C., Ghisletti, D. and Perego, C. (2003) *Catal. Today*, **81**, 405–12.
19. Corma, A., Diaz-Cabanas, M.J., Moliner, M. and Martinez, C. (2006) *J. Catal.*, **241**, 312–18.
20. Cukic, T., Kraehnert, R., Holena, M., Herein, D., Linke, D. and Dingerdissen, U. (2007) *Appl. Catal. A: Gen.*, **323**, 25–37.

21. Wolf, D., Buyevskaya, O.V. and Baerns, M. (2000) *Appl. Catal. A: Gen.*, **200**, 63–67.
22. Rodemerck, U., Baerns, M., Holena, M. and Wolf, D. (2004) *Appl. Surf. Sci.*, **223**, 168–74.
23. Holena, M. (2004) Present trends in the application of genetic algorithms to heterogeneous catalysis, in *High-Throughput Screening in Chemical Catalysis* (eds A. Hagemeyer, P. Strasser and J.A.F. Volpe), Wiley-VCH Verlag GmbH, Weinheim, pp. 153–73.
24. Holena, M., Cukic, T., Rodemerck, U. and Linke, D. (2008) *J. Chem. Inf. Model.*, **48**, 274–82.
25. Buyevskaya, O.V., Wolf, D. and Baerns, M. (2000) *Catal. Today*, **62**, 91–99.
26. Grubert, G., Wolf, D., Dropka, N., Kolf, S. and Baerns, M. (2001) Rapid discovery of new catalytic materials for the oxidative dehydrogenation of ethane to ethylene by an evolutionary approach, *4th World Congress on Oxidation Catalysis*. DECHEMA e.V, Berlin, Potsdam.
27. Langpape, M., Grubert, G., Wolf, D. and Baerns, M. (2001) *DGMK-Tagungsbericht*, **4**, 227–34.
28. Baerns, M., Buyevskaya, O., Grubert, G. and Rodemerck, U. (2002) Combinatorial methodology and its experimental validation by parallel synthesis, testing and characterization of solid catalytic materials, in *Principles and Methods for Accelerated Catalyst Design and Testing* (eds E.G. Derouane *et al.*), Kluwer Academic Publishers, Dordrecht, pp. 85–100.
29. Grubert, G., Kondratenko, E., Kolf, S., Baerns, M., van Geem, P. and Parton, R. (2003) *Catal. Today*, **81**, 337–45.
30. Buyevskaya, O.V., Brückner, A., Kondratenko, E.V., Wolf, D. and Baerns, M. (2001) *Catal. Today*, **67**, 369–78.
31. Cawse, J.N., Baerns, M. and Holena, M. (2004) *J. Chem. Inf. Comput. Sci.*, **44**, 143–46.
32. Tompos, A., Margittfalvi, J.L., Tfirst, E. and Vegvari, L. (2006) *Appl. Catal. A: Gen.*, **303**, 72–80.
33. Rodemerck, U., Wolf, D., Buyevskaya, O.V., Claus, P., Senkan, S. and Baerns, M. (2001) *Chem. Eng. J.*, **82**, 3–11.
34. Corma, A., Serra, J.M. and Chica, A. (2002) Application of genetic algorithms to the development and optimization of light paraffin isomerization catalysts, in *Principles and Methods for Accelerated Catalyst Design and Testing* (eds E.G. Derouane, V. Parmon, F. Lemos and F.R. Ribeiro), Kluwer, Dordrecht, pp. 153–72.
35. Paul, J.S., Janssens, R., Denayer, J.F.M., Baron, G.V. and Jacobs, P.A. (2005) *J. Comb. Chem.*, **7**, 407–13.
36. Ohrenberg, A., von Törne, C., Schuppert, A. and Knab, B. (2005) *QSAR Comb. Sci.*, **24**, 29–37.
37. Pereira, S.R.M., Clerc, F., Farrusseng, D., van der Waal, J.C., Maschmeyer, T. and Mirodatos, C. (2005) *QSAR Comb. Sci.*, **24**, 45–57.
38. Huang, K., Zhan, X.-L., Chen, F.-Q. and Lu, D.-W. (2003) *Chem. Eng. Sci.*, **58**, 81–87.
39. Hanak, J.J. (1970) *J. Mater. Sci.*, **5**, 964.
40. Xiang, X.-D., Sun, X., Briceno, G., Lou, Y., Wang, K.-A., Chang, H., Wallace-Freedman, W.G., Chen, S.-W. and Schultz, P.G. (1995) *Science*, **268**, 1738–40.
41. Briceño, G., Chang, H., Sun, X., Schultz, P.G. and Xiang, X.-D. (1995) *Science*, **270**, 273–75.
42. Danielson, E., Golden, J.H., McFarland, E.W., Reaves, C.M., Weinberg, W.H. and Wu, X.D. (1997) *Nature*, **389**, 944–48.
43. Danielson, E., Devenney, M., Giaquinta, D.M., Golden, J.H., Haushalter, R.C., McFarland, E.W., Poojary, D.M., Reaves, C.M., Weinberg, W.H. and Wu, X.D. (1998) *Science*, **279**, 837–39.
44. Schultz, P.G. and Xiang, X.-D. (1998) *Curr. Opin. Solid State Mater. Sci.*, **3**, 153–58.

45. Baker, B.E., Kline, N.J., Treado, P.J. and Natan, M.J. (1996) *J. Am. Chem. Soc.*, **118**, 8721–22.
46. Dover, R.B., Schneemeyer, L.F. and Fleming, R.M. (1998) *Nature*, **392**, 162–64.
47. Bergh, H.S. (2004) High-throughput workflow development: strategies and examples in heterogeneous catalysis, in *High-Throughput Screening in Chemical Catalysis* (eds A. Hagemeyer, P. Strasser and J.A.F. Volpe), Wiley-VCH Verlag GmbH, Weinheim, pp. 63–88.
48. Cong, P., Doolen, R.D., Fan, Q., Giaquinta, D.M., Guan, S., McFarland, E.W., Poojary, D.M., Self, K., Turner, H.W. and Weinberg, W.H. (1999) *Angew. Chem. Int. Ed.*, **38**, 483–88.
49. Senkan, S., Krantz, K., Ozturk, S., Zengin, V. and Onal, I. (1999) *Angew. Chem. Int. Ed.*, **38**, 2794–99.
50. Senkan, S.M. and Ozturk, S. (1999) *Angew. Chem. Int. Ed.*, **38**, 791–95.
51. Krantz, K., Ozkru, S. and Senkan, S. (2000) *Catal. Today*, **62**, 281–89.
52. Miyazaki, T., Ozturk, S., Onal, I. and Senkan, S. (2003) *Catal. Today*, **81**, 473–84.
53. Zech, T., Bohner, G. and Klein, J. (2005) *Catal. Today*, **110**, 58–67.
54. Schüth, F. et al. (2006) *Catal. Today*, **117**, 284–90.
55. Gobin, O.C., Martinez Joaristi, A. and Schüth, F. (2007) *J. Catal.*, **252**, 205–14.
56. Schwickardi, M., Johann, T., Schmidt, W. and Schüth, F. (2002) *Chem. Mater.*, **14**, 3913–19.
57. Schüth, F. (2003) *Angew. Chem. Int. Ed.*, **42**, 3604–22.
58. Kapteijn, F., Singoredjo, L., Dekker, N. and Moulijn, J. (1993) *Ind. Eng. Chem. Res.*, **32**, 445–52.
59. Perez-Ramirez, J., Berger, R.J., Mul, G., Kapteijn, F. and Moulijn, J.A. (2000) *Catal. Today*, **60**, 93–109.
60. Hoffmann, C., Wolf, A. and Schüth, F. (1999) *Angew. Chem. Int. Ed.*, **38**, 2800–3.
61. Rodemerck, U., Ignaszewski, P., Lucas, M. and Claus, P. (2000) *Chem. Eng. Technol.*, **23**, 413–16.
62. Hoffmann, C., Schmidt, H.-W. and Schüth, F. (2001) *J. Catal.*, **198**, 348–54.
63. Senkan, S.M. and Ozturk, S. (1999) *Angew. Chem.*, **111**, 867–71.
64. Senkan, S., Krantz, K., Ozturk, S., Zengin, V. and Onal, I. (1999) *Angew. Chem.*, **111**, 2965–71.
65. Rodemerck, U., Ignaszewski, P., Lucas, M., Claus, P. and Baerns, M. (2000) *Top. Catal.*, **13**, 249–52.
66. Claus, P., Hönicke, D. and Zech, T. (2001) *Catal. Today*, **67**, 319–39.
67. Thomson, S., Hoffmann, C., Ruthe, S., Schmidt, H.-W. and Schüth, F. (2001) *Appl. Catal. A: Gen.*, **220**, 253–64.
68. Hahndorf, I., Buyevskaya, O., Langpape, M., Grubert, G., Kolf, S., Guillon, E. and Baerns, M. (2002) *Chem. Eng. J.*, **89**, 119–25.
69. Schüth, F., Busch, O., Hoffmann, C., Johann, T., Kiener, C., Demuth, D., Klein, J., Schunk, S., Strehlau, W. and Zech, T. (2002) *Top. Catal.*, **21**, 55–66.
70. Grasso, G., Harji, B., Xue, E., Belochapkine, S. and Ross, J.R.H. (2003) *Catal. Today*, **81**, 369–75.
71. Geisler, S., Vauthey, I., Farusseng, D., Zanthoff, H. and Muhler, M. (2003) *Catal. Today*, **81**, 413–24.
72. Serra, J.M., Chica, A. and Corma, A. (2003) *Appl. Catal. A: Gen.*, **239**, 35–42.
73. Corma, A., Serra, J.M. and Chica, A. (2003) *Catal. Today*, **81**, 495–506.
74. Yamada, Y., Ueda, A., Shioyama, H. and Kobayashi, T. (2003) *Appl. Catal. A: Gen.*, **254**, 45–58.
75. Gomez, S., Peters, J.A., Waal, J.Cvd. and Maschmeyer, T. (2003) *Appl. Catal. A: Gen.*, **254**, 77–84.
76. Chen, L., Derouane, E.G. and Vedrine, J.C. (2004) *Appl. Catal. A: Gen.*, **270**, 157–63.
77. An, H., Kilroy, C. and McGinn, P.J. (2004) *Catal. Today*, **98**, 423–29.
78. Tibiletti, D., de Graaf, E.A.B., Pheng Teh, S., Rothenberg, G., Farrusseng, D. and Mirodatos, C. (2004) *J. Catal.*, **225**, 489–97.

79. Wang, H., Liu, Z., Shen, J., Liu, H. and Zhang, J. (2005) *Catal. Commun.*, **6**, 343–46.
80. Grubert, G., Kolf, S., Baerns, M., Vauthey, I., Farrusseng, D., van Veen, A.C., Mirodatos, C., Stobbe, E.R. and Cobden, P.D. (2006) *Appl. Catal. A: Gen.*, **306**, 17–21.
81. Moehmel, S., Steinfeldt, N., Engelschalt, S., Holena, M., Kolf, S., Baerns, M., Dingerdissen, U., Wolf, D., Weber, R. and Bewersdorf, M. (2008) *Appl. Catal. A: Gen.*, **334**, 73–83.
82. Kiener, C., Kurtz, M., Wilmer, H., Hoffmann, C., Schmidt, H.-W., Grunwaldt, J.-D., Muhler, M. and Schuth, F. (2003) *J. Catal.*, **216**, 110–19.
83. Omata, K., Hashimoto, M., Watanabe, Y., Umegaki, T., Wagatsuma, S., Ishiguro, G. and Yamada, M. (2004) *Appl. Catal. A: Gen.*, **262**, 207–14.
84. Omata, K., Watanabe, Y., Hashimoto, M., Umegaki, T. and Yamada, M. (2004) *Ind. Eng. Chem. Res.*, **43**, 3282–88.
85. Liu, Y., Cong, P., Doolen, R.D., Guan, S., Markov, V., Woo, L., Zeyss, S. and Dingerdissen, U. (2003) *Appl. Catal. A: Gen.*, **254**, 59–66.
86. Abelló, S. and Pérez-Ramírez, J. (2006) *Adv. Mater.*, **18**, 2436–39.
87. Santiago, M., Yalfani, M.S. and Pérez-Ramírez, J. (2006) *J. Mater. Chem.*, **16**, 2886–89.
88. Akporiaye, D.E., Dahl, I.M., Karlsson, A. and Wendelbo, R. (1998) *Angew. Chem.*, **110**, 629–31.
89. Choi, K., Gardner, D., Hilbrandt, N. and Bein, T. (1999) *Angew. Chem. Int. Ed.*, **38**, 2891–94.
90. Pescarmona, P.P., Rops, J.J.T., van der Waal, J.C., Jansen, J.C. and Maschmeyer, T. (2002) *J. Mol. Catal. A: Chem.*, **182–183**, 319–25.
91. Pescarmona, P.P., van der Waal, J.C., Maxwell, I.E. and Maschmeyer, T. (2001) *Angew. Chem.*, **113**, 762–65.
92. Corma, A., Diaz-Cabanas, M.J., Jorda, J.L., Martinez, C., Moliner, M. (2006) *Nature*, **443**, 842–45.
93. Klein, J., Lehmann, C.W., Schmidt, H.-W. and Maier, W.F. (1998) *Angew. Chem.*, **110**, 3557–61.
94. Corma, A., Serra, J.M., Serna, P., Valero, S., Argente, E. and Botti, V. (2005) *J. Catal.*, **229**, 513–24.
95. Holzwarth, A., Schmidt, H.-W. and Maier, W.F. (1998) *Angew. Chem.*, **110**, 2788–92.
96. Klein, S., Thorimbert, S. and Maier, W.F. (1996) *J. Catal.*, **163**, 476–88.
97. Lettmann, C., Hinrichs, H. and Maier, W.F. (2001) *Angew. Chem.*, **113**, 3258–62.
98. Orschel, M., Klein, J., Schmidt, H.-W. and Maier, W.F. (1999) *Angew. Chem.*, **111**, 2961–65.
99. Holzwarth, A. and Maier, W.F. (2000) *Platinum Metals Rev.*, **44**, 16–21.
100. Paul, J.S., Urschey, J., Jacobs, P.A., Maier, W.F. and Verpoort, F. (2003) *J. Catal.*, **220**, 136–45.
101. Saalfrank, J.W. and Maier, W.F. (2004) *Angew. Chem. Int. Ed.*, **43**, 2028–31.
102. Paul, J.S., Jacobs, P.A., Weiss, P.-A.W. and Maier, W.F. (2004) *Appl. Catal. A: Gen.*, **265**, 185–93.
103. Dai, Q.X., Xiao, H.Y., Li, W.S., Na, Y.Q. and Zhou, X.P. (2005) *Appl. Catal. A: Gen.*, **290**, 25–35.
104. Kim, D.K. and Maier, W.F. (2006) *J. Catal.*, **238**, 142–52.
105. Olong, N.E., Stowe, K. and Maier, W.F. (2007) *Appl. Catal. B: Environm.*, **74**, 19–25.
106. Procelewska, J., Galilea, J.L., Clerc, F., Farrusseng, D. and Schuth, F. (2007) *Comb. Chem. High Throughput Screen.*, **10**, 37–50.
107. Desrosiers, P., Guan, S., Hagemeyer, A., Lowe, D.M., Lugmair, C., Poojary, D.M., Turner, H., Weinberg, H., Zhou, X., Armbrust, R., Fengler, G. and Notheis, U. (2003) *Catal. Today*, **81**, 319–28.
108. Mayer, R., Fischer, A., Wolf, D., Kohle, N., Dingerdissen, U. (2004) WO 2005/058499 A1.
109. Mayer, R.W., Quandt, T., Schimmer, K., Rotgerink, H.L. and Tacke, T. (2006) *Stud. Surf. Sci. Catal.*, **162**, 235–42.

110. Mayer, R., Wolf, D. and Dingerdissen, U. (2004) WO 2005/039765 A1.
111. Lugmair, C., Hagemeyer, A., Erden, L.V., Volpe, A.F., Lowe, D.M. and Liu, Y. (2002) 2002/0014546 A1.
112. Lucas, M. and Claus, P. (2003) *Appl. Catal. A: Gen.*, **254**, 35–43.
113. Jähnisch, K., Hessel, V., Löwe, H. and Baerns, M. (2004) *Angew. Chem. Int. Ed.*, **43**, 406–46.
114. Müller, A. and Drese, K. (2004) Integrated microreactor set-ups for high-throughput screening and methods for the evaluation of “low-density” screening data, in *High-Throughput Screening in Chemical Catalysis* (eds A. Hagemeyer, P. Strasser and J.A.F. Volpe), Wiley-VCH Verlag GmbH, Weinheim, pp. 89–128.
115. Zech, T., Hönicke, D., Lohf, A., Golbig, K. and Richter, T. (2000) Simultaneous screening of catalysts in microchannels: methodology and experimental setup, in *Microreaction Technology: Industrial Prospects* (ed. W. Ehrfeld), Springer, Berlin, pp. 260–66.
116. Müller, A., Drese, K., Gnaser, H., Hampe, M., Hessel, V., Lowe, H., Schmitt, S. and Zapf, R. (2003) *Catal. Today*, **81**, 377–91.
117. Dingerdissen, U. and Linke, D. (2006) *Stud. Surf. Sci. Catal.*, **162**, 1–12.
118. Renneke, R., McIntosh, S., Arunajatesan, V., Cruz, M., Chen, B., Tacke, T., Lansink-Rotgerink, H., Geisselmann, A., Mayer, R., Hausmann, R., Schinke, P., Rodemerck, U. and Stoyanova, M. (2006) *Top. Catal.*, **38**, 279–87.

PART II

Case Studies

12

Concepts for Preparation of Zeolite-Based Catalysts

Metin Bulut and Pierre A. Jacobs

12.1

Introduction and Scope

Today the Structure Commission of the International Zeolite Association (IZA) has accepted 176 different framework types of different zeolite structures or topologies [1] with discrete acronyms [2]. They will be given in brackets when referring to zeolite samples. Each of the different framework topologies with distinct pore size and architecture can vary in chemical composition, as each framework type can be viewed as a tridimensional silicate in which Si–O₄ tetrahedra have common apices, several elements may be fully or partly substituted for Si and give rise to discrete materials encompassing a range of different hydrophilicity/hydrophobicity ratios, framework charge densities and framework compositions yielding different strengths of Brønsted/Lewis acid sites and redox properties.

The definition for catalytic purposes of a “zeolite” reads as follows: a crystalline material with micropores and cation-exchange capacity that is insoluble in water and common organic solvents and has sufficient thermal stability that allows removal of all pore-filling agents present in the as-synthesized materials. This definition is narrower than that of the IZA Constitution, which includes mesoporous solids, metal organic frameworks (MOFs), cationic and anionic clays [3].

An inspection of the industrial use of zeolites as catalysts shows, however, that only a rather limited number of zeolite topologies are currently used in major industrial processes. Among the more important ones are ultrastable Y (USY) (FAU), rare-earth-exchanged faujasite-type (X, Y) (FAU) and ZSM-5-type (MFI) zeolites in fluid catalytic cracking (FCC) of oil fractions [4]; noble-metal-loaded USY for hydroisomerization and hydrocracking of naphtha feedstocks [5]; mordenite (MOR) and zeolite Omega (MAZ) -based catalysts for C₄-C₆ alkane isomerization [6]; zeolites ZSM-23 (MTT), ZSM-35 (FER), ZSM-5 for selective oil dewaxing [7]; ZSM-5, silicalite (MFI), MCM-22 (MWW), Beta-type (BEA) zeolites for aromatics alkylation to yield ethylbenzene, p-xylene,

cumene, p-ethyltoluene [8]; zeolites ZSM-5, SAPO-34 (CHA) for methanol to olefins and/or larger hydrocarbons [9]; transition-metal-exchanged faujasite for catalytic combustion of volatile organic chemicals (VOCs) [10]; Fe, Cu, Cr, V, Ce-containing mordenite, ZSM-5, and faujasite-type zeolites for NO_x reduction with ammonia [11]; Beta-type zeolites in Friedel–Crafts catalysis, viz. acetylation of anisole [12]; ZSM-5-type zeolites for synthesis of pyridines from acetaldehyde, formaldehyde, and ammonia [13]; TS-1 (MFI) for liquid-phase oxygenation, viz. of phenol, propene, and oximes [14]; Fe-ZSM-5 for benzene oxygenation conversion to phenol with nitrous oxide [15]; Zeolite RHO for dimethylamine from methanol and ammonia [16]; and ZSM-22 (TON) and ZSM-23 for propene trimerization [17].

Most petrochemical catalysis involving transformations of crude oil derived fractions uses the Brønsted acidity spectrum of zeolites, often combined with the specific shape selectivity resulting from their pore architecture. In organic catalysis, a high number of different zeolites is used for a large number of organic reactions for chemical intermediates and fine chemicals [18].

Although topology and chemical composition determined by zeolite synthesis are at the basis of the shape, size, dimensionality, intersections of pores, and cages formed in the zeolite crystals and therefore are directly responsible for shape selectivity and diffusivity, the catalyst in the final process always requires further fine tuning by a number of secondary treatments. A notorious example consists in the ultrastabilization of zeolite Y, via subsequent exchanges with ammonium ions, steaming, and mineral acid treatment [19].

The size of the zeolite crystals determines the role of the external surface and the relative importance of diffusion-based shape selectivity in catalysis. So, the external surface of zeolite Beta, often in the form of nanosized crystallites, is crucial for catalysis. Some topologies like MWW (MCM-22) show structural features that result in the formation of typical half-cages at the external surface. Such confinement effects for molecules can also be the result of delamination of specific structures, viz. ITQ-2 [20].

Modified zeolites for use in an industrial reactor should have the right physical form and shape implied by the choice of the reactor (Chapter 9). FCC in a fluid-bed reactor requires spherical particles (70–100 μm), obtained by spray drying of the μm-sized USY zeolite crystals in the presence of a binder, viz. silica, alumina, and clays [21]. Extrusion requires a binding agent that attributes to the zeolite/binder mixture tixotropic properties in the extruder [22]. As the catalyst binder may be active, it exceeds the role of diluent agent for the active zeolite [21]. Indeed, the steam stability of some zeolites is known to be enhanced in a binder-containing zeolite particle [23].

The preparation of an industrial zeolite-based catalyst encompasses (i) synthesis of zeolite crystals with a given composition and morphology, including intergrowths or overgrowths of different structure types; (ii) modification of as-synthesized zeolite crystals, viz. template removal, ion exchange or impregnation, steam stabilization; (iii) shaping, viz. spray drying

and extrusion in presence of binder. For zeolite modification there is broad basic understanding [24], while shaping is treated in Chapter 9.

Before discussing aspects of zeolite synthesis relevant for catalysis, an overview of specific zeolite effects will be given, aiming at a conceptual overview of rules, hypotheses, and rationalizations that could be at the basis of *a-priori* design of zeolite crystals with predetermined topology, composition, and morphology. In this chapter a personal conceptual approach to zeolite catalyst preparation is given as needed by this catalyst designer. Emphasis is therefore on established zeolite effects and on ways to bring them into expression in synthesized materials. On many of the topics treated, several good reviews are available.

12.2

Zeolite Effects in Catalysis

12.2.1

Brønsted Acidity in Metallosilicate Zeolites

Whereas in zeolites Si^{4+} is substituted for M^{3+} elements, viz. Al, Ga, B, or Fe, the majority of the work on isomorphic substitution refers to aluminosilicates. The substitution is governed by Loewenstein's rule, stating that only Si–O–Si and Si–O–Al bonds are stable, excluding formation of Al–O–Al bonds. The resulting negative framework charges, if compensated by H^+ , are at the basis of formation of a solid Brønsted acid, with zeolite-specific bridging hydroxyl groups. Such bridged silanol groups [25] used for catalyst-activity-type relationships and catalytic-activity rationalizations, are viewed as resonance hybrids between two extreme structures (Figure 12.1), viz. “a fully bridged oxygen with a weakly bound proton,” and “a silanol group with a weak Lewis acid interaction of the hydroxyl oxygen with Al” [26]. The latter structure would represent the site in amorphous silica-alumina in which no stabilization by long-range symmetry exists [27]. Parameters affecting the zeolite acidity spectrum are shown in Figure 12.2.

The effect of chemical composition of a zeolite on its average Brønsted acidity, can be accounted for by its average Sanderson electronegativity, allowing

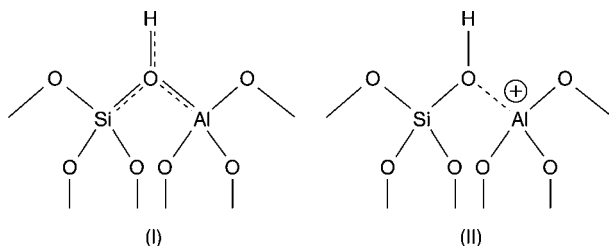


Figure 12.1 Brønsted acid sites in zeolites represented as a resonance hybrid between two extreme structures I and II [26].

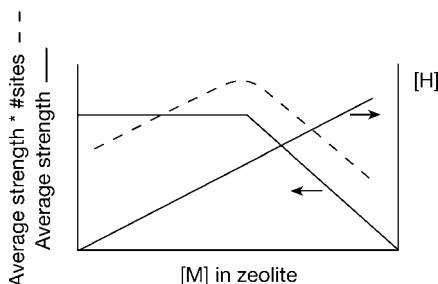


Figure 12.2 Schematic overview of zeolite parameters determining acidity in silicate-based zeolites [28]. M, trivalent element in tetrahedral coordination in the framework.

calculation of the average charge per proton present in the composition [29]. The maximum number of protons in siliceous materials, like USY, ZSM-5, Beta, usually varies from 0.2 till 1.2 mmol g⁻¹.

The effect of topology or structure on acid strength is expressed by the Si–O–M angle. The higher the angle, the higher the acid strength of the proton neutralizing the negative charge generated by substitution of M [30]. This topology-dependent Brønsted acidity rationalizes the existence of a spectrum of site strength. The Si–O–M bond angles ranging from 143 to 180° in H-MOR, from 133 to 177° in H-MFI and from 138 to 147° in H-FAU, are in line with observed decreasing catalytic activity, basicity of reactants affecting this spectrum [28].

The proton concentration in a zeolite depends on the degree of cation exchange for H⁺ and on the exchange capacity, viz. the M/(Si+M) fraction. In fully exchanged H-zeolites, the number of Brønsted sites will therefore increase linearly with the M/(Si + M) fraction, as predicted by the electronegativity concept. The strength of Brønsted sites is also influenced by the number of nearest neighbors (NNNs) [30]. In the tetrahedral zeolite environment, each Al (or M) atom has four nearest neighbors and depending on the topology between 9 and 12 NNNs in the second layer. The strength of the sites is maximal at low Al (M) concentration where the sites are isolated; it is minimal at the highest Al (M) concentration [31]. Including topologic densities, and the effect of up to five layers surrounding the central active site, the values of framework Si/Al yielding only isolated Brønsted sites (with maximum average Brønsted site strength) were found between 5.8 and 10.5 for different zeolites [32].

12.2.2

Zeolite Protonic Superacidity

Acid zeolites compared to their amorphous compositional counterparts often show several orders of magnitude enhanced intrinsic activity. Parameters invoked to rationalize this behavior are the higher concentration of Al^{IV} in the respective matrices, the higher intrinsic turnovers of each of such sites, as well as the enhanced reactant concentration in the intracrystalline

voids [33], favoring intermolecular hydrogen transfer. The latter effect is more pronounced in monodimensional tubular channels compared to cages, viz. in mordenite or mazzite compared to faujasite, suggesting that enhanced activity due to enhancement of bimolecular reaction rates contains a geometric component [33b].

Whereas the regularity of the Brønsted sites in terms of constant Si–O–Al bond angles for a given topology explains the rate enhancement compared to amorphous materials, the molecular origin of the *superacidity*, resulting in further rate enhancement, has been attributed to a favorable interaction with a neighboring Lewis site, viz. extra-framework $(\text{Al}_x\text{O}_y)^{z+}$ – species (EF_{Al}), or even to intrazeolitic silica-alumina species [34]. Their interaction with bridging hydroxyl groups yields enhanced acidity, as is evident from increased catalytic activity and infrared (IR) bathochromic shifts of the O–H stretching [35]. This is in line with electron withdrawal from the silanol O by EF_{Al} , leading to a decreased O–H bond strength and enhanced Brønsted acidity [36]. An overview of potential EF_{Al} species as probed by different techniques is available [37]. However, superacidic sites in zeolites, viz. USY, compared to real superacids at low temperature are unable to activate σ -bonds in alkanes. They have strengths only comparable to that of sulfuric acid [38, 39].

Recently, Brønsted sites are viewed to be of bifunctional nature, the H^+ protonating the adsorbed molecule, and the basic lattice oxygens converting the charged species into covalent ones. Thus, acid catalysis is not only controlled by protonation, but also by interaction with the zeolite oxygen atoms. The relative stability of intermediates is determined by the deprotonation energy and the stabilization by lattice (oxygen), the former being sensitive to zeolite composition and local geometric effects [40].

12.2.3

Brønsted Acidity in Substituted Four-Coordinated Aluminophosphates

Isomorphic substitution in microporous aluminophosphates ($\text{AlPO}_4\text{-n}$) is more complex than in traditional M^{3+} -containing metallosilicate zeolites. Crystalline microporous aluminophosphates [41], showing alternation between P^{4+} and Al^{3+} T-atoms in tetrahedrally arranged frameworks, do not show residual negative framework charges and do not contain Brønsted acidity. Al–OH groups present in AlPO_4 -hydrates, AlPO_4 -hydroxides, and AlPO_4 -fluorides [42, 43] show insufficient acid strength and/or stability for vapor-phase catalysis. No attempts are reported for use of such materials in liquid-phase low-temperature catalysis.

In the compositional family of four-coordinated aluminophosphate materials, many structure types and topologies are available for the catalyst designer [2]. Among the substitution possibilities with ions of different valence, the use of Si to achieve thermally stable solids is obvious. Substitution with M^{3+} occurs mainly for Al yielding neutral frameworks. With Si, isomorphic substitution

of P (IS_P) or simultaneous replacement of a set of adjacent {Al, P} ions ($IS_{Al,P}$) is possible [44].

The framework charges generated by substitution in a M, Al, P-containing synthesis gel, are neutralized by a template to allow crystallization of a four-coordinated $MAIPO_4$ -n framework. The size of and charge density on a template molecule, often protonated amines or tetraalkylammonium ions, will determine the degree of substitution. The concept of template/framework stoichiometry [45], that is, the maximum framework charge that can be balanced by a template molecule, dictates the substitution limit. When this ratio is exceeded, viz. with low-valent ions, the substituting ions are accommodated in charge-compensating cation positions [46]. With Co^{2+} , Fe^{2+} , and Mn^{2+} , charge compensation occurs already at low substitution degrees [47].

Si substitution in $AlPO_4$ -n is complex and even for a given topology can yield a whole family of $SiAlPO_4$ (SAPOs) with a variety of acid properties [42] (Figure 12.3). Via pathway IS_P a neutral framework is obtained with Si(4Al) environments. The $IS_{Al,P}$ path yields thermodynamically unstable Si–O–P bonds and is only hypothetical. The recurrent application of substitution mechanism $IS_{Al,P}$ starting from the crystal rim circumvents this problem, yielding a neutral $AlPO_4$ -n framework with a topotactic siliceous overlayer. At the boundary between the two domains electroneutral environments, viz. Si(3Si,1Al) and Si(1Al, 3Si), appear.

When Si substitution occurs via a combination of both pathways, the formation of Si-O-P bonds is avoided, resulting in the formation of silicon patches with $AlPO_4$ -n topology. In the majority of $SAPO_4$ -n materials, isolated Si is first accommodated in P sites [49], often significantly before the stoichiometric ratio is obtained. Further on, simultaneous substitution by the two mechanisms results in extensive silica patch formation. Zeolitic acidity is then generated via Al incorporation in the silica islands. It is clear that correlations between Brønsted acidity and degree of overall substitution will be complex. All synthesis parameters such as degree of substitution, nature of the organic template, crystallization temperature, and time, which may affect the relative importance of the substitution mechanisms, influence the Brønsted acid spectrum of the resulting materials [42].

Discrimination among rival substitution mechanisms has been attempted for several $SAPO_4$ -n topologies. In SAPO-5 up to 25% of the T atoms was replaced by large siliceous patches [48], concentrating at the crystals surface [50]. During SAPO-11 crystallization, the IS_P mechanism dominates with dipropylamine as template, while with diisopropylamine both IS_P mechanisms occur [51].

SAPO-34 synthesized with fluoride containing triethylamine also showed evidence for substitution via both mechanisms [52]. Unfortunately, the relative importance of formation of patches versus silica overlayers and Brønsted acid sites formation in each of them is not known.

SAPO-37 (FAU) has a potential interest for catalyst design, since a steam-stable pure FAU topology devoid of mesopores can be obtained, which is

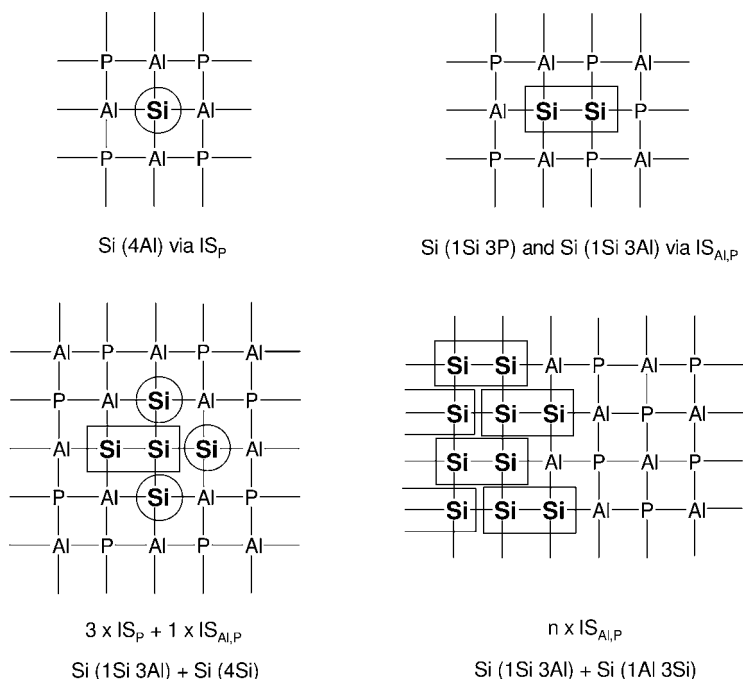


Figure 12.3 2-Dimensional grid representation of possible T-atom configurations in an $SiAlPO_4-n$ framework obtained by substitution of P (IS_P , circles; top left), of both one P and one Al atom

($IS_{Al,P}$, rectangles, top right), via recurrent replacement of Al, P couples ($n \times IS_{Al,P}$, bottom right), and via a combination of both pathways (bottom left). Si–P represent unstable chemical bonds [48].

impossible to achieve via the aluminosilicate variant [53]. According to the IS_P substitution mechanism, Si can be homogeneously distributed among the T-sites of SAPO-37, yielding a T-atom % of 12.5, 50, and 37.5 for Si, Al, and P, respectively [54]. The respective T-atoms have the following environments: Si(4Al), P(4Al), and Al(3P,1Si), negative framework charges being balanced by two tetrapropylammonium (TPA) ions and one tetramethylammonium (TMA) ion. Two models have been presented for substitution, though the assignment of the peaks of a deconvoluted ^{29}Si NMR spectrum could only be made via substitution, giving rise to siliceous domains near the crystal surface [55]. Brønsted acid sites (bridging silanol groups) can be present in the SAPO and silica-alumina domains as well as at their interphases. In this class of catalytic solids, there is no longer a linear correlation between Brønsted acid sites and degree of substitution or intensity of the Al^{IV} NMR line.

The contribution of different Brønsted acid sites in SAPO has been investigated:

- there is topology-dependent catalytic activity in SAPO-5, SAPO-11, and SAPO-37 [49a],

- in SAPO-5 isolated bridged OH groups in the SAPO domains [48a] are the active sites, with constant activity per site for SAPO-5 with different Si content [56],
- in SAPO-11 synthesized with dipropylamine, the active sites are located exclusively at domain interphases, while in SAPO-37 they were found at each of the three locations [49a],
- the thermal stability of hydroxyls in siliceous SAPO-37 is comparable to that in USY [57],
- hydrogen atom charges from molecular orbital calculations (CNDO/2), indicate that protons at border sites are most active [58].

12.2.4

Zeolite Shape Selectivity

Catalytic sites associated with a zeolite often affect reaction selectivity. A number of classical concepts are useful to the catalyst designer for their rationalizing and even predicting power. Molecules can be excluded from chemical activation at intracrystalline active sites, depending on the size, shape of the pores, and the reactant. To all such phenomena the concept of *reactant shape selectivity* (RSS) was coined. From a mixture of product molecules desorbing from the intracrystalline active sites the faster-diffusing “slimmer” molecules will be abundantly present, generating a pseudothermodynamic equilibrium in the bulk. The phenomena are described as *product diffusion shape selectivity* (PDSS). Geometric restrictions near the active site can inhibit formation of some transition states and affect product selectivity. The phenomena are known as *transition-state shape selectivity* (TSSS).

Whereas for RSS and PDSS crystallite encapsulated sites are needed, TSSS may occur in half-open cages at crystal terminating locations as well. Although such effects were mainly reported for hydrocarbons and alkylaromatics in medium-pore zeolites with 10-membered rings (10-MRs) of lattice atoms, viz. MFI, MEL, TON, the concepts are applicable to functionalized organics and other topologies as well. The nature of the sites is also not limited to Brønsted acid sites, but also applies to metal and redox sites. The area has been reviewed thoroughly [59]. The use of the concepts implies compositional homogeneity across the crystals and the existence of only intracrystalline sites that all show identical selectivity.

Initially, it was proposed that pore size and tortuosity, as well as pore architecture determined by the zeolite topology, were influencing intrazeolitic fields and field gradients, thus affecting differently the relative rates of primary and secondary reactions and overall selectivity [60]. Recently, effects of confinement on various kinetic and even thermodynamic effects were shown that provide an understanding of the confinement effect on adsorption and diffusion [61]. *Configurational-bias Monte Carlo* techniques allowed simulation of slowly diffusing molecules, trapped in cages or at adsorption sites in zeolite

topologies. This approach consisting of mapping the free-energy landscape in the intracrystalline space [61], ignores effects of local differences in site architecture, or concentration on reaction selectivity.

To a number of unexpected shape-selectivity phenomena with long alkane hydroconversion the term *inverse shape selectivity* was coined [62]. In zeolite pore widths of 0.65–0.74 nm, the opposite was encountered, as expected from mere geometric effects, that is, preferential formation of branched over linear hydrocarbons, viz. the formation of high yields of dibranched from n-alkanes over 10-MR zeolites like AFI (SAPO-5), the phenomenon being confirmed by adsorption experiments [63]. The molecular basis of such effects has been attributed to a purely entropic effect in monodimensional pores at high pressures expelling larger molecules by smaller ones [64].

Several shape-selective phenomena were attributed to topology-dependent structural sites. Such *nest effects* were the result of tuning of the curved catalyst surface to the configuration of adsorbed species, entropic effects governing the fitting [65]. A distinction between two types of *extra-framework catalysis* mainly in ZSM-22 (TON), was made using the terms of *pore mouth* and *key-lock* selective catalysis (Figure 12.4). Apparently, it is possible for alkanes via hydroconversion to be transformed in a selective way into products that are unable to be formed in or desorb from the zeolite. The abundant formation of some molecules, viz. 2-methylbranched alkanes from n-alkanes, was assigned to transformation in a single pore mouth. Others, viz. 2,4-dimethyloctane from n-decane, happened to be formed at neighboring pore mouths, as their selectivity was chain length as well as topology dependent [66]. However, the underlying hypothesis that intracrystalline conversion has been excluded for

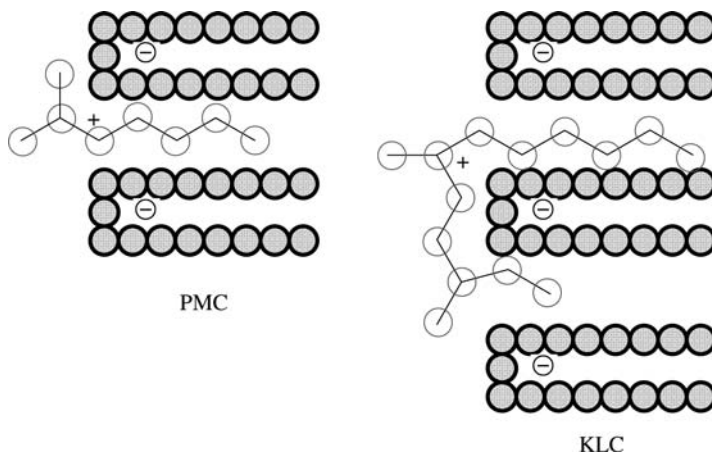


Figure 12.4 Schematic representation of methyl branching at the chain end of n-alkanes via pore-mouth catalysis (PMC) and dibranching at specific positions via molecular recognition in neighboring pore mouths (key-lock catalysis (KLC)) [66].

geometric reasons has been questioned. Simulation methods were assumed to prove the possibility of intracrystalline conversion, viz. via reverse shape selectivity [67].

Given this unsettled debate, the catalyst designer is recommended to continue taking possible effects of external surface catalysis into account. Indeed, the poisoning of the external surface of MWW zeolites (MCM-22) is not only selectivity but simultaneously activity determining [68]. Moreover, upon exfoliation of such structures the catalytic activity is much enhanced [69]. ITQ-2 being an exfoliated structure with external 12-MR cups, has a large external surface and allows conversion of molecules that are unable to enter the 10-MR pore system (Figure 12.5) [70]. For monomolecular reactions, viz. isomerization of *m*-xylene, Brønsted sites on the external surface and in micropores in the 10-MR of MWW (MCM-22) were active [71]. Whereas bimolecular reactions, viz. alkylation of aromatics in the liquid phase, occurred at the external surface of MCM-22, high-temperature toluene disproportionation has catalytic sites located in the 10-MR with 12-MR cages [72].

A review on cage and window effects in mainly hydroconversion of alkanes with zeolites [73] shows that bi- and even trinodal distributions of product carbon numbers can be formed. In the erionite (ERI) cage C_8 hydrocarbon fragments are selectively trapped, thus undergoing intense secondary cracking. This effect was confirmed in the ketonization of carboxylic acids [74]. Alternatively, in cases of slow diffusion (and counterdiffusion), viz. in the liquid-phase propylation of benzene in mordenite, the possibility of having pore-mouth catalysis was advanced [75]. Multinodal product distributions from

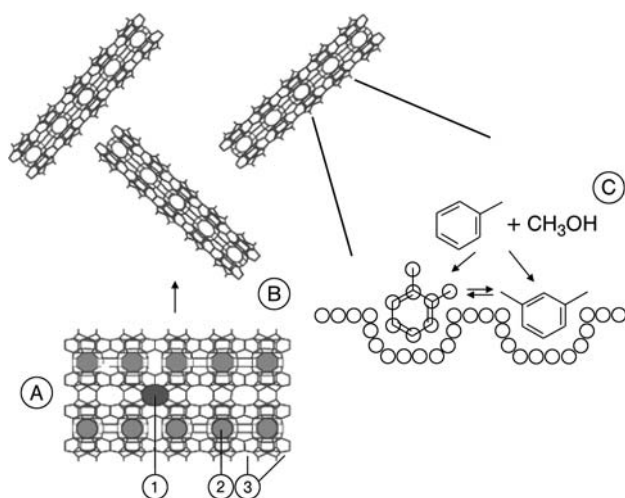


Figure 12.5 Schematic representation of geometric elements in MWW (MCM-22) (a), layers formed upon defoliation (ITQ-2) (b) and presence of 12-MR cups at the external surface (c) (3); 1, 10-MR pores with 12-MR cages; 2, 10-MRs [70].

alkane hydroconversion in ZSM-5, Beta, and even twinned faujasites, are the result of reduced central cracking of the alkane chain when the latter is stretched across neighboring cages separated by a window, thus forming a barrier for methyl shifts [72].

Catalysis at the external surface or in the intracrystalline voids emerges from the methylation of naphthalene over 10-MR zeolites. Whereas discrimination of the slim isomers, viz. 2,6-; 2,7-, from the bulky dimethylnaphthalenes in the methylation of 2-methylnaphthalene for steric reasons was proposed to occur in the nest sites at the external surface [76], it was convincingly shown afterwards that in a series of 10-MR zeolites, 2-methylnaphthalene already enters the pores below the reaction temperature [77], thus making it an example of intracrystalline PDSS.

12.2.5

Concentration Effects by Specific Adsorption

Adsorption equilibria determining concentration of reactants, products, and solvents near the catalyst active site, can differ significantly inside and outside the intracrystalline zeolite space. Control of the hydrophobicity/hydrophilicity balance in the voids and consequently of the polarity can be done by changing the Si/Al (or Si/M) ratio during synthesis or by postsynthesis treatment [26]. Column perturbation chromatography provides numerous examples with hydrocarbons and functionalized organics [78]. In zeolite Beta synthesis, either hydrophobic or hydrophilic samples can be obtained. Whereas in fluoride medium, highly hydrophobic samples with high Si/Al free of defects are synthesized, in standard conditions hydrophilic Beta that preferentially adsorbs polar over apolar adsorbate is found [79].

Competitive adsorption between n-alkanes depends on the zeolite pore architecture [78b]. In zeolite Y with 3D connection of large cages via 12-MRs, at high saturation degrees liquid-like behavior occurs, adsorption being unselective, independent of chain length and governed by chain-segment interactions. At low degree of pore filling, n-alkanes adsorb preferentially over shorter ones as enough space is available for maximum surface interaction. In MFI with 2D arrangements of 10-MRs, they show enhanced interaction with the pore walls as they exhibit stretched configurations. Consequently, reduced sorbate–sorbate interactions allow enhanced competitive sorption and discrimination according to chain length. The effect is, in a given topology, composition or surface polarity dependent. Competitive sorption effects are at the basis of selectivity in the hydroconversion of such molecules [80]. Whereas in liquid-phase hydroconversion of hydrocarbon mixtures, the behavior was predicted assuming no sorption preference, in vapor phase the adsorption preferences could be rationalized using adsorption–reaction models [81].

On ZSM-22, modeling of alkane hydroconversion needed to differentiate between pore, pore mouth and external surface adsorption [82]. The issue

remains whether external surface effects are needed to rationalize this behavior. Molecular simulations suggest that *n*-as well as iso-alkanes have access to the micropores of ZSM-22 and ZSM-23 and hydroconversion can be rationalized via intracrystalline catalysis [83]. The use of zeolite samples with open and template-filled pores, showed that methyl-branched C₅-C₉ alkanes neither from the vapor nor the liquid phase adsorb in the voids of ZSM-23. However, they adsorb from the liquid phase in the pores of ZSM-22 [84]. In vapor-phase Diels–Alder reactions of a diene and a dienophile, viz. butadiene and vinylcyclohexene, rate enhancements of several orders of magnitude occur as a result of concentration effects in zeolite cages [85].

When in catalysis with functionalized molecules unfavorable sorption ratios in the intracrystalline space occur, significant reduction of turnovers is encountered [86]. Therefore, zeolite-catalyzed conversion of reactants with strongly different polarity, remains a challenge [86], though this phenomenon is less of a problem in the gas phase [87]. A number of observations in oxidations with H₂O₂ over TS-1 have been rationalized in this way [88]. Benign effects on Friedel–Crafts reactions by zeolites in supercritical CO₂ [89] are not unexpected as its density is between that of liquid and vapor phase.

12.2.6

Site Isolation or the Role of Zeolites as Solid Solvents

Catalytic centers can be easily isolated in the intracrystalline space of zeolites. As discussed above, the Brønsted acid sites are isolated from a certain concentration, viz. critical Si/Al ratio, onwards. As a result it is possible to promote/suppress intramolecular versus intermolecular reactions depending on the overall chemical composition of the intracrystalline zeolite space [90]. Also, occluded metal complexes can be isolated and give rise to new catalytic chemistry [91, 92].

12.3

Zeolitization

Whereas formation of natural zeolites required geological timescales, the schools around Barrer and Milton, Breck, Flanigen, and Wilson have been able to reduce this to days/hours, using more severe conditions with respect to alkalinity and synthesis temperature [24a, 93]. Numerous studies [94] allowed the scientific basis of a number of phenomena related to zeolite synthesis to be established. As a result, zeolite synthesis is now backed up by many scientific concepts, allowing occasionally tailor-made synthesis [95]. In the present section *zeolitization* concepts will be discussed to facilitate the catalyst manufacturer's task.

12.3.1

Overall Steps in Zeolite Crystallization

Most industrial zeolite-based catalysts originate from the hydrothermal conversion in supersaturated conditions of Si and Al components in the presence of aqueous alkali, with occasionally added alkali-metal salts and organic molecules [96]. The whole process of *zeolitization* is schematically presented in Figure 12.6.

The traditionally used sources for the different elements, viz. Si, Al, Na, are transformed via liquid-phase mediation into a hydrogel or precipitate with the required chemical composition. The latter is converted into precursor species possibly with the help of mineralizing agents functioning as catalyst for the transformation. Via classical crystallization theory it is assumed that the precursors assemble into nuclei that are transformed into crystals via successive growth. It is claimed that in certain cases crystallization occurs via a solid-state transformation involving direct conversion of the gel (solid) into the crystal [97]. Models for zeolite crystallization assume nucleation followed by growth, or cluster–cluster aggregation. The former model, also referred to as monomer–cluster growth, is often used for inorganic gels, while the cluster–cluster growth model for solutions rich in organics [98]. Whereas structure-directing agents (SDAs) or template molecules, viz. alkylammonium ions, function as true topology-determining template or pore-filling agents, mineralizing agents such as alkali (alkaline earth) salts, OH^- , or F^- , are assumed to be catalysts for the gel to precursor/nucleus transformation.

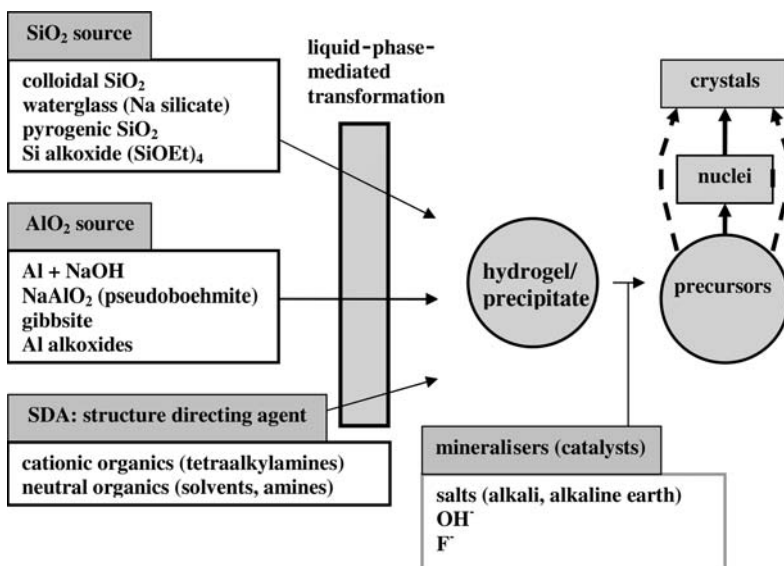


Figure 12.6 Schematic presentation of overall process of zeolitization [96].

The dissolved reactants during zeolite synthesis undergo a sequence of transformations during the so-called induction period (Figure 12.7). The formation of a visible gel is often denoted as the formation of the *primary amorphous phase*, consisting of a heterogeneous nonequilibrated product containing amorphous aluminosilicates, unchanged reactants, coagulated silica, and alumina [95b]. The latter probably stem from precipitated reactants (Si and/or Al) destabilized by changes in pH and salt concentrations. In diluted conditions, often denoted as *clear solution synthesis*, the solution remains colloidal, though the same phenomena occur.

Upon aging and/or temperature increase the primary amorphous phase obtains local order, either via successive depolymerization/polymerization of aluminosilicate catalyzed by hydroxyl ions [99], or releases species in solution and equilibrates with the surrounding liquid phase [100]. The *secondary amorphous phase* then obtained equilibrates with its solution. At this stage, typical structure-determining silicate and aluminosilicate anions are present [95b]. In the case of high-silica zeolite synthesis, from this stage on the crystallization progress can be monitored via pH measurement in the synthesis solution [101]. A pH drop points to the hydrolysis of an amorphous aluminosilicate, consuming hydroxyl ions. Subsequently, during condensation reactions and formation of Si(Al)–O–Si bridges, the pH rises with the parallel appearance of solids exhibiting order as pointed out by X-ray diffraction (XRD).

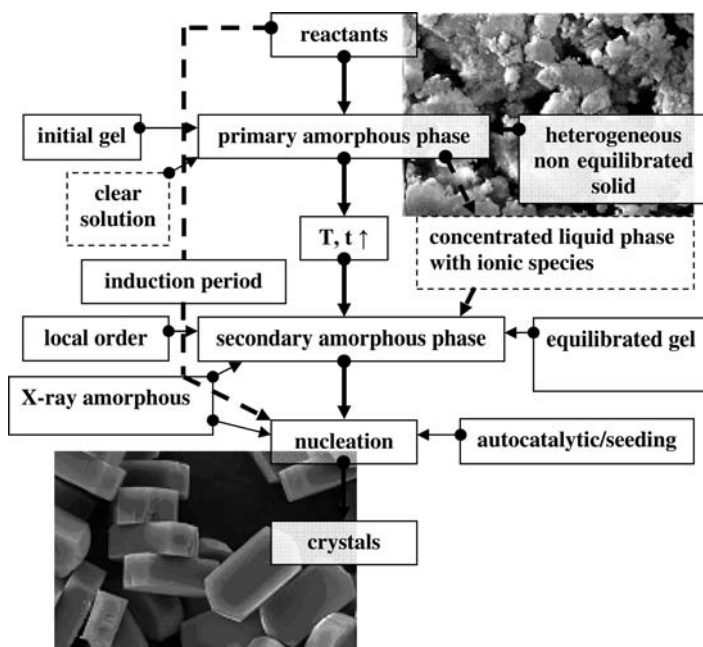


Figure 12.7 Scheme of equilibration and change of order during a zeolite synthesis [95b].

The latter transformation, autocatalytic in nature, can be regulated with the help of seed crystals.

The same multistage nature of zeolite synthesis was derived from characterization of a sequence of gels obtained during a crystallization of tetraethylammonium ion containing aluminosilicates [102]. Equilibrated gels, clearly different from the initial ones, have several physicochemical properties in common with high-silica zeolites. The same is true for the so-called *X-ray amorphous zeolites*, which were gels taken from an interrupted crystallization before long-range order established by XRD was present, while specific sorption and shape-selective catalytic properties were already present [103]. Before long-range order in the synthesis gel is established, it has to approach a pseudosteady-state equilibrium with solution containing ionic species with a wide range of mass/charge ratio [95b, 104].

12.3.2

Classic Model for Zeolite Growth

Zeolite synthesis can also be approached from classical nucleation–crystallization theory [105]. A viable nucleus is estimated to have a size between one and eight unit cells, depending on the structure type and the experimental synthesis conditions [106]. However, because of crystallization from high surface area systems, the energetics of zeolite nucleation can be significantly different from that of more dense phases [107]. Advanced techniques such as HRTEM and cryo-TEM are the basis of the experimental information about zeolite nucleation [108].

Nucleation involves activation of dormant nuclei in the amorphous phase upon release in the solution phase via gel dissolution [109]. The dormant nuclei are located near the surface of the gel particles, thus becoming activated in the early phase of the gel dissolution/growth process [110]. For ZSM-5 synthesis, gel dissolution and nucleation were experimentally proven and successfully modeled to be interfacial phenomena at the gel/solution boundary [111].

According to classic nucleation theory, *primary nucleation* from a supersaturated solution can be homogeneous, viz. spontaneous, or heterogeneous, viz. affected by impurities and thus eliminated by careful filtration of reactants. On the other hand, *secondary nucleation* is crystal catalyzed [112]. In zeolite synthesis, there is evidence that primary nucleation dominates [105a]. The distinction between homogeneous and heterogeneous secondary nucleation is often subtle, depending on whether the influence of a colloidal phase is considered to be heterogeneous or not [95b]. So it was established with the help of direct techniques such as scattering and electron microscopy that in the early stages of a clear solution synthesis of aluminum-rich zeolite phases, heterogeneous nucleation occurred [95a, 113], viz. at the surface of raft-like gel [114].

Experimentally observed nucleation rates typically go through a maximum with increasing degree of supersaturation of the synthesis solution, and thus are related to the increasing viscosity of the medium, inhibiting migration of intermediate species [98]. If nucleation and growth consume the same species, this phenomenon, viz. the maximum observed in the nucleation rate, is rationalized.

The degree of supersaturation in the synthesis gel influences crystal size and morphology. In Figure 12.8 the effect of alkalinity on average crystal size and morphology of a typical ZSM-5 synthesis gel is shown. At high alkalinity, commonly expressed as OH/SiO_2 molar ratio, massive nucleation occurs together with an increased rate of redissolution of the crystals formed. This results in the formation of smaller crystals with less well-defined or even changed morphology. At lower alkalinity, a lower number of nuclei grow into well-defined and large crystals.

The alkalinity of the synthesis hydrogel was shown to affect the aspect ratio, that is, length over width, of the crystals formed during synthesis of silicalite-1 [115]. At increasing alkalinity this ratio (c/a) was shown to decrease gradually. The growth rate along the a and b crystallographic directions, was found to decrease in a nonlinear way with the alkalinity, while it is independent for the c direction. The straight channels in the MFI topology to which silicalite-1 belongs, have their pore mouths at the (010) planes, and run through the crystals parallel with the b direction. The sinusoidal pores surface at the (100) planes run parallel to the a direction. Such phenomena can significantly affect shape selectivity in an otherwise identical zeolite sample. Attempts have been reported to correlate this alkalinity effect with condensation/dissolution of certain precursor species [116].

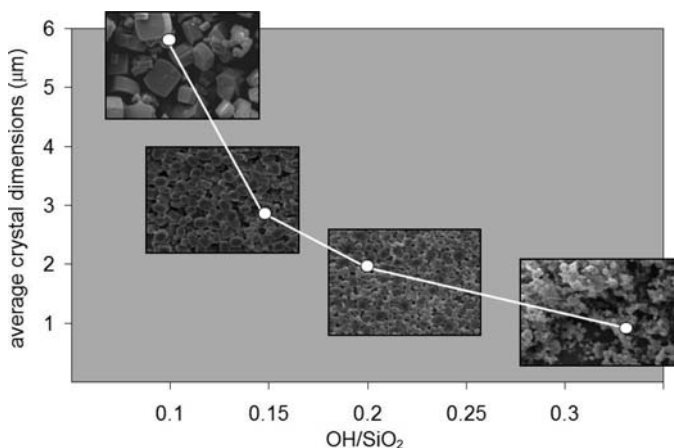
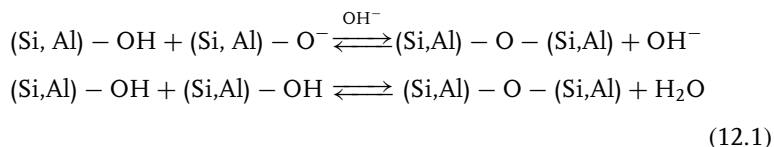


Figure 12.8 Influence of alkalinity (OH/SiO_2) of a typical ZSM-5 synthesis gel on the average crystal size and zeolite morphology.

Chemically, the increase in ordering degree of the primary gel has been visualized as follows [117]:



representing the forming and breaking of T–O–T bonds, viz. Si–O–Al and Si–O–Si, catalyzed by hydroxyl ions, and cations used for charge neutralization. The latter play a crucial role in the ordering process leading to minimization of the potential energy of the intermediates [118].

To bypass the induction period and eliminate the nucleation stage, seed crystals can be added to the system [119], directing synthesis to a desired topology [120]. The above-mentioned interface surface area necessary for nucleation, is now generated by the surface of the seed crystals, indicating that significant amounts of seeds have to be added to observe effects. As can be predicted, the use of colloidal zeolites (with high surface area) as seeds, can be very effective [121]. The need for high surface area and reactive seeds has been demonstrated with delayered or delaminated zeolites [122]. Seeds of MWW crystals were less reactive than their delaminated forms for the synthesis of MCM-22. Upon addition, the latter could eliminate the induction period, while significantly increasing the crystallization rate. The seeding had an effect on the crystal morphology as well, as it yielded smaller and thinner crystals. As among seed structures like MCM-41, ITQ-6, and ITQ-2, the latter was most effective, the similarity in structure elements between ITQ-2 and MCM-22 is obvious [122].

12.3.3

The Aggregation Model

The detection of discrete nanometric agglomerates in the zeolite synthesis gel, viz. with dynamic light scattering, small-angle X ray scattering, and small-angle neutron scattering [98], suggests that nanoclusters can aggregate into larger units, ending up with the formation of crystals. The reported preparation of a number of zeolite topologies such as MTW, BEA [123], and FAU [124] as nanoparticles or in colloidal form seems to confirm this. Moreover, the presence of nanosized particles during synthesis has been observed directly [125, 126]. The involvement of sheets and “columnar substructures” has been invoked in the synthesis of hexagonal faujasites [127]. In the synthesis of MFI-type topologies, the formation of silica oligomers with specific size, shape, and connectivity has been postulated as a result of template-directed self-organization [128].

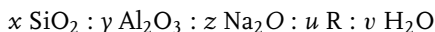
In a clear solution, the amphiphilic TPA ions position preferably at the interphase between the aqueous and organosilicon (tetraethylorthosilicon (TEOS)) phase. Subsequently, the silicate condenses around TPA ions shielding the template from the aqueous environment. The formed precursors are proposed to encapsulate a single TPA ion, and are already reminiscent of the ultimately formed zeolite topology (Figure 12.9). The precursors assumed to undergo aggregation via self-organization and to form elements consisting of 12 members are denoted in the original work as *nanoslabs*. Alternatively, the precursor can be added as a “monomer” to a growing crystal as expected from classical synthesis pathways [129].

Although much evidence exists for the occurrence of the former mechanism [130], the distinction between both pathways is far from obvious, explaining the contestation of the existence of such species [131]. However, recent diffusive light scattering (DLS) data showed the existence of fast relaxation attributed to a collective diffusion process of 2-nm precursors, viz. nanoslab-like species [130].

12.3.4

Zeolitization Parameters

The composition and the basicity of the synthesis gel, the presence of mineralizing agents and salts or ion pairs and template molecules, the synthesis temperature and time, are all important parameters determining the outcome of a synthesis experiment in terms of nature of the crystalline phase, composition and compositional homogeneity, purity, size, and morphology of the crystals [98]. The typical *chemical composition* of a synthesis hydrogel, commonly expressed in terms of molar composition of the oxides, is as follows:



with R an organic species (salt or molecule). As an example, the synthesis of MFI (ZSM-5) in an inorganic medium in the absence of R, occurs for a rather narrow compositional range, viz. at low $\text{SiO}_2/\text{Al}_2\text{O}_3$ and $\text{Na}_2\text{O}/\text{SiO}_2$ ratios in the gel [132].

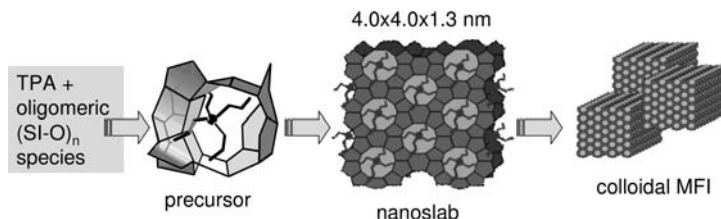


Figure 12.9 Schematic representation of the successive agglomeration of Si–O intermediates in the synthesis of MFI structures, with nanoslabs as key intermediates [128].

An *aqueous medium* is mostly used for zeolite synthesis, though organic solvents via their viscosity and permittivity can affect the solvating capacity of the medium [133]. When molecules like amines and alcohols are substituting a significant part of the water from the mixture, large crystals can be easily obtained [134]. Zeolites can be synthesized in *nonaqueous* solvents, provided the used SDAs remain isolated in solution, and thus show intermediate interactions, in terms of H-bonding capacity of the solvent. This interaction should not prevent the SDAs from accessing the framework precursors or intermediates [135]. In ferrierite (FER) synthesis in pyridine medium, propylamine is needed as buffer, preventing the pyridine from being protonated, and as template for nucleation of pyridine-stabilized silicate sheets, which grow upon layer-by-layer deposition [136]. Minor changes in the synthesis conditions may yield other topologies.

Most zeolites are crystallized at pH values ranging from 9 to 13, the OH^- anions functioning as catalyst for the mineralization (*vide supra*). Enhanced alkalinity of the medium, necessary to reach the supersaturated state, shortens the induction period, increases the nucleation and growth rate, while reducing the Si/Al ratio of the crystals [137]. Gel dissolution in basic medium seems to occur via a nucleophilic $\text{S}_{\text{N}}2$ reaction, in which fivefold-coordinated Si weakens siloxane bridges [133]. pH changes during crystallization, even used as a diagnostic means to follow crystallization, have already been mentioned. In aluminosilicate gels, silicate species become more deprotonated at higher alkalinity, resulting in a decreased condensation rate. The condensation rate of silicate with aluminate at higher alkalinity, however, is much less affected [133, 137].

Added F^- anions take the role of mineralizing catalyst in acid medium, via complexation with Si(Al) atoms [137]. Other elements, viz. Ga and Ti, forming complexes with fluoride, can be substituted in the zeolite framework. High F^- concentrations may also impart coordination ability from tetrahedral into octahedral. As in such conditions, the degree of supersaturation is rather limited, nucleation and growth is reduced and slow growth occurs with formation of a decreased number of structural defects.

Zeolite crystallization is thermally activated and enhanced at higher *temperatures*, viz. from 373 to 473 K. If the micropore-filling agents like water or organics are becoming too volatile at high temperatures, zeolite formation ceases at the expense of layered structures like clay minerals [93]. Very high temperature synthesis of porous open structures with pore fillers of low volatility is expected to be possible [98].

Zeolites are thermodynamically metastable phases that can be transformed at longer *synthesis times* into more stable (and more dense) structures [93]. This phenomenon is known as the *Ostwald rule of successive phase transformations*. The transformation of NaY into a gismondine-type framework (GIS) or into ZSM-4 (mazzite) (MAZ) is well known [138]. Typically, Al-rich zeolites, viz. A and X, yield the dense sodalite structure. When overexposed to the reaction medium, Si-rich zeolites are transformed into dense quartz phases, while in

the intermediate composition range, like for Al-rich ZSM-5, often the presence of a dense siliceous phase (quartz) is accompanied by a more Al-rich zeolite (mordenite) [95].

Templates, also known as structure-directing agents, influence the zeolization process markedly. The template molecule is surrounded by (aluminosilicate) species in a particular geometry, thus providing building units for a particular zeolite phase [139]. The pore-filling effect of the template lowers the interfacial energy and thus the chemical potential of the growing zeolite via additional interactions such as H-bond formation, electrostatic, and van der Waals interactions. Its geometry (form and size) is to a certain extent topology controlling [98, 137]. Directed template design has been successfully used for the forced synthesis of certain topologies [140]. Neutral molecules, cations and ion pairs, organic or inorganic in nature, are known to fulfill the dual role of a template, viz. structure or composition directing [98].

In aqueous solutions, small *cations* with high charge density, viz. Na^+ and Li^+ , are able to break the H-bonding network of water and become integrated in this network as strongly hydrated ions. They are categorized as *structure making* [111b]. Hydrated large cations, viz. K^+ , Cs^+ , TMA^+ , form transient cage or ring structures and have water *structure-breaking* properties. (Alumino)silicate oxygen anions are able to substitute water in such cages. Thus, K^+ has a preference for location into a double six-ring (D6R) of Si(Al) atoms formed via Si(Al)–O–Si bonds, while TMA^+ provokes formation of double four-ring (D4R) (cubic octamer) [140]. TPA^+ ions seem to favor formation of five-ring motives [128]. Organic and alkali cations might mutually disturb each other's effect, possibly resulting in formation of incompatible (alumino)silicate species [141].

Water, next to its hydration and hydrolyzing ability, is a *pore-filling agent* stabilizing the structure. Other neutral molecules, viz. ethers, alcohols, and polyols, also operate as pore-filling agents [133, 137]. Alkali- and alkaline-earth metal salts are nonvolatile pore-filling agents for high-temperature applications [142].

The complex interplay between several templating agents and the gel composition, viz. its Si/Al ratio, is shown schematically in Figure 12.10. Hydrated Na^+ ions are templating four-rings (4Rs) of aluminosilicate. Whereas at high concentration of Al, two 4R form a D4R, yielding aluminum-rich zeolite A (LTA), in silicon-rich conditions three 4R form a D6R, giving NaY (cubic siliceous faujasite). At high concentration of Al, D6R are formed yielding zeolite NaX (cubic faujasite with low Si/Al ratio), provided hydrated K ions are present as a second templating agent. In the presence of 18-crown-6 as a second template, D6Rs are now converted into EMT topology, that is, faujasite with hexagonal symmetry. The presence of Ge in the synthesis mixture can also introduce 4-MR and D4R in a framework. Ge substitution makes the rings more stable provided no Ge–O–Ge bonds are formed [143].

Templated synthesis assumes a direct correlation between shape and size of a SDA and of the surrounding cage. Whereas such direct action is only observed exceptionally [144], the use of a triquat molecule with D_{3h} symmetry

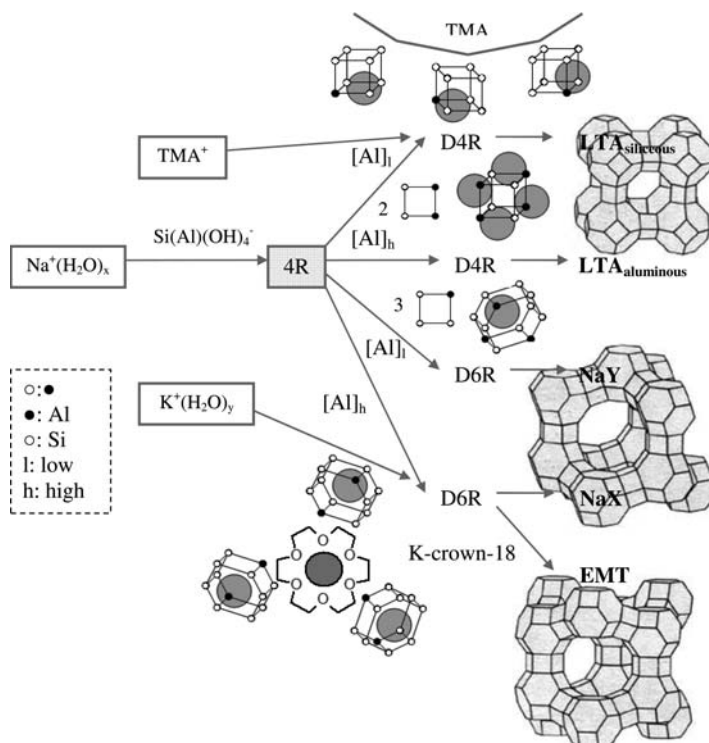


Figure 12.10 Influence of nature of template (Na^+ , K^+ , TMA^+ , 18-crown-6) and Si/Al ratio of the zeolite synthesis gel on the nature and composition of the (Al)silicate polyanions and the structures formed. 4R: four-ring consisting of four T atoms interconnected via oxygen anions; D4R: double four-ring; D6R: double six-ring [98].

for the synthesis of ZSM-18 is a case of “true templation.” Indeed, the isolated template molecules are stuck in cages with C_{3v} symmetry [144]. In cases where the same template is effective for the synthesis of different zeolite topologies, viz. Beta, EU-1, ZSM-11, and ZSM-12, it could be calculated that depending on conditions, the system is either in thermodynamic or kinetic control [145].

Use of microemulsions has been proposed for the synthesis of zeolites, their confined spaces acting as nanoreactors for growth [146]. The concept works with branched chain surfactant molecules at low temperature (368 K for 96 h), yielding silicalite-1 (MFI) crystals with narrow sizes tunable between 240 and 540 nm. Salt content is the morphology-determining parameter, which is consistent with the salt screening of the surfactant-electrostatic forces [147]. The zeolite does not nucleate in the microemulsion, and not before amorphous silica formed in the microemulsion separates from this medium. Whereas in conventional silicalite-1 synthesis conditions (433 K), the morphology is only sensitive to the electrostatic forces between the silicate and the surfactant

[148], it was concluded that surfactant adsorption on the growing silicate was crucial. The method can be extrapolated to the synthesis of other topologies, as shown by the growth of zeolite A (LTA) in the presence of nonionic microemulsions [149].

Zeolite crystal growth and *dissolution* occur in the same medium. Thus, zeolite synthesis constitutes a “complex equilibrium between crystal growth and dissolution,” the dissolution rate being determined by the surface area of the crystals and the degree of “undersaturation” of the medium [94b]. Dissolution of twinned ZSM-5 crystals [150] in hot aqueous NaOH, first showed surface pitting, followed by preferential attack at the twin boundaries, the minor component being dissolved eventually. Reflux of calcined ZSM-5 with aqueous 0.5 M Na₂CO₃, resulted in removal of siliceous material from the crystal’s interior, yielding zeolites enriched in Al with enhanced catalytic activity [150]. The method has been applied to develop mesoporosity in siliceous zeolites and to enhance diffusivity [151].

When in a hydroxy-catalyzed synthesis, there are not enough trivalent ions, viz. Al, B, Ga, Fe, and so on, and consequently an insufficient number of negative charges in the framework, the presence of extra-framework cations like Na⁺ or charged SDAs, requires the presence of *negatively charged siloxy defects* [152]. Therefore, nuclei with a high concentration of such defects are prone to dissolution [153]. High-silica gels possessing a lower concentration of charged SDAs (or a low SDA/SiO₂ ratio) preferably yield more dense topologies [152b].

12.3.5

Nanocrystalline Zeolites

The scaling of zeolite crystals from the micrometer to nanometer scale, will provide crystals with enhanced external surface and decreased diffusion path lengths. Control of composition, temperature/time, yields zeolite nanocrystals with a narrow size distribution [154]. Unfortunately, isolation of such small crystals is not evident due to their colloidal properties.

Via *confined space synthesis* with porous carbon as inert support material, synthesis of nanosized zeolite crystals of several topologies is possible and their recovery via controlled pyrolysis of the carbon becomes feasible [155]. In the 45-nm carbon black pores nanocrystals of ZSM-5 (MFI) of about the same size were obtained. The method is of general utility, as it seems possible to make nanosized zeolites of Beta zeolite X and Y and L (LTL), which can be easily washed, ion exchanged and finally isolated via calcination [156].

Thermoreversible polymer hydrogels also represent a medium for synthesis of nanosized zeolite crystals. This support is recyclable and stable in the temperature range of interest for zeolite synthesis. In aqueous media, the voids between monodisperse polymer spheres can serve as a nanoreactor for controlled growth [157]. Recycling of the support can be done via dissolution of

the polymer spheres in an appropriate solvent [158]. Thus, nanosized crystals of Beta, ZSM-5, and TS-1 were obtained. The corresponding (classical) gels were mixed with the emulsion containing the monodisperse polymer spheres and autoclaved. The product was treated with ethylacetate, and washed with water till all the polymer disappears [159].

12.3.6

Zeolite Synthesis via the Dry Gel Route

In most work on zeolite synthesis, crystallization is assumed to occur via solution-mediated transformations. In some cases the participation of the solid amorphous phase in the formation of nuclei has been clearly established [160].

The existence of X-ray amorphous MFI zeolites (*vide supra*) points to amorphous gel nucleation. ZSM-5 synthesis from silica solutions with low Si/Al and Na/SiO₂ ratios were shown to be liquid-phase phenomena, whereas the transformations with high Si/Al and Na/SiO₂ ratios, were proposed to be governed by solid hydrogel transformations [161]. From a starting aqueous solution containing mainly monomeric silica (ingredients mixed at acid pH), a hydrogel was formed at pH = 11 after NaOH addition, the high molar ratios favoring nucleation through interaction with TPA cations. It is postulated that local crystallization in the gel occurs since the Si/Al ratio of the whole solid phase remains constant during the crystallization [161a]. Others suggested that nucleation is heterogeneous either at the external surface of the gel or in inner gel pockets via autocatalytic nucleation [162]. As nucleation of ZSM-5 is complete before 10% crystallinity is reached, this proposal is rather unlikely [163].

The invention of the so-called *vapor-phase transport* (VPT) method [164] is another argument for the existence of a solid-phase transformation mechanism (Figure 12.11). A dried aluminosilicate gel (423–473 K) was contacted only with vapors of an aqueous SDA phase. The solution is placed at the bottom of an autoclave, while the dry gel was on top of a supporting device half-way up the autoclave [165]. In a variation of the method denoted as steam-assisted crystallization (SAC), the dry SDA-containing gel was activated with steam [166]. The method gives high yields of crystals and is useful for several zeolite phases such as Al- and Ti-Beta (BEA), TS-1 (MFI), TS-2 (MEL), and EU-1

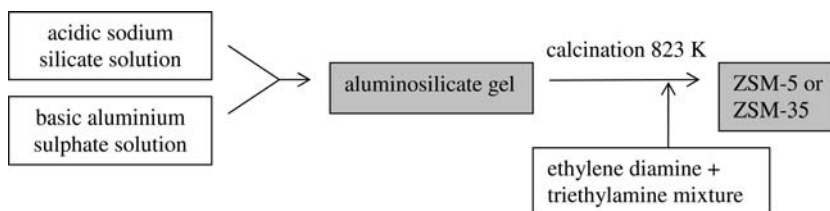


Figure 12.11 Scheme for the water-free synthesis of zeolites [199].

(EUO) [166, 167]. During the SAC synthesis of Beta, it was discovered [168] that initially defect SiOH groups, viz. Si(1Si,3OH), Si(2Si,2OH), Si(3Si, 1OH), were abundantly formed, while later they decreased, pointing to the successive generation and condensation of the defect species mentioned.

12.3.7

AlPO₄-n-Based Molecular Sieve Zeolites

The synthesis of AlPO₄-based materials with different topologies has been achieved via the hydrothermal synthesis method. The reaction mixtures besides Al and P as T atoms may contain one or more of 13 additional elements [169]. The family of materials shows a very large compositional and structural diversity, viz. at least 36 structures of which several are new [170].

The acronyms given to these materials together with the T atoms present, are shown in Table 12.1. Up to 15 elements, with various oxidation states, viz. from +1 till +5, have been incorporated [169, 170]. The preferred phosphate source is orthophosphoric acid, consisting essentially of monomeric PO₄. The corresponding “hydroxide” is acidic, so that the pH of the starting synthesis mixture is initially much lower than in traditional zeolite synthesis [171]. The most frequently used Al source is pseudoboehmite. For SAPO synthesis, colloidal, precipitated, fumed, and alkoxide silica has been successfully used. The M and El elements can be soluble salts or oxides dissolved in phosphoric acid. Organic amines and alkylammonium ions play the role of SDA [169]. During crystallization the pH of the synthesis mixture is between 3 and 10, and goes to neutral pH, the relative amounts of phosphoric acid and template determining the initial pH. For pH values <3, dense phases are usually formed, while above pH 10, crystallization is difficult as several elements form insoluble oxides [169, 171].

Synthesis in diluted solutions is also possible as well [173], while the presence of F[−] hardly shows any effect [174]. Crystallization occurs in the temperature–time regime of zeolites, viz. around 150 °C. Using the following molar composition

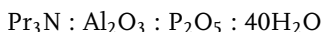


Table 12.1 Acronyms and T atom composition of AlPO₄-n-based molecular sieve zeolites [172].

Acronym	T atoms
AlPO ₄ -n	Al, P
SAPO-n	Si, Al, P
MAPO-n	M (Co, Fe, Mg, Mn, Zn)
MAPSO-n	M, Al, P, Si
ElAPO	El (As, B, Be, Ga, Ge, Li, Ti)
ElAPSO	El, Al, P, Si

$\text{AlPO}_4\text{-5}$ (AFI) is fully crystallized after 3 hours [167, 169]. The system, in particular that to synthesize $\text{AlPO}_4\text{-11}$ (AEL), requires vigorous stirring to remove heterogeneities [175].

While water is the most frequently used solvent, SAPO synthesis has been reported in a biphasic system, viz. water, containing Al and P sources, and hexanol with TEOS as Si source [176]. Also, the SAC method has been used to synthesize $\text{AlPO}_4\text{-11}$ [177]. Monitoring the crystallization with ^{17}O -labeled water gave useful mechanistic information, indicating that water reacts first with alumina in the dry gel before hydrolyzing Al–O–P. Afterwards P–O–H and Al–O–P bonds are broken and reformed.

The use of two different SDAs simultaneously in the synthesis of $\text{AlPO}_4\text{-n}$ materials or their substituted analogs has become commonplace [170]. Emphasis was on synthesis of SAPO-34 or SAPO (CHA) with improved purity/quality.

12.3.8

Ionothermal Synthesis Method

The use of ionic liquids (ILs) or eutectic mixtures as solvent in zeolite synthesis has been reported [178]. The IL, viz. 1-methyl-3-ethylimidazolium bromide, was used both as solvent and as SDA. It solubilizes all components involved in the synthesis, while the electrostatic interaction between cations, IL and framework species form the basis of a strong templating effect [165, 178]. It was shown that the IL also works as a microwave absorber [172] and is suited for microwave-assisted zeolite synthesis. Because of the low vapor pressure of IL, the synthesis occurs at low pressure. The addition of amines to such synthesis mixtures yields pure AFI and ATV structures. The amine as well as the IL seem to exert a structure-directing effect [179]. This method is particularly useful for preparation of transition-metal functionalized frameworks, viz. Co- $\text{AlPO}_4\text{-n}$ [180]. New zeotypes were obtained in the Al, P system, viz. SIZ-7, as well as in the Si system, viz. SIZ-12.

12.3.9

Zeolites with Pores Beyond the 12-MR

For obvious catalytic reasons, synthesis of large-pore zeolites has been sought. 14-, 18-, 20-, and even 24-MR materials have been made with different T atoms in the framework [181]. Unfortunately, most of the materials show monodimensional pores and limited stability in catalytic conditions. Aluminophosphates with 14-MR and 18-MR, denoted as $\text{AlPO}_4\text{-8}$ (AET) [182] and VPI-5 (VFI) [183] have been synthesized with di-propylamine as pore-filling agent.

Several aluminosilicate zeolites with 14-MR have been made, denoted as UTD-1 (DON) [184], CIT-5 (CFI) [185], SSZ-53 (SFH) and SSZ-59 (SFN) [186].

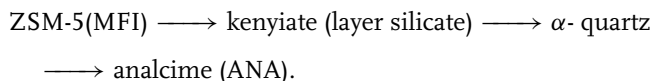
In most cases, SDAs are being used that are not commercially available. Moreover, the detailed catalytic potential of such materials remains unknown at this time. Sometimes such materials, viz. CIT-5, exhibit lower activity than standard zeolites [187].

Large-pore materials with other T-atom composition, viz. the galliumphosphate 20-MR cloverite (CLO) [188] and JDF-20 [189] have an interrupted framework with low thermal stability. The 18-MR galliumsilicate ECR-34 (ETR) [190] is of potential interest for catalysis. Recently developed germanates with intersecting 12- and 14-MR, denoted as ITQ-15 [191] and IM-12 [192] also have potential catalytic interest.

12.3.10

Upscaling of Zeolite Synthesis

For upscaling of zeolite synthesis, two issues are of key importance [193], viz. the reactor vessel and all EHS (environmental, health, safety) aspects. Reaction over-run has to be avoided, as illustrated by the phase sequence in MFI synthesis:



“Memory effects” associated with the presence of traces of species from a previous reaction in reactors or autoclaves or on stirrers may influence the outcome of a large-scale synthesis [193]. A cleaning with 1 M aqueous NaOH at 160 °C for 1 hour is often sufficient, though specific synthesis procedures may require specific cleaning treatments [194]. Considerations on source reactants in zeolite materials synthesis are available [195].

From the economic and environmental point of view, the dry-gel synthesis method for large-scale zeolite synthesis seems promising, due to the low template amount needed, the short synthesis time [196], the possibility of direct forming of the dry paste, and elimination of filtration [197]. The use of preformed porous silica spheres has been proposed for impregnation of reactants and *in-situ* synthesis of zeolites [198].

References

1. <http://izasc.ethz.ch/fmi/xsl/IZA-SC/ft.xsl> (last consulted: January 29th 2008).
2. <http://www.iza-online.org>.
3. http://www.iza-online.org/IZA_const_IZA.pdf (last consulted January 30th 2008).
4. Habib, E.T., Zhao, X., Yaluri, G., Cheng, W.C., Boock, L.T. and Gilson, J.-P. (2002) in *Zeolites for Cleaner Technologies* (eds M. Guisnet and J.-P. Gilson), Imperial College Press, Chapter 5.
5. van Veen, J. A.R. (2002) in *Zeolites for Cleaner Technologies* (eds M. Guisnet

- and J.-P. Gilson), Imperial College Press, Chapter 6.
6. Schmidt, F. and Köhler, E. (2002) in *Zeolites for Cleaner Technologies* (eds M. Guisnet and J.-P. Gilson), Imperial College Press, Chapter 7.
 7. Daage, M. (2002) in *Zeolites for Cleaner Technologies* (eds M. Guisnet and J.-P. Gilson), Imperial College Press, Chapter 8.
 8. (a) Beck, J.S., Dandekar, A.B. and Degnan, T.F. (2002) in *Zeolites for Cleaner Technologies* (eds M. Guisnet and J.-P. Gilson), Imperial College Press, Chapter 11; (b) Degnan, T.F. (2007) *Stud. Surf. Sci. Catal.*, **170A**, 54.
 9. Barger, P. (2002) in *Zeolites for Cleaner Technologies* (eds M. Guisnet and J.-P. Gilson), Imperial College Press, Chapter 12.
 10. Delahaye, G. and Coq, B. (2002) in *Zeolites for Cleaner Technologies* (eds M. Guisnet and J.-P. Gilson), Imperial College Press, Chapter 16.
 11. Kapteyn, F., Rodriguez-Mirasol, J., Moulijn, J.A. *et al* (1996) *Appl. Catal. B.*, **9**, 25–64.
 12. Marion, P., Jacquot, R., Ratton, S. and Guisnet, M. (2002) in *Zeolites for Cleaner Technologies* (eds M. Guisnet and J.-P. Gilson), Imperial College Press, Chapter 14.
 13. (a) Calvin, J.R., Davis, R.D. and McAteer, C.H. (2005) *Appl. Catal. A.*, **285**, 1; (b) McAteer, C.A., Colin, H. and Scriven, E.F.V. (2001) in *Fine Chemicals through Heterogeneous Catalysis* (eds H. Van Bekkum and R. Sheldon), Wiley VCH Verlag GmbH, p. 275.
 14. (a) Notari, B. (1991) *Stud. Surf. Sci. Catal.*, **67**, 243–56; (b) Clerici, M.G. (1993) *Stud. Surf. Sci. Catal.*, **78**, 21.
 15. Uriarte, A.K., Rodkin, M.A., Gross, M.J., Kharithonov, A.S. and Panov, G.I. (1997) *Stud. Surf. Sci. Catal.*, **110**, 857.
 16. Shannon, R.D., Keane, M., Abrams, L., Staley, R.H., Gier, T.E., Corbin, D.R. and Sonnichsen, G.C. (1988) *J. Catal.*, **114**, 8.
 17. Martens, J.A., Verrelst, W.H., Mathys, G.M., Brown, S.H. and Jacobs, P.A. (2005) *Angew. Chem. Int. Ed.*, **44**, 5687.
 18. (a) Venuto, P.B. and Landis, P.S. (1968) *Adv. Catal.*, **18**, 259; (b) Hölderich, W.F., Hesse, M. and Naumann, F. (1988) *Angew. Chem.*, **100**, 232; (c) Hölderich, W.F. and Van Bekkum, H. (1991) *Stud. Surf. Sci. Catal.*, **58**, 631; (d) Hölderich, W.F. (1996) *Comprehensive Supramolec. Chem.*, **7**, 671; (e) Hölderich, W.F. (2000) *Catal. Today*, **62**, 115; (f) Hölderich, W.F. and Kollmer, F. (2002) in *Catalysis*, Vol. **16**, RSC, London, p. 43.
 19. (a) Maher, P.K., Hunter, F.D. and Scherzer, J. (1971) *Adv. Chem. Ser.*, **101**, 266; (b) Ward, J.W. (1972) *J. Catal.*, **27**, 157; (c) Jacobs, P.A. and Uytterhoeven, J.B. (1972) *J. Catal.*, **27**, 161.
 20. (a) Springuel-Huet, M.-A., Guenneau, F., Gedeon, A. and Corma, A. (2007) *J. Phys. Chem. C*, **111**, 5694; (b) Galletero, M.S., Corma, A., Ferrer, B., Fornes, V. and Garcia, H. (2003) *J. Phys. Chem. B*, **107**, 1135; (c) Corma, A., Fornes, V., Guil, J.M., Pergher, S., Maesen, T.L.M. and Buglass, J.G. (2000) *Microporous Mesoporous Mater.*, **38**, 301.
 21. Roberie, T.G., Hildebrandt, D., Creighton, J. and Gilson, J.-P. (2002) in *Zeolites for Cleaner Technologies* (eds M. Guisnet and J.-P. Gilson), Imperial College Press, Chapter 3.
 22. (a) Doesburg, E.B.M., de Jong, K.P. and van Hooft, J.H.C. (1999) *Stud. Surf. Sci. Catal.*, **123**, 433; (b) Lepage, J.F. (1987) in *Applied Heterogeneous Catalysis*, Technip, Paris, p. 75; (c) Stiles, A.B. (1983) in *Catalyst Manufacture*, Marcel Dekker, New York; (d) Moulijn, J.A., Makkee, M. and van Diepen, A. (2004) *Chemical Process Technology*, John Wiley & Sons, Inc., New York, Chapter 9.
 23. Corma, A., Grande, M., Fornés, V., Cartledge, S. and Shatlock, M.P. (1990) *Appl. Catal. A.*, **66**, 45.
 24. (a) Breck, D.W. (1974) *Zeolite Molecular Sieves, Structure, Chemistry and Use*, John Wiley & Sons, Inc.,

- New York; (b) Kuhl, G.H. (1999) in *Catalysis and Zeolites*, Springer, Berlin, Chapter 3; (c) Vansant, E.F. (1988) *Stud. Surf. Sci. Catal.*, **37**, 143; (d) Szostak, R. (1991) *Stud. Surf. Sci. Catal.*, **58**, 153; (d) Szostak, R. (1991) in *Introduction to Zeolite Science and Practice*, Elsevier, Amsterdam, Chapter 5.
25. (a) Uytterhoeven, J.B., Christner, L.G. and Hall, W.K. (1964) *J. Phys. Chem.*, **69**, 2117; (b) Jacobs, P.A. (1976) in *Carboniogenic Activity of Zeolites*, Elsevier, Amsterdam.
 26. Corma, A. (2003) *J. Catal.*, **216**, 298.
 27. Gajda, G.J. and Rabo, J.A. (1994) in *Acidity and Basicity of Solids*, NATO ASI Series, vol. 444 (eds J. Fraissard and L. Petrakis), Kluwer Academic Press, Dordrecht, p. 127.
 28. Guisnet, M. and Gilson, J.-P. (2002) in *Zeolites for Cleaner Technologies* (eds M. Guisnet and J.-P. Gilson), Imperial College Press, Chapter 1.
 29. (a) Jacobs, P.A. and Mortier, W.J. (1982) *Zeolites*, **2**, 226; (b) Jacobs, P.A., Mortier, W.J. and Uytterhoeven, J.B. (1978) *J. Inorg. Nucl. Chem.*, **40**, 1919.
 30. Rabo, J. and Gajda, G.J. (1990) in *Guidelines for Mastering Properties of Molecular Sieves*, NATO ASI Series B, vol. 221, Plenum Press, New York, p. 273.
 31. Pines, L.A., Maher, P.J. and Wachter, W.A. (1984) *J. Catal.*, **85**, 466.
 32. Barthomeuf, D. (1987) *Mater. Chem. Phys.*, **17**, 49.
 33. (a) Chen, N.Y. and Haag, W.O. (1988) in *Hydrogen Effects in Catalysis* (eds Z. Paal and P.G. Menon), Dekker, p. 695; (b) Chen, N.Y. (1986) *Stud. Surf. Sci. Catal.*, **28**, 653; (c) Espeel, P., Parton, R., Toufar, H., Martens, J., Hölderich, W. and Jacobs, P. (1999) in *Catalysis and Zeolites* (eds J. Weitkamp and L. Puppe), Springer, p. 377.
 34. (a) Dwyer, J. (1988) *Stud. Surf. Sci. Catal.*, **37**, 333; (b) Lunsford, J.H. (1986) *J. Phys. Chem.*, **90**, 4847; (c) Mirodatos, D. and Barthomeuf, D. (1981) *Chem. Commun.*, 39; (d) Corma, A., Fornez, F., Martinez, A., Melo, F. and Pallato, O. (1988) *Stud. Surf. Sci. Catal.*, **37**, 495.
 35. Mirodatos, C. and Barthomeuf, D. (1981) *Chem. Commun.*, **181**, 38.
 36. Khabtou, S., Chevreau, T. and Lavalley, J.C. (1994) *Microporous Mater.*, **3**, 134.
 37. Szosak, R. (1991) *Stud. Surf. Sci. Catal.*, **58**, 153.
 38. Sommer, J., Hachoumy, M., Garin, F. and Barthomeuf, D. (1994) *J. Am. Chem. Soc.*, **116**, 5491.
 39. (a) Martens, J.A. and Jacobs, P.A. (1991) *Stud. Surf. Sci. Catal.*, **58**, 445; (b) Martens, J.A. and Jacobs, P.A. (1990) in *Theoretical Aspects of Heterogeneous Catalysis*, Van Nostrand-Reinhold Catalysis Series, New York, vol. 52 (ed. J.B. Moffat).
 40. van Santen, R.A. (1994) *Stud. Surf. Sci. Catal.*, **85**, 273.
 41. Wilson, S.T., Lok, B.M., Messina, C.A., Cannan, T.R. and Flanigen, E.M. (1982) *J. Am. Chem. Soc.*, **104**, 1146.
 42. Martens, J.A. and Jacobs, P.A. (1994) *Stud. Surf. Sci. Catal.*, **85**, 653.
 43. Goepper, M., Guth, F., Delmotte, L., Guth, J.L. and Kessler, H. (1989) *Stud. Surf. Sci. Catal.*, **49B**, 857.
 44. (a) Lok, B.M., Messina, C.A., Patton, R.L., Gajek, R.T., Cannan, T.R. and Flanigen, E.M. (1984) *J. Am. Chem. Soc.*, **106**, 6092; (b) Flanigen, E.M., Lok, B.M., Patton, R.L. and Wilson, S.T. (1986) *Proceedings of the 7th International Zeolite Conference* (eds Y. Murakami, A. Lijima and J.W. Ward), Kodansha-Elsevier, Amsterdam, Tokyo, p. 103.
 45. Flanigen, E.M., Patton, R.L. and Wilson, S.T. (1988) *Stud. Surf. Sci. Catal.*, **37**, 13.
 46. Wilson, S.T. and Flanigen, E.M. (1989) *ACS Symp. Ser.*, **398**, 329.
 47. (a) Ernst, S., Puppe, L. and Weitkamp, J. (1988) *Stud. Surf. Sci. Catal.*, **49A**, 231; (b) Schoonheydt, R.A., De Vos, R., Pelgrims, J. and Leeman, H. (1988) *Stud. Surf. Sci. Catal.*, **49A**, 559; (c) Wenquin, P., Shilun, Q., Qiubin, K., Zhiyun, W.

- and Shaoji, P. (1988) *Stud. Surf. Sci. Catal.*, **49A**, 281.
48. Mertens, M., Martens, J.A., Grobet, P.J. and Jacobs, P.A. (1990) *NATO ASI Ser., Ser. B*, **221**, 1.
 49. (a) Martens, J.A., Grobet, P.J. and Jacobs, P.A. (1990) *J. Catal.*, **126**, 299; (b) Young, D. and Davis, M.E. (1991) *Zeolites*, **11**, 277; (c) Biaglow, A.I., Adamo, A.T., Kokotailo, G.T. and Gorte, R.J. (1991) *J. Catal.*, **131**, 252; (d) Blackwell, C.S. and Patton, R.L. (1988) *J. Phys. Chem.*, **92**, 3965.
 50. Young, D. and Davis, M.E. (1991) *Zeolites*, **11**, 277.
 51. Yang, L., Aizhen, Y. and Qinhu, X. (1991) *Appl. Catal.*, **67**, 169.
 52. Yang, L., Maddox, P. and Couves, J.W. (1990) *J. Chem. Soc., Faraday Trans.*, **86**, 425.
 53. Szostak, R. (1991) *Stud. Surf. Sci. Catal.*, **58**, 153.
 54. Sierra de Saldariaga, L. and Davis, M. (1987) *J. Am. Chem. Soc.*, **109**, 2686.
 55. Martens, J.A., Janssens, C., Grobet, P.J., Beyer, H.K. and Jacobs, P.A. (1989) *Stud. Surf. Sci. Catal.*, **46**, 215.
 56. (a) Halik, C., Chaudhari, S.N. and Lercher, J.A. (1989) *JCS Faraday I*, **85**, 3879; (b) Halik, C. and Lercher, J.A. (1988) *JCS Faraday I*, **84**, 4457; (c) Meusinger, J., Vionek, H., Dworeckow, G., Goepfer, M. and Lercher, J.A. (1991) *Stud. Surf. Sci. Catal.*, **69**, 373.
 57. (a) Dzwigaj, S., Briend, M., Shikoleslamy, A., Peltre, M.J. and Barthomeuf, D. (1990) *Zeolites*, **10**, 157; (b) Martens, J.A., Grobet, P.J. and Jacobs, P.A. (1990) *J. Catal.*, **126**, 299.
 58. Ojo, A.F., Dwyer, J., Dewing, J., O'Mally, P.J. and Nabhan, A. (1992) *JSC Faraday*, **88**, 105.
 59. (a) Weisz, P.B. and Frilette, V.J. (1964) *J. Phys. Chem.*, **64**, 382; (b) Scicsery, S.M. (1976) in *Zeolite Chemistry and Catalysis*, ACS Monograph, American Chemical Society, Washington DC, vol. **181** (ed. J.A. Rabo), p. 680; (c) Chen, N.Y., Garwood, W.E. and Dwyer, F.G. (1996) *Shape Selective Catalysis in Industrial Applications*, Marcel Dekker, New York, Basel, Hong Kong; (d) Guisnet, M. (1990) *Acc. Chem. Res.*, **23**, 392; (e) Weitkamp, J. and Ernst, S. (1994) *Catal. Today*, **19**, 107; (f) Espeel, P., Parton, R., Toufar, H., Martens, J., Hölderich, W. and Jacobs, P. (1999) in *Catalysis and Zeolites* (eds J. Weitkamp and L. Puppe), Springer, p. 377; (g) Song, C., Garces, J.M. and Sugi, Y. (2000) *ACS Symp. Ser.*, **738**, 1.
 60. Mirodatos, C. and Barthomeuf, D. (1985) *J. Catal.*, **93**, 246.
 61. Smit, B. and Maesen, T.L.M. (2008) *Nature*, **451**, 671.
 62. Santilly, D.S. and Zones, S.I. (1990) *Catal. Lett.*, **7**, 383.
 63. Denaeyer, J.F., Ocakoglu, A.R., Martens, J.A. and Baron, G.V. (2004) *J. Catal.*, **226**, 240.
 64. Schenk, M., Calero, S., Maesen, T.L.M., van Benthem, L.L., Verbeek, M.G. and Smit, B. (2002) *Angew. Chem. Int. Ed.*, **41**, 2500.
 65. (a) Derouane, E.G., André, J.M. and Lucas, A.A. (1988) *J. Catal.*, **110**, 58; (b) Degnan, T.F. (2003) *J. Catal.*, **213**, 32.
 66. (a) Martens, J.A., Parton, R., Uytterhoeven, L., Jacobs, P.A. and Froment, G.F. (1991) *Appl. Catal.*, **76**, 95; (b) Martens, J.A., Vanbutsele, G., Jacobs, P.A., Denaeyer, J., Okacoglu, R., Baron, G.V., Munoz Arroyo, J.A., Thybaut, J. and Marin, G.B. (2001) *Catal. Today*, **65**, 111; (c) Claude, M.C. and Martens, J.A. (2000) *J. Catal.*, **190**, 39; (d) Claude, M.C., Vanbutsele, G. and Martens, J.A. (2001) *J. Catal.*, **203**, 213.
 67. Maesen, T.L.M., Schenk, M., Vlucht, T.J.H., de Jonge, J.P. and Smit, B. (1999) *J. Catal.*, **188**, 403.
 68. Inagaki, S., Kamino, K., Kikuchi, E. and Matsukata, M. (2007) *Appl. Catal. A*, **318**, 22.
 69. Corma, A., Fornes, V., Pergher, S.B., Maesen, T.L.M. and Buglass, J.G. (1998) *Nature*, **396**, 353.
 70. (a) Corma, A., Fornes, V., Guil, J.M., Pergher, S.B., Maesen, T.L.M. and Buglass, J.G. (2000) *Microporous Mesoporous Mater.*, **38**, 301;

- (b) Corma, A., Fornes, V., Martinez-Triguero, J. and Bergher, S.B. (1999) *J. Catal.*, **186**, 57;
 (c) Corma, A. and Fornes, V. (2001) *Stud. Surf. Sci. Catal.*, **135**, 73.
71. (a) Laforge, S., Martin, D., Paillaud, J.L. and Guisnet, M. (2003) *J. Catal.*, **220**, 92; (b) Laforge, S., Martin, D. and Guisnet, M. (2004) *Microporous Mesoporous Mater.*, **67**, 235.
 72. Corma, A., Martinez-Soria, V. and Schoenfeld, J. (2000) *J. Catal.*, **192**, 163.
 73. Martens, J.A. and Jacobs, P.A. (1992) *NATO ASI Ser., Ser. C*, **352**, 511.
 74. Martens, J.A., Wydoodt, M., Espeel, P. and Jacobs, P.A. (1993) *Stud. Surf. Sci. Catal.*, **78**, 527.
 75. Katzer, J.R. (1969) Ph.D. thesis, MIT, Cambridge Mass.
 76. (a) Deroaune, E.G. (1986) *J. Catal.*, **100**, 541; (b) Derouane, E.G., André, J.M. and Lucas, A.A. (1986) *J. Catal.*, **110**, 58.
 77. Neuber, M. and Weitkamp, J. (1991) *Stud. Surf. Sci. Catal.*, **60**, 291.
 78. (a) Stelzer, J., Paulis, M., Unger, M. and Weitkamp, J. (1998) *Microporous Mesoporous Mater.*, **22**, 1; (b) Denaeyer, J.F., Bouyermaouen, A. and Baron, G.V. (1998) *Ind. Eng. Chem. Res.*, **37**, 3698.
 79. (a) Corma, A., Domine, M.E., Gaona, J.A., Navarro, M.T., Rey, F. and Valencia, S. (2001) *Stud. Surf. Sci. Catal.*, **135**, 1812; (b) Stelzer, J., Paulis, M. and Weitkamp, J. (1998) *Microporous Mesoporous Mater.*, **22**, 18; (c) Weitkamp, J., Ernst, S., Roland, E. and Thiele, G.F. (1997) *Stud. Surf. Sci. Catal.*, **105**, 763.
 80. Denaeyer, J.F., Baron, G.V., Jacobs, P.A. and Martens, J.A. (2000) *Phys. Chem. Chem. Phys.*, **2**, 1007.
 81. Denaeyer, J.F.M., De Jonckheere, D., Hloch, M., Marin, G.B., Vanbutsele, G., Martens, J.A. and Baron, G.V. (2002) *J. Catal.*, **210**, 445.
 82. Denaeyer, J.F., Baron, G.V., Vanbutsele, G., Jacobs, P.A. and Martens, J.A. (1999) *Chem. Eng. Sci.*, **54**, 3553.
 83. (a) Maesen, T.L.M., Schenk, M., Vlugt, T.J.H., de Jonge, J.P. and Smit, B. (1999) *J. Catal.*, **188**, 403; (c) Raybaud, P., Patriceon, A. and Toulhoat, H. (2001) *J. Catal.*, **197**, 98.
 84. Denaeyer, J.F., Ocakoglu, A.R., Huybrechts, W., Martens, J.A., Thybaut, J.W., Marin, G.B. and Baron, G.V. (2003) *Chem. Commun.*, 1880.
 85. Dessau, M. (1986) *Chem. Commun.*, 1167.
 86. Sheldon, R.A. and Downing, R.S. (1999) *Appl. Catal. A*, **189**, 163.
 87. Corma, A., Garcia, H., Leyva, A. and Primo, A. (2003) *Appl. Catal. A*, **247**, 41.
 88. (a) Langendries, G., De Vos, D.E., Baron, G.V. and Jacobs, P.A. (1999) *J. Catal.*, **197**, 453; (b) Wilkenhöner, U., Langendries, G., Van Laar, F., Baron, G.V., Gammon, D.W., Jacobs, P.A. and van Steen, E. (2001) *J. Catal.*, **203**, 201; (c) De Vos, D. and Jacobs, P.A. (2004) *Stud. Surf. Sci. Catal.*, **154A**, 66.
 89. (a) Alvaro, M., Das, D., Cano, M. and Garcia, H. (2003) *J. Catal.*, **219**, 464; (b) Corma, A. and Garcia, H. (2003) *Chem. Rev.*, **103**, 4307.
 90. Tatsumi, T., Sakashita, H. and Asano, K. (1993) *Chem. Commun.*, 1264.
 91. Knops-Gerrits, P.P., De Vos, D.E., Baron, G.V. and Jacobs, P.A. (1994) *Nature*, **369**, 543.
 92. (a) De Vos, D., Hermans, I., Sels, B. and Jacobs, P. (2006) in *Catalysis for Fine Chemical Synthesis* (ed. E.G. Derouane), John Wiley & Sons, Inc., New York, Chapter 10, p. 207; (b) Dooos, B.M.L., Sels, B.F. and Jacobs, P.A. (2007) *Stud. Surf. Sci. Catal.*, **168**, 915.
 93. Barrer, R.M. (1982) *Hydrothermal Chemistry of Zeolites*, Academic Press, London, p. 360.
 94. (a) Martens, J.A. and Jacobs, P.A. (1987) *Stud. Surf. Sci. Catal.*, **33**, 390; (b) Byrappa, K. and Yoshimura, M. (2001) *Handbook of Hydrothermal Technology*, Noyes, New York, p. 875; (c) Balkus, K.J. (2001) in *Progress in Inorganic Chemistry* (ed K.D. Karlin), John Wiley & Sons, Inc., New York,

- Vol. 50, p. 217; (d) Soler-Illia, G.J.A.A., Sanchez, C., Lebeau, B. and Patarin, J. (2002) *Chem. Rev.*, **102**, 4093; (e) Caullet, P., Paillaud, J.L., Simon-Masseron, A., Soulard, M. and Patarin, J. (2005) *C. R. Chim.*, **8**, 245; (f) Robson, H. (ed.) (2001) *Verified Syntheses of Zeolitic Materials*, Elsevier, Amsterdam, p. 266; (g) Tosheva, L. and Valtchev, V.P. (2005) *Chem. Mater.*, **17**, 2494; (h) Lethbridge, Z.A.D., Williams, J.J., Walton, R.I., Evans, K.E. and Smith, C.W. (2005) *Microporous Mesoporous Mater.*, **79**, 339.
95. (a) Cundy, C.S. and Cox, P.A. (203) *Chem. Rev.*, **103**, 663; (b) Cundy, C.S. and Cox, P.A. (2005) *Microporous Mesoporous Mater.*, **82**, 1.
96. Kuhl, G. (2001) in *Verified Syntheses of Zeolitic Materials* (ed. H. Robson), Elsevier, Amsterdam, p. 19.
97. (a) Mintova, S., Olson, N.H., Valtchev, V. and Bein, T. (1999) *Science*, **283**, 958; (b) Serrano, D.P. and van Grieken, R. (2001) *J. Mater. Chem.*, **11**, 2391.
98. Kirschhock, G., Feyen, E.J.P., Jacobs, P.A. and Martens, J.A. (2008) in *Handbook of Heterogeneous Catalysis*, 2nd edn (eds G. Ertl, H. Knözinger, F. Schüth and J. Weitkamp), Wiley-VCH Verlag GmbH, Chapter 2.3.5.
99. Breck, D.W. (1964) *J. Chem. Educ.*, **41**, 678.
100. (a) Kerr, G.T. (1966) *J. Phys. Chem.*, **70**, 1047; (b) Zhdanov, S.P. (1971) *Adv. Chem. Ser.*, **101**, 20.
101. Casci, J.L. and Lowe, B.M. (1983) *Zeolites*, **3**, 186.
102. Nicolle, M.A., Di Renzo, F., Fajula, F., Espiau, P. and des Courières, T. (1993) in *Proceedings of the 9th International Zeolite Conference* (eds R. von Ballmoos, J.B., Higgins and M.M.J. Treacy), Butterworth-Heinemann, Boston, p. 313.
103. (a) Jacobs, P.A., Derouane, E.G. and Weitkamp, J. (1981) *Chem. Commun.*, 591; (b) Mintova, S., Olson, N.H., Senker, J. and Bein, T. (2002) *Angew. Chem. Int. Ed.*, **41**, 2558.
104. Bell, A.T. (1989) *ACS Symp. Ser.*, **398**, 66.
105. (a) Thompson, R.W. (1999) in *Molecular Sieves* (eds H.G. Karge and J. Weitkamp), Springer-Verlag, Berlin, Vol. 1, p. 1; (b) Thompson, R.W. (1992) in *Modeling and Reactivity in Zeolites* (eds C.R.A. Catlow and R. Vetrivel), Academic Press, London, p. 231; (c) Barrer, R.M. (1982) *Hydrothermal Chemistry of Zeolites*, Academic Press, London, p. 133.
106. Thompson, R.W. and Dyer, A. (1985) *Zeolites*, **5**, 292.
107. Pope, C.G. (1998) *Microporous Mesoporous Mater.*, **21**, 333.
108. (a) Regev, O., Cohen, Y., Kebat, E. and Talmon, Y. (1994) *Zeolites*, **14**, 314; (b) Mintova, S., Olson, N.H., Valtchev, V. and Bein, T. (1999) *Science*, **283**, 958.
109. Zhdanov, S.P. (1971) *Adv. Chem. Ser.*, **101**, 20.
110. Falamaki, C., Edrissi, M. and Sohrabi, M. (1997) *Zeolites*, **19**, 2.
111. (a) Nikolakis, V., Vlachos, D.G. and Tsapatsis, M. (1998) *Microporous Mesoporous Mater.*, **21**, 337; (b) McCormick, A.V. and Bell, A.T. (1989) *Catal. Rev. Sci. Eng.*, **31**, 97.
112. Feijen, E.J.P., Martens, J.A. and Jacobs, P.A. (1994) *Stud. Surf. Sci. Catal.*, **84**, 3.
113. Schoeman, B.J. and Regev, O. (1996) *Zeolites*, **17**, 447.
114. Aiello, A., Barrer, R.M. and Kerr, I.S. (1971) *Adv. Chem. Ser.*, **101**, 44.
115. Hayhurst, D.T., Nastro, A., Aiello, R., Crea, F. and Gordan, G. (1983) *Zeolites*, **3**, 416.
116. van Santen, R.A., Keijsper, J., Ooms, G. and Kortbeek, A.G.T.G. (1986) *Stud. Surf. Sci. Catal.*, **28**, 169.
117. Chang, C.D. and Bell, A.T. (1991) *Catal. Lett.*, **8**, 305.
118. Brunner, G.O. (1992) *Zeolites*, **12**, 428.
119. McCormick, A.V. and Bell, A.T. (1989) *Catal. Rev. Sci. Eng.*, **31**, 97.
120. (a) Gonthier, S. and Thompson, R.W. (1994) *Stud. Surf. Sci. Catal.*, **85**, 43; (b) Kacirek, H. and Lechert, H. (1975) *J. Phys. Chem.*, **79**, 1589;

- (c) Cundy, C.S., Forrest, J.O. and Plaisted, R.J. (2003) *Microporous Mesoporous Mater.*, **66**, 143.
121. Cundy, C.S., Palisted, R.J. and Zhao, J.P. (1998) *Chem. Commun.*, 1465.
 122. Souverijns, W., Verrelst, W., Vanbutsele, G., Martens, J.A. and Jacobs, P.A. (1994) *Chem. Commun.*, 1671.
 123. de Moor, P.P.E.A., Beelen, T.P.M., van Santen, R.A., Tsuji, K. and Davis, M.E. (2000) *Chem. Mater.*, **12**, 845.
 124. Mintova, S., Petkov, N., Karaghiossoff, K. and Bein, T. (2002) *Mater. Sci. Eng.*, **C19**, 111.
 125. Valtchev, V.P. (2004) *J. Phys. Chem. B*, **108**, 15587.
 126. Nikolakis, V., Kokkoli, E., Tirrell, M., Tsapatsis, M. and Vlachos, D.G. (2000) *Chem. Mater.*, **12**, 845.
 127. (a) Feijen, E.J.P., De Vadder, K., Bosschaerts, M.H., Lievens, J.L., Martens, J.A., Grobet, P.J. and Jacobs, P.A. (1994) *J. Am. Chem. Soc.*, **116**, 2950; (b) Vaughan, D.E.W. (1991) *Stud. Surf. Sci. Catal.*, **65**, 275.
 128. Kirschhock, C.A.E., Ravishankar, R., Verspeurt, F., Grobet, P.J., Jacobs, P.A. and Martens, J.A. (1999) *J. Phys. Chem. B*, **103**, 4965.
 129. Davis, T.M., Drews, T.O., Ramanan, H., He, C., Dong, J., Schnablegger, H., Katsoulakis, M.A., Kokkoli, E., McCormick, A.V., Penn, R.L. and Tsapatsis, M. (2006) *Nature Mater.*, **5**, 400.
 130. Kirschhock, C.E.A., Aerts, A. and Martens, J.A. (2007) *Stud. Surf. Sci. Catal.*, **170B**, 1473.
 131. Knight, C.T.G. and Kinrade, S.D. (2002) *J. Phys. Chem. B*, **106**, 3329.
 132. Dai, F.Y., Suzuki, M., Takahashi, H. and Saito, Y. (1986) *Stud. Surf. Sci. Catal.*, **28**, 223.
 133. Jansen, J.C. (1991) *Stud. Surf. Sci. Catal.*, **58**, 77.
 134. Kuperman, A., Nadimi, S., Oliver, S., Ozin, G.A., Ozin, J.M. and Olkin, M.M. (1993) *Nature*, **365**, 239.
 135. Morris, R.E. and Weigel, S.J. (1997) *Chem. Soc. Rev.*, **26**, 309.
 136. Weigel, S., Gabriel, J.C., Guittierez-Puebla, E., Moge-Breavo, A., Bull, L.M., Henson, N.J. and Cheetham, A.K. (1996) *J. Am. Chem. Soc.*, **118**, 11849.
 137. (a) Barrer, R.M. (1981) *Zeolites*, **1**, 130; (b) Guth, J.L., Caullet, P., Seive, A., Patarin, J. and Delprato, F. (1990) *NATO ASI Ser.*, **221**, 69.
 138. (a) Dwyer, F.C. and Chu, P. (1979) *J. Catal.*, **59**, 263; (b) Katovic, A., Subotic, B., Smit, I., Despotovic, L.A. and Curic, M. (1989) *ACS Symp. Ser.*, **398**, 124.
 139. (a) Lok, B.M., Cannan, T.R. and Messina, C.A. (1983) *Zeolites*, **3**, 382; (b) Gilson, J.P. (1992) *NATO ASI Ser.*, **352**, 19.
 140. Lobo, R.F., Pan, M., Chan, I., Medrud, R.C., Zones, S.I., Crozier, P.A. and Davis, M.A. (1994) *J. Phys. Chem.*, **98**, 12040.
 141. Hasegawa, I. and Sakka, S. (1989) *ACS Symp. Ser.*, **398**, 140.
 142. Barrer, R.M. (1981) *Zeolites*, **1**, 130.
 143. Blasco, T., Corma, A., Diaz-Cabanas, M.J., Rey, F., Vidal-Moya, J.A. and Zicovich-Wilson, C.M. (2002) *J. Phys. Chem. B*, **106**, 2634.
 144. Schüth, F. (2005) *Ann. Rev. Mater. Res.*, **35**, 209.
 145. Sastre, G., Leiva, S., Sabater, M.J., Gimenez, I., Rey, F., Valencia, S. and Corma, A. (2004) *J. Phys. Chem. B*, **107**, 5432.
 146. Axnanda, S. and Shantz, D.F. (2005) *Microporous Mesoporous Mater.*, **84**, 236.
 147. Lee, S. and Santz, D.F. (2005) *Microporous Mesoporous Mater.*, **84**, 268.
 148. Carr, C.S. and Shantz, D.F. (2005) *Microporous Mesoporous Mater.*, **85**, 284.
 149. Cundy, C.S., Henty, M.S. and Plaisted, R.J. (1995) *Zeolites*, **15**, 342.
 150. Dessau, R.M., Valyocsic, E.W. and Goeke, N.H. (1992) *Zeolites*, **12**, 776.
 151. Groen, J.C., Peffer, L.A.A., Moulijn, J.A. and Perez-Ramirez, J. (2004) *Microporous Mesoporous Mater.*, **69**, 29.
 152. (a) Koller, H., Lobo, R., Burkett, S. and Davis, M. (1995) *J. Phys. Chem. B*, **99**, 12588; (b) Burton, A.W., Zones, S.I. and Elomari, S. (2005)

- Curr. Opin. Colloid Interface Sci.*, **10**, 211.
153. Cambor, C., Villaescusa, L. and Diaz-Cabanas, M. (1999) *Top. Catal.*, **9**, 59.
 154. (a) Persson, A.E., Schoeman, B.J., Sterte, J. and Ottersted, J.E. (1994) *Zeolites*, **14**, 557; (b) Cambor, M.A., Corma, A., Mifsud, A., Perez-Pariente, J. and Valencia, S. (1997) *Stud. Surf. Sci. Catal.*, **105**, 341; (c) Larsen, S.C. (2007) *J. Phys. Chem. C*, **111**, 18464.
 155. (a) Madsen, C. and Jacobsen, C.J.H. (1999) *Chem. Commun.*, 673; (b) Jacobson, C.J.H., Madsen, C., Janssens, T.V.W., Jakobsen, H.J. and Skibsted, J. (2000) *Microporous Mesoporous Mater.*, **39**, 393.
 156. Schmidt, I., Madson, C. and Jacobsen, C.J.H. (2000) *Inorg. Chem.*, **39**, 2279.
 157. (a) Zhang, G., Yu, Y., Chen, X., Han, Y., Di, Y., Yang, B., Xiao, F.S. and Shen, J.C. (2003) *J. Colloid Interface Sci.*, **263**, 461; (b) Holland, B.T., Blanford, C.F. and Stein, A. (1998) *Science*, **281**, 538.
 158. Bronich, T.K., Kabanov, A.V., Kabanov, V.A., Yu, K. and Eisenberg, A. (1997) *Macromolecules*, **30**, 3519.
 159. Yang, X., Feng, Y., Tian, G., Du, Y., Ge, X., Di, Y., Zhang, Y., Sun, B. and Cio, F.S. (2005) *Angew. Chem. Int. Ed.*, **44**, 2563.
 160. Serrano, D.P. and van Grieken, R. (2001) *J. Mater. Chem.*, **11**, 2391.
 161. (a) Derouane, E.G., Detremmerie, S., Gabelica, Z. and Blom, N. (1981) *Appl. Catal.*, **1**, 101; (b) Gabelica, Z., Derouane, G. and Blom, N. (1984) *ACS Symp. Ser.*, **248**, 219.
 162. Subotic, B. and Graovac, A. (1985) *Stud. Surf. Sci. Catal.*, **24**, 199.
 163. Thompson, R.W. (1992) *Zeolites*, **12**, 837.
 164. Wu, D., Dong, J., Li, J., Li, J. and Wu, F. (1990) *Chem. Commun.*, 755.
 165. Yu, J. (2007) *Stud. Surf. Sci. Catal.*, **168**, 40.
 166. Matsukata, M., Ogura, M., Osaki, T., Rao, P., Nomura, M. and Kikuchi, E. (1999) *Top. Catal.*, **9**, 77.
 167. (a) Rao, P. and Matsukata, M. (1996) *Chem. Commun.*, 4041; (b) Rao, P., Leon, C., Ueyama, K. and Matsukata, M. (1998) *Microporous Mesoporous Mater.*, **21**, 305; (c) Georgen, S., Guillon, E., Rebours, B., Sorbier, L., Patarin, J. and Rouleau, L. (2007) *Stud. Surf. Sci. Catal.*, **170A**, 444.
 168. Weitkamp, J. and Hunger, M. (2005) *Stud. Surf. Sci. Catal.*, **155**, 1.
 169. Wilson, S.T. (1991) *Stud. Surf. Sci. Catal.*, **58**, 137.
 170. Wilson, S.T. (2007) *Stud. Surf. Sci. Catal.*, **168**, 105.
 171. Wilson, S.T., Lok, B.M., Messina, C.A., Cannan, T.R. and Flanigen, E.M. (1983) *ACS Symp. Ser.*, **218**, 79.
 172. Xu, Y., Tian, Z., Wang, S., Hu, Y., Wang, L., Wang, B., Ma, Y., Hou, L., Yu, J. and Lin, L. (2006) *Angew. Chem. Int. Ed.*, **45**, 3965.
 173. Wenqin, P., Shilun, Q., Quibin, K., Zhiyun, W. and Shaoyi, P. (1989) *Stud. Surf. Sci. Catal.*, **49A**, 281.
 174. Kessler, H. (1989) *Stud. Surf. Sci. Catal.*, **52**, 17.
 175. Tapp, N.J., Milestone, N.B. and Bibby, D.M. (1988) *Zeolites*, **8**, 183.
 176. Derouane, E.G. and von Ballmoos, R. (1987) US P 4,673,559.
 177. Chen, B. and Huang, Y. (2006) *J. Am. Chem. Soc.*, **128**, 6437.
 178. Cooper, E.R., Andrews, C.D., Wheatly, P.S., Webb, P.B., Wormald, P. and Morris, R.E. (2004) *Nature*, **430**, 1012.
 179. Wang, L., Xu, Y., Wei, Y., Duan, J., Chen, A., Wang, B., Ma, H., Tian, Z. and Li, L. (2006) *J. Am. Chem. Soc.*, **128**, 7432.
 180. Parnham, E.R. and Morris, R.E. (2007) *Acc. Chem. Res.*, **40**, 1005.
 181. (a) Cejka, J. (2005) *Stud. Surf. Sci. Catal.*, **157**, 111; (b) Corma, A. and Davis, M.E. (2004) *ChemPhysChem*, **5**, 304; (c) Casci, J.L. (1994) *Stud. Surf. Sci. Catal.*, **85**, 329.
 182. Richardson, J.W. and Vogt, E.T.C. (1992) *Zeolites*, **12**, 13.
 183. Davis, M.E., Saldiariagga, C., Montes, C., Garces, J. and Crowder, C. (1998) *Nature*, **331**, 98.

184. Lobo, R.F., Tsapatsis, M., Fryhardt, C.C., Khodabandeh, S., Wagner, P., Chen, C.Y., Balkus, K.J., Zones, S.I. and Davis, M.E. (1997) *J. Am. Chem. Soc.*, **119**, 8474.
185. Yoshikawa, M., Wagner, P., LOvallo, M., Tsuji, K., Takewaki, T., Chen, C.Y., Beck, L.W., Jones, C., Tsapatsis, M., Zones, S.I. and Davis, M.E. (1998) *J. Phys. Chem. B*, **102**, 7139.
186. Burton, A., Elomari, S., Chen, C.Y., Medrud, R.C., Chan, I.Y., Bull, L.M., Kibby, C., Harris, T.V., Zones, S.I. and Vittoratos, E.S. (2003) *Chem. Eur. J.*, **9**, 5737.
187. Cejka, J. (2005) *Stud. Surf. Sci. Catal.*, **157**, 111.
188. Estermann, M., McCusker, L.B., Baerlocher, C., Merrouche, A. and Kessler, H. (1991) *Nature*, **352**, 320.
189. Jones, R.H., Thomas, J.M., Chen, J., Xu, R., Huo, Q., Li, S., Ma, Z. and Chippindale, A.M. (1993) *J. Solid State Chem.*, **102**, 204.
190. Stromaier, K.G. and Vaughan, D.E.W. (2003) *J. Am. Chem. Soc.*, **125**, 16035.
191. Corma, A., Diaz-Cabanas, M.J., Rey, F., Nicolopoulos, S. and Boulayha, K. (2004) *Chem. Commun.*, 1356.
192. Paillaud, J.L., Harbuzaru, B., Patarin, J. and Bats, N. (2004) *Science*, **304**, 990.
193. Casci, J.L. (2005) *Microporous Mesoporous Mater.*, **82**, 217.
194. Nee, J.R.D., Lowe, B.M. and Casci, J.L. (1994) *Zeolites*, **14**, 610.
195. Kuhl, G. (1988) *Microporous Mater.*, **22**, 515.
196. Schmidt, F. (2001) *Appl. Catal. A*, **221**, 15.
197. Miller, S.J. (1996) USP 5,558,851.
198. Murrell, L., Overbeek, R.A., Chang, Y., van der Puil, N. and Yeh, C. (1999) PCT WO 99/16709.
199. Wenyang, X., Jianquan, L., Wenyang, L., Huiming, Z. and Bingchang, L. (1989) *Zeolites*, **9**, 468.

Further Reading

- De Vos, D. and Jacobs, P.A. (2004) *Stud. Surf. Sci. Catal.*, **154A**, 66.
- Lobo, R.F., Zones, S.I. and Davis, M.E. (1995) in *Inclusion Chemistry with Zeolites* (eds N., Herron and D.R., Corbin), Kluwer, Dordrecht, Vol. 1, p. 47.
- Caratzoulas, S., Vlachos, D. and Tsapatsis, M. (2005) *J. Phys. Chem. B*, **109**, 10429.

13

Ordered Mesoporous Materials

Ying Wan and Dongyuan Zhao

13.1

Introduction

Periodic mesoporous materials represent a new class of porous solids, which possess uniform pore sizes (1.5–40 nm), large surface areas (up to 2500 m²/g) and tunable structures [1–3]. These materials are amongst the most promising candidates to be used as nanoreactors of large molecules. These solids are of great interest, in particular, for catalysts and catalyst carriers. They are becoming a commercial reality and will continue to grow in significance coupled to the need for efficient and environmentally benign processes [4–11]. This chapter will summarize the synthesis of mesoporous solids according to the compositions, namely silica, functionalized silica, metal substituted mesoporous silica, carbon, metal oxides and nonoxides.

13.2

Mesoporous Silica

The essence for the construction of ordered porous materials is the self-assembly in which molecules (or parts of molecules) spontaneously organize stable, structurally well-defined aggregates (in nanometer length scale). By utilizing the self-assembling approach, a family of ordered mesoporous silicas, the pore size ranging from 2 to 50 nm, emerged in the early 1990 s [1, 2].

The self-assembling process involves noncovalent or weak interactions (van der Waals, electrostatic, and hydrophobic interactions, hydrogen and coordination bonds, and π – π stacking). This process corresponds to a variation of “reversed” pore structures. Most ordered mesoporous materials are derived from the thermodynamically stable and ordered aggregates spontaneously driven by the noncovalent interactions between molecules. These aggregates come from the cationic, anionic and nonionic surfactants, neutral amines, block copolymers, or their mixtures (Figure 13.1). They are disordered on the atomic or

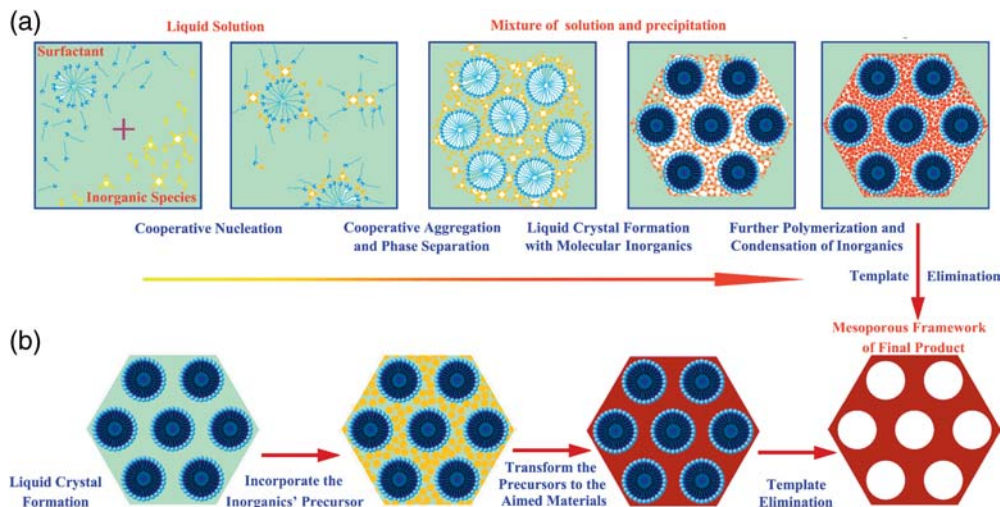


Figure 13.1 Synthetic strategy of mesoporous materials: (a) The cooperative interaction between inorganic and organic species at the molecular scale leads to assembly to 3D ordered arrangements. (b) The true or semiliquid-crystal phase

forms 3D ordered arrangements, and then incorporates the inorganic precursors. (Reprinted with permission from [12]. Copyright 2007 American Chemical Society.)

molecular scale, but display periodical mesoscopic morphology. Supramolecular aggregates pack into three-dimensional (3D) ordered mesostructures according to the corresponding symmetries. Route A is the cooperative self-assembly of surfactants and silica sources to form mesostructures, and route B is a so-called “true” liquid-crystal template pathway. At the final stage, the aggregates are removed by calcination, extraction, microwave digestion, or oxidative decomposition. Pores are opened, the dimension, shape, and topology depend on the size and morphology of supramolecular aggregates [4, 6, 12].

Several tens of kinds of different ordered mesoporous silicates have been synthesized and named. However, there are far fewer different mesostructures. Most of the mesostructures belong to hexagonal and cubic phases.

2D mesostructured silica with the hexagonal symmetry are most easily produced, the classical products being MCM-41, FSM-16, SBA-3, and SBA-15 [1–3, 13]. The ideal models for these structures are hexagonally close-packed cylindrical pores, belonging to the $p6mm$ space group (Figure 13.2). Typical transmission electron microscope (TEM) images can show two features: hexagonal structures along the channel system and parallel stripes if viewed perpendicular to the channel directions. The 3D mesostructures possess the intergrowth of hexagonal close packing (hcp) and cubic close-packing (ccp) phases (SBA-2, SBA-7 and SBA-12) [14, 15], cubic bicontinuous structures with the $1a\bar{3}d$ (MCM-48, FDU-5, KIT-6) [16–18], and $Pn\bar{3}m$ (AMS-10) [19]

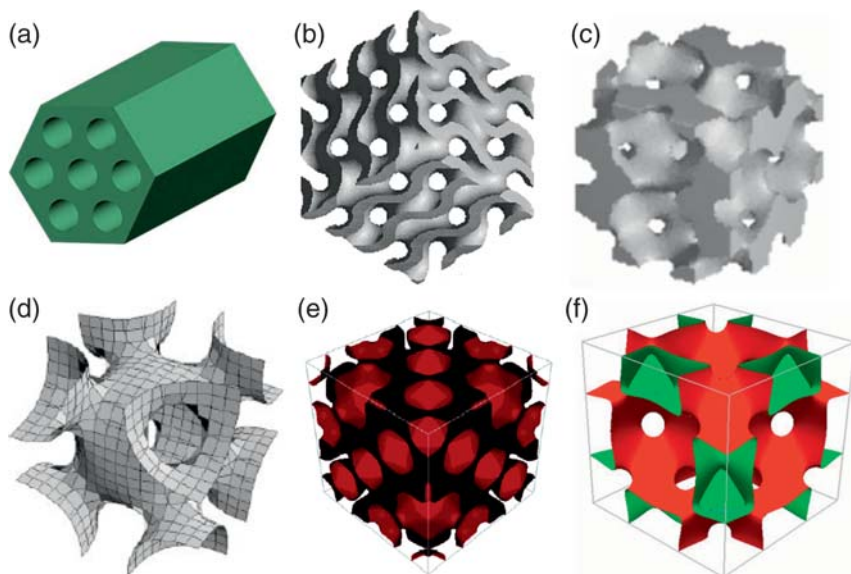


Figure 13.2 Pore models of mesostructures with symmetries of (a) $p6mm$, (b) $Ia\bar{3}d$, (c) $Pm\bar{3}n$, (d) $Im\bar{3}m$, (e) $Fd\bar{3}m$, and (f) $Fm\bar{3}m$. (Reprinted with

permission from [20, 24, 26, 27]. Copyright 2002, 2004, and 2007 American Chemical Society, and copyright 2000, *Nature*.)

symmetries, simple cubic structures with the $Pm\bar{3}n$ ($Pm\bar{3}m$) symmetry (SBA-1, SBA-6, and SBA-11) [13, 15, 20], face-centered cubic structures with the $Fm\bar{3}m$ (FDU-12 and KIT-5) [21, 22], and $Fd\bar{3}m$ (FDU-2 and AMS-8) [23, 24] symmetries and body-centered cubic structures with the $Im\bar{3}m$ symmetry (SBA-16 and IBN-1) [15, 25]. Figure 13.2 shows the typical pore-structural models. Among them, MCM-41, SBA-15, and MCM-48 are the extensively investigated mesoporous silica molecular sieves.

13.2.1

MCM-41

The first synthesis of MCM-41 mesoporous silica was reported by Mobil scientists using quaternary cationic surfactants $C_nH_{2n+1}N(CH_3)_3X$ ($n = 8-10, 12, 14$, and 16 ; $X = Cl$ and Br) as templates under basic conditions [1, 16].

The cell parameter of MCM-41 (~ 4.0 nm) can be easily obtained from the X-ray diffraction (XRD) and TEM analysis. The pore channels in MCM-41 are often simply approximated as cylinders [28], although at least three kinds of shapes have been proposed. The other two models are the hexagonal prism and a so-called “cucurbit” that can be envisaged as a string of connected spherical cages along the $[001]$ direction [29, 30]. Typical isotherms of MCM-41

show no obvious hysteresis loop. The pore-wall thickness is estimated to be about 1 nm and the BET surface area is generally higher than 1000 m²/g. In addition, micropores are not detected.

The solid-state magic-angle sample spinning nuclear magnetic resonance (MAS-NMR) spectra show that ²⁹Si signals of MCM-41 are wide, similar to those of amorphous silica. The Si-O-Si bonds are irregularly distributed in the MCM-41 framework with wide-range bond angles. Two overlapping signals with chemical shifts at -100 and -110 ppm correspond to the Si(OSi)₃OH group (labeled as Q³), and the Si(OSi)₄ group (denoted as Q⁴), respectively. The Q³ groups reflect the abundance of silanol groups on mesoporous silica that are beneficial for further functionalization. The silicon content in silanols is calculated to be 8–27% of the total silicon atoms in MCM-41 [31], which is close to the theoretical value (17–28%) from the structural model. MCM-41 materials may show different fine chemical structures of frameworks according to various procedures despite having the same pore channels.

13.2.2

SBA-15

The second important 2D hexagonally mesostructured silica is SBA-15 molecular sieve, first reported by Zhao *et al.* in 1998 [3, 15]. The results suggest that SBA-15 has a highly ordered 2D hexagonal mesostructure (space group *p6mm*) with a very uniform pore-size distribution. SBA-15 materials prepared from P123 at 40–100 °C (hydrothermal temperature) have uniform pore sizes from ~6.5 to 10 nm. The pore-wall thickness is calculated to be 3.1–4.8 nm, much thicker than that of MCM-41, which results in higher thermal and hydrothermal stability [3, 15].

More importantly, people have revealed that the wall structure of SBA-15 is quite different from that of MCM-41, although the two materials have the same space group (*p6mm*) [32]. Triblock copolymers not only play a role of templates but also insert into silica frameworks with EO blocks and form organic–inorganic hybrid frameworks. ¹H, ¹³C, and ²⁹Si NMR results have provided direct evidence for this [33]. After calcination, micropores or small mesopores are left in the frameworks and connections between the mesopores are generated owing to the removal of triblock copolymers. No diffraction peak assigned to these micropores is detected in XRD patterns due to the disordered arrangement. Nitrogen sorption techniques reveal pore sizes between 1 and 3 nm [34, 35]. The intraframework pore volumes contribute about 30% of total volume [36]. Complementary porosity of SBA-15 can be retained to a significant extent even after calcination at 900 °C, but probably completely disappears at 1000 °C. Adding a cosolvent like ethanol and a small amount of salts manipulates the P123 micellar environment and hence eliminates the microporosity of SBA-15 after a microwave hydrothermal treatment.

Modification of SBA-15 surface by octyldimethylsilyl groups can also block these small pores [35].

13.2.3

MCM-48

MCM-48 is defined by a so-called minimal surface, the gyroid (G-surface), which was first proposed by Monnier *et al.* [37]. This attractive mesostructure stimulated intensive research efforts. Also, the synthesis of cubic MCM-48 mesostructure with $Ia\bar{3}d$ symmetry (Figure 13.2b) is a good example to explain the effects of packing parameters of surfactants (g) values on the final mesostructures. The g value is widely used in predicting and explaining the final mesostructures [14]. The calculation of g value is simple but of great significance and guidance: $g = V/a_0l$. Here, V is the total volume of surfactant hydrophobic chains plus any cosolvent (organic molecules) between the chains, a_0 is the effective hydrophilic headgroup area at the aqueous-micelle surface, and l is the kinetic surfactant tail length. The expected mesophase sequence as a function of g value is cubic ($Pm\bar{3}n$) and 3D hexagonal ($P6_3/mmc$) with $g < 1/3$, 2D hexagonal ($p6mm$) with $1/3 < g < 1/2$, cubic ($Ia\bar{3}d$) with $1/2 < g < 2/3$ and lamellar with $g \approx 1$.

In the basic synthesis, with the increase of g values and the reduction of surface curvature around the surfactant micelles, the cubic $Ia\bar{3}d$ structure becomes favored over the hexagonal one [14, 38]. Therefore, the enlargement of surfactant hydrophobic volume or the enhancement of hydrophobic property can easily induce the formation of MCM-48 mesostructure. The characteristics for the synthesis are:

1. TEOS is the best silica precursor in the synthesis of MCM-48, which generates ethanol during the hydrolysis. Polar ethanol tends to enter the hydrophobic zone but cannot penetrate into the surfactant micelle core [39]. The enlarged surfactant hydrophobic volume decreases the interfacial curvature around the surfactant micelles, and thus results in the formation of MCM-48. Although Ryoo and coworker synthesized MCM-48 using colloidal silica as a source, adding ethanol was also necessary [38].
2. The pH value is generally higher than that for MCM-41.
3. Moderate polar molecules, for example, triethanolamine, favor the retention of periphery in the hydrophobic zone of surfactant micelles, which gives rise to MCM-48 mesostructure [39].
4. Cationic surfactants are used, the most common one being CTAB. The surfactant concentration is higher than that for MCM-41. Gemini surfactants and large head-group cationic surfactant $C_{16}H_{33}(CH_3)_2N(CH_2)(C_6H_5)$ can easily template the MCM-48 mesostructure. The alkyl chains or benzene groups that link with the polar heads of surfactants favor

staying in the outer shell of hydrophobic regions of micelles due to their hydrophobicity and large volumes, and hence reduce the curvature. Gemini surfactant $C_{22-12-22}$ is very efficient in directing MCM-48 mesostructure even at room temperature.

5. Cosurfactants with negative charge (e.g. $C_nH_{2n+1}COOH$ and $C_nH_{2n+1}SO_3H$) can interact with a small amount of cationic surfactants to form ion pairs. The mixture shows low hydrophilicity, increases the g value and assists the phase transformations from $p6mm$ to $Ia\bar{3}d$ [40].
6. Hydrothermal treatment and recrystallization is needed to improve the mesostructural regularity.

13.2.4

Pore-Size Control

Several methods can be relied on to adjust the pore sizes of mesoporous silica molecular sieves, as mentioned above, such as the selection of surfactants, hydrothermal treatment, and organic additives. Table 13.1 illustrates the pore sizes obtained by various methods.

1. Surfactant: Pore sizes of mesoporous silica materials mainly depend on the hydrophobic groups of surfactants. Cationic quaternary surfactants with longer alkyl chains can yield larger pore sizes. The chain is, however, limited to C_{22} , because surfactants with long alkyl chains are insoluble in water and lead to the formation of disordered products. As for the conventional PEO-PPO-PEO triblock copolymers, the pore

Table 13.1 Pore sizes of ordered silica mesostructures obtained by various methods.

Pore size (nm)	Method
2–5	Surfactants with different chain lengths including long-chain quaternary cationic salts and neutral organoamines
4–7	Long-chain quaternary cationic salts as surfactants High-temperature hydrothermal treatment
5–8	Charged surfactants with the addition of organic swelling agents such as TMB and midchain amines
2–8	Nonionic surfactants
4–20	Triblock copolymer surfactants
4–11	Secondary synthesis, for example water–amine postsynthesis
10–27	High-molecular-weight block copolymers, such as PI- <i>b</i> -PEO, PIB- <i>b</i> -PEO and PS- <i>b</i> -PEO triblock copolymers with the addition of swelling agents TMB and inorganic salts low-temperature synthesis

sizes are enlarged with increasing molecular weights of the hydrophobic blocks rather than those of copolymers [41]. Diblock copolymers always direct larger pore sizes compared to triblock copolymers with similar molecular weights or PPO chains because the latter tend to “U”-type bending aggregation. The bent hydrophobic PPO chains lead to a smaller size of micelles. High molecular weight block copolymers are of great interest owing to the relatively large mesopores in the resultant aluminosilicates and silicates that were first demonstrated by Wiesner and coworkers [42]. These lab-made copolymers include poly(isoprene)-poly(ethylene oxide) (PI-PEO), poly(styrene)-*block*-poly(4-vinylpyridine) (PS-P4VP) and poly(isobutylene)-*block*-poly(ethylene oxide) (PIB-PEO) that can template the mesopores with sizes larger than 20 nm [42–44]. However, the expected large mesopore sizes are not obtained. N₂ adsorption measurements show that the BET surface areas are close to zero. This is probably due to the isolated sphere packing model that results in thick pore walls and no micropore connection between mesopores [45]. The use of block copolymers with high molecular weights and long PEO chains (PEO₁₂₅-PS₂₃₀) provides a facile pathway to give ordered silica-type mesostructures that extend the accessible pore width to ~31 nm and the BET surface area to 360 m²/g [46]. The insertion of long PEO chains inside the silica pore walls facilitates the formation of tunnels connecting primary mesopores of silicates.

2. Organic swelling agent: Adding organic swelling agents is an important way to expand pore sizes. The hydrophobic organic species can be dissolved inside the hydrophobic regions of surfactant micelles, which leads to a swelling of the micelles. The pore sizes are expanded by the additives of large organic hydrocarbons such as dodecane, trimethyl benzene (TMB), triisopropylbenzene, tertiary amines, and poly(propylene glycol).
3. Hydrothermal treatment: Changing the hydrothermal temperature can tailor the pore size [47]. During the hydrothermal treatment at higher temperatures, the PEO blocks become hydrophobic and retract from the silicate walls. The hydrolysis and crosslinkage of inorganic species and assembly with surfactant continue in this stage. The enlarged surfactant micelles result in large-pore SBA-15, thin pore walls, and low micropore volumes [48]. The mesopore sizes of SBA-15 can be easily tuned from 4.6 to 10 nm and from 9.5 to 11.4 nm by increasing the hydrothermal temperature from 70 to 130 °C and by prolonging the hydrothermal time from 6 hours to four days, respectively. Considering the large cage sizes, the window sizes of cage-type mesostructures are too small. Expanding entrance sizes is a key factor for the immobilization of enzymes and the fabrication of cubic mesoporous carbon replicas with ordered mesopores. Fan *et al.* [21] enlarged the window sizes by the simple hydrothermal treatment of as-synthesized cage-type mesoporous

materials. The sizes of the entrances in face-centered cubic FDU-12 mesostructures ($Fm\bar{3}m$) can be continuously adjusted in the range of 4–9 nm by increasing the hydrothermal treatment temperature from 100 to 140 °C.

13.3

Organic Group Functionalized Mesoporous Silicates

13.3.1

Organic Groups Anchored to Mesoporous Silicates

Organic group functionalized mesoporous silicas take advantage of the large surface areas, high stability, and the confined mesopores in the inorganic solids, together with the tunable functionality of the organic moieties, such as hydrophobicity/hydrophilicity and acid/base properties. Two basic approaches for the incorporation of organic moieties have been developed, that is, grafting and cocondensation methods (Figure 13.3) [10]. Cocondensation is a synthetic approach in which tetraalkoxysilanes $(RO)_4Si$ and trialkoxyorganosilanes $(RO)_3Si-R'$ (where R is Et or Me and R' is a nonhydrolyzable ligand) coassemble with amphiphilic surfactants. Alternatively, by utilizing various methods, reactive organosilane species can be grafted on the surface or pore channels of mesoporous silicates. A wide range of functional organic groups have been incorporated in or on the pore walls of mesoporous silicates, including thiol, amine, epoxide, imadizole, cyanide, methyl, and phenyl groups [10, 49, 50]. These functional sites can further react or chelate with active molecules to gain rich functionalities. Their applications such as catalysis, separation,

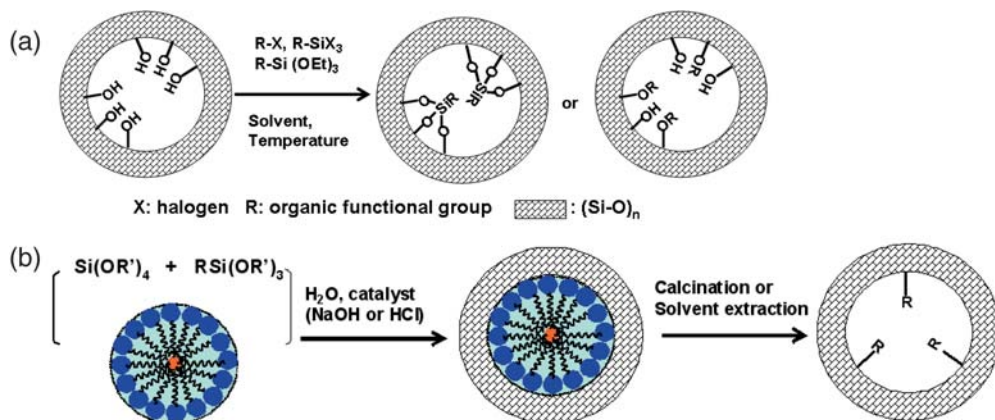


Figure 13.3 Schematic diagram for the (a) grafting and (b) cocondensation method in the preparation of organic groups functionalized materials.

irradiation, sensing, and adsorption of contaminations require accessibility of to the active sites.

13.3.2

Periodic Mesoporous Organosilicas

Unlike the functionalized mesoporous silicates mentioned above, where the organic ligands are anchored in or on the pore walls, periodic mesoporous organosilicas (PMOs) contain unique organic groups embedded inside the pore walls [51–53]. They are prepared through the surfactant-templated condensation of silsequioxane precursors like $(\text{RO})_3\text{-Si-R''-Si-(OR)}_3$. Both of the terminal groups in the precursors can hydrolyze and crosslink, resulting in preservation of the C–Si bonds and the frameworks on account of the tetra-coordinated silicate species. Therefore, fully organically functionalized mesoporous silicas can be produced by using 100% $(\text{RO})_3\text{-Si-R''-Si-(OR)}_3$ as silicate sources.

Owing to the similar synthetic strategy as for mesoporous silicas, PMOs have been fabricated by using nonionic surfactants as structure-directing agents (SDAs) via the hydrothermal and EISA methods. Enlarging pores and molding solid shapes including thin films, monoliths, spheres, polyhedrons, and so on, is also possible by analogous pathways. Both chain and cyclic organic compounds have been integrated into the inorganic matrices, including methylene, ethane, ethylene, benzene, ethylbenzene, 4-phenylether, and 4-phenylsulfide [49]. However, the reported mesostructures ($p6mm$, $1a\bar{3}d$, $Im\bar{3}m$, $Pm\bar{3}n$, intergrowth of 3D hexagonal with cubic mesophases) are limited, even if cationic surfactants are used, compared to their pure silica counterparts.

It is worth mentioning that periodic mesoporous benzene-silica represents a kind of ordered organic–inorganic hybrid mesoporous material possessing a crystal-like periodic pore-wall structure [54]. This is due to the strong π – π stacking of benzenes and the ordered layer structure owing to the alternating distribution of phenyl groups and silanols groups, which constructs, in turn, an ordered mesostructure and hierarchical PMOs (Figure 13.4).

13.3.3

Adsorption and Catalysis

The textural properties govern the diffusion process so that a well-defined structure may facilitate diffusion-controlled reactions. For example, the adsorption of heavy-metal ions (Hg^{2+} and Cu^{2+}) reveals a dramatic discrepancy between ordered and disordered mesoporous silica grafted with the aminopropyl or mercaptopropyl group [55]. The ordered mesostructure with a mean pore size of 6.5 nm brings about complete accessibility of the functional groups. While

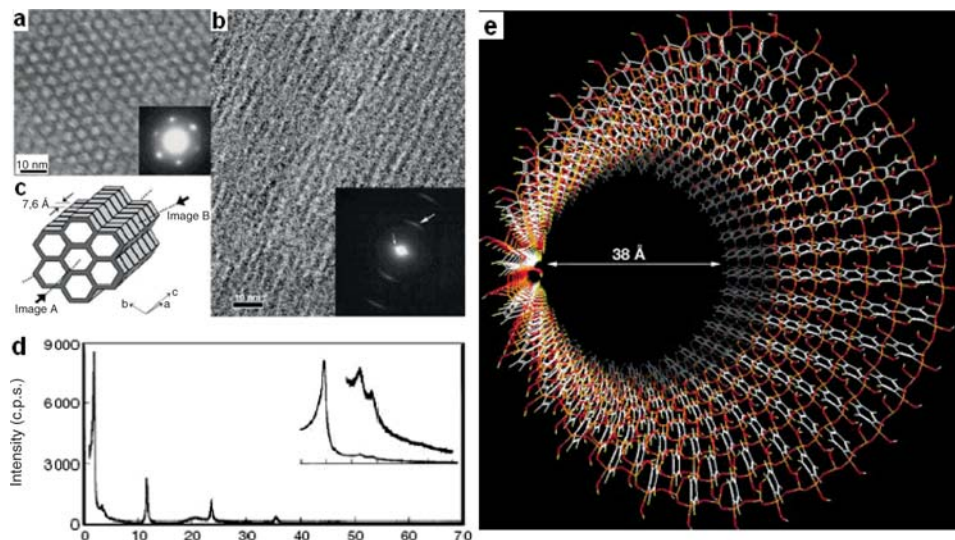
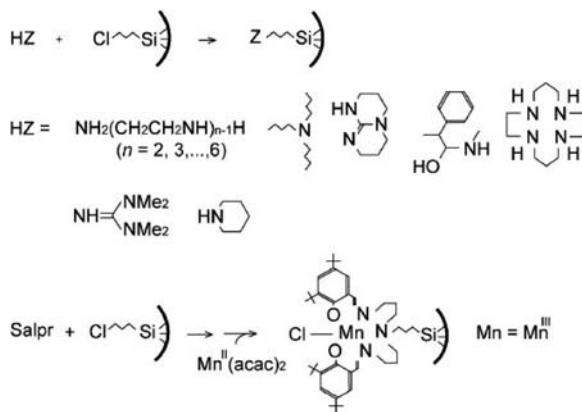


Figure 13.4 TEM images of PMO from a precursor of 1,4-bis(triethoxysilyl)benzene $[(\text{C}_2\text{H}_5\text{O})_3\text{Si}-(\text{C}_6\text{H}_4)-\text{Si}(\text{OC}_2\text{H}_5)_3]$ viewed along [001] (a) and [100] (b) directions, respectively. Structural model (c), XRD diffractions (d) and pore-wall structure (e) of calcined PMO sample. Insets (a) and (b) show the electron-diffraction patterns of the same area. (Adapted from [54].)

the disordered one reveals 87%, possibly because of pore lockage during the grafting process.

To obtain mesoporous molecular sieves with a strong basic nature, Rodriguez *et al.* [56] grafted $(\text{CH}_3\text{O})_3\text{Si}-(\text{CH}_2)_3\text{NH}_3^+ \text{Cl}^-$ on MCM-41, and then exchanged it with base in order to achieve the functional group transformation to $-(\text{CH}_2)_3\text{NH}_3^+\text{OH}^-$. Sulfonated mesoporous silica can be produced by oxidizing mercapto-functionalized materials. This solid displays a stronger acidity than Al-modified MCM-41. The oxidation reaction can also be carried out on the organic ligands in PMOs. Benzene groups can be sulfonated in benzene-PMOs to get solid acids, showing potential applications in catalysis and fuel cells [57]. Typically, an organosilane, protein, organometal, polymer, and metal can be further integrated on the organic groups functionalized mesoporous silica irrespective of the means by which it is obtained. For example, functional groups, such as amine, mercapto, or chloropropyl groups are incorporated on the surface of mesoporous silica SBA-15. The following iterative reactions with organic metal complexes, proteins, dendrimers precursors, or metal solution produce the second-class hybrid materials, possessing organometals, proteins, dendrimers, or metal nanowires within the mesopores (Figure 13.5) [58, 59].

A hydrophobic nature of the pore surface facilitates the adsorption of organic compounds. We tested the Ullmann coupling reaction of iodobenzene in water



salpr = 3-[N,N'-bis-3-(salicylidenamino)propyl]amine

Figure 13.5 Amine reactions with surface chloropropyl groups on mesoporous silica. (Adapted from [59].)

on palladium-supported pure siliceous and phenyl group functionalized MCM-41 samples [60]. Only 23% yield of biphenyl was observed on the Pd/MCM-41 catalyst. Pd/Ph-MCM-41 in which phenyl groups anchored on MCM-41 pore walls exhibited relatively high yield of biphenyl (74%). The Pd/Ph-PMO catalyst with phenylene moieties embedding inside silica matrix showed an even higher yield of biphenyl (94%) owing to the hydrophobic surface. This can be attributed, at least partly, to the hydrophobic surface of the Ph-MCM-41 and the Ph-PMO support.

13.4

Metal-Substituted Mesoporous Silica Molecular Sieves

In general, the surface of pure silicate mesostructures is weakly acidic. It is found that the incorporation of metal ions into the framework can introduce acidic and ion-exchange functionality and catalytically active sites. Various metal ions, such as Al^{3+} , Ti^{4+} , V^{5+} , Ga^{3+} , and Fe^{3+} , have been incorporated into SBA-15 to enhance its catalytic performance. In contrast to zeolites, which have crystalline structures, the incorporation of metal ions in mesoporous silicates cannot be strictly defined as intra- or extra-framework incorporation since these ions are highly dispersed on the framework. A wide range of compositions with different coordination numbers and chemical environments can contribute to amorphous framework structures. For example, both tetrahedrally and octahedrally coordinated aluminum in SBA-15 are involved in the formation of the amorphous pore walls, and may be defined as “intraframework Al.” The former may exist inside the pore walls, while the latter may be located on the pore surface.

Here, we give an example for the synthesis of Ti-containing mesoporous silicas. This kind of catalyst has abilities for the selective oxidation of olefin and other unsaturated compounds, such as the epoxidation of 1-hexene, cyclohexene, and styrene [61, 62]. The ratio of Si/Ti, structure, and hydrophobic nature of the material are the three most important factors in the catalytic activity. Therefore, a full understanding of the synthesis is necessary.

In contrast to mesoporous silicas, the balance of the hydrolysis and condensation rates between silica and titania sources should be thoroughly considered. Several methods have been used to improve the hydrolysis of TEOS or to decrease that of Ti precursors. The initial report on mesoporous titanium-containing mesoporous silicas used chemically modified Ti-alkoxide species to limit the rate of hydrolysis of the metal precursor [63]. Other reported titanium sources are $(\text{NH}_4)_2\text{TiF}_6$ [64] and TiCl_3 [65]. The low hydrolysis rate of TiCl_3 facilitates the incorporation of titanium in the silica framework. Mesoporous Ti-MCM-41 catalysts prepared from TiCl_3 and colloidal silica with the assistance of TMAOH and TEAOH are active in the epoxidation of cyclohexene using dilute H_2O_2 as the oxidant (Table 13.2). Using chelating agents, including tartatic acid and acetylacetone, can also decrease the hydrolysis rate of titanium sources. A time-delay hydrolysis method can be adopted by adding titanium sources in a gel of the prehydrolysis product of TEOS [61].

Normally, the Ti content is limited to 0.15–3 wt%. Too high a content would lead to the destruction of the ordered mesostructure or the aggregation of titania particles. The addition of *n*-(trimethoxysilylpropyl)ethylenediaminetriacetic acid (EDATAS) during the hydrothermal synthesis may improve the titanium

Table 13.2 Selective oxidation of cyclohexene on Ti-MCM-41 with different contents of titanium.

Sample ^a	Ti/Si ratio	Conversion (%)	Selectivity (%)					H_2O_2 efficiency
			A	B	C	D	E	
Ti-MCM-41(200)	0.0105	25	55	19	14	7	4.9	90
Ti-MCM-41(120)	0.0162	43	54	17	15	12	3.1	89
Ti-MCM-41(80)	0.0235	45	52	14	14	16	3.2	89
Ti-MCM-41(40)	0.0373	67	47	11	16	24	2.2	87

Reprinted with permission from [65].

^a The numbers in parentheses are the Si/Ti molar ratios in the synthesis gel.

A = epoxides; B = cyclohexene-1-ol; C = cyclohexene-1-one;

D = cyclohexanediol; E = others.

content and change the surface chemical state of titanium from four-coordination to six-coordination [66].

To improve the hydrophobicity of Ti-containing mesoporous silicas, cocondensation and grafting method with the organosilanes can be used as mentioned above [67].

13.5 Carbon

13.5.1

The Hard-Templating Approach

Ordered mesoporous carbons are generally fabricated by a hard-templating approach (Figure 13.6) [8, 11]. The hard-templating approach or so-called nanocasting, is an extension of the templating concept in the preparation of zeolites and mesoporous materials. Instead of organic amines or surfactants, highly ordered mesoporous silicates are employed as templates, which provide a scaffold for the formation of other materials. The precursors can be incorporated in the channels of mesoporous silicates by impregnation, sorption, phase transition, ion exchange, and coordination or covalent grafting. By a heat treatment, the precursors are thermally decomposed, and nanoparticles are formed and grow in the pore channels, by interconnection to each other combined with a crystallization process. The resulting by-products generally leave the channels via the gas phase. If the loading level of the precursors is sufficiently high, the nanocrystals may interlink with each other during the annealing process and form continuous frameworks. After the mesoporous silica templates are dissolved, the mesostructures are negatively copied by the nanocrystals, and replica materials such as unique nanorod or nanowire arrays are obtained.

In 1999, almost seven years after the first report of M41S by Mobil scientists, ordered mesoporous carbons were synthesized by Ryoo's and Hyeon's

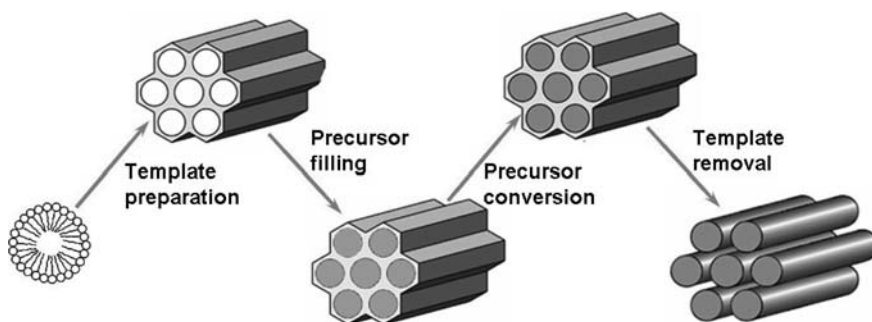


Figure 13.6 Schematic illustration for the nanocasting strategy.

group, respectively [68, 69]. The hard templates that have interconnected micro/mesopores in the frameworks are efficient in supporting the carbon periodical arrays and preserving the ordered mesostructures. The idea for the nanocasting strategy in preparing ordered mesoporous carbon replicas was not new, coming from the hard-templating route to microporous carbon molecular sieves. In 1997, Kyotani *et al.* [70] first reported the synthesis of porous carbon with large surface area ($\sim 2200 \text{ m}^2/\text{g}$) by using zeolite Y as a hard template. However, the micropore channels are too small to accommodate large carbon molecules and further carbonization. Porous carbons have disordered microstructures and could not faithfully replicate zeolite structures. By comparison, mesoporous silicates have larger pore channels that provide enough room to accommodate a large amount of carbon sources and allow the carbon molecules reconstructed. As a result, highly ordered mesoporous carbon replicas have been obtained. Later, ordered microporous carbon molecular sieves were synthesized more successfully via a chemical vapor deposition (CVD) method by using small organic molecules such as acetylene as a carbon source and zeolite Y as the hard template [71].

The distinct advantage for the nanocasting process is the avoidance of organic surfactants as SDAs and the hydrolysis and condensation process of precursors, which evokes extensive explorations for materials scientists. It is extremely suitable for the materials such as mesoporous metals, metal oxides, sulfides, carbides, and nitrides that cannot be synthesized via the surfactant-templating approach. Various carbon precursors, for example, sucrose, furfuryl alcohol, naphthalene, mesophase pitch, C_2H_2 , polyacrylonitrile, phenolic resins, can be utilized. The resultant mesostructures include $I4_132$, $Ia\bar{3}d$, $p6mm$, and $Im\bar{3}m$, and the macroscopic morphologies vary from films, rods, spheres, “single crystals” to monoliths. However, these mesoporous carbons are constructed by amorphous carbon rod (wire) nanoarrays (only a few cases are partially graphitized). Mesochannels are produced by the voids between carbon rods. Therefore, the pore-size distribution is relatively wider than the silica template.

13.5.2

The Supramolecular-Templating Approach

The preparation of mesoporous carbon materials with ordered open-pore structures by the supramolecular-templating approach is extremely difficult in solution and remains challenging, owing to the intrinsic characters of organic molecules and the high formation energy of C–C bonds.

More recently, Dai and coworkers successfully prepared ordered mesoporous carbon films with open-framework structures by using resorcinol and formaldehyde as carbon sources and diblock copolymer polystyrene-poly(4-vinylpyridine) (PS-P4VP) as a template [72]. Similar results were reported by Tanaka *et al.* [73], in which the same carbon precursor and triblock copolymer F127 ($\text{EO}_{106}\text{PO}_{70}\text{EO}_{106}$) were used for organic–organic self-assembly. Triethyl

orthoacetate was added as a carbon coprecursor, which may decrease the polymerization rate of resorcinol and formaldehyde under strong acid conditions and enhance the interaction between them and the surfactant templates.

Meng *et al.* [74, 75] demonstrated a reproducible synthesis of highly ordered mesoporous polymers and carbons from an organic–organic EISA process of low molecular weight and water-soluble phenolic resins (resols) and commercial copolymers PEO-PPO-PEO (Figure 13.7). A family of highly ordered mesoporous polymer resins and carbons have been synthesized, including mesostructures with lamellar, 2D hexagonal $p6mm$ (FDU-15), body-centered cubic $Im\bar{3}m$ (FDU-16), and bicontinuous cubic $Ia\bar{3}d$ (FDU-14) symmetries. The mesoporous polymer resins and carbons exhibit highly ordered structures, high surface areas ($\sim 1500 \text{ m}^2/\text{g}$), large pore volumes ($\sim 0.85 \text{ cm}^3/\text{g}$), and uniform pore sizes. In addition, the open carbon frameworks with covalently bonded construction and thick pore

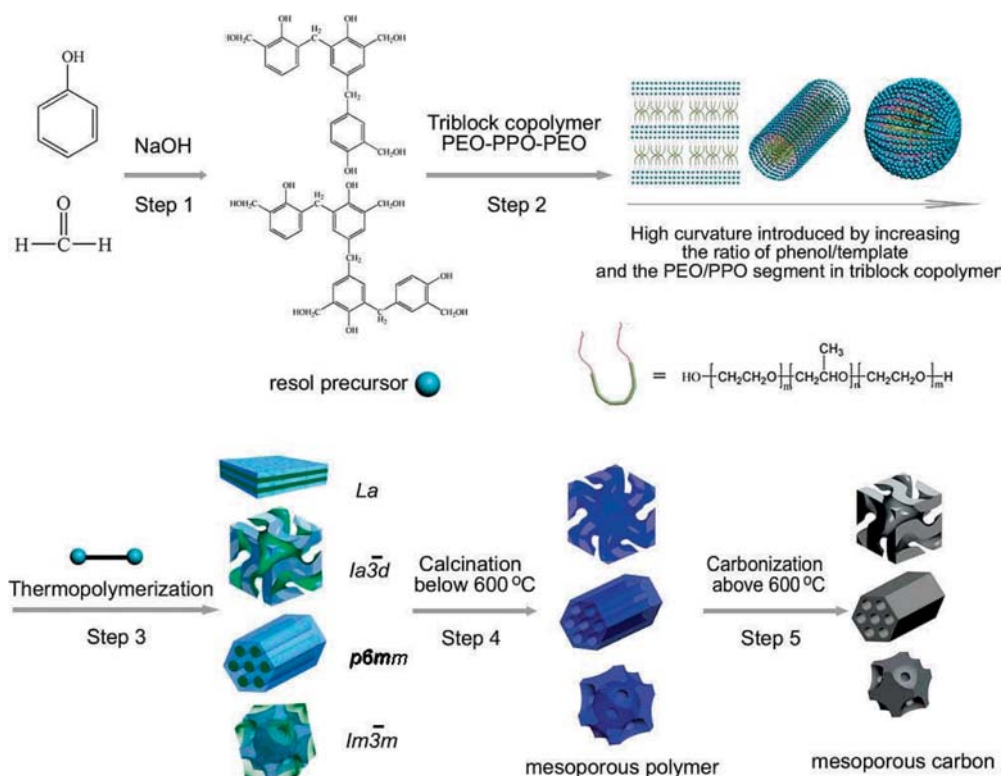


Figure 13.7 The scheme for the preparation of ordered mesoporous polymer resins and carbon frameworks. (Reprinted with permission from [75]. Copyright 2006 American Chemical Society.)

walls (thickness ~ 8 nm) exhibit highly thermal stability ($> 1400^\circ\text{C}$). Organic mesoporous materials and homologous carbons with open frameworks can also be prepared in aqueous media [76].

Inherent to the surfactant-templating approach, the interactions on surfactant/precursor species interfaces and inside species themselves play important roles on the polymer and carbon mesostructures. Several issues should be addressed:

1. SDAs: Block copolymers with one block sufficiently compatible with a thermosetting resin and one other block sufficiently repulsive are good SDAs.
2. Templating: The strong interaction between the SDAs and organic precursor is a key issue. Several cases have been shown here to highlight the importance for the strong hydrogen-bonding interaction in the preparation of ordered mesoporous carbonaceous materials. For example, highly ordered mesoporous polymers and carbons have been successfully synthesized in the system of low molecular weight basically catalyzed phenolic resols as precursors and PEO-containing block copolymers as templates. The precursors have plenty of hydroxyl and benzyl groups that can form strongly hydrogen-bonding interactions with amphiphilic block copolymers. Secondly, the precursors should be small enough to assemble around the amphiphilic block copolymer aggregates. The prepolymerization of polymeric oligomers is a choice to control the condensation of the monomers. Self-assembly of block copolymers induces the highly ordered mesostructure.
3. Crosslinking: Curing the polymer fixes the framework. The polymeric framework should be rigid enough to resist the polymerization-induced macroscopic phase separation. Base-catalyzed condensation of phenol and formaldehyde results in phenolic resin of a "rigid" 3D network structure with benzene rings as three or four crosslinking sites. This kind of crosslinked structure is similar to that of covalently bonded silicate zeolite frameworks, in which one silicon atom is linked to four other silicon atoms through Si—O bonds. In contrast, linear novolac resin may lack this property, leading to an unstable framework.
4. Template removal: The feature that the polymeric frameworks are more stable than block copolymers facilitates the elimination of templates with the maintenance of the mesostructured matrices.
5. Carbonization: The key point in this process is the assurance of the mesostructural stability. A uniform shrinkage is required. Therefore, pure inert carbonizing atmosphere such as nitrogen and argon is favorable. A small amount of oxygen in N_2 or Ar gas generates micropores in the carbonaceous pore walls. Similarly, the addition of CO_2 and H_2O in the carbonizing atmosphere could cause micropores. The temperature is generally above 600°C . The carbonization under an atmosphere of 4% O_2 (in volume) in N_2 at 700°C would lead to the agglomeration of pore walls.

This simple, reproducible approach by self-assembling low-molecular-weight polymers and triblock copolymers opens an avenue to diverse polymer and carbon mesostructures that have great potentials in many high-tech applications.

13.6

Nonsiliceous Oxides

13.6.1

The Supramolecular-Templating Approach

Yang *et al.* [77] prepared metal-oxide frameworks by using anhydrous inorganic salts instead of alkoxides or organic metal complexes as the soluble and hydrolyzable inorganic precursors. The preparation involves an acid-catalyzed sol-gel process. The alcoholysis of inorganic salts generates $M(OEt)_nCl_m$ species with a low polymerization rate that slowly react with water in air via hydrolysis and crosslinkage to form mesostructures.

On the basis of the compatibility of acid and base precursors, an “acid–base pair” concept was established for guiding the selection of precursors in fabricating mesoporous metal oxides with various components under nonaqueous conditions [78, 79]. Firstly, the inorganic precursors are divided into “acid” and “base” according to their alcoholysis (here, alcohol is used as the solvent) behaviors. Inorganic metal or nonmetal chlorides are considered as strong “acids” since a large amount of acid is generated during the alcoholysis process. Hydrated metal salts and inorganic acids (Brönsted acid) are classified as middle acidic precursors. Metal alkoxides and nonmetal alkoxides (e.g. phosphatides) are classified as “base” because acid substances are rarely generated from such precursors.

Guided by the “acid–base pair” concept, a wide variety of well-ordered, large-pore, homogeneous, multicomponent, mesostructured solids have been synthesized, including metal phosphates, silico-aluminophosphates, metal borates, as well as various metal oxides and mixed-metal oxides [79]. Most of these mesoporous products possess semicrystalline pore walls and relatively high thermal stability. These materials show high surface areas, uniform pore sizes and tunable periodic structures, which may cause fascinating chemical and physical properties. Some composites, such as TiPO and AlPO, are stable up to 800 °C. Moreover, such materials can be easily processed as thin films, monoliths, and multiscale ordered coatings.

This concept, together with the increased understanding of the EISA strategy, sol-gel chemistry, and organic–inorganic interaction, which are interdependent will pave the way for preparing various ordered mesoporous nonsiliceous materials.

13.6.2

The Hard-Templating Approach

For the oxides that cannot be synthesized by the surfactant self-assembly, the hard-templating approach is a good choice. The key point for the nanocasting method is to increase the loading level of the precursors in the mesopore channels of the templates. Evidently, improving the interactions between template and precursor and between precursors themselves are essential in the hard-templating approach [11].

For example, microwave-digested mesoporous silicas with large pore volumes, high surface areas, and most important of all, abundant silanols are expected to serve as ideal hard templates for nanocasting replicas. The interaction between the precursors and the silicate walls is enhanced by the abundant silanols and the mesopore channels are filled by using simple inorganic precursors such as metal chlorides or metal nitrates in an ethanol solution. After the solvents are naturally evaporated and the silica templates are dissolved, highly ordered metal-oxide nanowire arrays can be replicated with various compositions including Cr_2O_3 , Mn_xO_y , Fe_2O_3 , Co_3O_4 , NiO , CuO , WO_2 , CeO_2 , and In_2O_3 . The structures of these secondary mesophase materials can vary from hexagonally packed nanowire arrays ($p6mm$), 3D bicontinuous nanowire arrays ($1a\bar{3}d$), to nanosphere arrays ($Im\bar{3}m$) derived from SBA-15, FDU-5 or KIT-6, and SBA-16, respectively. More interestingly, they show doubly ordered structures on both meso- and atomic scales (Figure 13.8) [80, 81].

13.7

Nonoxides

Nonoxides such as silicon carbides, nitrides, metal sulfides, and so on, possess unique chemical, thermal, and mechanical properties and can be used as catalysts and catalyst carriers. The properties can be further enhanced by the confined-space effect in nanospace, high surface areas, and large pore volumes.

13.7.1

SiC-Based Materials

Nanoporous SiC-based materials are difficult to obtain due to the high formation temperature. Disordered nanoporous silicon carbide ceramics can be fabricated by a solid–gas reaction of ordered mesoporous carbon replica with silicon vapor [82], and a chemical vapor infiltration of dimethyldichlorosilane inside mesoporous silica following by the removal of silica [83]. Recently, highly ordered mesoporous SiC materials with uniform pore sizes and ultralarge surface areas have been synthesized by fully impregnating polycarbosilane

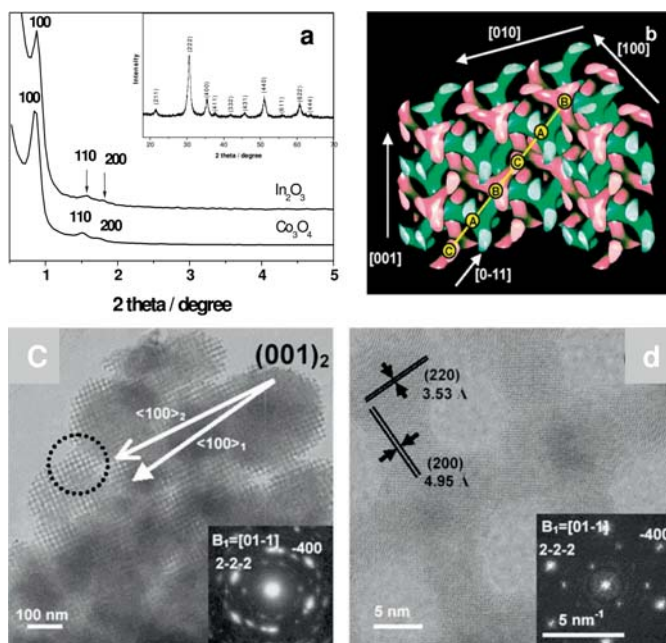


Figure 13.8 (a) Small-angle XRD patterns of In_2O_3 and Co_3O_4 nanowire arrays replicated by microwave-digested SBA-15. The inset is the wide-angle XRD pattern of an In_2O_3 nanowire replica material. (b) A model of the bicontinuous cubic mesostructure model with $Ia\bar{3}d$ symmetry. (c) TEM image of single-crystal In_2O_3 nanowire arrays with $I4_32$ symmetry from a template of FDU-5. (d) High-resolution TEM (HRTEM) image of the circled area. Insets of

c and d are the corresponding SAED patterns. The arrows in (c) represent the $[100]$ plane directions of the microstructure and mesostructure; and the arrows in (d) show the distance of In_2O_3 single crystal along the (220) and (200) directions. (Data and images are reproduced with permission from [81]. Copyright 2004 American Chemical Society.)

(PCS) inside the channels of mesoporous silicates, annealing and then removing hard templates of silicates [84–86]. The key point is the use of PCS that can decompose to silicon carbides during the annealing process.

A casting-by-casting method is also a solution to give mesoporous ceramics with open frameworks. Ordered mesoporous carbon replicas that are cast from mesoporous silicates are used as the hard templates. The final goal materials replicate the pore topologies of these carbons and have almost the same frameworks as the original mesoporous silica scaffolds. Miele and coworkers [87] employed this casting-by-casting method to synthesize mesoporous BN–C nanocomposites by using polyborazine as precursors. Shi *et al.* [88] combined this strategy with the atmosphere-assisted *in-situ* transformation to fabricate ordered mesoporous silicon oxycarbide and carbonitride ceramics with high surface areas. Air and ammonia are used to transform SiC–C composites

to highly ordered mesoporous ceramics accompanied with the removal of mesoporous carbon template.

13.7.2

Metal Sulfides

Stupp and coworkers first prepared mesostructured sulfides with oligomeric alkyl ethylene oxides [89, 90]. Lyotropic surfactant liquid-crystal phases are generated with the addition of appropriate metal ions, for example, Cd^{2+} . Hydrogen sulfide or hydrogen selenide gas is then fed into the solution to solidify the mesostructured organic–inorganic composites. The difficulty in this process remains the removal of the surfactants. A family of mesostructured solids, such as CdS, ZnS, and CdSe, have been successfully synthesized.

The hard-templating route has also been explored to fabricate ordered metal sulfide replicas by using mesoporous silica as a hard template. Utilizing $[\text{Cd}_{10} \text{S}_{16} \text{C}_{32} \text{H}_{80} \text{N}_4 \text{O}_{28}]$ cluster as a precursor, Gao *et al.* [91] fabricated ordered 2D hexagonal mesoporous CdS nanowire arrays. $[\text{Cd}_{10} \text{S}_{16}]^{4+}$ is a soluble cadmium sulfide cluster with ample –OH groups, which favors a large loading rate of $[\text{Cd}_{10} \text{S}_{16}]^{4+}$. The precursor also contains both Cd and S, and can be thermally decomposed to CdS at 160 °C in air. Liu *et al.* [92] nanocasted a mixture of thiourea and metal nitrates into mesoporous silica channels to prepare mesoporous CdS, ZnS, and In_2S_3 with nanoparticle pore walls and the 2D hexagonal structure. Thiourea serves as a sulfide source that can slow down the formation rate of metal sulfides. A novel high-temperature reductive sulfuration approach was demonstrated by Shi *et al.* [93] to fabricate highly ordered mesoporous crystalline WS_2 and MoS_2 . The metal precursors are phosphotungstic acid (PTA) and phosphomolybdic acid (PMA). The metal precursors (PTA and PMA)/silica composites can be converted to WS_2 and MoS_2 crystallites by using H_2S gas as a sulfuration agent at a high temperature of 600 °C. Mesoporous WS_2 and MoS_2 replicas have large surface areas, pore volume, and narrow pore-size distributions. Layered WS_2 and MoS_2 nanocrystals are partially oriented along the mesochannels of the silica templates (Figure 13.9). This high-temperature reductive sulfuration method is a general strategy, and can be extended to synthesize other mesoporous metal sulfides such as CdS.

13.8

Summary and Remarks

Heterogeneous catalysis is of fundamental importance in the chemical industry and in other technologically relevant applications. This chapter mainly illustrates the synthesis for the mesoporous solids that can be used as catalysts and catalysts carriers, such as silica, organic-group-functionalized silica, metal-substituted silica, phosphate, carbon, nonsiliceous oxides, nonoxides, and so

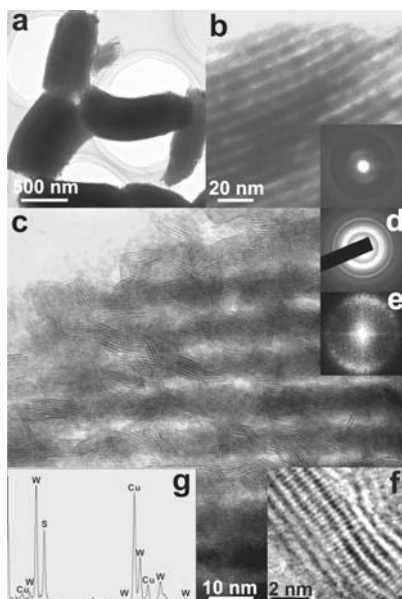


Figure 13.9 TEM images and energy dispersive X-ray spectroscopy (EDX) spectrum of mesoporous WS_2 -SBA-15 replicas prepared via a high-temperature reductive sulfuration method with H_2S gas at 600°C : (a) low-magnification TEM image; (b) high-magnification TEM image; (c) and (f) HRTEM images; inset (b) and (d) the corresponding SAED patterns of (b); (e) the corresponding FFT diffractogram of (c); and (g) EDX spectrum. (Reprinted with permission from [93]. Copyright 2007 American Chemical Society.)

on. Two synthetic pathways are introduced, that is, the supramolecular-templating and the hard-templating approaches.

To enhance the adsorptive and catalytic performance, both tailoring the pore structure and tuning the pore chemistry should be considered. The former is related to the internal mass-transfer resistance, while the latter contributes to selective adsorption and nature of the active center. High-efficiency porous heterogeneous catalysts could be produced on the basis of the synergistic effect of the high surface area, uniform pore channel, and the reactivity.

Acknowledgments

This work was supported by the NSF of China (20873086 and 20521140450), the State Key Basic Research Program of the PRC (2006CB202502 and 2006CB932302), the Shanghai Science & Technology and Education Committee (07QH14011, 07SG49, and 08JC1417100), Shanghai Nanotech Promotion Center (0652 nm024), the Program for New Century Excellent Talents in Universities (NCET-07-0560).

References

1. Kresge, C.T., Leonowicz, M.E., Roth, W.J., Vartuli, J.C. and Beck, J.S. (1992) *Nature*, **359**, 710.
2. Yanagisawa, T., Shimizu, T., Kuroda, K. and Kato, C. (1990) *Bull. Chem. Soc. Jpn.*, **63**, 988.

3. Zhao, D.Y., Feng, J.L., Huo, Q.S., Melosh, N., Fredrickson, G.H., Chmelka, B.F. and Stucky, G.D. (1998) *Science*, **279**, 548.
4. Corma, A. (1997) *Chem. Rev.*, **97**, 2373.
5. Davis, M.E. (2002) *Nature*, **417**, 813.
6. Ying, J.Y., Mehnert, C.P. and Wong, M.S. (1999) *Angew. Chem. Int. Ed.*, **38**, 56.
7. Schüth, F. and Schmidt, W. (2002) *Adv. Mater.*, **14**, 629.
8. Schüth, F. (2001) *Chem. Mater.*, **13**, 3184.
9. Wan, Y., Shi, Y.F. and Zhao, D.Y. (2007) *Chem. Commun.*, 897.
10. Stein, A., Melde, B.J. and Schroden, R.C. (2000) *Adv. Mater.*, **12**, 1403.
11. Wan, Y., Yang, H.F. and Zhao, D.Y. (2006) *Acc. Chem. Res.*, **39**, 423.
12. Wan, Y. and Zhao, D.Y. (2007) *Chem. Rev.*, **107**, 2821.
13. Huo, Q.S., Margolese, D.I., Ciesla, U., Feng, P.Y., Gier, T.E., Sieger, P., Leon, R., Petroff, P.M., Schüth, F. and Stucky, G.D. (1994) *Nature*, **368**, 317.
14. Huo, Q.S., Margolese, D.I. and Stucky, G.D. (1996) *Chem. Mater.*, **8**, 1147.
15. Zhao, D.Y., Huo, Q.S., Feng, J.L., Chmelka, B.F. and Stucky, G.D. (1998) *J. Am. Chem. Soc.*, **120**, 6024.
16. Beck, J.S. et al. (1992) *J. Am. Chem. Soc.*, **114**, 10834.
17. Liu, X.Y., Tian, B.Z., Yu, C.Z., Gao, F., Xie, S.H., Tu, B., Che, R.C., Peng, L.M. and Zhao, D.Y. (2002) *Angew. Chem. Int. Ed.*, **41**, 3876.
18. Kleitz, F., Choi, S.H. and Ryoo, R. (2003) *Chem. Commun.*, 2136.
19. Gao, C.B., Sakamoto, Y., Sakamoto, K., Terasaki, O. and Che, S.N. (2006) *Angew. Chem. Int. Ed.*, **45**, 4295.
20. Sakamoto, Y., Kaneda, M., Terasaki, O., Zhao, D.Y., Kim, J.M., Stucky, G., Shim, H.J. and Ryoo, R. (2000) *Nature*, **408**, 449.
21. Fan, J., Yu, C.Z., Gao, T., Lei, J., Tian, B.Z., Wang, L.M., Luo, Q., Tu, B., Zhou, W.Z. and Zhao, D.Y. (2003) *Angew. Chem. Int. Ed.*, **42**, 3146.
22. Kleitz, F., Liu, D.N., Anilkumar, G.M., Park, I.S., Solovyov, L.A., Shmakov, A.N. and Ryoo, R. (2003) *J. Phys. Chem. B*, **107**, 14296.
23. Shen, S.D., Li, Y.Q., Zhang, Z.D., Fan, J., Tu, B., Zhou, W.Z. and Zhao, D.Y. (2002) *Chem. Commun.*, 2212.
24. Garcia-Bennett, A.E., Miyasaka, K., Terasaki, O. and Che, S.N. (2004) *Chem. Mater.*, **16**, 3597.
25. Han, Y. and Ying, J.Y. (2005) *Angew. Chem. Int. Ed.*, **44**, 288.
26. Kaneda, M., Tsubakiyama, T., Carlsson, A., Sakamoto, Y., Ohsuna, T., Terasaki, O., Joo, S.H. and Ryoo, R. (2002) *J. Phys. Chem. B*, **106**, 1256.
27. Yu, T., Zhang, H., Yan, X.W., Chen, Z.X., Zou, X.D., Oleynikov, P. and Zhao, D.Y. (2006) *J. Phys. Chem. B*, **110**, 21467.
28. Feuston, B.P. and Higgins, J.B. (1994) *J. Phys. Chem.*, **98**, 4459.
29. Behrens, P. and Stucky, G.D. (1993) *Angew. Chem. Int. Ed. Engl.*, **32**, 696.
30. Garces, J.M. (1996) *Adv. Mater.*, **8**, 434.
31. Chen, C.Y., Li, H.X. and Davis, M.E. (1993) *Microporous Mesoporous Mater.*, **2**, 17.
32. Lukens, W.W., Schmidt-Winkel, P., Zhao, D.Y., Feng, J.L. and Stucky, G.D. (1999) *Langmuir*, **15**, 5403.
33. De Paul, S.M., Zwanziger, J.W., Ulrich, R., Wiesner, U. and Spiess, H.W. (1999) *J. Am. Chem. Soc.*, **121**, 5727.
34. Miyazawa, K. and Inagaki, S. (2000) *Chem. Commun.*, 2121.
35. Ryoo, R., Ko, C.H., Kruk, M., Antochshuk, V. and Jaroniec, M. (2000) *J. Phys. Chem. B*, **104**, 11465.
36. Ravikovitch, P.I. and Neimark, A.V. (2001) *J. Phys. Chem. B*, **105**, 6817.
37. Monnier, A. et al. (1993) *Science*, **261**, 1299.
38. Kim, J.M., Kim, S.K. and Ryoo, R. (1998) *Chem. Commun.*, 259.
39. Schumacher, K., Grun, M. and Unger, K.K. (1999) *Microporous Mesoporous Mater.*, **27**, 201.
40. Chen, F.X., Huang, L.M. and Li, Q.Z. (1997) *Chem. Mater.*, **9**, 2685.
41. Yu, C.Z., Fan, J., Tian, B.Z., Stucky, G.D. and Zhao, D.Y. (2003) *J. Phys. Chem. B*, **107**, 13368.
42. Templin, M., Franck, A., DuChesne, A., Leist, H., Zhang, Y.M.,

- Ulrich, R., Schadler, V. and Wiesner, U. (1997) *Science*, **278**, 1795.
43. Yu, K., Hurd, A.J., Eisenberg, A. and Brinker, C.J. (2001) *Langmuir*, **17**, 7961.
44. Groenewolt, M., Brezesinski, T., Schlaad, H., Antonietti, M., Groh, P.W. and Ivan, B. (2005) *Adv. Mater.*, **17**, 1158.
45. Smarsly, B., Xomeritakis, G., Yu, K., Liu, N.G., Fan, H.Y., Assink, R.A., Drewien, C.A., Ruland, W. and Brinker, C.J. (2003) *Langmuir*, **19**, 7295.
46. Deng, Y.H. et al. (2007) *J. Am. Chem. Soc.*, **129**, 1690.
47. Kim, S.S., Karkamkar, A., Pinnavaia, T.J., Kruk, M. and Jaroniec, M. (2001) *J. Phys. Chem. B*, **105**, 7663.
48. Galarneau, A., Cambon, N., Di Renzo, F., Ryoo, R., Choi, M. and Fajula, F. (2003) *New J. Chem.*, **27**, 73.
49. Hoffmann, F., Cornelius, M., Morell, J. and Froba, M. (2006) *Angew. Chem. Int. Ed.*, **45**, 3216.
50. Wan, Y., Zhang, D.Q., Hao, N. and Zhao, D.Y. (2007) *Int. J. Nanotechnol.*, **4**, 66.
51. Asefa, T., MacLachan, M.J., Coombs, N. and Ozin, G.A. (1999) *Nature*, **402**, 867.
52. Inagaki, S., Guan, S., Fukushima, Y., Ohsuna, T. and Terasaki, O. (1999) *J. Am. Chem. Soc.*, **121**, 9611.
53. Melde, B.J., Holland, B.T., Blanford, C.F. and Stein, A. (1999) *Chem. Mater.*, **11**, 3302.
54. Inagaki, S., Guan, S., Ohsuna, T. and Terasaki, O. (2002) *Nature*, **416**, 304.
55. Walcarius, A., Etienne, M., Sayen, S. and Lebeau, B. (2003) *Electroanalysis*, **15**, 414.
56. Rodriguez, I., Iborra, S., Rey, F. and Corma, A. (2000) *Appl. Catal., A Gen.*, **194**, 241.
57. Yang, Q.H., Kapoor, M.P. and Inagaki, S. (2002) *J. Am. Chem. Soc.*, **124**, 9694.
58. Corriu, R.J.P., Mehdi, A. and Reye, C. (2005) *J. Mater. Chem.*, **15**, 4285.
59. Yoshitake, H. (2005) *New J. Chem.*, **29**, 1107.
60. Wan, Y., Zhang, D.Q., Zhai, Y.P., Feng, C.M., Chen, J. and Li, H.X. (2007) *Chem. Asian J.*, **2**, 875.
61. Chen, Y.Y., Huang, Y.L., Xiu, J.H., Han, X.W. and Bao, X.H. (2004) *Appl. Catal. A Gen.*, **273**, 185.
62. Blasco, T., Corma, A., Navarro, M.T. and Pariente, J.P. (1995) *J. Catal.*, **156**, 65.
63. Tanev, P.T., Chibwe, M. and Pinnavaia, T.J. (1994) *Nature*, **368**, 321.
64. Niessen, T.E.W., Niederer, J.P.M., Gjervan, T. and Holderich, W.F. (1998) *Microporous Mesoporous Mater.*, **21**, 67.
65. Yu, J.Q., Feng, Z.C., Xu, L., Li, M.J., Xin, Q., Liu, Z.M. and Li, C. (2001) *Chem. Mater.*, **13**, 994.
66. Markowitz, M.A., Jayasundera, S., Miller, J.B., Klaehn, J., Burleigh, M.C., Spector, M.S., Golledge, S.L., Castner, D.G. and Gaber, B.P. (2003) *Dalton Trans.*, 3398.
67. Bhaumik, A. and Tatsumi, T. (2000) *J. Catal.*, **189**, 31.
68. Ryoo, R., Joo, S.H. and Jun, S. (1999) *J. Phys. Chem. B*, **103**, 7743.
69. Lee, J., Yoon, S., Hyeon, T., Oh, S.M. and Kim, K.B. (1999) *Chem. Commun.*, 2177.
70. Kyotani, T., Nagai, T., Inoue, S. and Tomita, A. (1997) *Chem. Mater.*, **9**, 609.
71. Hou, P.X., Yamazaki, T., Orikasa, H. and Kyotani, T. (2005) *Carbon*, **43**, 2624.
72. Liang, C.D., Hong, K.L., Guiochon, G.A., Mays, J.W. and Dai, S. (2004) *Angew. Chem. Int. Ed.*, **43**, 5785.
73. Tanaka, S., Nishiyama, N., Egashira, Y. and Ueyama, K. (2005) *Chem. Commun.*, 2125.
74. Meng, Y., Gu, D., Zhang, F.Q., Shi, Y.F., Yang, H.F., Li, Z., Yu, C.Z., Tu, B. and Zhao, D.Y. (2005) *Angew. Chem. Int. Ed.*, **44**, 7053.
75. Meng, Y., Gu, D., Zhang, F.Q., Shi, Y.F., Cheng, L., Feng, D., Wu, Z.X., Chen, Z.X., Wan, Y., Stein, A. and Zhao, D.Y. (2006) *Chem. Mater.*, **18**, 4447.
76. Zhang, F.Q., Meng, Y., Gu, D., Yan, Y., Yu, C.Z., Tu, B. and Zhao, D.Y. (2005) *J. Am. Chem. Soc.*, **127**, 13508.

77. Yang, P.D., Zhao, D.Y., Margolese, D.I., Chmelka, B.F. and Stucky, G.D. (1998) *Nature*, **396**, 152.
78. Tian, B.Z., Yang, H.F., Liu, X.Y., Xie, S.H., Yu, C.Z., Fan, J., Tu, B. and Zhao, D.Y. (2002) *Chem. Commun.*, 1824.
79. Tian, B.Z., Liu, X.Y., Tu, B., Yu, C.Z., Fan, J., Wang, L.M., Xie, S.H., Stucky, G.D. and Zhao, D.Y. (2003) *Nature Mater.*, **2**, 159.
80. Tian, B.Z., Liu, X.Y., Yang, H.F., Xie, S.H., Yu, C.Z., Tu, B. and Zhao, D.Y. (2003) *Adv. Mater.*, **15**, 1370.
81. Tian, B.Z. *et al.* (2004) *J. Am. Chem. Soc.*, **126**, 865.
82. Liu, Z.C., Shen, W.H., Bu, W.B., Chen, H.R., Hua, Z.L., Zhang, L.X., Li, L., Shi, J.L. and Tan, S.H. (2005) *Microporous Mesoporous Mater.*, **82**, 137.
83. Krawiec, P., Weidenthaler, C. and Kaskel, S. (2004) *Chem. Mater.*, **16**, 2869.
84. Shi, Y.F., Meng, Y., Chen, D.H., Cheng, S.J., Chen, P., Yang, T.F., Wan, Y. and Zhao, D.Y. (2006) *Adv. Funct. Mater.*, **16**, 561.
85. Yant, J., Wang, A.J. and Kim, D.P. (2006) *J. Phys. Chem. B*, **110**, 5429.
86. Krawiec, P., Geiger, D. and Kaskel, S. (2006) *Chem. Commun.*, 2469.
87. Dibandjo, P., Bois, L., Chassagneux, F., Cornu, D., Letoffe, J.M., Toury, B., Babonneau, F. and Miele, P. (2005) *Adv. Mater.*, **17**, 571.
88. Shi, Y.F., Wan, Y., Zhai, Y.P., Liu, R.L., Meng, Y., Tu, B. and Zhao, D.Y. (2007) *Chem. Mater.*, **19**, 1761.
89. Braun, P.V., Osenar, P. and Stupp, S.I. (1996) *Nature*, **380**, 325.
90. Rabatic, B.M., Pralle, M.U., Tew, G.N. and Stupp, S.I. (2003) *Chem. Mater.*, **15**, 1249.
91. Gao, F., Lu, Q.Y. and Zhao, D.Y. (2003) *Adv. Mater.*, **15**, 739.
92. Liu, X.Y., Tian, B.Z., Yu, C.Z., Tu, B. and Zhao, D.Y. (2004) *Chem. Lett.*, **33**, 522.
93. Shi, Y.F., Wan, Y., Liu, R.L., Tu, B. and Zhao, D.Y. (2007) *J. Am. Chem. Soc.*, **129**, 9522.

14

Hydrotreating Catalysts

Sonja Eijssbouts

14.1

Introduction

Hydrotreating, or hydroprocessing, technology associated with crude oil is over 70 years old as an industrial process. This refinery processing function is designed to remove the S, N, O, and metal contaminants from the crude oil, saturate the aromatic hydrocarbons and olefins and ultimately reduce the molecular weight. During crude oil hydroprocessing, an oil is contacted with a catalyst in the presence of hydrogen at temperatures ranging from 200 to 450 °C and pressures between 5 and 300 bar. Numerous reactions take place simultaneously, namely:

- Hydrogenation of unsaturated hydrocarbons (HDOlef and HDA),
- (Mild) hydrocracking of large molecules ((M)HC),
- Hydrodesulfurization of sulfur-containing molecules (HDS),
- Hydrodenitrogenation of nitrogen-containing molecules (HDN)
- Hydrodeoxygenation of oxygen-containing molecules (HDO)
- Hydrodemetallation of Ni and V metalloporphyrins (HDMe).

Today, every refinery product has invariably been hydrotreated to some degree at some stage of its processing life. The most important constituents of the hydrotreating technology and approach have hardly changed during the past 70 years. Alumina (Al_2O_3) supported Co-, Ni-, Mo-, and W-based catalysts are still the industry favorites as a result of their favorable chemical, physical, and mechanical properties, activity response, availability, and costs. With oil consumption having risen from 70 to over 80 million barrels per day from 1995 to 2005, and expected to grow to over 90 million barrels per day in 2020, the demand for hydrotreating catalysts will continue to grow.

14.2

Typical Hydrotreating Catalyst

14.2.1

Typical Catalyst Composition

Typical commercial hydroprocessing catalysts consist of Ni/Co-promoted Mo/W sulfides supported on an inorganic matrix of γ -alumina (γ -Al₂O₃) or mixed silica-alumina (SiO₂-Al₂O₃). Acidic inorganic additives such as phosphorus, P, and zeolites are also widely applied. Co-Mo- and Ni-Mo-P-based catalysts are typically used for HDS and HDN applications, respectively, whilst zeolite and amorphous SiO₂-Al₂O₃ containing catalysts are applied for (M)HC.

Any active hydrotreating catalyst must have a pore-size distribution suitable for the feed to be treated. The distillate HDS and HDN catalysts typically have a surface area between 150 and 250 m²/g and a narrow pore-size distribution, where 75% of the total pore volume is in pores having diameters from 7 to 13 nm [1]. The pore volume is typically lower than 0.7 cm³/g in order to have a sufficient activity per reactor volume. Heavier, high boiling feeds, for example, residue, require a larger average pore diameter to increase access to the inner part of the catalyst particles for the large oil molecules, plus a larger pore volume to increase the capacity for metals deposition. Demetallization catalysts typically have a lower surface area than distillate HDS and HDN catalysts (normally still above 120 m²/g), a pore volume larger than 0.7 cm³/g and an average pore diameter larger than 12.5 nm [2]. Some materials have pore volumes up to 1.1 cm³/g and contain pores with diameters larger than 100 nm [3]. Examples of pore-size distribution of catalysts used in the different hydroprocessing applications are shown in Figure 14.1.

Furthermore, the catalyst must have outstanding mechanical properties such as side crushing strength, bulk crushing strength, or abrasion [4, 5]. Such properties are necessary to prevent large catalyst beds in commercial reactors from collapsing under their own weight or catalyst fines leading to an increased pressure drop over the catalyst bed or creating maldistribution. Furthermore, such mechanical properties ensure that the used catalyst can be successfully regenerated and reused.

14.2.2

Literature Describing the Preparation of Hydrotreating Catalysts

The open and patent literature dealing with the preparation of hydrotreating catalysts is very extensive. The open literature typically describes the effect of the various preparation variables on the sample performance and other characteristics, mostly using catalysts with low metal loadings. They are prepared in a way ensuring that the materials are homogeneous and highly

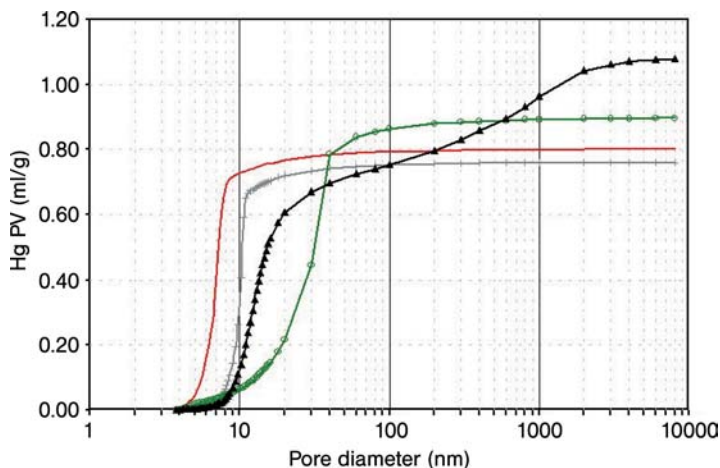


Figure 14.1 Examples of Hg pore-size distributions of catalysts used for diesel (red), vacuum gas oil (VGO) (gray), and residue (black and green) hydrotreatment.

dispersed (free of bulky active phase species) and therefore are suitable for analysis using advanced analytical techniques. The patent literature typically describes commercially viable materials with much higher metal loading, aiming for maximum performance rather than high dispersion and homogeneity. This is the primary reason for the large gap between the materials described in the scientific studies and those described in the patent literature and then produced commercially. Consequently, not all aspects relevant for the commercial catalyst preparation are addressed in the scientific literature. In the present chapter we do not attempt to give a complete overview of the available literature. The references included in the text are only examples chosen to illustrate the different preparation issues.

14.3

Support Preparation

14.3.1

Precipitation of γ -Alumina

γ - Al_2O_3 is often used as the support for hydrotreating catalysts. The boehmite (α - AlOOH) precursor to γ - Al_2O_3 can be prepared by the precipitation of:

- Al^{3+} compounds such as $\text{Al}(\text{NO}_3)_3$, AlCl_3 or $\text{Al}_2(\text{SO}_4)_3$ with a basic compound such as NaHCO_3 , Na_2CO_3 , NH_4OH or $(\text{NH}_4)_2\text{CO}_3$ [6].
- $\text{Al}_2\text{O}_4^{2-}$ compounds such as NaAlO_2 (i.e. $\text{Na}_2\text{O} \cdot \text{Al}_2\text{O}_3$ or $\text{Na}_2\text{Al}_2\text{O}_4$) with a strong acid such as HNO_3 or H_2SO_4 [6].

- $\text{Al}_2\text{O}_4^{2-}$ compounds such NaAlO_2 with Al^{3+} compounds such as $\text{Al}(\text{NO}_3)_3$, AlCl_3 or $\text{Al}_2(\text{SO}_4)_3$, HNO_3 , and/or H_2SO_4 followed by reacting the product with NaHCO_3 , Na_2CO_3 , NH_4OH , or $(\text{NH}_4)_2\text{CO}_3$ [7].

The precipitation conditions have to be chosen to ensure a sufficient yield as well as a suitable precipitate morphology. The typical conditions include temperatures between 20 and 100 °C, pH between 5.5 and 10.5 and precipitation times being from minutes up to several hours [6, 7].

Besides the “conventional” materials mentioned above, a wide range of materials can be prepared. For example, fibrillar boehmite can be prepared by treating aluminum chlorohydrate $[\text{Al}_n\text{Cl}_{(3n-m)}(\text{OH})_m]$ solutions in an autoclave at temperatures between 145 and 180 °C [8–10]. Mesoporous alumina, having an average pore diameter from 1.5 to 4 nm, with an average surface area above 500 m^2/g , can be prepared by treating an Al source such as Al sec-butoxide $\text{Al}[\text{OCH}(\text{CH}_3)\text{C}_2\text{H}_5]_3$ or Al isopropoxide $\text{Al}[\text{OCH}(\text{CH}_3)_2]_3$ in an alcohol–aqueous solvent with an organic template such as propionic ($\text{CH}_3\text{CH}_2\text{COOH}$) or stearic acid $[\text{CH}_3(\text{CH}_2)_{16}\text{COOH}]$ [11]. The precipitate morphology predetermines the surface area of the final support. To obtain supports with physical properties suitable for hydrotreating catalysts [1–3], preparing alumina precipitates with very small particles, that is, a very high surface area but a very small pore diameter, is hardly meaningful. (Pore diameter can be increased to the normal level on support calcination, but this is at the expense of surface area.) Different alumina precursors follow the same trend and fit inside the same relatively narrow band when attempting to adjust their pore diameter by calcination (Figure 14.2). Al_2O_3 precipitates

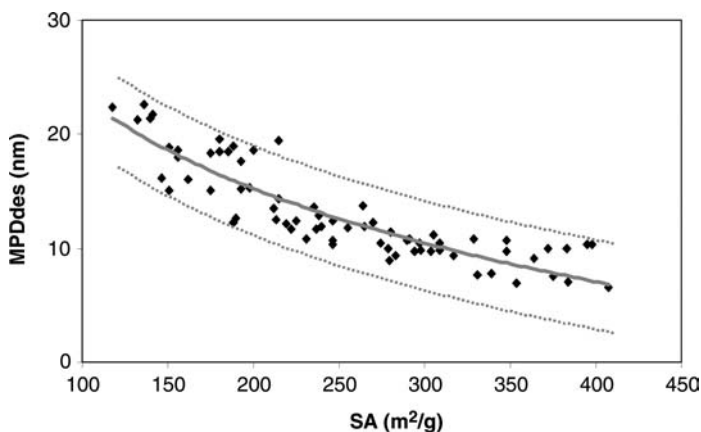


Figure 14.2 N_2 desorption data showing changes of textural properties of different alumina supports during the calcination treatment. Surface area decreases and pore diameter increases with increasing

calcination temperature. The solid line is the trend line for the present data set. The dashed lines mark the boundaries of the data range.

with very large particles, that is, a low surface area but a high pore diameter, are only suitable as supports for residue hydrotreating catalysts. Unless the precipitate is redissolved and reprecipitated [12], the surface area cannot be increased during the further preparation steps.

14.3.2

Addition of SiO₂

Silica, SiO₂, can be added during different stages involved in the preparation of the SiO₂–Al₂O₃ support. The addition of SiO₂ increases the surface area of the alumina support and introduces acid sites required for some hydrotreating reactions [13, 14]. Furthermore, SiO₂ reduces the interaction between the active phase and the support and thereby stimulates the formation of the more active Co-Mo-S-II/Ni-Mo-S-II phase [15–17]. However, the lower active phase – support interaction also makes the impregnation of the metals and the consecutive thermal treatments more critical [17–20].

The most typical SiO₂ reagent used in these preparations is water glass (aqueous solution of various Na_xSiO_y compounds). Alternatively, compounds such as tetraethoxysilane (TEOS, Si[OC₂H₅]₄) can be used [21, 22]. SiO₂ can be added prior to, during or after the precipitation of Al₂O₃. The order of precipitation and the SiO₂ to Al₂O₃ ratio determine the morphology as well as surface acidity, that is, number of Lewis and Brønsted acid sites, associated with the final SiO₂–Al₂O₃ support [13, 14]. For example:

- Al₂O₃-coated SiO₂ can be prepared by impregnating the SiO₂ hydrogel with an aluminum salt and then the Al₂O₃ gel is precipitated in the pores of the SiO₂ hydrogel by contact with NH₄OH [23].
- Homogeneous SiO₂–Al₂O₃ cogels can be prepared by precipitating water glass with a solution of AlCl₃ acidified with acetic acid salt at pH = 3.0, followed by the precipitation with NH₄OH at pH = 5–9 [24].
- SiO₂-coated Al₂O₃ support can be obtained by depositing hydrolyzed TEOS on Al(OH)₃ at 40 °C, using NH₄NO₃ as a catalyst for the hydrolysis of TEOS [21].

SiO₂–Al₂O₃ cogels are typically quite homogeneous and have higher acidity as compared to Al₂O₃-coated SiO₂ and SiO₂-coated Al₂O₃ supports, which often have an inhomogeneous distribution of silica throughout the alumina matrix, resulting in morphology and acidity (isoelectric point) differences between the different areas of the support [19, 25, 26].

14.3.3

Addition of Other Components (e.g. Zeolites) and Extrusion

To further process the washed and/or (spray-) dried alumina or silica-alumina precipitates, a “dough” is prepared by mixing the precipitate with water.

The dough typically also contains an acid to ensure Al_2O_3 peptization (i.e. deagglomeration by charging of the Al_2O_3 particles), resulting in a higher mechanical strength.

A dough suitable for monomodal Al_2O_3 supports is, for example, prepared by mixing boehmite gel and Al_2O_3 powder with 5% CH_3COOH . Addition of microcrystalline cellulose to the mixture generates macropores in addition to the mesopores [27]. A double-step based peptization of boehmite is also possible and includes, for example, a treatment with HNO_3 at 75–85% moisture level, followed by a treatment with CH_3COOH at 70–72% moisture level [28]. Solid additives such as zeolites or amorphous $\text{SiO}_2\text{--Al}_2\text{O}_3$ can be added to the alumina dough at this stage. A convenient method of preparing a multicomponent dough is to comull an alumina hydrogel with amorphous $\text{SiO}_2\text{--Al}_2\text{O}_3$, zeolite and a peptizable Al_2O_3 binder, followed by the addition of water and acid [29]. It is also possible to combine several alumina or $\text{SiO}_2\text{--Al}_2\text{O}_3$ precursors with different morphologies in a single support or to add other components. Depending on how many different components have been combined, what was their particle-size distribution and how well were they mixed, a wide range of support morphologies can be obtained (Figure 14.3).

The water content of the dough needs to be adjusted to ensure that the dough is suitable for further processing. The dough may also be kneaded to better mix the different components. The water content of the dough determines the pore volume of the final (Al_2O_3) support. A high water content in combination with a low amount of acid leads to a high pore volume but also to a lower mechanical strength of the final support. A high amount

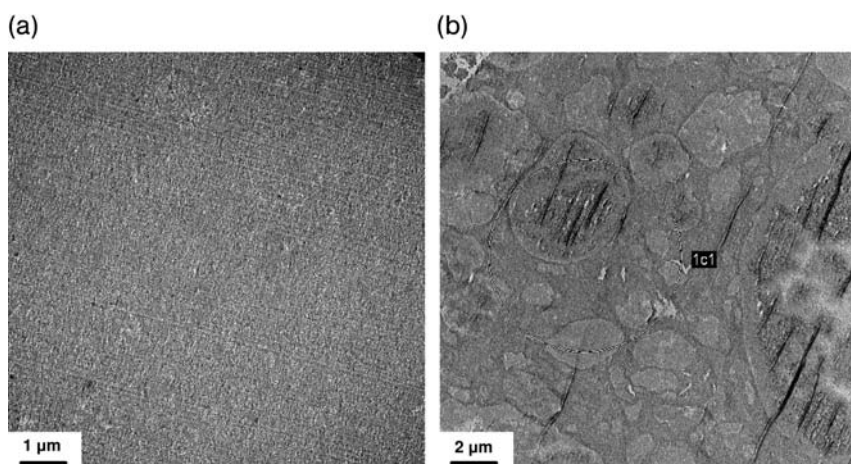


Figure 14.3 TEM micrographs of $\gamma\text{-Al}_2\text{O}_3$ supports: (a) homogeneous support prepared from a single alumina precursor and (b) heterogeneous support prepared by combining two alumina precursors of different densities embedded in a peptizable alumina matrix

of acid means a higher mechanical strength but this is at the expense of surface area and pore volume [30]. The most usual way of further processing is the extrusion process. Typical extrudate shapes are cylinders, trilobes or quadrilobes, having diameters from 1 to 3 mm. Larger-diameter extrudates are used in applications, which are pressure-drop limited, as well as for top and bottom layers in a reactor.

14.3.4

Drying and Calcination of Al_2O_3 and $\text{SiO}_2\text{-Al}_2\text{O}_3$ Supports

The extrudates once prepared then require to be dried and calcined. The drying is usually carried out using a belt dryer or a rotary dryer at a temperature between 100 and 200 °C. The calcination is typically carried out in a rotary kiln at a temperature in excess of 600 °C. The calcination is required to transform boehmite to $\gamma\text{-Al}_2\text{O}_3$ in order to make the extrudates mechanically strong and suitable for the subsequent impregnation steps. Dried only extrudates would disintegrate on impregnation. The pore diameter and surface area of the Al_2O_3 obtained are a function of the calcination conditions. High calcination temperature and/or high water partial pressure reduce the surface area and increase the pore diameter (Figure 14.2). Pore volume does not change on calcination. The presence of SiO_2 typically increases the thermal stability of the Al_2O_3 [31] so that combined $\text{SiO}_2\text{-Al}_2\text{O}_3$ supports require more severe calcination conditions (i.e. higher temperature, steam) than pure Al_2O_3 in order to modify their surface area and pore diameter. Thermal spreading of SiO_2 on Al_2O_3 [32] and the migration of silica into the alumina pores [13] are only expected at temperatures above 750 °C in a high steam content atmosphere.

14.4

Metal Comixing/Coextrusion and Coprecipitation Routes

14.4.1

Addition of Metals to the Al_2O_3 Dough

The active components can be added to the support prior to the shaping, for example, by coprecipitation or by adding a metal containing solution to the dough [33–36]. For example, a washed alumina precipitate can be mixed with dry water-soluble salts of Co and/or Ni and Mo and/or W or with a solution containing salts of Co and/or Ni and Mo and/or W at 25–100 °C and pH 4–8 [33]. It is also possible to mix boehmite with a slurry of MoO_3 in H_2O , followed by calcination [37–39]. Again, the water and acid contents of the dough need to be adjusted in a way ensuring that the dough is suitable for further processing.

These types of preparations typically ensure a very good distribution of the active metals in the Al_2O_3 support [35]. However, there is a high chance that stable (inactive) crystalline compounds such as $\text{Al}_2(\text{MoO}_4)_3$ or CoAl_2O_4 (NiAl_2O_4) would be formed during further processing. The metals are also very likely to have a strong interaction with the Al_2O_3 support and are consequently more difficult to sulfide than in catalysts prepared by the impregnation of metals on the $\gamma\text{-Al}_2\text{O}_3$ support [34].

14.4.2

Bulk Catalysts

The bulk catalysts are typically coprecipitated. The precipitate is filtered off, washed and optionally (spray) dried. For example, an aqueous slurry of $(\text{NH}_4)_2\text{Mo}_2\text{O}_7$ and NiCO_3 can be reacted at 80°C under pressure in a stirred autoclave. After cooling and depressurizing, SiO_2 powder, dispersed in ammonia solution, is added to the mixture that is then again reacted at 80°C under pressure. The solids are then recovered by spray drying at a temperature not exceeding 300°C [40]. The precipitate is then mixed with water and, optionally, a binder material such as Al_2O_3 or an acid in order to prepare a dough suitable for shaping/extrusion.

Bulk catalysts have the highest concentration of active metals. However, the active metals may have low dispersion and a high probability exists that inactive crystalline compounds, for example, CoMoO_4 (NiMoO_4), will be formed during their thermal treatment [41–43].

14.4.3

Drying and Calcination of Catalysts Prepared by Comixing/Coextrusion and Coprecipitation Routes

Since the metal-containing materials have specific thermal properties and sintering kinetics different from those of pure Al_2O_3 or $\text{SiO}_2\text{-Al}_2\text{O}_3$, the drying and calcination conditions must be tailored to match the composition of each material. The temperature chosen must be sufficiently high to obtain material with the required textural properties (surface area, pore diameter) and adequate mechanical strength. At the same time, the formation of stable, inactive crystalline compounds, for example, $\text{Al}_2(\text{MoO}_4)_3$, CoAl_2O_4 (NiAl_2O_4), or CoMoO_4 (NiMoO_4), should be prevented or at least minimized. Consequently, the range of drying and calcination conditions that can be applied is much more limited, making the pore-diameter and surface-area control of the metal containing materials more difficult than in the case of pure Al_2O_3 or $\text{SiO}_2\text{-Al}_2\text{O}_3$ supports. Metal-containing Al_2O_3 hydrogels are typically calcined at lower temperatures than pure Al_2O_3 , for example, at temperatures around

500 °C [36]. Bulk metal oxide catalysts are often not calcined but only dried at temperatures as low as 300 °C [40].

14.5

Impregnation of Metals

14.5.1

Typical Additives and Solution Stabilizers

The vast majority of catalysts are prepared by impregnation of the active metals on the compacted support. The metal-containing solutions and cosolutions are typically highly concentrated and stabilized by a diverse range of inorganic, as well as organic, additives. The impregnation solution must be completely clear and stable on storage/transportation. The solution viscosity should also not be too high to prevent difficulties in the impregnation process. Phosphoric acid, ammonia, and H_2O_2 are among the most frequently used inorganic additives, for example:

- Ni-Mo-P cosolution can be prepared by using $(\text{NH}_4)_6\text{Mo}_7\text{O}_{24}\cdot 4\text{H}_2\text{O}$, $\text{Ni}(\text{NO}_3)_2\cdot 6\text{H}_2\text{O}$, and H_3PO_4 as starting materials [44].
- $(\text{NH}_4)_6\text{Mo}_7\text{O}_{24}\cdot 4\text{H}_2\text{O}$ and aqueous H_2O_2 can be dissolved in water, producing highly stable peroxymolybdates. Subsequently, an appropriate amount of aqueous $\text{Co}(\text{NO}_3)_2\cdot 6\text{H}_2\text{O}$ is added [45].
- A stable solution is obtained by combining NH_4OH , $(\text{NH}_4)_2\text{Mo}_2\text{O}_7$, and $\text{Co}(\text{NO}_3)_2\cdot 6\text{H}_2\text{O}$ [46].

Nitrilo triacetic acid (NTA), ethylene diamine tetraacetic acid (EDTA), ethylene diamine ($\text{C}_2\text{H}_8\text{N}_2$), and citric acid (2-hydroxypropane-1,2,3-tricarboxylic acid) are the most frequently used organic additives. A clear aqueous impregnation solution can be prepared by:

- Preparing a slurry of MoO_3 and EDTA in H_2O , followed by adding $(\text{NH}_4)_2\text{CO}_3$ and N_2H_4 and heating the mixture [47]
- Preparing an aqueous slurry of MoO_3 and diethylenetriamine and heating the slurry [47]
- Dissolving NTA in NH_4OH , adding MoO_3 and heating the mixture [47]
- Combining, MoO_3 , CoCO_3 , H_3PO_4 , and citric acid and heating the mixture [48]
- Dissolving the Mo and/or Co/Ni salts in NH_4OH and adding citric acid to stabilize the solution [49].

Most of the solutions used are aqueous – there are only a few examples of preparations using organic solvents. For instance, magnesia-supported Ni–Mo catalysts can be prepared by nonaqueous impregnation using dimethyl sulfoxide and methanol as solvents [50]. Dimethyl formamide was used as a solvent for the impregnation of phosphomolybdates on $\gamma\text{-Al}_2\text{O}_3$ [51].

Depending on the metal concentrations and the solution stabilizers applied, the impregnation solutions can contain a wide range of species such as

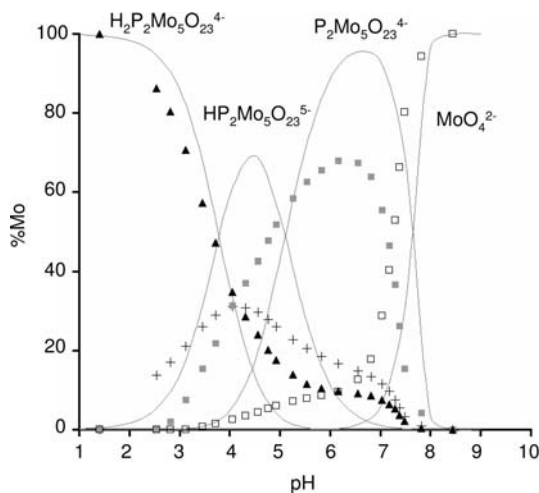


Figure 14.4 Calculated composition of 1.0 M Mo/1.0 M PO_4^{3-} cosolution as the function of pH content. (Reprinted with permission from [52]: J. A. Bergwerff, PhD Thesis, Utrecht University, The Netherlands, 2007.) While $\text{H}_x\text{P}_2\text{Mo}_5$ are the dominant species at low pH, MoO_4^{2-} prevails at high

pH. Solid lines are derived from calculations using complex formation constants. The separate data points represent the concentrations of the different complexes obtained from fitting the Raman spectra of synthesized solutions (pH adjustment by NaOH or HCl addition).

molybdates, iso-polymolybdates, Mo–P heteropolycompounds, as well as complexes of metals with organic ligands. The compositions of the cosolutions can be calculated using the equilibrium constants available in the literature. Figure 14.4 shows an example of the calculated composition of the Mo–P cosolution with variable pH. The chemistry of the impregnation solutions is very complex and can be studied by techniques such as Raman (Figure 14.5) [52–54] or Fourier transform infrared (FTIR) [55, 56].

Phosphoric acid and phosphates react with the alumina support and remain on the catalyst after its drying, calcination, and sulfidation. Most organic complex forming agents are removed on drying and calcination. Phosphorus and organic complexes still present during the catalyst sulfidation reduce the interaction between the active phase and the support, thus stimulating the formation of the more active Co–Mo–S-II/Ni–Mo–S-II phase [57–59].

14.5.2

Pore-Volume Impregnation versus Dipping/Equilibrium Impregnation of Compacted Support Particles

Methods such as dipping/equilibrium impregnation are only used to a limited extent. When dipping, the Al_2O_3 support is placed in a stainless steel basket and dipped into an aqueous impregnating solution, for example, prepared by

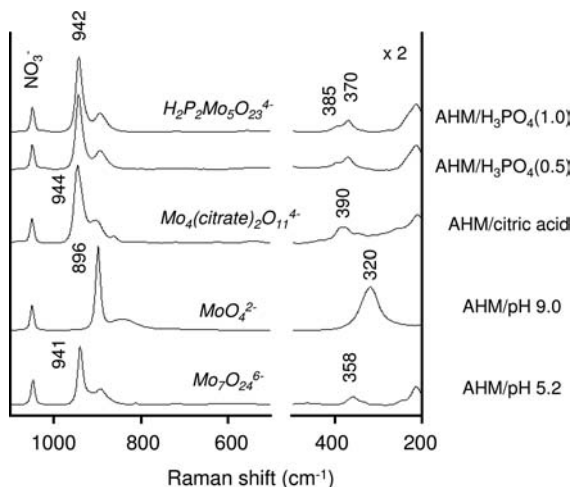


Figure 14.5 Raman spectra show that different Mo complexes are present in 1.0 M molybdate solutions with different pH and containing different solution stabilizers. (Reprinted with permission from [52]: J.A. Bergwerff, PhD Thesis, Utrecht University, The Netherlands, 2007). $\text{H}_2\text{P}_2\text{Mo}_5\text{O}_{23}^{4-}$ and $\text{Mo}_4(\text{citrate})_2\text{O}_{11}^{4-}$ are present in

phosphate- and citrate-stabilized solutions, respectively. $(\text{NH}_4)_6\text{Mo}_7\text{O}_{24}$ (AHM) solutions contain MoO_4^{2-} at high pH and $\text{Mo}_7\text{O}_{24}^{6-}$ at low pH. (The 1.0 M PO_4^{3-} solution pH was adjusted to 2. The 0.5 M PO_4^{3-} solution natural pH was 2. The 1.0 M citrate solution natural pH was 0.5. NH_4OH was used for pH adjustment.)

dissolving MoO_3 and NiO in a dilute H_3PO_4 and adding solid EDTA. The impregnating solution is recirculated over the basket for about 1 hour. The wet impregnated support is then removed from the basket and centrifuged [12]. Catalysts can also be prepared by equilibrium impregnation using an excess of aqueous $(\text{NH}_4)_6\text{Mo}_7\text{O}_{24} \cdot 4\text{H}_2\text{O}$ solutions (with or without NH_4OH as a competitor). Large solution volumes favor larger amounts of Mo in the Al_2O_3 pores and a higher proportion of octahedrally coordinated Mo being deposited. Stirring the solution during the impregnation step helps to achieve a uniform Mo profile [60–62], except perhaps for the outer surface of the particles, where Mo concentrations may still remain higher [62, 63].

The majority of impregnations are pore volume (i.e. incipient wetness) impregnations, that is, the solution volume added is equal to the pore volume of the support. At least several minutes are required to achieve a thorough wetting of the support particles. Longer times (up to several hours) are required for larger particles and larger catalyst batches.

During the impregnation, a small-scale “chromatographic” process takes place, which may lead to an inhomogeneous distribution of the solution components across the impregnated particles. While certain solution species may react with the support and decompose or precipitate others are stable throughout the entire impregnation process [55, 56]. FTIR, Raman and ^{31}P solid-state nuclear magnetic resonance (NMR) measurements showed that

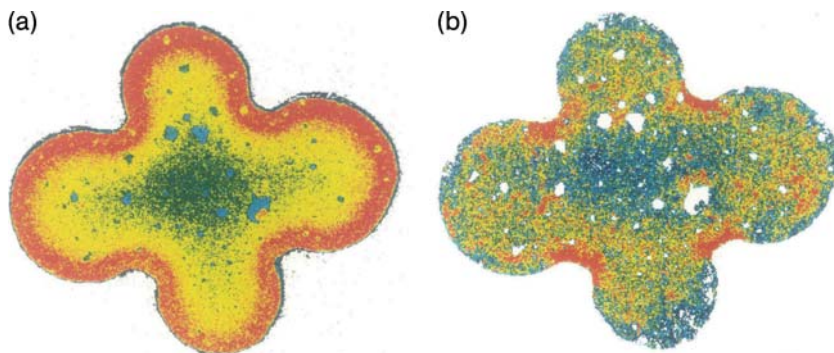


Figure 14.6 Scanning electron microscopy-electron micro probe analysis (SEM-EPMA) of P and Mo distributions in a quadrulobe shaped extrudate: (a) P map with egg-shell P profile and (b) Mo map with inhomogeneously distributed Mo (high concentration = red, medium concentration = yellow, low concentration = blue).

$(\text{NH}_4)_6\text{Mo}_7\text{O}_{24}\cdot 4\text{H}_2\text{O}$ and phosphomolybdates react with the basic surface OH groups of $\gamma\text{-Al}_2\text{O}_3$ and $\alpha\text{-AlOOH}$, leading to depolymerization of the adsorbing species. Phosphate reacts readily with bridging hydroxyls to form an AlPO_4 -like phase [55, 56, 64]. That is why phosphorus addition reduces the surface area of the final catalyst and why often the P-containing catalysts have “egg-shell P profiles” (Figure 14.6) [51, 64]. The surface AlPO_4 -like phase also functions as an acidic promoter for the HDN reaction [58, 59].

The impregnation process is particularly complex and the active metals can become inhomogeneously distributed if multicomponent supports, for example, those containing amorphous $\text{SiO}_2\text{-Al}_2\text{O}_3$ and/or zeolite, are being impregnated. Due to the different isoelectric points of the different support components, resulting in a much higher affinity of molybdates and phosphomolybdates for the Al_2O_3 than for the SiO_2 -containing support components, higher concentration of metals and different promoter to Mo ratios will be present in the Al_2O_3 as compared to the $\text{SiO}_2\text{-Al}_2\text{O}_3$ or zeolite (Figure 14.7) [19, 65]. Also, the morphology and density differences between different alumina components combined in a single support will result in an inhomogeneous distribution of the active components (Figure 14.8).

The impregnated material is typically aged for some time to allow this impregnation/chromatographic process to take place. The goal of most impregnations is the homogeneous distribution of active components throughout the catalyst particles. However, there are also catalyst applications where an inhomogeneous distribution of active components may be advantageous. Impregnation with larger solution species such as ammonium meta tungstate $[(\text{NH}_4)_6\text{H}_2\text{W}_{12}\text{O}_{40}]$ can lead to egg-shell profiles, while the impregnation with a small species such as sodium or ammonium tungstate leads to a flat profile [66]. Supported Mo-based catalysts with egg-shell

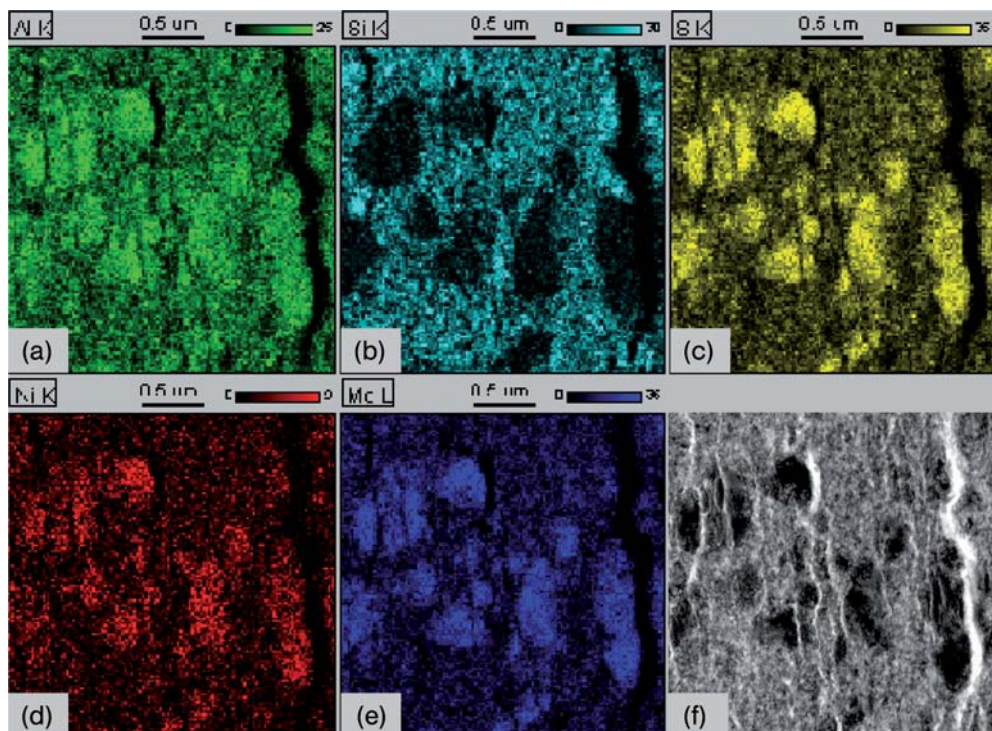


Figure 14.7 Scanning transmission electron microscopy combined with energy-dispersive X-ray analysis (STEM-EDX) of Ni-Mo/ Al_2O_3 - SiO_2 . (a) Al-K map, (b) Si-K map, (c) S-K map, (d) Ni-K map, (e) Mo-L map, and (f) STEM image.

Active metals are inhomogeneously distributed on a mixed Al_2O_3 - SiO_2 support. Ni and Mo sulfides have much higher concentrations in the dense Al-rich areas (i.e. in γ - Al_2O_3) than in the Si-rich areas (i.e. in SiO_2 - Al_2O_3) of the mixed support.

or uniform Mo radial profiles can be prepared by impregnating γ - Al_2O_3 extrudates with acidic or alkaline $(\text{NH}_4)_6\text{Mo}_7\text{O}_{24} \cdot 4\text{H}_2\text{O}$ solutions, respectively [67]. Furthermore, an egg-white profile can be obtained from an egg-shell profile, and an egg-yolk profile from a uniform profile, by impregnations of the Mo-containing extrudates with aqueous NH_4OH [67] or aqueous NH_4F and HCl [68]. Egg-yolk active metal profiles are expected to provide higher stability in the processing of heavier oil fractions [68]. The prediction of Mo or W concentration profiles is possible using a theoretical model of diffusive impregnation. However, it should be noted that the concentration profiles can become modified due to the redistribution of the impregnated components during the drying step [63, 69]. The impregnation process as well as the consecutive drying steps can be monitored by using *in-situ* techniques such as micro-Raman (Figure 14.9) [25, 52, 53, 70–72], ultraviolet-visible spectroscopy (UV-VIS) [52, 53, 71] ^{95}Mo -NMR [25], or nuclear resonance imaging (NRI)

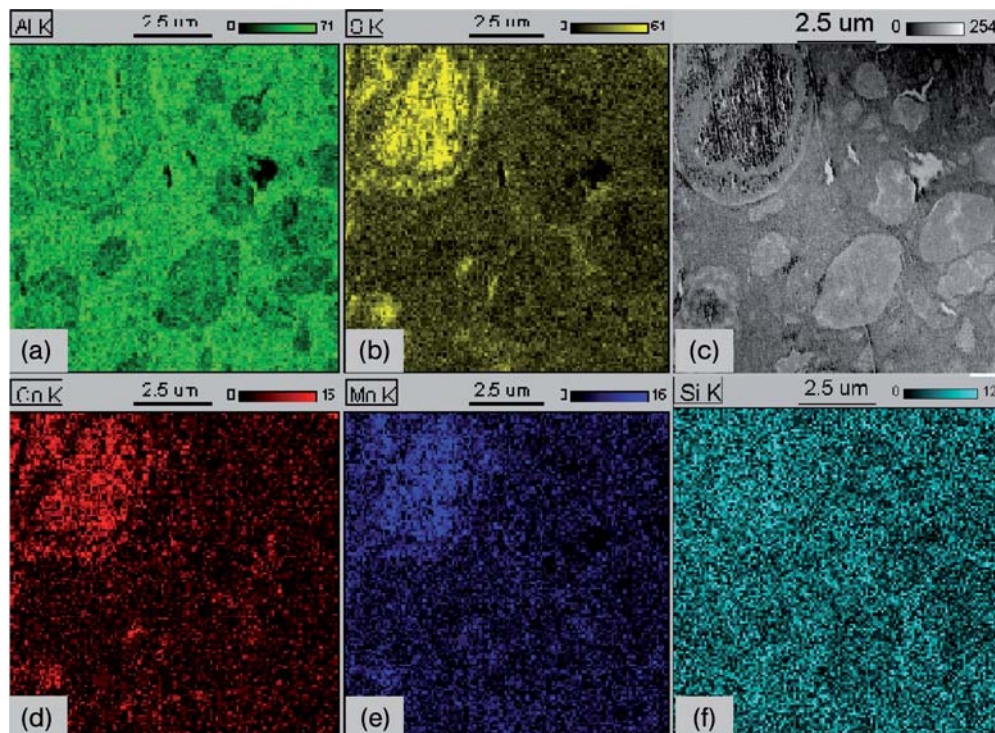


Figure 14.8 STEM – EDX analysis of Co-Mo/ Al_2O_3 catalyst: (a) Al K-map, (b) S-K map, (c) STEM image, (d) Co-K map, (e) Mo-K map, and (f) Si-K map. Active metals are inhomogeneously distributed in a Co-Mo/ Al_2O_3 catalyst containing three

different types of alumina with different morphologies/densities. Higher concentrations of Co and Mo sulfides are found in alumina areas with higher density, that is, higher specific surface area per unit volume.

[52, 53]. For details on the technique of microspectroscopy to study catalyst preparation with extrudates, we refer to Chapter 10.

14.5.3

Sequential versus Coimpregnation

If no stable coimpregnation solutions can be obtained, sequential impregnations can be used instead. Obviously, this process is more elaborate and time consuming, involving a series of impregnation and drying/calcination steps. Sequential impregnations seem attractive from the fundamental point of view as they enable the impregnation of anions at pH below the support isoelectric point followed by the impregnation of cations at pH above the support isoelectric point (cf. Chapter 3). This should result in the most effective adsorption of

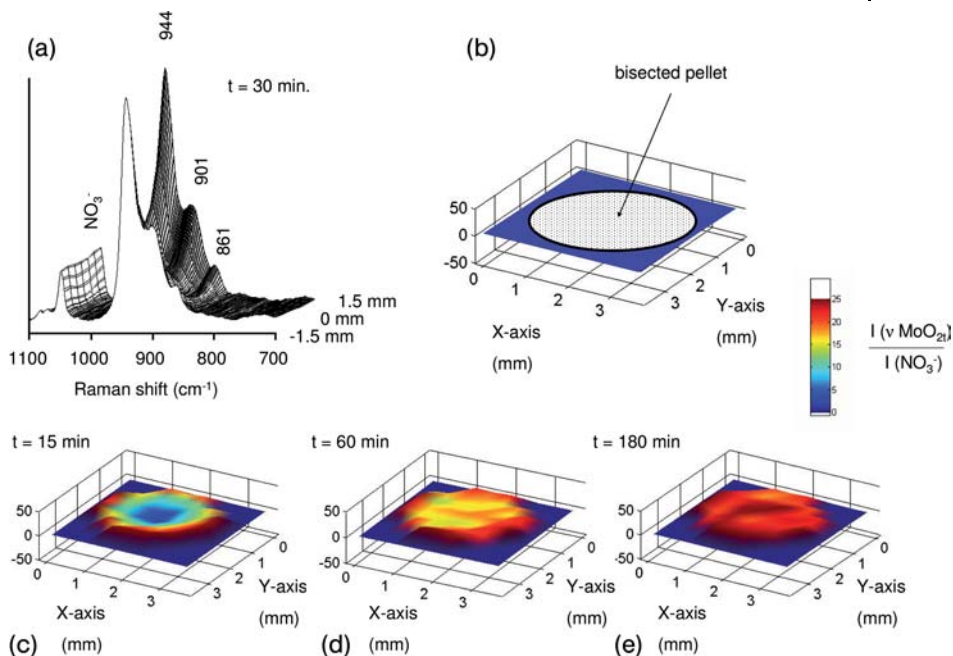


Figure 14.9 *In-situ* Raman microspectroscopy study on the evolution of Mo concentration profiles during the impregnation of Mo on the Al_2O_3 support. (Reprinted with permission from [52]: J.A. Bergwerff, PhD Thesis, Utrecht University, The Netherlands, 2007.) (a) Raman spectra recorded 30 minutes after impregnation of (b) bisected cylindrical Al_2O_3 pellets with 1.0 M Mo/1.0 M citrate solution.

Three-dimensional plots illustrate the spatial distribution of the $[\text{Mo}_4(\text{Hcitrate})_2\text{O}_{11}]^{4-}$ complex in 3-mm Al_2O_3 pellets (c) 15, (d) 60, and (e) 180 minutes after impregnation. The intensity plots are obtained by referencing to the NO_3^- Raman band. While Mo is only present in the outer part of the pellets after 15 minutes, a homogeneous Mo distribution is observed after 180 minutes after impregnation.

the respective ions from the solution on the support surface. However, there is a distinct possibility that the components impregnated in the initial impregnation step(s) will redissolve and redistribute in the consecutive steps. In addition to that, the multiple drying and calcination steps may be detrimental to the catalyst quality. That is why coimpregnation is typically more favorable for the dispersion of Co and Mo species [73] and leads to higher HDS activity [74] than sequential impregnation.

14.5.4

Drying and Calcination

The drying and calcination steps, where the metal salts are dehydrated and/or converted to oxides, are very critical. The optimum conditions are required

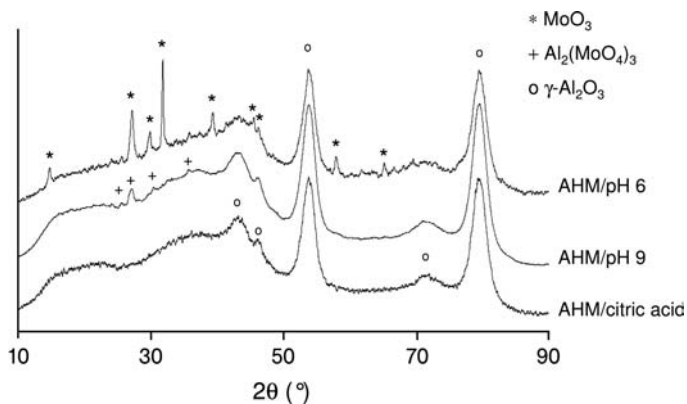


Figure 14.10 X-ray diffraction (XRD) patterns of 500 °C calcined 19 wt% MoO₃/Al₂O₃ catalysts prepared using different precursors. (Reprinted with permission from [52]: J.A. Bergwerff, PhD Thesis, Utrecht University, The Netherlands, 2007.) The catalyst prepared using the 1.8 M Mo/1.8 M citrate cosolution only contains

diffraction lines corresponding to the presence of γ -Al₂O₃ (o). Al₂(MoO₄)₃ (+) and MoO₃ (*) are formed in samples prepared with 1.8 M Mo solutions without an additional solution stabilizer, that is, with AHM-pH = 9 (NH₄OH added) and AHM pH = 6 (natural pH) solutions, respectively.

to prevent/control the sintering of the active components and the formation of stable crystalline compounds, in addition to ensuring that the drying and calcination steps are completed in a reasonably short period of time. For example, MoO₃ gets distributed on the support by thermal spreading, that is, by solid–solid wetting of MoO₃ on the Al₂O₃ surface [37–39]. However, calcination at temperatures exceeding 600 °C volatilizes Mo species, reduces the catalyst surface area and the amounts of surface Mo and yields various aluminates [75]. High-temperature calcination also stimulates the formation of crystalline Al₂(MoO₄)₃ [19], CoAl₂O₄/NiAl₂O₄ [76], and CoMoO₄/NiMoO₄ (Figures 14.10 and 14.11). The rapid sintering of the surface AlPO₄-like phase further reduces the surface area of the final catalyst. Most of these sintering processes are enhanced under high-humidity conditions.

Thermal treatment of still wet impregnated material may lead to the redistribution of the active components. Rapid drying, particularly at reduced pressure, can induce a transport of Mo oxides to the outer surface of the extrudates, leading to a sharp Mo egg-shell profile. A low drying rate is favorable for a homogeneous distribution of Mo [63]. Most importantly, some of the side reactions taking place during the drying and calcination may be exothermic. To such reactions belong the oxidation of organic compounds used as solution stabilizers and redox reactions occurring in materials containing, for example, a combination of ammonium salts and nitrates. That is why careful temperature control is required during the entire drying/calcination process.

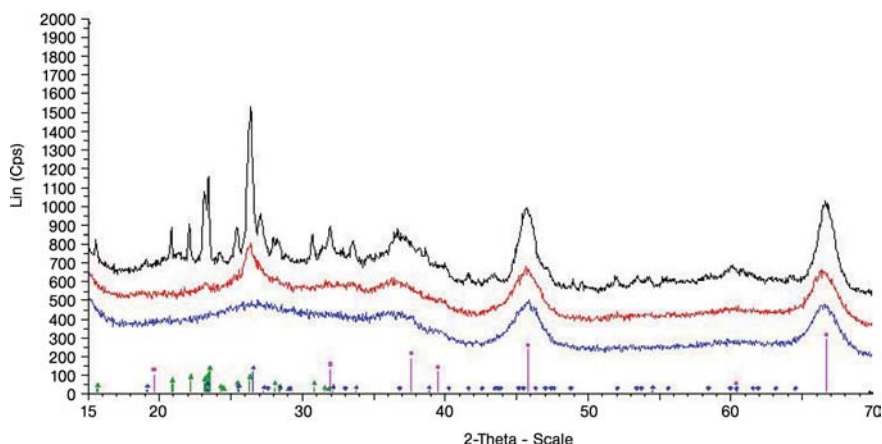


Figure 14.11 XRD patterns of calcined Co-Mo/Al₂O₃ catalysts, indicating the formation of CoMoO₄ and Al₂(MoO₄)₃ after 600 and 700 °C calcination, respectively. (From bottom to top: 500 (blue), 600 (red), and 700 °C (black) calcination; reference stick patterns of γ -Al₂O₃ (magenta), CoMoO₄ (blue), and Al₂(MoO₄)₃ (green) are included at the bottom.)

The drying is typically carried out using a belt dryer or a rotary dryer at temperatures between 100 and 200 °C. The calcination is normally carried out in a rotary kiln at temperatures between 400 and 600 °C. For instance, the impregnated composition is allowed to age for 2 hours, following which it is dried at 110 °C and then calcined at 480–550 °C for 1/2 hour in flowing air [77, 78]. The calcination is usually carried out in an oxygen-containing atmosphere (air). In principle, the calcination can be carried out in an inert atmosphere. This is an effective method to suppress the exotherms. For example, a cogelled silica-alumina carrier material impregnated with a nonaqueous dimethylformamide solution of nickel nitrate and ammonium metatungstate can be dried and then calcined in a nitrogen atmosphere at 593 °C [79]. The calcination in an inert atmosphere can, however, affect the chemical processes occurring on calcination very significantly. One of the common redox reactions occurring on calcination is related to the use of (NH₄)₆Mo₇O₂₄ in catalyst preparation. While the oxidative decomposition (NH₄)₆Mo₇O₂₄ leads to MoO₃ formation accompanied by NO_x emissions, its thermal decomposition in an inert (Ar) atmosphere can yield Mo₄O₁₁, Mo(V) species and MoO₂ (Figure 14.12) [80].

When the calcination step is not well controlled, or when it is not desirable to remove the organic additives from the catalyst before the sulfidation, it may be possible to dry the catalyst only at low temperature and to skip the calcination step. High activity can be obtained, for example, with dried-only Co/Ni-Mo/W hydrotreating catalysts containing particular carboxylic acids (e.g. glycolic acid or lactic acid) and particular organic S compounds

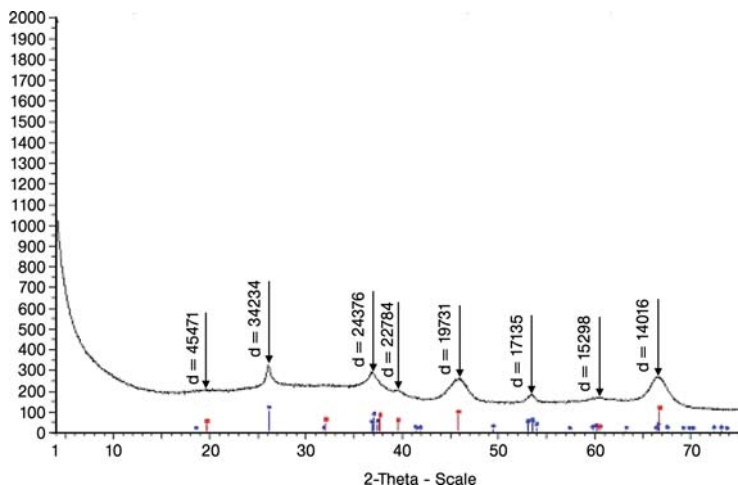


Figure 14.12 XRD pattern of Co-Mo/Al₂O₃ catalysts calcined in an inert atmosphere, indicating the formation of MoO₂. (Reference stick pattern of γ -Al₂O₃ (red) and MoO₂ (blue) are included at the bottom.)

(e.g. mercaptoacetic acid or 1-mercaptopropionic acid) [81]. However, the refinery end user generally prefers that the catalyst is free of water and any other compounds that may decompose or evaporate during the reactor start-up.

14.6

Presulfiding as the Last Stage in Hydrotreating Catalyst Preparation

14.6.1

Presulfiding Goals

The presulfiding can be considered as the last step in the preparation of the hydroprocessing catalyst before its active use on a process situation. It certainly is a very important process that must be appropriately optimized. The catalyst's metal oxides are not stable under the hydrotreating reaction conditions when the catalyst is contacted with oil at high pressure and temperature, with H₂ and H₂S present. Primarily the goal of the presulfiding is to bring the catalyst in equilibrium with its reaction environment. This needs to be conducted in an efficient and controlled manner rather than letting the presulfiding take place in the initial period of the run. The presulfided catalyst contains metal sulfides (e.g. MoS₂, WS₂, Co₉S₈, or Ni₃S₂) and is mostly referred to as a “sulfidic catalyst.” Ideally, the sulfidic Co and Ni species decorate the edges of the MoS₂ slabs and stacks, forming the so-called Co-Mo-S/Ni-Mo-S active phase [15–17].

14.6.2

Gas-Phase versus Liquid-Phase Presulfiding

Presulfiding can be carried out in the gas phase, using, for example, $\text{H}_2\text{S}/\text{H}_2$ mixtures. Such sulfidation can be carried out off-line by exposing it to H_2S - and H_2 -rich streams [82]. The $\text{H}_2\text{S}/\text{H}_2$ mixture often contains 10% H_2S and the typical sulfidation temperatures are between 325 and 360 °C [83]. Catalysts prepared by incorporating active metals into an Al_2O_3 hydrogel are typically sulfided with $\text{H}_2\text{S}/\text{H}_2$ at higher temperature (i.e. at least 482 °C) [34] than catalysts prepared by the impregnation of metals on the $\gamma\text{-Al}_2\text{O}_3$ support. When recycle gas is used, the sulfiding mixture may also contain CH_4 in addition to H_2S and H_2 . H_2S adsorbs on the catalyst already at 40 °C. H_2S consumption and water production are observed above 140 °C. The sulfidation is completed at 300 °C but H_2S adsorption continues above 350 °C [84].

The gas-phase presulfiding can also be carried out using CS_2 , mercaptan compounds (e.g. ethanethiol), thiophenic compounds or organosulfides such as dimethylsulfide (DMS) or dimethyldisulfide (DMDS) containing H_2 gas. H_2S can be used in combination with sulfur-containing compounds, which decompose at temperatures below 370 °C [85]. In such a case, a sulfur-rich recycle stream of a hydrocarbon gas (e.g. methane, ethane), preferably containing 5–80% by weight H_2S , can be used as the H_2S source [85, 86]. The actual benefit of organosulfides as activating agents observed in industrial practice is not just chemical but it is related to the lower exothermicity of the oxide-sulfide transformation [87]. It has been found that O–S exchange and intramolecular redox reactions can be initiated at low temperatures ($\sim 150^\circ\text{C}$) even when supplying H_2S to the catalyst at a low concentration ($\text{ppH}_2\text{S} \leq 3.3$ kPa). This leads to a sufficient level of sulfidation before reaching 300 °C, that is, before the competition between reduction and sulfidation starts. Due to their inability to provide H_2S at low reaction temperature, organosulfides are less efficient sulfiding agents than H_2S , which makes the exotherms occurring on sulfidation less pronounced [88].

As the presulfiding is accompanied by large heat effects, the catalyst sulfiding procedures must be designed with great caution and often tailor-made for specific catalysts [89, 90]. Instead of the formation of the active Co-Mo-S/Ni-Mo-S phase, uncontrolled exotherms may lead to the sintering of MoS_2 and to the subsequent segregation of the promoter as crystalline Ni_3S_2 and Co_9S_8 , resulting in a significantly lower catalyst activity. The temperature control of the presulfiding process is easier when the presulfiding is carried out in the liquid phase. Liquid is able to act as a far more efficient heat sink, as compared to gas phase. That is primarily why the *in-situ* presulfiding in industrial units is typically carried out at high temperature and pressure, using light feed such as straight run gas oil spiked with S-containing compound such as, for example, CS_2 or DMDS. An intermediate option is to prewet the catalyst with hydrocarbon prior to gas-phase sulfidation. For example, the catalyst is

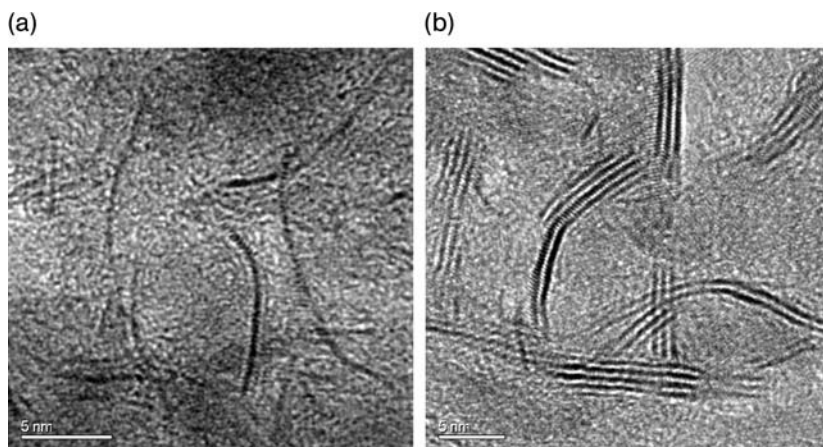


Figure 14.13 TEM micrographs of sulfided Ni-Mo/Al₂O₃ catalysts [92]: (a) after liquid-phase sulfidation (DMDs spiked straight run gas oil (SRGO), 30 bar, 320 °C) and (b) after H₂S/H₂ sulfidation (10% H₂S in H₂, 1 bar, 300 °C).

contacted with a hydrocarbon with a boiling range of 150–500 °C such as gasoline, white spirit, diesel, gas oil, mineral lube oil, or white oil, followed by contacting with H₂S/H₂ at a temperature of 150–450 °C [91]. As a consequence of the lower availability of H₂S in the initial stages of sulfidation as well as a better temperature control, liquid-phase sulfided catalysts typically contain single layers of MoS₂ as compared to MoS₂ stacks observed in catalysts after gas-phase-based H₂S/H₂ sulfidation (Figure 14.13) [92, 93].

14.6.3

***Ex-situ* versus *In-situ* Presulfiding**

The presulfiding can be carried out *ex-situ* (off-site), that is, outside the refinery reactor in a specialized equipment/company, as well as *in situ* (on site), that is, in the refinery reactor. *Ex-situ* presulfiding is carried out when the refinery reactor does not have the flexibility to carry out a well-controlled presulfiding. For example, there is no possibility to supply high concentration of S-containing compounds in the gas phase or in the liquid phase, or to use light feed.

Ex-situ presulfiding can be carried out in two steps. First, the oxidic catalyst is impregnated with a sulfur-containing compound. Various methods exist for such a procedure, for example, the catalyst is:

- Mixed with elemental sulfur and heated to a temperature above the melting point of sulfur in an inert atmosphere (Figure 14.14) [94],
- Contacted with molten sulfur at a temperature of 100–150 °C in an inert atmosphere [95], or

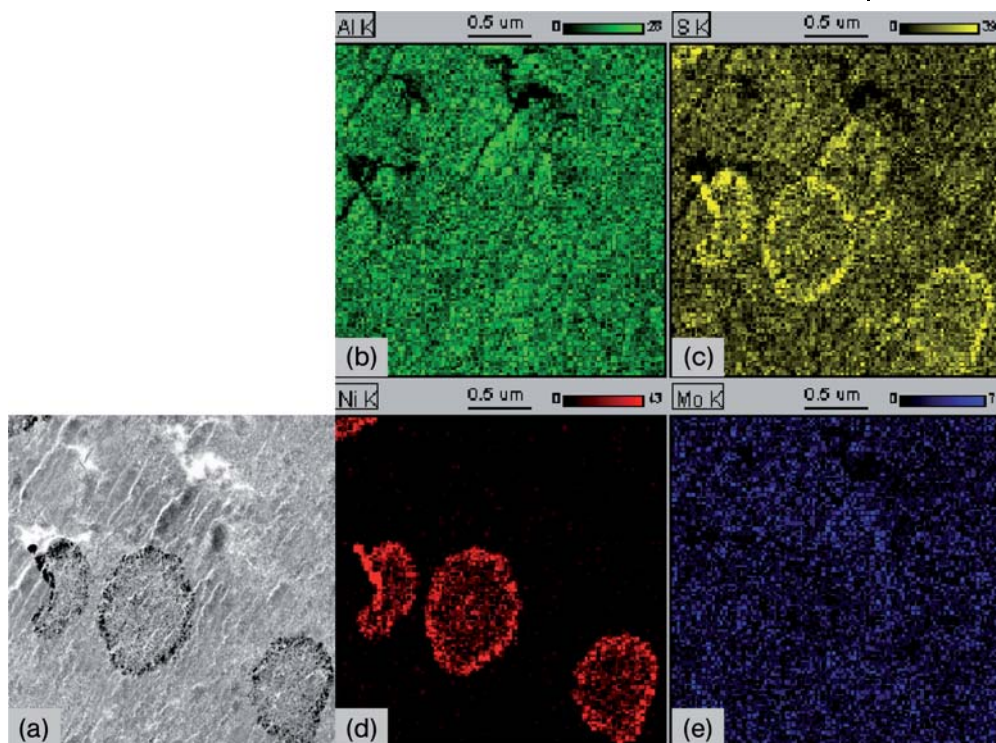


Figure 14.14 STEM-EDX analysis of Ni-Mo/Al₂O₃ catalyst *ex-situ* presulfided using powdered elemental sulfur: (a) STEM image, (b) Al K-map, (c) S-K map, (d) Ni-K map, and (e) Mo-K map. Sulfur is inhomogeneously distributed. S-rich areas coincide with Ni-rich areas.

- Contacted with a mixture of powdered elemental sulfur and a liquid olefinic hydrocarbon followed by heating to a temperature above 150 °C in an inert atmosphere [96].

The catalyst can also be impregnated with inorganic polysulfide, for example (NH₄)₂S_x [97] or with organic polysulfide R-Sn-R' such as di-tert-nonyl or di-tert-dodecyl pentasulfides (Figure 14.15) [98, 99] dissolved in an organic solvent and dried in an inert atmosphere. As shown in the examples in Figures 14.14 and 14.15, the impregnation of the S-containing components may result in an inhomogeneous distribution of the S-components throughout the catalyst particles. Second, the catalyst is loaded in the refinery reactor and contacted with a hydrocarbon feed and H₂ at high pressure and temperature.

Ex-situ presulfiding is also preferred if it is not possible to efficiently control the exotherms occurring during metal-oxide sulfidation or when the refinery cannot handle the compounds formed during the decomposition of organic additives during the presulfiding. The latter is often the case with

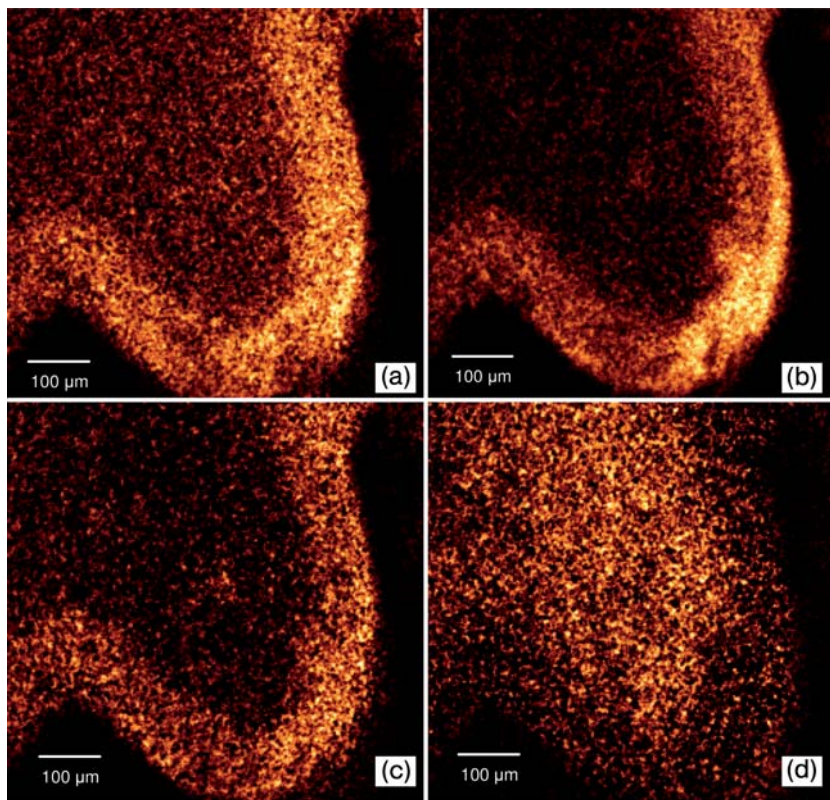


Figure 14.15 X-ray photoelectron spectroscopy (XPS) element mapping of an ex situ presulfided Ni–Mo hydroprocessing catalyst: (a) C–C (1 s); (b) S (2p); (c) Mo^{4+} (3p); (d) Mo^{6+} (3p). Different Mo species

are present on the outside (Mo^{4+}) and on the inside (Mo^{6+}) of the extrudates. The C–C and S remnants of the organic S-compound are found predominantly on the outside of the extrudate.

catalysts containing organic additives, which have not been calcined prior to the presulfiding.

An increasingly attractive option is the complete off-site presulfiding of the catalyst. This can again be done by impregnating the sulfur component (as described above) followed by H_2 activation, or by $\text{H}_2\text{S}/\text{H}_2$ sulfidation. The complete off-site presulfiding can, for example, be carried out by passing a gaseous stream comprising H_2 and H_2S upwardly in an ebullating or expanded bed [100]. It is again advantageous to pretreat the catalyst with a hydrocarbon liquid with a boiling range of 150–500 °C prior to contacting with H_2 and H_2S at a temperature of 150–450 °C [91]. In addition to placing some/all of the difficult handling steps outside the refinery reactor, the advantage of the complete off-site presulfiding is that commercial reactor start-up is much faster as compared to the on-site presulfiding procedure.

In-situ presulfiding is carried out in the process unit reactor in the gas phase using either $\text{H}_2\text{S}/\text{H}_2$ mixtures [34], sulfur-rich recycle stream [85, 86] or in the liquid phase by contacting the catalyst with H_2 and a S-spiked hydrocarbon feed [86, 101]. Good results were obtained by sulfidation at 350°C using SRGO spiked with DMDS [102]. Also, other hydrocarbon feeds and blends can be spiked with DMDS and used for the presulfiding [101]. Alternatively, a liquid hydrocarbon can be spiked with DMDS in combination with dimethyl polysulfide or di-tert-nonyl polysulfide [86, 103]. In cases where spiking or using a light feed with high S content is not possible, the catalyst can be contacted with a hydrocarbon solvent with very low olefin and organic nitrogen content such as highly hydrotreated jet fuel, diesel fuel, or kerosene, while adding the sulfiding agent such as H_2S , di-tert-nonyl poly sulfide (TNPS), DMDS or CS_2 in the gas phase [104]. Clearly, the *in-situ* sulfidation requires extra time during the reactor start-up. Moreover, *in-situ* sulfidation may sometimes be inhomogeneous in its sulfur distribution in the catalyst bed, as a result of maldistribution and channeling effects that can occur in large process reactors.

14.7

Industrial Process for the Production of the Oxidic Catalyst

14.7.1

Industrial Equipment

The equipment used in the industrial production is quite conventional, including stirred precipitation tanks, filters, extruders, concrete mills, spray, belt and rotary dryers, rotary kilns, and so on. The modernization of the industrial plants has been driven by the need to increase the production capacities (debottlenecking) and to commercialize new generations of catalysts as well as by health, safety, and environmental issues.

14.7.2

Health, Safety, and Environmental Issues

Environmental concerns and legislations play an ever-increasingly important part in the selection of catalyst components and raw materials used in their preparation. Most commercial production plants in Western Europe and in the United States must have zero emissions to the environment (i.e. air, waste water, particulate matter). For the same reason, the preparation yields must be as close to 100% as possible.

However, numerous materials used or formed during the production of hydroprocessing catalysts are toxic or dangerous to the environment. For example, some Ni compounds used are reprotoxic, genotoxic, or (suspected) carcinogens. During the catalyst drying and calcination, the decomposition

products of metal salts used in the catalyst production (e.g. nitrate and ammonia) are liberated as gases, for example, NO_x . Many raw materials are supplied as powders and any mechanical handling of the catalyst may produce fine metal-containing dust.

Consequently, great care must be taken that any personnel involved in catalyst production are adequately protected. Among hazards to be considered are that any skin contact with catalyst or its components, as well as any possibility to inhale fine catalyst dust particles, must be excluded. This handling situation is best achieved by using appropriate protective clothing, respiratory protection and by working in either sealed or well-ventilated installations. In addition, no gaseous, liquid, or solid waste may be released into the environment. This is achieved by purification and correct means of disposal of gaseous, liquid, and solid waste streams.

Typical examples of such waste streams are:

- the filtrate of the alumina and silica-alumina precipitation containing, for example, Na^+ , NH_4^+ , SO_4^{2-} , or NO_3^-
- the off-gas of the (spray-) drying of the alumina and silica-alumina containing, for example, SO_x or NO_x
- the off-gas of the drying and calcination of the final catalyst containing, for example, NO_x .

Currently, many new catalyst production installations are built in a way to prevent any escape of the waste streams into the environment. For example, these installations are sealed from the surroundings, having their own air circulation and purification systems, whilst the process water runs through a closed circuit involving purification and recycling.

14.8

Summary

At first sight, the preparation of hydrotreating catalysts appears to be a mature industrial process involving relatively simple experimental needs and procedures. However, the need to continuously produce more active catalysts requires ever more careful control of the preparation conditions and steps to achieve an optimal product. Furthermore, ever-increasingly strict environmental regulations for handling of the hydrotreating catalysts, related raw materials, and resulting process streams are additional demands beyond the continuous innovation required of this process.

References

1. Simpson, H.D., Richardson, R.L. and Baron, K. Union Oil Co. (1985) US Patent US4500424.
2. Hensley, A.L. and Hopkins, P.D. Standard Oil Co. (1980) British Patent GB2032796.

3. Klusdahl, H.E. Chevron Research Co. (1980) US Patent US4192736.
4. Poels, E.K., Staal, L.H., van Leeuwen, W.A. and Unilever, N.V. (1986) European Patent EP177102.
5. Kukes, S.G., Davis, T. and Brandes, K. Phillips Petroleum Co. (1988) US Patent US4778587.
6. Schoenthal, G.W. and Slaugh, L.H. Shell Oil Co. (1986) US Patent US4579729.
7. Yang, Q., Liu, B., Nie, H., Liu, X., Li, D., Shi, Y. and Zhuang, F. China Petro-Chemical Corporation Research Institute Petroleum Processing Sinopec (2001) US Patent US6518219.
8. Gevert, B.S. and Ying, Z.S. (1999) *J. Porous Mater.*, **6**, 63.
9. Ying, Z.S., Sterte, J., Gevert, B. and Otterstedt, J.E. (1995) *Ind. Eng. Chem. Res.*, **34**, 1566.
10. Iler, R. (1961) *J. Am. Ceram. Soc.*, **44**, 618.
11. Davis, M.E. and Vaudry, F.J. California Institute of Technology (1999) US Patent US5863515.
12. Shukis, P.J., Carruthers, J.D. and Lostaglio, V.J. Cytec Technology Corporation (2000) US Patent US6015485.
13. Murrel, L.L., Dispenziere, N.C. Jr. and Kim, K.S. (1989) *Catal. Lett.*, **2**, 263.
14. Kunisada, N., Choi, K.-H., Korai, Y., Mochida, I. and Nakano, K. (2004) *Appl. Catal., A: General*, **273**, 287.
15. Bouwens, S.M.A.M., van Dijk, M.P., van der Kraan, A.M., Koningsberger, D.C., van Zon, F.B.M., de Beer, V.H.J. and van Veen, J.A.R. (1994) *J. Catal.*, **146**, 375.
16. van Veen, J.A.R., Gerkema, E., van der Kraan, A.M. and Knoester, A. (1987) *Chem. Soc., Chem. Commun.*, **22**, 1684.
17. Hensen, E.J.M., Kooyman, P.J., van der Meer, Y., van der Kraan, A.M., de Beer, V.H.J., van Veen, J.A.R. and van Santen, R.A. (2001) *J. Catal.*, **199**, 224.
18. Caceres, C.V., Fierro, J.L.G., Lazaro, J., Lopez Agudo, A. and Soria, J. (1990) *J. Catal.*, **122**, 113.
19. Henker, M., Shpiro, E.S., Wendlandt, K.P. and Tkachenko, O.P. (1990) *Appl. Catal.*, **61**, 253.
20. Laine, J., Brito, J.L. and Severino, F. (1991) *J. Catal.*, **131**, 385.
21. Iwasaki, M., Yasumori, A., Kawazoe, H. and Yamane, M. (1990) *J. Non-Cryst. Solids*, **121**, 147.
22. Sato, S., Takahashi, R., Sodesawa, T., Shin, D., Ichikawa, N. and Ogura, K. (2006) *Bull. Chem. Soc. Jpn.*, **79**, 649.
23. Ward, J.W. Union Oil Co. (1983) US Patent US4419271.
24. Timken, H.K.C. Chevron U.S.A. Inc. (2004) US Patent US2004092390.
25. Luthra, N.P. and Cheng, W.C. (1987) *J. Catal.*, **107**, 154.
26. Kim, S.I. and Woo, S.I. (1992) *J. Catal.*, **133**, 124.
27. Tischer, R.E., Narain, N.K., Stiegel, G.J. and Cillo, D.L. (1985) *J. Catal.*, **95**, 406.
28. Levin, O.V., Golubev, A.B., Vlasov, V.G., Loginova, A.N. and Oltrev, A.G. Novokuibyshev Catalyst Works Co. Ltd (2002) Russian Patent RU2189860.
29. Ward, J.W. Union Oil Co. (1987) European Patent EP0220616.
30. Brundage, K.R. and Swaroop, S.H. Corning Inc. World Intellectual Property Organisation (2000) WO0043325.
31. Iler, R.K. (1964) *J. Am. Ceram. Soc.*, **47**, 339.
32. Knoezinger, H. and Taglauer, E. (1994) *Catalysis*, **10**, 1.
33. Kemp, R.A. Shell Oil Co. (1988) US Patent US4717705.
34. Kemp, R.A. Shell Oil Co. (1991) US Patent US5001101.
35. Kemp, R.A. and Adams, C.T. (1996) *Appl. Catal. A: General*, **134**, 299.
36. Kemp, R.A. Shell Oil Co. (1987) US Patent US4716140.
37. Kaluza, L. and Zdrzil, M. (2005) *React. Kinet. Catal. Lett.*, **85**, 391.
38. Knoezinger, H. (1991) *Dechema Monogr.*, **122**, 225.
39. Knoezinger, H. (1988) *Proc. 9th Int. Catal. Congr.*, **5**, 20.
40. Domokos, L., Jongkind, H. and van Veen, J.A.R. Shell International

- Research, World Intellectual Property Organisation (2004) WO2004073859.
41. Guenter, J.R., Koranyi, T.I., Marks, O. and Paal, Z. (1988) *Appl. Catal.*, **39**, 285.
 42. Koranyi, T.I., Marks, O., Manninger, I., Paal, Z. and Guenter, J.R. (1989) *J. Catal.*, **116**, 422.
 43. Brito, J.L. and Barbosa, A.L. (1997) *J. Catal.*, **171**, 467.
 44. Joseph, D.C. and Chomitz, N. American Cyanamid Co. (1966) US Patent US3287280.
 45. Cheng, W.C. and Pereira, C.J. (1987) *Appl. Catal.*, **33**, 331.
 46. Maslyanskij, G.N., Glozshitejn, A.Ya., Polotskaya, G.E., Shapiro, R.N., Vereshchagina, T.E., Zharkov, B.B., Krasij, B.V., Shavandin, Yu.A., Lugovskoj, A.I., Petrov, A.Yu. and Bubnov, Yu.N. Leningrad Petrochem Processes Development Association (1997) USSR Patent SU1557742.
 47. Thompson, M.S. Shell Internationale Research Massatsch. (1986) European Patent EP181035.
 48. Amano, T. and Morinaga, K. Japan Energy Corporation (1994) Japanese Patent JP6339635.
 49. Fang, W., Sun, J. and Sun, S. China Petro-Chemical Corporation, (2000) Chinese Patent CN1249327.
 50. Hillerova, E., Vit, Z. and Zdrzil, M. (1994) *Appl. Catal. A: General*, **118**, 111.
 51. Vazquez, P.G., Gonzalez, M.G., Blanco, M.N. and Caceras, C.V. (1995) *Stud. Surf. Sci. Catal.*, **91**, 1121.
 52. Bergwerff, J.A. (2007) PhD Thesis, Utrecht University, The Netherlands.
 53. Bergwerff, J.A., Jansen, M.A., Leliveld, R.G., Visser, T., de Jong, K.P. and Weckhuysen, B.M. (2006) *J. Catal.*, **243**, 292.
 54. Verbruggen, N.F.D., Lengeler, B., Mestl, G., von Hippel, L.M.J. and Knoezinger, H. (1994) *Langmuir*, **10**, 3063.
 55. van Veen, J.A.R., Hendriks, P.A.J.M., Romers, E.J.G.M. and Andrea, R.R. (1990) *J. Phys. Chem.*, **94**, 5275.
 56. van Veen, J.A.R., Hendriks, P.A.J.M., Andrea, R.R., Romers, E.J.G.M. and Wilson, A.E. (1990) *J. Phys. Chem.*, **94**, 5282.
 57. Kemp, R.A., Ryan, R.C. and Smegal, J.A. (1988) *Proc. 9th Int. Catal. Congr.*, **1**, 128.
 58. Eijssbouts, S., van Gestel, J.N.M., van Veen, J.A.R., de Beer, V.H.J. and Prins, R. (1991) *J. Catal.*, **131**, 412.
 59. van Veen, J.A.R., Colijn, H.A., Hendriks, P.A.J.M. and van Welsenens, A.J. (1993) *Fuel Process. Technol.*, **35**, 137.
 60. Blanco, M.N., Fierro, J.L.G., Caceres, C.V. and Thomas, H.J. (1987) *Appl. Catal.*, **33**, 231.
 61. Okamoto, Y., Arima, Y., Nakai, K., Umeno, S., Akai, Y., Ushikubo, T., Katada, N., Hasegawa, S., Isoda, T., Yoshida, H., Yamada, M., Segawa, K., Nishijima, A., Matsumoto, H., Uchijima, T., Hagio, M., Uchikawa, K., Inamura, K. and Tanaka, T. (1998) *Appl. Catal. A: General*, **170**, 329.
 62. Okamoto, Y., Umeno, S., Arima, Y., Nakai, K., Chiyoda, O., Yoshida, H., Akai, Y., Hasegawa, S., Shishido, T., Katada, N., Segawa, K., Yamada, M., Mochida, I., Ishihara, A., Nishijima, A., Matsumoto, H. and Uchijima, T. (1998) *Appl. Catal. A: General*, **170**, 359.
 63. Okamoto, Y., Umeno, S., Arima, Y., Nakai, K., Takahashi, T., Uchikawa, K., Chiyoda, O., Katada, N., Shishido, T., Hasegawa, S., Yoshida, H., Segawa, K., Koizumi, N., Nishijima, A., Kabe, T., Isoda, T. and Matsumoto, H. (1998) *Appl. Catal. A: General*, **170**, 343.
 64. Lopez Cordero, R., Gil Llambias, F.J., Palacios, J.M., Fierro, J.L.G. and Lopez Agudo, A. (1989) *Appl. Catal.*, **56**, 197.
 65. van Veen, J.A.R. and Hendriks, P.A.J.M. (1986) *Polyhedron*, **5**, 75.
 66. Pizzio, L.R., Caceres, C.V. and Blanco, M.N. (1995) *Catal. Lett.*, **33**, 175.
 67. Goula, M.A., Fierro, J.L.G., Kordulis, Ch., Lycourghiotis, A. (1992) *J. Catal.*, **137**, 285.

68. Oishi, Y., Kawakatsu, K. and Inoue, A. Nippon Oil Co. Ltd (1986) European Patent EP0204314.
69. Vazquez, P.G., Caceres, C.V., Blanco, M.N. and Thomas, H.J. (1989) *Int. Commun. Heat Mass Transfer*, **16**, 581.
70. Knozinger, H. and Jeziorkowski, H. (1978) *J. Phys. Chem.*, **82**, 2002.
71. Jeziorkowski, H. and Knozinger, H. (1979) *J. Phys. Chem.*, **83**, 1166.
72. Payen, E., Grimblot, J. and Kasztelan, S. (1987) *J. Phys. Chem.*, **91**, 6642.
73. Nava, R., Morales, J., Alonso, G., Ornelas, C., Pawelec, B. and Fierro, J.L.G. (2007) *Appl. Catal. A: General*, **321**, 58.
74. Rana, M.S., Ramirez, J., Gutierrez-Alejandre, A., Ancheyta, J., Cedeno, L. and Maity, S.K. (2007) *J. Catal.*, **246**, 100.
75. Stanislaus, A., Absi-Halabi, M., Al-Dolama, K., Katrib, A. and Ismail, M. (1988) *Appl. Catal.*, **41**, 109.
76. Atanasova, P., Lopez Agudo, A., Tabakova, T., Vladov, Ch. and Halachev, T. (1997) *Appl. Catal. A: General*, **161**, 105.
77. Simpson, H.D. Union Oil Co. (1990) European Patent EP0349223.
78. Simpson, H.D. and Borgens, P.D. Union Oil Co. (1989) European Patent EP0341893.
79. O'Hara, M.J. and Johnson, R.W. UOP Inc. (1985) US Patent US4497704.
80. Afanasiev, P., Martin, V. and Thomazeau, C. (2000) *Appl. Catal. A: General*, **199**, 61.
81. Kamo, T. and Kanai, Y. Sumitomo Metal Mining Co. (1992) European Patent EP496592.
82. MacArthur, J.B. IFP North America Inc. (2001) US Patent US6291391.
83. Ho, T.C. and McCandlish, L.E. Exxon Research Engineering (1986) US Patent US4595672.
84. Echard, M. and Leglise, J. (2001) *Catal. Lett.*, **72**, 83.
85. Bachtel, R.W., Earls, D.E., Johnson, D.R., Leung, P.C., Reynolds, B.E. and Trimble, H.J. Chevron USA Inc. (2005) US Patent US2005006283.
86. Hallie, H. (1982) *Oil Gas J. Dec.*, **20**, 69.
87. Texier, S., Berhault, G., Perot, G., Harle, V. and Diehl, F. (2004) *J. Catal.*, **223**, 404.
88. Texier, S., Berhault, G., Perot, G. and Diehl, F. (2005) *Appl. Catal. A: General*, **293**, 105.
89. Ho, T.C. and Reyes, S.C. (1990) *Chem. Eng. Sci.*, **45**, 2633.
90. Ho, T.C. and Reyes, S.C. (1988) *AIChE J.*, **34**, 314.
91. Eijsbouts, S., Dufresne, P., Labruyere, F., Plantenga, F.L., Gerritsen, L.A. and Akzo Nobel, N.V. Eurecat European Retrait Catalys, World Intellectual Property Organisation (2001) WO0176741.
92. Eijsbouts, S., van den Oetelaar, L.C.A. and van Puijenbroek, R.R. (2005) *J. Catal.*, **229**, 352.
93. Eijsbouts, S., van den Oetelaar, L.C.A., Louwen, J.N., van Puijenbroek, R.R. and van Leerdam, G.C. (2007) *Ind. Eng. Chem. Res.*, **46**, 3945.
94. Seamans, J.D., Gasser, N.G., Welch, J.G. and Adams, C.T. CRI Ventures Inc. (1990) European Patent EP359356.
95. Herrington, D.R. and Schwerko, A.P. Standard Oil Co. (1979) US Patent US4177136.
96. Ginestra, J.M., Lee, K.S. and Seamans, J.D. (2005) US Patent US2005159295.
97. Lockemeijer, J.R. Shell Oil Co. (1998) US Patent US5786293.
98. Gueguen, C., Gusnet, P., Jacquez, H. and Savin, G. ELF Aquitaine, ELF France (1988) European Patent EP298111.
99. van Gestel, J.N.M., Leglise, J. and Duchet, J.C. (1994) *J. Catal.*, **145**, 429.
100. Creager, T., Neuman, D.J. and Semper, G.K. Tricat Industries Inc. World Intellectual Property Organisation (1998) WO9806493.
101. Smegal, J.A., Ryan, R.C. and Nash, R.M. Shell Oil Co. (1991) US Patent US5008003.
102. Marroquin, G., Ancheyta, J. and Diaz, J.A.I. (2004) *Catal. Today*, **98**, 75.

103. Tuszynski, W.J. (1988) US Patent US4725571.
104. Ho, P.K., Loescher, M.E. and Podrebarac, G.G. Catalytic

Distillation Technology, World Intellectual Property Organisation (2002) WO02062471.

15

Methanol Catalysts

S. Schimpf and M. Muhler

15.1

Binary Cu/ZnO Catalysts

Methanol is one of the top 10 basic chemicals with a worldwide production from synthesis gas (CO , CO_2 , H_2) of 38 million tons in 2008 [1]. Methanol is used not only as solvent, but also as feedstock for several important chemicals such as acetic acid, methyl *tert*-butylether (MTBE), formaldehyde, methyl methacrylate (MMA), dimethyl terephthalate (DMT), chloromethane, and as gasoline extender [2, 3]. Methanol could provide convenient energy storage for fuel-cell applications, particularly in transportation and mobile devices, and it can be used as a clean fuel in combustion engines [4]. The booming Asian methanol market, coal-and biomass-based methanol production, and the growing role of methanol as a transportation and power-generation fuel all lead to an ongoing interest in methanol synthesis.

In the early 1920s it was known that the rate of catalyst deactivation in methanol synthesis was lower when the synthesis gas was purified from sulfur and Fe carbonyls [5], and BASF commercialized a high-pressure process using a catalyst consisting of zinc oxide and chromium oxide [6]. Soon, much more active copper-based catalysts were described in the literature [2]. Therein, Cu was identified as the active site [7–9]. In the early 1960s the careful purification of the feedstock originating from steam reforming of naphtha and natural gas, especially of sulfur, made it possible for Imperial Chemical Industries (ICI) to develop the low-pressure, low-temperature technology based on Cu. Initially, chromium oxide [10] was used, but was soon substituted by alumina [11, 12]. Nowadays, alumina is applied exclusively in the ternary Cu/ZnO/ Al_2O_3 catalysts used in industry [2], which are synthesized by coprecipitation. Other preparation methods are kneading, impregnation or leaching [2], gel-network coprecipitation [13], and intermetallic Cu catalysts by *in-situ* activation of binary and ternary Cu alloys [14].

At present, the development of more active catalysts operating at lower temperatures is key to improving the methanol synthesis process [15]. Many catalytic systems with different compositions have been found to be active

and selective for methanol synthesis so far, but Cu/ZnO (CZ) prepared by the classical coprecipitation technique still remains as the most active and selective binary catalyst [16, 17]. Therefore, we first concentrate on binary catalysts. It is generally known that copper is an active metal for methanol synthesis and is crucial for high activity. But catalysts consisting only of Cu or ZnO are hardly active [18, 19]. Slow CO hydrogenation takes place on ZnO and can be neglected, when Cu is present. The synergistic effect is highest at a composition of about 70 mol% Cu, where the maximum activity for methanol synthesis is reached. Nevertheless, the active site and the role of ZnO are still vividly discussed.

Nakamura *et al.* [20] showed that the deposition of Zn on Cu(111) increases methanol synthesis by an order of magnitude, underlining the necessity to maximize the number of neighboring Cu and Zn atoms. A high contact area between metallic Cu and ZnO is achieved, when partially reduced ZnO_x species in CZ migrate partly onto the copper particles under strongly reducing conditions [21–25]. This effect is caused by strong interactions between the metal and the reducible support (strong metal-support interactions, SMSI), and was recently visualized impressively by Schlögl and coworkers by high-resolution transmission electron microscopy (TEM) as shown in Figure 15.1 [19].

The contact area between Cu and ZnO is also strongly influenced by the composition of the gas phase. Grunwaldt *et al.* [24] investigated CZ catalysts with low copper loading. The highest activity was found under the most strongly reducing conditions, corresponding to low Cu–Cu coordination numbers. The Cu–Cu coordination number changed reversibly depending on the gaseous atmosphere applied. These dynamic reversible changes due to the gaseous environment were confirmed by Hansen *et al.* [26] using *in-situ* TEM, who investigated model catalysts prepared by impregnation with aqueous solutions of Cu acetate. They showed that the changes are caused both by adsorbate-induced changes in surface energies and by changes in the interfacial energy. The change in contact surface energy is related to the changes in number

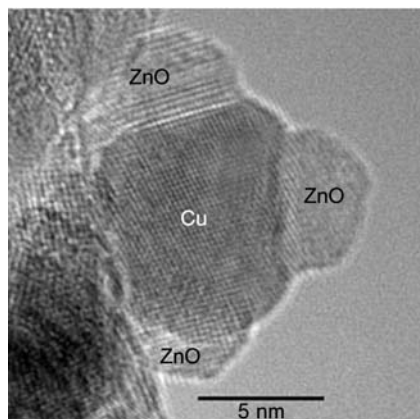


Figure 15.1 Metallic Cu particle partially covered by ZnO. The catalyst was prepared by coprecipitation with a molar ratio of Cu/Zn/Al of about 60 : 30 : 10 [19].

of oxygen vacancies at the interface [27, 28], which was also supported by infrared (IR) spectroscopy [29]. Only under severe reduction conditions was significant alloying of Cu and Zn observed, in addition to the morphological changes. Bulk alloying can be excluded under typical reaction conditions [24]. A dynamic model that correlated the relative interfacial area between copper metal and ZnO in CZ catalysts with the partial reduction of the ZnO component and the consequent spreading of Cu metal species on ZnO was established by the Topsøe group [27]. The dynamical changes were integrated into a microkinetic model, which can be used for extrapolation to industrially relevant reaction conditions [27, 28]. The dynamic changes under the reducing methanol synthesis conditions were also confirmed by X-ray diffraction (XRD) line analysis. A mutual structural interaction of the two components Cu and ZnO leads to strained copper particles stabilized by the unstrained state of the ZnO microcrystallites [30]. The induced microstructural strain influences the catalytic activity under the highly reducing conditions of methanol synthesis, and these microstructural changes of copper can be traced back to the phase composition of the corresponding hydroxycarbonate [30].

In summary, ZnO plays a dual role:

- It is a structural promoter serving as spacer between Cu particles maintaining a high dispersion of the Cu crystallites.
- It is an electronic promoter providing Zn+O adspecies [31–34].

These characterization results provide two guidelines for the *synthesis strategy*: to maximize the specific copper surface area and to maximize the contact area between Cu and ZnO. The second guideline suggests that a precursor with a high degree of mixing of the components, for example, where all the metal ions are located in a single phase, should lead to the best results. The most promising preparation method for such multicomponent catalysts satisfying all requirements is the coprecipitation technique, by which a precursor can be made, in which all the elements are mixed on the atomic level [35]. Therefore, we focus on this preparation method in the following and consider all the preparation parameters influencing the performance of the catalyst in detail. Other methods are presented in Section 15.4 on alternative preparation routes.

15.2 Coprecipitation

The coprecipitation method is one of the most important preparation methods, especially when high metal loadings are required (Chapter 7). A very high and homogeneous dispersion of the active components is achieved, and the components can be merged in stoichiometric ratios in the precursor material. Commercial Cu/ZnO/Al₂O₃ catalysts are produced exclusively by the coprecipitation method. The process shown systematically in Figure 15.2 can be basically described as coprecipitation of salts, most notably nitrates of Cu, Zn, Al by

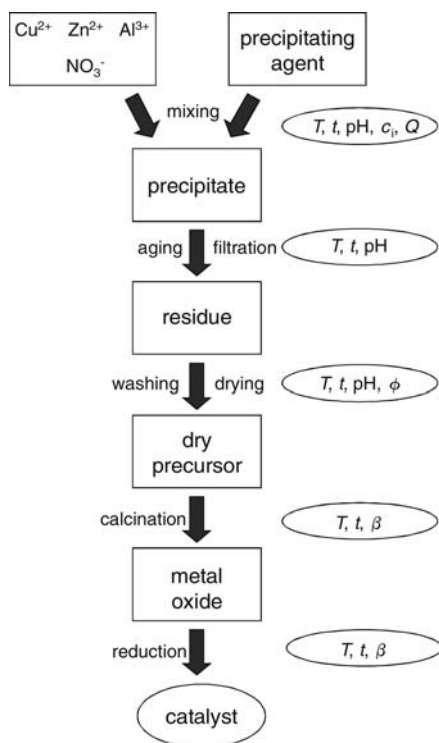


Figure 15.2 Schematic preparation procedure of Cu/ZnO/Al₂O₃ catalysts via the coprecipitation method and the parameters influencing the process: temperature T , time t , pH value of the solution, concentration c , volumetric rates of adding the metal nitrate solution and the precipitating agent Q , extent of the washing procedure ϕ , heating rate β .

means of a basic precipitating agents such as carbonates, hydroxycarbonates, or hydroxides of alkali metals. The chronological order of addition can differ: the base can be added to the metal salts or vice versa (inverse precipitation), or the two solutions can be added to the preparation vessel simultaneously [2]. Generally, an aqueous solution of Na₂CO₃ is employed as precipitating agent and is added under pH control to an aqueous solution of Cu(NO₃)₂, Zn(NO₃)₂, and Al(NO₃)₃ at elevated temperatures (323–363 K) [2, 36]. The structural and catalytic properties of the catalysts are influenced by all the precipitation conditions applied. Intimate mixing, uniform distribution, and high dispersion of the individual phases are required. Therefore, extremely careful control of parameters such as temperature, pH value, the concentration of the solutions and ionic strength, the mixing, and the aging procedure during the precipitation step as well as the washing of the metastable precipitated sample is of utmost importance and has to be optimized for each set of starting compounds and compositions [27, 36, 37]. The microstructural properties predefined during precipitation, such as size and strain of copper crystallites, are traceable throughout the next two steps of preparation: the calcination of the precursor to CuO/ZnO/Al₂O₃, and the reduction of the calcined material to the final catalyst. Bems *et al.* [37] used the term “chemical memory” for this phenomenon.

A typical laboratory preparation recipe for this coprecipitation route is provided hereafter. The experimental setup consists of a computer-controlled automatic titrator, a syringe pump, and a reactor, heated by a thermostat. An aqueous solution of $\text{Cu}(\text{NO}_3)_2$, $\text{Zn}(\text{NO}_3)_2$, and $\text{Al}(\text{NO}_3)_3$ in the case of ternary catalysts is prepared using high-purity water. High-purity chemicals were used in order to avoid impurities such as chlorine and sulfur. In our example 8.54 g $\text{Cu}(\text{NO}_3)_2$ and 4.86 g $\text{Zn}(\text{NO}_3)_2$ are dissolved in 35 ml of water ($c(\text{Cu} + \text{Zn} + \text{Al}) = 1.5 \text{ M}$) for a catalyst consisting of 70 at% Cu and 30 at% Zn. This solution is filled in the syringe of the pump by reverse pumping. 1.2 M Na_2CO_3 is employed as a precipitating agent and is filled in the tank of the automatic titrator. Fifty milliliters of water is added to the reaction container, which is thermostatted to 338 K and stirred by a magnetic stirrer during precipitation and the aging period. The pump, which feeds 1.5 ml nitrate solution per minute and 30 ml in total, and the computer-controlled automatic titrator are started at the same time. The addition of the Na_2CO_3 solution to maintain a pH value of 7.0 and the recording of the pH value is controlled by a computer program. After adding the first drops of the precursor and the precipitation agent a cloudy bluish precipitate can be observed. In our example, 39.6 ml are added at 338 K and vigorous stirring, which takes about 20 minutes.

After the precipitation an aging period follows, where the metastable precipitate is stirred at 338 K for another 2 hours. During this period of time the color of the precipitate changes from blue to green after about 30 minutes. The aged precipitate is filtered off using a glass frit and afterwards washed five times. For washing, 30 ml of high-purity water are added to the content of the glass frit, stirred for several minutes using a magnetic stirrer, and pumped off. The aged precipitate is dried at 383 K for 24 hours. Before calcination the precipitate is grounded. The calcination is performed in synthetic air at a flow rate of 75 ml/minute at 573 K for 3 hours using a heating rate of 2 K/minute. Reduction is performed at 513 K, using a heating rate of 1 K/minute in diluted H_2 up to 458 K and then up to 513 K in pure H_2 .

To optimize a catalyst with respect to its catalytic properties, it is imperative to characterize the physicochemical properties of the precursors during each step of preparation.

15.2.1

Precipitation

Depending on the precipitation parameters, different single and mixed phases (metal carbonates, hydroxycarbonates, hydroxynitrates, hydroxides, or oxides) are formed during precipitation. The phases identified in the precipitate in the literature mostly after aging and washing are summarized in Table 15.1. It is important to note that phase transformations occur during the aging period, as discussed later.

Table 15.1 Phases containing one or both metals identified in the precipitate. Adapted from [2].

Chemical formula	Name	References
Single metal		
$\text{Cu}_2(\text{OH})_2\text{CO}_3$	Malachite	[18, 30, 35, 38–40]
$\text{Cu}_2(\text{OH})_3\text{NO}_3$	Gerhardtite	[39, 41, 42]
$\text{Zn}_5(\text{OH})_6(\text{CO}_3)_2$	Hydrozincite	[18, 38, 39, 41]
$\text{Zn}_4(\text{OH})_6\text{CO}_3 \cdot \text{H}_2\text{O}$	Zinc hydroxycarbonate	[41]
Binary		
$(\text{Cu}_x\text{Zn}_{1-x})_5(\text{OH})_6(\text{CO}_3)_2$	Copper hydrozincite ($x < 0.1$)	[16, 18, 30, 37, 38, 41–43]
$(\text{Cu}_x\text{Zn}_{1-x})_5(\text{OH})_6(\text{CO}_3)_2$	Aurichalcite ($0.27 < x < 0.45$)	[16, 18, 30, 35–38, 43–45]
$(\text{Cu}_{1-x}\text{Zn}_x)_2(\text{OH})_2\text{CO}_3$	Zincian-Malachite ^a	[16, 30, 35–37, 39, 43–48]

^aSometimes named roasite (mineralogical name).

Due to the synthesis strategy at constant pH, Cu and Zn should be precipitated simultaneously to achieve a high contact area. So, the mixed Cu/Zn hydroxycarbonates are of interest as precursors for the synthesis of these catalysts. The chemical and structural identity of these precursors is linked to the activity of the final catalyst, that is, the catalyst has a chemical memory of its origin [37, 38, 45]. Generally, zinc-rich samples comprising hydrozincite and aurichalcite and with increasing copper ratio (zincian)-malachite were found to form at different Cu/Zn ratios [37, 49]. These hydroxycarbonates decompose slowly, whereas hydroxynitrates formed at $\text{pH} \leq 6$ decompose abruptly. As a consequence, decomposition of Cu nitrates leads to large Cu particles and low copper surface areas resulting in less-active catalysts [42].

As there is no break regarding the phase transformations at the end of the precipitation step and the beginning of the aging period, these solid-state reactions are discussed together in the following.

15.2.2

Aging

During the postprecipitation aging period in the mother liquid, a continuous increase of the pH of about one unit is normally observed due to the continuous incorporation of carbonate into the solid releasing hydroxide. In our example, a pronounced drop in the pH value can be observed after about 30 minutes

as shown in Figure 15.3. Similar striking features were observed in the composition range of 40:60 to 90:10 after various induction times by Bems *et al.* [37].

As already mentioned, a color change from blue to green is observed after about half an hour, obviously associated with the pH drop or the increase thereafter. Aging of the initially amorphous precipitates in their own solutions is accompanied by spontaneous crystallization. This can be seen in Figure 15.4: On the left side (a) the XRD pattern of the amorphous, blue precipitate without aging is shown, that is, a sample of the precipitate was taken directly after precipitation, washed and dried. In Figure 15.4b, the XRD pattern of the crystallized green sample after aging is shown. The diffraction lines originate from Cu/Zn-malachite $(\text{Cu}_{1-x}\text{Zn}_x)_2(\text{OH})_2\text{CO}_3$ and aurichalcite $(\text{Zn}_{1-x}\text{Cu}_x)_5(\text{OH})_6(\text{CO}_3)$. High background contributions to the XRD pattern indicate that an appreciable amount of amorphous material is still present in the sample.

Bems *et al.* [37] investigated the aging period by XRD. They took samples every 3 minutes during the first half hour of aging. They found that the initial (Cu,Zn) precipitate is X-ray amorphous exhibiting only the peaks of admixed NaNO_3 . Crystallization of Zn-malachite and aurichalcite starts simultaneously, coinciding with the drop of pH value. Therefore, they concluded that the pH drop is a direct indicator of the transformation of the solid, as there were no further shifts or alternations of shape after 30 minutes.

Bems *et al.* [37] tried to formulate the solid-formation steps of copper-rich precursors based on their results obtained by thermogravimetry (TG). Similar solid-formation steps were proposed by Li *et al.* [42] for Cu precipitation. Accordingly, when Na_2CO_3 is added under pH control to an aqueous solution of $\text{Cu}(\text{NO}_3)_2$ and $\text{Zn}(\text{NO}_3)_2$, the solid formation starts with the initial precipitation of amorphous copper hydroxide, that is, this initial solid formation is not

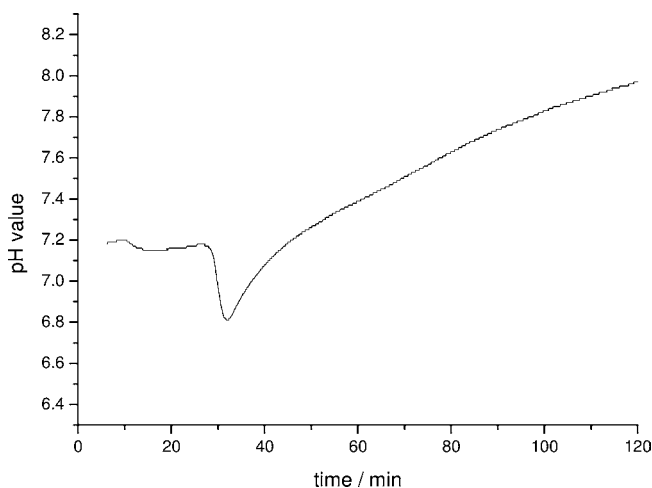


Figure 15.3 Changes of the pH value during aging of the precipitate.

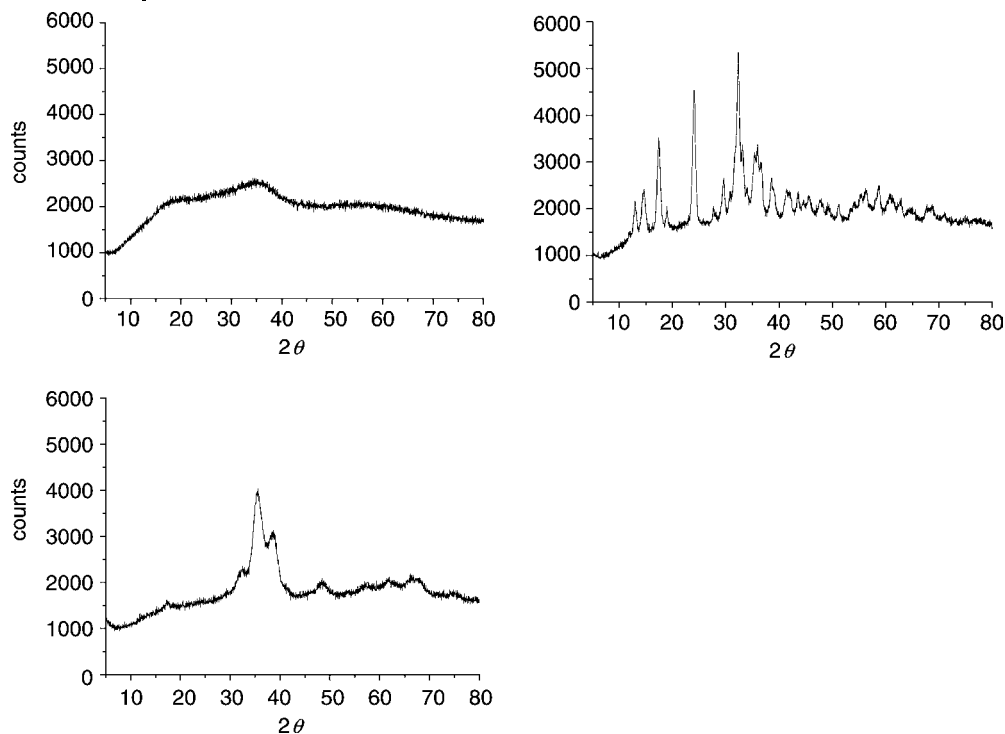
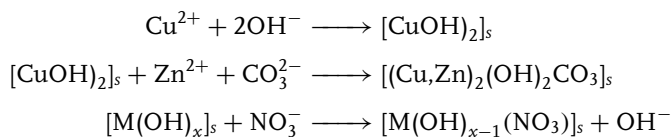
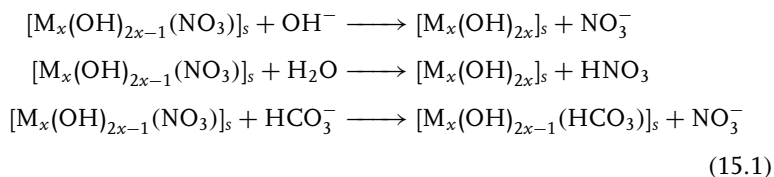


Figure 15.4 XRD pattern before (a) and after aging (b) as well as after calcination (c).

actually coprecipitation, and the kinetic effects on the complex sequence of events that are necessary to finally obtain a mixed hydroxycarbonate are of great importance to achieve active catalysts. Nevertheless, the copper hydroxide then reacts with Zn^{2+} and CO_3^{2-} to a mixed amorphous hydroxycarbonate (georgeite) having the same anionic composition as Zn-malachite. Concurrently, the more slowly solidifying zinc forms a hydroxy-rich material together with the residual Cu^{2+} ions, which is assumed to incorporate the main fraction of nitrate found in the precursors. The process of precursor formation does not stop at the end of the precipitation, but continues during the aging period. The transformations of the initial solids occur by partial dissolution/reprecipitation, for example by direct action of hydroxide or hydrolysis, leading to a removal of nitrate and an enrichment of hydroxide. Carbonate or bicarbonate can be incorporated by anion exchange in a slow reaction. Additionally, cation exchange cannot be excluded during ripening:





The reorganization of the solid eventually leads to the formation of nuclei of the two crystalline final phases Zn-malachite and aurichalcite from either georgeite or the amorphous hydroxy-rich material. During the aging period, Spencer *et al.* [36] found that the ratio of these two phases differ: aurichalcite, which is less stable than Zn-malachite, dissolves to some extent, whereas the amount of the more active Zn-malachite increases. The modifications of structural, optical, and thermal properties during the aging period influence the activity of the resulting catalyst significantly.

15.2.3

Washing

The number of washing steps and the amount of water influence the catalytic activity. Therefore, it is necessary to pay attention to carefully remove nitrate as well as sodium completely, and to prevent the precipitate from reprecipitating, forming a sol. In particular, the removal of nitrate is a crucial point. Nitrate, occurring as NaNO_3 or gerhardtite, is known to lower the activity of the final catalyst because of enhanced sintering of the final Cu particles due to the abruptly occurring decomposition of residual Cu nitrate. Bems *et al.* [37] investigated the change of the anionic composition regarding hydroxide and carbonate and found that the XRD patterns change with each washing step, although the removal of crystalline NaNO_3 is completed after the first washing step. Another unexpected negative effect of nitrate impurities is that nitrate inhibits the formation of the so-called high-temperature carbonate (HT-CO_3), which is assumed to play an essential role as “glue” between copper and zinc oxide [37]. In our example, NaNO_3 or gerhardtite were not found by XRD, and sodium was not detected either by elementary analysis.

15.2.4

Drying and Calcination

Calcination transforms basic carbonates into oxides by endothermic processes. (Cu,Zn)-hydroxycarbonates are identified as especially adequate precursor phases, which transform into a mixture of oxides. To gain more insight into the transformations, which depend mainly on composition (phases), but also on crystallite size and the chosen conditions, the calcination process can be

monitored by differential thermal gravimetry (DTG). The DTG and mass spectroscopy (MS) traces during thermal decomposition of our example are shown in Figure 15.5.

Two pronounced peaks at 567 and 727 K and two small shoulders at 341 and 444 K were found by DTG. The effluent gas was analyzed by quadrupole mass spectroscopy (QMS). The mass traces of H_2O , CO_2 , NO , and NO_2 are also shown in Figure 15.5 (right y-axis). Mass traces 30 and 46 indicate the absence of NO and NO_2 as expected. The small peak at 341 K originates from water only. The small peak at 444 K and the pronounced one at 567 K are due to a simultaneous release of water and CO_2 . For the pronounced peak at 727 K, the decomposition temperature is above the temperature used for the calcination, which means that this phase must still exist in the working catalyst. Mass spectroscopic analysis of the effluent gas flow indicates that this peak is caused by the release of CO_2 only. This species was also found by Bems *et al.* [37] who introduced the name HT-CO_3 due to its high thermal stability. The authors suggest a correlation with the existence of aurichalcite in the sample. As the DTG of aurichalcite revealed only one sharp decomposition peak at 675 K, a phase similar to aurichalcite or kinetic hindrance of some occluded carbonate was proposed. However, the XRD pattern only revealed ZnO and CuO in the calcined samples. Schur *et al.* [44] claimed that this HT-CO_3 species correlates with high dispersion and thus high activity. In contrast to Bems *et al.* [37] we identify small amounts of zincian malachite at $17.8^\circ 2\theta$ in the XRD pattern (see Figure 15.4c). Similar to our example, Baltes [50, 51] also identified small amounts of Zn-malachite after calcination and detected high activities for those malachite-containing calcined catalysts.

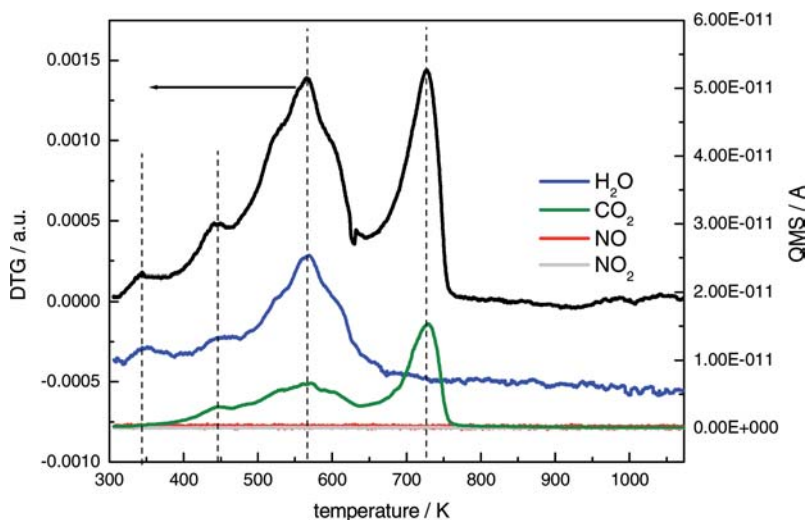


Figure 15.5 DTG and MS traces of the binary sample $\text{Cu/Zn} = 70/30$. Conditions: synthetic air, heating rate 2 K/min.

The BET (Brunauer-Emmett-Teller) surface area after calcination was found to amount to be $98 \text{ m}^2/\text{g}$. The surface area is therefore in the typical range of ternary industrial catalysts, which are between 60 and $100 \text{ m}^2/\text{g}$.

15.2.5

Reduction

The activation of the catalysts occurs by careful reduction of the Cu component (CuO), which is reduced to metallic Cu, whereas Zn and Al remain as oxide(s), independent of whether the reduction is performed in diluted H_2 or in synthesis gas. Industrially, the reducing gas (pure H_2 or make-up gas from the synthesis gas preparation) is diluted with inert gas (maximum 2–4% reducing gas) in order to limit the adiabatic temperature rise, which may cause Cu particle sintering. The catalyst is heated to 450 K at low pressure and high space velocity, then H_2 is introduced. Finally, the temperature is raised to 490 – 510 K . As the reduced catalyst is pyrophoric, the reduction procedure is usually performed in the reactor [2].

To investigate the reduction process, temperature-programmed reduction (TPR) can be performed. The TPR profile of our sample is shown in Figure 15.6. The features of the TPR profiles providing information about the catalyst are the peak positions, areas, and peak widths. Generally, it is beneficial when the reduction starts at low temperature to minimize particle growth. Reduction of CuO in binary catalysts is retarded compared to pure CuO [52–54].

The ratio of CuO in the calcined sample can be derived from the amount of hydrogen consumed using the peak area for a given stoichiometry of

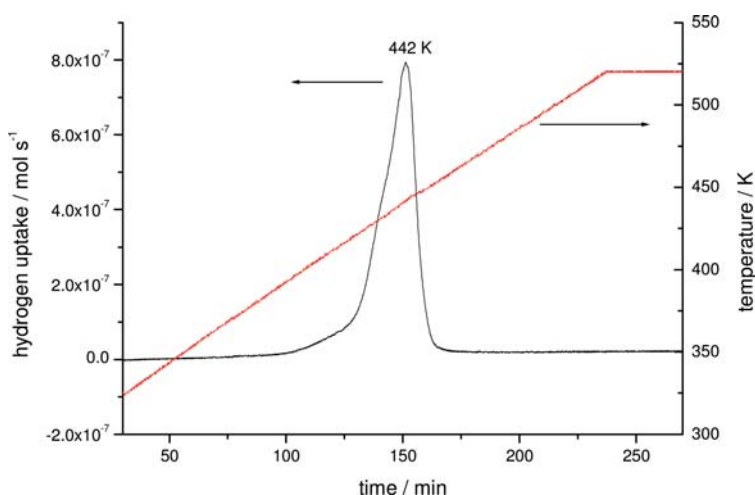


Figure 15.6 TPR profile of Cu/Zn = 70/30; conditions: heating rate 1 K/min , $4\% \text{ H}_2$ in argon.

the reduction reaction ($\text{H}_2:\text{CuO} = 1:1$). In our example, 63 wt% CuO was calculated instead of 69.5 wt% expected. A possible explanation is the remaining small amount of Zn-malachite in the calcined sample. The copper area was obtained by N_2O RFC (reactive frontal chromatography) amounting to $22 \text{ m}^2/\text{g}$.

In our example, we did not investigate parameters such as Cu/Zn ratio, concentration of the reagent solution, pH value, and sequence of adding the precipitation/precursor solution. Regarding the Cu/Zn ratio, different ratios were found to deliver the best catalysts, for example, 75:25 [18], 70:30 [30], or about 2:1[55]. This fact alone indicates that the composition alone is not a sufficient criterion for a good catalyst. Furthermore, better catalysts were achieved, when lower concentrations of the reagent solution were applied [44]. Another parameter expanding the parameter space is the pH value during precipitation, which can be kept constant at different values. Precipitation at about neutral pH values was found to give the best catalysts by several authors [2, 37, 45]. Bems *et al.* [37] also investigated a decreasing pH method, where a hydroxy-rich material consisting of basic copper nitrate (gerhardtite) as an intermediate was identified. A higher degree of crystallinity and a higher thermal decomposition temperature were found. The differences in the microstructure were traced back to the different pathways of solid formation for the two preparation methods. At pH values below 6 hydroxynitrate was detected by Li and Inui [42] leading to low activities. Furthermore, the particle size depends on the pH value. Under acidic and alkaline conditions, large particles are produced, whereas under neutral conditions they were found to be much smaller [45].

To summarize the insights originating from our research, the aims concerning each step are listed:

- Precipitation: Small particles with homogeneous distribution of the elements in preferred composition require intimate mixing, neutral pH, elevated temperature to form amorphous precursors of small particle size.
- Aging: Depending on the temperature an optimum time (at 60°C 2 h, at 70°C about 1 h) has to be maintained, so that the phase transformations, accompanied by the color change from blue to green, can take place. Zn-malachite and aurichalcite are formed out of either georgeite or the amorphous hydroxy-rich material and are detectable by XRD.
- Washing: Nitrate and sodium have to be removed carefully to avoid the formation of components that decompose abruptly.
- Calcination: Residual Zn-malachite is claimed to be beneficial.
- Reduction: The reduction gas has to be diluted with inert gas to limit the adiabatic temperature rise, which may cause Cu particle sintering.

In the multistep preparation procedure each treatment adds to the structural characteristics of the final catalyst. The discussed parameters should lead to the two goals of the synthesis strategy: maximum copper area and maximum contact area between the metallic Cu particles and the ZnO particles.

15.3

The Role of Alumina in Ternary Catalysts

The addition of a third component, in this case alumina, leads to a huge increase of the dimensions of the parameter range. First, there are several possibilities in which form Al is added, followed by the question as to when the Al component is to be added. For the commercial production, the raw materials have to be chosen carefully regarding the impurities. In 1965 Gallagher and Kidd [11] from ICI used sodium aluminate as starting material, which was dissolved in water by adding concentrated nitric acid. Aluminum hydroxide was precipitated first, but redissolved on stirring. To the resulting solution the copper and zinc nitrate solution was added. Rasmussen *et al.* [18] used a pseudoboehmite as the source of aluminum, which is insoluble under precipitation conditions. Consequently, they found only AlOOH and no hydrotalcite phase or any other phase containing Al together with Cu and/or Zn. Cornthwaite [12] employed a two-step procedure, where first a zinc aluminate is produced, and then copper and zinc are precipitated in the aqueous suspension.

Nowadays, mostly Al nitrate salt is used, and the nitrates of copper zinc and aluminum are added simultaneously. So, the following questions have to be answered: after adding the first drops, which component precipitates first, and which compound deposits onto the first one? And what is the resulting dispersion of the component, respectively? Is it congruent precipitation? Several Al-containing phases were identified in the literature, depending on the Cu/Zn/Al ratios and the preparation conditions applied, which are summarized in Table 15.2. Mainly, they were identified by XRD after aging, washing, and drying of the precipitate, as they are amorphous directly after precipitation. The lack of any long-range order in the XRD pattern could be an indicator of high dispersion.

Table 15.2 Additional Al-containing phases identified in the precipitate of ternary catalysts. Adapted from [2].

Chemical formula	Name	References
$(\text{Cu,Zn})_6\text{Al}_2(\text{OH})_{16}\text{CO}_3 \cdot 4\text{H}_2\text{O}$	(Cu, Zn, Al) hydroxycarbonate 'Hydrotalcite-like components'	[40], [42], [46], [47]
$\text{MAl}_2\text{O}_4 (\text{M} = \text{Cu,Zn})$	Spinel	[47, 56]
$\text{Al}(\text{OH})_3 \cdot \text{Al}_2(\text{CO}_3)_3$	Scarbroite	[16]
$\text{Al}(\text{OH})_3$	Aluminum hydroxide	[40, 57]
AlOOH	Boehmite	[18]

The third component not only influences the precipitation, but also the reduction step. The rate of reduction of CuO in ternary catalysts is increased compared to pure CuO. In the presence of ZnO the reduction of amorphous CuO is retarded, whereas Al_2O_3 induces the opposite effect. This is explained by interactions between Cu^{2+} and Zn^{2+} in solid solution, whereas Al_2O_3 as support with high surface area causes a high dispersion of the copper oxide particles and therefore an enhanced reduction [50, 52, 58]. The formation of unreducible spinel (CuAl_2O_4), especially at high temperatures, has to be avoided [2]. The ultimate goal during synthesis and activation should be to maintain the high degree of dispersion of the components as long as possible, that is, segregation has to be avoided.

Due to the complexity of the system *a-priori* criteria or some indicators would be helpful to predict the properties of the final catalyst. Two characteristic

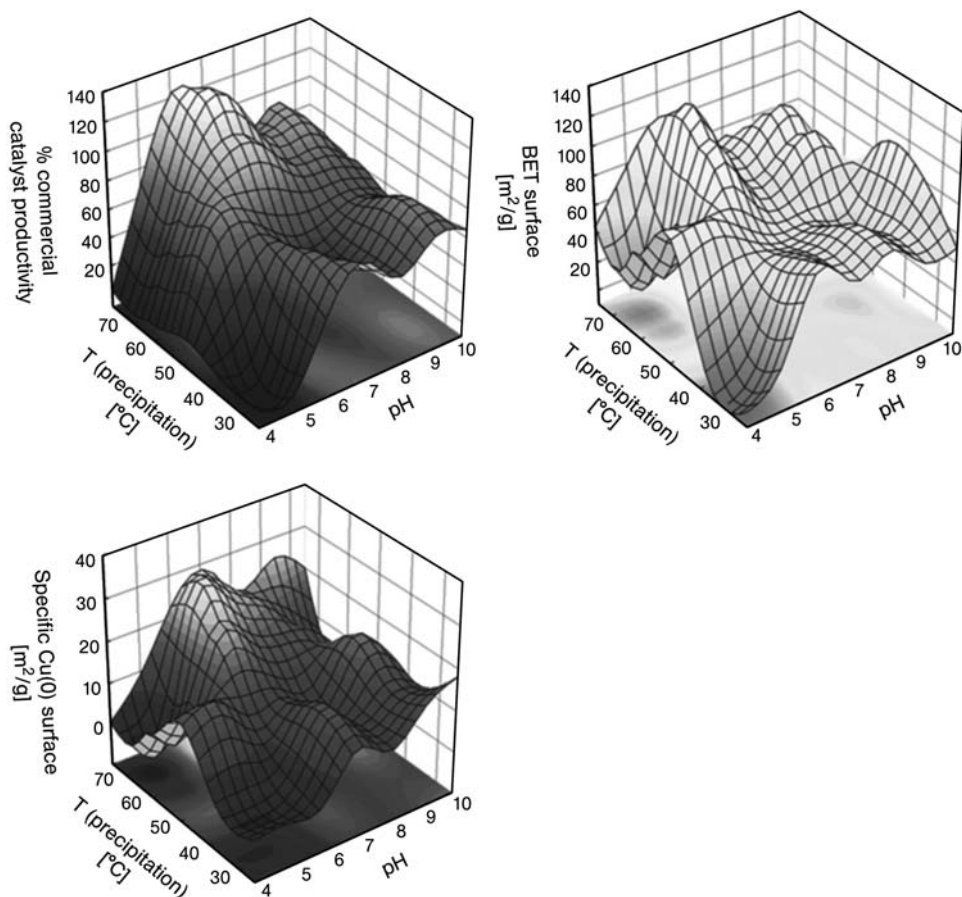


Figure 15.7 Resulting specific surface area, copper area, and activity as a function of pH and temperature of the precipitation [50, 51].

features were found to be valuable indicators: the specific surface area of the calcined catalyst, and the copper area of the reduced catalyst. This was recently shown by Baltes *et al.* [50, 51] who used high-throughput experimentation methods to investigate the whole range of precipitation parameters. Figure 15.7 shows the activity, the specific surface area, and the copper area in dependence of the preparation parameters temperature and pH value of the precipitation [50, 51].

The maxima show good coincidence with the highest BET and Cu areas leading to the highest activity. There are local maxima of the BET and Cu areas at low pH and 50 °C correlated with low productivity, because at this precipitation temperature separated Cu and ZnO particles were formed.

Baltes [50] suggested in his outlook to vary other precipitation parameter, as the nucleation process is crucial for the mixing and the interaction of the resulting active phases, which emerge out of the precipitate. For example, to perform a two-stage precipitation, where two metal compounds were precipitated simultaneously, followed by the dosing of the third metal-salt solution. The third metal would then precipitate on the already existing precipitate, providing new structural effects in the catalyst.

In comparison to binary catalysts, ternary Cu/ZnO/Al₂O₃ catalysts were found to be more active. Figure 15.8 shows the activity versus specific copper area for binary and ternary Cu-based catalysts [21]. A linear correlation between specific copper area and activity (given in methanol produced per hour and per mass of catalyst) was found for the binary as well as for the ternary catalysts. Deactivation was found to be slower for ternary catalysts.

This led the authors to the classification of the investigated Cu catalysts into three groups (families): Cu/Al₂O₃, CZ, and Cu/ZnO/Al₂O₃ differ significantly

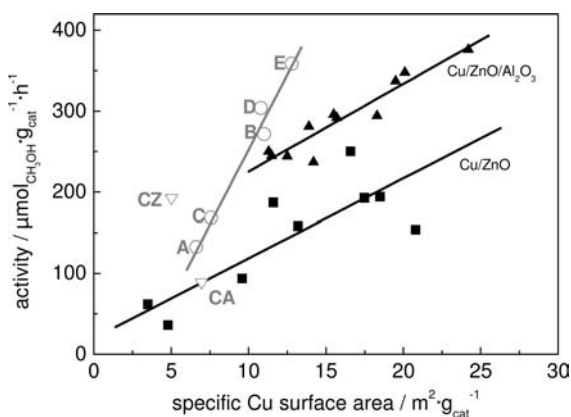


Figure 15.8 Area–activity relationship for binary (■) and ternary (▲) Cu-based catalysts [21]. The grey-colored measurements (open symbols) are discussed in Section 15.4.1. Conditions: 493 K, atmospheric pressure.

in their activity for the synthesis of methanol, while the activity is linearly correlated with the free specific Cu surface area derived from N_2O frontal chromatography within each group [60]. Alumina was clearly identified as a mandatory structural promoter to achieve high activity and stability [59, 60].

15.4

Alternative Preparation Routes

15.4.1

Alternative Anions

A promising solid-state preparation procedure aiming at an improvement of a better contact between Cu and ZnO is the so-called molten citric acid method, where citrate instead of carbonate is used. Various Cu/ZnO/ Al_2O_3 catalysts are prepared adapting the procedure developed by Courty *et al.* [61] which is described as follows: a mixture of $\text{Cu}(\text{NO}_3)_2 \cdot (x)\text{H}_2\text{O}$, $\text{Zn}(\text{NO}_3)_2 \cdot 6\text{H}_2\text{O}$, $\text{Al}(\text{NO}_3)_3 \cdot 9\text{H}_2\text{O}$, and the appropriate amount of citric acid is heated at 358 K for 2 hours to obtain a homogeneous melt. Then, it is gradually evacuated to a final pressure of 700 Pa in a rotary evaporator at the same temperature over night. During evacuation the melt transforms to a foamy solid, whereupon the volume expands by a factor of 10. After drying (383 K, 4 hours) and calcination in flowing air hygroscopic Cu/ZnO/ Al_2O_3 catalysts are obtained, which show structureless diffraction patterns, that is, these catalyst precursors are X-ray amorphous. They were further characterized by TG-DTA (thermogravimetry-differential thermal analysis) to achieve the optimum calcination temperature. The DTA (differential thermal analysis) profile originating from the decomposition in air reveals the occurrence of four exothermic transformations at 379, 448, 519, and 563 K. The TG-MS (thermogravimetry-mass spectrometry) data show that the decomposition of the amorphous solid catalyst precursor in air occurs via the following transformations: the low-temperature decomposition (363–383 K, 20% of mass loss) indicates the elimination of most of the ionic nitrates, free carboxyl groups, and water, related to the hygroscopic properties of the catalyst precursor. The CO_2 evolution during the evaporation is explained by the reaction of nitrate with the citric acid to NO , H_2O , and CO_2 . This reaction may also proceed during the first decomposition step, indicating that the precursor contained a certain amount of unreacted citric acid. The presence of the nitrate ions leads us to the conclusion that the reaction between the metal-nitrate salts and the citric acid was not completed during evacuation. During the second decomposition step (413–453 K, 38% mass loss) only CO_2 and H_2O are released, corresponding mainly to the dehydration and decarboxylation of the remaining citric acid. During the third decomposition step (453–523 K, 8% mass loss) only CO_2 is released. The high-temperature decomposition (523–573 K, 10% mass loss) indicates the oxidation of the remaining citrate (release of CO_2 and water).

Table 15.3 Results of the BET and N₂O RFC measurements [59] as a function of the different compositions of the catalysts and the temperature of calcination.

Catalyst	Composition CuO/ZnO/Al ₂ O ₃ (wt%)	BET (m ² g ⁻¹)	Cu surface area (m ² g ⁻¹)	Temperature of calcination (K)
A	65/28/07	n.d. ^b	6.6	673
B	65/28/07	n.d.	11	623
C	65/28/07	n.d.	7.6	593
D	65/28/07	n.d.	10	Four-step calcinations up to 623
E	65/28/07	44.4	13	Four-step calcinations up to 593
CZ	70/30/0	15.0	5.0	Four-step calcinations up to 593
CA	70/0/30	48.2	7.0	Four-step calcinations up to 593
CZA_coprec. ^a	65/28/07	53.7	24	593

^aCu/ZnO/Al₂O₃ catalyst, prepared by coprecipitation [2, 42, 48, 62] for comparison.

^bNot determined.

The characteristics of the calcined samples are summarized in Table 15.3. The addition of Al₂O₃ to the catalyst results in a higher BET surface area, but lower compared to the catalyst prepared by the coprecipitation (CZA_coprec.). To demonstrate the effect of the calcination on the activity, we calcined the ternary catalysts, which were synthesized by the new preparation procedure in five different steps (see Table 15.3). The correlation of the activity of the different samples and the specific copper surface area is shown in Figure 15.8. The Cu/ZnO/Al₂O₃ catalysts prepared using citric acid and calcined in one step are found to exhibit a lower catalytic activity for methanol synthesis compared to the catalysts calcined in a four-step calcination. The decomposition of the precursor is exothermic. In the one-step calcination procedure the local temperature of the CuO crystallites rises strongly, leading to a coalescence of the copper crystallites and therefore to the formation of larger Cu particles, that is, sintering is obviously responsible for the lower activity and the smaller copper surface area. Comparing the catalysts prepared by the citric acid method among each other also leads to the conclusion that a higher Cu surface area is necessary for a higher activity for methanol synthesis. The catalysts calcined in four steps show a lower specific copper surface area compared to the catalysts with a similar Cu

content made by the classical coprecipitation method. Nevertheless, comparing similar Cu surface areas they exhibit a higher intrinsic catalytic activity for the methanol synthesis. The high activity is believed to result from a strong interaction between Cu and ZnO. This could be explained by the formation of ZnO_{1-x} species at the interface between metallic Cu and ZnO leading to highly active CuZnO_{1-x} species. This investigation shows again that a high Cu surface area is necessary to get an active catalyst, but it is not the only parameter determining the activity. Comparing the ternary catalysts with the binary CZ catalyst, it can be concluded, in agreement with the results described in the previous section, that the addition of Al_2O_3 to the catalyst increases the catalytic performance.

In summary, the same conclusion can be drawn using citrate as for the ternary catalysts prepared by coprecipitation with aqueous Na_2CO_3 : the activity of a Cu/ZnO/ Al_2O_3 catalyst correlates with the copper surface area, and the larger the specific Cu surface area the higher is the activity for the synthesis of methanol.

By the use of other anions high degrees of mixing and dispersion can also be achieved. Eppele and coworkers synthesized Cu–Zn nanocomposites by thermolysis of copper–zinc cyanides. A coordination compound $\text{Zn}[\text{Cu}(\text{CN})_3]$ with both metals in the same crystal was achieved at low temperatures, whereas at higher temperatures a 1 : 1 mixture of CuO and ZnO was obtained, which can be reduced to CZ [63]. The catalytic activity in methanol synthesis of the oxides derived from precursor compounds containing Cu–Zn–CN and Cu–Zn–CN-ethylenediamine were tested. While the oxide mixture derived from $\text{Zn}[\text{Cu}(\text{CN})_3]$ was not catalytically active, the oxide mixture derived from crystalline compounds with ethylenediamine as ligand showed about 20–30% of the activity of an industrial catalyst [64]. Mixed Cu/Zn L-tartrates were then used as a precursor that contains both metals in one solid phase and decomposes at moderate temperatures because inorganic counterions such as alkali metals or carbonate were avoided. The maximum catalytic activity was found at about equimolar ratios of copper and zinc (40 mol% ZnO), although the BET surface area increases further with increasing ZnO content. The presence of this activity maximum reflects once again the interplay between Cu and ZnO and the necessity for a sufficiently high surface area [65].

An intimate mixture of CuO/ZnO nanocrystals was also obtained by a combination of sol-gel synthesis and photochemical oxidation. An easy sol-gel synthesis (precipitation in methanol by hydroxide in the presence of silane), where the organic substituents of the silane were almost completely removed by photochemical oxidation, provides an amorphous SiO_2 layer, which prevents the growth of the catalytically active particles to larger crystals. The coating layer of silica can easily be penetrated by gaseous reactants. High specific surface area (110–130 m^2/g) and good catalytic activity were achieved. The ratio of CuO to ZnO can be easily varied [66]. In another study, ZnO/ Al_2O_3 , CuO/ Al_2O_3 , and CuO/ZnO/ Al_2O_3 xerogels and aerogels were prepared by a sol-gel route using propylene oxide as gelation initiator. For aerogel preparation, the solvent was extracted with supercritical CO_2 . The aerogels revealed

a higher specific surface area and a higher Cu surface area than the corresponding xerogels, which resulted in a higher catalytic activity for methanol synthesis. The presence of ZnO significantly increased the catalytic activities of both the xerogel and the aerogel [67].

15.4.2

Chemical Vapor Deposition

Another new strategy, which allows a molecular control of the CZ interface and offers new possibilities to its maximization, is the chemical vapor deposition (CVD) technique. One approach was the combination of coprecipitation followed by CVD. Diethyl zinc (Et_2Zn) was deposited by CVD onto a coprecipitated reduced $\text{Cu}/\text{Al}_2\text{O}_3$. In spite of a small loss of Cu area, a large increase in TOF (turnover frequency) was found compared to the $\text{Cu}/\text{Al}_2\text{O}_3$, as well as an increase compared to the ternary catalysts synthesized by coprecipitation [21]. MOCVD (metal organic chemical vapor deposition) loading of mesoporous siliceous matrices (MCM-41 and MCM-48) with CZ was performed by Becker *et al.* [68] using $[\text{Cu}(\text{OCHMeCH}_2\text{NMe}_2)_2]$ as copper and diethyl zinc as zinc precursor. The specific copper areas were $5\text{--}6\text{ m}^2_{\text{Cu}}/\text{g}_{\text{cat}}$ before and after reaction. The rate of methanol production was in the range from $19\text{--}130\text{ }\mu\text{mol g}_{\text{cat}}^{-1}\text{ h}^{-1}$, similar to conventional coprecipitated binary catalysts. Both studies underline the importance of strong metal–substrate interactions, leading to highly active CuZnO_x species under industrially relevant conditions [21].

Cu-MOCVD was also performed to prepare $\text{Cu}/\text{Al}_2\text{O}_3$ model catalysts in a fluidized-bed reactor, using $[\text{Cu}(\text{OCHMeCH}_2\text{Nalkyl})_2]$ containing ethyl or propyl groups, respectively, and a commercial alumina support. Although high copper loadings up to 10% were achieved, no free copper surface area was found after reduction [69].

Hermes *et al.* [70] tried to adsorb typical metal organic vapor deposition precursors into the cavities of MOF-5 (MOF = metal organic framework). In MOF-5(Zn_4O) building blocks are linked together by terephthalate bridges to form a zeolite-like, cubic framework [71]. The catalytic activity of Cu@MOF-5 ($70\text{ }\mu\text{mol MeOH g}_{\text{cat}}^{-1}\text{ h}^{-1}$) was found to be similar to the above-mentioned $\text{Cu}/\text{Zn@MCM-41}$ and $\text{Cu}/\text{Zn@MCM-48}$ [68].

15.4.3

Promising Strategies

Advanced unit operations such as micromixing could help to gain more constant precipitating conditions. The precipitation of large quantities of materials is an ill-defined process: the chemical potentials of the reagents are neither spatially nor temporally constant, when a drop of the precipitating agent is added to the reactor, in which precipitate and dissolved ions already

exist. During aging, washing, and drying, complex exchange reactions occur, particularly between the anions. A continuous precipitation process, in which in the shortest possible time a precipitate is formed in a small volume of solution and then collected, followed by conventional processing, could be a remedy [44]. High-throughput experimentation technologies for the simultaneous screening of characterization data and the catalytic activity have proven helpful to fully control all parameters possible in a relatively short period of time. In this way, a deeper insight into these complex preparation process can be achieved [51]. *In-situ* characterization during synthesis is another highly promising approach to understand the above-described complexity [19, 72].

15.5

Conclusions

Different preparation methods and preparation conditions as well as pretreatment conditions lead to remarkable effects on the structure of the catalyst, which influence the catalytic performance. The coprecipitation methods implicate high flexibility, but entail high complexity. So, not only chemical composition, but also the preparation parameters and activation conditions determine the resulting properties of the final catalyst, which makes reproducible preparation difficult, especially when different phases are present.

There is no single criterion to predict high activity. The catalytic properties of the final catalyst are governed by the following three key criteria:

- high Cu surface (small crystallites)
- high Cu/Zn contact area (high dispersion of the structural promoter ZnO)
- efficient structural promotion by Al_2O_3 .

To fulfill these criteria, coprecipitation at well-controlled temperature and constant pH value and ideal mixing are helpful. Precipitation leads to the mixed hydroxycarbonates after the aging period, which are suitable precursors. Careful washing has to remove sodium and nitrates without reprecipitation. These hydroxycarbonates have to be transformed to the oxides, and finally a careful reduction procedure is necessary to avoid sintering of the Cu particles. The accurate performance of all these steps is crucial to finally obtain a highly active Cu/ZnO/ Al_2O_3 catalyst.

Acknowledgment

We are grateful for the financial support by the Deutsche Forschungsgemeinschaft (DFG) within the scope of our Collaborative Research Center (SFB 558) “Metal-Substrate Interactions in Heterogeneous Catalysis.” The authors thank all staff members of our department who contributed to this work, especially Lamy Khodeir, as well as Melanie Kurtz, Natalia Bauer, Hagen

Wilmer, Christoph Büscher, Thomas Genger, Stefan Kaluza, Raoul Naumann d'Alnoncourt and Olaf Hinrichsen. We thank Robert Schlögl for fruitful discussions.

References

1. American Methanol Institute (2009) www.methanol.org.
2. Hansen, J.B. (1997) *Handbook of Heterogeneous Catalysis*, Vol. 4 Wiley-VCH Verlag GmbH, Weinheim, pp. 1856–1876.
3. Hansen, J.B. and Nielsen, P.E.H. (2008) *Handbook of Heterogeneous Catalysis*, Wiley-VCH Verlag GmbH, Weinheim, pp. 2920–2949.
4. Olah, G.A., Goepfert, A. and Surya Prakash, G.K. (2006) *Beyond Oil and Gas: The Methanol Economy*, Wiley-VCH Verlag GmbH, Weinheim.
5. I.G. FARBENINDUSTRIE AG (1928) DE462837.
6. Mittasch, A., Pier, M. and Winkler, K. BASF AG (1925) Patent DE415686.
7. Lormand, C. (1925) *Ind. Eng. Chem.*, **17**, 430–432.
8. Fenske, M.R. and Frohlich, P.K. (1929) *Ind. Eng. Chem.*, **21**, 1052–1055.
9. Frohlich, P.K., Fenske, M.R. and Quiggle, D. (1928) *Ind. Eng. Chem.*, **20**, 694–698.
10. Davis, P., Snowdon, F.F., Bridger, G.W., Hughes, D.O. and Young, P.W. (1965) US 1,010,871 (ICI).
11. Gallagher, J.T. and Kidd, J.M. (1969) US 1,159,035 ICI.
12. Cornthwaite, D. (1972) US 1,296,212 ICI.
13. Hong, Z.S., Cao, Y., Deng, J.-F. and Fan, K.-N. (2002) *Catal. Lett.*, **82**, 37–44.
14. Jennings, J.R., Owen, G., Nix, R.M. and Lambert, R.M. (1992) *Appl. Catal. A*, **82**, 65–75.
15. (a) Chen, Y.Z., Liaw, B.J. and Chen, B.J. (2002) *Appl. Catal. A*, **236**, 121–128; (b) Ohyama, S. (1997) *React. Kinet. Catal. Lett.*, **61**, 331–336.
16. Cybulski, A. (1994) *Catal. Rev. Sci. Eng.*, **36**, 557–615.
17. Polarz, S., Neues, F., van den Berg, M.W.E., Grünert, W. and Khodeir, L. (2005) *J. Am. Chem. Soc.*, **127**, 12028–12034.
18. Rasmussen, B.S., Nielsen, P.E.H., Villadsen, J. and Hansen, J.B. (1987) *Preparation of Catalysts IV*, pp. 785–794.
19. Kasatkin, I., Kurr, P., Kniep, B., Trunschke, A. and Schlögl, R. (2007) *Angew. Chem. Int. Ed. Engl.*, **46**, 7324–7327.
20. Nakamura, I., Nakano, H., Fujitani, T., Uchijima, T. and Nakamura, J. (1998) *Surf. Sci.*, **402–404**, 92–95.
21. Kurtz, M., Bauer, N., Büscher, C., Wilmer, H., Hinrichsen, O., Becker, R., Rabe, S., Merz, K., Dries, M., Fischer, R.A. and Muhler, M. (2004) *Catal. Lett.*, **92**, 49–52.
22. Kanai, Y., Watanabe, T., Fujitani, T., Saito, M., Nakamura, J. and Uchijima, T. (1994) *Catal. Lett.*, **27**, 67–78.
23. Fu, S.S. and Somorjai, G.A. (1990) *Surf. Sci.*, **237**, 87–98.
24. Grunwaldt, J.-D., Molenbroek, A.M., Topsøe, N.-Y., Topsøe, H. and Clausen, B.S. (2000) *J. Catal.*, **194**, 452–460.
25. Frohlich, P.K., Davidson, R.L. and Fenske, M.R. (1929) *Ind. Eng. Chem.*, **21**, 109–111.
26. Hansen, P.L., Wagner, J.B., Helveg, S., Rostrup-Nielsen, J.R., Clausen, B.S. and Topsøe, H. (2002) *Science*, **295**, 2053–2055.
27. Clausen, B.S., Schiøtz, J., Gråbæk, L., Ovesen, C.V., Jacobsen, K.W., Nørskov, J.K. and Topsøe, H. (1994) *Top. Catal.*, **1**, 367–376.
28. Ovesen, C.V., Clausen, B.S., Schiøtz, J., Stoltze, P., Topsøe, H. and Nørskov, J.K. (1997) *J. Catal.*, **168**, 133–142.

29. Topsøe, N.-Y. and Topsøe, H. (1999) *J. Mol. Catal. A*, **141**, 95–105.
30. Günter, M.M., Ressler, T., Bems, B., Büscher, C., Genger, T., Hinrichsen, O., Muhler, M. and Schlögl, R. (2001) *Catal. Lett.*, **71**, 37–44.
31. Naumann d'Alnoncourt, R., Xia, X., Strunk, J., Löffler, E. and Muhler, M. (2006) *Phys. Chem. Chem. Phys.*, **8**, 1525–1538.
32. Greeley, J., Gokhale, A.A., Kreuser, J., Dumesic, J.A., Topsøe, H., Topsøe, N.-Y. and Mavrikakis, M. (2003) *J. Catal.*, **213**, 63–72.
33. Wilmer, H. and Hinrichsen, O. (2002) *Catal. Lett.*, **82**, 117–122.
34. Wagner, J.B., Hansen, P.L., Molenbroek, A.M., Topsøe, H., Clausen, B.S. and Helveg, S. (2003) *J. Phys. Chem.*, **107**, 7753–7758.
35. Porta, P., De Rossi, S., Ferraris, G., Lo Jacono, M., Minelli, G. and Moretti, G. (1988) *J. Catal.*, **109**, 367–377.
36. Waller, D., Stirling, D., Stone, F.S. and Spencer, M.S. (1989) *Faraday Discuss. Chem. Soc.*, **87**, 107–120.
37. Bems, B., Schur, M., Dassenoy, A., Junkes, H., Herein, D. and Schlögl, R. (2003) *Chem. Eur. J.*, **9**, 2039–2052.
38. Fujitani, T. and Nakamura, J. (1998) *Catal. Lett.*, **56**, 119–124.
39. Okamoto, Y., Fukino, K., Imanaka, T. and Teranishi, S. (1983) *J. Phys. Chem.*, **87**, 3740–3747.
40. Höppener, R.H., Doesburg, E.B.M. and Scholten, J.J.F. (1986) *Appl. Catal.*, **25**, 109–119.
41. Garbassi, F. and Petrini, G. (1984) *J. Catal.*, **90**, 106–112.
42. Li, J.-L. and Inui, T. (1996) *Appl. Catal. A*, **137**, 105–117.
43. Porta, P., Fierro, G., Lo Jacono, M. and Maretti, G. (1998) *Catal. Today*, **2**, 675–683.
44. Schur, M., Bems, B., Dassenoy, A., Kassatkine, I., Urban, J., Wilmer, H., Hinrichsen, O., Muhler, M. and Schlögl, R. (2003) *Angew. Chem. Int. Ed.*, **42**, 3815–3817.
45. Spencer, M.S. (1999) *Top. Catal.*, **8**, 259–266.
46. Melián-Cabrera, I., López Granados, M. and Fierro, J.L.G. (2002) *J. Catal.*, **210**, 273–284.
47. Busetto, C., Del Piero, G., Manara, G., Trifiro, F. and Vaccari, A. (1984) *J. Catal.*, **85**, 260–266.
48. Himelfarb, P.B., Simmons, G.W., Klier, K. and Herman, R.G. (1985) *J. Catal.*, **93**, 442–450.
49. Fujitani, T. and Nakamura, J. (2000) *Appl. Catal. A*, **191**, 111–129.
50. Baltes, C. (2007) Ph.D. thesis, Ruhr University Bochum.
51. Baltes, C., Vukojević, S. and Schüth, F. (2008) *J. Catal.*, **258**, 334–344.
52. Fleisch, T.H. and Mieville, R.L. (1984) *J. Catal.*, **90**, 165–172.
53. Vong, M.S.W., Sermon, P.A. and Grant, K. (1990) *Catal. Lett.*, **4**, 15–24.
54. Ketchik, S.V., Minyukova, T.P., Kuznetsova, L.I., Plyasova, L.M., Yurieva, T.M. and Boreskov, G.K. (1982) *React. Kinet. Catal. Lett.*, **19**, 345–349.
55. Shimomura, K., Ogawa, K., Oba, M. and Kotera, Y. (1978) *J. Catal.*, **52**, 191–205.
56. Gusi, S., Pizzoli, F., Trifiro, F., Vaccari, F. and Piero, G.D. (1986) in *Preparation of Catalysts IV* (eds G. Poncelet, P. Grange and P.A. Jacobs), Elsevier, Amsterdam, p. 753–763.
57. Gherardi, P., Ruggeri, O., Trifiro, F., Vaccari, A. and Piero, G.D. (1983) in *Preparation of Catalysts III* (eds G. Poncelet, P. Grange and P.A. Jacobs), Elsevier, Amsterdam, p. 723–733.
58. Himelfarb, P.B., Wawner, F.E., Bieser, A. and Vines, S.N. (1983) *J. Catal.*, **8**, 469–471.
59. Wilmer, H., Genger, T. and Hinrichsen, O. (2003) *J. Catal.*, **215**, 188–198.
60. Kurtz, M., Wilmer, H., Genger, T., Hinrichsen, O. and Muhler, M. (2003) *Catal. Lett.*, **86**, 77–80.
61. Courty, P., Ajot, H., Marcilly, C. and Delmon, B. (1973) *Powder Technol.*, **7**, 21–38.
62. Herman, R.G., Klier, K., Simmons, G.W., Finn, B.P., Bulko, J.B. and

- Kobylinski, T.P. (1979) *J. Catal.*, **56**, 407–429.
63. Guo, Y., Weiss, R. and Epple, M. (2005) *Eur. J. Inorg. Chem.*, 3072–3079.
 64. Weiss, R., Guo, Y., Vukojević, S., Khodeir, L., Boese, R., Schüth, F., Muhler, M. and Epple, M. (2006) *Eur. J. Inorg. Chem.*, 1796–1802.
 65. Weiss, R., Vukojević, S., Baltes, C., Naumann d'Alnoncourt, R., Muhler, M. and Epple, M. (2006) *Eur. J. Inorg. Chem.*, 4782–4786.
 66. Rohe, B., Weiss, R., Vukojević, S., Baltes, C., Muhler, R.M., Tausch, M. and Epple, M. (2007) *Eur. J. Inorg. Chem.*, 1723–1727.
 67. Guo, Y., Meyer-Zaika, W., Muhler, M., Vukojević, S. and Epple, M. (2006) *Eur. J. Inorg. Chem.*, 4774–4781.
 68. Becker, R., Parala, H., Hipler, F., Tkachenko, O.P., Klementiev, K.V., Grünert, W., Wilmer, H., Hinrichsen, O., Muhler, M., Birkner, A., Wöll, C., Schäfer, S. and Fischer, R.A. (2004) *Angew. Chem. Int. Ed.*, **43**, 2839–2842.
 69. Naumann d'Alnoncourt, R., Becker, M., Sekulic, J., Fischer, R.A. and Muhler, M. (2007) *Surf. Coat. Technol.*, **201**, 9035–9040.
 70. Hermes, S., Schröter, M.K., Schmid, R., Khodeir, L., Muhler, M., Tissler, A., Fischer, R.W. and Fischer, R.A. (2005) *Angew. Chem. Int. Ed.*, **44**, 6237–6241.
 71. Li, H., Eddaoudi, M., O'Keeffe, M. and Yaghi, O.M. (1999) *Nature*, **402**, 276–279.
 72. Ressler, T., Knief, B.L., Kasatkin, I. and Schlögl, R. (2005) *Angew. Chem. Int. Ed.*, **44**, 4704–4707.

16

Case Studies of Nobel-Metal Catalysts

Stuart Soled

16.1

Introduction

Noble-metals catalysts are widely used in catalytic conversion reactions. Hydrogenation reactions are commonly practiced over noble-metal catalysts in the refining, pharmaceutical, specialty chemical, and food industries. In hydroisomerization and dehydrocyclization reactions, which take place during, for example, lubes dewaxing and catalytic reforming, respectively, noble metals play key catalytic roles. In automotive emission control, nitrogen-oxide reduction and carbon monoxide/hydrocarbon oxidations are catalyzed by noble metals. In polymer electrolyte membrane (PEM) fuel cells, noble metals are critical for catalyzing oxygen-reduction reactions. Noble-metal catalysts often show higher activity and superior selectivity and stability versus non-noble metal systems. Their cost requires preparation techniques that utilize low loadings. When hydrogen activation is the rate-determining step, catalytic activity correlates with the number of available surface metal sites, so synthesis techniques are needed that maximize exposure of metal atoms at surfaces (i.e. optimize dispersion). The proportionality of activity with the number of metal sites assumes that all metal sites have equivalent activity, which in the absence of structure sensitivity is valid; that is, surface metal atoms on different locations of the particle have the same activity [1]. The proportionality also assumes that the reaction is kinetically controlled without transport limitations. Although perhaps less well recognized, uniformity of nanoscale metal-particle distribution (i.e. a uniform metal-particle size distribution with maximum metal-particle separation) can be an important factor in minimizing coalescence and thereby maintaining the initial high site number, a concept we will illustrate below. For example, when metal particles cluster in localized areas of the support, agglomeration can be a problem and stability will be poor. For most practical catalysts, as an empirical rule of thumb, the particles must be at least two to three radii distance from each other to avoid coalescence. This chapter will focus on various synthetic methods to obtain and maintain high dispersion

of supported noble-metal catalysts. This chapter is not intended to serve as a review of noble-metal catalysts but rather as an examination of some practical aspects of preparation science drawn from the author's personal experiences.

Most supported noble-metal catalysts are prepared from their metal precursor salts, added either by incipient wetness or cation exchange and then dried and calcined to create the corresponding oxide or the metal itself (since at temperatures below 500 °C, some noble-metal oxides such as those of Pt and Au decompose to the metal). With impregnated catalysts, the interaction strength between the metal precursor and support influences reducibility and dispersion of the supported noble metal. Often, a moderate precursor–support interaction works best, allowing the metal precursor to spread out and disperse on the support but avoiding very strong metal precursor–support interactions that prevent facile reduction. Base-metal catalysts are substantially less expensive than noble-metal catalysts but they usually have lower site activity. As result, their loadings are much higher than supported noble metals, and therefore they contain metal particles much larger (>10 nm) than those found in lower-loaded noble-metal catalysts (1–3 nm).

16.2

Optimization of Catalyst Preparation

Several approaches are used to optimize support/metal precursor interactions during preparation. These mainly involve creating electrostatic or chemical interactions that are much stronger than the van der Waals dispersion forces that would prevail in their absence. When only physical forces are present, active components will deposit within support pores as evaporation leads to supersaturation of intrapore liquids. This process tends to form irreproducible metal-particle distributions containing local regions of closely spaced metal particle clusters in reduced catalysts – a situation that would lead to rapid coalescence. Creating electrostatic interactions between the precursor and the support requires matching the charge of the species in the impregnation solution with an opposite charge on the support surface. This approach has been widely used [2, 3], and we will show another example here for one of our experimental supported Pt catalysts. A second method of modifying the support–impregnate interaction involves creating strongly interacting “complexes” between the support and the active components in the impregnation solution [4, 5]. The use of a water-soluble organic compound (e.g. acids or polyols) in the impregnation solution often allows these complexes to form. This approach is illustrated in this chapter for the preparation of well-dispersed supported Ru catalysts on silica, in which organic complexes are used to wet the support. In this case, the specific complexes used also avoid the formation of mobile ruthenium oxides during the preparation process.

16.2.1

Electrostatic Interactions and the Use of Zeta Potential Measurements

Small metal-oxide particles, the elementary components of conventional support materials, lower their surface free energies by terminating surfaces with the lowest possible charge, which normally means the surface is terminated with oxygen. However, this would create a stoichiometry richer in oxygen than the (crystallographically imposed) bulk stoichiometry. For example MeO_x would become $\text{MeO}_{x+\delta}$, where δ becomes larger as the metal-oxide particle size decreases. This enrichment in oxygen relative to the metal cations often is energetically unfavorable. Nature rather accommodates an enhanced O/M ratio by conversion of the terminating oxygens into hydroxyls [6], which effectively lowers the surface anion charge from -2 to -1 . Consequently, the surface of oxide supports contains hydroxyl groups, some of which on calcination may condense with release of water. This condensation creates bridged oxygen anions or coordinatively unsaturated metal cations but it maintains the neutral charge of the metal oxide (or more correctly, metal oxyhydroxide) particle.

When the small support particles are in contact with liquid water they no longer have to remain electrically neutral; surface charges can develop because ions in solution are available to neutralize these charges by forming a classical double layer surrounding the particle. Consequently, surface hydroxyls on oxide supports in aqueous suspension will ionize and the oxide surface develops a net positive or negative charge as a function of the pH in the contacting solution, as represented in Figure 16.1. This surface-charging phenomena can be used to advantage when preparing supported catalysts by aqueous impregnation or exchange because it provides a mechanism to adjust the surface charge to become complementary to the charge of the impregnation species. Zeta potential refers to the charge at the interface of the shear plane separating the tightly held compact layer and the more loosely held diffuse layer of the classical double layer [7]. The isoelectric point (IEP) is defined as the pH at which the zeta potential equals zero, indicating the pH at which the particles become neutral, and it reveals information about the near surface cation composition of the oxide support. Although not precisely equal to the zero point of charge on the particle surface, these two properties become essentially equal in the absence of strong specific ion adsorption, that is, when

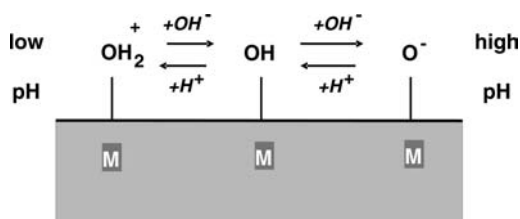


Figure 16.1 Representation of surface of small oxide support particle in aqueous suspension.

the anions in solution interact weakly with the support and do not interfere with proton equilibration reactions. At high solution ionic strength, the double layer breaks down and the surface charging does not occur by this mechanism.

At low pH (i.e. high hydronium ion concentrations), the equilibrium (Figure 16.1) shifts to the left so the concentration of protonated, positively charged $M(OH_2)^+$ species increases (i.e. the surface becomes positively charged). At high pH (low hydronium ion concentration), negatively charged surface species MO^- are in excess. At a specific pH for each solid, small but equal amounts of $M(OH_2)^+$ and MO^- coexist, and $M(OH)$ is the most abundant surface species; this represents the isoelectric point. Consequently, the zeta potential is positive at pH values below the isoelectric point and negative at pH values above the isoelectric point. The IEP gives information about the chemical nature of the metal oxide support because oxides containing cations with high charge to radius ratio (e.g. Si^{4+}) have low IEP and oxides with lower charge-density cations have higher IEP. This occurs because at high charge densities (e.g. for Si^{4+}) a large driving force (low pH) is required to protonate the OH group as it is close to the small and already highly charged Si^{4+} cation. In other words, a protonated OH_2^+ on silica (if it were even to exist) would donate its proton to a solution at low pH. For those of us in catalytic research this is an interesting phenomenon because it shows that silica suspended in aqueous slurry is acidic, whereas in normal heterogeneous catalysis practice, silica acts as a nonacidic inert support in gaseous environments typical of most catalytic reactions. In contrast, Al^{3+} cations have a lower charge than Si^{4+} and are also larger than tetravalent Si; consequently, its protonated form is more stable and alumina has a much higher isoelectric point (~ 9). Ti^{4+} has the same charge as Si^{4+} but with a much larger radius; hence titania is much easier to protonate and it shows an isoelectric point between 6 and 7 [8]. In this way, we can estimate the average near-surface population of the cations for mixed oxide supports as the measured IEP reflects a molar average of the individual metal oxide IEPs.

During the last 15 years, simple to operate laboratory instrumentation to measure zeta potential has evolved, so these measurements are now relatively inexpensive and straightforward. Most of these instruments measure the acoustic signal created when the double layer around small particles is distorted when the suspended particles are placed in a megahertz ac electric field. Another commonly practiced method of monitoring surface charge on small oxide particles involves measuring the buffering action of surfaces as they are exposed to solutions of changing acid or base concentration [9]. This approach is described by John Regalbuto in Chapter 3 of this book.

16.2.2

Noble-Metal Impregnation Example onto a Modified Silica-Alumina Support

Proper matching of the support surface charge with that of the active complex in the impregnating solution can maximize their electrostatic attraction and

lead to smaller metal particles upon reduction. This approach was elegantly reviewed in 1978 by Brunelle [10]. Our studies have attempted to apply this approach to the synthesis of Pt clusters on modified silica-alumina supports. The motivation behind the study was to examine if the acidity of amorphous silica-alumina could be tempered and brought into the range of the weaker acidity of chlorided or fluorided alumina by the dispersion of rare-earth and yttrium oxide surface coatings onto the silica-alumina [11]. Supports with this range of intermediate acidity are often used in bifunctional reactions, that is in conjunction with a supported metal, where the metal allows dehydrogenation and hydrogenation reactions and the solid acid is effective in isomerizing the olefins formed by paraffin dehydrogenation. To examine the bifunctional catalysis we needed to incorporate dispersed platinum on these modified silica-alumina supports.

The isomerization of 2-methyl-2-pentene was used as a probe reaction to monitor changes in acid-site strength of the oxide-modified supports [12]. The amounts of the different isomer products formed during the reaction provide a sensitive diagnostic for small changes in acid strength. The trivalent rare-earth oxides and yttrium oxide are mildly basic and disperse readily onto the silica-alumina surface [11]. Since they are trivalent with large cations they have isoelectric points above 11 [8]. In Figure 16.2 we show how increasing yttria content on an amorphous silica-alumina support (55 wt% SiO_2 and 45 wt% Al_2O_3) led to an increase in both the isoelectric point and the hydrogen chemisorption uptakes (when Pt is impregnated from a chloroplatinic acid solution). The IEP represents an average surface state, so that below monolayer coverage we measure a contribution from both the silica-alumina and the yttrium oxide. The dispersion of the platinum impregnated onto the modified silica-alumina catalysts was measured by hydrogen chemisorption uptakes at 40 °C by the classical volumetric technique [13]. The strong hydrogen chemisorption uptake (using a H/Pt adsorption stoichiometry of 1 : 1) derived from the difference between the total and back adsorption isotherms, was used

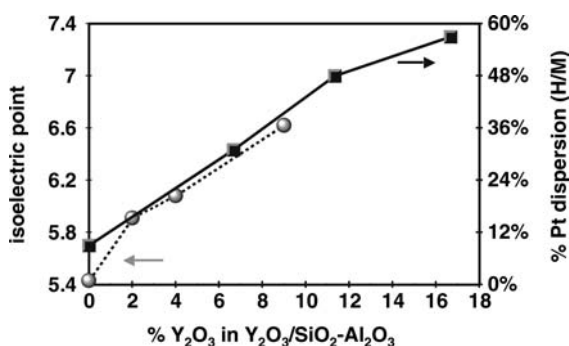


Figure 16.2 Change in isoelectric point (circles) and % Pt dispersion (squares) as a function of yttria addition onto amorphous silica-alumina.

to estimate the number of surface Pt atoms. This dual adsorption technique corrects for multilayer hydrogen adsorption and also for hydrogen weakly adhering to the support. With increasing yttria content, the surface becomes more positively charged at a given pH. As expected, the interaction of the anionic solution species (PtCl_6^{2-}) with the positively charged yttria-containing surface produces a higher dispersion of Pt metal particles on the support. This allowed for interesting bifunctional hydroisomerization of longer-chain paraffins [14].

16.2.3

A Novel Approach for the Preparation of Dispersed Ru on Silica

In a different problem, our objective was to prepare well-dispersed and homogeneously distributed Ru crystallites on a nonacidic support, such as silica. We knew that with silica supports, most metal ions adsorb weakly and that deposition of metal salts during drying from a supersaturated solution in a retreating meniscus will lead to nonuniform precipitation, making reproducible preparations difficult. There are several alternative ways of doing this preparation more effectively. Using electrostatic interaction would involve taking a high-pH solution of $(\text{NH}_3)_6\text{RuCl}_3$ and exchanging onto the (negatively charged) silica surface [15]. That would place a cationic form of Ru on the negative silica surface. Another approach involves the homogeneous precipitation by urea hydrolysis as pioneered by Geus [16] and applied specifically to supported Ru by de Jong *et al.* [17].

We chose instead to use strongly interacting Ru complexes that disperse well on silica and then exploit the strong hydrogenolysis activity of Ru metal to reductively decompose the complex. Since this will be an autocatalytic process the incipient introduction of the first metallic Ru sites will produce a rapid cascade of reduced Ru. Introducing water-soluble organics into impregnation solutions to induce complex formation is often practiced when a particular support has a weak affinity for the desired metal ions. For example, cobalt oxide on silica prepared by calcining impregnated cobalt nitrate species forms large clusters that easily reduce at 350–375 °C and create large Co crystallites (>15 nm) [18]. However, if citric acid is added to the impregnation solution, the supported oxide formed on calcining the complex interacts so strongly with the surface, that it requires temperatures approaching 600 °C to reduce [19]. In addition, silica-supported Ru catalysts present specific problems in that ruthenium oxide is mobile; therefore, it is advisable to avoid its formation in the process of creating metal clusters. For the Ru on silica catalysts studied here we used bifunctional water-soluble organics, specifically those containing amino groups together with either hydroxyl or carboxylate groups. Amino alcohols had been previously reported as additives in catalyst preparation for Fe–Mo-supported oxidation catalysts [20]. We hypothesized that amino groups might act as coordination sites for Ru and the hydroxyl or carboxylate

group could coordinate with the silica via condensation reactions leading to anchoring of Ru species to silica surfaces. Based on our unpublished studies with other supported catalysts, we had observed that monofunctional organic acid or polyol dispersion aids, while helping to form smaller metal crystallites, often created inhomogeneous nanoscale distributions. Among the bifunctional additives we investigated were the amino alcohol triethanolamine (TEA) and the aminoacid arginine (ARG).

We found that Ru-TEA and Ru-ARG impregnates decompose in a discrete multistep pattern, in which the impregnate converts into a more N-rich secondary complex that provides the starting point for reduction of Ru centers in these materials. This complex disperses well on silica and avoids the mobility problems associated with ruthenium oxide; it is also easily removed via hydrogenolysis reactions effectively catalyzed by Ru metal centers. In essence, this pathway allows *in-situ* formation of metalorgano complexes via thermal treatment with simple organic reactants. This approach does not require anaerobic conditions or unstable intermediates and differs from more conventional coordination chemistry techniques, which can use difficult to handle complexes such as carbonyls [21] or diphenylphosphines [22]. By reducing the Ru complex prepared from the partial decomposition of ARG or TEA impregnates, we obtain 1.2–1.5 nm Ru crystallites homogeneously distributed on the silica as demonstrated by chemisorption and TEM data shown below. This homogeneous distribution stands in sharp contrast to the distribution found using traditional aqueous-only impregnation procedures and it leads to enhanced resistance to reductive sintering. This approach is particularly well suited for metals with strong hydrogenolysis activity and whose oxides are mobile (Ru, Ir).

Figure 16.3 shows the gravimetric and heat changes for a 0.5% wt. Ru on SiO₂ triethanolamine-impregnate as it is heated in air. The multistep

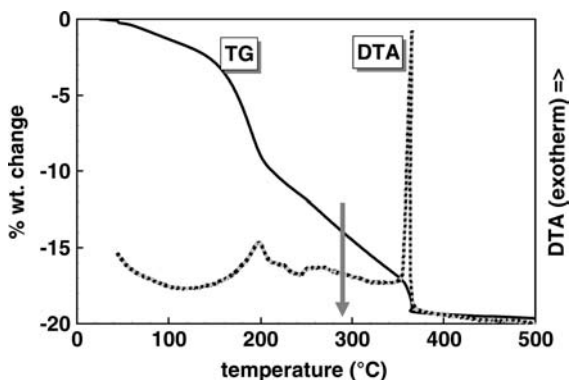


Figure 16.3 TG/DTA in air of 0.5% Ru/SiO₂ using triethanolamine impregnate – dried at 100°C. The arrow indicates the temperature to form the intermediate calcined state – that is, complex.

decomposition pattern contains three discrete exothermic regions. Some of the weight loss below 200 °C corresponds to the loss of excess TEA, as also seen with neat TEA/SiO₂. However, in that regime, an exothermic rather than endothermic event occurs, as expected from the simple evaporation of the TEA molecules. Clearly there is oxidative loss of hydrocarbon species even at this low temperature. The complex formation takes place at 200–300 °C as the sample traverses the first two exothermic events. During this treatment about 70% of the organic content is lost. By chemical analysis, the complex at this point contains C : H : N in a ratio of 2.7 : 8.5 : 1 indicating a higher relative nitrogen content than is present in the impregnate (6 : 15 : 1). The strongly exothermic decomposition around 370 °C represents the complete oxidation of the complex and is accompanied by evolution of water, carbon dioxide and nitrogen dioxide, consistent with the elemental analysis. This TGA-MS result is presented in Figure 16.4. Nitrogen complexation of the metal appears critical for forming such a high-temperature-stable metal-oxo-complex since non-N-containing complexes oxidize at substantially lower temperatures. The arrow in Figure 16.4 indicates the intermediate calcination point used to create the *in-situ*-formed complex.

The infrared spectra in Figure 16.5 show the genesis of the complex as it is formed from dried 0.5% Ru-TEA/SiO₂ impregnates. During thermal treatment in air, the overall intensity of C–H signals at 2920–2955 cm⁻¹ decrease, consistent with the loss of organic ligands. We do not observe any C_{sp2}–H vibrations at 3000–3100 cm⁻¹, indicating that no olefinic or aromatic hydrocarbons are present. We also do not observe any N–H stretches around 3100 cm⁻¹, indicating the absence of primary or secondary amines. Heating to 275 °C produces both carbonyl signals and a band at ~2290 cm⁻¹, characteristic of nitriles. This suggests that nitriles form during the final stages of TEA decomposition and form part of the Ru complex.

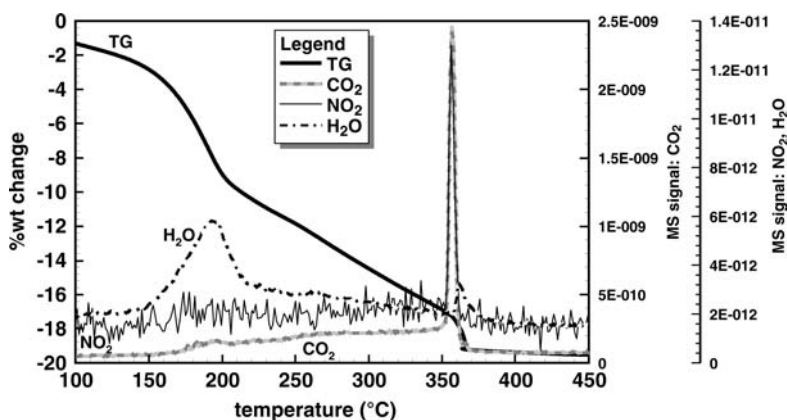


Figure 16.4 TGA-MS in air of 100 °C dried 0.5% Ru-TEA/SiO₂ impregnate.

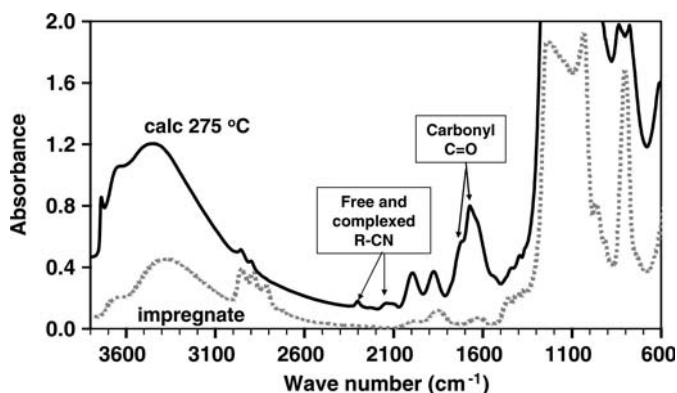


Figure 16.5 FT-IR spectra of 0.5% Ru-TEA/SiO₂ impregnate and calcined intermediate.

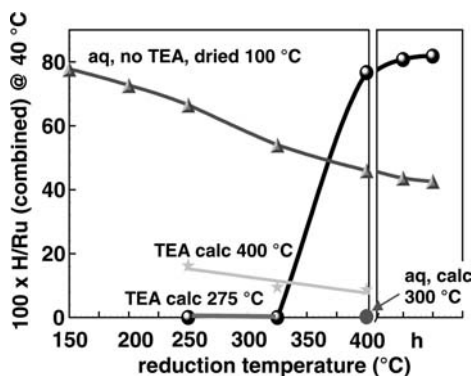


Figure 16.6 Ru dispersion ($100 \times \text{H/Ru}$, total isotherm) measured on 0.5% Ru/SiO₂.

Figure 16.6 compares H₂ chemisorption data for 0.5% Ru on Davisil 646 silica (270 m²/g) catalysts prepared via impregnation with an aqueous solution of Ru-nitrate either dried at 100 °C or calcined at 300 °C, as well as samples prepared with solutions containing TEA. The latter have been heated in air both at 275 °C to form the complex and 400 °C to form the oxide. High chemisorption values (>80%) were obtained on reducing either the aqueous sample that is dried at 100 °C or the TEA impregnate that is calcined at 275 °C. (For the lower surface area Davison 663 silica (80 m²/g) we measured a maximum dispersion of 68% for the TEA sample calcined at 275 °C.) The aqueously prepared, 100 °C dried sample had its highest chemisorption value after reduction at 150 °C, a temperature sufficient to reduce Ru oxide. Higher-temperature reductions of this sample consistently decreased chemisorption uptakes. If rather than drying at 100 °C, the sample is calcined at 300 °C, chemisorption uptakes become essentially undetectable. In contrast, the sample prepared from the partially decomposed impregnate does not give measurable chemisorption uptakes until reduction temperatures exceed 325 °C. This is consistent with

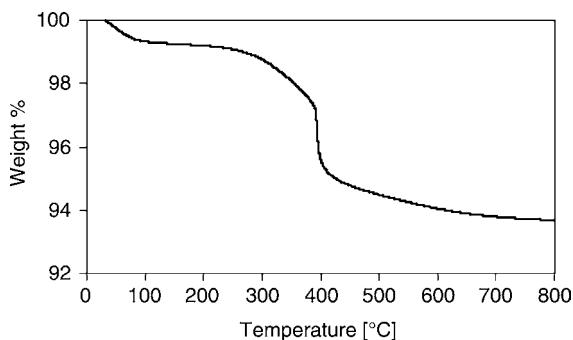


Figure 16.7 H_2 reduction of the 0.5% Ru-TEA/ SiO_2 impregnate after it is calcined at 275°C .

its TG reduction profile (see Figure 16.7) and the XANES and EXAFS results (not shown here) that indicate reduction of this complex begins above 325°C . The high temperature required for reduction of this Ru complex relative to supported RuO_2 reflects the strong interaction between the complex and the silica support. Most noteworthy is that the chemisorption of the Ru sample prepared from the complex does not decrease during sequential treatments in H_2 for 3 hours at 400°C , in sharp contrast with samples prepared by aqueous impregnations without organic complexes. Also, full oxidation of the organic complex at 400°C gives a sample with a lower but detectable chemisorption uptake. The surprising but dramatic difference in stability against reductive agglomeration starting with Ru particles of approximately the same size suggested a critical structural difference between the catalysts.

We used an *ex-situ* TEM reduction procedure to understand these distinctly different behaviors toward reductive sintering. Samples were crushed into pieces ($<0.1\ \mu\text{m}$ thick), dusted onto standard holey-carbon-coated TEM grids, and examined in bright-field TEM imaging mode using a Philips CM200F instrument. The same Ru crystals were examined following *ex-situ*-reduction treatments using a special cell that allows inert transfer to the microscope and viewing of the same sample area. The TEM micrographs provide compelling evidence to rationalize the different behaviors observed in the chemisorption results. As seen in Figure 16.8, the Ru crystallites produced from reduction of the complex are small and homogeneously distributed on the silica support. They remain in this morphology during successive reduction treatments as shown. The Ru crystallites in the aqueous prepared catalyst, although small, cluster together in “graveyards” on the silica surface, so when the sample is exposed to a higher reduction temperature, the clustered Ru crystallites coalesce into larger particles.

Some of the supported Ru catalysts were evaluated for phthalate hydrogenation activity [23]. The reaction is shown in Figure 16.9. Ru selectively hydrogenates the aromatic ring of the phthalate ester and this reaction offers a route to an alternative plasticizer precursor for polyvinyl chloride polymers.

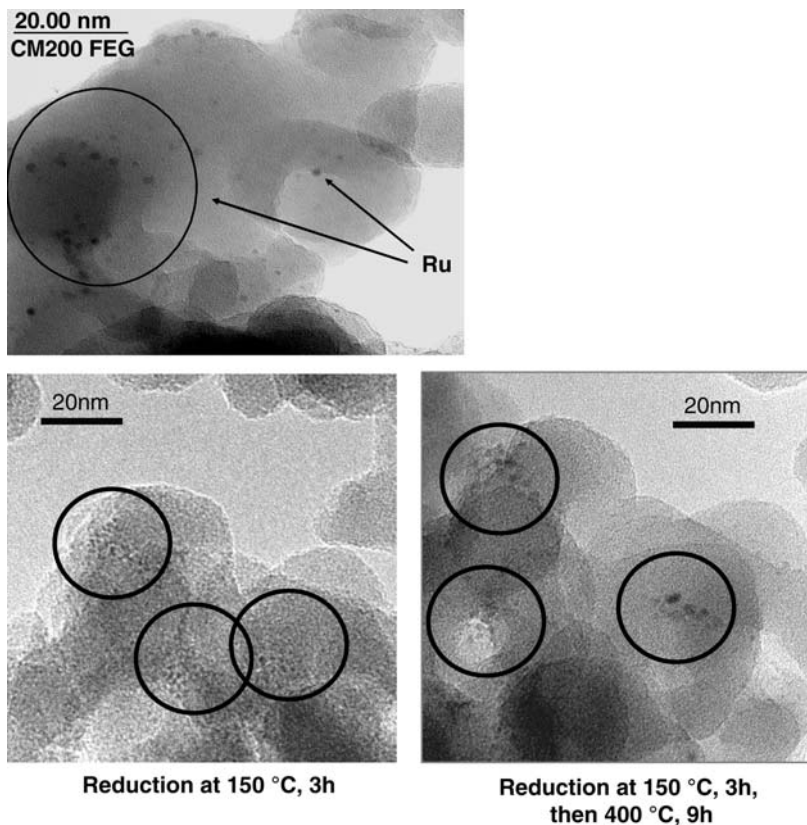


Figure 16.8 TEM of Ru complex on silica reduced at 400 °C for 9 hours (top) compared to aqueous preparation reduced first at 150 °C 3 hours (bottom left) and then 400 °C 6 hours (bottom right).

All the samples shown in Figure 16.9 contain 0.5% Ru so the dispersion on the x -axis is proportional to the number of surface metal sites. The phthalate hydrogenation reaction is well behaved with activities proportional to the number of metal sites – a phenomenon that occurs when there is no structure sensitivity nor any transport restrictions nor issues with aromatic adsorption on acid sites controlling hydrogenation rates. The most active sample is the one produced from the 400 °C reduction of the partially decomposed Ru impregnate.

16.2.4

Other Metals that Form Similar Supported Complexes as Ru

Clearly, the novel feature of the Ru on silica catalyst system described here involves forming a surface complex by partially decomposing the TEA or ARG

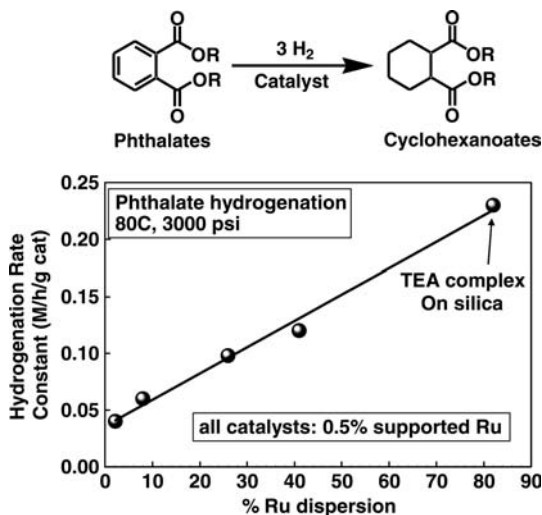


Figure 16.9 Phthalate hydrogenation by different 0.5% Ru-supported samples. The highest activity sample is the 0.5% Ru (TEA) on SiO₂ calcined at the intermediate decomposition temperature of 275 °C and reduced at 400 °C.

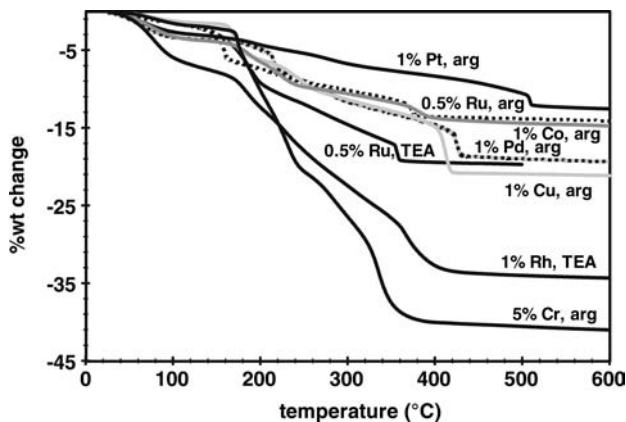


Figure 16.10 TG oxidation in air for transition-metal TEA or ARG oxo-complexes on silica.

impregnate. The thermal decomposition has a characteristic multistep pattern with the final oxidation of the carbon and nitrogen occurring at temperatures above 300 °C. Interestingly, other noble and non-noble metals appear to form analogous phases, particularly on silica supports, with qualitatively similar decomposition patterns. Figure 16.10 shows that silica-supported samples of Pd, Pt, Rh, Co, Cr, and Cu have the same type of decomposition curve as the Ru

Table 16.1 H₂ chemisorption (strong adsorption) measurements of 1% Pd/SiO₂ (Davison 62) using Pd nitrate in the impregnation solution.

Solution	Calcination temperature (°C)	Reduction temperature (°C)	% Dispersion
Aqueous	350	500	3
Arginine	450	400	43
		325	51
		400	47
Arginine	600	450	46
		400	9
		450	16
		500	20
		550	16
Arginine	300	600	10

complex described above. On the sample with Pd, we are able to fully calcine the complex to the oxide, since PdO does not have the same mobility as ruthenium oxide. In Table 16.1 we show by H₂ chemisorption (the strong uptakes are presented) that this Pd/SiO₂ catalyst has high chemisorption values when made with arginine and fully calcined to remove the organic. This catalyst has higher dispersion than an analogous sample prepared from an aqueous impregnation with no arginine present. Because Pd does not have the strong hydrogenolysis behavior of Ru, its partially decomposed complex (shown in Table 16.1 for the 300 °C calcined sample) actually has lower chemisorption uptakes than the calcined complex, probably as a result of incomplete cleaning of the residue from the Pd surface. Hence, differences in the Pd and Ru oxide mobilities and metal hydrogenolysis activities show that careful attention to detail of the treatment of impregnated complexes is necessary.

16.2.5

Conclusions

We have tried to demonstrate several approaches taken from our research to obtain well-dispersed and homogeneously distributed supported noble-metal catalysts. Use of zeta potential to understand the surface charge of the support coupled with the proper choice of the impregnating species is a common approach illustrated here on a Pt on yttria-modified silica-alumina sample. Also, the use of water-soluble organics to prepare strongly interacting surface complexes was also demonstrated for Ru on silica catalysts. The approach described here avoids the formation of mobile ruthenium oxide and takes advantage of the strong hydrogenolysis activity of Ru metal to remove the

complex. The optimization of supported noble-metal catalysts continues to provide new and exciting challenges.

Acknowledgments

The author gratefully acknowledges Sal Miseo and Joe Baumgartner for their many years of help in this and other research programs and Professor Enrique Iglesia for many helpful discussions on these topics. He also thanks Andre Malek for his close collaboration on the subject of supported Ru catalysts described here. Other colleagues who are gratefully acknowledged for providing important contributions for various parts of the work described here include Gary McVicker, Chris Kliewer, Bill Wachter, Shifang Luo, Richard Schlosberg, Jose Santiesteban, and Ed Mozeleski.

References

1. Kirlin, P.S. and Gates, B.C. (1987) *Nature*, **325**(6099), 38–40.
2. Mulcahy, F.M., Houalla, M. and Hercules, D.M. (1987) *J. Catal.*, **106**, 210–15.
3. Stelzer, J.B., Nitzsche, R. and Caro, J. (2005) *Chem. Eng. Technol.*, **28**(2), 182–86.
4. Wyrwalski, F., Lamonier, J.F., Siffert, S. and Aboukais, A. (2007) *Appl. Catal., B: Environ.*, **70**(1–4), 393–99.
5. Lensveld, D.J., Mesu, J.G., van Dillen, A.J. and de Jong, K.P. (2001) *Microporous Mesoporous Mater.*, **44–45**, 401–7.
6. Soled, S. (1983) *J. Catal.*, **81**(1), 252–57.
7. Hunter, R.J. (1981) *Zeta Potential in Colloid Science. Principles and Applications*, Academic Press, New York.
8. Parks, G.A. and De Bruyn, P.L. (1962) *J. Phys. Chem.*, **66**, 967–73.
9. Regalbuto, J.R., Agashe, K., Navada, A., Bricker, M.L. and Chen, Q. (1998) *Stud. Surf. Sci. Catal.*, **118**, 147–56.
10. Brunelle, J.P. (1978) *Pure Appl. Chem.*, **50**(9–10), 1211–29.
11. Soled, S.L., McVicker, G., Miseo, S., Gates, W. and Baumgartner, J. (1996) *Stud. Surf. Sci. Catal.*, **101A**, 563–72.
12. Kramer, G.M. and McVicker, G.B. (1986) *Acc. Chem. Res.*, **19**(3), 78–84.
13. Sinfelt, J.H. (1972) *Annu. Rev. Mater. Sci.*, **2**, 641–62.
14. Soled, S.L., McVicker, G.B. and Gates, W.E. (1993) US Patent 5208200.
15. Ian, P., Blanchard, J., Fajerwerk, K., Breyse, M., Vrinat, M. and Liu, Z. (2003) *Microporous Mesoporous Mater.*, **60**, 197–206.
16. Van Dillen, J.A., Geus, J.W., Hermans, L.A.M. and van der Meijden, J. (1977) Proceedings of the 6th International Congress on Catalysis, London, Vol. 2, pp. 677–85.
17. Toebe, M.L., van der Lee, M.K., Tang, L.M., Huis, M.H., Bitter, J.H., van Dillen, A.J. and de Jong, K.P. (2004) *J. Phys. Chem., B*, **108**, 11611–619.
18. Iglesia, E., Soled, S.L. and Fiato, R.A. (1992) *J. Catal.*, **137**(1), 212–24.
19. Soled, S.L., Iglesia, E., Fiato, R.A., Baumgartner, J.E., Vroman, H.B. and Miseo, S. (2003) *Top. Catal.*, **26**(1–4), 101–9.
20. Courty, P., Sugier, A. and le Page, J.F. (1973) German Patent DE2442311.

21. Di Silvestri, F., Moggi, P. and Predieri, G. (1998) *Stud. Surf. Sci. Catal.*, **118**, 219–28.
22. Li, H., Zhang, F., Wan, Y. and Lu, Y. (2006) *J. Phys. Chem., B*, **110**(45), 22942–946.
23. Schlosberg, R.H., Santiesteban, J.G., Soled, S.L., Malek, A., Baumgartner, J.E., Luo, S., Miseo, S. and Vartuli, J.C. (2004) World Patent Application 2004046078.

17

Gold Catalysts

Catherine Louis

17.1

Introduction

As is well known, gold is the most chemically inert metal, and as such the most noble metal. However, when it is present as particles of nanosize (<5 nm), it becomes reactive. This may be due to the increasing fraction of low coordination surface sites as particle size decreases, on which, for instance, CO molecules can adsorb, and H_2 can dissociate. This may be due also to changes in the electronic properties exemplified, for instance, by the contraction of the Au–Au bond when the gold particles are smaller than ~ 2 nm [1–3].

For years, gold was considered as a poorly active catalyst. In 1987, Haruta and his group discovered that gold particles were exceptionally active in the reaction of CO oxidation at room temperature (RT) and even much below, provided that the particles were smaller than 5 nm and supported on a reducible oxide support. Since then, gold has been extensively studied, and in many other reactions. For more information, we refer to several reviews [4–6], special issues in *Applied Catalysis A* **291** (2005) and *Topics in Catalysis* **44**(1–2) (2007), and also a book on gold catalysis [7].

The small size of gold particles is a crucial parameter to obtain active catalysts, not only for CO oxidation [8–12] but for many other reactions [4, 5, 13, 14]. The methods of preparation that lead to such types of catalysts are therefore very important.

Impregnation to incipient wetness, which is the simplest method, and that can be applied to almost any kind of supports (see Chapter 4), was the first method used for the preparation of supported gold catalysts with tetrachloroauric acid or gold trichloride as precursor [15–17]. However, thermal treatments performed to form metallic gold led to large particles (>10 nm) even for low gold loading, and to poorly active catalysts [18, 19]. The formation of large particles is now known to be due to the chlorides, which promote gold particle sintering during thermal treatments [14, 20, 21].

Haruta *et al.* was the first group to develop other methods of preparation that led to the formation of small gold particles, and as a consequence to active

catalysts. The first one was coprecipitation [22–24] (Section 17.5.1), and the second one was deposition-precipitation [25, 26] (Section 17.2.4).

The goal of this chapter is to gather the methods most commonly used for the preparation of gold catalysts supported on common oxide powders. For the sake of brevity, deposition on more specific supports, such as structured mesoporous supports, zeolites, and carbon is barely reported in this chapter, and we refer to Chapter 4 of the book on gold catalysis [7]. The methods described are mainly those performed in the liquid phase. The preparations of model catalysts, that is, on films or single crystals and those of bimetallics are excluded.

The gold precursor most used for catalyst preparation is tetrachloroauric acid ($\text{HAuCl}_4 \cdot 3\text{H}_2\text{O}$) whose gold is in the oxidation state III. This is a solid, orange in color, hygroscopic, and commercially available. When it is dissolved in water, chloroauric anions hydrolyze and form hydroxo-chloro gold(III) complexes, $[\text{Au}(\text{OH})_x\text{Cl}_{4-x}]^-$. The extent of hydrolysis depends on the pH, the ionic strength [27–29], the equilibration time [30–32], and the temperature of the solution [30, 33, 34]. These results, mostly based on XAFS and Raman experiments, do not report the presence of neutral gold species, as predicted by thermodynamic calculation [35].

Before describing methods of preparation of supported gold catalysts, a few other remarks must be made. Care must be taken to avoid uncontrolled reduction of gold during the drying step or sample storage after preparation, especially when gold is supported on titania. To avoid this problem it is advised to dry the samples at RT under vacuum and to store them in a refrigerator or a freezer [36, 37] or in a desiccator under vacuum and in the dark [38]. The thermal treatments performed to reduce supported gold precursors into Au^0 often consist in “calcination” treatments in air because the instability of Au_2O_3 induces the formation of metallic gold. Finally, the question of the hazards of explosive “fulminating” gold, which is a family of ill-defined gold compounds containing nitrogen, must be addressed. Reports mention that supported gold catalysts must never be prepared with solutions containing both gold salts and ammonia because the gold–nitrogen compounds contained in dried catalysts are extremely shock sensitive, and may explode [39, 40]. Other authors using ammonia, cyanide, or urea during catalyst preparation did not report such a problem [31, 41–44]. In any case, this type of catalysts must certainly be handled with care since the chemistry of “fulminating” gold is not well known.

17.2

Preparations Involving Aqueous Solutions

17.2.1

Impregnation to Incipient Wetness

In order to attempt to solve the problem of gold sintering because of the presence of chloride, impregnation with gold salts free of chlorides was

performed. Gold acetate [21] ($\text{Au}^{\text{III}}(\text{O}_2\text{CCH}_3)_3$) or potassium aurocyanide ($\text{KAu}^{\text{I}}(\text{CN})_2$) [16, 45] led to smaller particles (~ 5 nm) than HAuCl_4 . However, gold acetate is hardly soluble in water, and when $\text{KAu}(\text{CN})_2$ is used, potassium, which is also deposited onto the support, may have an influence on the catalytic properties.

17.2.2

Anion Adsorption

Adsorption of chloroauric anions on oxide support is in principle possible, provided that the point of zero charge (PZC) of the oxide support is higher than the pH of the solution, that is the support surface is positively charged (see Table 17.1). The pH conditions are roughly the same as for impregnation with HAuCl_4 or at slightly higher pH since usually the solutions are less concentrated.

The equilibrium adsorption of gold anions on TiO_2 ($50 \text{ m}^2 \text{ g}^{-1}$) at pH ~ 2 was reached rapidly (less than 15 minutes at 25 or 80°C) [46]. The Au loading did not exceed 1.5 wt%, and after washing with water, drying, and calcination at 300°C , the average particle size was ~ 5 nm. On alumina ($100 \text{ m}^2 \text{ g}^{-1}$), 1.9 wt% of gold could be deposited with a final gold particle size of ~ 4 nm [47]. It is possible to get smaller particles after reduction at 300°C under H_2 [47]; Au/ TiO_2 and Au/ Al_2O_3 samples (1 wt%) prepared by anion adsorption at natural pH (2.3 and 2.8) contained gold particles of 2.7 and 3.1 nm, respectively, but a high level of chloride remained on the support (0.4 and 1 wt%), especially on alumina.

Ivanova *et al.* [31] performed a systematic study of the anion adsorption on alumina at 70°C , using solutions at different pH, 1.5–4.5, which were obtained by varying the HAuCl_4 concentration (10^{-2} – 10^{-5} M). At the lowest pH when AuCl_4^- was the main species, and the alumina surface was the most positively charged, the amount of gold adsorbed was also the lowest. In contrast, at pH 4.5, when the main species in solution was $\text{AuCl}_2(\text{OH})_2^-$, more gold was adsorbed (~ 2 wt%). However, after washing with water and calcination at 300°C , the gold particles were large, 10–20 nm. The same group also studied the anion adsorption on other oxides at pH 3.5 (10^{-4} M) [48]. As shown in Table 17.1 (entry 1), the Au and Cl loadings after washing with water varied with both the PZC and the surface area of the supports, and again, after calcination at 300°C , the gold particles were large.

17.2.3

Small Particles from $\text{HAuCl}_4 \cdot 3\text{H}_2\text{O}$

Whether impregnation or anion adsorption was carried out, the gold complexes deposited on oxides contain chlorides, so the gold particles are rather large

Table 17.1 Gold loading and average particle size in supported gold catalysts prepared by anion adsorption, then either washed with water or with ammonia (4 M) [48]. All samples were prepared with an aqueous solution of HAuCl_4 (10^{-4} M, pH 3.5, nominal Au loading of 2 wt%) except for silica (10^{-2} M, pH 2) and calcined at 300°C .

Support	Surface area (m^2g^{-1})	PZC	Entry 1: washing with water			Entry 2: washing with ammonia		
			Au loading (wt%)	Cl loading (wt%)	$d\text{ Au}^0$ (nm)	Au loading (wt%)	Cl loading (ppm)	$d\text{ Au}^0$ (nm)
TiO_2	40	~ 6	1.53	480 ppm	–	1.19	≤ 150	3
ZrO_2	44	6–7	1.63	0.2	–	1.56	470	3
MgO	25	~ 12	0.53	0.2	–	^a	^a	–
Al_2O_3	200	7–9	2.0	0.33	16	1.38	≤ 150	1.9
CeO_2	240	6–7	1.97	0.66	–	1.98	≤ 150	$< 4^b$
SiO_2	530	1–2	120 ppm	≤ 150 ppm	–	^a	^a	–

^a Washings with ammonia not done because of the solubility of these oxides.

^b No contrast for TEM, but no visible XRD peak of Au^0 .

after calcination. However, remedies have been proposed to eliminate the chlorides after gold deposition. Two groups, Xu *et al.* [42] and Ivanova *et al.* [31, 48, 49] reported that after preparation of $\text{Au}/\text{Al}_2\text{O}_3$ by anion adsorption, washing with ammonia solution led to the elimination of the chlorides, without a drastic decrease in the gold loading. After calcination, much smaller gold particles were obtained as a consequence of chloride removal (entry 2 in Table 17.1).

On the basis of these results, Delannoy *et al.* [44] applied this method of ammonia washing to samples prepared by incipient wetness impregnation (Table 17.2). Small gold particles (~ 3 nm) were obtained after calcination at 300°C , even on silica and more surprisingly, most of the gold was retained even for nominal gold loadings of 4 wt%. TPD-MS led to the conclusion that the gold species formed during ammonia washing is an ammino-hydroxo or an ammino-hydroxo-aquo gold cation complex $[\text{Au}(\text{NH}_3)_2(\text{H}_2\text{O})_{2-x}(\text{OH})_x]^{(3-x)+}$ and not $\text{Au}(\text{OH})_3$ or $[\text{Au}(\text{OH})_4]^-$ as proposed in [31, 42]. It was proposed that cationic gold complexes can interact with the support negatively charged during washing, and this would explain that most of the gold is retained. Delannoy *et al.* used more diluted NH_3 solutions (1 M) than Ivanova *et al.* (4 and 25 M) [31, 48], and recent unpublished results [47] showed that still more diluted solutions (0.01 M) were as efficient, and prevented support dissolution. Li *et al.* [50] proposed

Table 17.2 Gold loading and average particle size in supported gold catalysts prepared by impregnation – ammonia washing (1 M, pH = 11.5), followed by calcination at 300°C [44]. The chloride content is below 200 ppm (detection limit) in all the samples.

Support	Nominal Au loading (wt%)	Au loading (wt%)	d_{Au^0} (nm)	Standard deviation (nm)
SiO ₂	1	0.94 ^a	4.0	1.67
TiO ₂	4	3.3	3.6	0.83
TiO ₂	1	0.97	3.2	0.6
TiO ₂	0.7	0.7	3.3	0.61
Al ₂ O ₃	4	3.4	3.8	0.82
Al ₂ O ₃	1	0.97	3.1	0.63

^aNote that the same sample washing with NaOH (10⁻³ M, pH = 11) leads to the full removal of gold (0.1 wt%).

a treatment with gaseous ammonia followed by washing with water to remove the chlorides after impregnation and obtain small gold particles on titania.

An alternative to the formation of large gold particles with HAuCl₄ precursor is to use other preparation methods, such as deposition-precipitation (Sections 17.2.4 and 17.2.6): the preparations are performed at higher pH, so most of the chlorides in the gold complexes are already hydrolyzed, and thorough washing with water removes the remaining chlorides.

17.2.4

Deposition-Precipitation with NaOH

This method of deposition-precipitation is probably the most used for the preparation of gold catalysts since it readily leads to the formation of small gold particles (2–3 nm). This method was first proposed by Haruta *et al.* [25, 26]. The pH of the solution containing HAuCl₄ and the oxide support is adjusted by addition of NaOH, often 7–8 for titania or alumina. The suspension is stirred for ~1 hour at 70–80°C. The catalyst is then washed with water to eliminate as much chloride and sodium ions as possible, dried between RT and 100°C, then usually calcined in air.

This method of deposition-precipitation is suitable for oxide supports whose PZC is higher than 5, such as MgO, TiO₂, Al₂O₃, ZrO₂, CeO₂ [14, 41, 51]. It is not suitable for SiO₂ (PZC ~2), SiO₂–Al₂O₃ (PZC ~1), WO₃ (PZC ~1) [14] or for supports such as activated carbon [52] or zeolites [53] due to their high acidity.

Several remarks can be made regarding this preparation method:

- The procedure of preparation does not correspond to that of deposition-precipitation as described by Geus *et al.* [54, 55] since pH is not gradually increased (see Chapter 6).
- The choice of pH of 7–8 results from a compromise between the yield of gold deposition (which usually does not reach 100%) and the gold particle size obtained after thermal treatment. It is noteworthy that the conditions of preparation are such that the support surface and the gold complex are both negatively charged, which may question the mechanism of interaction (see Section 17.2.5).
- In addition to NaOH, Na_2CO_3 , and NH_3 have also been used to adjust pH [30, 51], and the preparation was also performed at RT [56].

pH is one of the parameters most studied for this type of preparation, below and above the PZC of the oxide support [25, 51, 56–61]. The results obtained are roughly consistent. For example, if one considers the results of Moreau and Bond who performed the most extensive study on Au/TiO₂ with a nominal gold loading of about 1 wt% [56, 58–61], they show that the gold uptake versus pH looks like a kind of volcano curve (Figure 17.1). It slightly increases as pH increases from 2 to 6, passes through a maximum at pH 6 that is the PZC of TiO₂, then decreases drastically to a very low loading at pH 12. The gold particle size does not follow the same trend since it gradually decreases as pH increases. At pH 9 the gold particles are very small (~ 2 nm) compared to those formed at pH 6 (~ 10 nm) [62]. These trends were roughly the same for gold on alumina [30, 57]. The variations in particle size are easy to explain: when pH increases, the gold anion complexes are more hydrolyzed, the number of chlorides in the gold coordination sphere decreases, and therefore sintering of the gold particles is more limited during thermal treatment (see Section 17.1). The explanation for the variation of gold uptake with pH is more puzzling

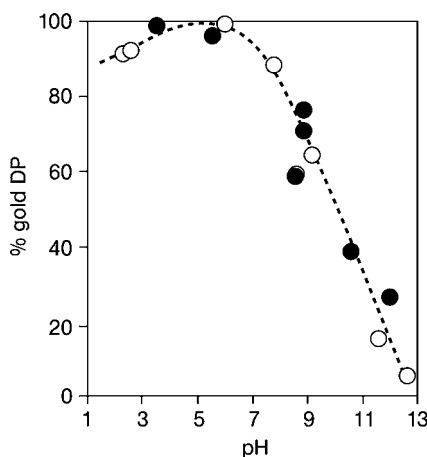


Figure 17.1 Gold uptakes on TiO₂ as a function of the pH upon addition of NaOH. (Reprinted from *Catalysis Today* [60] with permission from Elsevier.)

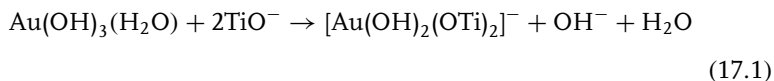
(Figure 17.1). When pH is lower than 6 (PZC), the conditions of preparation are those of anion adsorption (electrostatic interaction), so the smaller the pH, the higher the anion uptake expected (see Chapter 3); the opposite trend is observed: the gold uptake is maximum at the PZC when the surface is globally noncharged; this was also observed by Ivanova *et al.* [31] (see Section 17.2.2). Moreover, when pH is higher than the PZC, that is when the surface is negatively charged, there is still gold adsorption even though the uptake decreases.

17.2.5

Gold Complex Interaction with Oxide Supports

The explanations tentatively proposed in the literature [20, 25, 41, 61] for the variations of gold uptake with pH as shown in Figure 17.1, depend on the gold speciation that is considered. Some groups consider the presence of hydroxo-chloro anions as identified by Raman and XAFS [27–29], while others take into account the speciation deduced from thermodynamic data, that is the presence of neutral complexes, such as AuCl_3 at pH 2–5 [35] (see Section 17.1).

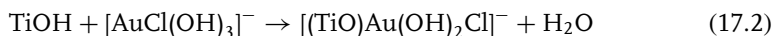
At pH above the PZC of titania ($\text{pH} > 6$) during deposition-precipitation, when the oxide surface is negatively charged and the predominant species in solution is $\text{AuCl}(\text{OH})_3^-$ and/or $\text{Au}(\text{OH})_4^-$, electrostatic attraction thus cannot take place. Haruta *et al.* [8, 25], however, proposed that $\text{AuCl}(\text{OH})_3^-$ adsorbs on specific surface sites of TiO_2 and acts as nucleation sites on which $\text{Au}(\text{OH})_3$ can precipitate. The decreasing Au loading when pH increases from 6 to 10, is attributed to the increasing solubility of $\text{Au}(\text{OH})_3$ with pH. However, there is no experimental proof that $\text{Au}(\text{OH})_3$ can precipitate under these conditions. Moreau and Bond [60, 61] proposed an adsorption of neutral $\text{Au}(\text{OH})_3(\text{H}_2\text{O})$, which may exist in equilibrium with the corresponding anion, on the oxide surface:



The decrease in gold uptake as pH increases is explained by an equilibrium between the adsorbed species and those in solution, which shifts toward the solution side as the pH is increased.

If one reconsiders the case of pH lower than the PZC of TiO_2 (conditions of anion adsorption), electrostatic adsorption of the gold anions is possible. However, the increasing gold uptake when pH increases is not consistent. The presence of neutral $\text{AuCl}_3(\text{H}_2\text{O})$ between pH 2 and 5 deduced from thermodynamic data, which may interact with the support, could explain that the gold uptake increases as pH increases and becomes closer to the PZC. Literature data in geochemistry reports the same type of observation, that is

a maximum of gold uptake as pH is close to the PZC of γ -alumina [63] for adsorptions performed between pH 4 and 10 and close to the PZC (~ 8) of goethite ($\text{FeO}(\text{OH})$) [64] for adsorptions between pH 4 and 8. Both groups also noted that this behavior is opposite to that of anion adsorption when pH is lower than PZC. They proposed a reaction between anion gold complexes and OHs of the support, leading to the formation of a surface gold complexes:



which is maximum as pH is close to the PZC because of the highest number of OH groups.

If one comes back to the case of pH above the PZC of the oxide, the decreasing gold loading as pH increases (Figure 17.1) may be due to the decreasing number of OH groups permitting the formation of surface gold complexes.

It is noteworthy that there is no direct experimental proof for any of these interpretations.

17.2.6

Deposition-Precipitation with Urea

The gradual rise in pH required in the “true” procedure of deposition-precipitation (see Chapter 6) was performed by the addition of urea ($\text{CO}(\text{NH}_2)_2$) for the preparation of gold catalysts. The procedure consists in stirring an aqueous solution containing HAuCl_4 , urea, and the oxide support in suspension, at $\sim 80^\circ\text{C}$ for a given time, then to wash the sample with water and dry it, and finally to apply a thermal treatment.

The first attempts performed were not very conclusive since large gold particles were obtained [65–67]. However, a more extensive study performed by Zanella *et al.* [41, 46] showed that small gold particles (~ 2 nm) could be obtained on various supports (TiO_2 , Al_2O_3 , and CeO_2), but not on silica (Table 17.3). All the gold of the solution, at least up to 8 wt% nominal Au loading, is deposited onto the supports within the first hour of preparation, when the suspension pH is still acidic (~ 3), then the sample “matures” while the pH of the suspension continues to increase up to a plateau at pH ~ 7 within 4 hours. The “maturation” time and the increase of pH lead to a decrease in the average gold particle size after sample calcination at 300°C (Table 17.3). Slightly smaller particles are obtained when preparation is performed at 90°C , or when the urea solution is more concentrated. When lower gold loading is required (~ 1 wt% Au), it is possible to drastically reduce the time of preparation to ~ 1 hour and to get small gold particles (Table 17.3).

Chemical analysis showed that the gold compound that precipitates on TiO_2 is close to $\text{Au}(\text{CO}(\text{NH}_2)_2)$ [41]. This compound results from a reaction between gold anions and urea or products of its decomposition, and forms only when the mixture is heated and reaches pH ~ 3 .

Table 17.3 Gold loading (DP) and average particle size in supported gold catalysts prepared by deposition-precipitation with urea at 80°C followed by calcination at 300°C.

Oxide support	PZC	Expected Au loading (wt%)	DP time (h)	Final pH	Au loading (wt%)	Cl loading (wt%)	d_{Au^0} (nm)	Reference
TiO ₂ (45 m ² g ⁻¹)	~6	8	1	3.0	7.8	0.041	5.6	[46]
			2	6.3	6.5	0.122	5.2	
			4	7.0	7.7	<0.03	2.7	
			16	7.3	6.8	<0.03	2.5	
			4 ^a	7.3	7.1	0.045	1.7	
			4 ^b	7.2	7.1	0.04	1.5	
CeO ₂ (260 m ² g ⁻¹)	~6	8	1	4.3	7.9	–	8.1	[41]
			16	6.6	8.2	–	<5 ^c	
Al ₂ O ₃ (100 m ² g ⁻¹)		8	1	4.3	6.9	–	6.9	[41]
			16	7.1	7.2	–	2.3	
		1	1	4.5	0.9	<0.03	2.2 ^d	[47]
			16	8	0.9	<0.03	2.1	
SiO ₂ (250 m ² g ⁻¹)	~2	8	1	5.2	2.9	–	>20	[41]
			16	7.0	3.7	–	>20	

^aAt 90°C.

^b0.84 M of urea instead of 0.42 M.

^cEstimation by XRD (poor contrast between gold particles and CeO₂ by TEM).

^dReduction H₂/300°C.

The chemical mechanism proposed by Zanella *et al.* [41] would first require the adsorption of anionic gold species, which is possible at the beginning of the preparation when pH is close to 2. The adsorbed gold species would act as nucleation sites for the precipitation of the gold compound at pH ~3. This method of preparation does not work properly with silica support, probably because the low PZC (~2) does not permit the adsorption of anionic gold species. The decrease in gold particle size as preparation time increases (Table 17.3) is related to a decrease in the size of the particles of gold precipitate. The increase of pH probably induces an increase in the density of negative charge at the surface of the precipitate and therefore an increase in repulsive

forces that lead to the fragmentation of the particles, according to a mechanism similar to peptization. Although the procedure of preparation is very similar to that of deposition-precipitation with a gradual increase of pH (see Chapter 6), the chemical phenomena involved are still different since all gold rapidly precipitates.

17.2.7

Cation Adsorption

Bis-ethanediamine gold(III) cation, $[\text{Au}(\text{en})_2]^{3+}$ ($\text{en} = \text{NH}_2\text{CH}_2\text{CH}_2\text{NH}_2$), first used for cationic exchange in zeolites [68, 69], was also used for cation adsorption on oxide supports. $[\text{Au}(\text{en})_2]\text{Cl}_3$ is not commercially available, but it is easy to synthesize [70]. The PZC of the oxide support must be lower than the pH of the precursor solution to make the support surface negatively charged (see Chapter 3). It is better to perform the adsorption at RT because $[\text{Au}(\text{en})_2]^{3+}$ decomposes at temperatures higher than 60°C. In Au/TiO₂ prepared at RT and pH 9, the gold loadings and particle sizes obtained after 1 and 16 hours of contact time, then washing with water, drying and calcination at 300°C were the same: 1.2 and 1.1 wt% Au and 2.5 and 2.7 nm in size [41].

This method has also been successfully applied for the preparation of gold on silica, conventional, or mesoporous (SBA-15). The particles appear smaller when they are reduced under H₂ rather than when they are calcined (Table 17.4). However, Zhu *et al.* [71] showed that the gold particles still retain residual organic compounds after reduction, and that it is necessary to proceed to further calcination at 400°C to completely eliminate them. TEM showed that the gold particles were located inside the pores of SBA-15. The same paper

Table 17.4 Gold loading and average particle size in supported gold catalysts prepared by $[\text{Au}(\text{en})_2]^{3+}$ adsorption.

Silica	Surface area (m ² g ⁻¹)	pH	Au loading (wt%)	Thermal treatment	<i>d</i> Au ⁰ (nm)	Reference
AD200	200	10.5	5.5	H ₂ /200°C	2.4	[73]
Cab-O-Sil	–	10	2.3	H ₂ /200°C and air/500°C	3.8	[71]
SBA-15	560	6.0	2.7	H ₂ /150°C and air/400°C	5.4	[74]
		7.4	7.4		5.2	
		8.5	6.9		4.9	
		9.6	9		4.9	

reports the gold speciation as a function of the pH of adsorption (6–10) as well as the gold loading, which increases with pH, and the gold particle size, which is rather constant.

$[\text{Au}(\text{en})_2]\text{Cl}_3$ was also successfully used for cation adsorption on activated carbon fibers [72].

17.3

Preparations Involving Organometallic Precursors

17.3.1

Impregnation of Phosphine-Based Gold Complexes

Phosphine gold complexes, $[\text{Au}^{\text{I}}(\text{PPh}_3)]\text{NO}_3$, and clusters, $[\text{Au}_9(\text{PPh}_3)_8](\text{NO}_3)_3$ (Au^{I} and Au^0), were first used by Iwasawa *et al.* [75] to prepare supported gold catalysts by the technique of impregnation. It was first performed in CH_2Cl_2 with oxide supports (TiO_2 , SiO_2 , and $\alpha\text{-Fe}_2\text{O}_3$), then in acetone with freshly precipitated metal hydroxides [76]. The second variant led to much smaller gold particles (~ 3 nm) after calcination than the first one (~ 30 nm) because amorphous hydroxides contain more surface OH and surface defects than the corresponding oxides, and therefore interact more efficiently with $[\text{Au}(\text{PPh}_3)]^+$ [77]. Moreover, upon calcination at 400°C , the simultaneous decomposition of the gold precursor into metal and of the hydroxide into oxide favors the gold–support interaction, and inhibits gold sintering.

$[\text{Au}_6(\text{PPh}_3)_6](\text{BF}_4)_2$ was also used for the impregnation of TiO_2 in CH_2Cl_2 (1 wt% Au) [78]. Small particles were obtained (4.7 nm) after a thermal cycle of reduction-oxidation treatment. Another series of gold organometallics has been recently used by the same group [79]: $[\text{Au}_2^{\text{I}}(\text{dppm})_2](\text{PF}_6)_2$, $\text{Au}_3^{\text{I}}(\text{Ph}_2\text{pz})_3$, $[\text{Au}_4^{\text{I}}(\text{dppm})_2(3,5\text{-Ph}_2\text{pz})_2](\text{NO}_2)_2$, and $\text{Au}_4^{\text{I}}(\text{form})_4$, (dppm = bis(diphenylphosphino)methane, form = formamidinates, pz = pyrazolate). After impregnation of 1 wt% Au under the same conditions, the average gold particles were 7.7, 4.8, 3.1, and 3.0 nm, respectively.

Another type of cluster, $\text{Au}_{13}^0[\text{PPh}_3]_4[\text{S}(\text{CH}_2)_{11}\text{CH}_3]_4$, dissolved in toluene was adsorbed onto TiO_2 (1 wt% Au) [80]. After washing with toluene, and drying at RT, the ligands were removed either by flowing ozone at RT or by calcination in air at 400°C , much smaller gold particles were obtained with ozone (1.2 instead of 2.7 nm). According to the authors, the adsorption of these Au_{13} clusters can be achieved on several high surface area supports, including carbon and SiO_2 , and with Au loadings > 1 wt%.

One advantage of using phosphine organogold complexes or clusters is that they do not contain chlorides, but one drawback is that they must be synthesized, and handled with care because of toxicity. Moreover, depending on the nature of the compounds, they are more or less stable in air and light,

but once they are supported, they become more air- and moisture-sensitive, and they must be stored in sealed ampoules.

17.3.2

Impregnation of Other Organogold Complexes

Isonitrile gold(I) nitrate, $\text{AuCNBu}^t\text{NO}_3$, was used as a precursor for the impregnation of Fe_2O_3 in acetone (3 wt% Au) [81]. After calcination at 400°C , gold particles probably smaller than 4 nm were obtained.

Haruta *et al.* [82] adsorbed di-methyl gold(III) acetylacetonate ($\text{Au}(\text{CH}_3)_2(\text{acac})$; commercial) on dehydrated oxides in acetone (equivalent to 3 wt% Au). After maturation, filtration, and calcination at 400°C , the Al_2O_3 , TiO_2 , and SiO_2 supports contained 2.8, 2.3, and 0.2 wt% Au, respectively, with average gold particle size of 6.6, 2.9, and 16 nm. According to the authors, the low gold loading on SiO_2 was due to competitive adsorption of the solvent, and the larger gold particles to weak interaction between gold acetylacetonate and silica. The same compound was used by the same group for chemical vapor deposition on TiO_2 , Al_2O_3 , SiO_2 [83], MCM-41, and activated carbon [84]. This method seems more suitable to prepare gold particles on silica since the gold particles are smaller (6.6 nm) and the gold loading higher (6.6 wt% Au). In MCM-41 structured silicas of different pore sizes, 2.2, 2.7, and 3.1 nm, the gold particle sizes were 4.2, 2.9, and 3.5 nm, respectively, after calcination at 400°C , that is smaller than on an amorphous silica, but probably obstructing the pores [84].

Gates' group has extensively used $\text{Au}(\text{CH}_3)_2(\text{acac})$ for the preparation of gold catalysts by impregnation of various supports in dried pentane or hexane: MgO [85], γ -alumina [86], TiO_2 [87], La_2O_3 [88], and Na-Y zeolites [89]. At RT, gold acetylacetonate reacts with surface OH groups of alumina and coordinatively unsaturated Al^{3+} centers, and forms $\text{AlO}_2\text{-Au}^{\text{III}}(\text{CH}_3)_2$ and $\{\text{Al}\}\text{-acac}$ species [86]. At 50°C under He, there is aggregation into gold oxide particles, then at temperatures higher than 200°C , 3-nm metallic gold particles form.

The obvious advantage of using organometallic gold precursors is that they do not contain chloride, and that any oxide support can be used. However, gold acetylacetonate is expensive, and the preparations must be performed in the absence of moisture and air.

17.4

Deposition of Gold Nanoparticles

17.4.1

Deposition of Gold Colloids

The colloidal route is an attractive strategy to prepare supported gold catalysts since metal particles of controlled size and narrow size distribution are formed

before deposition on the oxide support. The preparation consists of three main steps:

1. The preparation of the gold colloids by reduction of gold precursor, HAuCl_4 , or $\text{Au(PPh}_3)_3\text{Cl}$, in solution in the presence of a stabilizing or capping agent (thiol or amine ligands, or polymers, such as poly-vinylpyrrolidone (PVP), poly-vinylalcohol (PVA), poly-ethylene glycol (PEG) or tetrakis(hydroxymethyl)phosphonium chloride (THPC)); reduction can be performed with a chemical agent (sodium citrate, sodium borohydride, THPC) or by sonolysis or radiolysis [90]. The average size of the gold particles so-prepared and the size distribution depend on the conditions of synthesis, that are temperature, aging time, concentration, and nature of the different constituents (Table 17.5).
2. The deposition of gold is performed by dipping the support into the colloidal solution, followed by washing and drying; the colloids are generally negatively charged, so an electrostatic interaction is possible with the support. For instance, adsorption of gold colloids on titania and zirconia was performed at lower pH than the PZC of the supports (pH = 2) [92, 93] (entry 2 of Table 17.5). However, Porta *et al.* [100] also mentioned that the same type of sol obtained with THPC can be immobilized on carbon and alumina, independently of the pH of the sol. The step of deposition is not trivial; Porta *et al.* [100] showed that in order to obtain gold particles not significantly larger on activated carbon, SiO_2 , or Al_2O_3 than in the gold sol, a delicate balance must be achieved between several parameters, such as the nature and the concentration of the stabilizer, the stabilizer/Au ratio, and the nature of the support. If the stabilizing agent is appropriately chosen, and does not cover the whole gold particle, liquid-phase catalytic reactions can be directly performed.
3. For gas-phase reaction, the stabilizing agents must be decomposed by thermal treatment. This is also a crucial step during which the gold particles may sinter. Some of the studies gathered in Table 17.5 report the growth of the particles after thermal treatment (entries 1, 2, 4, 5), but not (entries 3, 6–8) for reasons that are not clear. Tsubota *et al.* [91] noted that the gold particles arising from colloidal route (entry 1) sinter more easily than in samples prepared by deposition-precipitation. A way to avoid sintering is to use a stabilizing agent, which decomposes at low temperature. This holds, for instance, for lysine, an α -amino acid ($\text{HO}_2\text{CCH(NH}_2\text{)(CH}_2\text{)}_4\text{NH}_2$), which does not interact strongly with gold, and can be decomposed at moderate temperature (200°C) [99] (entry 8).

Chemical agents were also used to reduce gold already deposited on oxide supports, for instance NaBH_4 to reduce gold first deposited on TiO_2 by deposition-precipitation [101] or using dimethylamine borane [102]. In both cases, the average gold particle size obtained was smaller than 5 nm.

Table 17.5 Examples of conditions of preparation of supported gold catalysts from colloidal gold route.

Gold colloid synthesis			Deposition of gold colloids on supports					Reference
Entry	Synthesis method	$d\text{ Au}^0$ in the sol (nm)	Deposition method	Support	Au loading wt%	$d\text{ Au}^0$ (nm) after drying/evaporation ($^{\circ}\text{C}$)	$d\text{ Au}^0$ (nm) after thermal treatment ($^{\circ}\text{C}$)	
1	Commercial	5	Impregnation	TiO_2	3	5.1 (200)	7.5 (400) 12 (600)	[91]
2	HAuCl_4 reduction by THPC in basic solution	2	Adsorption at pH 2	TiO_2 ZrO_2	1.7 and 17	2.0–2.5 (50)	<4–6 (400)	[92, 93]
3	$\text{Au}(\text{PPh}_3)_3\text{Cl}$ reduction in ethanol by NaBH_4		Adsorption	SiO_2	1.0	2.7 (100)	2.9 (400)	[94]
4	$\text{Au}(\text{PPh}_3)_3\text{Cl}$ reduction in toluene by NaBH_4 , capping by dodecylthiol	*	Impregnation	TiO_2	5	3.4 (RT)	4.6 (300)	[95]
5	HAuCl_4 reduction by NaBH_4 , capping by dodecanethiol	1.9	Impregnation	CeO_2	1	* (100)	3–4 (250)	[96]

6	Au(PPh ₃) ₃ Cl reduction in benzene or chloroform by <i>tert</i> - butylamine-borane, capping by dodecanethiol	3.5, 6.3, 8.2	Adsorption	Zeolite, TiO ₂ , Hydroxy apatite, Al ₂ O ₃ , ZnO, SiO ₂	5	* (100)	No change of size (300)	[97]
7	HAuCl ₄ reduction by NaBH ₄ , capping by PVA or glucose		Adsorption	TiO ₂ , ZnO, Al ₂ O ₃ , ZrO ₂	1	3.0 (PVA) 3.8 (glucose) (RT)	No change of size (250)	[98]
8	HAuCl ₄ reduction by NaBH ₄ and sonication, capping by lysine		Reduction in the presence of the support (pH 9)	α -Fe ₂ O ₃	5	<5 (100)	No change of size (300 or 500)	[99]

* Results non reported.

17.4.2

Deposition of Dendrimer-Encapsulated Gold Nanoparticles

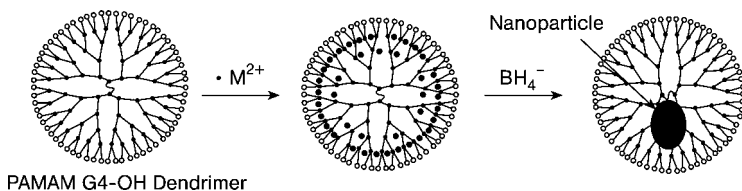
In this specific case, the colloid stabilizers are dendrimers, for instance, polyamidoamine (PAMAM), which are hyperbranched polymers that ramify from a single core and form a porous sphere [103, 104] (Scheme 17.1). Dendrimer-encapsulated nanoparticles (DENs) are synthesized by sequestering metal ions within appropriate dendrimers, and then by chemically reducing the resulting composite. They can be synthesized in various media, such as water or ethanol. The size of the nanoparticles is usually nearly monodisperse, and can be tuned by varying the metal-to-dendrimer ratio prior to reduction. Supported catalysts can then be prepared by immobilizing DENs onto a solid support. As in the case of colloids, the last step, which consists in the removal of dendrimers by thermal treatment, may lead to an increase in both the metal-particle size and particle-size distribution.

For instance, calcination temperatures of 500°C were required to remove PAMAM dendrimers from gold DENs impregnated on titania [105]. This led to particle growth from 1.7 to 7.2 nm. However, lower-temperature routes, such as oxygen plasma treatment, could lead to improved retention of the particle size. It is also possible to incorporate DENs into amorphous matrixes during sol-gel preparation, and then to calcine to remove the dendrimers. For instance, the average gold particle size and size distribution increased much less during calcination at 500°C after such sol-gel titania preparation (2.7 nm) than after impregnation (7.2 nm) [105]. In this approach, the dendrimer not only defined the size and monodispersity of the gold nanoparticles, but also the pore structure of titania. Another way to prevent sintering is to extract the nanoparticles from the dendrimers using an appropriate thiol. After deposition onto titania, smoother conditions for removing the thiols were found, such as temperatures of 160°C under O₂/He or below 300°C under H₂/N₂, and smaller gold particles were obtained (~3nm) [106].

17.5

One-Step Preparations

These methods permit simultaneously the preparation of the support and the deposition of gold.



Scheme 17.1 Preparation of gold particles in dendrimers. (Reprinted from *Chemistry of Materials* 15 (2003) 3873–3878 with permission from ACS.)

17.5.1

Coprecipitation

As mentioned in Section 17.1, the first method, which led to the formation of small gold particles supported on oxides, was coprecipitation [22–24]. This is a single-step method during which both the support oxide and the active phase are prepared (see Chapter 7). Coprecipitation is usually performed by addition of sodium carbonate to aqueous solutions containing both HAuCl_4 and the nitrates corresponding to the hydroxide support to be precipitated (probably rather an oxy-hydroxy-carbonate). Then, the coprecipitate is washed, dried, and calcined to obtain metallic gold on oxide. Coprecipitation can lead to high gold dispersion with gold particles smaller than 5 nm. It is easy to perform, but part of the gold particles could be embedded into the bulk of the support. It is important to carefully wash the samples to remove Na and Cl. This is possible by washing in water at 80°C [107, 108]. This method is valid for a limited number of supports, depending on the respective precipitation rates of support metal hydroxide and gold hydroxide, which is supposed to precipitate as such; their reciprocal affinity determines the gold particle size [22, 109].

The most detailed study is probably that reported by Al-Sayari *et al.* [110]. The authors investigated several parameters during the preparation of Au/ZnO by coprecipitation of HAuCl_4 and zinc nitrate with sodium carbonate at 80°C: the way the pH was adjusted (fixed pH or gradual increase of pH), the final pH, and the aging time. However the pH was adjusted, the Au loading decreased when the final pH increased (Table 17.6). Khoudiakov *et al.* [108] observed the same phenomenon during Au/ Fe_2O_3 preparation with final pH between 9.5 and 12; they explained that part of the gold was solubilized in the form of $[\text{Au}(\text{OH})_4]^-$. Aging at the final pH at 80°C led to a decrease of the Au content for the preparation at increasing pH, and no change at fixed pH (Table 17.6). The zinc and gold hydroxides precipitate roughly at the same pH (~7). In the case of Au/ Fe_2O_3 , the iron/hydroxide precipitates at lower pH (~3), that

Table 17.6 Au/ZnO preparation by coprecipitation at fixed or increasing pH [110].

Method	At increasing pH		At fixed pH	
	Final pH	Au loading (wt%) Au loading after aging	Au loading (wt%)	Au loading after aging
5	6.5	–	12	–
6	4.5	3.5 (80°C/3 h)	5	5
7	2.8	–	3	–
8	2.6	1 (80°C/1 h)	2	–
9	2.0	–	1	–
10	1.9	–	0.5	–

is, before gold, therefore the preparation of Au/Fe₂O₃ is in fact similar to a deposition-precipitation.

Solsona *et al.* [107] prepared Au/CoO_x, Au/MnO_x, Au/TiO₂, and Au/CuO (3 wt%) and Au/Fe₂O₃ and Au/CeO₂ (5 wt%) by dropwise addition of aqueous sodium carbonate up to pH 8.2. After washing, drying, and calcination at 400°C, the measured Au loading was that expected, and the mean gold particle size was found to depend drastically on the support: 8.2 nm on MnO_x, ~4 nm on Fe₂O₃, 3.0 nm on CeO₂, and 4.0 nm on TiO₂, nondetectable on CoO_x or CuO.

17.5.2

Sol-Gel Method

The sol-gel method is also a single-step method (see Chapter 5). It involves the hydrolysis of a metal alkoxide, precursor of the oxide support, in a water–alcohol solution containing HAuCl₄ [111–114], gold acetate, or hydrogen tetranitratoaurate [115]. Gold is then reduced thermally or by UV irradiation, followed by calcination so as to form oxide support. Gold was also introduced as colloids into the solution used for sol-gel synthesis of the support [116], but the use of alcohol and/or catalyst in the sol-gel process is responsible for the aggregation of the colloidal metal. According to the authors [116], several strategies allow this drawback to be avoided: (i) performing the reduction of the metal salt after the formation of the sol-gel; (ii) delaying the introduction of the metal colloid, that is, using the sol-gel matrix as a fixative agent; (iii) avoiding the use of alcohol or catalyst by using water-based precursors.

The sol-gel method does not seem to provide small gold particles on oxide supports (~20 nm), but it seems more suitable for oxides with mesoporous structures [7].

17.6

Special Methods

17.6.1

Photochemical Deposition

Photochemical deposition is based on the principle that metal cations with appropriate redox potentials can be reduced by photoelectrons created by bandgap illumination of semiconductors used as supports. Titania support was used, either as colloids [117, 118] or powder [26] or nanofibers [119]. UV irradiation of deaerated solutions containing HAuCl₄ and titania led to both the deposition of gold and its reduction. As a matter of fact, experimental conditions were such that at least part of [AuCl₄][−] or [AuCl₃OH][−] could adsorb

on titania before irradiation. In all cases, rather high gold loadings could be achieved (~ 4 wt%) with a 100% yield of deposition, but the average gold particles were always larger than 4 nm, even though in one case, organic capping agents (PVA, PVP, or PEG, see Section 17.4.1) were added [119]. Mechanisms of photoreduction were proposed [117, 118]. Attempts with tin and iron oxides were unsuccessful [119].

Note that UV irradiation was also used to photoreduce gold(III) precursors already supported on titania after deposition-precipitation (two-step preparation). The gold particles obtained were either larger (8.4 nm) than those obtained after thermal reduction (5 nm) [102] or smaller (1.9 instead of 3.3 nm) [120]. Other papers report the formation of large gold particles using this reduction method after sol-gel preparation (see Section 17.5.2).

17.6.2

Sonochemical Techniques

Gold particles can also be simultaneously deposited and reduced on a support by sonication. Sonication induces chemical changes due to cavitation phenomena involving the formation, growth, and implosive collapse of bubbles in liquid, which lead to the decomposition of water molecules in H^\cdot and OH^\cdot radicals. The H^\cdot radicals can trigger, for instance, the reduction of Au^{III} species in solution.

This method has been developed by Gedanken's group. It was applied for the deposition of gold on silica submicrospheres [121], and on powders of silica and titania [122] after immersion in a solution of HAuCl_4 in water or ethylene glycol basified with ammonia. The suspension was sonicated under Ar [121] or Ar and H_2 (5%) [122]. After sonication, washing, drying, and also calcinations in the case of silica submicrospheres, gold particles of ~ 4 –5 nm on average were obtained, and all gold was deposited onto the supports (7 or 5 wt%).

Sonication was also used to avoid aggregation of gold colloids and to favor the interaction with the support [99] (Table 17.5, entry 8).

17.7

Conclusion

By way of conclusion, one can summarize the most suitable preparation methods for each type of support. “Most suitable method” ideally means a method leading to small gold particles (< 5 nm), controlled gold loading, chloride content as low as possible, cheap, and commercially available precursors.

HAuCl₄ can be used as a precursor for preparations at low pH (impregnation, anion adsorption) since chlorides can be thereafter removed owing to a washing with ammonia (but beware of fulminating gold, see Section 17.1).

The methods of deposition-precipitation with NaOH and with urea performed at higher pH apply to the supports that have a PZC > 5, and lead to small gold particles (2–3 nm). The advantage of the preparation with urea over that with NaOH or NaCO₃ is that all the gold in solution is deposited onto the support, so there is no loss of gold in solution, and the gold loading can be controlled. Neither of these methods of deposition-precipitation is suitable for the deposition of gold on silica (with mesoporous structure or not) because of the too low PZC. However, other methods can be used for these supports, such as impregnation-washing with ammonia, adsorption of [Au(en)₂]³⁺, impregnation or chemical vapor deposition of gold acetylacetonate, or deposition of preformed gold colloids.

Before ending this chapter, it is interesting to mention that the World Gold Council (www.gold.org) can provide several reference gold catalysts: Au/TiO₂ prepared by deposition-precipitation, Au/Fe₂O₃ prepared by coprecipitation, Au/Fe₂O₃ on alumina beads prepared by deposition-precipitation and Au/C prepared from gold sol.

References

- Meyer, R., Lemire, C., Shaikhutdinov, S.K. and Freund, H.J. (2004) *Gold Bull.*, **37**, 72.
- Miller, J.T., Kropf, A.J., Zha, Y., Regalbuto, J.R., Delannoy, L., Louis, C., Bus, E. and van Bokhoven, J.A. (2006) *J. Catal.*, **240**, 222.
- Chen, M.S. and Goodman, D.W. (2006) *Catal. Today*, **111**, 22.
- Hashmi, A.S.K. and Hutchings, G.J. (2006) *Ang. Chem., Int. Ed.*, **45**, 7896.
- Thompson, D.T. (2006) *Top. Catal.*, **38**, 231.
- Corti, C.W., Holliday, R.J. and Thompson, D.T. (2007) *Top. Catal.*, **44**, 331.
- Bond, G.C., Louis, C. and Thompson, D. (2006) *Catalysis by Gold*, Vol. 6., Imperial College Press, London.
- Haruta, M. (1997) *Catal. Today*, **36**, 153.
- Haruta, M. (2003) *Chem. Record*, **3**, 75.
- Mavrikakis, M., Stoltze, P. and Nørskov, J.K. (2000) *Catal. Lett.*, **64**, 101.
- Valden, M., Lai, X. and Goodman, D.W. (1998) *Science*, **281**, 1647.
- Janssens, T.V.W., Clausen, B.S., Hvolbæk, B., Falsig, H., Christensen, C.H., Bligaard, T. and Nørskov, J.K. (2007) *Top. Catal.*, **44**, 15.
- Bond, G.C. and Thompson, D.T. (1999) *Catal. Rev. Sci. Eng.*, **41**, 319.
- Haruta, M. (2002) *Cattech*, **6**, 102.
- Cant, N.W. and Hall, W.K. (1971) *J. Phys. Chem.*, **75**, 2914.
- Galvagno, S. and Parravano, G. (1978) *J. Catal.*, **55**, 178.
- Sermon, P.A., Bond, G.C. and Wells, P.B. (1979) *J. Chem. Soc. Faraday Trans. I*, **75**, 385.
- Lin, S. and Vannice, M.A. (1991) *Catal. Lett.*, **10**, 47.
- Haruta, M., Tsubota, S., Kobayashi, T., Kageyama, H., Genet, M.J. and Delmon, B. (1993) *J. Catal.*, **144**, 175.
- Kung, H.H., Kung, M.C. and Costello, C.K. (2003) *J. Catal.*, **216**, 425.
- Oh, H.S., Yang, J.H., Costello, C.K., Wang, Y.M., Bare, S.R., Kung, H.H.

- and Kung, M.C. (2002) *J. Catal.*, **210**, 375.
22. Haruta, M., Kageyama, H., Kamijo, N., Kobayashi, T. and Delannay, F. (1988) *Stud. Surf. Sci. Catal.*, **44**, 33.
 23. Haruta, M., Kobayashi, T., Sano, H. and Yamada, N. (1987) *Chem. Lett.*, **2**, 405.
 24. Haruta, M., Yamada, N., Kobayashi, T. and Iijima, S. (1989) *J. Catal.*, **115**, 301.
 25. Tsubota, S., Cunningham, D.A.H., Bando, Y. and Haruta, M. (1995) *Stud. Surf. Sci. Catal.*, **91**, 227.
 26. Bamwenda, G.R., Tsubota, S., Nakamura, T. and Haruta, M. (1997) *Catal. Lett.*, **44**, 83.
 27. Peck, J.A. and Brown, G.E. (1991) *Geochim. Cosmochim. Acta*, **55**, 671.
 28. Farges, F., Sharp, J.A. and Brown, G.E. (1993) *Geochim. Cosmochim. Acta*, **57**, 1243.
 29. Murphy, P.J. and LaGrange, M.S. (1998) *Geochim. Cosmochim. Acta*, **62**, 3515.
 30. Lee, S.-J. and Gavrilidis, A. (2002) *J. Catal.*, **206**, 305.
 31. Ivanova, S., Petit, C. and Pitchon, V. (2004) *Appl. Catal. A*, **267**, 191.
 32. Moreau, F., Bond, G.C. and Taylor, A.O. (2004) *Chem. Commun.*, 1642.
 33. Belevantsev, V.I., Kolonin, G.R. and Ryakhovskaya, S.K.R. (1972) *Russ. J. Inorg. Chem.*, **17**, 1303.
 34. Murphy, P.L., Stevens, G. and LaGrange, M.S. (2000) *Geochim. Cosmochim. Acta*, **64**, 479.
 35. Nechayev, Y.A. and Zvonareva, G.V. (1983) *Geokhimiya*, **6**, 919.
 36. Daté, M., Ichihashi, Y., Yamashita, T., Chiorino, A., Boccuzzi, F. and Haruta, M. (2002) *Catal. Today*, **72**, 89.
 37. Schumacher, B., Plzak, V., Kinne, K. and Behm, R.J. (2003) *Catal. Lett.*, **89**, 109.
 38. Zanella, R. and Louis, C. (2005) *Catal. Today*, **107–108**, 768.
 39. (a) Cusumano, J.A. (1974) *Nature*, **247**, 456; (b) Fisher, J.M. (2003) *Gold Bull.*, **36**, 155.
 40. Steinhauser, G., Evers, J., Jakob, S., Klapötke, T. M. and Oehlinger, G. (2008) *Gold Bull.*, **41**, 305.
 41. Zanella, R., Delannoy, L. and Louis, C. (2005) *Appl. Catal. A*, **291**, 62.
 42. Xu, Q., Kharas, K.C.C. and Datye, A.K. (2003) *Catal. Lett.*, **85**, 229.
 43. Fu, Q., Kudriavtseva, S., Saltsburg, H. and Flytzani-Stephanopoulos, M. (2003) *Chem. Eng. J.*, **93**, 41.
 44. Delannoy, L., El Hassan, N., Musi, A., Le To, N.N., Krafft, J.-M. and Louis, C. (2006) *J. Phys. Chem. B*, **110**, 22471.
 45. Delgass, W.N., Boudart, M. and Parravano, G. (1968) *J. Phys. Chem.*, **72**, 3563.
 46. Zanella, R., Giorgio, S., Henry, C.R. and Louis, C. (2002) *J. Phys. Chem. B*, **106**, 7634.
 47. Hugon, A., Delannoy, L. and Louis, C. unpublished results.
 48. Ivanova, S., Pitchon, V. and Petit, C. (2006) *J. Mol. Catal. A*, **256**, 278.
 49. Ivanova, S., Pitchon, V., Zimmermann, Y. and Petit, C. (2006) *Appl. Catal. A*, **298**, 57.
 50. Li, W.-C., Comotti, M. and Schüth, F. (2006) *J. Catal.*, **237**, 190.
 51. Wolf, A. and Schüth, F. (2002) *Appl. Catal. A*, **226**, 1.
 52. Prati, L. and Martra, G. (1999) *Gold Bull.*, **32**, 96101.
 53. Lin, J.-N. and Wan, B.-Z. (2003) *Appl. Catal. B*, **41**, 83.
 54. Hermans, L.A. and Geus, J.W. (1979) *Stud. Surf. Sci. Catal.*, **4**, 113.
 55. van Dillen, J.A., Geus, J.W., Hermans, L.A. and van der Meijden, J. (1977) in *Proceedings of the 6th International Congress on Catalysis, London, 1976* (eds G.C. Bond, P.B. Wells and F.C. Tompkins), The Chemical Society, London, p. 677.
 56. Moreau, F. and Bond, G.C. (2006) *Appl. Catal. A*, **302**, 110.
 57. Chang, C.-K., Chen, Y.-J. and Yeh, C.-T. (1998) *Appl. Catal. A*, **174**, 13.
 58. Moreau, F. and Bond, G.C. (2006) *Catal. Today*, **114**, 362.
 59. Moreau, F. and Bond, G.C. (2007) *Catal. Today*, **122**, 215.

60. Moreau, F. and Bond, G.C. (2007) *Catal. Today*, **122**, 260.
61. Moreau, F., Bond, G.C. and Taylor, A.O. (2005) *J. Catal.*, **231**, 105.
62. Moreau, F. and Bond, G.C. (2007) *Topics Catal.*, **44**, 95.
63. Nechayev, Y.A. and Nikolenko, N.V. (1985) *Geochem. Intern.*, **11**, 1656.
64. Machesky, M.L., Andrade, W.O. and Rose, A.W. (1991) *Geochim. Cosmochim. Acta*, **5**, 769.
65. Dekkers, M.A.P., Lippits, M.J. and Nieuwenhuys, B.E. (1998) *Catal. Lett.*, **56**, 195.
66. Dekkers, M.A.P., Lippits, M.J. and Nieuwenhuys, B.E. (1999) *Catal. Today*, **54**, 381.
67. Grisel, R.J.H. and Nieuwenhuys, B.E. (2001) *Catal. Today*, **64**, 69.
68. Guillemot, D., Borovskov, V.Y., Kazansky, V.B., Polisset-Thfoin, M. and Fraissard, J. (1997) *J. Chem. Soc., Faraday Trans.*, **93**, 3587.
69. Guillemot, D., Polisset-Thfoin, M. and Fraissard, J. (1996) *Catal. Lett.*, **41**, 143.
70. Block, B.P. and Bailar, J.J.C. (1951) *J. Am. Chem. Soc.*, **73**, 4722.
71. Zhu, H., Ma, Z., Clark, J.C., Pan, Z., Overbury, S.H. and Dai, S. (2007) *Appl. Catal. A*, **326**, 89.
72. Bulushev, D.A., Yuranov, I., Suvorova, E.I., Buffat, P.A. and Kiwi-Minsker, L. (2004) *J. Catal.*, **224**, 8.
73. Zanella, R., Sandoval, A., Santiago, P., Basiuk, V.A. and Saniger, J.M. (2006) *J. Phys. Chem. B*, **110**, 8559.
74. Zhu, H., Liang, C., Yan, W., Overbury, S.H. and Dai, S. (2006) *J. Phys. Chem. B*, **110**, 10842.
75. Yuan, Y., Asakura, K., Wan, H., Tsai, K. and Iwasawa, Y. (1996) *Catal. Lett.*, **42**, 15.
76. Yuan, Y., Kozlova, A.P., Asakura, K., Wan, H., Tsai, K. and Iwasawa, Y. (1997) *J. Catal.*, **170**, 191.
77. Kozlov, A.I., Kozlova, A.P., Liu, H. and Iwasawa, Y. (1999) *Appl. Catal. A*, **182**, 9.
78. Choudhary, T.V., Sivadinarayana, C., Chusuei, C.C., Datye, A.K., Fackler, J.P. Jr. and Goodman, D.W. (2002) *J. Catal.*, **207**, 247.
79. Yan, Z., Chinta, S., Mohamed, A.A., Fackler, J.J.P. and Goodman, D.W. (2006) *Catal. Lett.*, **111**, 15.
80. Menard, L.D., Xu, F., Nuzzo, R.G. and Yang, J.C. (2006) *J. Catal.*, **243**, 64.
81. Mathieson, T.J., Langdon, A.G., Milestone, N.B. and Nicholson, B.K. (1998) *Chem. Commun.*, 371.
82. Okumura, M. and Haruta, M. (2000) *Chem. Lett.*, 396.
83. Okumura, M., Nakamura, S., Tsubota, S., Nakamura, T., Azuma, M. and Haruta, M. (1998) *Catal. Lett.*, **51**, 53.
84. Okumura, M., Tsubota, S. and Haruta, M. (2003) *J. Mol. Catal. A*, **199**, 73.
85. Guzman, J. and Gates, B.C. (2001) *Nano Lett.*, **1**, 689.
86. Guzman, J. and Gates, B.C. (2003) *Langmuir*, **19**, 3897.
87. Fierro-Gonzalez, J.C. and Gates, B.C. (2005) *J. Phys. Chem. B*, **109**, 7275.
88. Fierro-Gonzalez, J.C., Bhirud, V.A. and Gates, B.C. (2005) *Chem. Commun.*, 5275.
89. Fierro-Gonzalez, J.C. and Gates, B.C. (2004) *J. Phys. Chem. B*, **108**, 16999.
90. Daniel, M.-C. and Astruc, D. (2004) *Chem. Rev.*, **104**, 293.
91. Tsubota, S., Nakamura, T., Tanaka, K. and Haruta, M. (1998) *Catal. Lett.*, **56**, 131.
92. Grunwaldt, J.-D., Kiener, C., Wogerbauer, C. and Baiker, A. (1999) *J. Catal.*, **181**, 223.
93. Grunwaldt, J.D., Maciejewski, M., Becker, O.S., Fabrizioli, P. and Baiker, A. (1999) *J. Catal.*, **186**, 458.
94. Martra, G., Prati, L., Manfredotti, C., Biella, S., Rossi, M. and Coluccia, S. (2003) *J. Phys. Chem. B*, **107**, 5453.
95. Chou, J. and McFarland, E.W. (2004) *Chem. Commun.*, 1648.
96. Hickey, N., Arneodo Larochette, P., Gentilini, C., Sordelli, L., Olivi, L., Polizzi, S., Montini, T., Fornasiero, P., Pasquato, L. and Graziani, M. (2007) *Chem. Mater.*, **19**, 650.

97. Zheng, N. and Stucky, G.D. (2006) *J. Am. Chem. Soc.*, **128**, 14278.
98. Comotti, M., Li, W.-C., Spliethoff, B. and Schüth, F. (2006) *J. Am. Chem. Soc.*, **126**, 917.
99. Zhong, Z., Lin, J., Teh, S.-P., Teo, J. and Dautzenberg, F.M. (2007) *Adv. Funct. Mater.*, **17**, 1402.
100. Porta, F., Prati, L., Rossi, M., Coluccia, S. and Martra, G. (2000) *Catal. Today*, **61**, 165.
101. Mallick, K., Witcomb, M.J. and Scurrell, M.S. (2004) *Appl. Catal. A*, **259**, 163.
102. Isono, R., Yoshimura, T. and Esumi, K. (2005) *J. Colloid. Inter. Sci.*, **288**, 177.
103. Scott, R.W.J., Wilson, O.M. and Crooks, R.M. (2005) *J. Phys. Chem. B*, **109**, 692.
104. Chandler, B.D. and Gilbertson, J.D. (2008) in *Nanoparticles and Catalysis* (ed. D. Astruc), Wiley-VCH Verlag GmbH, Weinheim.
105. Scott, R.W.J., Wilson, O.M. and Crooks, R.M. (2004) *Chem. Mater.*, **16**, 5682.
106. Korkosz, R.J., Gilbertson, J.D., Prasifka, K.S. and Chandler, B.D. (2007) *Catal. Today*, **122**, 370.
107. Solsona, B.E., Garcia, T., Jones, C., Taylor, S.H., Carley, A.F. and Hutchings, G.J. (2006) *Appl. Catal. A*, **312**, 67.
108. Khoudiakov, M., Gupta, M.-C. and Deevi, S. (2005) *Appl. Catal. A*, **291**, 151.
109. Tsubota, S., Haruta, M., Kobayashi, T., Ueda, A. and Nakahara, Y. (1991) *Stud. Surf. Sci. Catal.*, **72**, 695.
110. Al-Sayari, S., Carley, A.F., Taylor, S.H. and Hutchings, G.J. (2007) *Top. Catal.*, **44**, 123.
111. Li, F.B. and Li, X.Z. (2002) *Appl. Catal. A*, **228**, 15.
112. Kozuka, H. and Sakka, S. (1993) *Chem. Mater.*, **5**, 222.
113. Akbarian, F., Dunn, B.S. and Zink, J.I. (1996) *J. Raman Spectrosc.*, **27**, 775.
114. Innocenzi, P., Brusatin, G., Martucci, A. and Urabe, K. (1996) *Thin Solid Films*, **279**, 23.
115. Seker, E. and Gulari, E. (2002) *Appl. Catal. A*, **232**, 203.
116. Smith, D.D., Snow, L.A., Sibille, L. and Ignont, E. (2001) *J. Non-Cryst. Solids*, **285**, 256.
117. Fernandez, A., Caballero, A., Gonzalez-Elise, A.R., Herrmann, J.-H., Dexpert, H. and Villain, F. (1995) *J. Phys. Chem.*, **99**, 3303.
118. Wang, C.-Y., Liu, C.-Y., Zheng, X., Chen, J. and Shen, T. (1998) *Colloids Surf., A*, **131**, 271.
119. Li, D., McCann, J.T., Gratt, M. and Xia, Y. (2004) *Chem. Phys. Lett.*, **394**, 387.
120. Soejima, T., Tada, H., Kawahara, T. and Ito, S. (2002) *Langmuir*, **18**, 4191.
121. Pol, V.G., Gedanken, A. and Calderon-Moreno, J. (2003) *Chem. Mater.*, **15**, 1111.
122. Perkasa, N., Pol, V.G., Pol, S.V. and Gedanken, A. (2006) *Cryst. Growth Design*, **6**, 293.

Index

a

adsorption 69, 285
 –anion 371
 –cation 378
 –concentration effect 253
 –monolayer 51
 –selective 51
 –strong 365
 aerogel 83
 –mixed-metal oxide 98
 –sol-gel entrapment 97
 –stabilization 90
 –Ti-Si 101
 AgPt/SiO₂ catalyst 127
 Ag/SiO₂ catalyst 124
 aggregation model 259
 aging 70, 89, 334
 Al₂(MoO₄)₃ 316
 [AlMo₆] 74 ff.
 alumina (Al₂O₃) 92, 154 ff., 183,
 312, 342
 – γ -Al₂O₃ 302 f., 312
 –catalyst 203 ff.
 –cluster-derived catalyst 160
 –dough 307
 –layer 192
 –mesoporous 304
 –precipitation 303
 –ternary catalyst 341
 alumina gel 196
 alumina support 52
 alumina xerogel 92
 aluminosilicate 163
 –zeolite 267
 aluminophosphates (AlPO₄-n) 247
 –four-coordinated 247
 aluminum isopropoxide 304
 aluminum phosphate hydrate (APH) 184
 aluminum *sec*-butoxide 304

aluminum silicate 98
 ammonium hexamolybdate (AHM) citrate
 202
 ammonium metavanadate 129
 anatase/impregnation solution interface
 21
 anion adsorption 371
 aperture 163
 atomizer 197
 Au/Al₂O₃ 371
 Au/C 388
 Au(CH₃)₂(acac) 380
 Au/Co₃O₄ 226
 [Au(en)₂]³⁺ 378
 Au/Fe₂O₃ 388
 Au(OH)₃ 375
 [Au^I(PPh₃)]NO₃ 379
 Au/TiO₂ 226, 371, 388
 Au/ZnO 385
 aurichalcite (Zn_{1-x}Cu_x)₅(OH)₆(CO₃)
 335

b

bayerite 142
 bentonite 196
 beta zeolite (BEA) 243, 259 ff.
 bimetallic catalyst 54, 122 ff.
 bimetallic nanoparticle
 –cluster derived 159
 bioceramics 105
 bis-ethanediamine gold(III) cation
 [Au(en)₂]³⁺ 378
 boehmite 195
 –fibrillar 142
 –microporous 142
 –precursor 303
 bonding mode 162
 Brønsted acid 245

- buffer effect 68
- bulk catalyst 308
- c**
 - calcination 60, 77, 315, 337
 - alumina 307
 - high throughput catalysis 231
 - silica-alumina 307
 - capping agent 381
 - carbon 156, 289
 - carbon nanofiber (CNF)
 - support 119
 - surface-oxidized CNF (CNF-O) 119
 - carbonate
 - high-temperature 337 f.
 - casting-by-casting method 295
 - catalysis 285
 - cluster 157
 - high throughput 219
 - homogenous 158
 - hydrodesulfurization (HDS) 4
 - catalyst
 - acid 87
 - attrition-resistant microspheroidal 196
 - base 87
 - bimetallic 54, 122 ff.
 - bulk 308
 - drying and calcination 308
 - egg-shell 186
 - entrapped 98 ff.
 - Fischer–Tropsch 148
 - fixed-bed 174, 186
 - fluidized 181
 - fluidized-bed 175, 186, 196
 - heterogenous 158
 - hybrid organic-inorganic 168
 - library 223 ff.
 - methanol 329 ff.
 - noble-metal 353 ff.
 - optimization 222, 354
 - solid, *see* solid catalyst
 - shaping 173 ff.
 - sulfidic 318
 - ternary 341
 - zeolite-based 243 ff.
 - catalyst body 201 ff.
 - catalytic material 97
 - catalytic phase material
 - bulk 91
 - cation
 - adsorption 378
 - charge reversal 25
 - charge transfer 204
 - chemical vapour deposition (CVD) 290, 347
 - chemisorption 365
 - clear solution synthesis 256
 - cluster 153 ff.
 - catalysis 157
 - cobalt
 - particle 9
 - Keggin-type Co-Mo complex 209
 - Co²⁺ complex 206 ff.
 - speciation 212
 - Co/Al₂O₃ 128
 - CoAl₂O₄ 316
 - Co(H₂O)₆²⁺ aqua complex 27 f., 210 f.
 - Co-Mo complex 209
 - CoMoO₄ 316
 - Co-Mo-S-II/phase 310
 - Co(NO₃)₂ · 6H₂O 309
 - Co/Ni-Mo/W 317
 - Co-oxide/ γ -Al₂O₃ catalyst 130
 - coimpregnant 72
 - coimpregnation 314
 - combinatorial strategy 220
 - comixing/coextrusion and coprecipitation
 - route 308
 - condensation
 - aprotic 89
 - configurational-bias Monte Carlo 250
 - confined space synthesis 264
 - constant-rate period 65
 - conversion 86
 - copper 121
 - copper nitrate 121, 340
 - copper phyllosilicate 48
 - copper tetraammine adsorption 48
 - copper/zinc methanol catalyst 147
 - coprecipitate
 - highly dispersed 139
 - coprecipitation 135 ff., 331, 385
 - process operation 142
 - sequential 143
 - counterion 73
 - crystal growth 138
 - crystallization 91
 - zeolite 255
 - Cu/Al₂O₃ 343
 - CuFe alloy particle 130
 - CuFe/ γ -Al₂O₃ catalyst 129
 - Cu₂(NO₃)(OH)₃ 121
 - CuO 342
 - CuO/Al₂O₃ 346
 - Cu/SiO₂ catalyst 104
 - Cu/Zn-malachite (Cu_{1-x}Zn_x)₂(OH)₂CO₃ 335

Cu/ZnO (CZ) catalyst 226, 329 ff., 343
 CuZnO_{1-x} 346
 Cu/ZnO/Al₂O₃ catalyst 331 f., 343 ff.
 cyclohexene
 –selective oxidation 288

d

deagglomeration
 –chemical 195
 –mechanical 195
 degree of reduction 145
 dehydration 155
 dehydroxylation 156
 dendrimer-encapsulated nanoparticle (DEN) 384
 density functional theory 18
 deposition
 –Co(H₂O)₆²⁺ aqua complex on titania surface 27
 deposition mode 20
 deposition precipitation (DP) 37 ff., 111 ff., 381
 –equipment 113 ff.
 –injection method 123
 –kinetics 115
 –molecular details 118
 –NaOH 373
 –urea 121, 376
 design of experiment (DoE) 220
 diffuse layer model 21
 dimethyl gold(III) acetylacetonate 380
 dimethyldisulfide (DMDS) 319 ff.
 dimethylsulfide (DMS) 319
 dipping/equilibrium impregnation 310
 dissolution 47, 264
 dodecaheteropolyacid H_n[XM₁₂O₄₀]
 –Keggin-type 104
 dough 306
 drip coagulation 196
 dry gel route 265
 –zeolite synthesis 265
 drying 14, 59 ff., 315, 337
 –alumina 307
 –high throughput catalysis 231
 –parameter 76
 –silica-alumina 307
 –supercritical 90

e

egg-shell profile 64
 egg-shell structure 186
 electric double-layer theory 40

electrical resistance tomography (ERT) 149
 electrochemical (equilibrium) modeling 26 ff.
 electrokinetic charge 24
 electrophilic cleavage of M–C bond 161
 electrostatic adsorption 33 ff.
 –deposition-precipitation 45
 –ion exchange 41
 –metal respeciation 38
 –purely 37
 electrostatic interaction 69, 354 f.
 electrostatics 47
 electrostatics-based design 47
 encapsulation 103
 entrapment
 –sol-gel 97 ff.
 –steric 105
 enzyme 105
 epoxide 101
 equilibrium adsorption 14
 equilibrium deposition filtration (EDF) 14 f., 130
 evolutionary strategy 222 f.
 extended Stern model 21
 extended X-ray absorption fine structure (EXAFS) 25, 159
 extrusion 181 ff., 305

f

falling-rate period 65 f.
 faujasite-type zeolite (FAU) 243 ff., 259
 ferrierite (FER) synthesis 261
 Fischer–Tropsch catalyst 148
 –iron-based 148
 fixed-bed reactor 177, 187, 234
 flame spray pyrolysis (FSP) 194
 flexible ligand method 166
 fluidized bed 196
 foam monolith 192
 freeze-drying method 231

g

gas-phase presulfiding 319
 gas–solid surface reaction 13
 gel drying 90
 gelation 89
 –encapsulation 103
 gelation time 89
 georgeite 336
 gerhardtite 337 ff.
 Gibbs free energy change 113

gismondine-type framework
(GIS) 261

goethite 376

gold

–colloids 380

–fulminating 370

–loading 372 ff.

–particle 387

gold catalyst 369 ff.

–colloidal gold route 382 f.

gold complex

–interaction 375

–phosphine-based 379

gold nanoparticle 380 ff.

–dendrimer-encapsulated 384

gold organometallics 379

grafting 69, 284

granulation 179

h

$\text{HAuCl}_4 \cdot 3 \text{H}_2\text{O}$ 370 f.

$\text{H}_2\text{PMo}_{11}\text{CoO}_{40}^{5-}$ 209 ff.

$\text{H}_n[\text{XM}_{12}\text{O}_{40}]$ 104

hard templating approach 289 ff.

heteropolyacid (HPA)

–Keggin-type 166

heteropolyanion 71

hexachloroplatinate (CPA) $[\text{PtCl}_6]^{-2}$
33 ff.

high throughput experimentation 217 ff.

homocondensation 94

homogeneous deposition–precipitation
15, 22 f.

honeycomb 187

–ceramic 188

–metallic 190

hot-gas granulator 181

hybrid organic-inorganic catalyst 168

hybrid organic-inorganic interphase
catalyst 100

hydrodenitrogenation (HDN) 301

hydrodesulfurization (HDS) 301 f.

–catalysis 4

hydrogel 83

hydroprocessing 301

hydrotalcite 96, 140

hydrothermal synthesis 230

hydrothermal treatment 283

hydrotreating

–unsupported metal sulfide catalyst 148

hydrotreating catalyst 301 ff.

–preparation 302, 318

–typical 302

hydroxo-chloro gold(III) complex 370

i

immobilization 153

impregnation 59 ff., 77, 379

–capillary impregnation 61

–catalyst library 227

–concentration 67

–counterion 73

–diffusional 62

–dry 61

–extended mixed phase 72

–high throughput preparation 226

–incipient wetness (IWI) 14 f., 61,
370

–ligand 71

–metal 309

–method 61

–noble-metal 356

–pH 67

–physical model 62

–precursor 71

–wet 61

inorganic oxide 154 f.

inorganic support

–modified 167

interface

–arrangement of ion 20

–diffuse part 18

–structure 18

interface speciation/structure of the
deposited precursor species 26

interfacial chemistry 13 ff.

–liquid/solid 13

interfacial deposition 14 f.

–determination of the mode 23

–mode 20 ff.

interphase catalyst 102

inverse shape selectivity 251

ion adsorption (IA) 119

ion exchange (IE) 41

ion pair formation 21

ion pairing 161

ionothermal synthesis method
267

IR microspectroscopy 203

isoelectric point (IEP) 24, 356

k

kaolin 196

Keggin-type Co-Mo complex 209

Keggin-type dodecaheteropolyacid

$\text{H}_n[\text{XM}_{12}\text{O}_{40}]$ 104

Keggin-type heteropolyacid (HPA)
166

key-lock catalysis (KLC) 251

I

layer 18
 –compact 18
 –mobile–diffuse 19
 –stagnant–diffuse 19
 ligand 22, 71
 –exchange 161
 –in solution 76
 –nucleophilic or electrophilic attack 161
 –removal 128
 liogel 83
 liquid-crystal template pathway 278
 liquid-phase photodeposition (LPPD) 130
 liquid-phase presulfiding 319

m

$M(NO_3)_x \cdot \gamma H_2O$ 73
 macroscopic adsorption data 27
 manganese hydroxide 115
 manganese(III) salen species 168
 mazzite (MAZ) 261
 MCM-41 279, 347
 MCM-48 281, 347
 memory effect 268
 mesoporous material
 –ordered 277 ff.
 mesoporous molecular sieve 286
 mesoporous silica 277 ff.
 –organic group functionalized 284
 –periodic 285
 mesoporous silica molecular sieve 287
 –metal-substituted 287
 mesostructure 278
 –pore model 279
 metal
 –comixing/coextrusion and coprecipitation route 307
 –impregnation 309
 –promoted 52
 metal carbonate 140
 metal cluster 162
 –formation 162
 metal complex
 –zeolite-entrapped 164
 metal hydroxide 140
 metal nitrate 73
 metal organic framework (MOF) 243, 347
 metal sulfide 296
 metal-oxide phase 91
 metallosilicate zeolite 245
 methanol catalyst 329 ff.
 MFI 243 ff., 264
 $MgAl_2O_4$ spinel phase 96

micelle 83
 microelectrophoretic mobility 24
 microspectroscopic method
 –invasive 202
 mixed metal oxide catalyst 230
 mixed phase
 –formation 70
 mixer agglomerator 180
 mixing
 –diffusive 144
 –dispersive 144
 –distributive 144
 $[Mn(X_2\text{-haacac})Cl]$ 166
 Mo(III) deposition onto silica 129
 Mo/Al_2O_3 catalyst 207 f.
 MoO_3 309 ff.
 MoO_x/Al_2O_3 catalyst 74 ff.
 Mo-oxide 130
 modifier 97
 MOF, *see* metal organic framework
 MOF-5 347
 molecular catalyst
 –inorganic 104
 –physically entrapped (adsorbed) 103
 molecular sieve 266
 –acronym 266
 – $AlPO_4$ -n-based 266
 molybdenum
 –alumina-supported catalyst 77
 –egg-yolk distribution 126
 molybdenum (hydr)oxide 125
 molybdenum speciation 74
 –in solution 74
 12-molybdophosphoric acid 166
 monolayer adsorption 51
 monolith 83, 187 ff.
 –coating 194
 monomer–cluster growth model 255
 monometallic catalytic material 91
 moving-bed reactor 195
 MRI technique 205
 MWW zeolite 243 ff., 259

n

$(NH_4)_6H_2W_{12}O_{40}$ 312
 $(NH_4)_6Mo_7O_{24} \cdot 4H_2O$ 309 ff.
 $NaNO_3$ 337
 nanocasting strategy 289
 nanoparticle
 –supported 159
 nanoslab 260
 nature's nanotechnology 7
 nest effect 251

- network
 - 3D 100
- Ni(II) complex 166
- NiAl₂O₄ 71
- Ni₆Al₂(OH)₁₆CO₃ · 4H₂O 145
- Ni(en)₃²⁺ 203
- Ni/SiO₂ catalyst 143
- nickel 130
 - deposition 127
 - precipitate 141
- nickel alumina catalyst 145
- high nickel loading 145
- single-step sulfur-promoted 146
- nickel hydroxide 118 ff., 141
- noble-metal catalyst 353 ff.
- noble-metal impregnation 356
- noninvasive method 205
- nucleation 136
 - primary 257
 - rate 137
 - secondary 257
- o**
 - open-cell foam 192
 - organic catalyst
 - functionalized 103
 - organogold complex 379 f.
 - organometallic precursor 379
 - Ostwald ripening 139
 - Ostwald rule of successive phase transformation 261
 - oxide
 - nonsiliceous 293
 - support 375
 - oxide/gas interface 77
 - oxide/water interface 77
 - oxidic support 15 ff.
 - oxo–/hydroxo–group 16 ff.
- p**
 - palladium
 - deposition 127
 - palladium tetraammine (PdTA)
 - [(NH₃)₄Pd]²⁺, [Pd(NH₃)₄]²⁺ 37, 56
 - PAMAM, *see* polyamidoamine
 - pan granulation 179
 - Pauling valence bond 17
 - Pd/Al₂O₃ 127
 - Pd/MCM-41 catalyst 287
 - Pd/ZrO₂ catalyst 123
 - pelletting 177 ff.
 - PEO-PPO-PEO 291
 - peptization 183, 195
 - perovskite 96
 - phosphine gold complex 379
 - phosphine ligand
 - chelating 168
 - phosphomolybdic acid (PMA) 296
 - phosphotungstic acid (PTA) 296
 - photochemical deposition 386
 - phyllosilicate 118
 - plasticizer 182 f.
 - platinum
 - deposition 127
 - platinum tetraammine (PTA) [(NH₃)₄Pt]²⁺, [Pt(NH₃)₄]²⁺ 33 ff., 69, 167
 - poly(isobutylene)-*block*-poly(ethylene oxide) (PIB-PEO) 283
 - poly(isoprene)-poly(ethylene oxide) (PI-PEO) 283
 - poly(styrene)-*block*-poly(4-vinylpyridine) (PSB-P4VP) 283
 - poly(styrene)-poly(4-vinylpyridine) (PS-P4VP) 290
 - polyamidoamine (PAMAM) 384
 - polycarbosilane (PCS) 294 f.
 - polycondensation 87
 - polyhedral oligomeric silsesquioxanes (POSS) 156
 - polysilsesquioxanes structure 100
 - polysilylated organic molecule 100
 - pore model
 - mesostructure 279
 - pore size control 282
 - pore size distribution 184, 302
 - tailoring 184
 - pore system
 - chemistry 67
 - pore-filling agent 262
 - pore-mouth catalysis (PMC) 251
 - pore-volume impregnation 310
 - porous solid catalytic phase 86
 - positron-emission particle tracking (PEPT) 149
 - potentiometric titration 23
 - precipitation 136 ff., 333
 - condition 141
 - high throughput preparation 226
 - precursor distribution
 - egg-shell 66 f.
 - egg-yolk 66 f.
 - uniform 66 f.
 - precursor-support interaction 69
 - presulfiding 318
 - ex-situ* 320
 - goal 318
 - in-situ* 320

- primary amorphous phase 256
- primary screening 223
- process monitoring 149
- product diffusion shape selectivity (PDSS) 250
- promoter 51
- pseudoboehmite 341
- Pt/ γ -Al₂O₃ 130
- [PtCl₆]²⁻ 33 ff.
- [Pt(NH₃)₄]²⁺ 33 ff., 69, 167
- Pt(NH₃)₄(NO₃)₂ 123
- PtRu₅C(CO)₁₆ 159
- PTA, *see* phosphotungstic acid or platinum tetraammine
- pzc (point of zero charge) determination 25, 33

- q**
- quantum-mechanical calculation 26 ff.

- r**
- Raman microspectroscopy 202 f.
- reactant shape selectivity (RSS) 250
- reactive adsorption 37
- reactor
 - catalyst library 234
 - fixed-bed 177, 187, 234
 - moving-bed 195
- recrystallization 139
- redeposition 47
- reduction 339
- reduction deposition precipitation (RDP) 124
- rehydroxylation 156
- replication method 193
- reticulated foam 192
- revised physical adsorption (RPA) model 35 ff.
- [Rh₆(CO)₁₅]²⁻ 167
- Rh/MnO/SiO₂ catalyst 122
- rotary press 178
- Ru
 - dispersed on silica 358
 - Ru(NO)(NO₃)₃(H₂O)₂ 123
 - Ru-TEA/SiO₂ impregnate 360 ff.

- s**
- safety 323
- salen complex 166
- SAPO-n 248, 267
- SAPO-5 248 ff.
- SAPO-11 248 ff.
- SAPO-14 248
- SAPO-37 (FAU) 248 ff.
- SBA-15 280 ff., 378
- Schiff base complex 166
- SDA 285 ff.
- secondary amorphous phase 256
- secondary screening 225
- selective catalytic reduction (SCR) 188
- selective metal partitioning 54
- sequential impregnation 314
- shape selectivity 250
 - zeolite 250
- shaping 173 ff.
 - high throughput catalysis 231
- shear plane 19
- ship-in-a-bottle synthesis 163
- Si–O–M bond angle 246
- Si(OR)₄ precursor 105
- SiAlPO₄ (SAPO) 248
- SiC-based material 294
- silanol 155
- silica (SiO₂) 87, 118, 154 f., 305
 - Al₂O₃-coated 305
 - cluster-derived catalyst 160
 - dispersed Ru 358
 - mesoporous 277 ff.
 - nanostructured 7
- silica catalyst
 - Ti- and Zr-doped 101
- silica-alumina 183, 196, 302 ff.
 - drying and calcination 307
 - yttria-modified 357 f.
 - modified 356
- silicate 87
- silicon 87
 - wafer 224
- silicon alkoxide 90
- siloxyl defect
 - negatively charged 264
- simple electrostatic adsorption 21
- single bead 225
- single pellet 224
- single-screw extruder 182
- site isolation 254
- sodium hydroxide 142 f.
- sol-gel chemistry 231
 - catalyst library 232 f.
 - high throughput catalysis 231
- sol-gel entrapment 97 ff.
- sol-gel method 386
- sol-gel processing 83
 - hydrolytic 83
 - nonhydrolytic 83
 - physicochemical principle 85

- sol-gel processing *contd.*
 - preparation of solid catalyst 91
 - solid catalyst 3
 - development 4
 - preparation 91
 - shaping 173 ff.
 - synthesis 5
 - solid/fluid interfacial energy 137
 - solid–solid reaction 14
 - solution
 - impregnating 27
 - viscosity 63
 - solvent evaporation 90
 - sonochemical technique 387
 - space-resolved spectroscopy 201 ff.
 - spacer 141, 167
 - spinel 342
 - spinel compound 95
 - split-and-pool synthesis 221
 - spray drying 196
 - stabilizer 141, 309
 - stabilizing agent 381
 - steam-assisted crystallization (SAC) 265
 - Stern–Gouy–Chapmann model 21
 - streaming potential measurement 24
 - strong electrostatic adsorption (SEA) 36 ff.
 - structure-directing agent (SDA) 255
 - successive phase transformation
 - Ostwald rule 261
 - superacidity 247
 - protonic 246
 - supercage 163
 - supercritical fluid reactive deposition (SFRD) 194
 - supersaturation 137
 - support
 - oxidic 15 ff.
 - preparation 303
 - surface 154
 - support dissolution
 - ligand-promoted 75
 - supported complex 363
 - supramolecular-templating approach 290 ff.
 - surface
 - charged 15
 - unmodified 160
 - surface binding 16
 - surface complexation 16
 - surface ionization
 - homogeneous 16
 - interfacial model 26
 - model 15 ff.
 - surface loading 36
 - surface organometallic chemistry 160
 - surface oxygen
 - bridging bonded (BO) 28
 - terminal bonded (TO) 28
 - surface reaction 161
 - surface siloxane group 155
 - surface speciation/structure of the deposited precursor species 23 ff.
 - surface reaction 46
 - suspension
 - impregnating 27
 - synthesis
 - clear solution 256
 - confined space 264
 - ferrierite (FER) 261
 - hydrothermal 230
 - ionothermal synthesis method 267
 - ship-in-a-bottle 163
 - split-and-pool 221
 - surface-mediated 162
 - templated 262
 - water-free zeolite 263
- t**
- takovite $\text{Ni}_6\text{Al}_2(\text{OH})_{16}\text{CO}_3 \cdot 4\text{H}_2\text{O}$ 145
 - TEDDI method 206 ff.
 - temperature-programmed desorption (TPD) 156
 - temperature-programmed reduction (TPR) 339
 - template 262
 - templated synthesis 262
 - tertiary nonyl poly sulfide (TNPS) 323
 - tethering 167
 - tetraalkoxysilane 284
 - tetrachloroauric acid 370 f.
 - tetraethylorthosilicon (TEOS) 260, 281, 305
 - tetrakis(hydroxymethyl)phosphonium chloride (THPC) 381
 - tetramethylammonium (TMA) ion 249, 262
 - tetrapropylammonium (TPA) ion 249, 262
 - thermolysis 91
 - Thiele modulus 117
 - three plane model 21 ff.
 - Ti(III) deposition 129
 - Ti-MCM-41 288
 - selective oxidation of cyclohexene 288
 - Ti-SiO₂ catalyst 102

time-resolved spectroscopy 201
 titania 93, 386 f.
 titania surface 18
 transition-metal ionic species (TMIS)
 14, 22
 –ligand 22
 transition-state shape selectivity 250
 trialkoxyorganosilane 284
 triethanolamine (TEA) 359
 triple-layer model 21

u

urea hydrolysis 116
 urea method 120 f.
 UV-Vis-NIR DR microspectroscopy
 204

v

V_2O_5/SiO_2 129
 V_2O_5/TiO_2 194
 vapor-phase transport (VPT) 265
 viscosity 63
 volatile organic compound (VOC) 193

w

wafer-based preparation 223
 washcoating 194
 washing 89, 337

x

xerogel 83, 93 ff.
 –alumina 92
 –mixed-metal oxide 98
 –sol-gel entrapment 97
 –stabilization 90

X-ray fluorescence analysis (RFA)
 220

y

yttria 357 f.

z

zeolite 43 f., 161, 243 ff., 305
 –beta-type (BEA) 243, 259 ff.
 –catalyst 243 ff.
 –crystallization 255
 –dry gel route 265
 –growth 257
 –modification 244
 –nanocrystalline 264
 –pores beyond the 12-MR 267
 –protonic superacidity 246
 –shape selectivity 250
 –ship-in-a-bottle concept 163
 –silicate-based 246
 –solid solvent 254
 –synthesis 256, 268
 –water-free synthesis 263
 zeolitization 254
 –parameter 260
 zeozyme 165
 zeta potential (ζ -potential) 24
 –measurement 355
 zinc silicate 71
 Zn-malachite 336 f.
 $(Zn_{1-x}Cu_x)_5(OH)_6(CO_3)$ 335
 ZnO 330 f.
 ZnO/ Al_2O_3 346
 ZSM-4 261
 ZSM-5 243 ff., 257 ff.
 ZSM-22 244 ff.